Acoustic and elastic wave propagation in microstructured media with interfaces: homogenization, simulation and optimization

Marie Touboul

NNT/NL : 2021AIXM0437/026ED353

Aix-Marseille Université

École Doctorale 353 – Sciences pour l'Ingénieur : Mécanique, Physique, Micro et Nanoélectronique

Laboratoire de Mécanique et d'Acoustique

Thèse

présentée en vue de l'obtention du grade universitaire de docteur

Discipline : Sciences pour l'Ingénieur
Spécialité : Mécanique des Solides

par

Marie TOUBOUL

Acoustic and elastic wave propagation in microstructured media with interfaces: homogenization, simulation and optimization

Thèse soutenue le 13 octobre 2021 devant le jury composé de :

Claude BOUTIN	Professeur, ENTPE	Président / Rapporteur
Sonia FLISS	Professeur associée, ENSTA Paris	Rapporteure
Hélène BARUCQ	Directrice de Recherche, INRIA	Examinatrice
Richard CRASTER	Professeur, Imperial College London	Examinateur
Vincent PAGNEUX	Directeur de Recherche, CNRS	Examinateur
William PARNELL	Professeur, University of Manchester	Examinateur
Cédric BELLIS	Chargé de Recherche, CNRS	Directeur de thèse
Bruno LOMBARD	Directeur de Recherche, CNRS	Directeur de thèse

Je soussignée, Marie Touboul, déclare par la présente que le travail présenté dans ce manuscrit est mon propre travail, réalisé sous la direction scientifique de Bruno Lombard et Cédric Bellis, dans le respect des principes d'honnêteté, d'intégrité et de responsabilité inhérents à la mission de recherche. Les travaux de recherche et la rédaction de ce manuscrit ont été réalisés dans le respect à la fois de la charte nationale de déontologie des métiers de la recherche et de la charte d'Aix-Marseille Université relative à la lutte contre le plagiat.

Ce travail n'a pas été précédemment soumis en France ou à l'étranger dans une version identique ou similaire à un organisme examinateur.

Fait à Marseille le 29 juillet 2021

Abstract/Résumé

Acoustic and elastic wave propagation in microstructured media with interfaces: homogenization, simulation and optimization

■ *Abstract.* In this thesis, the focus is on wave propagation in periodic microstructured media in the presence of interfaces. The dynamic homogenization of these media and the design of the microstructures to achieve a given macroscopic effect are studied. In a first part, homogenization and optimization are carried out for thin microstructured layers. In a second part, the homogenization of periodic microstructures in all spatial dimensions is addressed.
The first part concerns the case where the heterogeneities constitute a periodic row of inclusions immersed in a homogeneous matrix. When the physical parameters of the inclusions are strongly contrasted with those of the matrix, internal resonances can occur and be used to maximise acoustic absorption. The homogenization of such a resonant microstructured layer is studied using a method of matched asymptotic expansions and leads to non-local jump conditions. The introduction of auxiliary variables allows to get a local evolution problem in time which is then solved numerically by an ADER scheme coupled with an immersed interface method. This methodology is validated (local truncation error analysis, comparison with analytical solutions) and makes possible wave diffraction simulations by resonant meta-interfaces. Finally, the sensitivity of the effective parameters to the geometry of the microstructure is determined using topological derivatives. We then implement a topological optimization procedure for the design of non-resonant thin microstructured layers.
On the other hand, it is often assumed that the contact between the inclusions and the homogeneous matrix is perfect. Some models, such as spring-mass conditions, account for the behaviour of imperfect contacts between solids. In the second part of the thesis, low-frequency volume homogenization of such configurations is carried out to obtain the expression of the homogenized fields at order 1, and an extension to non-linear contacts is presented. Finally, dispersion diagrams in 1D solids with spring-mass conditions are studied. The framework of high-frequency homogenization is used and an approximation of the fields to the leading order, as well as dispersion relations near the edges of the Brillouin zone is obtained.

Keywords : Homogenization in dynamics, Resonant effective interfaces, Immersed interface method, Auxiliary variables, Topological optimization, Imperfect interfaces.

Propagation d'ondes acoustiques et élastiques dans des milieux microstructurés avec interfaces : homogénéisation, simulation et optimisation

■ *Résumé.* Dans cette thèse, on s'intéresse à la propagation des ondes dans des milieux microstructurés périodiques en présence d'interfaces. On étudie l'homogénéisation en dynamique de ces milieux ainsi que le design des microstructures pour obtenir un effet macroscopique donné. Dans une première partie, l'homogénéisation et l'optimisation sont menées pour des couches minces microstructurées. Dans une seconde partie, on traite de l'homogénéisation de microstructures périodiques selon toutes les dimensions de l'espace.
La première partie concerne le cas où les hétérogénéités constituent une rangée périodique d'inclusions plongées dans une matrice homogène. Lorsque les paramètres physiques des inclusions sont fortement contrastés avec ceux de la matrice, des résonances internes peuvent se produire et être utilisées pour maximiser l'absorption acoustique. L'homogénéisation d'une telle couche microstructurée résonante est étudiée grâce à une méthode de développements asymptotiques

raccordés, et conduit à des conditions de saut non locales en temps. L'introduction de variables auxiliaires permet de se ramener à un problème d'évolution local en temps qui est ensuite résolu numériquement par un schéma ADER couplé à une méthode d'interface immergée. Cette méthodologie est validée (analyse d'erreur locale de troncature, comparaison à des solutions analytiques) et rend possible des simulations de diffraction d'ondes par des méta-interfaces résonantes. Enfin, la sensibilité des paramètres effectifs à la géométrie de la microstructure est déterminée à l'aide de dérivées topologiques. On met alors en œuvre une procédure d'optimisation topologique en vue du design de couches minces microstructurées non résonantes.
D'autre part, il est souvent supposé que le contact entre les inclusions et la matrice homogène est parfait. Certains modèles, par exemple les conditions masse-ressort, rendent compte du comportement des contacts imparfaits entre solides. Dans la deuxième partie de la thèse, l'homogénéisation volumique à basse fréquence de telles configurations est menée pour obtenir l'expression des champs homogénéisés à l'ordre 1, et une extension à des contacts non-linéaires est présentée. Enfin, on étudie les diagrammes de dispersion dans des solides 1D avec conditions de masse-ressort. On se place ainsi dans le cadre de l'homogénéisation haute fréquence et on obtient une approximation des champs à l'ordre dominant, ainsi que des relations de dispersion près des bords de la zone de Brillouin.

Mots-clés : Homogénéisation en dynamique, Interfaces effectives résonantes, Méthode d'interface immergée, Champs auxiliaires, Optimisation topologique, Interfaces imparfaites.

Acknowledgments

Déjà plus de trois ans que je suis arrivée au LMA pour mon stage de fin d'étude ainsi que la thèse qui y a suivi ! A ce titre, j'aimerais remercier tout le personnel du LMA pour leur accueil et leur contribution à mon intégration. Un grand merci également à tous ceux qui ont collaboré à ce travail en dehors des murs du LMA. En particulier, un grand merci à Raphael Assier pour son implication, son accueil lors de mon séjour à Manchester et ses nombreux conseils pour la suite.

Je tiens également à remercier Claude Boutin d'avoir accepté le double rôle de président du jury et de rapporteur, ainsi que Sonia Fliss d'avoir accepté de rapporter mon manuscrit. Enfin, merci aux examinateurs Hélène Barucq, Richard Craster, William Parnell et Vincent Pagneux pour votre intérêt et vos questions lors de la soutenance.

Évidemment, un grand merci à mes directeurs de thèse, Cédric Bellis et Bruno Lombard pour ces trois années. Merci pour votre implication remarquable : je m'estime très chanceuse d'avoir eu la chance d'évoluer à vos côtés pendant cette thèse ! Grâce à vous, j'ai énormément appris à la fois sur un plan scientifique mais également humain, voire même sportif entre les conseils de Bruno et les itinéraires de randonnée de Cédric. Ces trois années ont été faites de plusieurs belles rencontres dont vous faites indéniablement partie ! Bruno, ou plutôt maître pâtissier, je me souviendrai particulièrement de tes nombreux conseils mais aussi de ton humour avec la boule bleue, la boule verte et leurs amis, ainsi que le chef-d'oeuvre sur le tableau de ton bureau. Cédric, merci pour ton écoute et ta bienveillance qui m'ont particulièrement touchée à de nombreuses reprises.

Une mention particulière pour les doctorants et post-doctorants que j'ai rencontrés lors de ces trois ans : l'agent Rando Polish Man Tic Prof Padawan 1310 et Youyou fidèles compagnons de randonnée, Rémi qui m'a supportée comme co-bureau pendant deux ans, Patryk avec ses post-it verts et son fameux chocolat pour lutter contre le stress, Harold et tes conseils de grand frère de thèse, mais aussi Christelle, Daria, Ana, Martin, Louis, Augustin... pour votre écoute, vos conseils et toutes ces pauses, afterworks, courses, randonnées,.. partagés !

Merci à mes amis avec qui j'ai passé de merveilleux moments au cours de ces années et qui ont su être présents et à l'écoute ! Petite mention spéciale à certains en particulier. J'ai été ravie de vous retrouver Ornina et Sophie après toutes ces années, ainsi que Sarah à chacun de tes rapides retours depuis l'Angleterre. Merci Thibaud et Eléonore pour vos nombreux encouragements et votre présence tout le long de ma soutenance ! Je mentionnerai évidemment notre groupe d'ENSTA et tout particulièrement le quatuor de choc JMCA (Julianie-Marie-Claire-Alix) qui a su résister à la distance Paris-Marseille et saura, j'en suis sûre, traverser les années.

Enfin, merci à ma famille, surtout à mes parents, pour votre soutien et vos encouragements depuis toujours et surtout durant ces derniers mois de thèse. Et merci Anthony pour ton optimisme sans faille, et ta patience que j'ai sûrement mise à rude épreuve ces derniers temps !

Contents

CHAPTER 1

Introduction

1.1 Context

The design of composite media allows to control wave propagation in a fine way and leads to exotic effects that cannot be found in nature e.g. negative refraction, subwavelength imaging, lensing and cloaking, noise and vibration control, to cite a few. It constitutes the paradigm of metamaterials, which have undergone spectacular developments since the early 2000's, see Deymier, 2012; Craster and Guenneau, 2013 and references therein for an overview. They are most often constructed by repeating periodically a unit cell.

When the periodicity is of the same order of magnitude than the characteristic wavelength, it results in a structure of *crystal* type and this is known as the area of *phononic metamaterials*. These materials present exotic behaviours due to Bragg scattering mechanism, the scattering of waves by a periodic arrangement of scatterers of dimensions comparable to the wavelength. An example is the sculpture described in Martinez-Sala et al., 1995, see Figure 1.1. It is a two-dimensional periodic arrangement of steel tubes. They behave as scatterers for soundwaves and their periodic arrangement leads to destructive interferences at some frequencies. Consequently, the amplitude of transmitted waves is highly attenuated at these frequencies. The sculpture exhibits band gaps, i.e. spectral bands where propagation of waves is forbidden. One drawback of the phononic crystals is that their period is of order of magnitude of the wavelength associated with the first band gap. For example, in the context of low-frequency sound reduction, a sound attenuation for frequencies ranging from 10 Hz to 10 KHz would requiere a structure of a few meters to ensure band gaps in this regime.

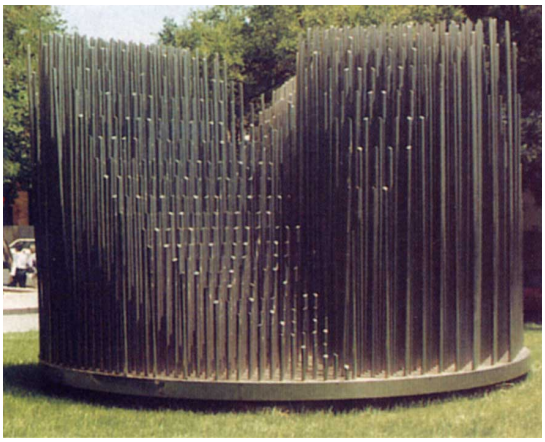

Figure 1.1 – Eusebio Sempere's sculpture in Madrid (after Martinez-Sala et al., 1995).

This motivates the use of another type of metamaterials: the *locally resonant* metamaterials. These ones can also exhibit spectral gaps and particular behavior but at frequencies well below those of Bragg scattering. The resonant structure is then characterized by a *subwavelength* unit cell. In elasticity, an example is given by Liu, 2000 with a heavy material coated with a soft one and embedded in a hard matrix, see Figure 1.2. A structure of some centimeters size then allows gaps at low frequency.

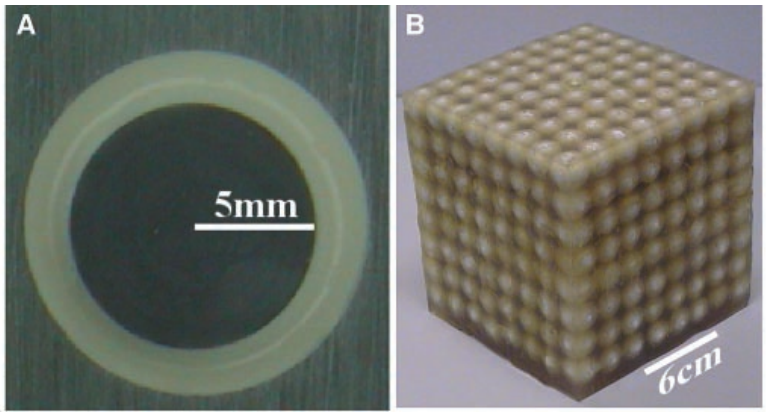

Figure 1.2 – (a) Basic unit cell and (b) resulting structure (after Liu, 2000)

The materials being structured at subwavelength lengthscales, they can be seen as a homogeneous medium described by effective parameters. Then, it turns out that the band gaps can be interpreted in terms of negative effective parameters (the mass density in elasticity, the permeability in electromagnetism). These locally resonant metamaterials have been studied for various applications: design of a perfect lense that allows to focus all Fourier components of an image so that the sharpness of the image is not limited anymore (Pendry, 2000), optical cloaking (Cai, Chettiar, Kildishev, & Shalaev, 2007), maximisation of sound absorption (Ma, Yang, Xiao, Yang, & Sheng, 2014; Schwan, Umnova, & Boutin, 2017; Huang et al., 2019; Maurel, Mercier, Pham, Marigo, & Ourir, 2019a), mitigation of waves (Su, Lu, & Norris, 2018), seismic shields (Colombi, Roux, Guenneau, Gueguen, & Craster, 2016; Palermo, Vitali, & Marzani, 2018; Zaccherini et al., 2019), etc.

Consequently, the interest for modeling microstructured media, performing numerical simulations and designing microstructures has increased. Thanks to *homogenization* methods, the

microstructure can be advantageously replaced, at the macro-scale, by a homogeneous effective medium. From a numerical point of view, it avoids having to mesh fine spatial scales and thus leads to enormous computational gains compared with full-field simulations. It is also a way to obtain analytically some information (e.g. expression of the macroscopic field, of the scattering coefficients, or dependance of the wave behaviour on the constitutive parameters or geometry) in an explicit way since the effective medium obtained is homogeneous. Once these microstructured media are modelled thanks to homogenization methods, it raises the question of mathematical tools that can aid to design the microstructures in order to achieve a desired macroscopic effect. On the one hand, when the geometry of the microstructure is imposed (periodic arrangement of circles, rectangles,...), one aims at optimizing the physical or geometric parameters. On the other hand, when the metamaterial is designed only from selected constitutive materials with no requirement on the geometry, *topological optimization* is deployed to determine the material distribution within the unit cell.

In this context, this thesis has focused on different aspects of homogenization (obtaining effective media in different physical configurations, optimization of microstructures) and has required the development of a numerical method to handle the resonant behaviour in the presence of interfaces. Consequently, the next two sections give an overview of the usual homogenization and numerical techniques in this context, with a more detailed description of the results to be used in the rest of the dissertation.

1.2 Homogenization

1.2.1 Classical techniques

Homogenization is an up-scaling technique that allows to replace the microscopic description of a given microstructured medium by a macroscopic model endowed with effective parameters. The different homogenization methods can then be divided into analytical and computational categories (Geers, Kouznetsova, & Brekelmans, 2010).

Among the analytical methods, the asymptotic homogenization (Sánchez-Palencia, 1980; Bensoussan, Lions, & Papanicolaou, 2011), which we use here, has been extensively used for periodic microstructures. The effective homogeneous medium is obtained for a periodicity $h > 0$ of the structure that tends to 0. The simplest problem is the classical elliptic equation in $\Omega \subset \mathbb{R}^d$

$$-\operatorname{div}(\boldsymbol{A}_h(\boldsymbol{X})\boldsymbol{\nabla} u_h)(\boldsymbol{X}) = f(\boldsymbol{X}) \text{ in } \Omega, \tag{1.1}$$

with $\boldsymbol{A}_h : \mathbb{R}^d \mapsto \mathbb{R}^d$ being uniformly bounded and h-periodic, and some boundary conditions to be considered. One introduces the unit cell $\mathcal{Y} = (0,1)^d$ which is reproduced periodically. Then one writes $\boldsymbol{A}_h(\boldsymbol{X}) = \boldsymbol{A}(\boldsymbol{X}/h)$ such that the elliptic equation can be recast as

$$-\operatorname{div}(\boldsymbol{A}(\boldsymbol{X}/h)\boldsymbol{\nabla} u_h)(\boldsymbol{X}) = f(\boldsymbol{X}) \text{ in } \Omega. \tag{1.2}$$

The aim of homogenization is to study the limit of $(u_h)_h$ as h tends to zero. This is obtained assuming scale seperation, i.e. that $\boldsymbol{X}$ and $\boldsymbol{Y} = \boldsymbol{X}/h$ are two independant variables. They account for the slow continuous variations and the small-scale fast variations of the fields, respectively. Then, the following two-scale expansion ansatz is written

$$u_h(\boldsymbol{X}) = u_0(\boldsymbol{X}, \boldsymbol{X}/h) + h u_1(\boldsymbol{X}, \boldsymbol{X}/h) + h^2 u_2(\boldsymbol{X}, \boldsymbol{X}/h) + \cdots \tag{1.3}$$

where the functions $u_i(\boldsymbol{X}, \boldsymbol{Y})$ are assumed to be periodic with respect to the second variable. Assuming that f does not scale in h, an identification order by order leads to the homogenized problem

$$\begin{cases} u_0(\boldsymbol{X}, \boldsymbol{Y}) = u_0(\boldsymbol{X}) \\ -\operatorname{div}(\boldsymbol{A}_{\text{eff}}\boldsymbol{\nabla} u_0)(\boldsymbol{X}) = f(\boldsymbol{X}) \text{ in } \Omega, \end{cases} \tag{1.4}$$

where the homogenized tensor A_{eff} does not depend on $\boldsymbol{X}$. It only depends on the cell distribution, the material properties and the determination of the periodic solutions Ψ_j, $j = 1, \cdots, d$, to the cell problems

$$-\operatorname{div}(\boldsymbol{A}(\boldsymbol{Y})(\boldsymbol{\nabla}_{\boldsymbol{Y}}\Psi_j + \boldsymbol{e}_j))(\boldsymbol{Y}) = 0 \text{ in } \mathcal{Y} \tag{1.5}$$

in the unit cell. Once u_0 is computed, these cell problems also allow to get the first-order corrector term u_1 as

$$u_1(\boldsymbol{X}, \boldsymbol{Y}) = \sum_{j=1}^{d} \frac{\partial u_0}{\partial X_j}(\boldsymbol{X})\Psi_j(\boldsymbol{Y}). \tag{1.6}$$

One notes that this method is heuristic since the ansatz (1.3) is postulated. The convergence can then be proved using two-scale convergence (Nguetseng, 1989; Allaire, 1992) or Γ-convergence (Dal Maso, 2012).

This multiscale expansion method has also been used to study problems in dynamics. Then, in the so-called *low-frequency / long-wavelength* framework, the small parameter that tends to zero is the ratio between the characteristic size of the microstructure and a typical wavelength. This is illustrated by Figure 1.3 in a 2D setting where Ω is made of the periodic repetition of inclusions Ω_i embedded in a homogeneous matrix Ω_m.

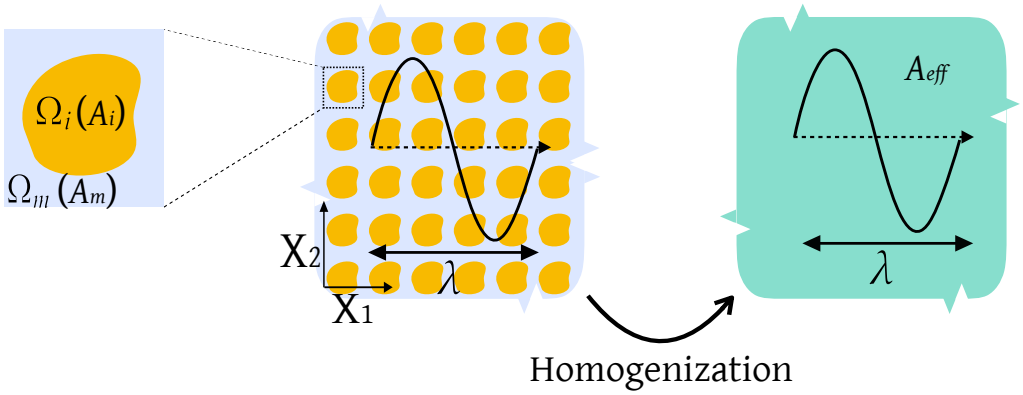

Figure 1.3 – Homogenization process for a 2D periodic medium. *(left)* Original configuration with zoom on a unit cell, *(right)* Homogenized model.

Other analytical methods can be mentioned: for example, the *Willis* approach is based on variational principles. First developped in statics (Hashin & Shtrikman, 1963; Willis, 1977), it has then been adapted to dynamic problems (Willis, 1981; Willis, 2011; Nassar, He, & Auffray, 2015) for random microstructures.

This thesis makes use of *two-scale asymptotic expansions* in different frameworks: the classical low-frequency regime for periodic microstructures, but also the homogenization and optimization of thin microstructured layers. The high-frequency homogenization is also used for media with imperfect contacts. Consequently more details are given in the three next subsections about the state of art and the main ideas of the homogenization in these three contexts.

1.2.2 Homogenization of thin microstructured layers

An active direction of research concerns the size reduction of microstructures. It is often advantageous to replace a volume microstructure by a surface (in 3D) or a line (in 2D) one. This is the idea of metasurfaces or meta-interfaces that are more compact and less lossy than their bulk counterparts. Different metasurfaces and their exotic behaviour have been devised in acoustics: tapered labyrinthine unit cells (Xie et al., 2014) allow wavefront modulation, conversion from bulk

waves to surface waves, beam-steering and effective negative refraction; perfect absorption can be reached thanks to a membrane in the unit cell (Ma et al., 2014; Yang, Ma, Yang, & Sheng, 2015). Sound absorption can also be maximized thanks to an array of resonators (Schwan et al., 2017) or of porous layers of resonant inclusions (Lagarrigue, Groby, Tournat, Dazel, & Umnova, 2013). In elasticity, source illusion using space-coiling metasurfaces (Liu et al., 2017) is also possible as well as the use of torus-like tapers for the design of acoustic metasurfaces to control elastic guided waves (Zhu & Semperlotti, 2016). The periodic repetition of supercells made by several different unit cells allows to reach wave trapping in an elastic waveguide and wave focusing in a semi-infinite medium (Ahn, Lee, Lee, & Kim, 2019). One can also mention Su and Norris, 2016; Su et al., 2018 where the metasurface is an array of uniform parallel plate separated by equally spaced rectangular cracks and is designed to focus SV-waves while remaining transparent for P-waves, see Figure 1.4. This section therefore focuses on the homogenization of thin microstructured layers.

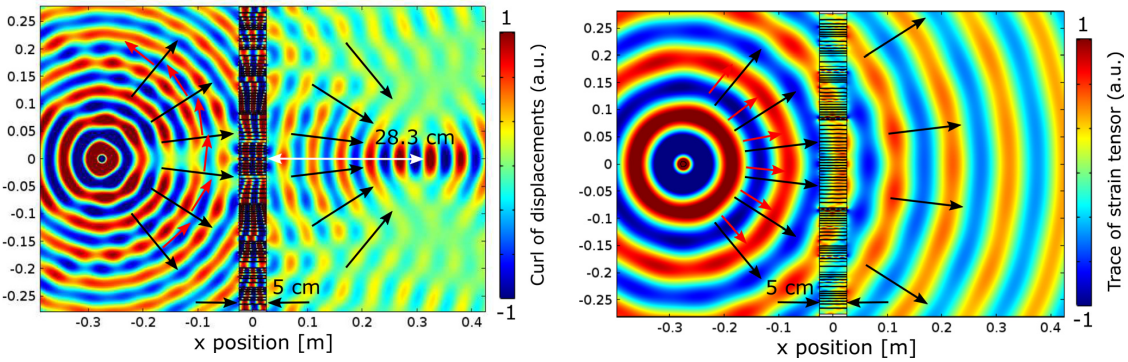

(a) Focusing a cylindrical SV-wave source

(b) Cylindrical P-wave incidence

Figure 1.4 – Simulations of Su, Lu, and Norris, 2018.

1.2.2.1 Previous works

The two-scale homogenization method is a privileged tool to simulate wave propagation in bulk microstructured media (Sanchez-Hubert & Sanchez-Palencia, 1992; Bensoussan et al., 2011). However, the usual homogenization methods used for volumic microstructures fail when considering a thin row of scatterers (Lapine, McPhedran, & Poulton, 2016; Marigo & Maurel, 2016a; Marigo & Maurel, 2017b): the behaviour of the fields is dominated by boundary layer effects which are not taken into account by bulk effective medium theories. To recover their efficiency, these methods must then be combined with matched-asymptotic expansions, yielding effective jump conditions on an equivalent meta-interface.

These methods have been used in static elasticity (Marigo & Pideri, 2011; David, Pideri, & Marigo, 2012). For wave propagation, they have been adapted in acoustics (Bonnet-Bendhia, Drissi, & Gmati, 2004; Marigo & Maurel, 2016a; Marigo & Maurel, 2017b), and electromagnetism (Delourme, Haddar, & Joly, 2012; Delourme, Haddar, & Joly, 2013; Ourir, Gao, Maurel, & Marigo, 2017). For wave propagation in elasticity, studies focused on rows of non-resonant inclusions (Marigo, Maurel, Pham, & Sbitti, 2017a; Pham, Maurel, & Marigo, 2021) and then on resonant inclusions (Pham, Maurel, & Marigo, 2017). One also notes that similar methods can also be used to get effective jump conditions for stratified media (Marigo & Maurel, 2017c), metallic structures (Marigo & Maurel, 2016b; Maurel, Marigo, & Ourir, 2016), Helmholtz resonators (Mercier, Marigo, & Maurel, 2017; Maurel, Marigo, Mercier, & Pham, 2018), bubble screens (Pham, Mercier, Fuster, Marigo, & Maurel, 2020), adhesive layers (Abdelmoula, Coutris, & Marigo, 1998; Burel, 2014; Rizzoni, Dumont, Lebon, & Sacco, 2014; Rizzoni, Dumont, & Lebon, 2017) and for the latter

the results are equivalent to those obtained with energy-based methods (Lebon & Rizzoni, 2011; Dumont, Rizzoni, Lebon, & Sacco, 2018; Lebon & Rizzoni, 2018). The case of non-periodic layers has also been studied for seismic waves (Capdeville & Marigo, 2012).

The first part of this thesis extensively uses the results of (Marigo et al., 2017a; Pham et al., 2017), i.e. the results concerning the homogenization of a thin microstructured layer in the time domain, and of a thin resonant microstructured layer in the frequency-domain, respectively. Consequently, the Sections 1.2.2.2, 1.2.2.3, and 1.2.2.4 expose the framework and results of these papers that will be used afterwards.

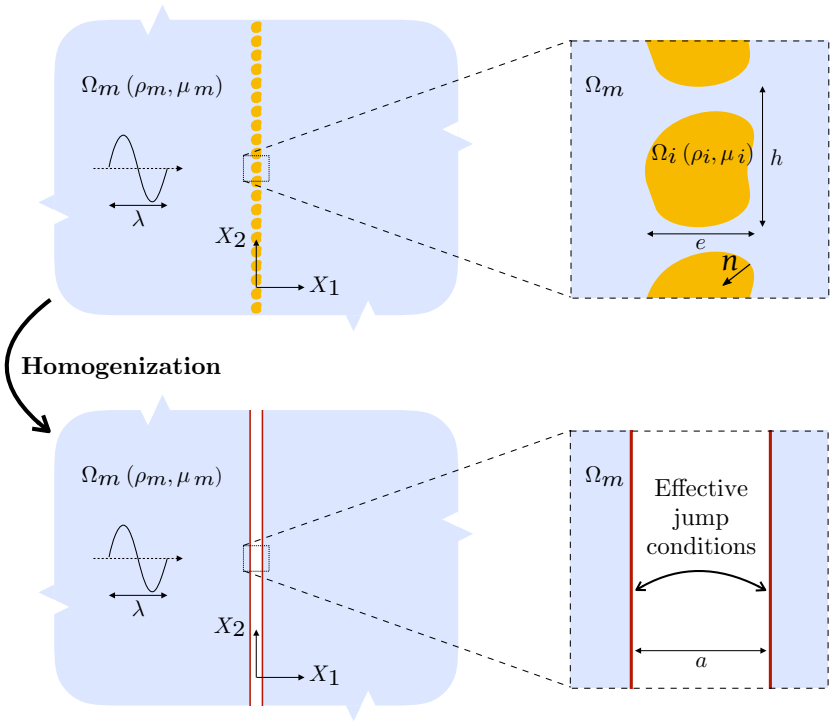

Figure 1.5 – Homogenization process for a single periodic array of inclusions. *(top)* Original configuration with a thin microstructured layer, *(bottom)* Homogenized interface model.

1.2.2.2 Physical configuration

Let us consider the propagation of *scalar* waves in 2D across a periodic row of inclusions $\cup_i \Omega_i$ embedded within a homogeneous matrix Ω_m, with both media being assumed to be isotropic. The thickness and the period of the row are denoted by e and h, respectively, and we assume that $e = O(h)$. The time and the spatial coordinates are denoted by t and $\boldsymbol{X} = (X_1, X_2)$, respectively, with X_2 being the direction of periodicity of the inclusions as shown in Figure 1.5. The microstructured medium is characterized by two constitutive parameters, the mass density ρ_h and the shear modulus μ_h, that are piecewise constant:

$$(\rho_h, \mu_h)(\boldsymbol{X}) = \begin{cases} (\rho_m, \mu_m) & \text{in the matrix,} \\ (\rho_i, \mu_i) & \text{in the inclusions.} \end{cases}$$

The problem is considered within the framework of the linear anti-plane elasticity model. The time-domain governing equation for the scalar out-of-plane displacement U_h writes:

$$\operatorname{div}\left(\mu_h(\boldsymbol{X})\boldsymbol{\nabla} U_h(\boldsymbol{X}, t)\right) = \rho_h(\boldsymbol{X})\frac{\partial^2 U_h}{\partial t^2}(\boldsymbol{X}, t).$$

Introducing the scalar velocity field $V_h = \partial U_h/\partial t$, this system can be rewritten as a first-order system in time for V_h and for the stress vector $\boldsymbol{\Sigma}_h = (\Sigma_{1h}, \Sigma_{2h})^T$:

$$\begin{cases} \dfrac{\partial \boldsymbol{\Sigma}_h}{\partial t}(\boldsymbol{X}, t) = \mu_h(\boldsymbol{X}) \boldsymbol{\nabla} V_h(\boldsymbol{X}, t), \\ \rho_h(\boldsymbol{X}) \dfrac{\partial V_h}{\partial t}(\boldsymbol{X}, t) = \boldsymbol{\nabla} \cdot \boldsymbol{\Sigma}_h(\boldsymbol{X}, t), \end{cases} \tag{1.7}$$

with V_h and $\boldsymbol{\Sigma}_h \cdot \boldsymbol{n}$ being continuous at each matrix/inclusion interface $\partial\Omega_i$, given that $\boldsymbol{n}$ is the *inward* unit normal on each $\partial\Omega_i$. The system (1.7) is also relevant to other physical phenomena, such as acoustic waves for which the fields $\boldsymbol{\Sigma}_h$, V_h, ρ_h and $1/\mu_h$ would stand instead for velocity, pressure, compressibility and mass density, respectively.

1.2.2.3 Homogenization in the non-resonant case

In this subsection, one is interested in the *non-resonant* case i.e. when the physical parameters are comparable. One first reminds the assumptions of the homogenization process and then the main steps and the results obtained in Marigo et al., 2017a.

■ *Hypotheses of the homogenization process.* Considering an illumination by an incident wave or external sources, a characteristic wavelength λ within the matrix is assumed to be much larger than the period h. Defining the wavenumber within the matrix as $k_m = 2\pi/\lambda$, we introduce the parameter

$$\eta = k_m h \tag{1.8}$$

and we assume that $\eta \ll 1$ for the configurations of interest. This geometrical assumption allows to homogenize the microstructure in the so-called long-wavelength regime.

Assumption 1.1

The configuration satisfies $\eta = k_m h \ll 1$ while $\rho_i/\rho_m = O(1)$ and $\mu_i/\mu_m = O(1)$.

■ *Main steps.* Two-scale homogenization techniques and matched-asymptotic expansions are applied to the microstructured problem defined above. They involve five steps:

1. two space coordinates are introduced to describe both the slow variations and the small-scale fast variations of the fields;
2. the fields are expanded using the ansatz of a two-scale asymptotic expansion;
3. matching conditions between the far field in the outer region and the near field in the inner region are formulated in an intermediate region close to the inclusions, see Figure 1.6;
4. an identification order by order provides the jump conditions for the effective fields up to $O(\eta^2)$;
5. the interface of zero thickness on which the jump conditions apply is then replaced by an equivalent enlarged interface of thickness $a = O(h)$, as sketched in Figure 1.5. This enlargement is needed for the final effective model to be stable.

■ *Notations.* The fast scale of coordinates is $\boldsymbol{y} = \boldsymbol{X}/h = (y_1, y_2)^\top$. The domain Ω is the elementary cell $\mathbb{R} \times [-1/2, 1/2]$ in $\boldsymbol{y}$-coordinates that contains one single inclusion Ω_i, and $(\boldsymbol{e}_1, \boldsymbol{e}_2)$ is the canonical basis of $\mathbb{R}^2$. For any function $f(x_1)$, we define the jump and the mean value around the (centered) enlarged interface of thickness a:

$$[\![f]\!]_a = f(a/2) - f(-a/2) \qquad \text{and} \qquad \langle\!\langle f \rangle\!\rangle_a = \frac{1}{2}\big(f(a/2) + f(-a/2)\big). \tag{1.9}$$

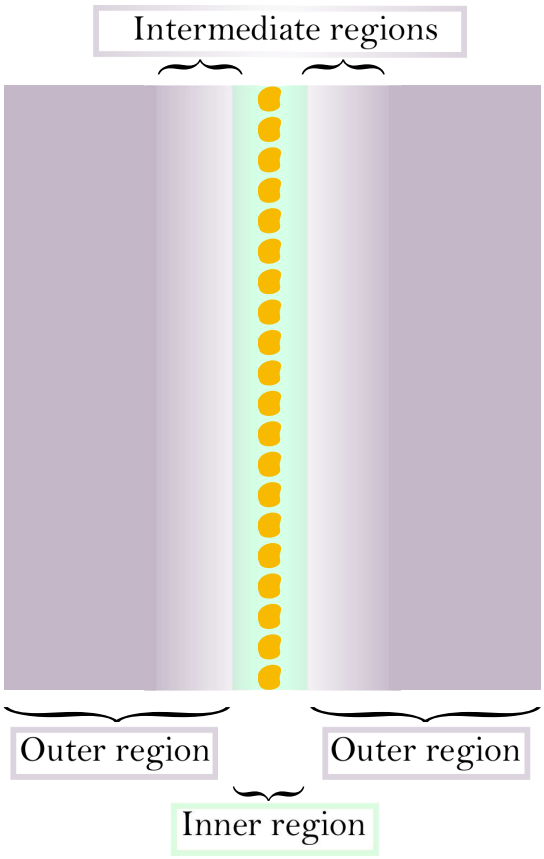

Figure 1.6 – Inner, outer and intermediate regions.

■ *Cell problems.* The homogenization process requires the computation of the fields $\Phi^{(j)}$ for $j = 1, 2$ which are y_2-periodic and solutions of the following cell problems:

$$\begin{cases} \nabla_{\boldsymbol{y}} \cdot \left(\mu(\boldsymbol{y}) \left(\nabla_{\boldsymbol{y}} \Phi^{(j)}(\boldsymbol{y}) + \boldsymbol{e}_j \right) \right) = 0 \text{ in } \Omega, \\ \mu(\boldsymbol{y}) [\nabla_{\boldsymbol{y}} \Phi^{(j)}(\boldsymbol{y}) + \boldsymbol{e}_j] \cdot \boldsymbol{n} \text{ and } \Phi^{(j)} \text{ continuous on } \partial\Omega_i, \\ \lim\limits_{y_1 \to \pm\infty} \nabla_{\boldsymbol{y}} \Phi^{(j)}(y_1, y_2) = \boldsymbol{0}. \end{cases} \tag{1.10}$$

Consequently, $\Phi^{(j)} \in L^2_{\text{loc}}(\Omega)$ and $\nabla\Phi^{(j)} \in L^2(\Omega)$, which allows the definition of the following constants for $j = 1, 2$:

$$\begin{cases} \mathcal{B}_j = \lim\limits_{y_1 \to +\infty} \left[\Phi^{(j)}(y_1, y_2) - \Phi^{(j)}(-y_1, y_2) \right], \\ C_j = \displaystyle\int_\Omega \frac{\mu(\boldsymbol{y})}{\mu_m} \frac{\partial \Phi^{(j)}}{\partial y_2}(\boldsymbol{y}) \, \mathrm{d}\boldsymbol{y}. \end{cases} \tag{1.11}$$

Furthermore, one can notice that $\Phi^{(j)}$ is defined up to a constant, which will not be a problem since the quantities of interest are the constants defined in (4.2).

■ *Final homogenized model.* From Marigo et al., 2017a, we know that the homogenization at order $O(\eta)$ of such a configuration yields the following homogenized model:

Jump conditions 1.1: Non-resonant case

$$\begin{cases} \dfrac{\partial \boldsymbol{\Sigma}}{\partial t} = \mu_m \boldsymbol{\nabla} V & (|X_1| \geq a/2,\ X_2 \in \mathbb{R}), \\ \rho_m \dfrac{\partial V}{\partial t} = \boldsymbol{\nabla} \cdot \boldsymbol{\Sigma} & (|X_1| \geq a/2,\ X_2 \in \mathbb{R}), \\ [\![V]\!]_a = h \left\{ \mathcal{B} \left\langle\!\!\left\langle \dfrac{\partial V}{\partial X_1} \right\rangle\!\!\right\rangle_a + \mathcal{B}_2 \left\langle\!\!\left\langle \dfrac{\partial V}{\partial X_2} \right\rangle\!\!\right\rangle_a \right\} & (X_2 \in \mathbb{R}), \\ [\![\Sigma_1]\!]_a = h \left\{ \mathcal{S} \langle\!\langle \operatorname{div} \boldsymbol{\Sigma} \rangle\!\rangle_a - C_1 \left\langle\!\!\left\langle \dfrac{\partial \Sigma_1}{\partial X_2} \right\rangle\!\!\right\rangle_a - C \left\langle\!\!\left\langle \dfrac{\partial \Sigma_2}{\partial X_2} \right\rangle\!\!\right\rangle_a \right\} & (X_2 \in \mathbb{R}). \end{cases} \tag{1.12}$$

with the effective parameters being defined as

$$\begin{cases} \mathcal{B} = \dfrac{a}{h} + \mathcal{B}_1, \\ C = \dfrac{a}{h} + \left(\dfrac{\mu_i}{\mu_m} - 1 \right) \displaystyle\int_{\Omega_i} \mathrm{d}\boldsymbol{y} + C_2, \\ \mathcal{S} = \dfrac{a}{h} + \left(\dfrac{\rho_i}{\rho_m} - 1 \right) \displaystyle\int_{\Omega_i} \mathrm{d}\boldsymbol{y}. \end{cases} \tag{1.13}$$

1.2.2.4 Homogenization in the resonant case

As already discussed, interesting effects can be achieved when local resonances occur within the microstructure and subwavelength design of metamaterials are then possible. In electromagnetism, they yield doubly negative metamaterials on a range of frequencies, paving the way to negative refraction (see Chapter 1-4 in Craster and Guenneau, 2013). In elasticity, the resonances are exploited to maximise sound absorption (Ma et al., 2014; Schwan et al., 2017; Huang et al., 2019; Maurel et al., 2019a) or to mitigate waves (Su et al., 2018). They can help to the design of vibration suppression bands (D'Alessandro et al., 2017; Xu, Barnhart, Li, Chen, & Huang, 2019) or of seismic shields (Colombi et al., 2016; Palermo et al., 2018; Zaccherini et al., 2019) as illustrated in Figure 1.7.

These resonances can be induced by particular geometries (e.g. split ring resonators, Helmholtz resonators) or by a large contrast of physical parameters (e.g. hard inclusions with a soft coating embedded in a hard matrix, soft inclusions in stiff matrix). The latter case is considered here with a unit cell made of a soft inclusion embedded in a hard matrix with a high contrast in the physical parameters. In this case, the resonances are of the so-called Mie type and occur at frequencies associated to wavelengths which are about the size of the inclusion and much smaller than the wavelength in the matrix.

More precisely, when $\rho_i/\rho_m = O(1)$ and $\mu_i/\mu_m = O(\eta^2)$, then the inclusion is the seat of local resonances. When the microstructure occupies the whole space, this resonant configuration has been studied in Auriault and Bonnet, 1985; Zhikov, 2000; Felbacq and Bouchitté, 2005; Zhikov, 2005; Auriault and Boutin, 2012; Bouchitté, Bourel, and Felbacq, 2015; Comi and Marigo, 2019. The transmission problem between a highly contrasted microstructure and a homogeneous half-plane has been tackled in Vinoles, 2016. When the microstructure is localized in a single thin row, this additional scaling in the shear modulus leads to new effective jump conditions that have been derived in the frequency domain in Pham et al., 2017. They are presented in this subsection.

First, the Fourier transform in time of a function $g(t)$ is defined by:

$$\mathscr{F}[g](\omega) = \hat{g}(\omega) = \int_{\mathbb{R}} g(t) e^{-i\omega t} \, \mathrm{d}t, \tag{1.14}$$

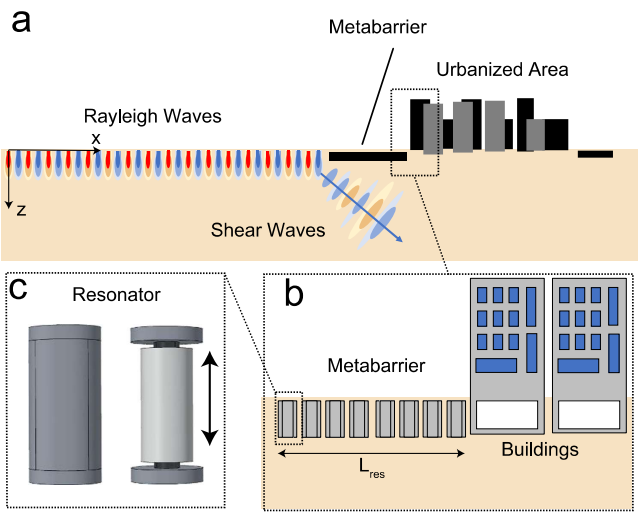

Figure 1.7 – (a) Surface to shear waves conversion - (b) Zoom on the metabarrier - (c) Zoom on one resonator (after Palermo, Vitali, and Marzani, 2018)

where ω is the angular frequency.

■ *Hypotheses of the homogenization process.* Secondly, the assumptions of the resonant case are recalled.

Assumption 1.2

The configuration satisfies $\eta = k_m h \ll 1$ while $\rho_i/\rho_m = O(1)$ and $\mu_i/\mu_m = O(\eta^2)$.

■ *Methodology.* As in the non-resonant case, the jump conditions are derived thanks to matched asymptotic expansions. The main lines of the methodology are unchanged.

■ *Cell problems.* However, the occurence of resonances leads to a slight modification of the cell problems. Indeed, instead of (1.10), for $j = 1, 2$ the fields $\Phi^{(j)}$ are now y_2-periodic and solutions of:

$$\begin{cases} \Delta_{\boldsymbol{y}} \Phi^{(j)}(\boldsymbol{y}) = 0 & \text{in } \Omega \backslash \Omega_i, \\ [\nabla_{\boldsymbol{y}} \Phi^{(j)}(\boldsymbol{y}) + \boldsymbol{e}_j] \cdot \boldsymbol{n} = 0 & \text{on } \partial\Omega_i, \\ \lim\limits_{y_1 \to \pm\infty} \nabla_{\boldsymbol{y}} \Phi^{(j)}(y_1, y_2) = \boldsymbol{0}. \end{cases} \tag{1.15}$$

As in the non-resonant case, it allows to introduce the following constants for $j = 1, 2$:

$$\begin{cases} \mathcal{B}_j = \lim\limits_{y_1 \to +\infty} \left[\Phi^{(j)}(y_1, y_2) - \Phi^{(j)}(-y_1, y_2) \right], \\ C_j = -\int_{\Omega \backslash \Omega_i} \dfrac{\partial \Phi^{(j)}}{\partial y_2}(\boldsymbol{y}) \, \mathrm{d}\boldsymbol{y}. \end{cases} \tag{1.16}$$

■ *Elementary problem.* Moreover, in the resonant case, the homogenized model also involves the following Dirichlet problem:

$$\begin{cases} \Delta_{\boldsymbol{y}} \psi_\infty(\boldsymbol{y}, \omega) + \kappa_\infty^2(\omega) \, \psi_\infty(\boldsymbol{y}, \omega) = 0 & (\boldsymbol{y} \in \Omega_i), \\ \psi_\infty(\boldsymbol{y}, \omega) = 1 & (\boldsymbol{y} \in \partial\Omega_i), \end{cases} \tag{1.17}$$

with

$$\kappa_\infty^2(\omega) = \frac{\rho_i h^2}{\mu_i}\,\omega^2. \tag{1.18}$$

Remark 1. *The notation ∞ for ψ_∞ or κ_∞^2, stands for the fact that the inviscid case is considered and the dissipation parameter γ that will be introduced later on then equals to $+\infty$.*

■ *Final homogenized model.* The resulting jump conditions on the enlarged interface are

Jump conditions 1.2: Resonant case

$$\begin{cases} \left[\!\left[\hat{V}\right]\!\right]_a = h\left\{\mathcal{B}\left\langle\!\left\langle\dfrac{\partial \hat{V}}{\partial X_1}\right\rangle\!\right\rangle_a + \mathcal{B}_2\left\langle\!\left\langle\dfrac{\partial \hat{V}}{\partial X_2}\right\rangle\!\right\rangle_a\right\} & (X_2 \in \mathbb{R}) \\ \left[\!\left[\hat{\Sigma}_1\right]\!\right]_a = h\left\{\mathcal{S}\left\langle\!\left\langle\dfrac{\partial \hat{\Sigma}_1}{\partial X_1}\right\rangle\!\right\rangle_a + C_1\left\langle\!\left\langle\dfrac{\partial \hat{\Sigma}_1}{\partial X_2}\right\rangle\!\right\rangle_a + C_2\left\langle\!\left\langle\dfrac{\partial \hat{\Sigma}_2}{\partial X_2}\right\rangle\!\right\rangle_a + \mathscr{D}_\infty(\omega)\left\langle\!\left\langle \operatorname{div}\hat{\boldsymbol{\Sigma}}\right\rangle\!\right\rangle_a\right\} & (X_2 \in \mathbb{R}), \end{cases} \tag{1.19}$$

with the constant effective parameters defined by (1.16) and

$$\begin{cases} \mathcal{B} = \dfrac{a}{h} + \mathcal{B}_1, \\ \mathcal{S} = \dfrac{a}{h} - \displaystyle\int_{\Omega_i} \mathrm{d}\boldsymbol{y}. \end{cases} \tag{1.20}$$

The frequency-dependent coefficient $\mathscr{D}_\infty(\omega)$ is defined by

$$\mathscr{D}_\infty(\omega) = \frac{\rho_i}{\rho_m}\int_{\Omega_i} \psi_\infty(\boldsymbol{y},\omega)\,\mathrm{d}\boldsymbol{y}. \tag{1.21}$$

The explicit dependency of $\mathscr{D}_\infty$ on the frequency is reached through a modal expansion of ψ_∞ on the basis of the eigensystems $(\lambda_r, P_r)_{r\geq 1}$ that is associated with the following self-adjoint eigenvalue problem posed on a single inclusion:

$$\begin{cases} \Delta_{\boldsymbol{y}} P_r(\boldsymbol{y}) + \lambda_r P_r(\boldsymbol{y}) = 0 & (\boldsymbol{y} \in \Omega_i), \\ P_r(\boldsymbol{y}) = 0 & (\boldsymbol{y} \in \partial\Omega_i). \end{cases} \tag{1.22}$$

Let us define the real-valued coefficients $\{\alpha_r\}_{r\geq 0}$ and the resonant frequencies $\{\omega_r\}_{r\geq 1}$:

$$\alpha_0 = \frac{\rho_i}{\rho_m}\int_{\Omega_i}\mathrm{d}\boldsymbol{y} \qquad \alpha_r = \sqrt{\frac{\rho_i}{\rho_m}}\int_{\Omega_i} P_r(\boldsymbol{y})\,\mathrm{d}\boldsymbol{y} \qquad \text{and} \qquad \omega_r = \frac{1}{h}\sqrt{\frac{\mu_i}{\rho_i}\,\lambda_r}. \tag{1.23}$$

It is proven in Pham et al., 2017 that the frequency-dependent coefficient $\mathscr{D}_\infty(\omega)$ in (1.19) and (1.21) can be recast as the infinite series

Jump conditions 1.3: Frequency-dependent coefficient

$$\mathscr{D}_\infty(\omega) = \alpha_0 - \sum_{r\geq 1}\alpha_r^2\,\frac{\omega^2}{\omega^2-\omega_r^2}. \tag{1.24}$$

The coefficient $\mathscr{D}_\infty$ depends on the constitutive parameters of the inclusions as well as their geometries. On the contrary, the five other effective parameters in (1.19) depend only on the geometry of the inclusions whereas in the non-resonant case (1.12) their constitutive properties were also involved. Moreover, due to the expression of α_r in (1.23), the eigenmodes P_r that have zero mean value do not contribute to the effective model.

1.2.3 High-frequency homogenization

While the previous section focused on a specific example of low-frequency homogenization, this section will give an overview of the main ideas of high-frequency homogenization which will be used in Chapter 6 of this thesis.

One introduces $\boldsymbol{h}$ the vector containing the periodicity of the medium among the different directions of the space. It is well known from the Bloch-Floquet theory that for $\boldsymbol{h}$-periodic media, the displacement satisfies:

$$\hat{U}(\boldsymbol{X}+\boldsymbol{h},\boldsymbol{k}) = \hat{U}(\boldsymbol{X},\boldsymbol{k})e^{i\boldsymbol{k}\cdot\boldsymbol{h}},$$

where $\boldsymbol{k}$ is the Bloch wavenumber. Its real part represents the phase velocity and its imaginary part accounts for the damping of waves. The Bloch wavenumber depends on the angular frequency ω through dispersion relations. The part of the wavenumber domain defined by $[0, \pi/h_i]$ in each direction completely defines the dispersion relation and is called the irreducible Brillouin zone. Typically in such problems, the dispersion diagram displays band-gaps, i.e. regions in the angular frequency domain where waves cannot propagate because the Bloch wavenumber is purely imaginary. There are infinite number of branches of the dispersion diagram, i.e. for a given Bloch wavenumber, one can find an infinite (countable) set of angular frequencies leading to propagating waves. Figure 1.8 displays a dispersion diagram and illustrates the domain validity of the low-frequency homogenization.

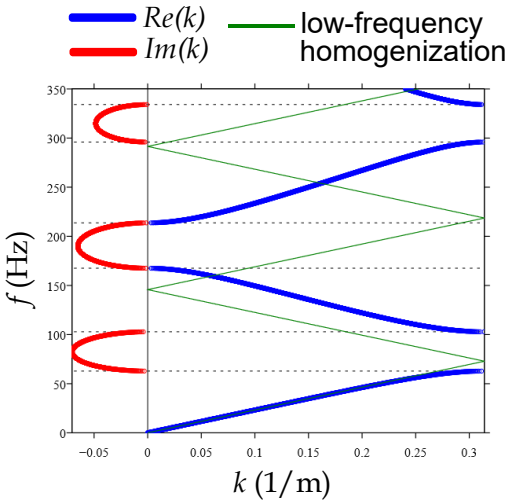

Figure 1.8 – Example of dispersion diagram and approximation in the *low-frequency* regime.

These bandgaps and some of the exotic behaviours of wave phenomena in periodic media such as negative refraction (Willis, 2016) or topologically protected states (Lee-Thorp, Weinstein, & Zhu, 2018) occur at high frequencies. For these frequencies, the wavelength is comparable to the periodicity of the microstructures. This is hence beyond the assumption of a wavelength much larger than the periodicity which allows to introduce two scales in the low-frequency homogenization framework. This problem is tackled by the *high-frequency homogenization* introduced in Craster, Kaplunov, and Pichugin, 2010a.

The objective of the high-frequency homogenization is to approximate how the dispersion relation and the wavefield behave for angular frequencies ω that are close to the angular frequencies ω_0 (eigenfrequencies) corresponding to an edge of the Brillouin zone on the dispersion diagram, see Figure 1.9. The main idea of Craster et al., 2010a is to combine both Floquet-Bloch theory and two-scale expansions. One main difference with the low-frequency framework is the type of scale separation: the fast scale still represents the variation within a cell while the slow scale accounts

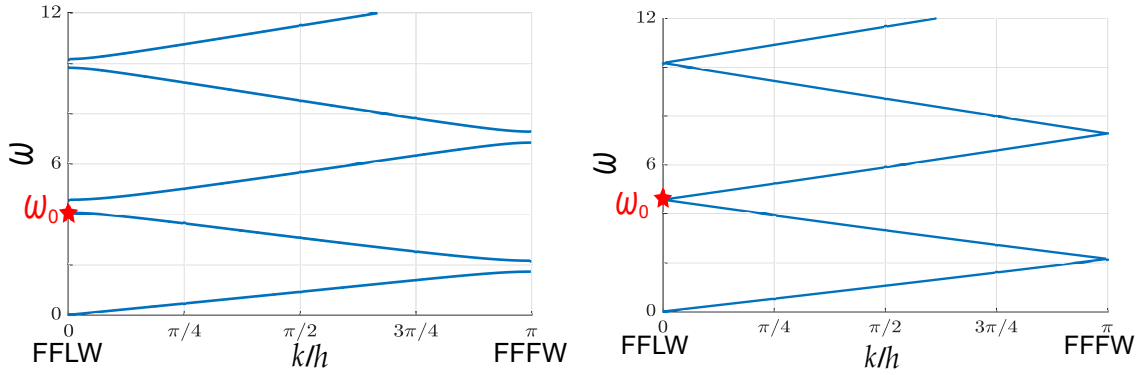

(a) Single eigenvalue (b) Double eigenvalue

Figure 1.9 – Example of dispersion diagram with the FFFW and FFLW case. The red star denotes an eigenfrequency ω_0 close to which we want to approximate the dispersion relation and wavefield. It is either a single eigenvalue (a) or a double eigenvalue (b)

for the modulation of these rapide oscillations. This comes from the fact that there exist standing waves at the wavenumbers ω_0 corresponding to the edges of the Brillouin zone. Close to these eigenfrequencies, the behaviour is the same up to a modulation. One can consider for the wavefield its projection onto the associated highly oscillating Bloch eigenfunctions. These rapidly oscillating solutions are modulated by a long-scale solution. The modulation length is denoted by L and is much larger than the periodicity.

In a 1D case, and adopting the terminology of Guzina, Meng, and Oudghiri-Idrissi, 2019, we will refer to the homogenization near the left edge of the Brillouin zone $k \approx 0$ as Finite Frequency Low Wavenumber (FFLW), while the homogenization near the right edge ($k \approx \pi/h$) will be referred to as Finite Frequency Finite Wavenumber (FFFW), see Figure 1.9. Upon introducing $\tilde{k}$ as

$$(\text{FFLW}) : \tilde{k} = k \quad \text{and} \quad (\text{FFFW}) : \tilde{k} = \pi/h - k, \tag{1.25}$$

the end result of the high-frequency homogenization technique is an approximation of the type

$$\omega^2 = \omega_0^2 + \mathcal{T}\tilde{k}^2 h^2 + o\left(\frac{h^2\tilde{k}^2}{L^2}\right), \tag{1.26}$$

where the parameter $\mathcal{T} \in \mathbb{R}$ can be determined explicitly. This angular frequency approximation comes together with an associated leading-order approximation of the wave field $U_h(X)$ of the form

$$U_h(X) = U^{(0)}\left(X, \frac{X}{\delta}\right) + O\left(\frac{h\tilde{k}}{L}\right), \tag{1.27}$$

with $\delta = h/L$ the small parameter which is the ratio between the periodicity and the modulation length L. One the contrary, in the case of low-frequency homogenization, the zeroth-order field can be shown to be independent of the fast variable; this is one of the main differences between low- and high-frequency homogenization.

When ω_0 is a double eigenfrequency, two branches of the dispersion diagrams intersect with non-zero slope at an edge of de Brillouin zone, see Figure 1.9b. Such intersections are also known in the literature (see e.g. Lee-Thorp et al., 2018, Ochiai and Onoda, 2009 and Guzina et al., 2019) as *Dirac points* or *Dirac cones*. Then, the method has to be adapted to recover the sought approximations. One advantage of this approach compared to the Bloch wave decomposition is

that it allows to get additional information such as the nature of the modulation which differs for the simple or double eigenvalue case.

In Guzina et al., 2019, the technique is generalized in any dimension, and the asymptotic analysis is pushed one order further. A uniform approximation is also derived, considering the fact that some branches do not intersect at the edges of the Brillouin zone but are close to each other. Other works concerned the inclusion of a source term (Meng, Oudghiri-Idrissi, & Guzina, 2020) and the derivation of the process in the time domain (Harutyunyan, Milton, & Craster, 2016). The methodology has also been applied to several other configurations such as discrete lattice media (Craster, Kaplunov, & Postnova, 2010b; Colquitt, Craster, & Makwana, 2015), frame structures (Nolde, Craster, & Kaplunov, 2011), optics (Craster, Kaplunov, Nolde, & Guenneau, 2011), elastic plates (Antonakakis & Craster, 2012), full vector wave systems (Antonakakis, Craster, & Guenneau, 2014), elastic composites (Boutin, Rallu, & Hans, 2014), reticulated structures (Rallu, Hans, & Boutin, 2018).

1.2.4 Optimization

In the context of metamaterials, the optimization of the microstructures is a useful tool in order to determine the designs that exhibit interesting macroscopic behaviours. To this purpose, different types of optimization can be considered:

- the *parametric* optimization when the shapes are parameterised by a fixed number of variables (thickness, dimensions, etc.)
- the *shape* optimization when, from an initial shape, the position of the boundaries of the microstructure is changed without changing its topology
- the *topological* optimization when the best possible shape is sought, even if it means changing the topology

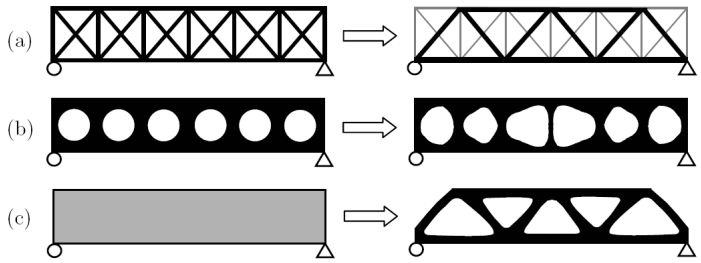

Figure 1.10 – Three types of optimization (a) parametric (b) shape (c) topological. Initial designs on the left and final designs on the right. (Martin Ph. Bendsoe, 2003)

Figure 1.10 illustrates these differences. In this work, we are interested in topological optimization which leaves more freedom compared to the first two methods. Indeed, these ones can easily converge to a local minimum with poor performance. The mathematical tool allowing to perform this type of optimization is the *topological derivative* (Martin Ph. Bendsoe, 2003). It measures the sensitivity of a cost functional to topological perturbations. A perturbation is a small inhomogeneity of size ε introduced at a point $\boldsymbol{z}$ of the unit cell that defines the microstructure. This perturbation induces new material properties $\boldsymbol{m}_{\boldsymbol{z},\varepsilon}$ instead of the initial ones $\boldsymbol{m}$. Then, the so-called topological derivative of a given function f of the material properties $\boldsymbol{m}$ denoted by $\mathcal{D}f$

is defined thanks to the following asymptotic expansion in 2D:

$$f(\boldsymbol{m}_{\boldsymbol{z},\varepsilon}) \underset{\varepsilon\to 0}{=} f(\boldsymbol{m}) + \varepsilon^2 \mathcal{D}f(\boldsymbol{m},\boldsymbol{z},\mathcal{P},\Delta\boldsymbol{m}) + o(\varepsilon^2) \tag{1.28}$$

with $\mathcal{P}$ the shape of the inhomogeneity and $\Delta\boldsymbol{m}$ the material perturbation in the inhomogenity. Therefore, the topological derivative describes the influence on the functional f of a perturbation located at $\boldsymbol{z}$, of shape $\mathcal{P}$ and material perturbation $\Delta\boldsymbol{m}$. Consequently, the more negative $\mathcal{D}f(\boldsymbol{m},\boldsymbol{z},\mathcal{P},\Delta\boldsymbol{m})$ is, the more efficient a perturbation at $\boldsymbol{z}$ would be to decrease f.

Then, different numerical methods are possible to update the material properties based on the knowledge of the topological derivatives. One method used in this dissertation is the *level-set* method. For a two-phase material distribution, it relies on the characterization of this distribution thanks to a level-set function which is stricly positive in one phase and strictly negative in the other phase. This has first been introduced for *shape* optimization and is based on the fact that the interface between phases, which corresponds to a level-set function which is equal to 0, can evolve based on the shape derivative of the cost functional with respect to a perturbation of this interface (Allaire, de Gournay, Jouve, & Toader, 2005; Allaire & Yamada, 2018). This methodology has then been adapted to topological perturbation based on a projection algorithm (Amstutz & Andrä, 2006; Amstutz, Giusti, Novotny, & de Souza Neto, 2010; Giusti, Ferrer, & Oliver, 2016; Oliver, Ferrer, Cante, Giusti, & Lloberas-Valls, 2017).

A strategy of optimization of microstructures, in line with the homogenization considered in this dissertation, is to perform the optimization from the homogenized model that describes the material. It relies on the expression of a cost function to be minimized in terms of the effective coefficients that characterize the homogenized model. At low frequency, this method has been used in statics (Amstutz et al., 2010; Giusti, Novotny, & de Souza Neto, 2010; Oliver et al., 2017), in dynamics for a low constrast (Allaire & Yamada, 2018), and a high contrast (Vondřejc, Rohan, & Heczko, 2017) of the physical properties. It has also been extended to high-frequency homogenization (Noguchi, Yamada, Izui, & Nishiwaki, 2018).

In this framework, a topological optimization procedure is presented in Cornaggia and Bellis, 2020 to optimize dynamical properties for antiplane shear waves based on homogenization. The main ingredients are the following ones:

1. the two-scale asymptotic homogenization method is deployed
2. a cost functional is considered on the basis of the homogenized model
3. topological derivatives are computed
4. the minimization is performed thanks to a level-set algorithm
5. each iteration of the level-set requires the computation of cell problems which are solved using FFT-accelerated solvers

Works on the optimization in dynamics of microstructured thin layers are more scarce and recent: Matsushima, Isakari, Takahashi, and Matsumoto, 2020 for an optimization of slabs based on far-field behaviour and Noguchi and Yamada, n.d. for a design of acoustic metasurfaces based on a homogenization model.

1.3 Discretization of interfaces

From a numerical point of view, the difficulty of the problems tackled in this thesis is the presence of interfaces. In particular, Chapter 3 aims at presenting a numerical method to simulate the interaction of transient waves with resonant meta-interfaces. By opposition with frequency-domain

approaches, time-domain formulations have two main advantages: i) they allow to simulate wide-band wave phenomena in a single computation; ii) they pave the way to problems involving nonlinearities, for which even a monochromatic forcing would require to solve numerous Helmholtz equations due to the generation of harmonics.

1.3.1 Existing methods

Without claiming to be exhaustive, below are the broad outlines of numerical methods that have been developped to take into account interfaces.

■ *Finite differences on uniform grids.* Finite differences are a commonly used discretization method for the numerical simulation of wave propagation. It is an easy-to-implement method which involves uniform Cartesian grids. However, this method suffers from considerable drawbacks when interfaces are considered, see Figure 1.11. Indeed, it yields spurious diffractions, and a drop in order of convergence. Moreover, if jump conditions, i.e. discontinuities of the fields, are considered at the interfaces, these numerical methods also fail to satisfy them due to the stairstep approximation.

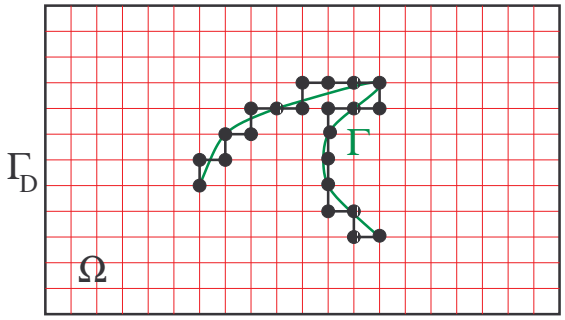

Figure 1.11 – Stairstep approximation of an interface Γ in green (Lombard, 2010).

■ *Numerical methods for boundary conditions.* When an interface has to be considered for boundary conditions, several methods can be mentioned. For example, with the fictitious domain method, one introduces a Lagranger multiplier that can be interpreted as a surface current in order to deal with boundary conditions (Collino, Joly, & Millot, 1997; Becache, Joly, & Tsogka, 2001). This method allows to work with a uniform mesh whatever the geometry is. Another approach is the penalization one: a source term is added to the evolution equations to account for the boundary condition (Fornet & Guès, 2009). However, the extension of these methods for jump conditions is not obvious.

■ *Avaraging the coefficients.* An easy-to-implement solution is to average the coefficients of the partial differential equation (from the values of the physical parameters on each part of the interface) near the interface. The averaged coefficients can be chosen to optimize the stability condition and the order of convergence, which is still reduced but controlled (Cohen & Joly, 1996). However, this method does not allow to deal with the case of jump conditions at the interface and even for perfect contacts the order of convergence is reduced to 1.

■ *Mesh refinement.* A possibility with finite differences is to perform a local mesh refinement around the interface. However, it will still lead to a failure to respect jump conditions. In the same spirit, another possibility is to use an unstructured mesh to get a mesh adapted to the interface, which is commonly used with finite elements, finite volumes and the discontinuous Galerkin method. For

example, the spectral element method is an unstructured method that allows to take into account jump conditions at the interface via a variational formulation (Komatitsch & Vilotte, 1998).Then, one gets a good description of the geoemetry of the interface. However, if this geometry is complex, see Figure 1.12, the meshing step can be difficult.

Furthermore, one main drawback of these methods is the requirement on the time step. Indeed,

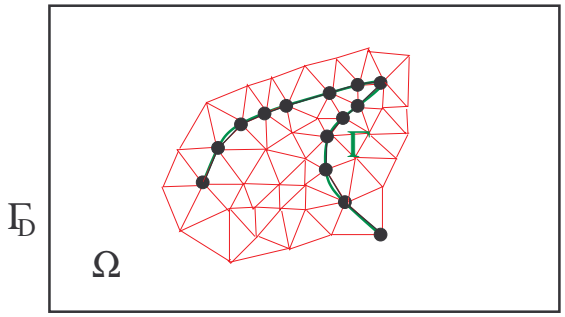

Figure 1.12 – Adaptative mesh for an interface Γ in green (Lombard, 2010).

when the meshes are of constant spatial step h and time step Δt, the finite difference schemes are stable under the Courant–Friedrichs–Lewy (CFL) condition

$$\frac{c\Delta t}{h} \leq \alpha \tag{1.29}$$

where c denotes the propagation velocity and α is the CFL number that depends on the scheme considered and the space dimension. This value α is a stability parameter and also an optimal value in the sense that the ratio $c\Delta t/h$ cannot be chosen too small since the numerical dispersion increases when this ratio decreases. When a local refinement is considered, the stability condition (1.29) will be given by the finest grid. As a result, the calculation time can increase significantly due to a small time step Δt. Another drawback is the fact that having a ratio $c\Delta t/h$ much smaller than its optimal value (1.29) in the regions where the grid is coarse will increase the dispersion phenomena. With unstructured meshes and finite elements, the same drawback holds with a time step linked by the CFL stability condition to the smallest step of the mesh. As a result, the calculation time can increase significantly.

■ *Immersed Interface methods.* With this type of methods, the interface is immersed in the meshing, in the sense that it does not have to coincide with the mesh, see Figure 1.13. To do so, at grid points in the vicinity of the interface, the numerical scheme is modified to ensure a given local truncation error (Zhang & LeVeque, 1997). This is done by using the jump conditions as well as the geometry of the interface (its relative position in the grid and its curvature). The advantage is that discontinuities of the fields at the interfaces can be taken into account and that there is no additional requirement on the time step. The drawback of this method is that the stability issue is not addressed.

1.3.2 Explicit Simplified Interface Method

In this dissertation, we have chosen to work with an Immersed Interface Method which is the Explicit Simplified Interface Method presented in this subsection. As previously said, the Immersed Interface Methods is an efficient way to take into account jump conditions on an arbitrary interface. A scheme is used far from the interface and a new scheme is applied at the calculation points

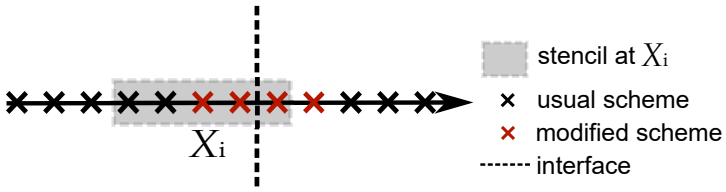

Figure 1.13 – Immersed Interface Method for a 1D setting.

close to the interfaces. This yields to a difficulty of generalization at higher-order schemes, and a difference of nature between the scheme used at the interface and the one used near the interface (in terms of numerical dispersion for example). These limitations have motivated the development of the Explicit Simplified Interface Method (ESIM) and its application to a variety of wave propagation problems (Lombard & Piraux, 2004, 2006; Lombard, Piraux, Gélis, & Virieux, 2008; Lombard, 2010; Chiavassa & Lombard, 2011).

The principle of the ESIM is the following: instead of building a new scheme in the vicinity of the interfaces, we apply at any computational point the same scheme (i.e. the one chosen in a homogeneous medium). This is possible thanks to a modification of the numerical values used by the scheme to do the time-stepping at points near the interface. The main difficulty is then to build these modified values while taking into account the jump conditions and the geometry of the interface. Their expression are then independent of the scheme chosen and it is therefore easier to extend the method to a large class of numerical schemes.

A local truncation error analysis can been performed to check that the order of the scheme in a homogeneous medium can be reached if the parameters of the ESIM are well chosen. Regarding stability, the classical Von Neumann analysis cannot be applied, as it is only valid in homogeneous media. Energy techniques, valid in the case of variable coefficients, are well suited to discretisations arising from a variational formulation, which is not the case for this method. The only way to study the stability seems to be the Gustafsson, Kreiss, Sundström (GKS) analysis by discrete normal modes (Lombard, 2010). One notes that it is purely numerical (given physical and numerical parameters) and does not offer a theoretical expression such as the classical CFL condition. However, stability under the usual CFL condition is generally observed in numerical experiments as well as an order of convergence which is coherent with the local truncation error analysis.

1.4 Overview of the thesis

The design of media at a microstructured scale allows to control wave propagation in a fine way and to obtain exotic effects at the macroscopic scale. Thanks to homogenization methods, the microstructure can be advantageously replaced, at the macro scale, by a homogeneous effective medium. Then, it raises the question of optimization tools in order to design the microstructure that allows to achieve a desired macroscopic effect. In this context, the consideration of interfaces (microstructured interfaces, imperfect interfaces) can lead to modifications in the homogenization methods, the numerical methods, or the optimization methods classically used. Therefore, the present thesis has focused on the study of waves propagation in microstructured media with interfaces through homogenization, time-domain simulations and optimization. The research described in this dissertation has been performed at the Laboratory of Mechanics and Acoustics under the supervision of Bruno Lombard and Cédric Bellis. Parts of this work were also carried out through other collaborations which are detailed below. The dissertation is divided into two parts that are independent.

■ *Part I*. The first part concerns the case where the heterogeneities constitute a periodic row of inclusions embedded in a homogeneous matrix, see Section 1.2.2. When the physical parameters of the inclusions are strongly contrasted with those of the matrix, internal resonances can occur and can be used in turn to maximise acoustic absorption. In Chapter 2, the homogenization of such a resonant microstructured layer in the time domain is studied using a method of matched asymptotic expansions and leads to non-local jump conditions. The derivation of the jump conditions follows the work Pham et al., 2017 in the frequency domain whose main results have been introduced in Section 1.2.2.4. An energy analysis then provides a condition on the thickness of the enlarged effective interface. Time-domain simulations are then performed in order to assess the validity of the homogenized model. This chapter mainly reproduces [A2] and results from a collaboration with Kim Pham (IMSIA, ENSTA Paris), Agnès Maurel (Institut Langevin, ESPCI ParisTech) and Jean-Jacques Marigo (Laboratoire de Mécanique des Solides, Ecole Polytechnique). The next section of this chapter, whose work appears in [A5], tackles the incorporation of dissipation: some numerical simulations are presented to investigate the effect of this new parameter.

A large part of the work consists of developing a numerical method to perform time domain simulations of wave propagation across resonant interfaces. Indeed, simulation of time-domain acoustic wave propagation across enlarged effective interfaces have been previously addressed in Lombard, Maurel, and Marigo, 2017 but in the case of *non-resonant* effective jump conditions (1.12). In the present study, the central question therefore concerns the discretization of interfaces characterized by *resonant* effective jump conditions (1.19) that are frequency-dependent in the harmonic regime, along with their implementation for wave propagation simulations in the time domain. This work is presented in Chapter 3 and mainly follows [A1]. The introduction of auxiliary variables allows to get a local evolution problem in time which is then solved numerically by a finite-difference scheme coupled with an immersed interface method. This methodology is validated through a local truncation error analysis and comparison with analytical solutions. In the line of the previous chapter, the modifications of the numerical method due to the incorporation of dissipation, which have been presented in [A5], is at stake in the last section.

Eventually, in Chapter 4, the sensitivity of the effective parameters to the geometry of the microstructure in the non-resonant case is determined using topological derivatives following Bonnet, Cornaggia, and Guzina, 2018. Then, we implement a topological optimization procedure for the design of non-resonant thin microstructured layers following Cornaggia and Bellis, 2020. Some preliminary numerical results are presented. It also required to propose a numerical method to solve cell problems on an infinite band. This was done thanks to FFT accelerated solvers developped in collaboration with Rémi Cornaggia (now at Institut Jean Le Rond d'Alembert, Sorbonne Université).

■ *Part II*. It is often assumed that the contact between the inclusions and the homogeneous matrix is perfect. Some models, such as linear spring-mass conditions, account for the behaviour of imperfect contacts between solids. In Chapter 5, low-frequency homogenization of such configurations is first carried out in 1D. The expression of the zeroth-order mean field and the first-order corrector is obtained and some numerical comparisons with full-field simulations are presented. This 1D linear case has led to an extension to non-linear contacts in [A4] so the main results of this paper are also presented. Then, the homogenization in the linear case is performed for the full 3D elasticity case.

Eventually, dispersion diagrams in 1D solids with linear spring-mass conditions are studied in Chapter 6. Contrary to the previous chapters that study the propagation of waves in time-domain, this chapter is a work in the frequency domain. The framework of high-frequency homogenization (Craster et al., 2010a) is used and an approximation for the fields and for the dispersion relations near the edges of the Brillouin zone is obtained. This chapter mainly reproduces [A3] and was initiated by a collaboration with Raphael Assier (Departement of Mathematics, University of

Manchester). We both developed the theoretical analysis, performed the numerical implementation and produced the figures jointly.

Published referred papers

[A1 = Touboul et al., 2020a] M. Touboul, B. Lombard, C. Bellis: "Time-domain simulation of wave propagation across resonant meta-interfaces", *Journal of Computational Physics* 414 (2020), 109474.

[A2 = Touboul et al., 2020b] M. Touboul, K. Pham, A. Maurel, J.-J. Marigo, B. Lombard, C. Bellis: "Effective resonant model and simulations in the time-domain of wave scattering from a periodic row of highly-contrasted inclusions", *Journal of Elasticity* 142, 53–82 (2020).

[A3 = Assier et al., 2020] R. Assier, M. Touboul, B. Lombard, C. Bellis: "High-frequency homogenization in periodic media with imperfect interfaces", *Proceedings of the Royal Society A* 476: 20200402 (2020).

[A4 = Bellis et al., 2021] C. Bellis, B. Lombard, M. Touboul, R. Assier: "Effective dynamics for low-amplitude transient elastic waves in a 1D periodic array of non-linear interfaces", *Journal of the Mechanics and Physics of Solids* 149: 104321 (2021).

[A5 = Touboul et al., 2021] M. Touboul, X. Gao, B. Lombard: "Damping in a row of locally-resonant inclusions: dynamic homogenization and scattering of transient shear waves", *Wave Motion* 107: 10281 (2021).

In preparation

[A6] R. Cornaggia, C. Bellis, M. Touboul: "FFT-based computation of cell problems in an infinite strip".

[A7] M. Touboul, R. Cornaggia, C. Bellis: "Topological optimization of the effective dynamics of microstructured interfaces".

[A8] M. Touboul, B. Lombard, C. Bellis, R. Assier: "Effective dynamics for transient elastic waves in an elastic media with linear spring-mass interfaces".

Part I

Homogenization and optimization of microstructured interfaces

CHAPTER 2

Homogenization and simulations in the time domain of scalar waves scattering from a periodic row of highly contrasted inclusions

This chapter aims at studying the propagation of waves across a periodic row of inclusions whose high contrast with the background matrix yields local resonances. The homogenization of such a resonant microstructure is performed in the transient regime, and effective jump conditions are obtained in Section 2.1. The resulting model is then analyzed based on energy balance in Section 2.2 and a condition on the thickness of the enlarged interface is obtained to ensure the stability. Section 2.3 aims at both illustrating the effective dynamical behavior obtained and at validating the effective model through comparisons with full-field, i.e. microstructure-based, simulations. Damping is then considered in Section 2.4 to be closer from real devices and to examine physical applications such as coherent perfect absoption. Appendix 2.A assesses the equivalence with the frequency-domain formulation of Pham et al., 2017.

This work started as a joint work with Kim Pham (IMSIA, ENSTA Paris), Agnès Maurel (Institut Langevin, ESPCI ParisTech) and Jean-Jacques Marigo (Laboratoire de Mécanique des Solides, Ecole Polytechnique) which has allowed to write the energy of the homogenized problem in a quadratic form and to discuss the results obtained in the inviscid case.

2.1 Effective jump conditions in the time domain

The homogenization of such a periodic row of highly-contrasted inclusions using matched asymptotic expansions has been investigated in (Pham et al., 2017) in the frequency domain. We follow the same method here and underline the differences associated to the time-domain approach for the derivation of the jump conditions at the second order.

2.1.1 Assumptions for the homogenization in the resonant case

As discussed in introduction, the microstructure of periodicity h and thickness e is homogenized in the long-wavelength regime, which means that the dimensionless parameter $\eta = k_m h$ defined in (1.8) is much smaller than 1. The choice of a characteristic wavelength and the associated small parameter is discussed in Section 2.3.1.3. With high material contrast, the microstructure can be the seat of local resonances. Introducing the wavenumber $k_i = \omega\sqrt{\rho_i/\mu_i}$ within the inclusions, then such resonances can occur when the wavelength within an inclusion is of order of h, i.e. $k_i h = O(1)$ (Auriault & Boutin, 2012; Pham et al., 2017). In particular, this assumption is met for a low contrast in mass density $\rho_i/\rho_m = O(1)$ and a high contrast in shear modulus $\mu_i/\mu_m = O(\eta^2)$, a configuration which we consider in the present study. These geometrical and material assumptions are recalled there for the sake of completeness:

Assumption 2.1

The configuration satisfies $\eta = k_m h \ll 1$ while $\rho_i/\rho_m = O(1)$ and $\mu_i/\mu_m = O(\eta^2)$. One rewrites the parameter μ_i as $\mu_i = \eta^2\mu_0$ where μ_0 is a reference modulus that satisfies $\mu_0/\mu_m = O(1)$

This Assumption of the *resonant* case differs from Assumption 1.1 in the *non-resonant* case by the high material contrast in the shear modulus. This additional scaling leads to substantial modifications in the homogenization process.

2.1.2 Nondimensionalization

New nondimensionalized space-time coordinates are introduced to formulate the homogenization problem independently of the wavelength λ, i.e. one defines $\boldsymbol{x} = k_m \boldsymbol{X}$ and $\tau = k_m\sqrt{\frac{\mu_m}{\rho_m}}\, t$. One introduces the nondimensionalized fields $v_\eta(\boldsymbol{x},\tau) = \sqrt{\frac{\rho_m}{\mu_m}} V_h(\boldsymbol{X},t)$ and $\boldsymbol{\sigma}_\eta(\boldsymbol{x},\tau) = \frac{1}{\mu_m}\boldsymbol{\Sigma}_h(\boldsymbol{X},t)$. The original system

$$\begin{cases} \dfrac{\partial \boldsymbol{\Sigma}_h}{\partial t}(\boldsymbol{X},t) = \mu_h(\boldsymbol{X})\boldsymbol{\nabla} V_h(\boldsymbol{X},t), \\ \rho_h(\boldsymbol{X})\dfrac{\partial V_h}{\partial t}(\boldsymbol{X},t) = \boldsymbol{\nabla}\cdot\boldsymbol{\Sigma}_h(\boldsymbol{X},t), \end{cases} \tag{2.1}$$

is then transformed into:

$$\begin{cases} \dfrac{\partial \boldsymbol{\sigma}_\eta}{\partial \tau}(\boldsymbol{x},\tau) = \dfrac{\mu_h(\boldsymbol{x})}{\mu_m}\boldsymbol{\nabla}_{\boldsymbol{x}}\, v_\eta(\boldsymbol{x},\tau), \\ \dfrac{\rho_h(\boldsymbol{x})}{\rho_m}\dfrac{\partial v_\eta}{\partial \tau}(\boldsymbol{x},\tau) = \boldsymbol{\nabla}_{\boldsymbol{x}}\cdot\boldsymbol{\sigma}_\eta(\boldsymbol{x},\tau), \end{cases} \tag{2.2}$$

while the continuity conditions on v_η and $\boldsymbol{\sigma}_\eta\cdot\boldsymbol{n}$ at the matrix/inclusion interfaces are preserved.

Remark 2. *In numerical examples, an initial condition or a point source will be added to the original system. They will be kept as such in the final effective model, which means that there is*

an implicit assumption that the source point is located in the homogeneous medium, far enough from the microstructured interface.

2.1.3 Matched asymptotic expansions

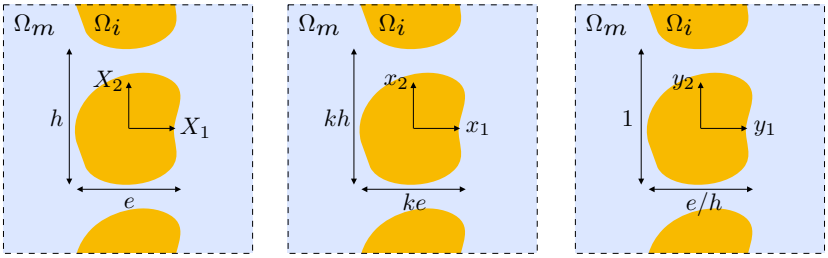

Figure 2.1 – The different coordinate systems considered: *(left)* original coordinates, *(center)* nondimensionalized coordinates, and *(right)* rescaled coordinates.

While the space coordinate $\boldsymbol{x} = (x_1, x_2)$ is appropriate to describe the *slow* variations of the wavefield, one introduces the *rescaled* coordinate $\boldsymbol{y} = \boldsymbol{x}/\eta$, see Figure 2.1, which will be used to describe its small-scale *fast* variations. Note that, with a slight abuse of notation, the inclusion domain is referred to as $\cup_i \Omega_i$ in all three coordinate systems. Depending on the region of space considered, the fields v_η and $\boldsymbol{\sigma}_\eta$ will be assumed to have specific dependencies on $\boldsymbol{x}$ and $\boldsymbol{y}$. In the far field, only the slow coordinate $\boldsymbol{x}$ is needed to describe the propagating field. Near the inclusions, dependence on the fast coordinate $\boldsymbol{y}$ is considered in order to describe field variations at the scale of the microstructure while slower variations along the interface are also accounted for through a dependence on x_2. Three regions are thus defined: an outer region (far field) for which $\boldsymbol{x} \in \mathbb{R}^2$, an inner region (near field) that excludes the inclusions, i.e. $\boldsymbol{y} \in \mathbb{R}^2 \setminus \cup_i \Omega_i$ and $x_2 \in \mathbb{R}$, and the inner region that coincides with the inclusions, i.e. $\boldsymbol{y} \in \cup_i \Omega_i$ and $x_2 \in \mathbb{R}$. In these three regions, the velocity and stress fields are expanded using the following ansatz:

$$
\begin{array}{ccc}
\text{Outer region} & \text{Inner region} & \text{Inclusions region} \\
(\boldsymbol{x} \in \mathbb{R}^2) & (\boldsymbol{y} \in \mathbb{R}^2 \setminus \cup_i \Omega_i,\ x_2 \in \mathbb{R}) & (\boldsymbol{y} \in \cup_i \Omega_i,\ x_2 \in \mathbb{R}) \\
\begin{cases} v_\eta = \displaystyle\sum_{j\geq 0} \eta^j v^j(\boldsymbol{x}, \tau) \\ \boldsymbol{\sigma}_\eta = \displaystyle\sum_{j\geq 0} \eta^j \boldsymbol{\sigma}^j(\boldsymbol{x}, \tau) \end{cases} &
\begin{cases} v_\eta = \displaystyle\sum_{j\geq 0} \eta^j w^j(\boldsymbol{y}, x_2, \tau) \\ \boldsymbol{\sigma}_\eta = \displaystyle\sum_{j\geq 0} \eta^j \boldsymbol{s}^j(\boldsymbol{y}, x_2, \tau) \end{cases} &
\begin{cases} v_\eta = \displaystyle\sum_{j\geq 0} \eta^j w_i^j(\boldsymbol{y}, x_2, \tau) \\ \boldsymbol{\sigma}_\eta = \displaystyle\sum_{j\geq 0} \eta^j \boldsymbol{s}_i^j(\boldsymbol{y}, x_2, \tau). \end{cases}
\end{array}
\tag{2.3}
$$

The terms $(w^j, \boldsymbol{s}^j)_{j\geq 0}$ of the expansion of the solution $(v_\eta, \boldsymbol{\sigma}_\eta)$ in the inner region are assumed to be periodic with respect to y_2. In addition, the continuity conditions on the inclusions interfaces read $w^j = w_i^j$ and $\boldsymbol{s}^j \cdot \boldsymbol{n} = \boldsymbol{s}_i^j \cdot \boldsymbol{n}$ on $\partial\Omega_i$. We consider the bounded domain described in $\boldsymbol{y}$-coordinates as $\Omega^b = [-y_1^b, y_1^b] \times [-1/2, 1/2]$ with $y_1^b > e/h$, see Figure 2.2. Later on, Ω_i will denote the inclusion in this bounded elementary cell. Moreover, one introduces the domain $\Omega = \lim_{y_1^b \to \pm\infty} \Omega^b = \mathbb{R} \times [-1/2, 1/2]$ which is the *elementary cell* generating the periodic row of inclusions.

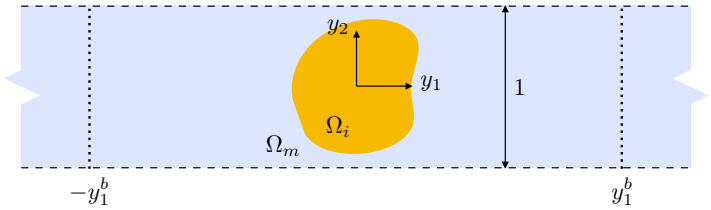

Figure 2.2 – Bounded elementary cell $\Omega^b = [-y_1^b, y_1^b] \times [-\frac{1}{2}, \frac{1}{2}]$ with $y_1^b > \frac{e}{h}$.

As is customary in the two-scale asymptotic expansion approach, the differential operators featured in (2.2) are rewritten in the inner regions as:

$$\boldsymbol{\nabla}_{\boldsymbol{x}} v_\eta \to \frac{1}{\eta}\boldsymbol{\nabla}_{\boldsymbol{y}} v_\eta + \frac{\partial v_\eta}{\partial x_2}\boldsymbol{e}_2 \qquad \text{and} \qquad \boldsymbol{\nabla}_{\boldsymbol{x}} \cdot \boldsymbol{\sigma}_\eta \to \frac{1}{\eta}\boldsymbol{\nabla}_{\boldsymbol{y}} \cdot \boldsymbol{\sigma}_\eta + \frac{\partial \boldsymbol{\sigma}_\eta}{\partial x_2} \cdot \boldsymbol{e}_2$$

in terms of the canonical unit vectors $\boldsymbol{e}_1, \boldsymbol{e}_2$.

Inserting (2.3) in (2.2) while using the previous differential operator identities, one obtains the following recursive differential problems at the orders $j \geq 0$ in the three regions:

$$\begin{cases} \dfrac{\partial \boldsymbol{\sigma}^j}{\partial \tau} = \boldsymbol{\nabla}_{\boldsymbol{x}} v^j, & \text{(2.4a)} \\ \dfrac{\partial v^j}{\partial \tau} = \boldsymbol{\nabla}_{\boldsymbol{x}} \cdot \boldsymbol{\sigma}^j, & \text{(2.4b)} \\ \dfrac{\partial \boldsymbol{s}^{j-1}}{\partial \tau} = \dfrac{\partial w^{j-1}}{\partial x_2}\boldsymbol{e}_2 + \boldsymbol{\nabla}_{\boldsymbol{y}} w^j, & \text{(2.4c)} \\ \dfrac{\partial w^{j-1}}{\partial \tau} = \dfrac{\partial \boldsymbol{s}^{j-1}}{\partial x_2} \cdot \boldsymbol{e}_2 + \boldsymbol{\nabla}_{\boldsymbol{y}} \cdot \boldsymbol{s}^j, & \text{(2.4d)} \\ \dfrac{\partial \boldsymbol{s}_i^j}{\partial \tau} = \dfrac{\mu_0}{\mu_m}\left(\dfrac{\partial w_i^{j-2}}{\partial x_2}\boldsymbol{e}_2 + \boldsymbol{\nabla}_{\boldsymbol{y}} w_i^{j-1}\right), & \text{(2.4e)} \\ \dfrac{\rho_i}{\rho_m}\dfrac{\partial w_i^{j-1}}{\partial \tau} = \dfrac{\partial \boldsymbol{s}_i^{j-1}}{\partial x_2} \cdot \boldsymbol{e}_2 + \boldsymbol{\nabla}_{\boldsymbol{y}} \cdot \boldsymbol{s}_i^j, & \text{(2.4f)} \end{cases}$$

where $\boldsymbol{s}^j$, $\boldsymbol{s}_i^j$, w^j and w_i^j vanish if $j < 0$. Consequently, one can identify the $O(\eta^{-1})$-terms in the inner region:

$$\begin{cases} \boldsymbol{\nabla}_{\boldsymbol{y}} w^0 = \boldsymbol{0}, & \text{(2.5a)} \\ \boldsymbol{\nabla}_{\boldsymbol{y}} \cdot \boldsymbol{s}^0 = 0. & \text{(2.5b)} \end{cases}$$

Then, in all three regions, the $\mathcal{O}(1)$-terms read

$$\begin{cases} \dfrac{\partial \boldsymbol{\sigma}^0}{\partial \tau} = \boldsymbol{\nabla}_{\boldsymbol{x}}\, v^0, & \text{(2.6a)} \\ \dfrac{\partial v^0}{\partial \tau} = \boldsymbol{\nabla}_{\boldsymbol{x}} \cdot \boldsymbol{\sigma}^0, & \text{(2.6b)} \\ \dfrac{\partial \boldsymbol{s}^0}{\partial \tau} = \dfrac{\partial w^0}{\partial x_2}\boldsymbol{e}_2 + \boldsymbol{\nabla}_{\boldsymbol{y}}\, w^1, & \text{(2.6c)} \\ \dfrac{\partial w^0}{\partial \tau} = \dfrac{\partial \boldsymbol{s}^0}{\partial x_2} \cdot \boldsymbol{e}_2 + \boldsymbol{\nabla}_{\boldsymbol{y}} \cdot \boldsymbol{s}^1, & \text{(2.6d)} \\ \dfrac{\partial \boldsymbol{s}_i^0}{\partial \tau} = \boldsymbol{0}, & \text{(2.6e)} \\ \dfrac{\rho_i}{\rho_m}\dfrac{\partial w_i^0}{\partial \tau} = \dfrac{\partial \boldsymbol{s}_i^0}{\partial x_2} \cdot \boldsymbol{e}_2 + \boldsymbol{\nabla}_{\boldsymbol{y}} \cdot \boldsymbol{s}_i^1. & \text{(2.6f)} \end{cases}$$

One notes that the stress vector in the inclusion (2.6e) equals zero at the order $\mathcal{O}(1)$ whereas there is a contribution at the zeroth order for the stress vector in the matrix (2.6c). This is due to the high contrast in η^2 between μ_m and μ_i as described in Assumption 2.1. Assuming that at the initial time $\boldsymbol{s}_i^0(\boldsymbol{y}, x_2, 0) = 0$, then (2.6e) implies

$$\boldsymbol{s}_i^0(\boldsymbol{y}, x_2, \tau) = 0 \qquad \forall \tau \geq 0. \tag{2.7}$$

Then the $\mathcal{O}(\eta)$-term within the inclusions reads

$$\frac{\partial \boldsymbol{s}_i^1}{\partial \tau} = \frac{\mu_0}{\mu_m}\boldsymbol{\nabla}_{\boldsymbol{y}}\, w_i^0. \tag{2.8}$$

Finally, the outer and the inner solutions have to match in an intermediate region, see Figure 1.6. Therefore, matching conditions are formulated in the limit $y_1 \longrightarrow \pm\infty$ for the near-field solution (inner region) and $x_1 \longrightarrow 0^{\pm}$ for the far-field solution (outer region) which are expressed using the ansatz (2.3):

$$\begin{cases} \lim\limits_{x_1 \to 0^{\pm}} \sum\limits_{j\geq 0} \eta^j v^j(\boldsymbol{x}, \tau) = \lim\limits_{y_1 \to \pm\infty} \sum\limits_{j\geq 0} \eta^j w^j(\boldsymbol{y}, x_2, \tau), & \text{(2.9a)} \\ \lim\limits_{x_1 \to 0^{\pm}} \sum\limits_{j\geq 0} \eta^j \boldsymbol{\sigma}^j(\boldsymbol{x}, \tau) = \lim\limits_{y_1 \to \pm\infty} \sum\limits_{j\geq 0} \eta^j \boldsymbol{s}^j(\boldsymbol{y}, x_2, \tau). & \text{(2.9b)} \end{cases}$$

Taylor expansions of the outer fields v^j and $\boldsymbol{\sigma}^j$ at $x_1 = 0$ are written out for $j = 0, 1$:

$$\begin{cases} v^j(x_1, x_2, \tau) = v^j(0^{\pm}, x_2, \tau) + \eta\, y_1 \partial_{x_1} v^j(0^{\pm}, x_2, \tau), \\ \boldsymbol{\sigma}^j(x_1, x_2, \tau) = \boldsymbol{\sigma}^j(0^{\pm}, x_2, \tau) + \eta\, y_1 \partial_{x_1} \boldsymbol{\sigma}^j(0^{\pm}, x_2, \tau). \end{cases} \tag{2.10}$$

Eventually, one inserts (2.10) in (2.9). The $\mathcal{O}(1)$-terms are then identified:

$$\begin{cases} v^0(0^{\pm}, x_2, \tau) = \lim\limits_{y_1 \to \pm\infty} w^0(\boldsymbol{y}, x_2, \tau), & \text{(2.11a)} \\ \boldsymbol{\sigma}^0(0^{\pm}, x_2, \tau) = \lim\limits_{y_1 \to \pm\infty} \boldsymbol{s}^0(\boldsymbol{y}, x_2, \tau), & \text{(2.11b)} \end{cases}$$

and the $\mathcal{O}(\eta)$-terms give:

$$\begin{cases} v^1(0^{\pm}, x_2, \tau) = \lim\limits_{y_1 \to \pm\infty} \left[w^1(\boldsymbol{y}, x_2, \tau) - y_1 \dfrac{\partial v^0}{\partial x_1}(0^{\pm}, x_2, \tau) \right], & \text{(2.12a)} \\ \boldsymbol{\sigma}^1(0^{\pm}, x_2, \tau) = \lim\limits_{y_1 \to \pm\infty} \left[\boldsymbol{s}^1(\boldsymbol{y}, x_2, \tau) - y_1 \dfrac{\partial \boldsymbol{\sigma}^0}{\partial x_1}(0^{\pm}, x_2, \tau) \right]. & \text{(2.12b)} \end{cases}$$

We will see in the following that these limits are independant of y_2.

2.1.3.1 Jump conditions at the order $\mathcal{O}(1)$

Introducing for any function $f(x_1)$ the notation $[\![f]\!] = f(0^+) - f(0^-)$ then the jump condition for v^0 reads:

$$[\![v^0(\cdot, x_2, \tau)]\!] = 0, \tag{2.13}$$

due to (2.11a) and (2.5a). More precisely, for the zeroth-order velocity field we have:

$$v^0(0^\pm, x_2, \tau) = w^0(x_2, \tau). \tag{2.14}$$

Integrating (2.5b) on $\Omega^b \backslash \Omega_i$ yields:

$$\int_{-\frac{1}{2}}^{\frac{1}{2}} [s_1^0(+y_1^b, y_2, x_2, \tau) - s_1^0(-y_1^b, y_2, x_2, \tau)] \mathrm{d}y_2 = 0, \tag{2.15}$$

where we used the continuity of $\boldsymbol{s}^0 \cdot \boldsymbol{n}$ on $\partial\Omega_i$, (2.6e) and the periodicity conditions with respect to y_2. Taking the limit when $y_1^b \to +\infty$, we get the integrated jump condition:

$$[\![\sigma_1^0(\cdot, x_2, \tau)]\!] = 0. \tag{2.16}$$

Remark 3. *We assume that v^0 and σ_1^0 are sufficiently smooth so that $\frac{\partial}{\partial\zeta}[\![v^0(\cdot, x_2, \tau)]\!] = [\![\frac{\partial}{\partial\zeta} v^0(\cdot, x_2, \tau)]\!]$ and $\frac{\partial}{\partial\zeta}[\![\sigma_1^0(\cdot, x_2, \tau)]\!] = [\![\frac{\partial}{\partial\zeta}\sigma_1^0(\cdot, x_2, \tau)]\!]$ for $\zeta = x_2$ or $\zeta = \tau$. Hence equations (2.13) and (2.16) imply:*

$$\left[\!\!\left[\frac{\partial}{\partial\zeta} v^0(\cdot, x_2, \tau) \right]\!\!\right] = 0, \tag{2.17}$$

and

$$\left[\!\!\left[\frac{\partial}{\partial\zeta} \sigma_1^0(\cdot, x_2, \tau) \right]\!\!\right] = 0, \tag{2.18}$$

for $\zeta = x_2$ or τ.

2.1.3.2 Jump conditions at the order $\mathcal{O}(\eta)$

■ *Jump condition for v^1.* Due to the continuity condition (2.18) with $\zeta = \tau$ and based on (2.6a), we get that $\partial v^0/\partial x_1$ is continuous at $x_1 = 0$. Thus, from (2.12a), one obtains the jump condition:

$$[\![v^1(\cdot, x_2, \tau)]\!] = \lim_{y_1 \to +\infty} \left[w^1(y_1, y_2, x_2, \tau) - w^1(-y_1, y_2, x_2, \tau) - 2y_1 \frac{\partial v^0}{\partial x_1}(0, x_2, \tau) \right]. \tag{2.19}$$

At this point, an expression for w_1 is needed. For this purpose, we combine (2.5b), (2.6c), (2.14), (2.11b), (2.6a) and the fact that $\partial \boldsymbol{s}^0/\partial\tau \cdot \boldsymbol{n} = \partial \boldsymbol{s}_i^0/\partial\tau \cdot \boldsymbol{n} = 0$ on $\partial\Omega_i$ due to (2.6e). Then, one obtains that the field w^1 is part of the following problem:

$$\begin{cases} \boldsymbol{\nabla}_y \cdot \dfrac{\partial \boldsymbol{s}^0}{\partial\tau} = 0 & \text{in } \Omega\backslash\Omega_i, \\ \dfrac{\partial \boldsymbol{s}^0}{\partial\tau} = \dfrac{\partial v^0}{\partial x_2}(0, x_2, \tau)\boldsymbol{e}_2 + \boldsymbol{\nabla}_y w^1 & \text{in } \Omega\backslash\Omega_i, \\ \dfrac{\partial \boldsymbol{s}^0}{\partial\tau} \cdot \boldsymbol{n} = 0 & \text{on } \partial\Omega_i, \\ \lim\limits_{y_1 \to \pm\infty} \dfrac{\partial \boldsymbol{s}^0}{\partial\tau} = \boldsymbol{\nabla}_x v^0(0, x_2, \tau). \end{cases} \tag{2.20}$$

The problem above being linear with respect to $\frac{\partial v^0}{\partial x_1}(0,x_2,\tau)$ and $\frac{\partial v^0}{\partial x_2}(0,x_2,\tau)$, the field w^1 can be written as

$$w^1(\boldsymbol{y},x_2,\tau)=\frac{\partial v^0}{\partial x_1}(0,x_2,\tau)[\Phi^{(1)}(\boldsymbol{y})+y_1]+\frac{\partial v^0}{\partial x_2}(0,x_2,\tau)\Phi^{(2)}(\boldsymbol{y})+\tilde{w}(x_2,\tau), \tag{2.21}$$

where the field $\tilde{w}$ does not depend on $\boldsymbol{y}$ and will not play any role in the following. For $j=1,2$ the fields $\Phi^{(j)}$ are y_2-periodic and solutions of:

$$\begin{cases} \Delta_{\boldsymbol{y}}\Phi^{(j)}(\boldsymbol{y})=0 & \text{in } \Omega\backslash\Omega_i,\\ [\boldsymbol{\nabla}_{\boldsymbol{y}}\Phi^{(j)}(\boldsymbol{y})+\boldsymbol{e}_j]\cdot\boldsymbol{n}=0 & \text{on } \partial\Omega_i,\\ \lim\limits_{y_1\to\pm\infty}\boldsymbol{\nabla}_{\boldsymbol{y}}\Phi^{(j)}(y_1,y_2)=\boldsymbol{0}. \end{cases} \tag{2.22}$$

Owing to the third equation in (2.22), some constants $\mathcal{B}_j$ are introduced for $j=1,2$ as

$$\mathcal{B}_j=\lim_{y_1\to+\infty}\left[\Phi^{(j)}(y_1,y_2)-\Phi^{(j)}(-y_1,y_2)\right]. \tag{2.23}$$

Since $\Phi^{(j)}\in L^2_{\text{loc}}(\Omega)$ and $\boldsymbol{\nabla}\Phi^{(j)}\in L^2(\Omega)$ the constants are well defined. Furthermore, due to their definition, the fact that $\Phi^{(j)}$ is defined up to a constant in (2.22) will not be a problem. Finally, inserting (2.21) in (2.19) leads to

$$[\![v^1(\cdot,x_2,\tau)]\!]=\mathcal{B}_1\frac{\partial v^0}{\partial x_1}(0,x_2,\tau)+\mathcal{B}_2\frac{\partial v^0}{\partial x_2}(0,x_2,\tau). \tag{2.24}$$

■ *Jump condition for σ_1^1.* Using both (2.17) and (2.18) with $\zeta=x_2$ and $\zeta=\tau$ together with (2.6a) and (2.6b) implies that $\frac{\partial}{\partial x_1}\sigma_1^0(\cdot,x_2,\tau)$ is continuous at $x_1=0$. The equation (2.12b) integrated along $y_2\in[-1/2,1/2]$ provides the jump condition for σ_1^1:

$$[\![\sigma_1^1(\cdot,x_2,\tau)]\!]=\lim_{y_1^b\to+\infty}\int_{-\frac{1}{2}}^{\frac{1}{2}}\left[s_1^1(y_1^b,y_2,x_2,\tau)-s_1^1(-y_1^b,y_2,x_2,\tau)\right]\mathrm{d}y_2-2y_1^b\frac{\partial\sigma_1^0}{\partial x_1}(0,x_2,\tau).$$

We start with (2.6d) integrated on $\Omega^b\backslash\Omega_i$:

$$\underbrace{\int_{\Omega^b\backslash\Omega_i}\frac{\partial w^0}{\partial\tau}\,\mathrm{d}\boldsymbol{y}}_{I_1}\underbrace{-\int_{\Omega^b\backslash\Omega_i}\frac{\partial\boldsymbol{s}^0}{\partial x_2}\cdot\boldsymbol{e}_2\,\mathrm{d}\boldsymbol{y}}_{I_2}\underbrace{-\int_{\Omega^b\backslash\Omega_i}\boldsymbol{\nabla}_{\boldsymbol{y}}\cdot\boldsymbol{s}^1\,\mathrm{d}\boldsymbol{y}}_{I_3}=0.$$

We introduce the parameter φ satisfying $0<\varphi<1$ and such that $S_i=\frac{e\varphi}{h}$ is the surface of the inclusion in $\boldsymbol{y}$-coordinates. Due to (2.14), the first integral I_1 can be computed:

$$I_1=\frac{\partial v^0}{\partial\tau}(0,x_2,\tau)\left[2y_1^b-\frac{e\varphi}{h}\right]. \tag{2.25}$$

The derivative $\frac{\partial}{\partial\tau}s_2^0(\boldsymbol{y},x_2,\tau)$ can be expressed thanks to the cell functions defined in (2.22) using the second equation of (2.20) together with (2.21) and (2.6a):

$$\frac{\partial s_2^0}{\partial\tau}(\boldsymbol{y},x_2,\tau)=\frac{\partial\sigma_1^0}{\partial\tau}(0,x_2,\tau)\frac{\partial\Phi^{(1)}}{\partial y_2}(\boldsymbol{y})+\frac{\partial\sigma_2^0}{\partial\tau}(0,x_2,\tau)\left[\frac{\partial\Phi^{(2)}}{\partial y_2}(\boldsymbol{y})+1\right]. \tag{2.26}$$

Integrating (2.26) in time and differentiating it with respect to x_2, the second integral I_2 writes:

$$I_2 = -\frac{\partial \sigma_1^0}{\partial x_2}(0,x_2,\tau)\int_{\Omega^b\setminus\Omega_i}\frac{\partial \Phi^{(1)}}{\partial y_2}(\boldsymbol{y})\,\mathrm{d}\boldsymbol{y} - \frac{\partial \sigma_2^0}{\partial x_2}(0,x_2,\tau)\left[\int_{\Omega^b\setminus\Omega_i}\frac{\partial \Phi^{(2)}}{\partial y_2}(\boldsymbol{y})\,\mathrm{d}\boldsymbol{y} + 2y_1^b - \frac{e\varphi}{h}\right]. \tag{2.27}$$

Owing to the periodicity of $\boldsymbol{s}^1$ with respect to y_2 and introducing the curvilinear abscissa ℓ on $\partial\Omega_i$, with $\boldsymbol{n}$ being the associated *inward* unit normal, then I_3 can be expressed as

$$I_3 = -\int_{-\frac{1}{2}}^{\frac{1}{2}}[s_1^1(y_1^b,y_2,x_2,\tau) - s_1^1(-y_1^b,y_2,x_2,\tau)]\,\mathrm{d}y_2 - \int_{\partial\Omega_i}\boldsymbol{s}^1\cdot\boldsymbol{n}\,\mathrm{d}\ell.$$

Due to the continuity condition $\boldsymbol{s}^1\cdot\boldsymbol{n} = \boldsymbol{s}_i^1\cdot\boldsymbol{n}$ on $\partial\Omega_i$, the second term in I_3 can be recast as

$$-\int_{\partial\Omega_i}\boldsymbol{s}^1\cdot\boldsymbol{n}\,\mathrm{d}\ell = \int_{\Omega_i}\nabla_{\boldsymbol{y}}\cdot\boldsymbol{s}_i^1\,\mathrm{d}\boldsymbol{y}.$$

We now use (2.6f) together with (2.7) and (2.8). For the boundary condition, the continuity condition $w^j = w_i^j$ on $\partial\Omega_i$ and (2.5a) with (2.11a) is used. Then, the field $\boldsymbol{s}_i^1$ satisfies

$$\begin{cases}\dfrac{\partial \boldsymbol{s}_i^1}{\partial\tau}(\boldsymbol{y},x_2,\tau) = \dfrac{\mu_0}{\mu_m}\nabla_{\boldsymbol{y}}\,w_i^0(\boldsymbol{y},x_2,\tau) & (\boldsymbol{y}\in\Omega_i),\\[2ex] \dfrac{\rho_i}{\rho_m}\dfrac{\partial w_i^0}{\partial\tau}(\boldsymbol{y},x_2,\tau) = \nabla_{\boldsymbol{y}}\cdot\boldsymbol{s}_i^1(\boldsymbol{y},x_2,\tau) & (\boldsymbol{y}\in\Omega_i),\\ w_i^0(\boldsymbol{y},x_2,\tau) = v^0(0,x_2,\tau) & (\boldsymbol{y}\in\partial\Omega_i).\end{cases}$$

Therefore, one concludes that the field w_i^0 is solution of

$$\begin{cases}\dfrac{\rho_i}{\rho_m}\dfrac{\partial^2 w_i^0}{\partial\tau^2}(\boldsymbol{y},x_2,\tau) - \dfrac{\mu_0}{\mu_m}\Delta_{\boldsymbol{y}}w_i^0(\boldsymbol{y},x_2,\tau) = 0 & (\boldsymbol{y}\in\Omega_i),\\ w_i^0(\boldsymbol{y},x_2,\tau) = v^0(0,x_2,\tau) & (\boldsymbol{y}\in\partial\Omega_i),\end{cases} \tag{2.28}$$

and one can rewrite

$$I_3 = -\int_{-\frac{1}{2}}^{\frac{1}{2}}[s_1^1(y_1^b,y_2,x_2,\tau) - s_1^1(-y_1^b,y_2,x_2,\tau)]\,\mathrm{d}y_2 + \frac{\rho_i}{\rho_m}\int_{\Omega_i}\frac{\partial w_i^0}{\partial\tau}\,\mathrm{d}\boldsymbol{y}. \tag{2.29}$$

Collecting the three integrals (2.25), (2.27) and (2.29) and using (2.6b), one gets

$$\begin{aligned}&\int_{-\frac{1}{2}}^{\frac{1}{2}}[s_1^1(y_1^b,y_2,x_2,\tau) - s_1^1(-y_1^b,y_2,x_2,\tau)]\,\mathrm{d}y_2 - 2y_1^b\frac{\partial\sigma_1^0}{\partial x_1}(0,x_2,\tau) = -\frac{e\varphi}{h}\frac{\partial\sigma_1^0}{\partial x_1}(0,x_2,\tau)\\ &\quad - \frac{\partial\sigma_1^0}{\partial x_2}(0,x_2,\tau)\int_{\Omega^b\setminus\Omega_i}\frac{\partial\Phi^{(1)}}{\partial y_2}(\boldsymbol{y})\,\mathrm{d}\boldsymbol{y} - \frac{\partial\sigma_2^0}{\partial x_2}(0,x_2,\tau)\int_{\Omega^b\setminus\Omega_i}\frac{\partial\Phi^{(2)}}{\partial y_2}(\boldsymbol{y})\,\mathrm{d}\boldsymbol{y} + \frac{\rho_i}{\rho_m}\int_{\Omega_i}\frac{\partial w_i^0}{\partial\tau}\,\mathrm{d}\boldsymbol{y}.\end{aligned} \tag{2.30}$$

Introducing the following two parameters

$$C_j = -\int_{\Omega\setminus\Omega_i}\frac{\partial\Phi^{(j)}}{\partial y_2}(\boldsymbol{y})\,\mathrm{d}\boldsymbol{y} \qquad \text{for } j=1,2 \tag{2.31}$$

and taking the limit $y_1^b\to+\infty$ in (2.30) finally entails the following jump condition

$$[\![\sigma_1^1(\cdot,x_2,\tau)]\!] = -\frac{e\varphi}{h}\frac{\partial\sigma_1^0}{\partial x_1}(0,x_2,\tau) + C_1\frac{\partial\sigma_1^0}{\partial x_2}(0,x_2,\tau) + C_2\frac{\partial\sigma_2^0}{\partial x_2}(0,x_2,\tau) + \frac{\rho_i}{\rho_m}\int_{\Omega_i}\frac{\partial w_i^0}{\partial\tau}\,\mathrm{d}\boldsymbol{y}. \tag{2.32}$$

2.1.3.3 Final effective jump conditions

The jump conditions derived in the previous sections are associated with an interface of zero thickness as one considers jumps in the limit $x_1 \longrightarrow 0^{\pm}$. Yet, it is proven in Marigo and Maurel, 2016a and Marigo et al., 2017a that a non-zero thickness a allows to define an interface energy $\mathcal{E}_a$, which would in turn ensure the stability of the effective model which means that V and $\boldsymbol{\Sigma}$ are bounded (Delourme et al., 2012). In practice, this condition prevents from instabilities which appear when the interface term $\mathcal{E}_a \longrightarrow -\infty$ as time increases and is compensated by a bulk energy term $\mathcal{E} \longrightarrow +\infty$ (Delourme et al., 2021).

Using such an energy-based argument, we will justify in the next section that an enlarged interface is also required in the resonant case considered here. Meanwhile, the present section establishes the final effective jump conditions expressed relatively to an enlarged interface of thickness $a > 0$ in the original system of space coordinates with $a/h = O(1)$. The effective jump conditions thus obtained are equivalent up to order $O(\eta^2)$ to the ones formulated in Section 2.1.3.2.

One considers the definition (1.9) of the jump and the mean value around a centered enlarged interface. Setting $f = v_\eta(\cdot, x_2, \tau)$ or $f = \sigma_{1\eta}(\cdot, x_2, \tau)$, we seek asymptotics of the form:

$$\llbracket f \rrbracket_{k_m a} = \llbracket f^0 \rrbracket_{k_m a} + \eta \llbracket f^1 \rrbracket_{k_m a} + O(\eta^2). \tag{2.33}$$

To do so, we consider the following Taylor expansions between $0^{\pm}$ and $\pm k_m a/2$ for the function f defined above

$$\begin{cases} \llbracket f^0 \rrbracket = \llbracket f^0 \rrbracket_{k_m a} - \eta \dfrac{a}{h} \left\langle\!\!\left\langle \dfrac{\partial f^0}{\partial x_1} \right\rangle\!\!\right\rangle_{k_m a} + O(\eta^2), \\ \llbracket f^1 \rrbracket = \llbracket f^1 \rrbracket_{k_m a} + O(\eta). \end{cases} \tag{2.34}$$

Likewise for $g = \partial v^0/\partial x_j(\cdot, x_2, \tau)$ or $g = \partial \sigma_k^0/\partial x_j(\cdot, x_2, \tau)$ with $j, k = 1, 2$ one considers

$$g(0) = \left\langle\!\!\left\langle g \right\rangle\!\!\right\rangle_{k_m a} + O(\eta). \tag{2.35}$$

Due to (2.35), the solution to (2.28) is expanded as $w_i^0 = w_i + O(\eta)$ where the field w_i is solution to the inner problem

$$\begin{cases} \dfrac{\rho_i}{\rho_m} \dfrac{\partial^2 w_i}{\partial \tau^2}(\boldsymbol{y}, x_2, \tau) - \dfrac{\mu_0}{\mu_m} \Delta_{\boldsymbol{y}} w_i(\boldsymbol{y}, x_2, \tau) = 0 & (\boldsymbol{y} \in \Omega_i), \\ w_i(\boldsymbol{y}, x_2, \tau) = \langle\!\langle v(\cdot, x_2, \tau) \rangle\!\rangle_{k_m a} & (\boldsymbol{y} \in \partial\Omega_i). \end{cases} \tag{2.36}$$

Introducing the following coefficients

$$\mathcal{S} = \frac{a}{h} - \frac{e\varphi}{h} \qquad \text{and} \qquad \mathcal{B} = \frac{a}{h} + \mathcal{B}_1, \tag{2.37}$$

then combining the equations (2.33–2.35), (2.13), (2.24), (2.16), (2.32) and (2.36), we get

$$\begin{cases} \llbracket v_\eta \rrbracket_{k_m a} = \eta \left\{ \mathcal{B} \left\langle\!\!\left\langle \dfrac{\partial v_\eta}{\partial x_1} \right\rangle\!\!\right\rangle_{k_m a} + \mathcal{B}_2 \left\langle\!\!\left\langle \dfrac{\partial v_\eta}{\partial x_2} \right\rangle\!\!\right\rangle_{k_m a} \right\} + O(\eta^2), \\ \llbracket \sigma_{1\eta} \rrbracket_{k_m a} = \eta \left\{ \mathcal{S} \left\langle\!\!\left\langle \dfrac{\partial \sigma_{1\eta}}{\partial x_1} \right\rangle\!\!\right\rangle_{k_m a} + C_1 \left\langle\!\!\left\langle \dfrac{\partial \sigma_{1\eta}}{\partial x_2} \right\rangle\!\!\right\rangle_{k_m a} + C_2 \left\langle\!\!\left\langle \dfrac{\partial \sigma_{2\eta}}{\partial x_2} \right\rangle\!\!\right\rangle_{k_m a} + \dfrac{\rho_i}{\rho_m} \displaystyle\int_{\Omega_i} \dfrac{\partial w_i}{\partial \tau} \, \mathrm{d}\boldsymbol{y} \right\} + O(\eta^2). \end{cases}$$

We now consider the associated approximation of the fields, as $(v, \boldsymbol{\sigma}) = (v^0 + \eta v^1, \boldsymbol{\sigma}^0 + \eta \boldsymbol{\sigma}^1)$, which are solution to (2.2) in the matrix domain while satisfying the jump conditions above but truncated at the second order. These fields are then transposed to the original coordinate system $(\boldsymbol{X}, t)$, as $(V, \boldsymbol{\Sigma})$, see Figure 2.1. This finally yields the following effective model at order $O(\eta)$:

Result 2.1: Resonant jump conditions in the time domain

$$\begin{cases} \dfrac{\partial \boldsymbol{\Sigma}}{\partial t} = \mu_m \boldsymbol{\nabla} V & (|X_1| \geq a/2,\ X_2 \in \mathbb{R}), \\ \rho_m \dfrac{\partial V}{\partial t} = \boldsymbol{\nabla} \cdot \boldsymbol{\Sigma} & (|X_1| \geq a/2,\ X_2 \in \mathbb{R}), \\ [\![V]\!]_a = h \left\{ \mathcal{B} \left\langle\!\!\left\langle \dfrac{\partial V}{\partial X_1} \right\rangle\!\!\right\rangle_a + \mathcal{B}_2 \left\langle\!\!\left\langle \dfrac{\partial V}{\partial X_2} \right\rangle\!\!\right\rangle_a \right\} & (X_2 \in \mathbb{R}), \\ [\![\Sigma_1]\!]_a = h \left\{ \mathcal{S} \left\langle\!\!\left\langle \dfrac{\partial \Sigma_1}{\partial X_1} \right\rangle\!\!\right\rangle_a + \mathcal{C}_1 \left\langle\!\!\left\langle \dfrac{\partial \Sigma_1}{\partial X_2} \right\rangle\!\!\right\rangle_a + \mathcal{C}_2 \left\langle\!\!\left\langle \dfrac{\partial \Sigma_2}{\partial X_2} \right\rangle\!\!\right\rangle_a + \rho_i \displaystyle\int_{\Omega_i} \dfrac{\partial W_i}{\partial t} \, \mathrm{d}\boldsymbol{y} \right\} & (X_2 \in \mathbb{R}). \end{cases} \tag{2.38}$$

In (2.38), $W_i(\boldsymbol{y}, X_2, t) = \sqrt{\frac{\mu_m}{\rho_m}}\, w_i(\boldsymbol{y}, x_2, \tau)$ so that W_i is solution of

$$\begin{cases} \dfrac{\partial \boldsymbol{\Sigma}_i}{\partial t}(\boldsymbol{y}, X_2, t) = \dfrac{\mu_i}{h} \boldsymbol{\nabla}_{\boldsymbol{y}} W_i(\boldsymbol{y}, X_2, t) & (\boldsymbol{y} \in \Omega_i), \\ \rho_i \dfrac{\partial W_i}{\partial t}(\boldsymbol{y}, X_2, t) = \dfrac{1}{h} \boldsymbol{\nabla}_{\boldsymbol{y}} \cdot \boldsymbol{\Sigma}_i(\boldsymbol{y}, X_2, t) & (\boldsymbol{y} \in \Omega_i), \\ W_i(\boldsymbol{y}, X_2, t) = \langle\!\langle V(\cdot, X_2, t) \rangle\!\rangle_a & (\boldsymbol{y} \in \partial\Omega_i). \end{cases} \tag{2.39}$$

One notices that the field W_i is a function of X_2 through the prescribed boundary condition $\langle\!\langle V(\cdot, X_2, t) \rangle\!\rangle_a$. The five effective parameters $\mathcal{B}$, $\mathcal{B}_2$, $\mathcal{S}$, $\mathcal{C}_1$ and $\mathcal{C}_2$ are given by (2.37), (2.23), and (2.31).

Remark 4. *When $\rho_i = 0$, as it is in the case when the inclusions are replaced by voids, the resonant term $\rho_i \int_{\Omega_i} \frac{\partial W_i}{\partial t} \mathrm{d}\boldsymbol{y}$ in (2.38) vanishes. Therefore, when the contribution of the resonances is not activated, one recovers the model of Marigo and Maurel, 2016a.*

Remark 5. *The equivalence between this model and the one obtained in the frequency-domain (1.19) in Pham et al., 2017 is assessed in Appendix 2.A and is based on the fact that*

$$\mathscr{F}\left[\rho_i \int_{\Omega_i} \frac{\partial W_i}{\partial t} \mathrm{d}\boldsymbol{y} \right] = \mathscr{D}_\infty(\omega) \left\langle\!\!\left\langle \boldsymbol{\nabla} \cdot \hat{\boldsymbol{\Sigma}} \right\rangle\!\!\right\rangle_a . \tag{2.40}$$

2.2 Energy analysis

2.2.1 Balance of energy

One advantage of the time-domain formulation is the possibility to perform an energy analysis, which is studied in this section. In the original microstructured configuration, a bounded domain $D = \cup_i D_i \cup D_m$ is considered in order to define the elastic energy for all time $t \geq 0$

$$\mathcal{E}_h(t) = \frac{1}{2} \int_D \left\{ \frac{1}{\mu_h(\boldsymbol{X})} (\boldsymbol{\Sigma}_h(\boldsymbol{X}, t))^2 + \rho_h(\boldsymbol{X}) (V_h(\boldsymbol{X}, t))^2 \right\} \mathrm{d}\boldsymbol{X}, \tag{2.41}$$

to get the conservation identity

$$\frac{\mathrm{d}}{\mathrm{d}t} \mathcal{E}_h(t) = 0. \tag{2.42}$$

Accordingly, in the homogenized problem, the elastic energy has to be defined in the bounded domain $D \backslash D_a$ that excludes the enlarged interface of width a, see Figure 2.3. In this configuration,

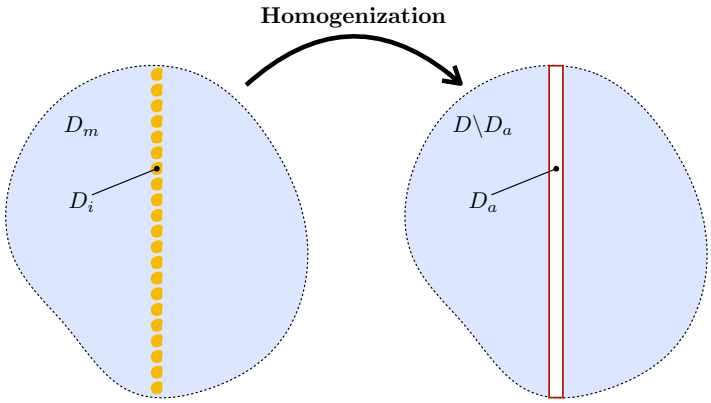

Figure 2.3 – *(left)* Domain $D = \cup_i D_i \cup D_m$ considered for the energy analysis in the original microstructured configuration, *(right)* domain $D\backslash D_a$ for the analysis of the effective problem.

a term $\mathcal{E}_a$ will be associated to the jump conditions at the effective interface. We expect it to account for the *bulk* energy of the microstructured region of thickness e in the original problem, so that $\mathcal{E}_a \geq 0$ is expected.

Multiplying the first equation of (2.38) by $\boldsymbol{\Sigma}$, the second by V, then after summation and integration over $D\backslash D_a$ one obtains:

$$\frac{\mathrm{d}}{\mathrm{d}t}\underbrace{\frac{1}{2}\int_{D\backslash D_a}\left\{\frac{1}{\mu_m}(\boldsymbol{\Sigma})^2+\rho_m(V)^2\right\}\mathrm{d}\boldsymbol{X}}_{\mathcal{E}}+\underbrace{\int_I [\![V\boldsymbol{\Sigma}\cdot\boldsymbol{e}_1]\!]_a\,\mathrm{d}X_2}_{\frac{\mathrm{d}}{\mathrm{d}t}\mathcal{E}_a}+\int_{\partial D}V\boldsymbol{\Sigma}\cdot\boldsymbol{n}\,\mathrm{d}\ell=0, \tag{2.43}$$

where the interval I is defined as $I = \{X_2 : \boldsymbol{X} \in D_a\}$ and $\boldsymbol{n}$ is the *inward* unit normal on ∂D. $\mathcal{E}$ and $\mathcal{E}_a$ are respectively *bulk* and *interface* energy terms. The third term involves the velocity and the normal component of the stress vector on the boundaries of the domain D. We assume that these wavefields have a compact support so that this third term vanishes if D is chosen large enough.

Focusing on the term $\mathcal{E}_a$, then using the relation $[\![fg]\!]_a = [\![f]\!]_a \langle\!\langle g\rangle\!\rangle_a + [\![g]\!]_a \langle\!\langle f\rangle\!\rangle_a$ together with the jump conditions of (2.38) one obtains

$$\begin{aligned}\frac{\mathrm{d}}{\mathrm{d}t}\mathcal{E}_a = &\int_I h\left\{\mathcal{B}\left\langle\!\!\left\langle\frac{\partial V}{\partial X_1}\right\rangle\!\!\right\rangle_a+\mathcal{B}_2\left\langle\!\!\left\langle\frac{\partial V}{\partial X_2}\right\rangle\!\!\right\rangle_a\right\}\langle\!\langle\Sigma_1\rangle\!\rangle_a\,\mathrm{d}X_2\\&+\int_I h\left\{\mathcal{S}\left\langle\!\!\left\langle\frac{\partial \Sigma_1}{\partial X_1}\right\rangle\!\!\right\rangle_a+\mathcal{C}_1\left\langle\!\!\left\langle\frac{\partial \Sigma_1}{\partial X_2}\right\rangle\!\!\right\rangle_a+\mathcal{C}_2\left\langle\!\!\left\langle\frac{\partial \Sigma_2}{\partial X_2}\right\rangle\!\!\right\rangle_a\right\}\langle\!\langle V\rangle\!\rangle_a\,\mathrm{d}X_2+\mathcal{J},\end{aligned}$$

where one has defined

$$\mathcal{J} = h\rho_i\int_I\left\{\int_{\Omega_i}\frac{\partial W_i}{\partial t}(\boldsymbol{y},X_2,t)\,\mathrm{d}\boldsymbol{y}\right\}\langle\!\langle V\rangle\!\rangle_a\,\mathrm{d}X_2. \tag{2.44}$$

The first two relations of (2.38) and integration by parts lead to

$$\begin{aligned}\frac{\mathrm{d}}{\mathrm{d}t}\mathcal{E}_a = \beta+\frac{h}{2}\frac{\mathrm{d}}{\mathrm{d}t}\int_I\left\{\mathcal{S}\rho_m\langle\!\langle V\rangle\!\rangle_a^2+\frac{\mathcal{B}}{\mu_m}\langle\!\langle\Sigma_1\rangle\!\rangle_a^2+\frac{\mathcal{S}-\mathcal{C}_2}{\mu_m}\langle\!\langle\Sigma_2\rangle\!\rangle_a^2\right\}\mathrm{d}X_2\\+h(\mathcal{B}_2-\mathcal{C}_1)\int_I\left\langle\!\!\left\langle\frac{\partial V}{\partial X_2}\right\rangle\!\!\right\rangle_a\langle\!\langle\Sigma_1\rangle\!\rangle_a+\mathcal{J},\end{aligned}$$

where β is a boundary term on ∂I.

Adapting the proof of Appendix A in Marigo et al., 2017a with an integration in the domain $\Omega\backslash\Omega_i$, one proves the following property.

Property 1. *The effective parameters $\mathcal{B}_2$ and C_1 defined in (2.23) and (2.31) satisfy*

$$\mathcal{B}_2 = C_1.$$

Proof. First, we establish a formal relation that will be used several times to perform the energy analysis. To do so, we consider a function $\tilde{\Phi} \in H^1_{\text{loc}}(\Omega\backslash\Omega_i)$ which is at most constant when $|y_1|$ goes to infinity and which is y_2-periodic. Then, the first equation of (2.22) is multiplied by $\tilde{\Phi}$ and integrated by parts. Using the boundary conditions, one obtains:

$$\int_{\Omega\backslash\Omega_i} \left[\nabla_{\boldsymbol{y}} \Phi^{(j)}(\boldsymbol{y}) + \boldsymbol{e}_j\right] \cdot \nabla_{\boldsymbol{y}} \tilde{\Phi}(\boldsymbol{y})\, \mathrm{d}\boldsymbol{y} - \lim_{y_1 \to +\infty} \int_{-1/2}^{1/2} \left[\tilde{\Phi}(y_1, y_2) - \tilde{\Phi}(-y_1, y_2)\right] \boldsymbol{e}_1 \cdot \boldsymbol{e}_j \, \mathrm{d}y_2 = 0. \quad (2.45)$$

Remark 6. *The equation (2.45) is a formal relation used in this part in order to obtain a lower bound for the effective parameters. However, this does not constitute a well-posed variational formulation. This would require to introduce suitable functional spaces and Dirichlet-to-Neumann operators in order to reformulate the problem in a bounded domain.*

■ *An expression for $\mathcal{B}_2$.* First, we consider the formal relation (2.45) that is satisfied by the field $\Phi^{(1)}$ with $\tilde{\Phi} = \Phi^{(2)}$. It yields

$$\mathcal{B}_2 = \int_{\Omega\backslash\Omega_i} \nabla_{\boldsymbol{y}} \Phi^{(1)}(\boldsymbol{y}) \cdot \nabla_{\boldsymbol{y}} \Phi^{(2)}(\boldsymbol{y})\, \mathrm{d}\boldsymbol{y} + \int_{\Omega\backslash\Omega_i} \nabla_{\boldsymbol{y}} \Phi^{(2)} \cdot \boldsymbol{e}_1 \, \mathrm{d}\boldsymbol{y}. \quad (2.46)$$

To have an explicit expression of the last term, we multiply the second cell problem (2.22) by the function y_1 and we integrate in the bounded domain $\Omega^b\backslash\Omega_i$, i.e.

$$\int_{\Omega^b\backslash\Omega_i} \Delta_{\boldsymbol{y}}(\Phi^{(2)} + y_2) y_1 \, \mathrm{d}\boldsymbol{y} = 0.$$

By integration by parts and due to the periodicity and boundary conditions for $\Phi^{(2)}$, this equation leads to

$$\int_{-1/2}^{1/2} \left[\nabla_{\boldsymbol{y}} \Phi^{(2)}(-y_1^b, y_2) + \nabla_{\boldsymbol{y}} \Phi^{(2)}(y_1^b, y_2)\right] \cdot y_1^b \boldsymbol{e}_1 \, \mathrm{d}y_2 - \int_{\Omega^b\backslash\Omega_i} \nabla_{\boldsymbol{y}} \Phi^{(2)} \cdot \boldsymbol{e}_1 \, \mathrm{d}\boldsymbol{y} = 0. \quad (2.47)$$

One can define the half-strips $]-\infty; -e/h[\times[-1/2; 1/2]$ and $]e/h; +\infty[\times[-1/2; 1/2]$ where $\Phi^{(2)}$ is harmonic. Then, due to the modal decomposition, it is straightforward that

$$\lim_{y_1 \to \pm\infty} \left[y_1 \nabla_{\boldsymbol{y}} \Phi^{(2)}(y_1, y_2)\right] = 0.$$

Consequently, due to (2.47) and (2.46)

$$\mathcal{B}_2 = \int_{\Omega\backslash\Omega_i} \nabla_{\boldsymbol{y}} \Phi^{(1)}(\boldsymbol{y}) \cdot \nabla_{\boldsymbol{y}} \Phi^{(2)}(\boldsymbol{y})\, \mathrm{d}\boldsymbol{y}. \quad (2.48)$$

■ *An expression for C_1.* We now consider the formal relation (2.45) that is satisfied by the field $\Phi^{(2)}$ with $\tilde{\Phi} = \Phi^{(1)}$. It yields

$$C_1 = \int_{\Omega\backslash\Omega_i} \nabla_{\boldsymbol{y}} \Phi^{(1)} \cdot \nabla_{\boldsymbol{y}} \Phi^{(2)} \, \mathrm{d}\boldsymbol{y}.$$

Combined with (2.48) this concludes the proof. □

As a consequence, the term involving $\mathcal{E}_a$ reduces to

$$\frac{\mathrm{d}}{\mathrm{d}t}\mathcal{E}_a = \beta + \frac{h}{2}\frac{\mathrm{d}}{\mathrm{d}t}\int_I \left\{ \mathcal{S}\rho_m \langle\!\langle V \rangle\!\rangle_a^2 + \frac{\mathcal{B}}{\mu_m}\langle\!\langle \Sigma_1 \rangle\!\rangle_a^2 + \frac{\mathcal{S}-C_2}{\mu_m}\langle\!\langle \Sigma_2 \rangle\!\rangle_a^2 \right\} \mathrm{d}X_2 + \mathcal{J}. \tag{2.49}$$

Next, we want to express $\mathcal{J}$ in (2.44) as a quadratic form. To do so, we use the field equations and the boundary conditions in (2.39) to rewrite $\mathcal{J}$ as follows:

$$\begin{aligned}\mathcal{J} &= -\int_I \int_{\partial\Omega_i} \boldsymbol{\Sigma}_i(\boldsymbol{y}, X_2, t)\cdot\boldsymbol{n}\, \langle\!\langle V(\cdot, X_2, t)\rangle\!\rangle_a \,\mathrm{d}\boldsymbol{y}\,\mathrm{d}X_2, \\ &= \int_I \int_{\Omega_i} \left\{ W_i\, \boldsymbol{\nabla}_{\boldsymbol{y}}\cdot\boldsymbol{\Sigma}_i + \boldsymbol{\Sigma}_i\cdot\boldsymbol{\nabla}_{\boldsymbol{y}} W_i \right\} \mathrm{d}\boldsymbol{y}\,\mathrm{d}X_2,\end{aligned}$$

from which one gets

$$\mathcal{J} = \frac{1}{2}\frac{\mathrm{d}}{\mathrm{d}t}\int_I\int_{\Omega_i}\left\{ h\rho_i {W_i}^2 + \frac{h}{\mu_i}\left|\boldsymbol{\Sigma}_i\right|^2 \right\}\mathrm{d}\boldsymbol{y}\,\mathrm{d}X_2.$$

Finally, the interface term (2.49) is recast as

$$\begin{aligned}\frac{\mathrm{d}}{\mathrm{d}t}\mathcal{E}_a = \beta &+ \frac{h}{2}\frac{\mathrm{d}}{\mathrm{d}t}\int_I \left\{ \mathcal{S}\rho_m \langle\!\langle V \rangle\!\rangle_a^2 + \frac{\mathcal{B}}{\mu_m}\langle\!\langle \Sigma_1 \rangle\!\rangle_a^2 + \frac{\mathcal{S}-C_2}{\mu_m}\langle\!\langle \Sigma_2 \rangle\!\rangle_a^2 \right\} \mathrm{d}X_2 \\ &+ \frac{h}{2}\frac{\mathrm{d}}{\mathrm{d}t}\int_I\int_{\Omega_i}\left\{ \rho_i {W_i}^2 + \frac{1}{\mu_i}\left|\boldsymbol{\Sigma}_i\right|^2 \right\}\mathrm{d}\boldsymbol{y}\,\mathrm{d}X_2.\end{aligned} \tag{2.50}$$

To conclude, the bounded domain D is chosen sufficiently large so that the remaining boundary terms on ∂D in (2.43) and β on ∂I in (2.50) vanish. The identity (2.43) finally reads as the following conservation equation:

Result 2.2: Conservation equation

$$\frac{\mathrm{d}}{\mathrm{d}t}(\mathcal{E} + \mathcal{E}_a) = 0, \tag{2.51}$$

with $\mathcal{E}$ defined in (2.43) and

$$\mathcal{E}_a = \frac{h}{2}\int_I \left\{ \mathcal{S}\rho_m \langle\!\langle V \rangle\!\rangle_a^2 + \frac{\mathcal{B}}{\mu_m}\langle\!\langle \Sigma_1 \rangle\!\rangle_a^2 + \frac{\mathcal{S}-C_2}{\mu_m}\langle\!\langle \Sigma_2 \rangle\!\rangle_a^2 + \int_{\Omega_i}\left(\rho_i {W_i}^2 + \frac{1}{\mu_i}\left|\boldsymbol{\Sigma}_i\right|^2 \right)\mathrm{d}\boldsymbol{y} \right\}\mathrm{d}X_2. \tag{2.52}$$

2.2.2 Positivity of the interface term $\mathcal{E}_a$

Lastly, the term $\mathcal{E}_a$ has to be positive to represent an energy. In this case, (2.51) is a conservation equation for the total energy $(\mathcal{E} + \mathcal{E}_a)$, a sufficient condition for the continuous homogenized problem considered to be stable. Since $\mathcal{E}_a$ is a quadratic form, a sufficient condition for $\mathcal{E}_a \geq 0$ is $\mathcal{B} \geq 0$, $\mathcal{S} \geq 0$ and $(\mathcal{S} - C_2) \geq 0$. These three terms can be bounded below as follows:

- $\mathcal{S} \geq 0$ if and only if $a/e \geq \varphi$.
- $\mathcal{B} \geq 0$. This condition has been proved in the 3D case in Maurel, Pham, and Marigo, 2019b when $a = e$. For completeness, it is proved for all a in the 2D case in Section 2.2.2.1.
- $(\mathcal{S} - C_2) \geq 0$ if $a \geq e$. This condition has been proved in the 3D case in Maurel et al., 2019b when $a = e$. For completeness, it is proved for all a in the 2D case in Section 2.2.2.2.

Result 2.3: Stability

To sum up, provided that $a \geq e$ then $\mathcal{E}_a$ can be defined as an energy for all $0 < \varphi < 1$, which is associated with the effective interface of finite thickness a. In turn, Equation (2.51) ensures that the homogenized problem (2.38) is stable.

2.2.2.1 Positivity of the parameter $\mathcal{B}$

We seek a lower bound for the parameter $\mathcal{B}$ that is defined by (2.37) and (2.23). To do so, let us define the following quadratic functional:

$$\mathcal{L}(\tilde{\Phi}) = \int_{\Omega\backslash\Omega_i} \left[\frac{1}{2}\nabla_{\boldsymbol{y}}\tilde{\Phi}(\boldsymbol{y}) + \boldsymbol{e}_1\right] \cdot \nabla_{\boldsymbol{y}}\tilde{\Phi}(\boldsymbol{y})\,\mathrm{d}\boldsymbol{y} - \lim_{y_1\to+\infty} \int_{-1/2}^{1/2} \left[\tilde{\Phi}(y_1, y_2) - \tilde{\Phi}(-y_1, y_2)\right]\mathrm{d}y_2.$$

Due to the formal relation (2.45) for $\Phi^{(1)}$, one has for all $\tilde{\Phi} \in H^1_{\mathrm{loc}}(\Omega\backslash\Omega_i)$ at most constant when $|y_1| \mapsto \infty$ and y_2-periodic:

$$\mathcal{L}\left(\Phi^{(1)} + \tilde{\Phi}\right) - \mathcal{L}\left(\Phi^{(1)}\right) = \frac{1}{2}\int_{\Omega\backslash\Omega_i} |\nabla_{\boldsymbol{y}}\tilde{\Phi}(\boldsymbol{y})|^2\,\mathrm{d}\boldsymbol{y} \geq 0. \tag{2.53}$$

Consequently,

$$\mathcal{L}\left(\Phi^{(1)}\right) \leq \mathcal{L}\left(\tilde{\Phi}\right) \tag{2.54}$$

for all $\tilde{\Phi} \in H^1_{\mathrm{loc}}(\Omega\backslash\Omega_i)$ at most constant when $|y_1| \mapsto \infty$ and y_2-periodic. Moreover, one has

$$\mathcal{L}\left(\Phi^{(1)}\right) = -\frac{\mathcal{B}_1}{2} + \frac{1}{2}\int_{\Omega\backslash\Omega_i} \nabla_{\boldsymbol{y}}\Phi^{(1)} \cdot \boldsymbol{e}_1\,\mathrm{d}\boldsymbol{y}. \tag{2.55}$$

To have an explicit expression of the second term, we multiply the first cell problem (2.22) by the function y_1 and we integrate in the bounded domain $\Omega^b\backslash\Omega_i$, i.e.

$$\int_{\Omega^b\backslash\Omega_i} \Delta_{\boldsymbol{y}}(\Phi^{(1)} + y_1)y_1\,\mathrm{d}\boldsymbol{y} = 0.$$

By integration by parts and due to the periodicity and boundary conditions for $\Phi^{(1)}$, this equation leads to

$$\int_{-1/2}^{1/2} \left[\nabla_{\boldsymbol{y}}\Phi^{(1)}(-y_1^b, y_2) + \nabla_{\boldsymbol{y}}\Phi^{(1)}(y_1^b, y_2)\right] \cdot y_1^b \boldsymbol{e}_1\,\mathrm{d}y_2 + 2y_1^b - \int_{\Omega^b\backslash\Omega_i} \nabla_{\boldsymbol{y}}\Phi^{(1)} \cdot \boldsymbol{e}_1\,\mathrm{d}\boldsymbol{y} - \int_{\Omega^b\backslash\Omega_i} \mathrm{d}\boldsymbol{y} = 0.$$

Given that the last integral is equal to $(2y_1^b - e\varphi/h)$, then considering the previous identity in the limit $y_1^b \to +\infty$ entails

$$\int_{\Omega\backslash\Omega_i} \nabla_{\boldsymbol{y}}\Phi^{(1)} \cdot \boldsymbol{e}_1\,\mathrm{d}\boldsymbol{y} = \frac{e\varphi}{h},$$

and thus, from (2.55), one gets

$$\mathcal{L}\left(\Phi^{(1)}\right) = -\frac{\mathcal{B}_1}{2} + \frac{e\varphi}{2h}.$$

As a consequence and due to (2.54), one obtains the following lower bound for $\mathcal{B}_1$:

$$\mathcal{B}_1 \geq \frac{e\varphi}{h} - 2\mathcal{L}\left(\tilde{\Phi}\right) \tag{2.56}$$

for all $\tilde{\Phi} \in H^1_{\text{loc}}(\Omega\backslash\Omega_i)$, $\tilde{\Phi}$ at most constant when $|y_1| \mapsto \infty$ and y_2-periodic. To have an explicit bound, we define $\tilde{\Phi}$ as the piecewise linear function:

$$\tilde{\Phi}(\boldsymbol{y}) = 2\tilde{\beta}h\frac{y_1}{e} \quad \text{if } 0 \leq |y_1| \leq \frac{e}{2h} \quad \text{and} \quad \tilde{\Phi}(\boldsymbol{y}) = \tilde{\beta}\,\text{sign}(y_1) \quad \text{if } |y_1| \geq \frac{e}{2h}$$

with $\tilde{\beta}$ a constant, from which one gets:

$$\mathcal{L}\big(\tilde{\Phi}\big) = 2\frac{h}{e}(1-\varphi)\tilde{\beta}^2 - 2\tilde{\beta}\varphi.$$

As a quadratic function of $\tilde{\beta}$, then $\mathcal{L}\big(\tilde{\Phi}\big)$ reaches a minimum for $\tilde{\beta} = \frac{e\varphi}{2h(1-\varphi)}$, which inserted in (2.56) yields:

$$\mathcal{B}_1 \geq \frac{e\varphi}{h} + \frac{e\varphi^2}{h(1-\varphi)}.$$

To conclude, using (2.37), one finally obtains the following positive lower bound for $\mathcal{B}$:

$$\mathcal{B} \geq \frac{a}{h} + \frac{e\varphi}{h} + \frac{e\varphi^2}{h(1-\varphi)} \geq 0.$$

2.2.2.2 Positivity of the term $(\mathcal{S} - C_2)$

We seek a lower bound for the term $(\mathcal{S} - C_2)$ that is featured in (2.52) and is defined by (2.37) and (2.31). Let us introduce $\boldsymbol{\Psi}^{(2)} = (\nabla_{\boldsymbol{y}}\Phi^{(2)} + \boldsymbol{e}_2)$ and the following admissibility space:

$$\mathcal{W}^{\text{per}}(\Omega\backslash\Omega_i) = \Big\{(\boldsymbol{f} - \boldsymbol{e}_2) \in L^2_{\text{loc}}(\Omega\backslash\Omega_i) \text{ with } \boldsymbol{f}(y_1, y_2+1) = \boldsymbol{f}(y_1, y_2) \text{ for all } \boldsymbol{y} \in \Omega\backslash\Omega_i$$
$$\text{and such that } \nabla_{\boldsymbol{y}} \cdot \boldsymbol{f} = 0 \text{ in } \Omega\backslash\Omega_i,\ \boldsymbol{f}\cdot\boldsymbol{n} = 0 \text{ on } \partial\Omega_i \text{ and } \lim_{y_1\to\pm\infty} \boldsymbol{f} = \boldsymbol{e}_2\Big\},$$

so that $\boldsymbol{\Psi}^{(2)} \in \mathcal{W}^{\text{per}}(\Omega\backslash\Omega_i)$. We also introduce for any $\tilde{\boldsymbol{\Psi}} \in \mathcal{W}^{\text{per}}(\Omega\backslash\Omega_i)$ the following functional:

$$\mathcal{M}\big(\tilde{\boldsymbol{\Psi}}\big) = \frac{1}{2}\int_{\Omega\backslash\Omega_i} \big|\tilde{\boldsymbol{\Psi}} - \boldsymbol{e}_2\big|^2 \,\mathrm{d}\boldsymbol{y}.$$

Upon noticing that for any admissible field $\tilde{\boldsymbol{\Psi}}$ the derivative of $\mathcal{M}$ in $\mathcal{W}^{\text{per}}(\Omega\backslash\Omega_i)$ satisfies

$$\mathcal{M}'\big[\boldsymbol{\Psi}^{(2)}\big]\tilde{\boldsymbol{\Psi}} = \int_{\Omega\backslash\Omega_i} \nabla_{\boldsymbol{y}}\Phi^{(2)} \cdot \tilde{\boldsymbol{\Psi}}\,\mathrm{d}\boldsymbol{y} = \int_{\partial(\Omega\backslash\Omega_i)} \Phi^{(2)}\tilde{\boldsymbol{\Psi}}\cdot\boldsymbol{n}\,\mathrm{d}\boldsymbol{y} - \int_{\Omega\backslash\Omega_i} \Phi^{(2)}\nabla_{\boldsymbol{y}}\cdot\tilde{\boldsymbol{\Psi}}\,\mathrm{d}\boldsymbol{y} = 0,$$

then $\boldsymbol{\Psi}^{(2)}$ minimizes the quadratic functional $\mathcal{M}$. Moreover, from the formal relation (2.45) that is satisfied by the field $\Phi^{(2)}$ with $\tilde{\Phi} = \Phi^{(2)}$ one has

$$C_2 = \int_{\Omega\backslash\Omega_i} \big|\nabla_{\boldsymbol{y}}\Phi^{(2)}\big|^2 \,\mathrm{d}\boldsymbol{y} = 2\mathcal{M}\big(\boldsymbol{\Psi}^{(2)}\big).$$

As a consequence, we obtain that $C_2 \leq 2\mathcal{M}\big(\tilde{\boldsymbol{\Psi}}\big)$ for all $\tilde{\boldsymbol{\Psi}} \in \mathcal{W}^{\text{per}}(\Omega\backslash\Omega_i)$. Finally, we define $\tilde{\boldsymbol{\Psi}}$ as

$$\tilde{\boldsymbol{\Psi}}(\boldsymbol{y}) = \boldsymbol{0} \quad \text{if } 0 \leq |y_1| < \frac{e}{2h} \quad \text{and} \quad \tilde{\boldsymbol{\Psi}}(\boldsymbol{y}) = \boldsymbol{e}_2 \quad \text{if } |y_1| \geq \frac{e}{2h}$$

from which one gets $\mathcal{M}(\tilde{\boldsymbol{\Psi}}) = e(1-\varphi)/(2h)$. From the minimization principle, we finally obtain the following lower bound $(\mathcal{S} - C_2) \geq (a-e)/h$, which proves that $(\mathcal{S} - C_2) \geq 0$ if $a \geq e$.

2.3 Numerical experiments

In the previous two sections we derived the resonant jump conditions in the time domain, and we used this formulation to perform an energy analysis. This allowed to get a sufficient condition for the problem to be stable. In this section, we now investigate numerically the propagation of waves in the effective media so obtained.

2.3.1 Configuration and numerical methods

2.3.1.1 Microstructured configuration

We consider the propagation of waves across a straight and h-periodic row of elliptic inclusions aligned with the X_2-axis and placed at $X_1 = 0\,\mathrm{m}$, see top of Figure 1.5. One sets $h = 2\,\mathrm{m}$ and the ellipses have semi-major axis $R_1 = 0.8\,\mathrm{m}$, semi-minor axis $R_2 = 0.5\,\mathrm{m}$ and tilt angle $\theta = 40°$ with respect to the X_1-axis, which results in a row thickness $e = 1.3838\,\mathrm{m}$. The inclusions are highly contrasted, with shear modulus $\mu_i = 10^{-2}\mu_m = 10^8\ \mathrm{kg}\cdot\mathrm{m}^{-1}\cdot\mathrm{s}^{-2}$ while their mass density is such that $\rho_i = \rho_m = 4.44\cdot 10^3\,\mathrm{kg}\cdot\mathrm{m}^{-3}$. The corresponding wave velocities are $c_m = 1500\,\mathrm{m}\cdot\mathrm{s}^{-1}$ and $c_i = 150\,\mathrm{m}\cdot\mathrm{s}^{-1}$.

A numerical approximation of the solution $\boldsymbol{U}_h = (V_h, \boldsymbol{\Sigma}_h)^\top$ in this microstructured configuration is obtained using the numerical method presented in Lombard et al., 2008. The system (2.1) is discretized on a Cartesian grid and solved using the ADER-4 scheme (Schwartzkopff, Dumbser, & Munz, 2004; Lorcher & Munz, 2006). As expected, the mesh size has to be much smaller than h for the inclusions geometry to be suitably approximated, which in turn implies high numerical costs in terms of computation time and memory requirements. Here, the interfaces $\partial\Omega_i$ are discretized using the Explicit Simplified Interface Method (ESIM).

2.3.1.2 Homogenized model

In the equivalent homogenized model (2.38), and owing to the analysis of Section 2.2, the interface thickness has to be chosen as $a \geq e$. Furthermore, in the *non-resonant* case the discrepancy on the fields has been shown to be minimized for $a = e$ (Marigo et al., 2017a). Consequently, the same thickness of the enlarged interface $a = e$ is chosen in the present numerical experiments for the resonant case.

The effective parameter $\mathcal{S}$ in (2.37) is calculated from the physical parameter values while the parameters $\mathcal{B}_1$, $\mathcal{B}_2$, $\mathcal{C}_1$ and $\mathcal{C}_2$ are computed numerically from the solutions $\Phi^{(j)}$ of the cell problems. They are approximated from the weak formulation (2.45) in a bounded domain $\Omega^b\backslash\Omega_i$ instead of $\Omega\backslash\Omega_i$. The bounded domain is $\Omega^b = [-y^b, y^b]\times[-\frac{1}{2}, \frac{1}{2}]$ with periodicity conditions in y_2 and Neumann conditions in y_1. The value y^b is chosen to be sufficiently large with $y^b = 5$ in order to approximate the Neumann condition at infinity. These approximations are computed using the finite-element method in FreeFem++ (Hecht, 2012) on a single cell. Once these two cell problems are solved numerically, then the four coefficients $\mathcal{B}_1$, $\mathcal{B}_2$, $\mathcal{C}_1$ and $\mathcal{C}_2$ are approximated based on (2.23) and (2.31). For the configuration considered, the obtained values are reported in Table 2.1.

Table 2.1 – Numerical values of the effective interface parameters featured in (2.38).

$\mathcal{B}_1$	$\mathcal{B}$	$\mathcal{B}_2$	$\mathcal{S}$	$\mathcal{C}_1$	$\mathcal{C}_2$
0.911	1.603	-0.142	0.378	-0.142	0.2

Finally, the solution $\boldsymbol{U} = (V, \boldsymbol{\Sigma})^\top$ of the time-domain effective problem (2.38) is discretized with a mesh size ΔX and a time step Δt, and we denote by $(\mathbf{U})_{i,j}^n$ the approximation of $\boldsymbol{U}$ at

point $(i\Delta X, j\Delta X)$ and time $t_n = n\Delta t$. A specific numerical method has been developed in Touboul et al., 2020a to handle the resonant jump conditions considered, which are non-local in time. The latter relies on the introduction of a set of *auxiliary variables*, locally along the interface, to derive equivalent jump conditions that are local in time. The resulting system is in turn discretized on a Cartesian grid and solved using the ADER-4 scheme while the geometry of the interface is handled using an extension of the ESIM to the resonant case. This numerical method is detailed in Chapter 3.

In the proposed numerical method, the auxiliary variables, which are introduced to derive a local-in-time system, rely on the expression of $\mathscr{D}_\infty(\omega)$ in (1.24). The values of the coefficients (α_r, ω_r) that define $\mathscr{D}_\infty(\omega)$ are obtained by solving numerically the eigenvalue problem (1.22) in FreeFem++ (Hecht, 2012). The first four modes P_r of the eigenvalue problem (1.22) are shown in Figure 2.4 for the elliptic inclusions case considered. Referring to the discussion in Section 1.2.2.4, then the modes P_1 and P_4 in Figure 2.4a and 2.4d have non-null mean values and are linked to resonances at ω_1 and ω_4. The modes P_2 and P_3 represented in Figures 2.4b and 2.4c have null mean values and the associated resonances ω_2 and ω_3 are not taken into account in the effective model. Numerically, the infinite sum in $\mathscr{D}_\infty(\omega)$ is truncated to the first eight resonances associated with modes that have non-null mean values. Computations have been performed to check that the resonances not taken into account have a negligible influence on the effective solution. The numerical values of the parameters α_0 and (α_r, ω_r) for $\alpha_r \neq 0$, which are used numerically, are reported in Table 2.2.

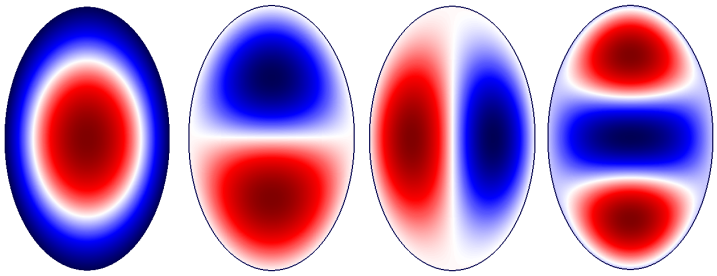

(a) P_1 (b) P_2 (c) P_3 (d) P_4

Figure 2.4 – First four modes P_r of the eigenvalue problem (1.22) for the elliptic inclusions considered.

Table 2.2 – Resonances parameters in (1.24).

r	0	1	4	8	9	13	16	21	23
α_r	0.314	0.462	0.144	0.148	0.069	0.078	0.037	0.053	0.081
ω_r (rad · s^{-1})		600	1101	1523	1637	1962	2178	2438	2463

2.3.1.3 Initial condition and forcing

To design the initial conditions or the forcing term, the following source function is introduced

$$F(\xi) = \begin{cases} \displaystyle\sum_{k=0}^{3} \alpha_k \sin(2^k k_m \xi) & \text{if } -\frac{c_m}{f_0} \leq \xi \leq 0 \\ 0 & \text{otherwise,} \end{cases} \tag{2.57}$$

with f_0 the central frequency, $\alpha_0 = 1$, $\alpha_1 = -21/32$, $\alpha_2 = 63/768$, and $\alpha_3 = -1/512$, which entails that F is of class C^6. Figure 2.5 displays the Fourier transform $\hat{F}$ of F as a function of

$$\eta(k) = kh \text{ for } f_0 \in \{25, 50, 100\} \text{ Hz.}$$

The dimensionless parameters corresponding to these central frequencies read

$$\eta_0 := \eta(2\pi f_0/c_m) \in \{0.21, 0.42, 0.84\}, \tag{2.58}$$

respectively. While in Figure 2.5 the dashed line indicates the central small parameter η_0, it should be noted that the frequency content of $\hat{F}$ extends to frequencies much higher than f_0 thus resulting in higher values of the parameter η for the associated wavelengths. In this figure, the blue crosses denote the dimensionless parameters $\eta_r := \eta(\omega_r/c_m)$ at the resonant frequencies ω_r in $\mathscr{D}_\infty(\omega)$ defined in (1.24) and associated with modes with non-zero mean (resonant frequencies with zero-mean modes are not displayed here).

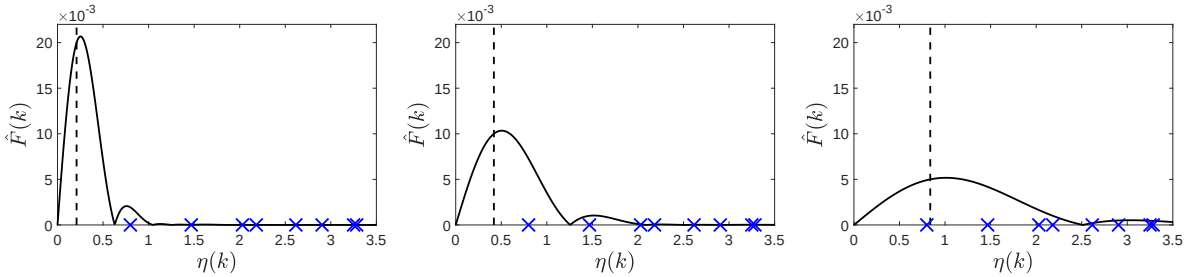

(a) $f_0 = 25\,\text{Hz}$ (b) $f_0 = 50\,\text{Hz}$ (c) $f_0 = 100\,\text{Hz}$

Figure 2.5 – Fourier transform $\hat{F}$ of the source function for the three different values f_0 considered (the associated dimensionless parameters η_0 are indicated by the dashed lines). The blue crosses denote the values η_r associated with resonances ω_r, see (1.24), of non-zero mean modes.

■ *Incident plane wave.* In a first case, an incident plane wave is considered and the initial conditions read

$$\boldsymbol{U}_h(\boldsymbol{X}, 0) = \begin{pmatrix} \dfrac{1}{\mu_m} \\ -\dfrac{1}{c_m} \\ 0 \end{pmatrix} F\big((\boldsymbol{X} - \boldsymbol{X}_I) \cdot \boldsymbol{e}_1\big) \tag{2.59}$$

where the initialization point $\boldsymbol{X}_I = (-2, 0)\,\text{m}$ is chosen such that compactly supported initial conditions (2.59) do not intersect the enlarged interface (or the inclusions for the microstructured configuration). The initial velocity field and profile are displayed in Figure 2.6 for $f_0 = 100\,\text{Hz}$. The velocity profile is normalized by the maximum homogenized velocity. From now on, it will be the case for each velocity profile displayed.

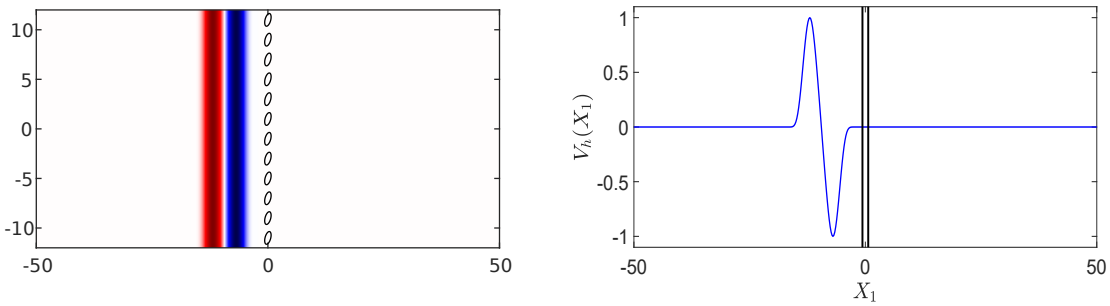

(a) Waveform (b) X_1-profile at $X_2 = -1\,\text{m}$

Figure 2.6 – Velocity field at the time $t = 0$ for the incident plane wave given by (2.59) with $f_0 = 100\,\text{Hz}$.

■ *Point source.* In a second case, we consider a point source located at $\boldsymbol{X}_S = (-35, 0)\,\mathrm{m}$ and such that (2.1) reads:

$$\begin{cases} \dfrac{\partial \boldsymbol{\Sigma}_h}{\partial t}(\boldsymbol{X}, t) = \mu_h(\boldsymbol{X}) \boldsymbol{\nabla} V_h(\boldsymbol{X}, t) \\ \rho_h(\boldsymbol{X}) \dfrac{\partial V_h}{\partial t}(\boldsymbol{X}, t) = \boldsymbol{\nabla} \cdot \boldsymbol{\Sigma}_h(\boldsymbol{X}, t) + \rho_m \, \delta(\boldsymbol{X} - \boldsymbol{X}_s) \, F(t c_m), \end{cases} \tag{2.60}$$

with $\delta(\boldsymbol{X} - \boldsymbol{X}_s)$ being a Dirac delta function at $\boldsymbol{X} = \boldsymbol{X}_s$.

2.3.1.4 Numerical errors

To assess whether the homogenized model provides a satisfying approximation of the original problem in the microstructured configuration, we compare the corresponding numerical solutions. With $\boldsymbol{U}_h$ and $\boldsymbol{U}$ being respectively the exact solution of the original problem in the microstructured configuration and in the homogenized model, we denote by $\mathbf{U}_h$ and $\mathbf{U}$ their numerical approximations. Defining the total *modeling* error $\varepsilon_T = \|\boldsymbol{U}_h - \boldsymbol{U}\|$, then one has formally by triangular inequality:

$$\varepsilon_T \leq \underbrace{\|\boldsymbol{U}_h - \mathbf{U}_h\|}_{\varepsilon_1} + \underbrace{\|\mathbf{U}_h - \mathbf{U}\|}_{\varepsilon_2} + \underbrace{\|\mathbf{U} - \boldsymbol{U}\|}_{\varepsilon_3}.$$

The term ε_1 is the numerical error associated with the simulation in the microstructured configuration while ε_3 is the one associated with the simulation based on the homogenized model. Both are governed and controlled by the numerical methods employed, see Lombard and Piraux, 2004, and Touboul et al., 2020a or Chapter 3, respectively. In appropriate numerical implementations, these errors are considered to be negligible compared to ε_2. As a consequence, we consider that the numerical error $\varepsilon_2 = \|\mathbf{U}_h - \mathbf{U}\|$ provides a reliable estimation of the total modeling error ε_T and can be used to measure the validity of the homogenized model.

The homogenized model of Section 2.1 is derived under Assumptions 2.1, i.e., with asymptotics being performed in the limit $\eta \to 0$ while it is assumed that $\mu_i/\mu_m = O(\eta^2)$ to preserve resonances. In practice, we apply this model to a given geometric and material configuration for which the parameters h, μ_i and μ_m are set. The signal (2.57) is also considered as a *source* term and the latter carries a range of wavelengths λ that are in turn associated with a parameter $\eta(2\pi/\lambda) = 2\pi h/\lambda = 2\pi h f/c_m$. For Assumptions 2.1 to hold then one must have both $\eta(2\pi/\lambda) \ll 1$ and $\eta(2\pi/\lambda) = O(\sqrt{\mu_i/\mu_m})$.

As a consequence, the agreement between simulations for the microstructured and the homogenized problems are expected to deteriorate as $\eta(2\pi/\lambda)$ approaches 1. For the source signal (2.57) considered, we will only focus on η_0 defined (2.58) but, as seen in Figure 2.5, the frequency content of this source extends to higher frequencies for which the associated wavelengths may lie beyond the validity domain of Assumptions 2.1.

2.3.2 Incident plane wave at normal incidence

In a first example, we consider an incident plane wave at normal incidence, see Section 2.3.1.3. The velocity profiles of the numerical solutions in the original microstructured configuration are presented in Figure 2.7a for different mesh sizes. Figure 2.7b compares the velocity profiles for the homogenized model, computed either numerically on a grid of mesh size $\Delta X = 0.2\,\mathrm{m}$ or semi-analytically. The numerical method for the homogenized model will be described in Chapter 3. The semi-analytical solution is described in Appendix 3.A.1. On the one hand, the numerical solution for the microstructured configuration on the fine grid $\Delta X = 0.025\,\mathrm{m}$ is assumed to have converged,

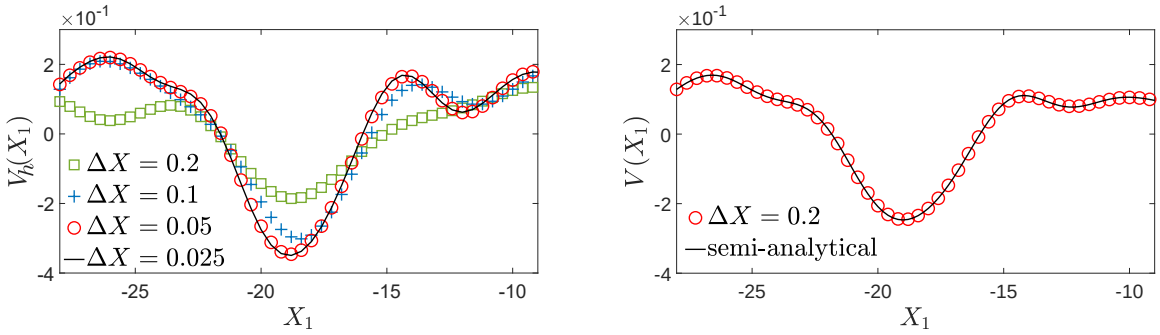

(a) Microstructured configuration: numerical solutions (b) Homogenized model: numerical and semi-analytical solutions

Figure 2.7 – Velocity profiles for the microstructured configuration and using the homogenized model. The source term is such that $f_0 = 100\,\text{Hz}$.

see Fig. 2.7a. On the other hand, a coarse grid $\Delta X = 0.2\,\text{m}$ is enough when using the homogenized model, see Fig. 2.7b. As an indication of the numerical gain, at $f_0 = 100\,\text{Hz}$, a computational time of 47 seconds for the homogenized model ($\Delta X = 0.2\,\text{m}$ in Fig. 2.7b) corresponds to a computational time of 4.8 hours for the original microstructured configuration ($\Delta X = 0.025\,\text{m}$ in Fig. 2.7a). The extra time needed for the original problem is due to the smaller mesh size but also to the smaller time step imposed by the CFL condition for numerical stability. These two mesh sizes will be used in numerical experiments from now on.

The velocity fields for the microstructured configuration and for the homogenized model together with their respective profiles along $X_2 = -1\,\text{m}$ are reported in Figure 2.8 at time $t = 31.7\,\text{ms}$ for $f_0 \in \{25, 50, 100\}\,\text{Hz}$. The corresponding discrepancies between both solutions is measured in the L^2-norm for $X_1 \in [-50; -5]\,\text{m}$ and at $X_2 = -1\,\text{m}$. The relative errors are of about 4%, 7% and 10%, respectively. For the stress component Σ_1, these errors are of about 3%, 7% and 13%. Since the errors measurements are comparable for the velocity and stress fields, we will now evaluate the agreement between the homogenized model and the microstructured problem only in terms of the velocity field. As expected from the discussion in Section 2.3.1.4, the solutions agree at low frequency but deviate from one another as the parameter η_0 in (2.58) increases to 1 and does not conform to the shear modulus ratio of Assumptions 2.1. Finally, in Figure 2.8, it can be observed that the dispersive nature of the material is amplified, in both the microstructured configuration and in the homogenized model, as f_0 increases. This behavior illustrates the fact that resonances play an increasing role. At low frequency, the observed wavefield is almost comparable to the case of a non-resonant interface (with low-constrasted inclusions), see Lombard et al., 2017, while at higher frequencies some energy is still radiated by the interface after the incident wave has crossed the former.

In the case $f_0 = 50$ Hz, the velocity in the microstructured and homogenized configuration is recorded from $t = 0$ to $t = 475$ ms at one receiver. This receiver is located on the right of the enlarged interface at $\boldsymbol{X}_T = (X_T, 0)$ m, with $X_T = 10$m. From these data, the Fourier transform of the transmitted velocity $\hat{V}(\boldsymbol{X}_T, \omega)$ is computed and its logarithm is displayed in Figure 2.9 after normalization. The dashed line indicates the logarithm of the Fourier transform of the incident wave. Around the resonances for the microstructured configuration, we can see within a small frequency band a high transmission followed by a high reflexion. A zoom on the first two resonances is also displayed. The first one is associated with a mode of non-null mean value, see Figure 2.4a, while the mode of the second one has a null mean value, see Figure 2.4b, and thus is not accounted for in the model. Around the first resonance taken into account in $\mathscr{D}_\infty(\omega)$ (1.24), we have a good

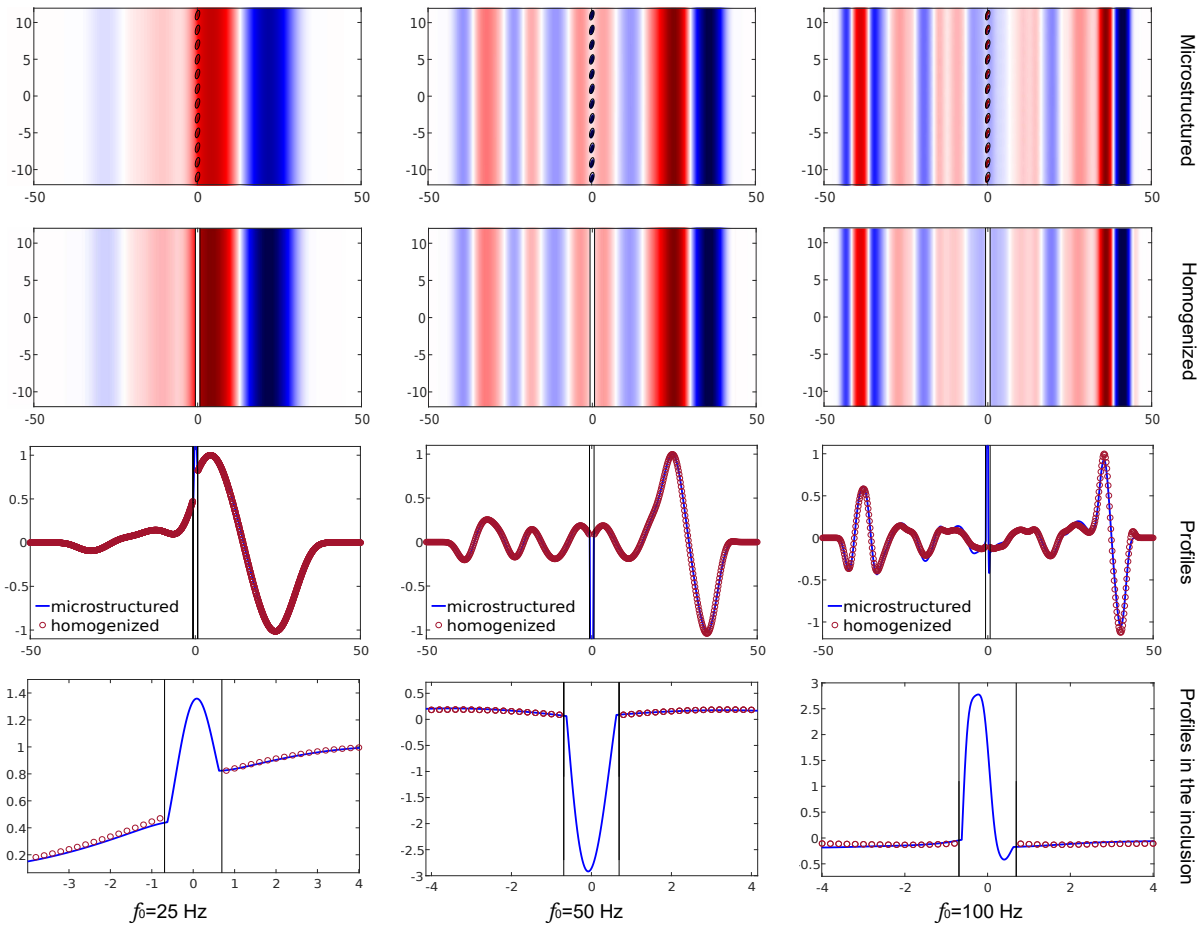

Figure 2.8 – *(Top two rows)* velocity fields for the microstructured configuration and for the homogenized model for an illumination by an incident plane wave at normal incidence. *(Third row)* comparison of the corresponding velocity profiles at $X_2 = -1\,\text{m}$. *(Bottom row)* zoom in the inclusion. *(left)* $f_0 = 25\,\text{Hz}$ so that $\eta_0 = 0.21$, *(center)* $f_0 = 50\,\text{Hz}$ so that $\eta_0 = 0.42$, and *(right)* $f_0 = 100\,\text{Hz}$ so that $\eta_0 = 0.84$.

agreement between both Fourier transforms. On the contrary, the behaviour of the solution is not well described by the homogenized solution around the second resonance. The same holds for each resonance associated with a mode of null mean value. However, these missed resonant frequencies also correspond to values of η which are around or higher than 1. Thus, even if the behaviour of the solution is not well described, it is in any case for a range of frequencies that go beyond the low-frequency hypothesis of homogenization. Furthermore, it can also be noticed that these missed resonant frequencies are not solicited a lot by the frequency content of the incident field. Therefore, it can be assumed that it does not induce a much greater error.

2.3.3 Source point

In the previous example of Section 2.3.2, the X_2-invariance of the incident plane wave considered implies that the X_2-derivatives vanish in the effective model (2.38) so that the associated homogenized coefficients $\mathcal{B}_2$, $\mathcal{C}_1$ and $\mathcal{C}_2$ play no role. To deal with a full 2D configuration, we consider the forcing by the source point described in (2.60). The physical and numerical parameters are the same as in the previous example. Moreover, the computational domain is defined as $[-70\ \text{m}; 35\ \text{m}] \times [-132\ \text{m}; 132\ \text{m}]$, i.e. it is chosen large enough along the X_2-axis to avoid reflections from the top and bottom boundaries while Perfectly Matched Layers are used in the background domain on the left and right boundaries.

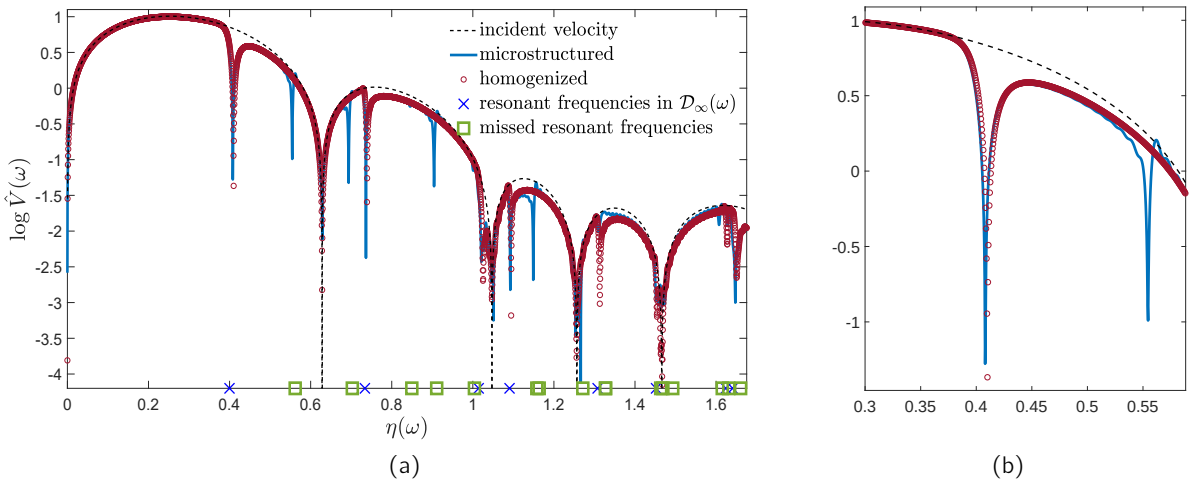

Figure 2.9 – (a) Logarithm of the Fourier transform $\hat{V}(\boldsymbol{X}_T, \omega)$ for the microstructured and the homogenized configuration. The dashed line indicates the logarithm of the Fourier transform of the incident velocity. The blue crosses denote the resonant frequencies taken into account in $\mathscr{D}_\infty(\omega)$ (1.24) and the green squares denote the missed resonant frequencies of zero mean modes. (b) Zoom on the first two resonances.

The velocity fields for the microstructured configuration and for the homogenized model are displayed at times $t \in \{t_1, t_2, t_3, t_4\} = \{25.3, 38.0, 50.7, 63.3\}$ ms on the figures 2.10, 2.11 and 2.12, which correspond to a source central frequency $f_0 \in \{25, 50, 100\}$ Hz, respectively. The X_1-profiles of both solutions at $X_2 = 1$ m are compared on Figure 2.13. Quantitatively, the discrepancies between solutions are again measured in the L^2-norm for $X_1 \in [-50 \text{ m} \,; -5 \text{ m}\,]$ and at $X_2 = 1\,\text{m}$. The associated relative errors are of about 2%, 9% and 13%, respectively, which is of same order than the ones obtained in Section 2.3.2.

As in the previous example, the agreement between solutions deteriorates as η approaches 1. Figure 2.13 also displays the velocity profiles zoomed in within a single inclusion in the microstructured configuration. As the frequency increases then shorter wavelengths are *trapped* within the inclusion and more resonant frequencies featured in (1.24) are solicited, thereby explaining the discrepancies between the two models.

2.4 Accounting for dissipation

In most of the works on homogenization of thin microstructured layers, dissipation is neglected. An exception is the Section 3 of Pham et al., 2017 where damping is introduced heuristically in the homogenized model. The assumption of inviscid media adopted in the previous sections simplifies the theoretical analyses and the numerical modeling. However, dissipation always occurs in real devices. It may modify notably the properties foreseen, degrade or amplify them. It may even been exploited to control wave propagation (Li et al., 2017). This section therefore considers dissipation in the full homogenization process and with the additional objective of presenting time-domain simulations.

This work started with the mentoring of the internship of Xinzhao Gao at Ecole Centrale Marseille which focused on the expression of the jump conditions and the development of a 1D numerical method when dissipation is considered.

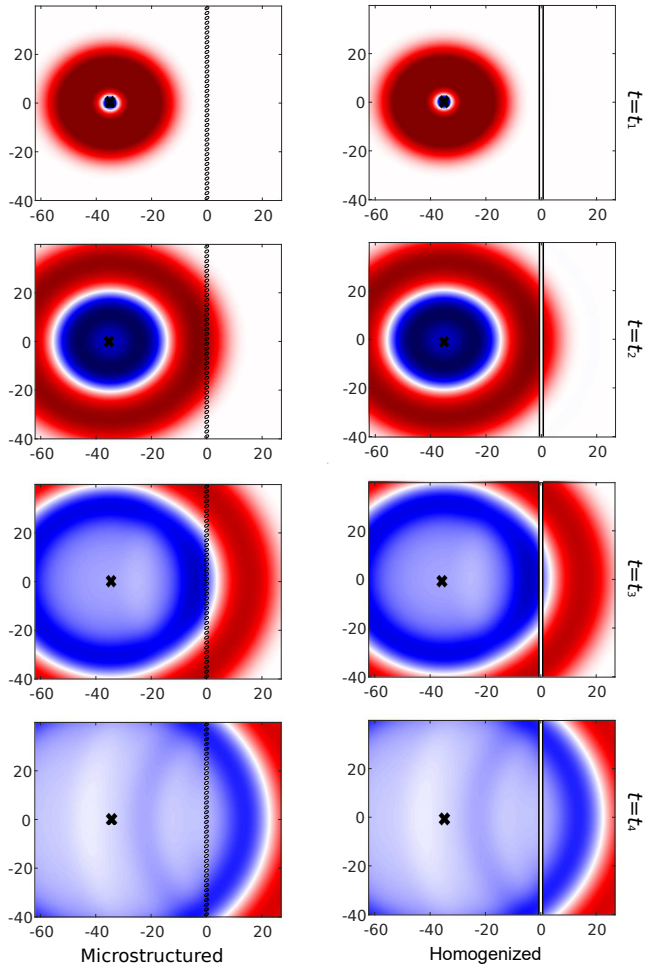

Figure 2.10 – *(Left)* velocity fields for the microstructured configuration and *(right)* for the homogenized model for $f_0 = 25\,\mathrm{Hz}$ (so that $\eta_0 = 0.21$) and at different times $t \in \{25.3, 38.0, 50.7, 63.3\}$ ms. A source point is located at $(-35, 0)$ m and is symbolized by a black cross. Only a subset of the computational domain is shown here.

2.4.1 Microstructured configuration

One introduces a dissipation parameter γ_h. The latter is inversely proportional to the damping, so that $\gamma_h = +\infty$ corresponds to an inviscid medium. Therefore, the microstructured configuration is unchanged except the fact that there is now three positive and piecewise constant parameters:

$$(\rho_h, \mu_h, \gamma_h)(\boldsymbol{X}) = \begin{cases} (\rho_m, \mu_m, +\infty) & \text{in the matrix,} \\ (\rho_i, \mu_i, \gamma) & \text{in the inclusions.} \end{cases}$$

The question adressed in this section is not to consider a particular constitutive dissipative mechanism but rather to exhibit a methodology and to present numerical experiments. Consequently, we find it more relevant to consider a structural dissipation model, where damping is introduced in the momentum equation. The evolution equations of linear anti-plane elasticity with damping hence write as the first-order system:

$$\begin{cases} \partial_t \boldsymbol{\Sigma}_h(\boldsymbol{X}, t) = \mu_h \boldsymbol{\nabla} V_h(\boldsymbol{X}, t), \\ \rho_h\, \partial_t V_h(\boldsymbol{X}, t) + \dfrac{1}{\gamma_h} V_h(\boldsymbol{X}, t) = \boldsymbol{\nabla} \cdot \boldsymbol{\Sigma}_h(\boldsymbol{X}, t). \end{cases} \tag{2.61}$$

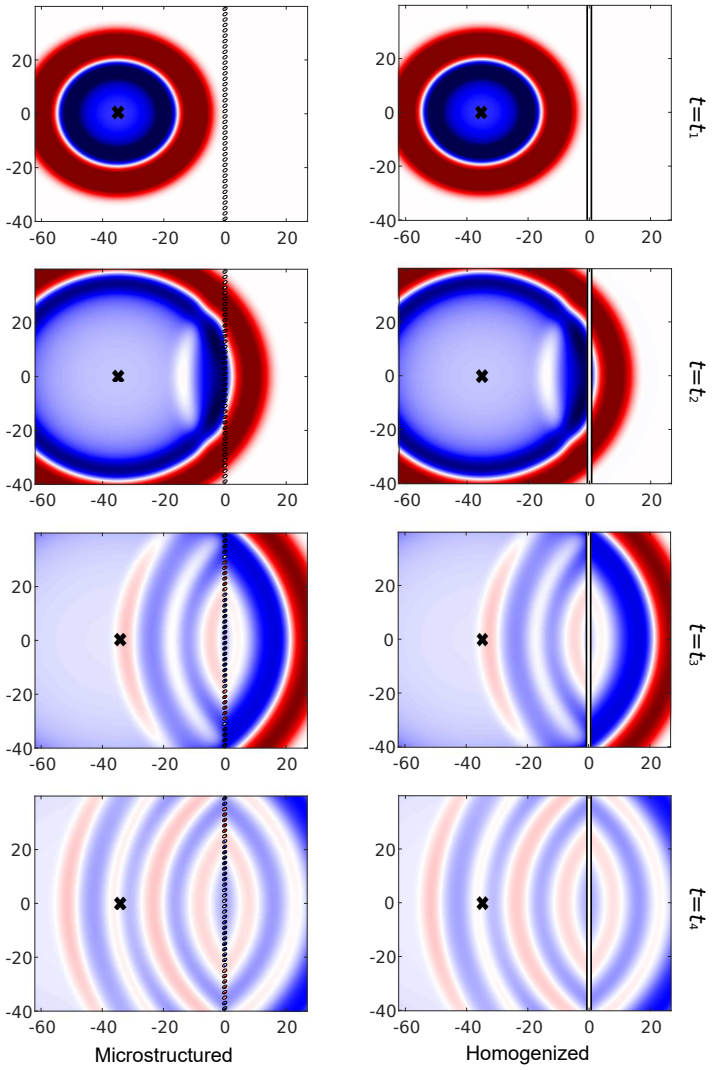

Figure 2.11 – *(Left)* velocity fields for the microstructured configuration and *(right)* for the homogenized model for $f_0 = 50\,\text{Hz}$ (so that $\eta_0 = 0.42$) and at different times $t \in \{25.3, 38.0, 50.7, 63.3\}$ ms. A source point is located at $(-35, 0)$ m and is symbolized by a black cross. Only a subset of the computational domain is shown here.

2.4.2 Frequency-domain formulation

The homogenization steps followed in Pham et al., 2017 can be extended to the case $\gamma \neq +\infty$. For the sake of brevity, the full derivation is not detailed here, since the findings can be obtained using the correspondence principle: see e.g. chapter 3 of Carcione, 2007. The microstructured problem (2.61) can be recast in the frequency domain as

$$\begin{cases} \mathrm{i}\omega\, \hat{\boldsymbol{\Sigma}}_h(\boldsymbol{X}, \omega) = \mu_h\, \boldsymbol{\nabla} \hat{V}_h(\boldsymbol{X}, \omega), \\ \mathrm{i}\omega\, \hat{\rho}_h^{\gamma}\, \hat{V}_h(\boldsymbol{X}, \omega) = \boldsymbol{\nabla} \cdot \hat{\boldsymbol{\Sigma}}_h(\boldsymbol{X}, \omega), \end{cases} \tag{2.62}$$

with

$$\hat{\rho}_h^{\gamma}(\boldsymbol{X}) = \begin{cases} \rho_m & \text{in the matrix,} \\ \rho_i \left(1 + \dfrac{1}{\mathrm{i}\omega\, \gamma\, \rho_i}\right) & \text{in the inclusions,} \end{cases}$$

which is exactly the same frequency-domain formulation as in the inviscid case. Consequently, one expects to find the same effective jump conditions (1.19) by replacing the term ρ_i by $\rho_i(1 + \frac{1}{\mathrm{i}\omega\gamma\rho_i})$

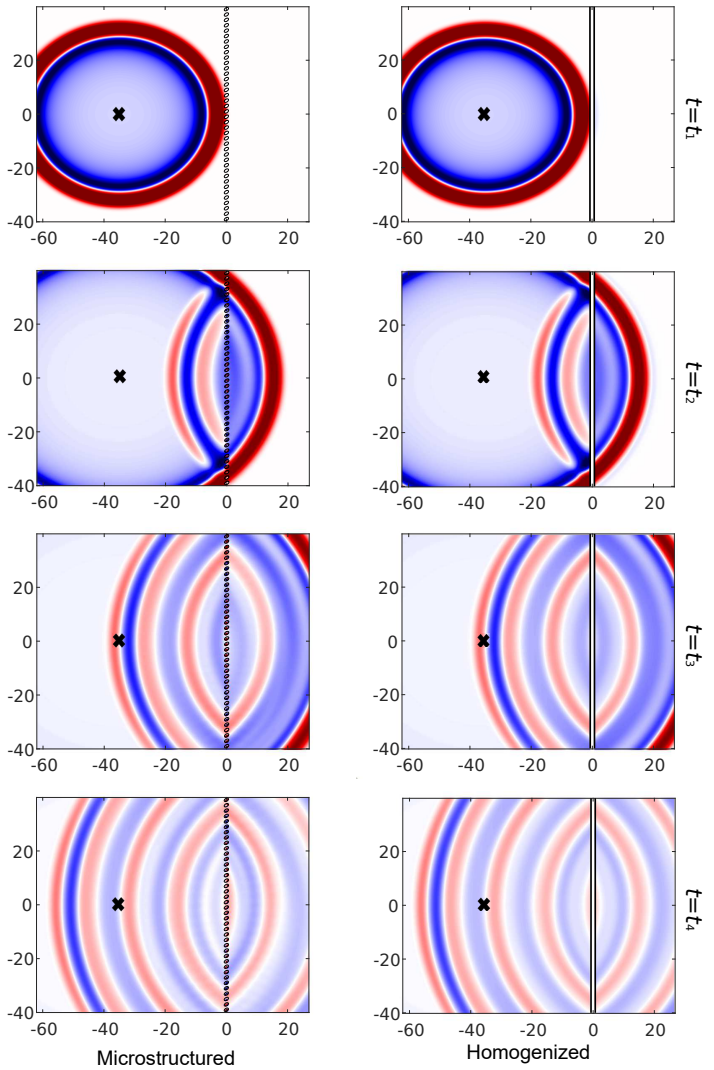

Figure 2.12 – *(Left)* velocity fields for the microstructured configuration and *(right)* for the homogenized model for $f_0 = 100\,\text{Hz}$ (so that $\eta_0 = 0.84$) and at different times $t \in \{25.3, 38.0, 50.7, 63.3\}$ ms. A source point is located at $(-35, 0)$ m and is symbolized by a black cross. Only a subset of the computational domain is shown here.

in the effective coefficients. This is possible because the contrast in the parameter ρ does not depend on a scaling in η. The coefficients $\mathcal{S}$, $\mathcal{B}$, $\mathcal{B}_2$, $\mathcal{C}_1$ and $\mathcal{C}_2$ do not depend on ρ_i, thus they are unchanged. On the contrary, $\mathscr{D}_\infty(\omega)$ depends implicitly on ρ_i, and thus it is changed into $\mathscr{D}_\gamma(\omega)$, leading to the new homogenized model with damping:

$$\begin{cases} \mathrm{i}\omega\,\hat{\boldsymbol{\Sigma}}(\boldsymbol{X},\omega) = \mu_m\,\boldsymbol{\nabla}\hat{V}(\boldsymbol{X},\omega) & (|X_1| \geq a/2, X_2 \in \mathbb{R}) \\ \mathrm{i}\omega\,\rho_m\,\hat{V}(\boldsymbol{X},\omega) = \boldsymbol{\nabla}\cdot\hat{\boldsymbol{\Sigma}}(\boldsymbol{X},\omega) & (|X_1| \geq a/2, X_2 \in \mathbb{R}) \\ \left[\!\left[\hat{V}\right]\!\right]_a = h\left\{B\left\langle\!\left\langle\partial_{X_1}\hat{V}\right\rangle\!\right\rangle_a + B_2\left\langle\!\left\langle\partial_{X_2}\hat{V}\right\rangle\!\right\rangle_a\right\} & (X_2 \in \mathbb{R}) \\ \left[\!\left[\hat{\Sigma}_1\right]\!\right]_a = h\left\{S\left\langle\!\left\langle\partial_{X_1}\hat{\Sigma}_1\right\rangle\!\right\rangle_a + C_1\left\langle\!\left\langle\partial_{X_2}\hat{\Sigma}_1\right\rangle\!\right\rangle_a + C_2\left\langle\!\left\langle\partial_{X_2}\hat{\Sigma}_2\right\rangle\!\right\rangle_a + \mathscr{D}_\gamma(\omega)\left\langle\!\left\langle\boldsymbol{\nabla}\cdot\hat{\boldsymbol{\Sigma}}\right\rangle\!\right\rangle_a\right\} & (X_2 \in \mathbb{R}). \end{cases} \tag{2.63}$$

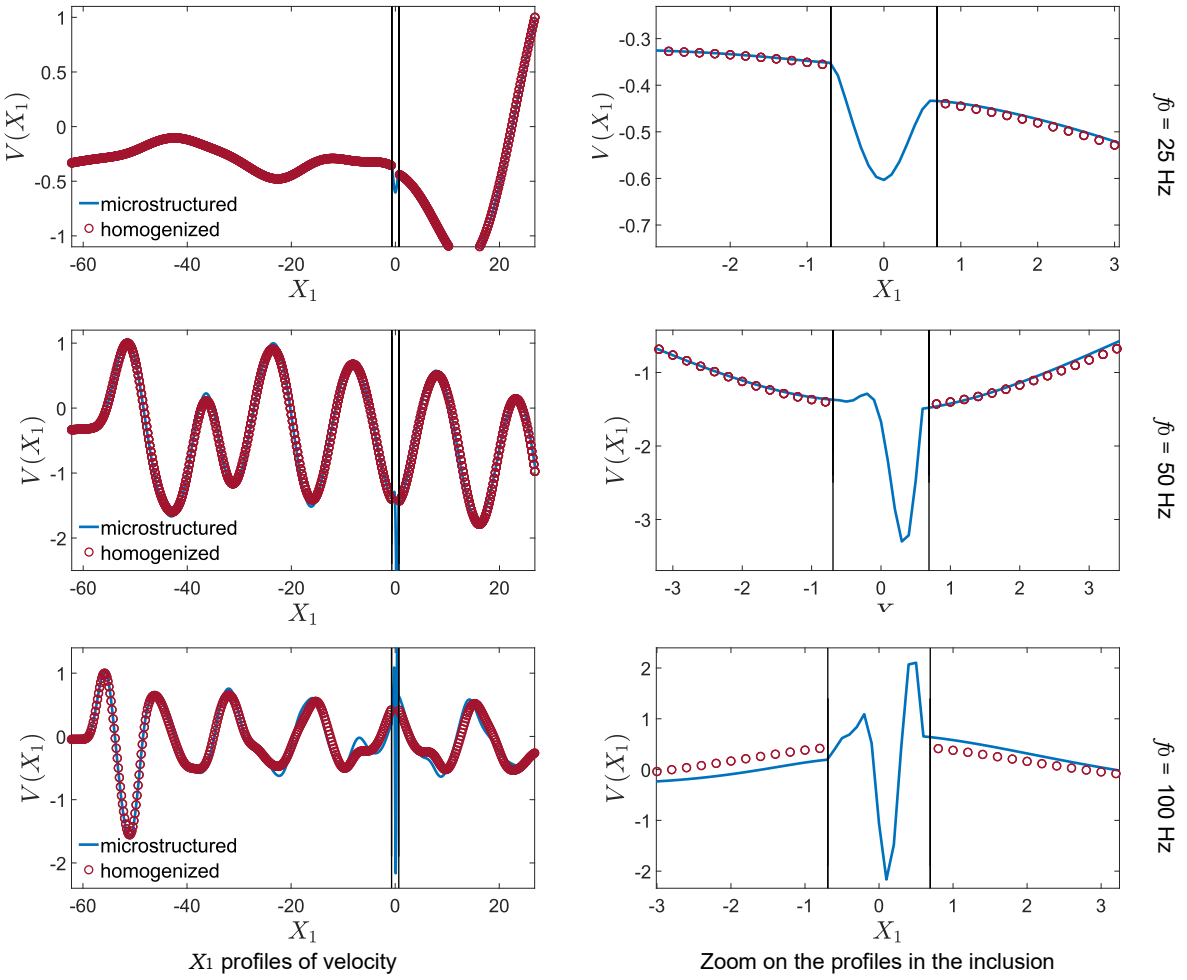

Figure 2.13 – Comparisons of the velocity profiles for the microstructured configuration and the homogenized model at $X_2 = 1\,\mathrm{m}$. *(Left)* subset of the computational domain, and *(right)* zoom in the inclusion region. From top to bottom rows: $f_0 \in \{25, 50, 100\}$ Hz, respectively, which corresponds to $\eta_0 \in \{0.21, 0.42, 0.84\}$.

The new effective coefficient $\mathscr{D}_\gamma(\omega)$ is obtained as follows. Replacing ρ_i by $\rho_i(1 + \frac{1}{\mathrm{i}\omega\gamma\rho_i})$, the Dirichlet problem (1.17) becomes

$$\begin{cases} \Delta_{\boldsymbol{y}}\psi_\gamma(\boldsymbol{y},\omega) + \kappa_\gamma^2(\omega)\,\psi_\gamma(\boldsymbol{y},\omega) = 0 & (\boldsymbol{y} \in \Omega_i), \\ \psi_\gamma(\boldsymbol{y},\omega) = 1 & (\boldsymbol{y} \in \partial\Omega_i), \end{cases} \tag{2.64}$$

where (1.18) is replaced by

$$\kappa_\gamma^2(\omega) = \frac{\rho_i h^2}{\mu_i}\,\omega^2\left(1 + \frac{1}{\mathrm{i}\omega\,\gamma\,\rho_i}\right).$$

Then the frequency-dependent coefficient in (1.21) becomes

$$\mathscr{D}_\gamma(\omega) = \frac{\rho_i}{\rho_m}\left(1 + \frac{1}{\mathrm{i}\omega\,\gamma\,\rho_i}\right)\int_{\Omega_i}\psi_\gamma(\boldsymbol{y},\omega)\,\mathrm{d}\boldsymbol{y}. \tag{2.65}$$

Keeping the same definitions of α_0, $\alpha_{r\geq 1}$ and ω_r than in (1.23), the modal expansion of (2.65) yields

Result 2.4: Frequency-dependant coefficient with dissipation

$$\mathscr{D}_\gamma(\omega) = \left(1 + \frac{1}{\mathrm{i}\omega\,\gamma\rho_i}\right)\left\{\alpha_0 - \sum_{r\geq 1}\alpha_r^2 \frac{\omega^2 - \dfrac{\mathrm{i}\omega}{\gamma\rho_i}}{\omega^2 - \dfrac{\mathrm{i}\omega}{\gamma\rho_i} - \omega_r^2}\right\}. \tag{2.66}$$

The frequency-dependent effective coefficient (2.66) recovers (1.24) in the limit-case $\gamma = +\infty$. As in (1.24), the infinite series is truncated to a finite number N_R of resonances, and the null-mean modes lead to $\alpha_r = 0$, so that they do not contribute to the effective model obtained. The effect of this limitation will be examined numerically in Section 3.6.

2.4.3 Time-domain formulation

2.4.3.1 Effective jump conditions

Replacing ρ_i by $\rho_i(1 + \frac{1}{\mathrm{i}\omega\gamma\rho_i})$ in (2.39) yields the inner problem in the frequency domain:

$$\begin{cases} \mathrm{i}\omega\,\hat{\boldsymbol{\Sigma}}_i(\boldsymbol{y}, X_2, \omega) = \dfrac{\mu_i}{h}\boldsymbol{\nabla}_{\boldsymbol{y}}\hat{W}_i(\boldsymbol{y}, X_2, \omega) & (\boldsymbol{y} \in \Omega_i), \\ \rho_i\left(1 + \dfrac{1}{\mathrm{i}\omega\,\gamma\rho_i}\right)\hat{W}_i(\boldsymbol{y}, X_2, \omega) = \dfrac{1}{h}\boldsymbol{\nabla}_{\boldsymbol{y}}\cdot\hat{\boldsymbol{\Sigma}}_i(\boldsymbol{y}, X_2, \omega) & (\boldsymbol{y} \in \Omega_i), \\ \hat{W}_i(\boldsymbol{y}, X_2, \omega) = \left\langle\!\left\langle \hat{V}(\cdot, X_2, \omega)\right\rangle\!\right\rangle_a & (\boldsymbol{y} \in \partial\Omega_i). \end{cases} \tag{2.67}$$

Similarly, (2.40) becomes

$$\begin{aligned} \mathrm{i}\omega\,\rho_i\left(1 + \frac{1}{\mathrm{i}\omega\,\gamma\rho_i}\right)\int_{\Omega_i}\hat{W}_i\,\mathrm{d}\boldsymbol{y} &= \frac{\rho_i}{\rho_m}\left(1 + \frac{1}{\mathrm{i}\omega\,\gamma\rho_i}\right)\int_{\Omega_i}\psi_\gamma(\boldsymbol{y}, \omega)\,\mathrm{d}\boldsymbol{y}\,\left\langle\!\left\langle\boldsymbol{\nabla}\cdot\hat{\boldsymbol{\Sigma}}\right\rangle\!\right\rangle_a \\ &= \mathscr{D}_\gamma(\omega)\,\left\langle\!\left\langle\boldsymbol{\nabla}\cdot\hat{\boldsymbol{\Sigma}}\right\rangle\!\right\rangle_a. \end{aligned} \tag{2.68}$$

Inverse Fourier transforms of (2.63), (2.68) and (2.67) yield the homogenized model in the time domain:

$$\begin{cases} \partial_t\boldsymbol{\Sigma} = \mu_m\,\boldsymbol{\nabla}V & (|X_1| \geq a/2,\ X_2 \in \mathbb{R}), \\ \partial_t V = \dfrac{1}{\rho_m}\boldsymbol{\nabla}\cdot\boldsymbol{\Sigma} & (|X_1| \geq a/2,\ X_2 \in \mathbb{R}), \\ [\![V]\!]_a = h\left\{B\,\langle\!\langle\partial_{X_1}V\rangle\!\rangle_a + B_2\,\langle\!\langle\partial_{X_2}V\rangle\!\rangle_a\right\} & (X_2 \in \mathbb{R}), \\ [\![\Sigma_1]\!]_a = h\left\{S\,\langle\!\langle\partial_{X_1}\Sigma_1\rangle\!\rangle_a + C_1\,\langle\!\langle\partial_{X_2}\Sigma_1\rangle\!\rangle_a + C_2\,\langle\!\langle\partial_{X_2}\Sigma_2\rangle\!\rangle_a \right. & \\ \qquad\qquad \left. + \rho_i\displaystyle\int_{\Omega_i}\partial_t W_i\,\mathrm{d}\boldsymbol{y} + \frac{1}{\gamma}\int_{\Omega_i}W_i\,\mathrm{d}\boldsymbol{y}\right\} & (X_2 \in \mathbb{R}), \end{cases} \tag{2.69}$$

where W_i is solution in each inclusion of the inner problem:

$$\begin{cases} \partial_t\boldsymbol{\Sigma}_i(\boldsymbol{y}, X_2, t) = \dfrac{\mu_i}{h}\boldsymbol{\nabla}_{\boldsymbol{y}}W_i(\boldsymbol{y}, X_2, t) & (\boldsymbol{y} \in \Omega_i), \\ \rho_i\partial_t W_i(\boldsymbol{y}, X_2, t) + \dfrac{1}{\gamma}W_i(\boldsymbol{y}, X_2, t) = \dfrac{1}{h}\boldsymbol{\nabla}_{\boldsymbol{y}}\cdot\boldsymbol{\Sigma}_i(\boldsymbol{y}, X_2, t) & (\boldsymbol{y} \in \Omega_i), \\ W_i(\boldsymbol{y}, X_2, t) = \langle\!\langle V(\cdot, X_2, t)\rangle\!\rangle_a & (\boldsymbol{y} \in \partial\Omega_i). \end{cases} \tag{2.70}$$

In the limit-case $\gamma = +\infty$, the equations (2.39) and (2.38) of the inviscid model are recovered.

2.4.3.2 Energy identity

For all time $t \geq 0$, one defines

$$\mathcal{F}_h^\gamma(t) = \frac{1}{\gamma}\int_{\cup_i \Omega_i} (V_h(\boldsymbol{X},t))^2 \mathrm{d}\boldsymbol{X}. \tag{2.71}$$

Then, the energy identity in the microstructured configuration holds

$$\frac{\mathrm{d}}{\mathrm{d}t}\mathcal{E}_h(t) = -\mathcal{F}_h^\gamma(t) \leq 0, \tag{2.72}$$

with $\mathcal{E}_h$ defined in (2.41). When $\gamma = +\infty$, the inviscid case (2.42) is recovered and the energy is conserved.

For the homogenized model, the energy balance can be calculated in the same way as in the case without dissipation. The expressions of $\mathcal{E}$ (2.43) and $\mathcal{E}_a$ (2.52) are unchanged. On the other hand, the term γ modifies the energy balance, which is written as follows

Result 2.5: Energy identity with dissipation

$$\frac{\mathrm{d}}{\mathrm{d}t}(\mathcal{E}+\mathcal{E}_a) = -\mathcal{F}_\gamma, \tag{2.73}$$

with

$$\mathcal{F}_\gamma = \frac{h}{\gamma}\int_I \int_{\Omega_i} W_i^2 \mathrm{d}\boldsymbol{y}\, \mathrm{d}X_2 \geq 0. \tag{2.74}$$

This underlines that $\mathcal{E}+\mathcal{E}_a$ is decreasing due to the dissipation.

2.4.4 Numerical experiments

The physical and geometrical parameters are unchanged compared to Section 2.3. The additional dissipation parameter γ is given for each numerical experiment later on. In the microstructured configuration, dissipation is taken into account with a Strang's splitting method (LeVeque, 2002). The incorporation of the dissipation parameter in the numerical method is tackled in the next chapter (see Section 3.6). The numerical method has been implemented for a dissipation parameter which is greater than a minimal value, see Assumption 3.2, which equals to $\gamma^\star = 1.87\,10^{-7}\,\mathrm{kg}^{-1}\cdot\mathrm{m}^3\cdot\mathrm{s}$ in the present configuration. This numerical method is used here to assess the reliability of the homogenized model and to investigate the effect of the dissipation parameter γ.

2.4.4.1 Validation of the homogenized model

■ *Incident plane wave at normal incidence.* Numerical simulations are first performed with the incident plane wave at normal incidence of Section 2.3.2. We compare the homogenized simulations with full-field simulations performed in the microstructured configuration. The dissipation parameter is $\gamma = 2\cdot 10^{-6}\,\mathrm{kg}^{-1}\cdot\mathrm{m}^3\cdot\mathrm{s}$. One investigates the agreement between both configurations for three values of central frequencies $f_0 = 36,\ 72,\ 108\,\mathrm{Hz}$ in (2.57) in the initial conditions (2.59) corresponding to dimensionless parameters $\eta_0 = 0.3,\ 0.6,\ 0.9$, respectively. The velocity fields for the microstructured configuration and for the homogenized model together with their respective profiles along $X_2 = -1\,\mathrm{m}$ are reported in Figure 2.14 at time $t = 31.7\,\mathrm{ms}$. The corresponding discrepancy between both solutions is measured in the L^2-norm for $X_1 \in [-50;-5]\,\mathrm{m}$ and at $X_2 = -1\,\mathrm{m}$. The relative errors are of about 3.8%, 5.7% and 7.4%, respectively. As expected, the solutions agree at low frequency but deviate from one another as the parameter η_0 increases to 1 and does not conform to Assumption 2.1.

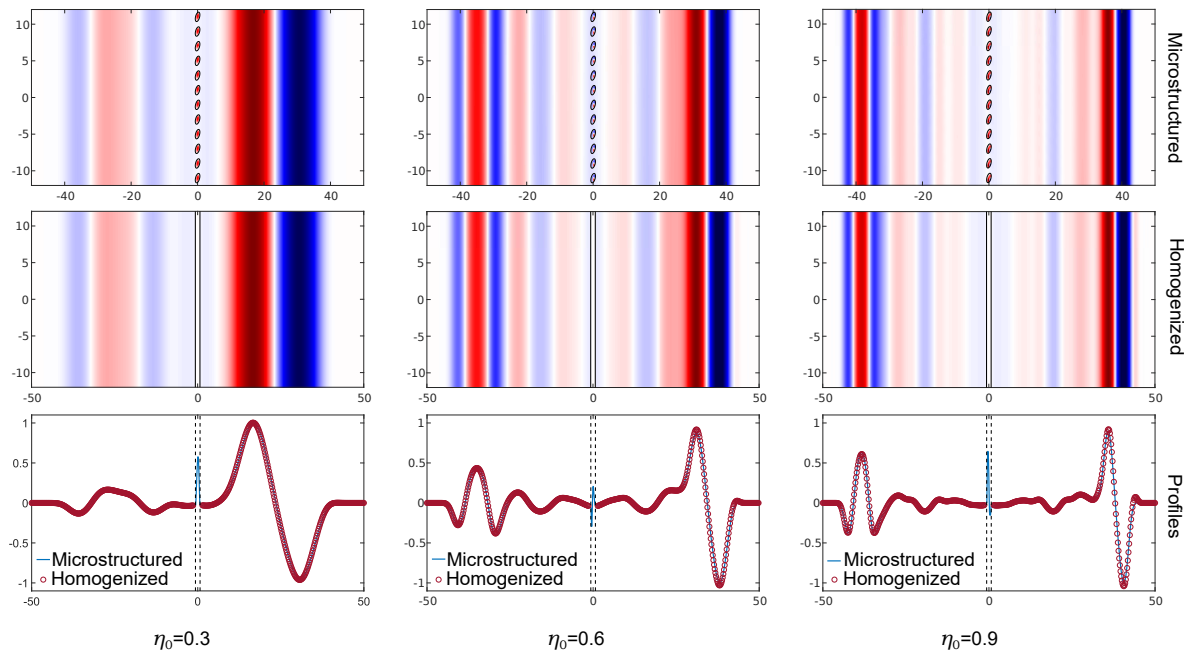

Figure 2.14 – *(Top two rows)* velocity fields for the microstructured configuration and for the homogenized model for an illumination by an incident plane wave at normal incidence when dissipation is considered ($\gamma = 2 \cdot 10^{-6}\,\mathrm{kg}^{-1} \cdot \mathrm{m}^3 \cdot \mathrm{s}$). *(Bottom row)* comparison of the corresponding velocity profiles at $X_2 = -1\,\mathrm{m}$. *(left)* $\eta_0 = 0.3$, *(center)* $\eta_0 = 0.6$, and *(right)* $\eta_0 = 0.9$.

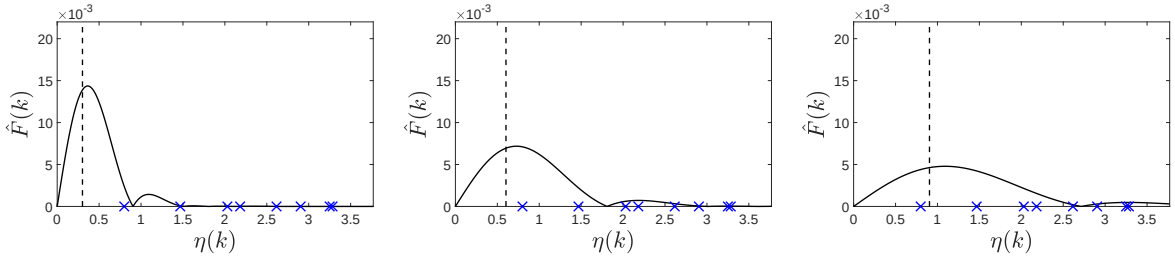

(a) $\eta_0 = 0.3$ (b) $\eta_0 = 0.6$ (c) $\eta_0 = 0.9$

Figure 2.15 – Fourier transform $\hat{F}$ of the source function for the three different values η_0 considered (here indicated by the dashed lines). The blue crosses denote the values $\eta_r = \omega_r h / c_m$ associated with resonances ω_r in (2.66).

As in the inviscid case, one has to remember that the frequency content of the source function is a wide-band signal that involves frequencies higher than f_0 for which the associated values η lie beyond the hypothesis of the small parameter of Assumption 2.1. This is confirmed by Figure 2.15 that displays the Fourier spectrum of the source function for the three different central frequencies considered here. Compared to Figure 2.5, only the central frequency changes but the resonant frequencies denoted by the blue crosses are the same. The comparison of the homogenized simulations with full-field simulations is then satisfying given the large values of η involved. In order to have a more precise comparison frequency by frequency, the transmission coefficients are now studied. To do so, the velocity of the microstructured configuration and of the homogenized model in the case $\eta_0 = 0.6$ is recorded from $t = 0$ to $t = 475$ ms at one receiver located at $(10, 0)\,\mathrm{m}$. The Fourier transform of the velocity is computed from these data and normalized by the one of the source function. The resulting transmission coefficient is displayed in Figure 2.16. One recovers the fact that the agreement between both transmission coefficients deteriorates around

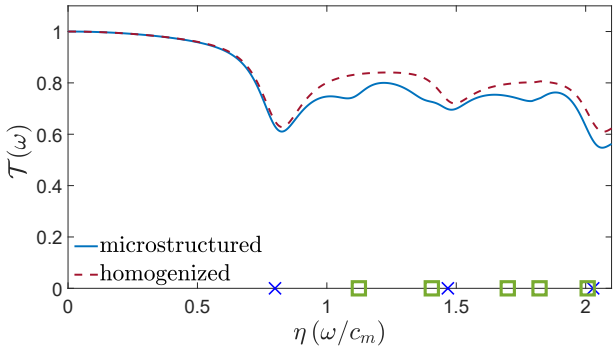

Figure 2.16 – Transmission coefficient for the microstructured configuration and the homogenized model. The blue crosses and the green squares denote the resonant frequencies taken into account in $\mathscr{D}_\gamma(\omega)$ and the missed resonant frequencies of zero mean modes, respectively.

the resonant frequencies that are not taken into account in $\mathscr{D}_\gamma(\omega)$. However, the agreement is better than the ones presented in Figure 2.9 for the inviscid case, explaining the good quality of the results in Figure 2.14 even for the higher values of η_0.

■ *Source point.* We now consider a full 2D configuration which solicits the five effective coefficients in the homogenized model with the case of a source point of Section 2.3.3. The velocity fields on a subset of the computational domain are displayed at times $t \in \{t_1, t_2, t_3, t_4\} = \{25.3, 38.0, 50.7, 63.3\}$ ms on the figures 2.17, 2.18 and 2.19 for $\eta_0 = 0.3,\ 0.6,\ 0.9$, respectively. The profiles at $X_2 = 1$ m are then compared on Figure 2.20. Quantitatively, the discrepancies between solutions of the microstructured problem and of the homogenized model are measured in the L^2-norm for $X_1 \in [-50\text{ m}\,; -5\text{ m}\,]$ and at $X_2 = 1\,\text{m}$. The associated relative errors for the three values of η_0 are of about 2.7%, 7% and 14%, respectively. A good agreement is again observed at low frequency and decreases as η_0 increases to 1.

2.4.4.2 Investigation of the effect of damping

In the previous section, we illustrated that the homogenized model seems to be an accurate approximation of the microstructured configuration. Consequently, we now investigate the effect of damping directly in the resonant homogenized model. This underlines the benefit of the homogenization process since simulations are much less costly and physical properties are easier to analyze.

To begin with, we again consider the incident plane wave at normal incidence so that the simulations can be performed in a 1D setting. Firstly, the velocity profiles of the effective model at $t = 31.7\,\text{ms}$ are presented in Figure 2.21 for different values of γ. In these examples, the central frequency f_0 of the source function (2.57) in the initial condition (2.59) is $f_0 = 72$ Hz. The resonant behaviour of the material leads to energy radiated by the enlarged interface even a long time after the incident wave has passed it. Close to the limit value $\gamma^\star$, for example $\gamma = 2 \cdot 10^{-7}\,\text{s} \cdot \text{kg}^{-1} \cdot \text{m}^3$, the dissipation is so high that we do not see this resonant behaviour anymore. On the other hand, close to $100\,\gamma^\star$, for example $\gamma = 2 \cdot 10^{-5}\,\text{kg}^{-1} \cdot \text{m}^3 \cdot \text{s}$, the dissipation has barely any influence and we almost recover the case $\gamma = +\infty$.

We now focus on a possible physical application of this work through the so-called property of Coherent Perfect Absorption. Schematically, resonant and dissipative scatterers behave as open systems, characterized by their energy leakage and intrinsic losses. The equilibrium between these two energy losses corresponds to a condition of critical coupling and gives rise to a maximum of energy absorption. The study of critical coupling is an active research topic in acoustics, especially

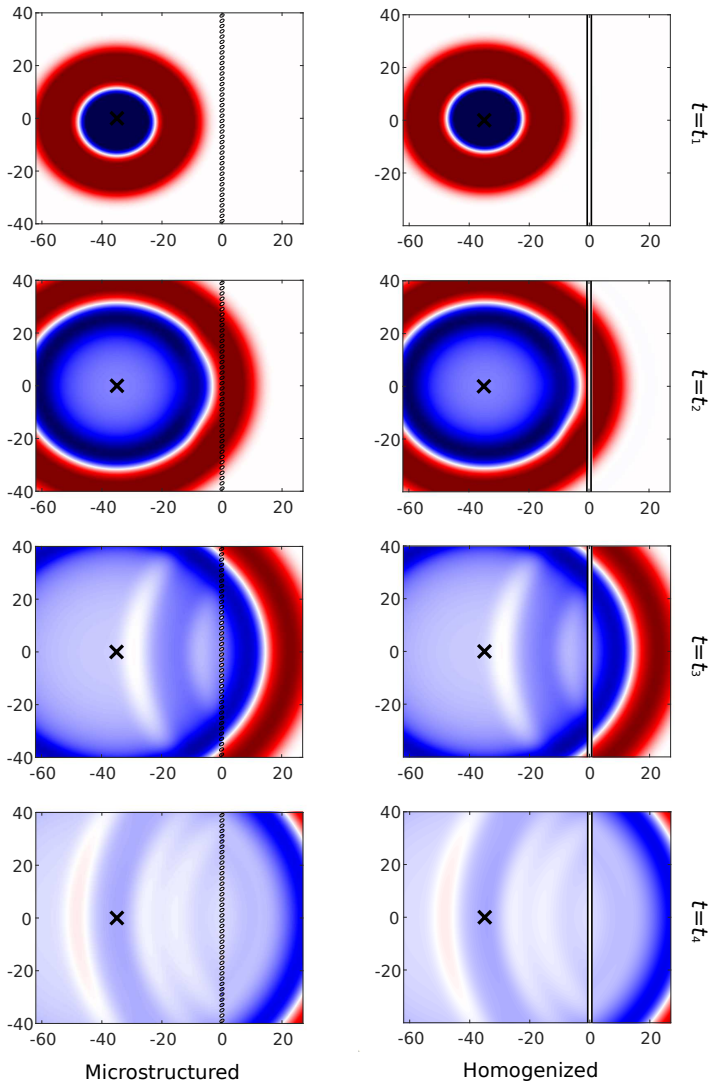

Figure 2.17 – *(Left)* velocity fields for the microstructured configuration and *(right)* for the homogenized model for $\eta_0 = 0.3$ and at different times $t \in \{25.3, 38.0, 50.7, 63.3\}$ ms. A source point is located at the black cross. Dissipation is considered ($\gamma = 2 \cdot 10^{-6}\,\mathrm{kg}^{-1} \cdot \mathrm{m}^3 \cdot \mathrm{s}$).

when the resonances is induced by geometry. The main application is the design of subwavelength panels made of Helmholtz resonators (Jiménez, Huang, Romero-Garcia, Pagneux, & Groby, 2016; Romero-Garcia et al., 2016; Jiang, Li, & Zhang, 2017; Jiménez, Romero-Garcia, Pagneux, & Groby, 2017; Leng et al., 2019; Romero-Garcia et al., 2020; Romero-Garcia et al., 2021). Here, the method is adapted to local resonances induced by the contrast of the physical properties. One recalls that the scattering matrix is defined by

$$\begin{pmatrix} c \\ d \end{pmatrix} = \mathbb{S} \begin{pmatrix} a \\ b \end{pmatrix}$$

with a and b the amplitudes of the incoming waves from the left and the right, respectively, and c and d the amplitudes of the corresponding outgoing waves. In particular, when there is a mirror symmetry, the scattering matrix writes

$$\mathbb{S} = \begin{pmatrix} \mathcal{T}(\omega) & \mathcal{R}(\omega) \\ \mathcal{R}(\omega) & \mathcal{T}(\omega) \end{pmatrix}, \tag{2.75}$$

with $\mathcal{R}(\omega)$ and $\mathcal{T}(\omega)$ the reflection and transmission coefficients computed in the next chapter,

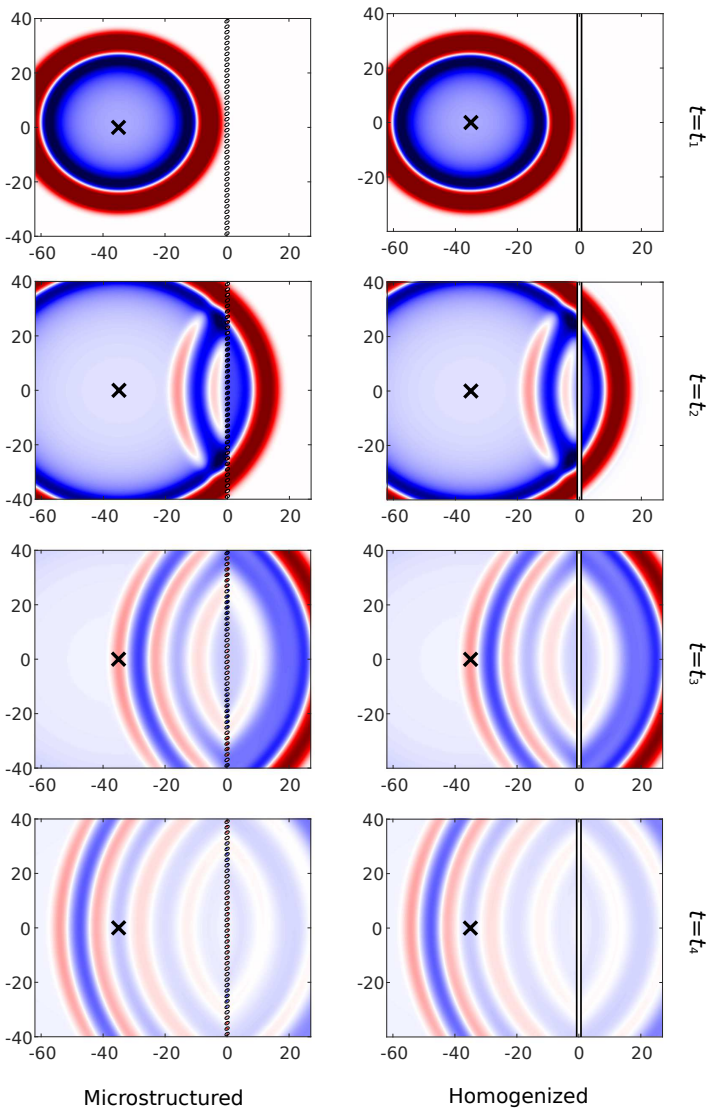

Figure 2.18 – *(Left)* velocity fields for the microstructured configuration and *(right)* for the homogenized model for $\eta_0 = 0.6$ and at different times $t \in \{25.3, 38.0, 50.7, 63.3\}$ ms. A source point is located at the black cross. Dissipation is considered ($\gamma = 2 \cdot 10^{-6}$ kg^{-1} · m^3 · s).

see(3.118). From their expressions for $\theta_I = 0$, one can fill in the scattering matrix $\mathbb{S}$ (Romero-Garcia et al., 2021). For a medium without dissipation, the zeros and poles of the determinant of $\mathbb{S}$ are off the real axis and complex conjugate, around each resonant frequency ω_r considered. By convention, we have chosen a time dependence in $e^{i\omega t}$, so that the poles are in the upper half-plane of $\mathbb{C}$, unlike (Romero-Garcia et al., 2021). This property is observed in Figure 2.22a, where we represent $\log(|\det(\mathbb{S})|)$ around the first four resonance frequencies ω_r taken into account in $\mathscr{D}_\gamma(\omega)$.

When attenuation is considered in the scatterers, the position of these zeros and poles evolves in the complex plane. The imaginary parts of the zeros grow strictly with the magnitude of the dissipative effects. Associated to each resonance ω_r, there is then a critical value of the attenuation for which the zero of $\det(\mathbb{S})$ lies on the real axis, at a frequency $\tilde{\omega}_r$. Figure 2.22b illustrates this property; for $\gamma = 4.47 \cdot 10^{-6}$, we observe that the zero of $\det(\mathbb{S})$ associated with the first resonance frequency lies on the real axis. This is not the case for the three following resonances at this value of γ. Figure 2.23 displays the trajectory of the zeros of $\det(\mathbb{S})$ in the complex plane. We note that there is a slight shift between ω_r and $\tilde{\omega}_r$.

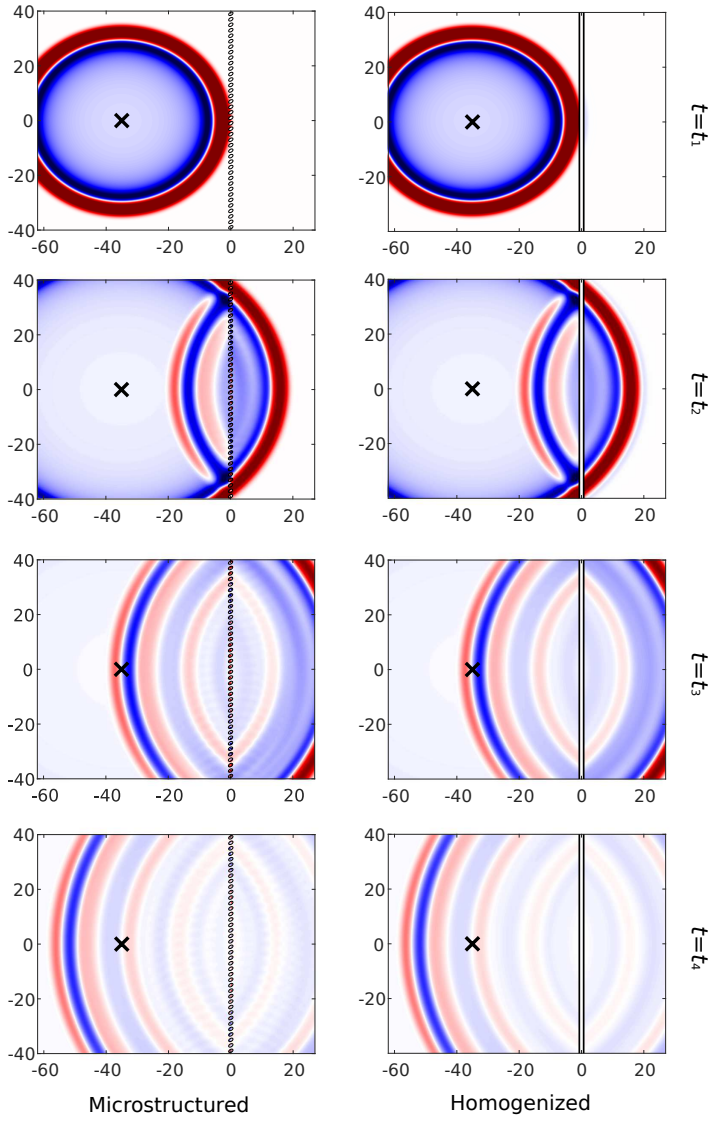

Figure 2.19 – *(Left)* velocity fields for the microstructured configuration and *(right)* for the homogenized model for $\eta_0 = 0.9$ and at different times $t \in \{25.3, 38.0, 50.7, 63.3\}$ ms. A source point is located at the black cross. Dissipation is considered ($\gamma = 2 \cdot 10^{-6}\,\mathrm{kg}^{-1} \cdot \mathrm{m}^3 \cdot \mathrm{s}$).

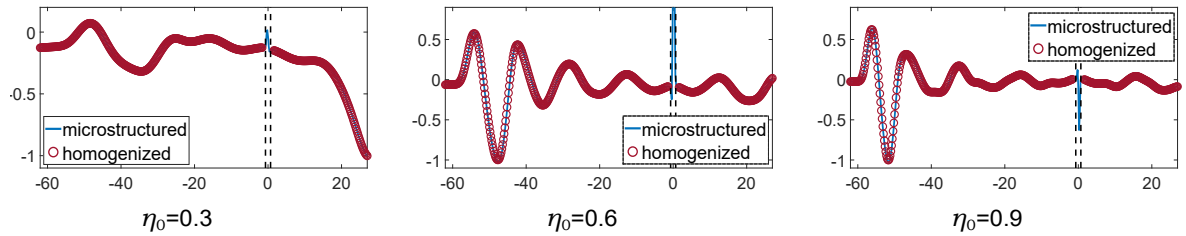

Figure 2.20 – comparison of the velocity profiles at $X_2 = 1\,\mathrm{m}$ in the case of a source point and the three different values of η_0. Dissipation is considered ($\gamma = 2 \cdot 10^{-6}\,\mathrm{kg}^{-1} \cdot \mathrm{m}^3 \cdot \mathrm{s}$).

The transmission and reflexion coefficients computed analytically in (3.118) are displayed in Figure 2.24 for the two values $\gamma = +\infty$ and $\gamma = 4.47 \cdot 10^{-6}\,\mathrm{kg}^{-1} \cdot \mathrm{m}^3 \cdot \mathrm{s}$. As said previously, this last value ensures the critical coupling at $\tilde{\omega_1}$. When dissipation is not considered, perfect transmission is reached followed by perfect reflection within a small band width around the resonant frequencies. With dissipation, these behaviors are smoothed. Besides, one notices that absorption

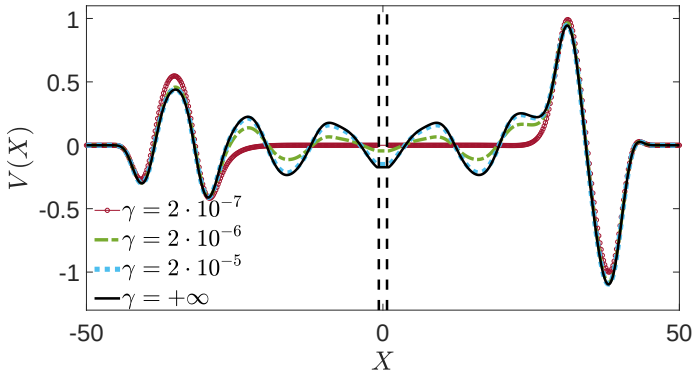

Figure 2.21 – Velocity profiles of the homogenized problem at time $t = t_f$ for different values of γ.

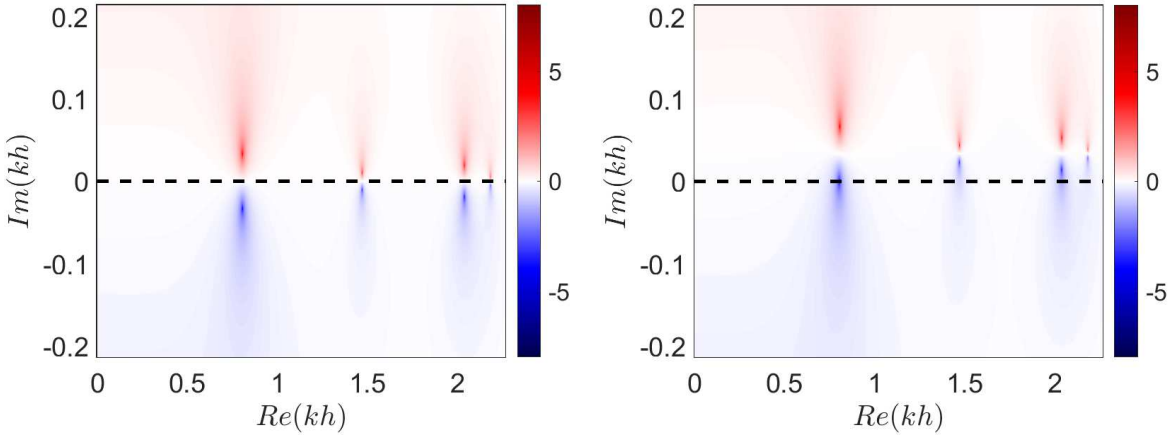

(a) $\gamma = +\infty$ (b) $\gamma = 4.47 \cdot 10^{-6}$

Figure 2.22 – Complex frequency map of $\log(|\det(\mathbb{S})|)$ for the invisicid case (a) and for the critical value of the dissipation parameter (b), where $\mathbb{S}$ is the scattering matrix. We observe three poles and three zeros, in the vicinity of the first three resonance frequencies taken into account in $\mathscr{D}_\gamma$.

$\alpha = 1 - |\mathcal{R}|^2 - |\mathcal{T}|^2$ is maximal around these resonant frequencies (see Figure 2.24c): the optimal value $\alpha = 0.5$ is reached at $\tilde{\omega_1}$. It is consistent with the perfect absorption of symmetric systems illuminated only on one side (Romero-Garcia et al., 2021).

To illustrate this behaviour around the resonant frequencies, we consider a causal monochromatic source point located at $X_S = -120\,\text{m}$. In (2.60), the forcing $F(tc_m)$ is thus replaced by $A\,\sin(\omega_S t)$ if $t \geq 0$, and 0 if $t < 0$. The angular frequency ω_S will be specified for each simulation later on. The velocity profiles at $t = 633\,\text{ms}$ are displayed in Figure 2.25. The magnitude A of the source is such that the amplitude of the emitted velocity is 0.5 m/s, which is denoted by horizontal dotted lines. At the considered time, the incident wave to the left of the source has almost left the domain, and the front of the reflected wave is located near -800 m; it is marked by a green arrow. For $\gamma = +\infty$ (Figure 2.25a), the angular frequency of the forcing is $\omega_S = \omega_{\text{min}}$ which corresponds to the minimum of the transmission coefficient. The time-domain simulations confirm that there is almost no transmitted signal quite quickly. Attenuation is considered in Figure 2.25b with $\gamma = 4.47 \cdot 10^{-6}\,\text{s} \cdot \text{kg}^{-1} \cdot \text{m}^3$, which ensures critical coupling around the first resonance, at $\tilde{\omega_1}$. The angular frequency for the forcing is $\omega_S = \tilde{\omega_1}$. In this second subfigure, the transmitted wave is greater, as expected. Between the front of the reflected wave (green arrow) and the interface, the amplitude of V is greater than 0.5, which confirms that the reflected wave is not absorbed.

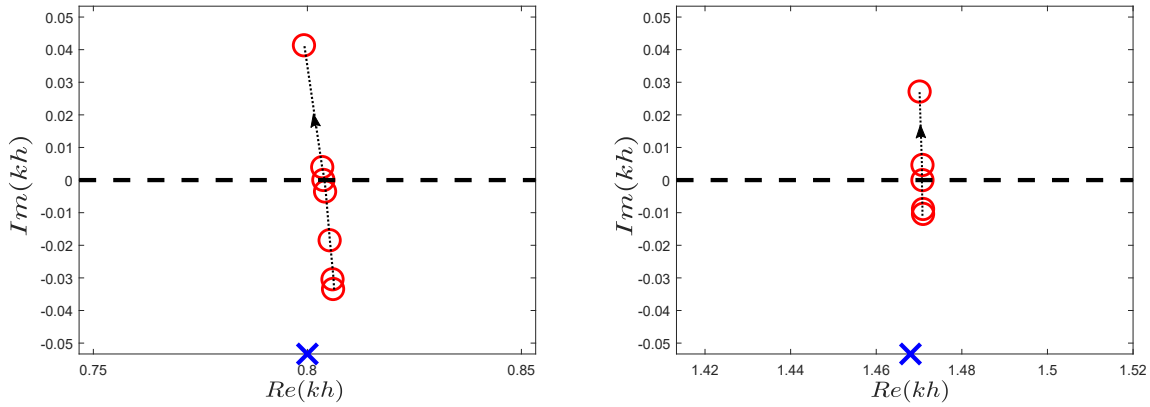

(a) first resonant frequency in $\mathscr{D}_\gamma(\omega)$

(b) second resonant frequency in $\mathscr{D}_\gamma(\omega)$

Figure 2.23 – Zeros of $\det(\mathbb{S})$ in the complex plane, where $\mathbb{S}$ is the scattering matrix, for various values of the dissipation parameter. The arrow shows the direction of the trajectory as losses are increased (i.e. γ is decreased). The red circles denote the zeros for $\gamma \in \{+\infty, 5\cdot10^{-5}, 1\cdot10^{-5}, 5\cdot10^{-6}, 4.47\cdot10^{-6}, 4\cdot10^{-6}, 2\cdot10^{-6}\}$ from bottom to top. The blue cross denotes the resonant frequency.

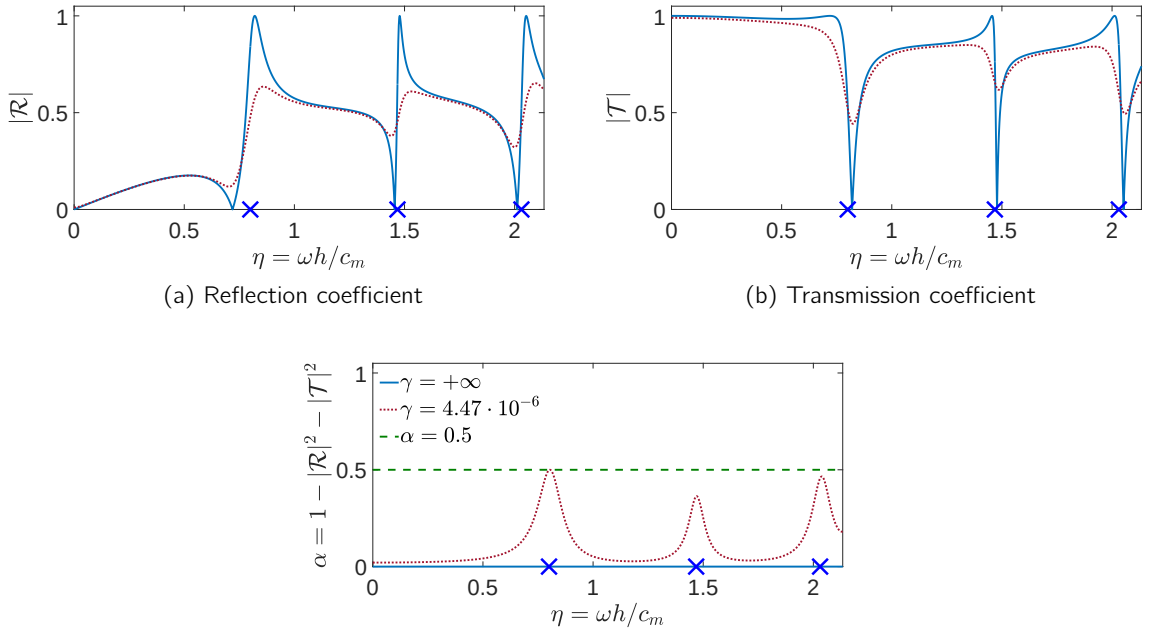

(a) Reflection coefficient

(b) Transmission coefficient

(c) Absorption coefficient

Figure 2.24 – Reflection, transmission and absorption coefficients (3.118). The blue crosses denote ω_r in $\mathscr{D}_\gamma(\omega)$.

To obtain Coherent Perfect Absorption, it is necessary to illuminate the resonant interface from both sides. To do this, two sources are placed symmetrically with respect to the interface and switched on at the same time. Figure 2.26 represents V at $t = 631$ ms. The dotted horizontal lines in ± 0.5 mark the amplitude of the incident wave emitted. At this moment, the incident waves emitted by the two sources have almost left the domain. On the other hand, the fronts of the reflected waves are visible and marked by green arrows. In the inviscid case (Figure 2.26a), the reflected waves are observed, which leads to an increase in the amplitude of the reflected

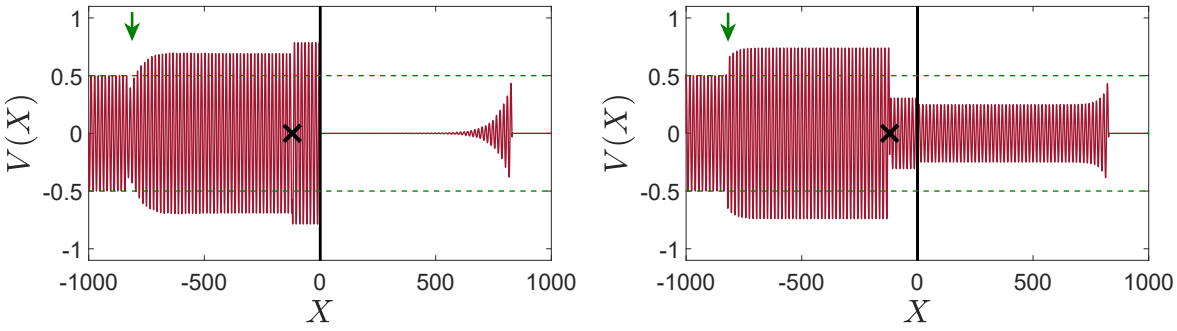

(a) $\gamma = +\infty$ (b) $\gamma = 4.47 \cdot 10^{-6}\,\mathrm{s} \cdot \mathrm{kg}^{-1} \cdot \mathrm{m}^3$

Figure 2.25 – Velocity profiles of the homogenized problem at $t = 633\,\mathrm{ms}$ with one source. Dissipation parameter $\gamma = +\infty$ (a) and $\gamma = 4.47 \cdot 10^{-6}\,\mathrm{s} \cdot \mathrm{kg}^{-1} \cdot \mathrm{m}^3$ (b). The monochromatic source point is located at the black cross and is switched on at $t = 0$. The angular frequency of the source is either $\omega_{\min}$ for which $\mathcal{T}$ is minimal without dissipation (a) or $\tilde{\omega}_1$ which is such that $\det(\mathbb{S})(\tilde{\omega}_1) = 0$ if $\gamma = 4.47 \cdot 10^{-6}\,\mathrm{s} \cdot \mathrm{kg}^{-1} \cdot \mathrm{m}^3$ (b). The green arrows denote the reflected wavefront.

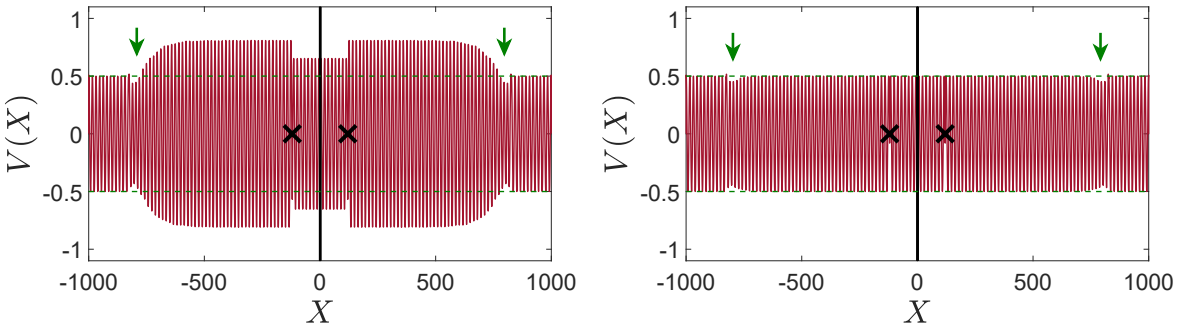

(a) $\gamma = +\infty$ (b) $\gamma = 4.47 \cdot 10^{-6}\,\mathrm{s} \cdot \mathrm{kg}^{-1} \cdot \mathrm{m}^3$

Figure 2.26 – Velocity profiles of the homogenized problem at $t = 631\,\mathrm{ms}$ with two sources. Dissipation parameter $\gamma = +\infty$ (a) and $\gamma = 4.47 \cdot 10^{-6}\,\mathrm{s} \cdot \mathrm{kg}^{-1} \cdot \mathrm{m}^3$ (b). The two monochromatic source points are located at the black crosses and are switched on at $t = 0$. The angular frequency of the source is $\tilde{\omega}_1$ is such that $\det(\mathbb{S})(\tilde{\omega}_1) = 0$ if $\gamma = 4.47 \cdot 10^{-6}\,\mathrm{s} \cdot \mathrm{kg}^{-1} \cdot \mathrm{m}^3$. The green arrows denote the reflected wavefronts.

waves. In the dissipative case with critical coupling (Figure 2.26b), the wave amplitude does not exceed 0.5 which is the amplitude of the emitted velocity. This means that the reflected waves have disappeared and have been completely absorbed by the dissipative resonant interface.

2.5 Conclusion and perspectives

This chapter has focused on the propagation of waves across a periodic row of highly-contrasted inclusions, a problem which has been tackled by a homogenization technique. More specifically, the homogenization process has been performed directly in the time domain. The high contrast between the inclusions and the matrix is described by a scaling of the shear moduli as η^2, where η is the usual small parameter corresponding to the long-wavelength regime. As a consequence, this produces wavelengths within the inclusions that are comparable to the size of the latter.

The specific homogenization process has led to effective jump conditions that are (i) non-local in time and (ii) apply on the boundaries of an equivalent interface possibly *enlarged* to maintain stability. One notes that no calculation is performed anymore within this region. Having the

thickness of the effective interface larger than the width of the original microstructured array has been shown to be a sufficient condition to have a stable effective problem. The agreement of this time-domain effective model with the frequency-dependent jump conditions developed in Pham et al., 2017 has also been established. Then, numerical examples have been provided to illustrate the model obtained and to compare its solutions with simulations involving the original microstructure. A good agreement has been found at low excitation frequency and it has been discussed how it deteriorates as the frequency increases. Eventually, the effective jump conditions have been rewritten in the frequency domain and the time domain when dissipation is considered. Simulations of the homogenized problem incorporating dissipation have also been performed. They have allowed to assess the reliability of the homogenized model when there is coexistence of resonances and dissipation. The role played by dissipation has then been illustrated: for each resonant frequency taken into account in the homogenized model, Coherent Perfect Absorption is observed for a critical value of the dissipation parameter.

Different follows-up can be identified at the end of this chapter:

- A first perspective is to perform the derivation of an effective model at higher order, as discussed in Felbacq and Bouchitté, 2005; Pham et al., 2017, to account for the resonances associated with modes with zero mean, which are missed in the current model. However, it seems that when dissipation is considered, this does not induce a large error compared to full-field solutions. Thus, it is important to assess to what extent these resonances play a role for the problem under consideration.

- The extension of this work to the full three-dimensional elasticity case is also of interest. It requires to introduce a scaling in η^2 for both Lamé's parameters and to perform the computation in a tensorial form but it should not pose major technical difficulties, see (Auriault & Bonnet, 1985; Auriault & Boutin, 2012; Comi & Marigo, 2019) for volumic microstructures.

- In the next chapter dedicated to the numerical modeling of resonant meta-interfaces, the proposed numerical method is shown to be an efficient tool to handle curved enlarged interface. However, the extension to curved interfaces will be purely heuristic. In the non-resonant case, the validity of this extension was discussed through numerical experiments in Lombard et al., 2017. This paper has illustrated that for small curvatures, the error remains the same as for a straight array. However, for high curvatures, the error increases and the jump conditions have to be modified. This numerical investigation could be performed for resonant interfaces in order to identify the maximum curvature below which the heuristic extension is suitable. In line with this point, a more demanding perspective would be to perform the homogenization process for inclusions located along a curved line. The homogenized model would be more complicated since, even in the non-resonant case, the local definition of the curvature will lead to a local expression of the effective parameters, see Rizzoni and Lebon, 2013 for thin curved interphases.

- Moreover, the discussion about Coherent Perfect Absorption was performed for normal incidence. This study could be generalized for different incident angles. This is of particular interest for the design of an optimal metasurface over a wide band of incidence angles (Jiménez et al., 2016). In this purpose, it would also be useful to consider several rows of inclusions in order to play with several geometries and reach wide bands of absorption instead of a single value around each resonance.

- We considered the damping through a structural model. Depending on the solid under consideration it may be relevant to model the energy dissipation by a Maxwell, Kelvin-Voigt,

standard rheological model or more sophisticated model (Krushynska, Kouznetsova, & Geers, 2016; Lewińska, Kouznetsova, van Dommelen, Krushynska, & Geers, 2017). Our approach was rather methodological but in order to describle precisely the dissipative process for a given model it could be interesting to consider these models, which require to introduce the damping in the constitutive equation instead of the balance of momentum.

- Finally, the thin microstructured layer was assumed to be infinite. However, as it is more realistic, it could be of interest to consider a layer of finite length. It requires to take into account both the boundary layer effects appearing near the microstructured layer and the corner singularities in the neighborhood of the extremities of the layer, see for example Semin, Delourme, and Schmidt, 2018 for a finite-length periodic array of holes.

2.A Agreement with the existing frequency-domain formulation

With the effective model (2.38) being derived in the time domain, this section focuses on assessing its equivalence with the frequency-domain formulation (1.19) obtained in Pham et al., 2017. Due to the final effective jump condition (2.38), we seek a closed-form identity for the field W_i solution of (2.39). To do so, let us consider the time-domain Green's function associated with the inclusion domain Ω_i and a source point $\boldsymbol{y}_0$, i.e. the field $G : (\boldsymbol{y}, t) \mapsto G(\boldsymbol{y}, \boldsymbol{y}_0, t)$ that is the fundamental solution of the problem:

$$\begin{cases} \dfrac{\partial^2 G}{\partial t^2}(\boldsymbol{y}, \boldsymbol{y}_0, t) - \dfrac{\mu_i}{\rho_i h^2} \Delta_{\boldsymbol{y}} G(\boldsymbol{y}, \boldsymbol{y}_0, t) = \delta(\boldsymbol{y} - \boldsymbol{y}_0)\delta(t) & (\boldsymbol{y} \in \Omega_i), \\ G(\boldsymbol{y}, \boldsymbol{y}_0, t) = 0 & (\boldsymbol{y} \in \partial\Omega_i), \\ G(\boldsymbol{y}, \boldsymbol{y}_0, 0) = \dfrac{\partial G}{\partial t}(\boldsymbol{y}, \boldsymbol{y}_0, 0) = 0 & (\boldsymbol{y} \in \Omega_i). \end{cases}$$

We define the convolution product:

$$[f * g](t) = \int_{\mathbb{R}} f(t - t')g(t)\,\mathrm{d}t'.$$

Then, the equations (2.39) at time $(t - t')$ are multiplied by G taken at time t' and integrated on $\Omega_i \times [0, t]$, which leads to

$$\int_{\Omega_i} \left\{ \left[\frac{\partial^2 W_i}{\partial t^2} * G \right](t) - \frac{\mu_i}{\rho_i h^2} \left[\Delta_{\boldsymbol{y}} W_i * G \right](t) \right\} \mathrm{d}\boldsymbol{y} = 0.$$

Integrating by parts twice, the first term in time and the second term in space, respectively, and using the boundary conditions for W_i and G yields:

$$W_i(\boldsymbol{y}_0, X_2, t) = -\frac{\mu_i}{\rho_i h^2} \left[\langle\!\langle V(\cdot, X_2, \cdot) \rangle\!\rangle_a * \int_{\partial\Omega_i} \boldsymbol{\nabla}_{\boldsymbol{y}} G(\boldsymbol{y}, \boldsymbol{y}_0, \cdot) \cdot \boldsymbol{n}\,\mathrm{d}\ell \right](t), \tag{2.76}$$

with $\mathrm{d}\ell$ the surface element associated to the $\boldsymbol{y}$-variable. Going back to (2.38), using the Fourier transform (4.70), we now get formally in the frequency domain:

$$\mathscr{F}\left[\rho_i \int_{\Omega_i} \frac{\partial W_i}{\partial t}\,\mathrm{d}\boldsymbol{y} \right](\boldsymbol{X}, \omega) = \frac{\rho_i}{\rho_m} \left\langle\!\!\left\langle \boldsymbol{\nabla} \cdot \hat{\boldsymbol{\Sigma}}(\cdot, X_2, \omega) \right\rangle\!\!\right\rangle_a \int_{\Omega_i} \left\{ -\frac{\mu_i}{\rho_i h^2} \int_{\partial\Omega_i} \boldsymbol{\nabla}_{\boldsymbol{y}_0} \hat{G}(\boldsymbol{y}, \boldsymbol{y}_0, \omega) \cdot \boldsymbol{n}\,\mathrm{d}\ell_0 \right\} \mathrm{d}\boldsymbol{y}, \tag{2.77}$$

where we have used the identity $i\omega\rho_m\hat{V} = \boldsymbol{\nabla}\cdot\hat{\boldsymbol{\Sigma}}$ and the fact that $\hat{G}(\boldsymbol{y},\boldsymbol{y}_0,\omega) = \hat{G}(\boldsymbol{y}_0,\boldsymbol{y},\omega)$. We define the field ζ as

$$\zeta(\boldsymbol{y},\omega) = -\frac{\mu_i}{\rho_i h^2}\int_{\partial\Omega_i} \boldsymbol{\nabla}_{\boldsymbol{y}_0}\hat{G}(\boldsymbol{y},\boldsymbol{y}_0,\omega)\cdot\boldsymbol{n}\,\mathrm{d}\ell_0. \tag{2.78}$$

Owing to the following relation satisfied by G in the frequency domain

$$\Delta_{\boldsymbol{y}}\hat{G}(\boldsymbol{y},\boldsymbol{y}_0,\omega) + \frac{\rho_i\mu_m}{\rho_m\mu_0}\hat{G}(\boldsymbol{y},\boldsymbol{y}_0,\omega) = -\frac{\rho_i h^2}{\mu_i}\delta(\boldsymbol{y}-\boldsymbol{y}_0),$$

then it turns out that ζ is the solution of the following problem:

$$\begin{cases} \Delta_{\boldsymbol{y}}\zeta(\boldsymbol{y},\omega) + \dfrac{\rho_i h^2}{\mu_i}\,\omega^2\,\zeta(\boldsymbol{y},\omega) = 0 & (\boldsymbol{y}\in\Omega_i), \\ \zeta(\boldsymbol{y},\omega) = 1 & (\boldsymbol{y}\in\partial\Omega_i), \end{cases} \tag{2.79}$$

Therefore, provided that the Fourier transforms are well-defined, then $\zeta = \psi_\infty$ with ψ_∞ defined in (1.17). Consequently, once this identity is used in (2.77) together with (1.21), the agreement of the time-domain effective model with the frequency-dependent jump conditions is established. Nonetheless, thanks to the time-domain formulation, an energy analysis is now accessible, which in turn provides a sufficient condition for the effective model to be stable.

CHAPTER 3

Numerical modeling for wave propagation across resonant meta-interfaces

This chapter aims at building a numerical method to simulate the interaction of transient waves with the effective resonant meta-interface studied in Chapter 2. The ESIM approach has been motivated and briefly explained in Section 1.3. This methodology has been used in Lombard et al., 2017 for the case of *non-resonant* effective interfaces. In the present study, the central question therefore concerns the case of *resonant* effective jump conditions that are frequency-dependent in the harmonic regime or non-local in time, along with their implementation for wave propagation simulations in the time domain. This chapter will thus develop a specific ESIM approach for the resonant case, based on the formalism of auxiliary variables.

In Section 3.1, this formalism is introduced and implemented to obtain an equivalent augmented system of first-order equations in time with transformed jump conditions that are local in time. Section 3.2 details the numerical implementation in 1D: the fourth-order finite-difference scheme ADER is used in combination with the ESIM. An error analysis is performed and sufficient conditions under which a given order of accuracy can be obtained are stated in Section 3.3. Then Section 3.4 extends the proposed numerical method to 2D. Numerical experiments in 1D and 2D are finally presented in Section 3.5, while comparisons with semi-analytical solutions allow to assess quantitatively the performance of the approach developed. The modifications of the numerical method in the case where damping is considered are presented in Section 3.6.

3.1 Formalism of auxiliary variables

The effective jump conditions associated with the resonant meta-interfaces are characterized by frequency-dependent terms in the harmonic regime (1.19) and consequently involve a convolution product in the time domain, see (2.38) and (2.76). Their implementation would therefore require to store the entire history of the traces of the solution at the enlarged interface while the computation of the time convolution integral itself would substantially increase the computational cost in a naive extension of the ESIM. As a consequence, it is required to develop a specific approach to handle efficiently this type of resonant interface models numerically. For this purpose, the auxiliary variables formalism has been previously employed in Tip, 1998; Gralak and Tip, 2010; Gralak and Maystre, 2012; Cassier, Hazard, and Joly, 2017a; Cassier, Joly, and Kachanovska, 2017b for Maxwell's equations and in Bellis and Lombard, 2019 for bulk dispersive metamaterials in acoustics. It is adapted here to deal with the resonant meta-interfaces considered.

First, let consider the effective jump conditions (1.19) in the harmonic regime. We assume that the sum in (1.24) can be truncated to a finite number N_R of resonances based on the analysis of the frequency content of a given illuminating wave, see Figure 2.5 in Section 2.3.1.3.
Accordingly, let define locally (along the enlarged interface) the so-called auxiliary variables $\hat{J}_r$ and $\hat{G}_r$, which are associated with the resonance index $r \in \{1, \dots, N_R\}$ and which satisfy the following equations:

$$\begin{cases} (\omega^2 - \omega_r^2)\hat{J}_r(X_2, \omega) = \alpha_r^2 \omega^2 \left\langle\!\left\langle \operatorname{div} \hat{\boldsymbol{\Sigma}}(\boldsymbol{X}, \omega) \right\rangle\!\right\rangle_a \\ \mathrm{i}\omega\, \hat{J}_r(X_2, \omega) = \hat{G}_r(X_2, \omega) \end{cases} \qquad \text{for } X_2 \in \mathbb{R}. \tag{3.1}$$

Setting

$$\begin{cases} \widetilde{\mathcal{B}}_1 = h\mathcal{B} \\ \widetilde{\mathcal{B}}_2 = h\mathcal{B}_2 \\ \widetilde{\mathcal{C}}_{11} = h(\mathcal{S} + \alpha_0) \\ \widetilde{\mathcal{C}}_{12} = h\mathcal{C}_1 \\ \widetilde{\mathcal{C}}_{22} = h(\mathcal{C}_2 + \alpha_0) \end{cases} \tag{3.2}$$

while combining (1.19) and (3.1) then yields the following system in the time domain for all $t > 0$

by a formal application of the inverse Fourier transform:

$$\begin{cases} \partial_t \boldsymbol{\Sigma}(\boldsymbol{X},t) = \mu_m \boldsymbol{\nabla} V(\boldsymbol{X},t) & (|X_1| \geq a/2, X_2 \in \mathbb{R}) \\ \partial_t V(\boldsymbol{X},t) = \dfrac{1}{\rho_m} \operatorname{div} \boldsymbol{\Sigma}(\boldsymbol{X},t) & (|X_1| \geq a/2, X_2 \in \mathbb{R}) \\ \partial_t J_r(X_2,t) = G_r(X_2,t) & (X_2 \in \mathbb{R},\ r = 1,\dots,N_R) \\ \partial_t G_r(X_2,t) = -\omega_r^2 J_r(X_2,t) + \mu_m \alpha_r^2 \partial_t \langle\!\langle \Delta V \rangle\!\rangle_a & (X_2 \in \mathbb{R},\ r = 1,\dots,N_R) \\ [\![V]\!]_a = \widetilde{B}_1 \langle\!\langle \partial_{X_1} V \rangle\!\rangle_a + \widetilde{B}_2 \langle\!\langle \partial_{X_2} V \rangle\!\rangle_a & (X_2 \in \mathbb{R}) \\ [\![\Sigma_1]\!]_a = \widetilde{C}_{11} \langle\!\langle \partial_{X_1} \Sigma_1 \rangle\!\rangle_a + \widetilde{C}_{12} \langle\!\langle \partial_{X_2} \Sigma_1 \rangle\!\rangle_a + \widetilde{C}_{22} \langle\!\langle \partial_{X_2} \Sigma_2 \rangle\!\rangle_a - h \sum_{r=1}^{N_R} J_r & (X_2 \in \mathbb{R}). \end{cases} \tag{3.3}$$

To be consistent with the definition (3.1), the auxiliary variables J_r are not averaged in the last equation of the above system.

Remark 7. *The auxiliary variables $\{\hat{J}_r\}$ are defined through (3.1) for all $\omega \neq \omega_r$. Therefore, in order to apply the inverse Fourier transform, care must be taken and a suitable approach relies on the introduction of an artificial damping parameter that is taken to zero once in the time domain. Studying such a limit amounts to investigate the existence of a limiting absorption principle for the system considered, which is beyond the scope of this work. Reference can be made to, e.g., Cassier et al., 2017b for such an anlysis for dispersive media in electromagnetism.*

Starting from the original variable $\boldsymbol{U} = (V, \boldsymbol{\Sigma})^\mathsf{T}$, the set $\boldsymbol{w} = (\{J_r\}, \{G_r\})^\mathsf{T}$ of auxiliary variables is introduced locally along the enlarged interface to allow the derivation of the system (3.3). The latter consists of first-order equations in time that are complemented by jump conditions that are local in time.

3.2 Numerical modeling in 1D

3.2.1 Preliminaries

In this section, we describe for simplicity the numerical implementation of the system (3.3) in a one-dimensional configuration which is representative of the propagation of a plane wave illuminating a straight enlarged interface at normal incidence. The stress reduces to the scalar field $\boldsymbol{\Sigma}(\boldsymbol{X}) = \Sigma(X)\,\boldsymbol{e}_1$ where $X = \boldsymbol{X} \cdot \boldsymbol{e}_1$ with $(\boldsymbol{e}_1, \boldsymbol{e}_2)$ being the canonical basis of $\mathbb{R}^2$. In this setting, the system (3.3) is recast for all $t > 0$ as:

$$\begin{cases} \partial_t \Sigma(X,t) = \mu_m\, \partial_X V(X,t) & (|X| \geq a/2), \quad (3.4a) \\ \partial_t V(X,t) = \dfrac{1}{\rho_m}\, \partial_X \Sigma(X,t) & (X| \geq a/2), \quad (3.4b) \\ \partial_t G_r(t) = -\omega_r^2 J_r(t) + \mu_m \alpha_r^2 \partial_t \left\langle\!\!\left\langle \partial_{XX}^2 V \right\rangle\!\!\right\rangle_a & (r = 1,\dots,N_R), \quad (3.4c) \\ \partial_t J_r(t) = G_r(t) & (r = 1,\dots,N_R), \quad (3.4d) \\ [\![V]\!]_a = \widetilde{B}_1 \langle\!\langle \partial_X V \rangle\!\rangle_a\,, & (3.4e) \\ [\![\Sigma]\!]_a = \widetilde{C}_{11} \langle\!\langle \partial_X \Sigma \rangle\!\rangle_a - h \sum_{r=1}^{N_R} J_r. & (3.4f) \end{cases}$$

One introduces the matrix

$$\mathbb{A} = \begin{pmatrix} 0 & -1/\rho_m \\ -\mu_m & 0 \end{pmatrix} \tag{3.5}$$

so that concatenating (3.4a) and (3.4b) yields

$$\partial_t \boldsymbol{U} + \mathbb{A}\,\partial_X \boldsymbol{U} = \boldsymbol{0} \qquad (|X| \geq a/2). \tag{3.6}$$

3.2.2 ADER-K scheme

The solution $\boldsymbol{U}$ is discretized on a uniform grid with a mesh size ΔX and a time step Δt. We denote by $\boldsymbol{U}_i^n$ the approximation of $\boldsymbol{U}$ at the point $X_i = i\Delta X$ and time $t_n = n\Delta t$. The explicit finite-difference ADER-K scheme (Schwartzkopff et al., 2004; Lorcher & Munz, 2006), with K an even integer (to have centered finite differences), is used to solve numerically (3.6). When applied to an equation such as (3.6) in a homogeneous domain, this scheme is of order K in both space and time for sufficiently smooth initial data and, for $K = 4$, it is stable under the CFL condition $\Delta t \leq \Delta X/c_m$. Its time-marching writes:

$$\boldsymbol{U}_i^{n+1} = \boldsymbol{U}_i^n - \sum_{s=-K/2}^{+K/2} \sum_{m=1}^{K} \nu_{K,m,s} \left(\frac{\Delta t}{\Delta X}\mathbb{A}\right)^m \boldsymbol{U}_{i+s}^n, \tag{3.7}$$

where the $\nu_{K,m,s}$ are a set of coefficients such that, if the solution $\boldsymbol{U}$ is of class C^K, then its m-th order derivative can be approximated as (Lombard, 2010):

$$\partial_X^m \boldsymbol{U}(X_j, t_n) = \frac{(-1)^{m+1}}{\Delta X^m} m! \sum_{s=-K/2}^{K/2} \nu_{K,m,s} \boldsymbol{U}(X_{j+s}, t_n) + O(\Delta X^{K+1}), \qquad m = 1, \ldots, K. \tag{3.8}$$

Inserting Taylor expansions for $\boldsymbol{U}(X_{j+s}, t_n)$ at (X_j, t_n) and up to the order K in the previous expression leads to the following relations that are satisfied by the coefficients $\nu_{K,m,s}$ for $0 \leq k \leq K$ and $1 \leq m \leq K$:

$$\sum_{s=-K/2}^{K/2} \nu_{K,m,s} s^k = \begin{cases} (-1)^{m+1} & \text{if } k = m \\ 0 & \text{else.} \end{cases} \tag{3.9}$$

From now on, we choose the ADER-K scheme with $K = 4$ which we consider to allow a good compromise between accuracy and computational cost.

3.2.3 Numerical scheme at the interfaces

Considering the time-marching (3.7), two types of points can be distinguished, see Figure 3.1: (i) *regular points* that are the grid nodes for which the stencil does not intersect the enlarged interface, and (ii) *irregular points* that are the nodes whose stencil includes at least one node within the enlarged interface where the solution is actually not defined. Such grid nodes X_i lying within the enlarged interface are referred to as *ghost points*. For time-marching at the irregular points, the scheme (3.7) is modified: *ghost values* $\boldsymbol{U}^*$ have to be defined and used at the ghost points X_i within the enlarged interface while standard numerical values can be used otherwise. In the framework of the Explicit Simplified Interface Method (ESIM), these ghost values are defined as smooth extrapolations of the solution at the ghost points from the values of the solution at the physical points $\pm a/2$. In the case of the ADER-4 scheme, they are given by

$$\begin{cases} \boldsymbol{U}^*(X_i, t_n) = \displaystyle\sum_{m=0}^{q} \frac{1}{m!} \left(X_i + \frac{a}{2}\right)^m \partial_X^m \boldsymbol{U}\left(-\frac{a}{2}, t_n\right) & \text{for } i = I_L + 1,\ I_L + 2, \\ \boldsymbol{U}^*(X_i, t_n) = \displaystyle\sum_{m=0}^{q} \frac{1}{m!} \left(X_i - \frac{a}{2}\right)^m \partial_X^m \boldsymbol{U}\left(\frac{a}{2}, t_n\right) & \text{for } i = I_R - 1,\ I_R - 2, \end{cases} \tag{3.10}$$

where I_L and I_R are the indices of the grid nodes that are the closest to the enlarged interface on each side and $q \geq 1$ is a user-chosen parameter that controls the accuracy of the approximation.

Remark 8. *In the definition* (3.10) *of the ghost values, the point* X_i *is a* grid node *that is in the enlarged interface while* $\pm a/2$ *is a* physical point *that may not coincide with a grid node. This is the whole feature of the ESIM, which allows to implement jump conditions at interfaces whose geometry may be independent of the computational grid of the finite-difference scheme considered.*

This methodology has been implemented in the case of non-resonant effective interface models in Lombard et al., 2017. It is extended here to the case of resonant models, which requires substantial modifications due to the use of auxiliary variables. In the sections 3.2.4 and 3.2.5, it is shown how the computation of the ghost values through (3.10) rely both on the use of the jump conditions (3.4e-3.4f) and on Taylor expansions on both sides of the enlarged interface.

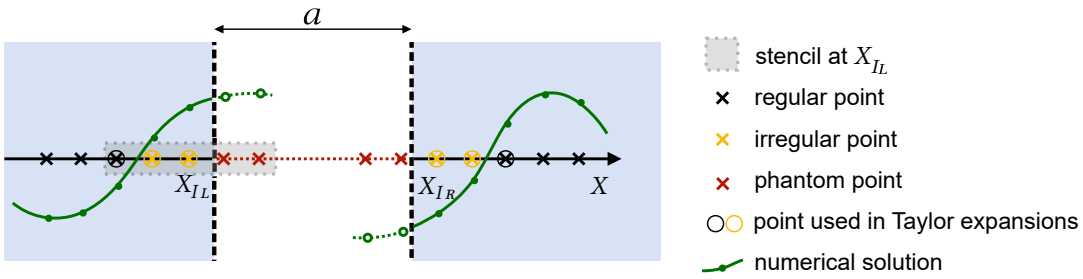

Figure 3.1 – Stencil at X_{I_L} and nodes around the enlarged interface.

3.2.4 High-order jump conditions

The ghost values $\boldsymbol{U}^*$ in (3.10) are expressed in terms of the spatial derivatives $\partial_X^m \boldsymbol{U}$ at $\pm a/2$. To estimate, one computes *qth-order jump conditions* relating the traces of the spatial derivatives of the solution, up to its qth derivative. The vectors $\boldsymbol{U}_+^q(t_n)$ and $\boldsymbol{U}_-^q(t_n)$ are also introduced and concatenate a number $q_U = 2q+2$ of unknowns which are the traces on each side of the spatial derivatives of the fields V and Σ up to the order q:

$$\boldsymbol{U}_\pm^q(t_n) = \left(V_\pm(t_n),\, \partial_X V_\pm(t_n), \ldots,\, \partial_X^q V_\pm(t_n),\, \Sigma_\pm(t_n),\, \partial_X \Sigma_\pm(t_n), \ldots,\, \partial_X^q \Sigma_\pm(t_n)\right)^\top \in \mathbb{R}^{q_U}, \quad (3.11)$$

where $V_\pm(t_n) \equiv V(\pm a/2, t_n)$ and $\Sigma_\pm(t_n) \equiv \Sigma(\pm a/2, t_n)$ and the same notation is employed for the spatial derivatives. The numbering of arrays begins at 1: for instance, $\boldsymbol{U}_\pm^q(t_n)[1] = V(\pm a/2, t_n)$. Moreover, the vector $\boldsymbol{Z}$ contains the $2N_R$ auxiliary variables at time t_n, i.e.

$$\boldsymbol{Z}(t_n) = (J_1(t_n), \ldots,\, J_{N_R}(t_n),\, G_1(t_n), \ldots,\, G_{N_R}(t_n))^\top \in \mathbb{R}^{2N_R}. \quad (3.12)$$

To obtain jump conditions at the order q, i.e. a relation between the vectors $\boldsymbol{U}_+^q$, $\boldsymbol{U}_-^q$ and $\boldsymbol{Z}$, the zeroth-order jump conditions (3.4e) and (3.4f) are first differentiated in time and the equations (3.4a) and (3.4b) are used to replace time derivatives by spatial derivatives. This yields a relation between the vectors $\boldsymbol{U}_+^1$, $\boldsymbol{U}_-^1$ and $\boldsymbol{Z}$. This process of differentiating in time the jump conditions is iterated up to the chosen value of q while the equation (3.4c) is used to express the term $\partial_t G_r$ using J_r and $\partial_t \left\langle\!\left\langle \partial_{XX}^2 V \right\rangle\!\right\rangle_a$ when necessary. The qth-order jump conditions so obtained are written as:

$$\mathbb{C}_+^q \boldsymbol{U}_+^q(t_n) + \boldsymbol{R}_+^q(t_n) = \mathbb{C}_-^q \boldsymbol{U}_-^q(t_n) + \boldsymbol{R}_-^q(t_n) + \mathbb{Q}^q \boldsymbol{Z}(t_n), \quad (3.13)$$

with $\mathbb{C}_\pm^q$ being $q_U \times q_U$ matrices that depend only on the interface parameters and $\mathbb{C}_+^q$ being invertible in the cases considered hereafter. $\mathbb{Q}^q$ is a $q_U \times 2N_R$ matrix that depends only on the

physical parameters and on the resonant frequencies. The q_U-element vectors $\boldsymbol{R}^q_\pm(t_n)$ contain the $(q+1)$-th order derivatives of V and Σ.

In the ensuing numerical examples, the values $q = 3$ and $q = 5$ are chosen and it is checked numerically that the corresponding matrices $\mathbb{C}^q_+$ are invertible. In the case $q = 3$ the entries of the above matrices are given below:

$$\begin{cases} \mathbb{C}^3_\pm[i,i] = 1, & \mathbb{C}^3_\pm[5,6] = \mp\dfrac{\widetilde{C}_{11}}{2}, \\ \mathbb{C}^3_\pm[1,2] = \mp\dfrac{\widetilde{B}_1}{2}, & \mathbb{C}^3_\pm[6,7] = \mp\dfrac{\widetilde{B}_1}{2}, \\ \mathbb{C}^3_\pm[2,3] = \mp\dfrac{\widetilde{C}_{11}}{2}, & \mathbb{C}^3_\pm[7,8] = \mp\dfrac{1}{2}\Big(\widetilde{C}_{11} - h\displaystyle\sum_{r=1}^{N_R}\alpha_r^2\Big), \\ \mathbb{C}^3_\pm[3,4] = \mp\dfrac{\widetilde{B}_1}{2}, & \mathbb{C}^3_\pm[i,j] = 0 \text{ else}, \end{cases} \tag{3.14}$$

$$\begin{cases} \mathbb{Q}^3[2,j] = -\dfrac{h}{\mu_m} & \text{if } j \in \{N_R+1,\dots,2N_R\}, \quad \mathbb{Q}^3[7,j] = \dfrac{h\omega_j^2}{c_m^2} \quad \text{if } j \in \{1,\dots,N_R\}, \\ \mathbb{Q}^3[4,j] = \dfrac{h\omega_{j-N_R}^2}{\mu_m c_m^2} & \text{if } j \in \{N_R+1,\dots,2N_R\}, \quad \mathbb{Q}^3[i,j] = 0 \quad \text{else}, \\ \mathbb{Q}^3[5,j] = -h & \text{if } j \in \{1,\dots,N_R\}, \end{cases} \tag{3.15}$$

$$\boldsymbol{R}^3_\pm[4] = \mp\frac{1}{2}\Big(\widetilde{C}_{11} - h\sum_{r=1}^{N_R}\alpha_r^2\Big)\partial_X^4 V_\pm, \quad \boldsymbol{R}^3_\pm[8] = \mp\frac{\widetilde{B}_1}{2}\partial_X^4\Sigma_\pm, \quad \boldsymbol{R}^3_\pm[i] = 0 \text{ else}. \tag{3.16}$$

3.2.5 Computation of the ghost values

Let define $\mathbb{T}^q_i(\pm a/2)$ as the $2 \times q_U$ matrices of the polynomial forms of the Taylor expansions at the order q between the grid node with index i and the physical point $\pm a/2$, which may not coincide with a grid point, see Remark 8, i.e.

$$\mathbb{T}^q_i(\pm a/2) = \begin{pmatrix} 1 & (X_i \pm a/2) & \dots & (X_i \pm a/2)^q/q! & 0 & 0 & \dots & 0 \\ 0 & 0 & \dots & 0 & 1 & (X_i \pm a/2) & \dots & (X_i \pm a/2)^q/q! \end{pmatrix}.$$

The equation (3.10) is now recast as

$$\begin{cases} \boldsymbol{U}^*(X_i,t_n) = \mathbb{T}^q_i\left(-\dfrac{a}{2}\right)\boldsymbol{U}^q_-(t_n) & \text{for } i = I_L+1,\, I_L+2, \\ \boldsymbol{U}^*(X_i,t_n) = \mathbb{T}^q_i\left(\dfrac{a}{2}\right)\boldsymbol{U}^q_+(t_n) & \text{for } i = I_R-1,\, I_R-2. \end{cases} \tag{3.17}$$

The vector $\boldsymbol{U}^q_+(t_n)$ can be expressed as a function of $\boldsymbol{U}^q_-(t_n)$ using the qth-order jump conditions (3.13). In order to determine $\boldsymbol{U}^q_-(t_n)$, Taylor expansions are written at the q_T nodes $X_i = X_{I_L-q_T+1},\dots,X_{I_L}$ on the left side of the enlarged interface as

$$\boldsymbol{U}(X_i,t_n) = \mathbb{T}^q_i\left(-\frac{a}{2}\right)\boldsymbol{U}^q_-(t_n) + O(\Delta X^{q+1}), \tag{3.18}$$

and at the q_T nodes $X_i = X_{I_R},\dots,X_{I_R+q_T-1}$ on the right side of the enlarged interface as

$$\begin{aligned} \boldsymbol{U}(X_i,t_n) &= \mathbb{T}^q_i\left(\frac{a}{2}\right)\boldsymbol{U}^q_+(t_n) + O(\Delta X^{q+1}) \\ &= \mathbb{T}^q_i\left(\frac{a}{2}\right)(\mathbb{C}^q_+)^{-1}\left[\mathbb{C}^q_-\boldsymbol{U}^q_-(t_n) + \mathbb{Q}^q\boldsymbol{Z}(t_n) + \boldsymbol{R}^q_-(t_n) - \boldsymbol{R}^q_+(t_n)\right] + O(\Delta X^{q+1}). \end{aligned} \tag{3.19}$$

In (3.19), we made use of (3.13) and, by an abuse of notations, the term $\mathcal{O}(\Delta X^{q+1})$ denotes a vector with entries of the order of ΔX^{q+1} and whose size may vary from line to line. The user-chosen parameter q_T will be specified later on. We introduce the $4q_T \times q_U$ block matrices $\mathbb{M}^q$ and $\mathbb{F}^q$ by blocks:

$$\mathbb{M}^q = \begin{pmatrix} \mathbb{T}^q_{I_L-q_T+1}(-\frac{a}{2}) \\ \vdots \\ \mathbb{T}^q_{I_L}(-\frac{a}{2}) \\ \mathbb{T}^q_{I_R}(\frac{a}{2})(\mathbb{C}^q_+)^{-1}\mathbb{C}^q_- \\ \vdots \\ \mathbb{T}^q_{I_R+q_T-1}(\frac{a}{2})(\mathbb{C}^q_+)^{-1}\mathbb{C}^q_- \end{pmatrix}, \qquad \mathbb{F}^q = \begin{pmatrix} \mathbf{0} \\ \vdots \\ \mathbf{0} \\ -\mathbb{T}^q_{I_R}(\frac{a}{2}) \\ \vdots \\ -\mathbb{T}^q_{I_R+q_T-1}(\frac{a}{2}) \end{pmatrix} (\mathbb{C}^q_+)^{-1}, \tag{3.20}$$

and the $4q_T$-element vectors $\boldsymbol{\mathcal{U}}(t_n)$ and $\boldsymbol{\Delta}(t_n)$:

$$\boldsymbol{\mathcal{U}}(t_n) = \begin{pmatrix} \boldsymbol{U}(X_{I_L-q_T+1}, t_n) \\ \vdots \\ \boldsymbol{U}(X_{I_L}, t_n) \\ \boldsymbol{U}(X_{I_R}, t_n) \\ \vdots \\ \boldsymbol{U}(X_{I_R+q_T-1}, t_n) \end{pmatrix}, \qquad \boldsymbol{\Delta}(t_n) = -\mathbb{F}^q\,(\boldsymbol{R}^q_-(t_n) - \boldsymbol{R}^q_+(t_n)). \tag{3.21}$$

Then, from (3.18) and (3.19), one obtains the following system:

$$\mathbb{M}^q\,\boldsymbol{U}^q_-(t_n) = \boldsymbol{\mathcal{U}}(t_n) + \mathbb{F}^q\,\mathbb{Q}^q\boldsymbol{Z}(t_n) - \boldsymbol{\Delta}(t_n) + \mathcal{O}(\Delta X^{q+1}). \tag{3.22}$$

When the parameter q_T is chosen as $4q_T = q_U$, then $\mathbb{M}^q$ is a square matrix that is formally checked to be invertible. This is possible only if q is odd which we assume in the 1D setting considered. If $4q_T > q_U$ then $\mathbb{M}^q$ is not square and we denote by $(\mathbb{M}^q)^{-1}$ its Moore-Penrose pseudo-inverse. Therefore, using the qth-order jump conditions (3.13), we obtain the following expressions for the vectors $\boldsymbol{U}^q_\pm(t_n)$:

$$\boldsymbol{U}^q_-(t_n) = (\mathbb{M}^q)^{-1}\big(\boldsymbol{\mathcal{U}}(t_n) + \mathbb{F}^q\mathbb{Q}^q\boldsymbol{Z}(t_n) - \boldsymbol{\Delta}(t_n) + \mathcal{O}(\Delta X^{q+1})\big), \tag{3.23}$$

and

$$\begin{aligned} \boldsymbol{U}^q_+(t_n) = (\mathbb{C}^q_+)^{-1}[\mathbb{C}^q_-(\mathbb{M}^q)^{-1}\big(\boldsymbol{\mathcal{U}}(t_n) + \mathbb{F}^q\mathbb{Q}^q\boldsymbol{Z}(t_n) - \boldsymbol{\Delta}(t_n) + \mathcal{O}(\Delta X^{q+1})\big) \\ + \mathbb{Q}^q\boldsymbol{Z}(t_n) + \boldsymbol{R}^q_-(t_n) - \boldsymbol{R}^q_+(t_n)]. \end{aligned} \tag{3.24}$$

One neglects the terms that do not depend on $\boldsymbol{\mathcal{U}}(t_n)$ or $\boldsymbol{Z}(t_n)$ in (3.23) and (3.24), and introduces the $q_U \times q_U$ matrix $\mathbb{G}^q$ as

$$\mathbb{G}^q = \mathbb{C}^q_-(\mathbb{M}^q)^{-1}\mathbb{F}^q + \mathbb{I}_{q_U}. \tag{3.25}$$

This allows us to formulate the numerical approximation $(\boldsymbol{U}^q_\pm)^n$ of the vectors $\boldsymbol{U}^q_\pm(t_n)$:

$$(\boldsymbol{U}^q_-)^n = (\mathbb{M}^q)^{-1}\,[\boldsymbol{\mathcal{U}}^n + \mathbb{F}^q\mathbb{Q}^q\boldsymbol{Z}^n], \tag{3.26}$$

and

$$(\boldsymbol{U}^q_+)^n = (\mathbb{C}^q_+)^{-1}[\mathbb{C}^q_-(\mathbb{M}^q)^{-1}\,\boldsymbol{\mathcal{U}}^n + \mathbb{G}^q\mathbb{Q}^q\boldsymbol{Z}^n]. \tag{3.27}$$

Due to (3.17), we finally get the approximation below for the ghost values.

Result 3.1: Numerical approximations of the ghost values

Approximation 1. *The numerical approximations* $(\boldsymbol{U}^*)_i^n$ *of the ghost values* $\boldsymbol{U}^*(X_i, t_n)$ *are computed using the formulae*

$$\begin{cases} (\boldsymbol{U}^*)_i^n = \mathbb{T}_i^q\left(-\frac{a}{2}\right)(\mathbb{M}^q)^{-1}\left[\boldsymbol{\mathcal{U}}^n + \mathbb{F}^q\mathbb{Q}^q\boldsymbol{Z}^n\right] & \text{for } i = I_L+1, I_L+2, \\ (\boldsymbol{U}^*)_i^n = \mathbb{T}_i^q\left(\frac{a}{2}\right)(\mathbb{C}_+^q)^{-1}\left[\mathbb{C}_-^q(\mathbb{M}^q)^{-1}\boldsymbol{\mathcal{U}}^n + \mathbb{G}^q\mathbb{Q}^q\boldsymbol{Z}^n\right] & \text{for } i = I_R-2, I_R-1, \end{cases} \tag{3.28}$$

in terms of the numerical approximations $\boldsymbol{\mathcal{U}}^n$, $\boldsymbol{Z}^n$ *of* $\boldsymbol{\mathcal{U}}(t_n)$, $\boldsymbol{Z}(t_n)$, *respectively.*

The quality of this approximation is quantified in Section 3.3 through a local error analysis. In practice, the matrices $\mathbb{T}_i^q(\pm\frac{a}{2})$, $\mathbb{C}_\pm^q$, $\mathbb{F}^q$, $\mathbb{G}^q$, $\mathbb{Q}^q$ and $(\mathbb{M}^q)^{-1}$ featured in (3.28) are computed in a pre-processing step once for all.

The ghost values (3.28) are used in the ADER-K scheme (3.7) at irregular points. For example, the time-stepping at the irregular point X_{I_L} on the left side of the enlarged interface is recast as

$$\frac{\boldsymbol{U}_{I_L}^{n+1} - \boldsymbol{U}_{I_L}^n}{\Delta t} + \frac{1}{\Delta t}\sum_{s=-K/2}^{0}\sum_{m=1}^{K} v_{K,m,s}\left(\mathbb{A}\frac{\Delta t}{\Delta X}\right)^m \boldsymbol{U}_{I_L+s}^n + \frac{1}{\Delta t}\sum_{s=1}^{K/2}\sum_{m=1}^{K} v_{K,m,s}\left(\mathbb{A}\frac{\Delta t}{\Delta X}\right)^m \boldsymbol{U}^{*n}_{I_L+s} = \boldsymbol{0}, \tag{3.29}$$

which can be written as

$$\boldsymbol{U}_{I_L}^{n+1} = \mathcal{H}_L(\boldsymbol{U}^n, \boldsymbol{Z}^n) \tag{3.30}$$

with $\boldsymbol{U}^n = \{\boldsymbol{U}_i^n\}_i$ being arranged as a vector and $\mathcal{H}_L$ defined by

$$\begin{aligned} \mathcal{H}_L(\boldsymbol{U}^n, \boldsymbol{Z}^n) = \boldsymbol{U}_{I_L}^n &- \sum_{s=-K/2}^{0}\sum_{m=1}^{K} v_{K,m,s}\left(\mathbb{A}\frac{\Delta t}{\Delta X}\right)^m \boldsymbol{U}_{I_L+s}^n \\ &- \sum_{s=1}^{K/2}\sum_{m=1}^{K} v_{K,m,s}\left(\mathbb{A}\frac{\Delta t}{\Delta X}\right)^m \mathbb{T}_{I_L+s}^q\left(-\frac{a}{2}\right)(\mathbb{M}^q)^{-1}\boldsymbol{\mathcal{U}}^n \\ &- \sum_{s=1}^{K/2}\sum_{m=1}^{K} v_{K,m,s}\left(\mathbb{A}\frac{\Delta t}{\Delta X}\right)^m \mathbb{T}_{I_L+s}^q\left(-\frac{a}{2}\right)(\mathbb{M}^q)^{-1}\mathbb{F}^q\,\mathbb{Q}^q\,\boldsymbol{Z}^n. \end{aligned} \tag{3.31}$$

The numerical approximation $\boldsymbol{\mathcal{U}}^n$ of $\boldsymbol{\mathcal{U}}(t_n)$ defined in (3.21) can be expressed as a function of $\boldsymbol{U}^n$. On the right side, we take the example of the irregular point I_R, where the time-stepping is written:

$$\boldsymbol{U}_{I_R}^{n+1} = \mathcal{H}_R(\boldsymbol{U}^n, \boldsymbol{Z}^n) \tag{3.32}$$

with $\mathcal{H}_R$ defined by

$$\begin{aligned} \mathcal{H}_R(\boldsymbol{U}^n, \boldsymbol{Z}^n) = \boldsymbol{U}_{I_R}^n &- \sum_{s=0}^{K/2}\sum_{m=1}^{K} v_{K,m,s}\left(\mathbb{A}\frac{\Delta t}{\Delta X}\right)^m \boldsymbol{U}_{I_R+s}^n \\ &- \sum_{s=-K/2}^{-1}\sum_{m=1}^{K} v_{K,m,s}\left(\mathbb{A}\frac{\Delta t}{\Delta X}\right)^m \mathbb{T}_{I_R+s}^q\left(\frac{a}{2}\right)(\mathbb{C}_+^q)^{-1}\mathbb{C}_-^q(\mathbb{M}^q)^{-1}\boldsymbol{\mathcal{U}}^n \\ &- \sum_{s=-K/2}^{-1}\sum_{m=1}^{K} v_{K,m,s}\left(\mathbb{A}\frac{\Delta t}{\Delta X}\right)^m \mathbb{T}_{I_R+s}^q\left(\frac{a}{2}\right)(\mathbb{C}_+^q)^{-1}\mathbb{G}^q\,\mathbb{Q}^q\,\boldsymbol{Z}^n. \end{aligned} \tag{3.33}$$

Remark 9. *In this section, the computation of the ghost values has been described for the ADER-4 scheme for the sake of simplicity. Yet, the only difference between the different ADER-K schemes is the number of irregular points and ghost points to be considered. Therefore, $\mathcal{H}_L$ and $\mathcal{H}_R$ at X_{I_L} and X_{I_R}, which are always irregular points, are introduced above for an arbitrary ADER-K scheme, with K being an even integer.*

3.2.6 Computation of the auxiliary variables

The computation of the ghost values $\boldsymbol{U}^*$ through Approximation 1 requires to determine an approximation $\boldsymbol{Z}^n$ of the vector $\boldsymbol{Z}(t_n)$ of auxiliary variables (3.12) at each time step. Assuming zero initial conditions for J_r and G_r, which is justified in the case where the enlarged interface is illuminated by an initially remote source, then integrating (3.4c-3.4d) yields

$$\begin{cases} J_r(t_n) = -\Lambda_r^1(t_n)\cos(\omega_r t_n) + \Lambda_r^2(t_n)\sin(\omega_r t_n), \\ G_r(t_n) = \omega_r \left(\Lambda_r^2(t_n)\cos(\omega_r t_n) + \Lambda_r^1(t_n)\sin(\omega_r t_n)\right), \end{cases} \tag{3.34}$$

where, owing to (3.4a-3.4b), one has for $i = 1, 2$:

$$\Lambda_r^i(t_n) = \frac{1}{\omega_r}\int_0^{t_n} \ell_r^i(\tau)\,\mathrm{d}\tau \quad \text{with} \quad \begin{cases} \ell_r^1(\tau) = \mu_m \alpha_r^2 \partial_t \left\langle\!\left\langle \partial_X^2 V \right\rangle\!\right\rangle_a (\tau)\sin(\omega_r \tau), \\ \ell_r^2(\tau) = \mu_m \alpha_r^2 \partial_t \left\langle\!\left\langle \partial_X^2 V \right\rangle\!\right\rangle_a (\tau)\cos(\omega_r \tau). \end{cases} \tag{3.35}$$

In practice, the functions Λ_r^i in (3.35) are computed iteratively as

$$\begin{cases} \Lambda_r^i(t_0) = 0, \\ \Lambda_r^i(t_{n+1}) = \Lambda_r^i(t_n) + \dfrac{1}{\omega_r}\displaystyle\int_{t_n}^{t_{n+1}} \ell_r^i(\tau)\,\mathrm{d}\tau, \end{cases} \tag{3.36}$$

where $t_0 = 0$ and the integral being computed using the extrapolative Newton-Cotes formulae (Vetterling, Teukolsky, Press, & Flannery, 1992), i.e.

$$\int_{t_n}^{t_{n+1}} \ell_r^i(\tau)\,\mathrm{d}\tau = \Delta t \sum_{w=0}^{q_I-2} \delta_w \ell_r^i(t_{n-w}) + \mathcal{O}(\Delta t^{q_I}). \tag{3.37}$$

The values of the parameters δ_w for $q_I = 2, \ldots, 5$ are reported in Table 3.1.

q_I	2	3	4	5
δ_0	1	3/2	23/12	55/24
δ_1		-1/2	-16/12	-59/24
δ_2			5/12	37/24
δ_3				-9/24

Table 3.1 – Numerical integration by the Newton-Cotes formulas: values of the parameter δ_w featured in (3.37).

Moreover, the computation of the terms $\ell_r^i(t_{n-w})$ defined through in (3.35) and used in (3.37) requires to approximate the temporal derivative $\partial_t \left\langle\!\left\langle \partial_X^2 V \right\rangle\!\right\rangle_a (t_{n-w})$, which is achieved using the following finite-difference approximation:

$$\partial_t \left\langle\!\left\langle \partial_X^2 V \right\rangle\!\right\rangle_a (t_{n-w}) = \frac{1}{\Delta t}\sum_{z=0}^{q_D} \beta_z \left\langle\!\left\langle \partial_X^2 V \right\rangle\!\right\rangle_a (t_{n-w-z}) + \mathcal{O}(\Delta t^{q_D}). \tag{3.38}$$

The values of β_z for $q_D = 1, \ldots, 4$ are listed in Table 3.2.

q_D	1	2	3	4
β_0	1	3/2	11/6	75/36
β_1	-1	-4/2	-18/6	-144/36
β_2		1/2	9/6	108/36
β_3			-2/6	-48/36
β_4				9/36

Table 3.2 – Numerical derivation: values of the parameter β_z featured in (3.38).

Remark 10. *Owing to* (3.4c)*, the term* $\langle\langle \partial_X^3 \Sigma \rangle\rangle_a$ *can be used in* (3.35) *instead of the quantity* $\partial_t \langle\langle \partial_X^2 V \rangle\rangle_a$ *with mixed derivatives in time and space. However, in practice, numerical instabilities have been observed in 2D when the third-order spatial derivative is used, contrary to the mixed approach described here. Such instabilities were not observed in 1D but we adopt this mixed approach for the 1D case as well for consistency.*

By inserting (3.37) and (3.38) in (3.36), while keeping track of the approximation order, we get the following expression for Λ_r^i:

$$\begin{cases} \Lambda_r^i(t_0) = 0, \\ \Lambda_r^i(t_{n+1}) = \Lambda_r^i(t_n) + \dfrac{\mu_m \alpha_r^2}{\omega_r} \displaystyle\sum_{w=0}^{q_I-2} \delta_w \sum_{z=0}^{q_D} \beta_z \langle\langle \partial_X^2 V \rangle\rangle_a (t_{n-w-z}) (\kappa_r^i)^{n-w} + O(\Delta t^{\min(q_D+1, q_I)}) \end{cases} \tag{3.39}$$

with $(\kappa_r^1)^s = \sin(\omega_r t_s)$ and $(\kappa_r^2)^s = \cos(\omega_r t_s)$. For $w = 0, ..., q_I - 2$ and $z = 0, ..., q_D$, we know from (3.11) that

$$\langle\langle \partial_X^2 V \rangle\rangle_a (t_{n-w-z}) = \frac{1}{2}(\boldsymbol{U}_-^q(t_{n-w-z}) + \boldsymbol{U}_+^q(t_{n-w-z}))[3], \tag{3.40}$$

where $\boldsymbol{U}[3]$ stands for the third term of the vector $\boldsymbol{U}$. Using the numerical approximations (3.26) and (3.27), we obtain the approximation of $\langle\langle \partial_X^2 V \rangle\rangle_a (t_{n-w-z})$:

$$\langle\langle \partial_X^2 V \rangle\rangle_a^{n-w-z} = \frac{1}{2}\left[(\mathbb{I}_{q_U} + (\mathbb{C}_+^q)^{-1}\mathbb{C}_-^q)(\mathbb{M}^q)^{-1} \boldsymbol{\mathcal{U}}^{n-w-z} + ((\mathbb{M}^q)^{-1}\mathbb{F}^q + (\mathbb{C}_+^q)^{-1}\mathbb{G}^q)\,\mathbb{Q}^q\, \boldsymbol{Z}^{n-w-z} \right][3], \tag{3.41}$$

leading to the final approximation below.

Result 3.2: Numerical approximation of $(\Lambda_r^i)^n$

Approximation 2. *The numerical approximation* $(\Lambda_r^i)^n$ *of* $\Lambda_r^i(t_n)$ *for* $i = 1, 2$ *is computed by the recurrence relation*

$$\begin{cases} (\Lambda_r^i)^0 = 0, \\ (\Lambda_r^i)^{n+1} = (\Lambda_r^i)^n + \dfrac{\mu_m \alpha_r^2}{\omega_r} \displaystyle\sum_{w=0}^{q_I-2} \delta_w \sum_{z=0}^{q_D} \beta_z (\langle\langle \partial_X^2 V \rangle\rangle_a)^{n-w-z} (\kappa_r^i)^{n-w} \end{cases} \tag{3.42}$$

with $(\langle\langle \partial_X^2 V \rangle\rangle_a)^s$ *denoting the numerical approximation* (3.41).

For $i = 1, 2$, we introduce the function $\mathcal{N}_r^i$ defined by

$$\mathcal{N}_r^i\left((\Lambda_r^i)^n, \boldsymbol{U}^n, ..., \boldsymbol{U}^{n-w-z}, \boldsymbol{Z}^n, ..., \boldsymbol{Z}^{n-w-z}, t_n\right)$$
$$= (\Lambda_r^i)^n + \frac{\mu_m \alpha_r^2}{2\omega_r} \sum_{w=0}^{q_I-2} \delta_w \sum_{z=0}^{q_D} \beta_z [(\mathbb{I}_{q_U} + (\mathbb{C}_+^q)^{-1}\mathbb{C}_-^q)(\mathbb{M}^q)^{-1}\boldsymbol{\mathcal{U}}^{n-w-z}][3](\kappa_r^i)^{n-w}$$
$$+ \frac{\mu_m \alpha_r^2}{2\omega_r} \sum_{w=0}^{q_I-2} \delta_w \sum_{z=0}^{q_D} \beta_z [((\mathbb{M}^q)^{-1}\mathbb{F}^q + (\mathbb{C}_+^q)^{-1}\mathbb{G}^q)\mathbb{Q}^q \boldsymbol{Z}^{n-w-z}][3](\kappa_r^i)^{n-w}, \quad (3.43)$$

which allows to write that

$$(\Lambda_r^i)^{n+1} = \mathcal{N}_r^i\left((\Lambda_r^i)^n, \boldsymbol{U}^n, ..., \boldsymbol{U}^{n-w-z}, \boldsymbol{Z}^n, ..., \boldsymbol{Z}^{n-w-z}, t_n\right). \quad (3.44)$$

We now introduce the $2N_R \times 2N_R$ matrix $\mathbb{P}(t_n)$ as follows:

$$\text{for } j \in \{1, ..., N_R\} \begin{cases} \mathbb{P}[j, j] = -\cos(\omega_j t_n), \\ \mathbb{P}[j, j+N_R] = \sin(\omega_j t_n), \\ \mathbb{P}[j+N_R, j] = \omega_j \sin(\omega_j t_n), \\ \mathbb{P}[j+N_R, j+N_R] = \omega_j \cos(\omega_j t_n), \\ \mathbb{P}[i, j] = 0 \quad \text{else.} \end{cases} \quad (3.45)$$

so that, owing to (3.34), we have the following approximation.

Result 3.3: Numerical approximation of the auxiliary variables

Approximation 3. *The numerical approximation* $\boldsymbol{Z}^n = \left(J_1^n, \ldots, J_{N_R}^n, G_1^n, \ldots, G_{N_R}^n\right)^\top$ *of the auxiliary variables vector* $\boldsymbol{Z}(t_n)$ *at the time step* t_n *writes:*

$$\boldsymbol{Z}^n = \mathbb{P}(t_n)\boldsymbol{\Lambda}^n \quad (3.46)$$

with $\boldsymbol{\Lambda}^n = \left((\Lambda_1^1)^n, \ldots, \left(\Lambda_{N_R}^1\right)^n, (\Lambda_1^2)^n, \ldots, \left(\Lambda_{N_R}^2\right)^n\right)^\top$.

In practice, owing to the formula (3.42), the computation of the auxiliary variables J_r^n, G_r^n at a given time step t_n only requires the knowledge of $(\Lambda_r^1)^{n-1}$, $(\Lambda_r^2)^{n-1}$ and $(\langle\partial_X^2 V\rangle_a)^{n-1-w-z}$ for $w = 0, \ldots, (q_I - 2)$ and $z = 0, \ldots, q_D$. These quantities constitute a set of *memory variables* which are necessary to store. We regroup them in the following vector

$$\boldsymbol{\Psi}^n = \left(\boldsymbol{\Lambda}^{n-1}, (\langle\partial_X^2 V\rangle_a)^{n-1}, \cdots, (\langle\partial_X^2 V\rangle_a)^{n+1-q_I-q_D}\right)^\top, \quad (3.47)$$

of size $(q_D+1)\times(q_I-1)+2N_R$. The vector $\boldsymbol{\Psi}^n$ is stored and updated during the entire simulation. For a given ghost point, once $\boldsymbol{Z}^n$ is computed, the resonant case only requires an additional matrix-vector product with a matrix computed in pre-processing. Therefore, in terms of computational time, these additional computations are negligible compared to the cost of the numerical scheme. Indeed, for the 1D examples investigated, the additional computational time for the resonant meta-interface is of about 11% compared to finite differences in a homogeneous medium.

3.2.7 Summary of the algorithm

Algorithm 1 Time-marching scheme with auxiliary variables and ghost values

- *Pre-processing:*
  - Detection of the irregular points surrounding the enlarged interface.
  - Computation of the matrices $(\mathbb{M}^q)^{-1}$, $\mathbb{C}_-^q$, $(\mathbb{C}_+^q)^{-1}$, $\mathbb{F}^q$, $\mathbb{G}^q$ and $\mathbb{Q}^q$.
  - Computation of $\mathbb{T}_i^q(-\frac{a}{2})(\mathbb{M}^q)^{-1}$ and $\mathbb{T}_i^q(-\frac{a}{2})(\mathbb{M}^q)^{-1}\mathbb{F}^q\mathbb{Q}^q$ for ghost values at the left side of the enlarged interface.
  - Computation of $\mathbb{T}_i^q(\frac{a}{2})(\mathbb{C}_+^q)^{-1}\mathbb{C}_-^q(\mathbb{M}^q)^{-1}$ and $\mathbb{T}_i^q(\frac{a}{2})(\mathbb{C}_+^q)^{-1}\mathbb{G}^q\mathbb{Q}^q$ for ghost values at the right side of the enlarged interface.
  - Computation of $(\mathbb{I}_{qU} + (\mathbb{C}_+^q)^{-1}\mathbb{C}_-^q)(\mathbb{M}^q)^{-1}$ and $((\mathbb{M}^q)^{-1}\mathbb{F}^q + (\mathbb{C}_+^q)^{-1}\mathbb{G}^q)\mathbb{Q}^q$.
- *Initialization:* set the solution $\boldsymbol{U}_i^0$ at $t_0 = 0$ while $\boldsymbol{\Psi}^0 = \mathbf{0}$ along the enlarged interface.
- *Iterate in time* $n \geq 0$:
  - Computation of the vector $\boldsymbol{\Lambda}^n$ from $\boldsymbol{\Psi}^n$ using Approximation 2.
  - Computation of $\mathbb{P}(t_n)$ and then of the auxiliary variables vector $\boldsymbol{Z}^n$ from $\boldsymbol{\Lambda}^n$ using Approximation 3.
  - Computation of $\boldsymbol{\mathcal{U}}^n$ in (3.21) from $\boldsymbol{U}_i^n$.
  - Computation of the ghost values $(\boldsymbol{U}^*)_i^n$ using Approximation 1.
  - Time-marching using (3.7) to compute the solution $\boldsymbol{U}_i^{n+1}$ for all i with the ghost values being used where necessary.
  - Computation of $\left\langle\left\langle \partial_X^2 V \right\rangle\right\rangle_a^n$ using (3.41) and update of the memory variables vector $\boldsymbol{\Psi}^{n+1}$ in (3.47).

3.3 Numerical analysis in 1D

To our knowledge, there is no theoretical result available on the numerical stability of the ESIM. In the non-resonant case, no stability issue has been observed on a large number of simulations that involved interfaces with various constitutive parameters and positions within the finite-difference grid (Lombard et al., 2017). In the resonant case considered in the present study, the stability is observed in practice to depend on the order of integration q_I in (3.37), on the order of derivation q_D in (3.38) and on the number q_T of grid nodes considered for the Taylor expansions (3.18-3.19). In practice, given (q_D, q_I), the stability is observed on numerical experiments for the minimal values of q_T that are reported in Table 3.3. The case $(q_D, q_I) = (4, 5)$ is not reported because q_T being too large, the use of the pseudo-inverse of the associated matrix $\mathbb{M}^q$ yields unacceptable numerical errors. When q_T is chosen according to Table 3.3, then the CFL condition $\Delta t \leq \Delta X / c_m$ of the ADER-4 scheme in a homogeneous domain seems to be the critical threshold for stability here as well.

In this context where no stability result is available then *global* error estimates, i.e. cumulative error over the iterations, cannot be derived for the proposed scheme. Rather, we focus here on a *local* in time error analysis. We assume that the numerical solution is the exact continuous one at time t_n and evaluate the error commited by the numerical scheme in one time step. The

q_D \ q_I	2	3	4	5
1	$q_U/4$	$q_U/4$	$q_U/4$	$q_U/4$
2	$q_U/4$	$q_U/4+1$	$q_U/4+1$	$q_U/4+1$
3	$q_U/4$	$q_U/4+1$	$q_U/4+2$	$q_U/4+2$
4	$q_U/4$	$q_U/4+1$	$q_U/4+2$	

Table 3.3 – Minimal value of the Taylor expansion parameter q_T for which the scheme is observed to be stable in the numerical experiments considered, given (q_D, q_I) and with $q_U = (2q+2)$ as in (3.11) for $q \in \{3, 5\}$.

expressions of the local errors $\mathcal{L}_{0,\boldsymbol{U}}$, $\mathcal{L}_{0,\boldsymbol{\Lambda}}$ and $\mathcal{L}_{0,\boldsymbol{Z}}$ on $\boldsymbol{U}$, $\boldsymbol{\Lambda}$ and $\boldsymbol{Z}$, respectively, at time t_n are introduced as:

$$\begin{cases} \mathcal{L}_{0,\boldsymbol{U}}(X_{I_L}, t_n) = \boldsymbol{U}(X_{I_L}, t_{n+1}) - \mathcal{H}_L(\boldsymbol{U}(\cdot, t_n), \boldsymbol{Z}(t_n)), \\ \mathcal{L}_{0,\boldsymbol{U}}(X_{I_R}, t_n) = \boldsymbol{U}(X_{I_R}, t_{n+1}) - \mathcal{H}_R(\boldsymbol{U}(\cdot, t_n), \boldsymbol{Z}(t_n)), \\ \mathcal{L}_{0,\Lambda_r^i}(t_n) = \Lambda_r^i(t_n) - \mathcal{N}\left(\Lambda_r^i(t_n), \boldsymbol{U}(\cdot, t_n), ..., \boldsymbol{U}(\cdot, t_{n-w-z}), \boldsymbol{Z}(t_n), ..., \boldsymbol{Z}(t_{n-w-z}), t_n\right) \\ \qquad\qquad\qquad\qquad\qquad\qquad\qquad\qquad \text{(for } i = 1,2, \text{ and } r = 1, \dots, N_R), \\ \mathcal{L}_{0,\boldsymbol{\Lambda}}(t_n) = \left(\mathcal{L}_{0,\Lambda_1^1}(t_n), \cdots, \mathcal{L}_{0,\Lambda_{N_R}^1}(t_n), \mathcal{L}_{0,\Lambda_1^2}(t_n), \cdots, \mathcal{L}_{0,\Lambda_{N_R}^2}(t_n)\right)^\top, \\ \mathcal{L}_{0,\boldsymbol{Z}}(t_n) = \mathbb{P}(t_{n+1})\mathcal{L}_{0,\boldsymbol{\Lambda}}(t_n). \end{cases} \tag{3.48}$$

These errors are analyzed at the irregular points in the general case of a ADER-K scheme. These points are chosen as they necessitate a special treatment. For a regular point, the analysis is simply the same as in a homogeneous medium. The example of the left irregular point X_{I_L} and the right one X_{I_R} is chosen because they are irregular points regardless of the choice of the even integer K.

Assumption 3.1

Let us assume sufficiently smooth initial data, so that the local truncation error for the ADER-K scheme in a homogeneous domain is $O(\Delta X^K)$. We consider the order $q \in \{3, 5\}$ and we set $q_T = q_U/4$ so that $\mathbb{M}^q$ in (3.20) is a square matrix.

Then, considering the approximations 1, 2 and 3, the local errors (3.48) are analysed in the three next subsections.

3.3.1 Estimation of $\mathcal{L}_{0,U}$

Property 2. *Under Assumptions 3.1, the local errors on $\boldsymbol{U}$ defined in (3.48) read*

$$\begin{cases} \mathcal{L}_{0,\boldsymbol{U}}(X_{I_L}, t_n) = O(\Delta X^{\min(K+1,q)}), \\ \mathcal{L}_{0,\boldsymbol{U}}(X_{I_R}, t_n) = O(\Delta X^{\min(K+1,q)}). \end{cases} \tag{3.49}$$

Proof. $\mathcal{L}_{0,\boldsymbol{U}}$ is defined in (3.48) for the two irregular points X_{I_L} and X_{I_R}. These local errors can

be expressed as:

$$\begin{aligned}\boldsymbol{\mathcal{L}}_{0,\boldsymbol{U}}(X_{I_L},t_n)=\boldsymbol{U}(X_{I_L},t_{n+1})-\boldsymbol{U}(X_{I_L},t_n)+\sum_{s=-K/2}^{0}\sum_{m=1}^{K}\nu_{K,m,s}\left(\mathbb{A}\frac{\Delta t}{\Delta X}\right)^m\boldsymbol{U}(X_{I_L+s},t_n)\\+\sum_{s=1}^{K/2}\sum_{m=1}^{K}\nu_{K,m,s}\left(\mathbb{A}\frac{\Delta t}{\Delta X}\right)^m\tilde{\boldsymbol{U}}^*(X_{I_L+s},t_n),\end{aligned}\tag{3.50}$$

and

$$\begin{aligned}\boldsymbol{\mathcal{L}}_{0,\boldsymbol{U}}(X_{I_R},t_n)=\boldsymbol{U}(X_{I_R},t_{n+1})-\boldsymbol{U}(X_{I_R},t_n)+\sum_{s=-K/2}^{-1}\sum_{m=1}^{K}\nu_{K,m,s}\left(\mathbb{A}\frac{\Delta t}{\Delta X}\right)^m\tilde{\boldsymbol{U}}^*(X_{I_R+s},t_n)\\+\sum_{s=0}^{K/2}\sum_{m=1}^{K}\nu_{K,m,s}\left(\mathbb{A}\frac{\Delta t}{\Delta X}\right)^m\boldsymbol{U}(X_{I_R+s},t_n),\end{aligned}\tag{3.51}$$

where $\tilde{\boldsymbol{U}}^*(X_i,t_n)$ denotes the ghost value obtained when replacing the numerical values $(\boldsymbol{U},\boldsymbol{\Lambda},\boldsymbol{Z})^n$ by their exact counterparts in Approximation 1. These fields are assumed to be as smooth as necessary.
To estimate (3.50) and (3.51), one first evaluates the approximation of the ghost values $\tilde{\boldsymbol{U}}^*(X_i,t_n)$. From Approximation 1, these quantities write:

$$\begin{cases}\tilde{\boldsymbol{U}}^*(X_{I_L+s},t_n)=\mathbb{T}_i^q\left(-\frac{a}{2}\right)(\mathbb{M}^q)^{-1}\left[\boldsymbol{\mathcal{U}}(t_n)+\mathbb{F}^q\mathbb{Q}^q\boldsymbol{Z}(t_n)\right] & \text{for } s=1,\dots,K/2,\\ \tilde{\boldsymbol{U}}^*(X_{I_R+s},t_n)=\mathbb{T}_i^q\left(\frac{a}{2}\right)(\mathbb{C}_+^q)^{-1}[\mathbb{C}_-^q(\mathbb{M}^q)^{-1}\boldsymbol{\mathcal{U}}(t_n)+\mathbb{G}^q\mathbb{Q}^q\boldsymbol{Z}(t_n)] & \text{for } s=-K/2,\dots,-1.\end{cases}\tag{3.52}$$

Using (3.23) and (3.24), one gets

$$\begin{cases}\tilde{\boldsymbol{U}}^*(X_{I_L+s},t_n)= & \mathbb{T}^q_{I_L+s}\left(-\frac{a}{2}\right)\boldsymbol{U}_-^q(t_n)+\mathbb{T}^q_{I_L+s}\left(-\frac{a}{2}\right)(\mathbb{M}^q)^{-1}\left[\boldsymbol{\Delta}(t_n)+\boldsymbol{O}(\Delta X^{q+1})\right]\\ & \qquad\qquad\qquad\qquad\qquad\qquad\qquad\qquad\qquad\qquad\qquad\qquad\text{for } s=1,\dots,K/2\\ \tilde{\boldsymbol{U}}^*(X_{I_R+s},t_n)= & \mathbb{T}^q_{I_R+s}\left(\frac{a}{2}\right)\boldsymbol{U}_+^q(t_n)-\mathbb{T}^q_{I_R+s}\left(\frac{a}{2}\right)(\mathbb{C}_+^q)^{-1}[\mathbb{G}^q(\boldsymbol{R}_-^q(t_n)-\boldsymbol{R}_+^q(t_n))\\ & \qquad\qquad+\mathbb{C}_-^q(\mathbb{M}^q)^{-1}\boldsymbol{O}(\Delta X^{q+1})]\quad\text{for } s=-K/2,\dots,-1.\end{cases}\tag{3.53}$$

Symbolic computations are then performed using Maple to estimate the leading contributions of the entries of the vectors in (3.53). Doing so provides, for $q=3$ or 5:

$$\begin{cases}\mathbb{T}^q_{I_L+s}\left(-\frac{a}{2}\right)(\mathbb{M}^q)^{-1}\boldsymbol{\Delta}(t_n)=\boldsymbol{O}(\Delta X^q),\\ \mathbb{T}^q_{I_L+s}\left(-\frac{a}{2}\right)(\mathbb{M}^q)^{-1}\boldsymbol{O}(\Delta X^{q+1})=\boldsymbol{O}(\Delta X^{q+1}),\\ \mathbb{T}^q_{I_R+s}\left(\frac{a}{2}\right)(\mathbb{C}_+^q)^{-1}\mathbb{G}^q(\boldsymbol{R}_-^q(t_n)-\boldsymbol{R}_+^q(t_n))=\boldsymbol{O}(\Delta X^q),\\ \mathbb{T}^q_{I_R+s}\left(\frac{a}{2}\right)(\mathbb{C}_+^q)^{-1}\mathbb{C}_-^q(\mathbb{M}^q)^{-1}\boldsymbol{O}(\Delta X^{q+1})=\boldsymbol{O}(\Delta X^{q+1}).\end{cases}\tag{3.54}$$

One notes that the first and third of the above estimates make use of the definition (3.16) of $\boldsymbol{R}_\pm^q(t_n)$, which are expressed in terms of the exact solution, and it is assumed that the latter is sufficiently smooth. Therefore, for $q=3$ or 5, we finally obtain the following estimate for the approximation of the ghost values:

$$\tilde{\boldsymbol{U}}^*(X_i,t_n)=\mathbb{T}_i^q\left(\mp\frac{a}{2}\right)\boldsymbol{U}_\mp^q(t_n)+\boldsymbol{O}(\Delta X^q).\tag{3.55}$$

The top (resp. bottom) sign corresponds to the left (resp. right) case, the order of this approximation being the same for both sides. Consequently, from now on we will only consider X_{I_R} to evaluate the order of $\mathcal{L}_{0,\boldsymbol{U}}$ but the final result will apply to any irregular point. We use Taylor expansions and (3.55) for each term of (3.51) to get:

$$\begin{cases} \boldsymbol{U}(X_{I_R+s}, t_n) = \displaystyle\sum_{\ell=0}^{q} \frac{1}{\ell!} \left(X_{I_R+s} - \frac{a}{2}\right)^{\ell} \partial_X^{\ell} \boldsymbol{U}\left(\frac{a}{2}, t_n\right) + \mathcal{O}(\Delta X^{q+1}), \\ \tilde{\boldsymbol{U}}^{*}(X_{I_R+s}, t_n) = \displaystyle\sum_{\ell=0}^{q} \frac{1}{\ell!} \left(X_{I_R+s} - \frac{a}{2}\right)^{\ell} \partial_X^{\ell} \boldsymbol{U}\left(\frac{a}{2}, t_n\right) + \mathcal{O}(\Delta X^{q}). \end{cases} \tag{3.56}$$

Since $\Delta t = \mathcal{O}(\Delta X)$ holds from the CFL condition of the ADER-K scheme, then one can write

$$\mathcal{L}_{0,\boldsymbol{U}}(X_{I_R}, t_n) = \mathcal{L}^0_{0,\boldsymbol{U}}(X_{I_R}, t_n) + \sum_{m=1}^{K} \mathcal{L}^m_{0,\boldsymbol{U}}(X_{I_R}, t_n) + \mathcal{O}(\Delta X^q), \tag{3.57}$$

when defining for $m = 1, \ldots, K$:

$$\begin{aligned} \mathcal{L}^0_{0,\boldsymbol{U}}(X_{I_R}, t_n) &= \boldsymbol{U}(X_{I_R}, t_{n+1}) - \boldsymbol{U}(X_{I_R}, t_n), \\ \mathcal{L}^m_{0,\boldsymbol{U}}(X_{I_R}, t_n) &= \sum_{s=-K/2}^{+K/2} \nu_{K,m,s} \left(\mathbb{A}\frac{\Delta t}{\Delta X}\right)^m \sum_{\ell=0}^{q} \frac{1}{\ell!} \left(X_{I_R+s} - \frac{a}{2}\right)^{\ell} \partial_X^{\ell} \boldsymbol{U}\left(\frac{a}{2}, t_n\right). \end{aligned} \tag{3.58}$$

From a Taylor expansion at the order K in time and using (3.6) in combination with Taylor expansions at the order $(q-m)$ in space, we can write

$$\begin{aligned} \boldsymbol{U}(X_{I_R}, t_{n+1}) = \boldsymbol{U}(X_{I_R}, t_n) + \sum_{m=1}^{K} \frac{\Delta t^m}{m!} (-1)^m \mathbb{A}^m \sum_{\ell=0}^{q-m} \frac{1}{\ell!} \left(X_{I_R} - \frac{a}{2}\right)^{\ell} \partial_X^{m+\ell} \boldsymbol{U}\left(\frac{a}{2}, t_n\right) \\ + \mathcal{O}(\Delta X^{q+1}) + \mathcal{O}(\Delta X^{K+1}). \end{aligned} \tag{3.59}$$

Combining (3.58) and (3.59), we can rewrite $\mathcal{L}_0(X_{I_R}, t_n)$ as follows:

$$\begin{aligned} \mathcal{L}^0_{0,\boldsymbol{U}}(X_{I_R}, t_n) = \sum_{m=1}^{K} \frac{\Delta t^m}{m!} (-1)^m \mathbb{A}^m \sum_{\ell=m}^{q} \frac{1}{(\ell-m)!} \left(X_{I_R} - \frac{a}{2}\right)^{\ell-m} \partial_X^{\ell} \boldsymbol{U}\left(\frac{a}{2}, t_n\right) \\ + \mathcal{O}(\Delta X^{q+1}) + \mathcal{O}(\Delta X^{K+1}). \end{aligned} \tag{3.60}$$

Summing $\mathcal{L}^0_{0,\boldsymbol{U}}$ and the terms $\mathcal{L}^m_{0,\boldsymbol{U}}$ yields:

$$\mathcal{L}_{0,\boldsymbol{U}}(X_{I_R}, t_n) = \sum_{m=1}^{K} \mathbb{A}^m \Delta t^m \sum_{\ell=0}^{q} \varepsilon_{\ell,m} \partial_X^{\ell} \boldsymbol{U}\left(\frac{a}{2}, t_n\right) + \mathcal{O}(\Delta X^{\min(K+1,q)}), \tag{3.61}$$

where, for $m = 1, \ldots, K$ and $\ell = 0, \ldots, q$, the parameter $\varepsilon_{\ell,m}$ is defined as

$$\varepsilon_{\ell,m} = \frac{(-1)^m}{m\,!(\ell-m)!} \left(X_{I_R} - \frac{a}{2}\right)^{\ell-m} \delta_{\ell \geq m} + \sum_{s=-K/2}^{K/2} \nu_{K,m,s} \frac{1}{\ell!\,\Delta X^m} \left(X_{I_R} - \frac{a}{2} + s\Delta X\right)^{\ell}, \tag{3.62}$$

with $\delta_{\ell \geq m} = 0$ if $\ell < m$ and $\delta_{\ell \geq m} = 1$ else. Expanding the second right-hand side term using the binomial expansion entails

$$\varepsilon_{\ell,m} = \frac{(-1)^m}{m!\,(\ell-m)!} \left(X_{I_R} - \frac{a}{2}\right)^{\ell-m} \delta_{\ell \geq m} + \sum_{j=0}^{\ell} \frac{\Delta X^{j-m}}{j!\,(\ell-j)!} \left(X_{I_R} - \frac{a}{2}\right)^{\ell-j} \sum_{s=-K/2}^{K/2} \nu_{K,m,s} s^j. \tag{3.63}$$

For $0 \leq j \leq K$ then (3.9) implies that it holds:

$$\frac{(-1)^m}{m!\,(\ell-m)!}\left(X_{I_R}-\frac{a}{2}\right)^{\ell-m}\delta_{\ell\geq m}+\sum_{j=0}^{\min(\ell,K)}\frac{\Delta X^{j-m}}{j!\,(\ell-j)!}\left(X_{I_R}-\frac{a}{2}\right)^{\ell-j}\sum_{s=-K/2}^{K/2}\nu_{K,m,s}s^j=0. \tag{3.64}$$

Therefore, if $\ell \leq K$ then $\varepsilon_{\ell,m}=0$ and when $\ell > K$ then (3.62) reduces to

$$\varepsilon_{\ell,m}=\sum_{j=K+1}^{\ell}\frac{\Delta X^{j-m}}{j!\,(\ell-j)!}\left(X_{I_R}-\frac{a}{2}\right)^{\ell-j}\sum_{s=-K/2}^{K/2}\nu_{K,m,s}s^j=\mathcal{O}(\Delta X^{\ell-m})\sum_{j=K+1}^{\ell}\sum_{s=-K/2}^{K/2}\frac{\nu_{K,m,s}s^j}{j!\,(\ell-j)!}.$$

For all (ℓ,m) the results for these two cases can be summarized as follows:

$$\varepsilon_{\ell,m}=\mathcal{O}(\Delta X^{\ell-m})\delta_{\ell>K}. \tag{3.65}$$

This allows to conclude the proof since, using (3.65) in (3.61), then for $q=3$ and $q=5$ one gets:

$$\mathcal{L}_{0,\boldsymbol{u}}(X_{I_R},t_n)=\mathcal{O}\left(\Delta X^{\min(K+1,q)}\right), \tag{3.66}$$

and the same holds for X_{I_L}, or any other irregular point. □

3.3.2 Estimation of $\mathcal{L}_{0,\Lambda_r^i}$

Property 3. *Under Assumptions 3.1, the local error on the auxiliary variables Λ_r^i defined in (3.48) is given by*

$$\mathcal{L}_{0,\Lambda_r^i}(t_n)=\mathcal{O}(\Delta X^{\min(q_I,q_D+1)})+\mathcal{O}(\Delta X^{q-1})\sum_{w=0}^{q_I-2}(\kappa_r^i)^{n-w}\qquad(i=1,2,\ r=1,\dots,N_R). \tag{3.67}$$

Proof. $\mathcal{L}_{0,\Lambda_r^i}$ is defined in (3.48) and can be expressed using Approximation 2 as

$$\mathcal{L}_{0,\Lambda_r^i}(t_n)=\Lambda_r^i(t_{n+1})-\Lambda_r^i(t_n)-\frac{\mu_m\alpha_r^2}{\omega_r}\sum_{w=0}^{q_I-2}\delta_w\sum_{z=0}^{q_D}\beta_z\left\langle\!\left\langle\widetilde{\partial_X^2V}\right\rangle\!\right\rangle_a(t_{n-w-z})(\kappa_r^i)^{n-w}, \tag{3.68}$$

where $\left\langle\!\left\langle\widetilde{\partial_X^2V}\right\rangle\!\right\rangle_a(t_s)$ denotes the trace value obtained when replacing the numerical values $(\boldsymbol{U}^s,\boldsymbol{\Lambda}^s,\boldsymbol{Z}^s)$ by the exact continuous solutions in (3.41). This term writes:

$$\begin{aligned}\left\langle\!\left\langle\widetilde{\partial_X^2V}\right\rangle\!\right\rangle_a(t_{n-w-z})=\frac{1}{2}[(\mathbb{I}_{q_U}+(\mathbb{C}_+^q)^{-1}\mathbb{C}_-^q)(\mathbb{M}^q)^{-1}\boldsymbol{\mathcal{U}}(t_{n-w-z})\\+((\mathbb{M}^q)^{-1}\mathbb{F}^q+(\mathbb{C}_+^q)^{-1}\mathbb{G}^q)\mathbb{Q}^q\boldsymbol{Z}(t_{n-w-z})][3],\end{aligned} \tag{3.69}$$

Using (3.40), (3.23) and (3.24), one gets

$$\begin{aligned}\left\langle\!\left\langle\widetilde{\partial_X^2V}\right\rangle\!\right\rangle_a(t_{n-w-z})&=\left\langle\!\left\langle\partial_X^2V\right\rangle\!\right\rangle_a(t_{n-w-z})\\&+\frac{1}{2}[-(\mathbb{C}_+^q)^{-1}\mathbb{G}^q(\mathbb{R}_-^q(t_{n-w-z})-\mathbb{R}_+^q(t_{n-w-z}))+(\mathbb{M}^q)^{-1}\boldsymbol{\Delta}(t_{n-w-z})][3]\\&-\frac{1}{2}[(\mathbb{I}_{q_U}+(\mathbb{C}_+^q)^{-1}\mathbb{C}_-^q)(\mathbb{M}^q)^{-1}\mathcal{O}(\Delta X^{q+1})][3]\end{aligned} \tag{3.70}$$

Symbolic computations are then performed using Maple to estimate the leading contributions of the entries of the vectors in (3.53). Doing so for $q=3$ or 5 yields:

$$\begin{cases}[-(\mathbb{C}_+^q)^{-1}\mathbb{G}^q(\mathbb{R}_-^q(t_{n-w-z})-\mathbb{R}_+^q(t_{n-w-z}))+(\mathbb{M}^q)^{-1}\boldsymbol{\Delta}(t_{n-w-z})][3]=\mathcal{O}(\Delta X^{q-1}),\\[(\mathbb{I}_{q_U}+(\mathbb{C}_+^q)^{-1}\mathbb{C}_-^q)(\mathbb{M}^q)^{-1}\mathcal{O}(\Delta X^{q+1})][3]=\mathcal{O}(\Delta x^q).\end{cases} \tag{3.71}$$

Using (3.70) and (3.71) combined with (3.39) in (3.68) concludes the proof. □

3.3.3 Estimation of $\mathcal{L}_{0,Z}$

Property 4. *Under Assumptions 3.1, the local error on the auxiliary variable vector $\boldsymbol{Z}$ defined in (3.48) is given by*

$$\mathcal{L}_{0,\boldsymbol{Z}}(t_n) = \left(\boldsymbol{O}\left(\Delta X^{\min(q,\, q_I,\, q_D+1)}\right), \boldsymbol{O}\left(\Delta X^{\min(q-1,\, q_I,\, q_D+1)}\right)\right)^\top, \tag{3.72}$$

with $\boldsymbol{O}(\Delta X^s)$ standing here for a vector of size N_R and whose entries are of order $O(\Delta X^s)$.

Proof. $\mathcal{L}_{0,\boldsymbol{Z}}$ is defined in (3.48). To compute it, we first introduce the vectors of size $2N_R$

$$\boldsymbol{\kappa}^{n-w} = \left(\left(\kappa_1^1\right)^{n-w}, \cdots, \left(\kappa_{N_R}^1\right)^{n-w}, \left(\kappa_1^2\right)^{n-w}, \cdots, \left(\kappa_{N_R}^2\right)^{n-w}\right)^\top, \tag{3.73}$$

and

$$\boldsymbol{D}^w = (\omega_1(w+1)O(\Delta t), \cdots, \omega_{N_R}(w+1)O(\Delta t), \omega_1 O(1), \cdots, \omega_{N_R} O(1))^\top \tag{3.74}$$

Then, using trigonometric formulas, one notices that

$$\mathbb{P}(t_{n+1})\boldsymbol{\kappa}^{n-w} = \boldsymbol{D}^w. \tag{3.75}$$

Using (3.68) and (3.75), one gets the expected result. □

3.3.4 Computation of the cumulative error

Even if one lacks of a theoretical stability property for the proposed scheme, we assume that, if applicable, the *global* error would be in agreement with the analysis of the *local* error and corresponds to the accumulation of the latter over iterations. Accordingly, a *cumulative* error at time t_n can be found from Propositions 2, 3 and 4 by repeating the scheme $O(\frac{1}{\Delta t})$ times. In numerical experiments, we measure *global* errors on $\boldsymbol{U}$ only. Consequently, in a second step of the analysis we evaluate the effect of the *cumulative* error regarding $\boldsymbol{Z}$ on the *local* error regarding $\boldsymbol{U}$. Therefore, the final *local* error on $\boldsymbol{U}$ after two time steps is defined by:

$$\begin{cases} \mathcal{L}_{\boldsymbol{U}}(X_{I_L}, t_n) = \boldsymbol{U}(X_{I_L}, t_{n+2}) - \mathcal{H}_L\left(\boldsymbol{U}(\cdot, t_{n+1}) + \mathcal{L}_{0,\boldsymbol{U}}(\cdot, t_n), \boldsymbol{Z}(t_{n+1}) + \dfrac{1}{\Delta t}\mathcal{L}_{0,\boldsymbol{Z}}(t_n)\right), \\ \mathcal{L}_{\boldsymbol{U}}(X_{I_R}, t_n) = \boldsymbol{U}(X_{I_R}, t_{n+2}) - \mathcal{H}_R\left(\boldsymbol{U}(\cdot, t_{n+1}) + \mathcal{L}_{0,\boldsymbol{U}}(\cdot, t_n), \boldsymbol{Z}(t_{n+1}) + \dfrac{1}{\Delta t}\mathcal{L}_{0,\boldsymbol{Z}}(t_n)\right), \end{cases} \tag{3.76}$$

and one arrives at the following result.

Result 3.4: Cumulative error

Property 5. *Let us introduce the cumulative error $\mathcal{E}(t_n) = \frac{1}{\Delta t}\mathcal{L}_{\boldsymbol{U}}(X_i, t_n)$.*
Then $\mathcal{E}(t_n) = O(\Delta X^\delta)$ is obtained with the parameter δ being given by

$$\delta = \min(K,\, q-1,\, q_I-1,\, q_D) \quad \text{for } q \in \{3,\, 5\}. \tag{3.77}$$

Proof. Due to the expression of $\mathcal{H}_L$ in (3.31) then $\mathcal{L}_{\boldsymbol{U}}(X_{I_L}, t_n)$ defined in (3.76) can be expressed as

$$\mathcal{L}_{\boldsymbol{U}}(X_{I_L}, t_n) = \mathcal{L}_{0,\boldsymbol{U}}(X_{I_L}, t_{n+1}) - \mathcal{H}_L\left(\mathcal{L}_{0,\boldsymbol{U}}(\cdot, t_n), \frac{1}{\Delta t}\mathcal{L}_{0,\boldsymbol{Z}}(t_n)\right), \tag{3.78}$$

and the same holds for the right side. Thus, we aim at evaluating the order of

$$\mathcal{H}_L(\boldsymbol{\mathcal{L}}_{0,\boldsymbol{U}}(\cdot,t_n),\frac{1}{\Delta t}\boldsymbol{\mathcal{L}}_{0,\boldsymbol{Z}}(t_n)) \qquad \text{and} \qquad \mathcal{H}_R(\boldsymbol{\mathcal{L}}_{0,\boldsymbol{U}}(\cdot,t_n),\frac{1}{\Delta t}\boldsymbol{\mathcal{L}}_{0,\boldsymbol{Z}}(t_n)).$$

To do so, symbolic computations are then performed using Maple to estimate the leading contributions of the entries of the vectors in $\mathcal{H}_L$ (3.31) and $\mathcal{H}_R$ (3.33). Doing so provides, for $q = 3$ or 5:

$$\begin{cases} \mathbb{T}^q_{I_L+s}\left(-\frac{a}{2}\right)(\mathbb{M}^q)^{-1} = \mathcal{O}(1), \\ \mathbb{T}^q_{I_L+s}\left(-\frac{a}{2}\right)(\mathbb{M}^q)^{-1}\mathbb{F}^q\mathbb{Q}^q = \mathbb{B}_{\Delta X}, \\ \mathbb{T}^q_{I_R+s}\left(\frac{a}{2}\right)(\mathbb{C}^q_+)^{-1}\mathbb{C}^q_-(\mathbb{M}^q)^{-1} = \mathcal{O}(1), \\ \mathbb{T}^q_{I_R+s}\left(\frac{a}{2}\right)(\mathbb{C}^q_+)^{-1}\mathbb{G}^q\mathbb{Q}^q = \mathbb{B}_{\Delta X}, \end{cases} \tag{3.79}$$

with $\mathbb{B}_{\Delta X}$ being a $2\times 2N_R$ matrix defined by

$$\mathbb{B}_{\Delta X}[i,j] = \begin{cases} \mathcal{O}(\Delta X^2) & \text{for } i \in \{1,\dots,N_R\} \text{ and } j \in \{N_R+1,\dots,2N_R\}, \\ \mathcal{O}(\Delta X) & \text{for } i \in \{N_R+1,\dots,2N_R\} \text{ and } j \in \{1,\dots,N_R\}, \\ 0 & \text{else.} \end{cases} \tag{3.80}$$

The term $\boldsymbol{\mathcal{L}}_{0,\boldsymbol{U}}(X_i,t_n)$ is determined in Property 2 for X_i an irregular point. For a regular point, the error analysis of a ADER-K scheme in a homogeneous medium can be used and $\boldsymbol{\mathcal{L}}_{0,\boldsymbol{U}}(X_i,t_n) = \mathcal{O}(\Delta X^{K+1})$. $\boldsymbol{\mathcal{L}}_{0,\boldsymbol{Z}}(t_n)$ is also determined in Property 4. Using these results combined with (3.79) in (3.31) and (3.33), we finally obtain

$$\boldsymbol{\mathcal{L}}_{\boldsymbol{U}}(X_{I_L},t_n) = \mathcal{O}(\Delta X^{\min(K+1,q,q_I,q_D+1)}), \tag{3.81}$$

and the same holds for X_{I_R}, or any other irregular point. Therefore, the final estimate given by Property 5 writes:

$$\mathcal{E}(t_n) = \mathcal{O}(\Delta X^{\min(K,q-1,q_I-1,q_D)}). \tag{3.82}$$

□

If stability holds then we expect the cumulative error $\mathcal{E}(t_n)$ to be consistent with the global error. Considering Property 5 and the above discussion on the numerical stability, then one can conclude that a third-order accuracy can be reached but the fourth-order accuracy of the ADER-4 scheme cannot be recovered. In the numerical experiments of Section 3.5.1, global errors are measured and they are found to be in agreement with the analysis of the local error provided in Property 5. Note that, even if Property 5 is relative to the 1D case, the numerical experiments of Section 3.5.2 suggest that similar results also hold in the 2D case.

Remark 11. *In the non-resonant case, no auxiliary variables need to be defined and* $\boldsymbol{Z}(t_n) = \boldsymbol{0}$ *can be set in* (3.13)*. In this case, the integration and derivation steps of Section 3.2.6 are irrelevant so that the associated parameters* q_I *and* q_D *can be removed from the estimates of Property 5. As a consequence, the error* $\mathcal{E}(t_n) = \mathcal{O}(\Delta X^{\min(K,q-1)})$ *for all* q *is recovered, which meets the result proven in Lombard and Piraux, 2003 for* $K = 2$*.*

3.4 Numerical modeling in 2D

3.4.1 Setting

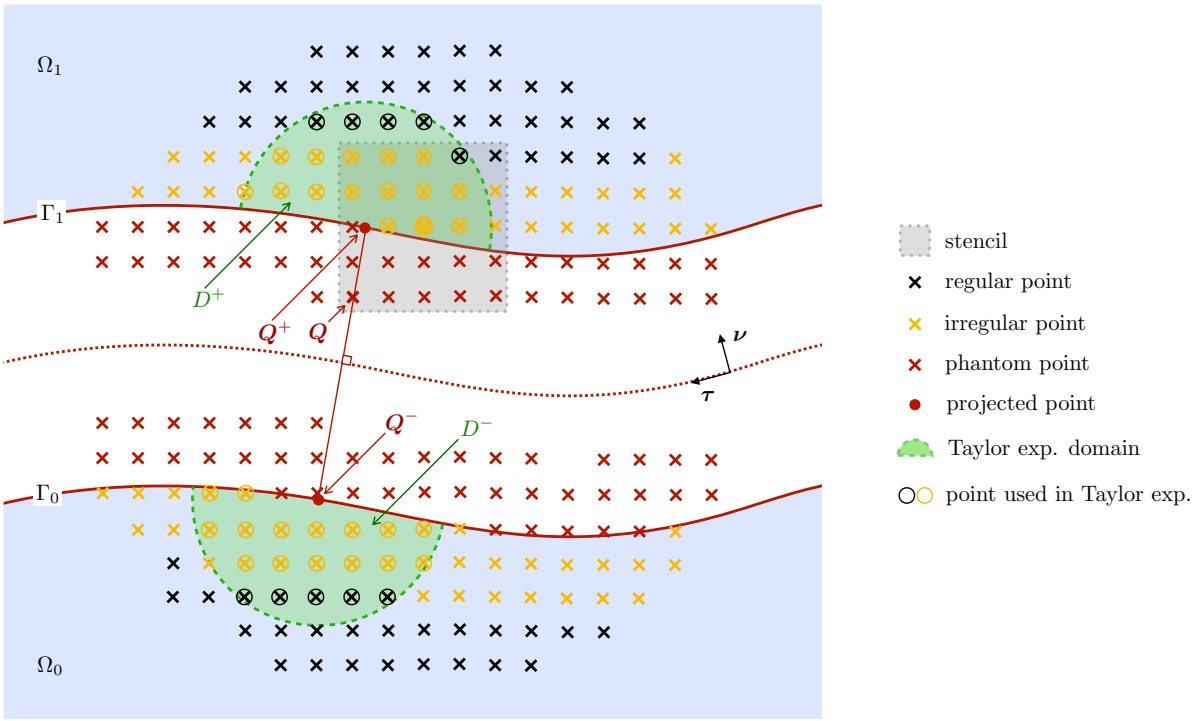

Figure 3.2 – Smooth enlarged interface of width a that separates the domains Ω_0 and Ω_1 in 2D. A ghost value is sought at the point $\boldsymbol{Q}$ whose orthogonal projections onto the interfaces Γ_0 and Γ_1 are denoted as $\boldsymbol{Q}^-$, $\boldsymbol{Q}^+$ respectively.

In this section, we formally extend the 2D model (3.3) to a configuration with a curved enlarged interface defined by two parallel curves $\Gamma_j = \Gamma_j(X_1(s), X_2(s))$, with $j = 0, 1$ and s being the associated curvilinear abscissa, see Figure 3.2. The solution is defined in the domains on each side, which are denoted as Ω_0 and Ω_1, while as previously no physical field is defined in the interspace of width a between Γ_0 and Γ_1. The jump conditions in (3.3), which are expressed in Cartesian coordinates, are directly transposed in the local frame defined by the normal and tangent vectors $\boldsymbol{\nu}$ and $\boldsymbol{\tau}$ at the interfaces:

$$
\begin{cases}
\partial_t \boldsymbol{\Sigma}(\boldsymbol{X}, t) = \mu_m \boldsymbol{\nabla} V(\boldsymbol{X}, t) \quad (\boldsymbol{X} \in \Omega_0 \cup \Omega_1), & \text{(3.83a)} \\
\partial_t V(\boldsymbol{X}, t) = \dfrac{1}{\rho_m} \operatorname{div} \boldsymbol{\Sigma}(\boldsymbol{X}, t) \quad (\boldsymbol{X} \in \Omega_0 \cup \Omega_1), & \text{(3.83b)} \\
\partial_t J_r(s, t) = G_r(s, t) \quad (s \in \mathbb{R},\ r = 1, \dots, N_R), & \text{(3.83c)} \\
\partial_t G_r(s, t) = -\omega_r^2 J_r(s, t) + (c_m \alpha_r)^2 \langle\!\langle \Delta \operatorname{div} \boldsymbol{\Sigma} \rangle\!\rangle_a \quad (s \in \mathbb{R},\ r = 1, \dots, N_R), & \text{(3.83d)} \\
[\![V]\!]_a = h\mathcal{B} \langle\!\langle \partial_\nu V \rangle\!\rangle_a + h\mathcal{B}_2 \langle\!\langle \partial_\tau V \rangle\!\rangle_a \quad (s \in \mathbb{R}), & \text{(3.83e)} \\
[\![\Sigma_\nu]\!]_a = h\mathcal{S} \langle\!\langle \partial_\nu \Sigma_\nu \rangle\!\rangle_a + hC_1 \langle\!\langle \partial_\tau \Sigma_\nu \rangle\!\rangle_a + hC_2 \langle\!\langle \partial_\tau \Sigma_\tau \rangle\!\rangle_a + h\alpha_0 \langle\!\langle \operatorname{div} \boldsymbol{\Sigma} \rangle\!\rangle_a - h \sum_{r=1}^{N_R} J_r. & \text{(3.83f)}
\end{cases}
$$

where $\Sigma_\nu = \boldsymbol{\Sigma}\cdot\boldsymbol{\nu}/\|\boldsymbol{\nu}\|$, $\Sigma_\tau = \boldsymbol{\Sigma}\cdot\boldsymbol{\tau}/\|\boldsymbol{\tau}\|$ and $\partial_\nu f = \boldsymbol{\nabla} f\cdot\boldsymbol{\nu}/\|\boldsymbol{\nu}\|$, $\partial_\tau f = \boldsymbol{\nabla} f\cdot\boldsymbol{\tau}/\|\boldsymbol{\tau}\|$. Moreover, $[\![f]\!]_a$ and $\langle\!\langle f\rangle\!\rangle_a$ stand for the 2D version of the jump and the mean value of f at the enlarged interface respectively.

Remark 12. *In the proposed extension* (3.83) *of the model* (3.3) *to a configuration involving a curved enlarged interface, we have chosen to keep the term* $\langle\!\langle \operatorname{div}\boldsymbol{\Sigma}\rangle\!\rangle_a$ *as such as it has a clear interpretation relatively to a homogenization process, see Pham et al., 2017. However, we do not claim that* (3.83) *is a* homogenized *model in the case of a curved enlarged interface. Indeed, to obtain such a model, the curvature should be taken into account in the homogenization process from the beginning, in line with the perspective mentioned at the end of Chapter 2. Our objective is rather to show that such a model can be efficiently handled using the proposed numerical approach.*

3.4.2 Numerical scheme at the interface

As previously, we use the ADER-4 scheme with a uniform Cartesian grid with $\boldsymbol{U}_{i,j}^n$ denoting the numerical value of the solution $\boldsymbol{U} = (V, \Sigma_1, \Sigma_2)^\top$ at the point $(X_i = i\Delta X, X_j = j\Delta X)$ and time t_n. In this framework, the approach adopted is as in 1D: the irregular points are detected and ghost values are computed at the grid points that are located in between Γ_1 and Γ_0 and used by the stencil. For $\boldsymbol{Q} = (X_I, X_J)$ being such a point, let Ω^+ and Ω^- denote the closest domain and the farthest one respectively (there is no ambiguity in these definitions as the width of the stencil is systematically chosen to be smaller than the width a of the enlarged interface). Then $\boldsymbol{Q}^\pm = (X_1^\pm, X_2^\pm)$ denotes the orthogonal projection of $\boldsymbol{Q}$ on $\Gamma^\pm = \partial\Omega^\pm$ (see Figure 3.2).

The coefficients of 2D Taylor expansions are put as the entries of the $3\times 3(q+1)(q+2)/2$ matrix

$$\mathbb{T}_{ij}^q(\boldsymbol{Q}^\pm) = \left(\mathbb{I}_3, \cdots, \frac{1}{\beta!(\alpha-\beta)!}(X_i - X_1^\pm)^{\alpha-\beta}(X_j - X_2^\pm)^\beta \mathbb{I}_3, \cdots, \frac{(X_j - X_2^\pm)^q}{q!}\mathbb{I}_3\right), \tag{3.84}$$

with $\alpha = 0,\cdots,q$ and $\beta = 0,\cdots,\alpha$. One also introduces the following vectors of size $q_U = 3(q+1)(q+2)/2$ that contain the boundary values of the 2D derivatives of $\boldsymbol{U}$ up to the chosen order q:

$$\boldsymbol{U}_\pm^q(t_n) = \left(\boldsymbol{U}^\pm, \cdots, \frac{\partial^\ell}{\partial X_1^{\ell-m}\partial X_2^m}\boldsymbol{U}^\pm, \cdots, \frac{\partial^q}{\partial X_2^q}\boldsymbol{U}^\pm\right)^\top \tag{3.85}$$

with $\ell = 0,\cdots,q$ and $m = 0,\cdots,\ell$. $\boldsymbol{U}^\pm$ stands for the value of $\boldsymbol{U}$ in $\boldsymbol{Q}^\pm$ and the same holds for the spatial derivatives. Extending to the 2D case the definition (3.10) and (3.17), a ghost value $\boldsymbol{U}^*$ at the point $\boldsymbol{Q}$ is defined as a smooth expansion of the value $\boldsymbol{U}_+^q(t_n)$ of the solution on the Γ^+ interface at the time step t_n:

$$\boldsymbol{U}_{IJ}^* = \mathbb{T}_{IJ}^q(\boldsymbol{Q}^+)\boldsymbol{U}_+^q(t_n). \tag{3.86}$$

3.4.3 High-order jump conditions and compatibility conditions

To compute the ghost values, high-order jump conditions relating $\boldsymbol{U}_+^q(t_n)$ and $\boldsymbol{U}_-^q(t_n)$ have to be used and these are obtained by differentiating in time the original jump conditions, as it was done in Section 3.2.4 in the 1D case. For $q \geq 0$, one introduces $q_B = (q+1)(q+2)$ and the vectors and matrices required to write the jump conditions: two matrices $\mathbb{C}_\pm^q$ of size $q_B \times q_U$, $\boldsymbol{R}_\pm^q(t_n)$ two q_B-element vectors containing the $(q+1)$-th order derivatives, $\boldsymbol{Z}^q(t_n)$ a $(q+1)(q+2)N_R$-element vector containing the auxiliary variables and their spatial derivatives until order q, and $\mathbb{Q}^q$ a $q_B \times (q+1)(q+2)N_R$ matrix.

For example, at the zeroth order, the jump conditions (3.83e)-(3.83f) are written

$$\mathbb{C}_+^0 \boldsymbol{U}_+^0(t_n) + \boldsymbol{R}_+^0(t_n) = \mathbb{C}_-^0 \boldsymbol{U}_-^0(t_n) + \boldsymbol{R}_-^0(t_n) + \mathbb{Q}^0 \boldsymbol{Z}^0(t_n). \tag{3.87}$$

The jump condition (3.87) is differentiated with respect to time, and then time derivatives are replaced by spatial derivatives thanks to (3.83a)-(3.83b) for $\boldsymbol{U}_\pm^0$ or (3.83d)-(3.83c) for $\boldsymbol{Z}^0(t_n)$. In 2D, the jump condition (3.87) is also differentiated with respect to the curvilinear abscissa s using the chain rule as

$$\frac{\partial}{\partial s}(\mathbb{C}_\pm^0 \boldsymbol{U}_\pm^0(t_n)) = \left(\frac{\partial}{\partial s}\mathbb{C}_\pm^0\right) \boldsymbol{U}_\pm^0(t_n) + \mathbb{C}_\pm^0 \left(X_1' \frac{\partial}{\partial X_1} \boldsymbol{U}_\pm^0(t_n) + X_2' \frac{\partial}{\partial X_2} \boldsymbol{U}_\pm^0(t_n) \right). \tag{3.88}$$

This process is iterated q times and leads to q_B equations overall:

$$\mathbb{C}_+^q \boldsymbol{U}_+^q(t_n) + \boldsymbol{R}_+^q(t_n) = \mathbb{C}_-^q \boldsymbol{U}_-^q(t_n) + \boldsymbol{R}_-^q(t_n) + \mathbb{Q}^q \boldsymbol{Z}^q(t_n). \tag{3.89}$$

Furthermore, the condition $\boldsymbol{\nabla} \wedge \boldsymbol{\Sigma} = \boldsymbol{0}$ holds outside the support of the external sources considered and writes

$$\frac{\partial \Sigma_2}{\partial X_1} = \frac{\partial \Sigma_1}{\partial X_2}. \tag{3.90}$$

This equation is differentiated with respect to X_1 and X_2 up to the qth order so that one gets $q_C = q(q+1)/2$ compatibility conditions. These equations are used to reduce the number of unknowns of $\boldsymbol{U}_\pm^q(t_n)$. Reduced vectors $\boldsymbol{V}_\pm^q(t_n)$ of size $q_U - q_C$ are thus introduced and satisfy

$$\boldsymbol{U}_\pm^q(t_n) = \mathbb{L}_\pm^q \boldsymbol{V}_\pm^q(t_n) \tag{3.91}$$

where $\mathbb{L}_\pm^q$ are $q_U \times (q_U - q_C)$ matrices. Inserting (3.91) in (3.89), the underdetermined system for $\boldsymbol{V}_-^q(t_n)$ writes

$$\mathbb{S}_-^q \boldsymbol{V}_-^q(t_n) = \mathbb{S}_+^q \boldsymbol{V}_+^q(t_n) + \boldsymbol{R}_+^q(t_n) - \boldsymbol{R}_-^q(t_n) - \mathbb{Q}^q \boldsymbol{Z}^q(t_n). \tag{3.92}$$

with $\mathbb{S}_\pm^q = \mathbb{C}_\pm^q \mathbb{L}_\pm^q$ $q_B \times (q_U - q_C)$ matrices. A singular value decomposition of $\mathbb{S}_-^q$ is used to build its least-squares pseudo-inverse $(\mathbb{S}_-^q)^{-1}$ and its kernel $\mathbb{K}_{\mathbb{S}_-^q}$. Since (3.92) is underdetermined, the solution $\boldsymbol{V}_-^q(t_n)$ is not unique and can be written

$$\boldsymbol{V}_-^q(t_n) = \left((\mathbb{S}_-^q)^{-1} \middle| \mathbb{K}_{\mathbb{S}_-^q} \right) \begin{pmatrix} \mathbb{S}_+^q \boldsymbol{V}_+^q(t_n) + \boldsymbol{R}_+^q(t_n) - \boldsymbol{R}_-^q(t_n) - \mathbb{Q}^q \boldsymbol{Z}^q(t_n) \\ \boldsymbol{\Lambda}^q \end{pmatrix} \tag{3.93}$$

with $(\cdot|\cdot)$ standing for the representation of a matrix by blocks, and $\boldsymbol{\Lambda}^q$ a set of $q_U - q_C - q_B$ Lagrange multipliers. Then, $\boldsymbol{U}_-^q(t_n)$ follows from (3.91).

3.4.4 Computation of the ghost values

To determine the traces $\boldsymbol{U}_+^q(t_n)$ in (3.86), as it was done in Section (3.2.5), 2D Taylor expansions are written out at the grid points that are contained in the domain D^+ (resp. D^-) defined as the intersection of the disk centered at $\boldsymbol{Q}^+$ (resp. $\boldsymbol{Q}^-$) with the domain Ω^+ (resp. Ω^-), see Figure 3.2. Using the definition (3.84) and the equation (3.91), these Taylor expansions write for a point (X_i, X_j) in D^+:

$$\boldsymbol{U}(X_i, X_j) = \mathbb{T}_{ij}^q(\boldsymbol{Q}^+) \mathbb{L}_+^q \left(\mathbb{I}_{q_U - q_C} \middle| \mathbb{0} \right) \begin{pmatrix} \boldsymbol{V}_+^q(t_n) \\ \boldsymbol{\Lambda}^q \end{pmatrix} + O(\Delta X^{q+1}) \tag{3.94}$$

with $\mathbb{0}$ the matrix of size $(q_U - q_C) \times (q_U - q_C - q_B)$ filled with zeros. Using (3.93), the Taylor expansions in D^- write:

$$\boldsymbol{U}(X_i, X_j) = \mathbb{T}_{ij}^q(\boldsymbol{Q}^-)\mathbb{L}_-^q \left((\mathbb{S}_-^q)^{-1}\middle|\mathbb{K}_{\mathbb{S}_-^q}\right)\begin{pmatrix} \mathbb{S}_+^q \boldsymbol{V}_+^q(t_n) + \boldsymbol{R}_+^q(t_n) - \boldsymbol{R}_-^q(t_n) - \mathbb{Q}^q \boldsymbol{Z}^q(t_n) \\ \boldsymbol{\Lambda}^q \end{pmatrix} + \boldsymbol{O}(\Delta X^{q+1}) \quad (3.95)$$

The derivatives of orders greater than $q+1$, i.e. $\boldsymbol{R}_\pm^q(t_n)$ and $\boldsymbol{O}(\Delta X^{q+1})$, are neglected in the expansions (3.94) and (3.95) that can be written in the matrix form:

$$\boldsymbol{\mathcal{U}}(t_n) = \mathbb{M}^q \begin{pmatrix} \boldsymbol{V}_+^q(t_n) \\ \boldsymbol{\Lambda}^q \end{pmatrix} + \mathbb{F}^q \begin{pmatrix} \boldsymbol{Z}^q(t_n) \\ \boldsymbol{0} \end{pmatrix} \quad (3.96)$$

with $\boldsymbol{\mathcal{U}}(t_n)$ containing the values of $\boldsymbol{U}$ at the points in $D^+ \cup D^-$. The radius of these half-disks is chosen large enough, $r = 3.2\Delta X$ for $q = 3$ for example, to ensure that the system (3.96) is overdetermined. The least-squares inverse of $\mathbb{M}^q$ is denoted by $(\mathbb{M}^q)^{-1}$, and we consider $\widetilde{(\mathbb{M}^q)^{-1}}$ its restriction so that one finally gets:

$$\boldsymbol{V}_+^q(t_n) = \widetilde{(\mathbb{M}^q)^{-1}}\left(\boldsymbol{\mathcal{U}}(t_n) - \mathbb{F}^q \begin{pmatrix} \boldsymbol{Z}^q(t_n) \\ \boldsymbol{0} \end{pmatrix}\right). \quad (3.97)$$

Finally the ghost values (3.86) are computed using (3.91) and (3.97) while taking the numerical counterparts $\boldsymbol{\mathcal{U}}^n$ and $(\boldsymbol{Z}^q)^n$ of $\boldsymbol{\mathcal{U}}(t_n)$ and $\boldsymbol{Z}^q(t_n)$, respectively

Result 3.5: Numerical approximations of the ghost values in 2D

$$\boldsymbol{U}_{IJ}^* = \mathbb{T}_{IJ}^q(\boldsymbol{Q}^+)\mathbb{L}_+^q \widetilde{(\mathbb{M}^q)^{-1}}\left(\boldsymbol{\mathcal{U}}^n - \mathbb{F}^q \begin{pmatrix} (\boldsymbol{Z}^q)^n \\ \boldsymbol{0} \end{pmatrix}\right). \quad (3.98)$$

This procedure constitutes an extension of the approach developed in Lombard et al., 2017 for non-resonant interface problems.

3.4.5 Computation of the auxiliary variables

Unlike the non-resonant case, it remains to compute the numerical approximations $(\boldsymbol{Z}^q)^n$ of $\boldsymbol{Z}^q(t_n)$. This vector contains the auxiliary variables $J_r(s,t)$ and $G_r(s,t)$ along the enlarged interface and their spatial derivatives up to order q. However, one recalls that the source term of the equation defining J_r and G_r (3.83d) is a third-order derivative. Therefore, when this equation is derived m times, the source term is of order $m+3$. Keeping in mind that the derivatives of order greater than $q+1$ will be neglected for the numerical computation when the ESIM is of order q, then this source term and the resulting derivatives of J_r and G_r will be neglected if $m \geq q-2$. Therefore $\boldsymbol{Z}^n$ is reduced to a size of $(q-2)(q-1)N_R$.

Here, we limit ourself to $q = 3$ to avoid the computation of new auxiliary variables in $\boldsymbol{Z}^n$. These new variables would be the spatial derivatives of J_r and G_r. This can be done but given the satisfying numerical results already obtained for $q = 3$ such technicalities will not be considered here. In this case, $\boldsymbol{Z}^n$ only contain the J_r and G_r, $r = 1, \cdots, N_R$. Then, one just has to perform numerical integration and numerical differentiation which extend Approximation 3 to 2D and allow to compute $J_r(s,t)$ and $G_r(s,t)$, solution of (3.83d) and (3.83c). In terms of memory requirements, the computation of the auxiliary variables in 2D requires the storage of the vector $\boldsymbol{\Psi}$ defined in (3.47) for the 1D case at each orthogonal projection point $Q^\pm$.

3.5 Numerical experiments

The derivation of the effective model has already been tackled in Chapter 2 and the latter is used in this section to perform wave propagation simulations and validate the proposed numerical method. In particular, the featured effective parameters will be chosen independently of a microstructure.

3.5.1 1D case

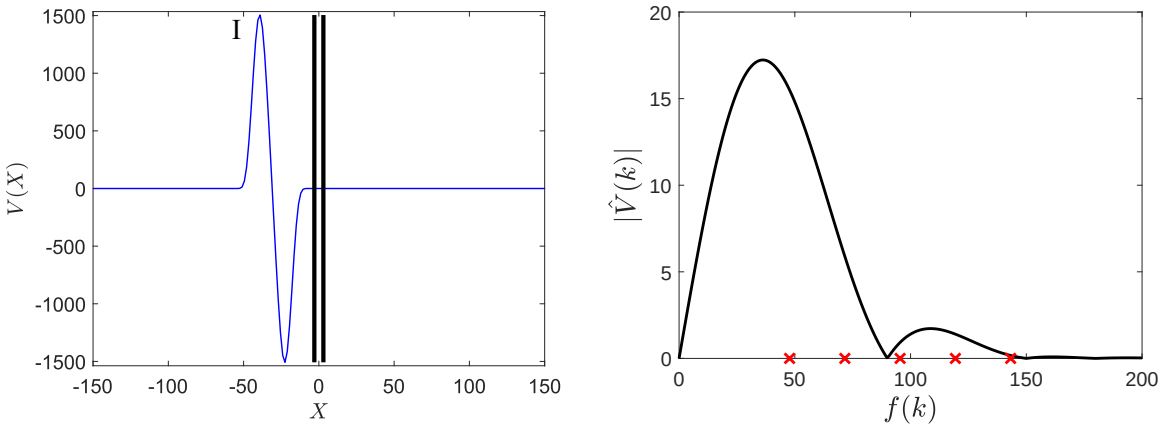

(a) Waveform (b) Fourier spectrum

Figure 3.3 – Initial condition (3.99): (a) velocity field V and (b) associated spectrum with the red crosses indicating the five resonant frequencies $f_r = \omega_r/2\pi$ considered.

$\mathcal{B}$ (m)	$\mathcal{S}$ (m)	h (m)
1.603	0.378	2

r	0	1	2	3	4	5
ω_r (rad·s^{-1})		300	450	600	750	900
α_r	0.314	0.462	0.4	0.2	0.1	0.1

Table 3.4 – Interface parameters for the 1D effective model (3.4).

μ_m (kg·m^{-1} · s^{-2})	c_m (m·s^{-1})	f_0 (Hz)	X_I (m)	a (m)	ΔX (m)	ζ
10^{-3}	1500	30	-9	6	1.5	0.95

Table 3.5 – Matrix properties and numerical parameters.

This section aims at validating the numerical method described in Section 3.2 in the 1D case. The chosen constitutive parameters and numerical ones are provided in the Tables 3.4 and 3.5 considering a number $N_R = 5$ of resonant frequencies. The time step follows from the CFL condition $\Delta t = \zeta \Delta X/c_m$ taken for $\zeta = 0.95$. The initial conditions are:

$$\boldsymbol{u}(X,0) = \begin{pmatrix} \dfrac{1}{\mu_m} \\ -\dfrac{1}{c_m} \\ 0 \end{pmatrix} F\big(X - X_I\big) \tag{3.99}$$

where the *source* function F is defined in (2.57) and is of class C^6. It depends on the choice of a central frequency f_0 given in Table 3.5. For the chosen values of c_m and ΔX in Table 3.5 then the

number of grid nodes is approximately 33 per wavelength at the central frequency f_0. Moreover, the initialization point X_I is chosen so that the support of the initial time conditions (3.99) does not intersect the enlarged interface. The corresponding initial velocity and its Fourier spectrum are shown in Figure 3.3. The final simulation time is chosen so that the wave has not hit yet the boundaries of the computational domain.

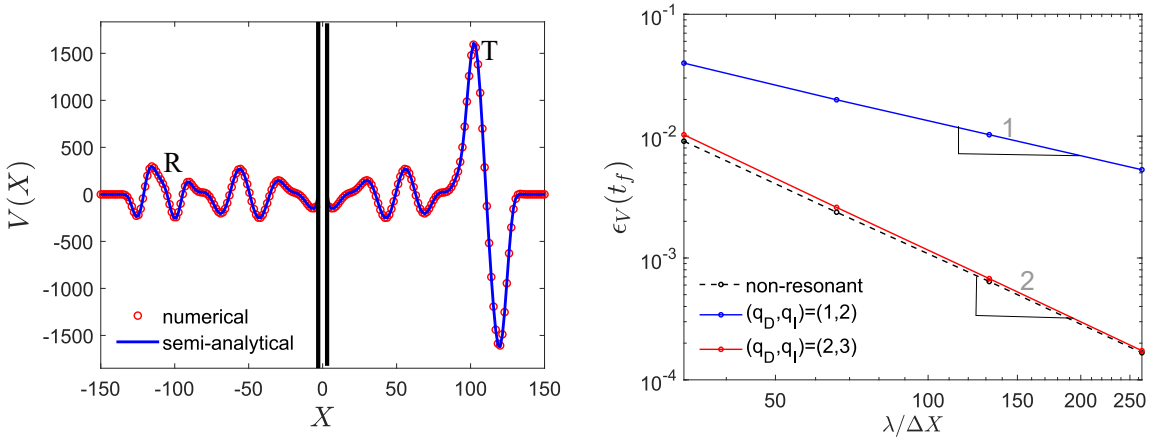

(a) V_{ref} (blue) and V (red) at the final simulation time $t_{\text{f}} = 94.05$ ms. R: reflected wave, T: transmitted wave.

(b) Relative error $\epsilon_V(t_{\text{f}})$ in a log-log scale.

Figure 3.4 – Numerical results for velocity field V in the 1D case: comparison with a semi-analytical solution V_{ref}.

Figure 3.4(a) displays the associated velocity V computed at the final simulation time $t_{\text{f}} = 94.05$ ms, together with a semi-analytical solution V_{ref}, which is derived in Appendix 3.A.1. The discrepancy between the two solutions is quantified by defining a global relative error at the final simulation time t_{f} as follows:

$$\epsilon_V(t_{\text{f}}) = \frac{\|V_{\text{ref}}(\cdot, t_{\text{f}}) - V(\cdot, t_{\text{f}})\|_{L^2(\Omega_{\text{obs}})}}{\|V_{\text{ref}}(\cdot, t_{\text{f}})\|_{L^2(\Omega_{\text{obs}})}},$$

where $\Omega_{\text{obs}} = [X_{\text{ini}}; X_{\text{end}}]\backslash[-a/2; a/2]$, with X_{ini} and X_{end} the left and right boundaries of the computational domain. One measures $\epsilon_V(t_{\text{f}}) = 1.5 \cdot 10^{-2}$ when $q = 3$, $(q_D, q_I) = (2,3)$ and $\lambda/\Delta X = 33$ for the characteristic wavelength $\lambda = c_m/f_0$. The relative error $\epsilon_V(t_{\text{f}})$ is represented as a function of $\lambda/\Delta X$ whose slope in a log-log scale graph characterizes the global order of the scheme, see Figure 3.4(b) for $q = 3$ and two values of (q_D, q_I). The errors obtained in the non-resonant case, with $\alpha_r = 0$ for $r = 0, \ldots, 5$, are included in Fig. 3.4(b) for comparison. It is seen that setting $(q_D, q_I) = (1,2)$ yields order 1, which is a drop in accuracy compared to the non-resonant case for which the global error considered is of order 2. The choice $(q_D, q_I) = (2,3)$ allows to recover this order with similar accuracy.

Table 3.6 reports the orders of accuracy measured using the *global* error metric $\epsilon_V(t_{\text{f}})$ for $q = 3$ and $q = 5$ depending on the chosen values (q_D, q_I). The parameter q_T is chosen to be the minimal value given by Table 3.3 for each value of (q_D, q_I). These orders, as well as Figure 3.4(b), are obtained with the relative position of the interfaces within the Cartesian grid being kept while the ratio $\lambda/\Delta X$ is increased. Even if the one lacks of a theoretical stability property for the proposed scheme, these numerical results are in agreement with the analysis of the *local* truncation error in Property 5. Note that, in practice, for the largest values of (q_D, q_I) considered then the Taylor expansion parameter q_T must be increased to maintain the numerical stability. Doing so, the matrix $\mathbb{M}^q$ is no longer a square matrix so that Property 5 does not apply anymore. However the corresponding orders measured remain compatible with the estimates of Property 5. The right

q_D \ q_I	2	3	4	5
1	1	1	1	1
2	1	2	2	2
3	1	2	2	2
4	1	2	2	

q_D \ q_I	2	3	4	5
1	1	1	1	1
2	1	2	2	2
3	1	2	3	3
4	1	2	3	

Table 3.6 – Convergence measurements in the 1D case: orders of accuracy for $q = 3$ *(left)* and $q = 5$ *(right)*.

bottom boxes are not filled in Table 3.6 because the associated values q_T being too large, the use of the pseudo-inverse of the matrix $\mathbb{M}^q$ yields unacceptable numerical errors.

3.5.2 2D case

In this section, we validate the method dicussed in Section 3.4 on three test cases: i) incident plane wave at normal incidence on a plane enlarged interface, ii) slanted incident plane wave on a tilted enlarged interface, and iii) incident plane wave on a circular enlarged interface. Semi-analytical solutions are computed in these three cases, see Sections 3.A.1 and 3.A.2. The initial conditions are

$$\begin{aligned}\boldsymbol{U}(\boldsymbol{X},0) &= \left(V,\, \Sigma_1,\, \Sigma_2\right)^{\mathsf{T}}(\boldsymbol{X},0)\\ &= \begin{pmatrix} \dfrac{1}{\mu_m} \\ -\dfrac{\cos\theta_I}{c_m} \\ -\dfrac{\sin\theta_I}{c_m} \end{pmatrix} F((\boldsymbol{X}-\boldsymbol{X}_I)\cdot\boldsymbol{e}_1\cos\theta_I + (\boldsymbol{X}-\boldsymbol{X}_I)\cdot\boldsymbol{e}_2\sin\theta_I),\end{aligned} \tag{3.100}$$

where F is defined in (2.57), θ_I is the angle between the direction of propagation of the plane wave and the horizontal axis and the initialization point $\boldsymbol{X}_I$ is chosen so that the support of the initial time conditions does not intersect the enlarged interface. The constitutive and numerical parameters are those of Tables 3.4 and 3.5 while the chosen additional effective interface parameters that are requested in 2D are reported in Table 3.7. The proposed numerical method is implemented taking $q = 3$ since, as previously discussed, the cases $q \geq 4$ are very demanding in 2D and require to handle additional auxiliary variables.

$\mathcal{B}_2$ (m)	$\mathcal{C}_1$ (m)	$\mathcal{C}_2$ (m)
0.142	0.142	0.2

Table 3.7 – Additional effective interface parameters for the 2D model (3.83).

3.5.2.1 Incident plane wave at normal incidence

First, we consider the case of normal incidence, i.e. $\theta_I = 0$, with a wave impacting a plane enlarged interface, in which case the fields are independent of X_2. Periodicity conditions are imposed at the bottom and top boundaries of the computational domain. Physically, the problem is 1D, but the full 2D algorithm is employed and one sets $(q_D, q_I) = (2, 3)$.

Figure 3.5 displays the velocity field V at the initial time $t = 0$, at which the initialization point in (3.100) is $\boldsymbol{X}_I = (-9\,\text{m}, 0\,\text{m})$, and at time $t_\text{f} = 94.05$ ms, while Figure 3.6 shows the profiles of the solution at $X_2 = 0$. The discrepancy between the numerical and the semi-analytical solutions

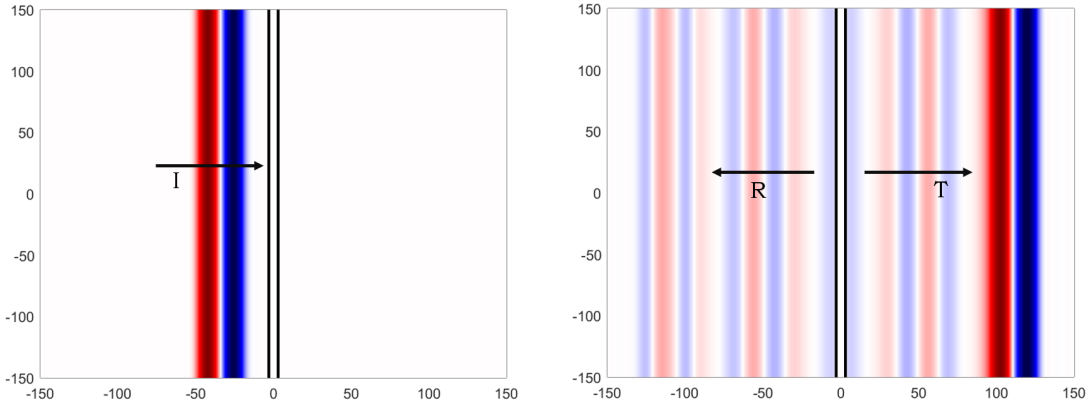

(a) $t = 0$ (b) $t_f = 94.05$ ms

Figure 3.5 – Velocity field V computed for an incident plane wave (I) at normal incidence on the enlarged interface. R: reflected wave, T: transmitted wave.

is comparable with the 1D results with $\epsilon_V(t_f) = 4.5 \cdot 10^{-2}$ for $\lambda/\Delta X = 33$. Table 3.8 reports the measured orders of accuracy, which are the same as in 1D.

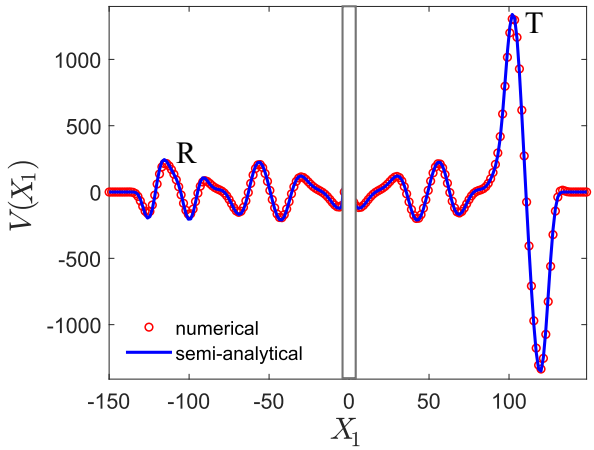

Figure 3.6 – Incident plane wave at normal incidence in 2D: semi-analytical and numerical velocity fields V_{ref} (blue) and V (red) at $X_2 = 0$ and for the final simulation time $t_f = 94.05$ ms.

3.5.2.2 Slanted incident plane wave on a tilted enlarged interface

The case of an incident wave at oblique incidence, with $\theta_I = 10°$ in (3.100), on an enlarged interface tilted from the vertical axis at $-7.2°$ is now considered. It allows us to inspect both the dependencies of the jump conditions on X_2 and the capability of the numerical method to account for the slope of the interface on a Cartesian grid. To perform the simulations, one imposes the semi-analytical solution of the problem on the domain boundary.

Figure 3.7 displays the velocity field computed at the initial time, at which the initialization point in (3.100) is $\boldsymbol{X}_I = (-21\,\text{m}, -150\,\text{m})$, and at time $t_f = 84.55$ ms when $(q_D, q_I) = (2, 3)$. Figure 3.8 compares the reference semi-analytical solution and the numerical one, with $\epsilon_V(t_f) = 4.1 \cdot 10^{-2}$ when $\lambda/\Delta X = 33$. This result is similar to that given in Section 3.5.2.1, which illustrates that the dependency of the jump conditions on X_2 and the slope of the interface are both accurately

q_D \ q_I	2	3	4	5
1	1	1	1	1
2	1	2	2	2
3	1	2	2	2
4	1	2	2	

Table 3.8 – Convergence measurements in the 2D case: orders of accuracy for $q = 3$.

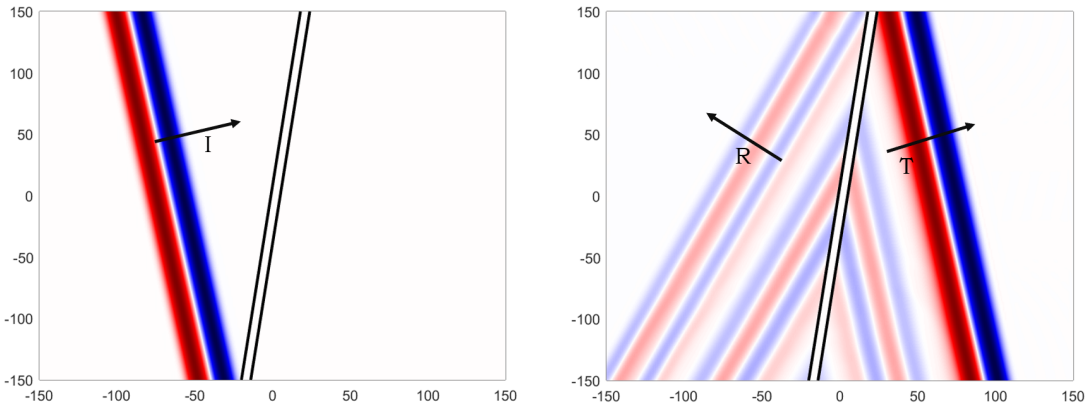

(a) $t = 0$ (b) $t_f = 84.55$ ms

Figure 3.7 – Velocity field V computed for an incident plane wave (I) at oblique incidence on a tilted enlarged interface. R: reflected wave, T: transmitted wave.

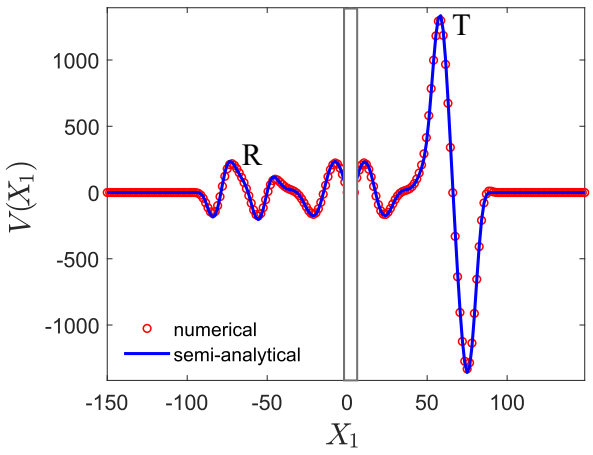

Figure 3.8 – Slanted incident plane wave on a tilted enlarged interface: semi-analytical and numerical velocity fields V_{ref} (blue) and V (red) at $X_2 = 0$ and for the final simulation time $t_f = 84.55$ ms.

accounted for by the proposed numerical method.

3.5.2.3 Incident plane wave on a circular enlarged interface

The case of an incident plane wave on a circular enlarged interface is now considered. This example allows to inspect the capability of the method to take into account a curved enlarged interface. A semi-analytical solution is derived in Section 3.A.2 in the resonant case with $\mathcal{B}_2 = C_1 = \alpha_0 = 0$.

Consequently, in this subsection, these interface parameters are set to zero to allow the comparison with the semi-analytical solution. The numerical parameters are $(q_D, q_I) = (2, 3)$.

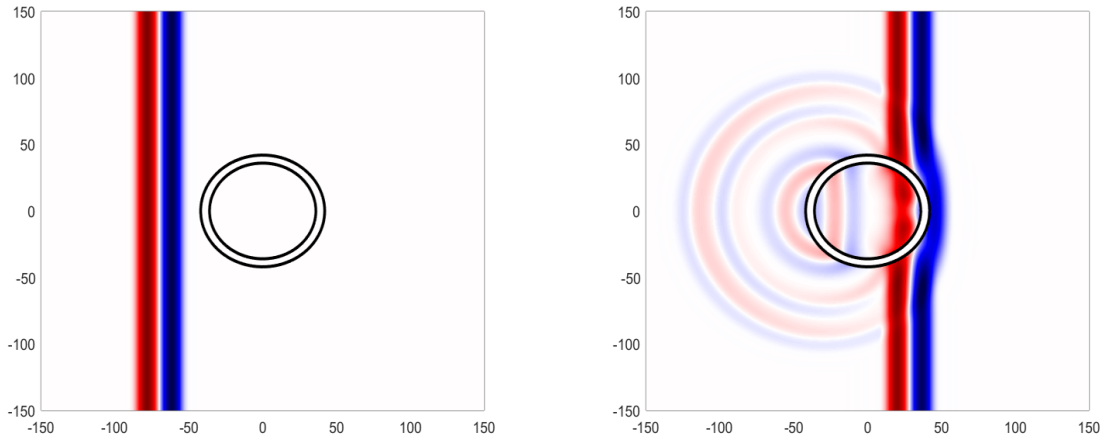

(a) $t = 0$ (b) $t_f = 63.3$ ms

Figure 3.9 – Velocity field V computed for an incident plane wave on a circular enlarged interface.

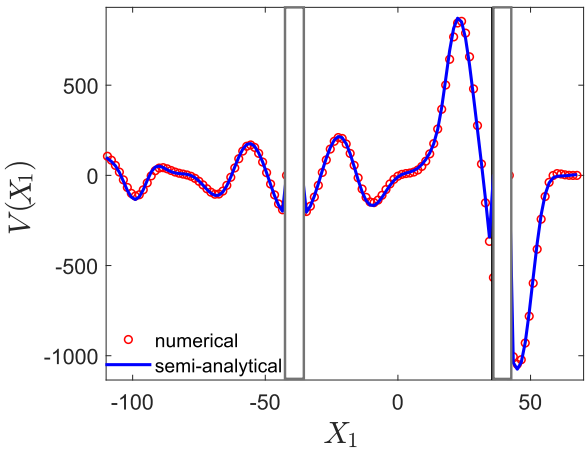

Figure 3.10 – Incident plane wave on a circular enlarged interface in 2D: semi-analytical and numerical velocity fields V_{ref} (blue) and V (red) at $X_2 = 0$ and for the final simulation time $t_f = 63.3$ ms. The vertical black lines denote the position of the enlarged circular interface.

We consider an incident plane wave with propagation direction along X_1 and periodicity conditions imposed on the top and bottom boundaries of the computational domain. The enlarged interface is defined by two circles of center $(0, 0)$ and radii $a^- = 42$ m and $a^+ = 36$ m. The velocity field at the initial time, at which the initialization point in (3.100) is $\boldsymbol{X}_I = (-45\,\text{m}, 0\,\text{m})$, and at final simulation time $t_f = 63.3$ ms are displayed in Figure 3.9. The comparison with the semi-analytical solution is reported in Figure 3.10 at $X_2 = 0$. The measured error is $\epsilon_V(t_f) = 2 \cdot 10^{-2}$ when $\lambda/\Delta X = 33$, which highlights the satisfying performances of the proposed approach with the circular enlarged interface being accurately handled numerically.

3.6 Accounting for dissipation

So far, the numerical method has been presented for jump conditions that relates to an inviscid microstructured configuration. As discussed in Section 2.4, it is also possible to take into account dissipation. The resulting jump conditions (2.63) can be discretized using the same numerical strategy involving an ADER-4 scheme, the ESIM and auxiliary variables. However, the jump conditions are substantially changed when dissipation is considered, and the main resulting changes for the numerical method will be presented in this section.

3.6.1 Formalism of auxiliary fields

Following the same method as in Section 3.1, we introduce the auxiliary variables $\hat{J}_r$ and $\hat{G}_r$ associated with the resonance index $r \in \{1, \cdots, N_R\}$ and which satisfy:

$$\begin{cases} \left(\omega^2 - \dfrac{1}{\gamma\rho_i}\mathrm{i}\omega - \omega_r^2\right)\hat{J}_r(X_2,\omega) = \alpha_r^2\left(1 + \dfrac{1}{\gamma\rho_i\,\mathrm{i}\omega}\right)\left(\omega^2 - \dfrac{1}{\gamma\rho_i}\mathrm{i}\omega\right)\left\langle\!\left\langle \operatorname{div}\hat{\boldsymbol{\Sigma}}\right\rangle\!\right\rangle_a \\ \mathrm{i}\omega\,\hat{J}_r(X_2,\omega) = \hat{G}_r(X_2,\omega) \end{cases} \qquad (X_2 \in \mathbb{R}). \tag{3.101}$$

Combining (2.63), (2.66) and (3.101), a formal inverse Fourier transform yields the system

$$\begin{cases} \partial_t \boldsymbol{\Sigma}(\boldsymbol{X},t) = \mu_m \boldsymbol{\nabla} V(\boldsymbol{X},t) & (|X_1| \geq a/2, X_2 \in \mathbb{R}), \\ \partial_t V(\boldsymbol{X},t) = \dfrac{1}{\rho_m}\operatorname{div}\boldsymbol{\Sigma}(\boldsymbol{X},t) & (|X_1| \geq a/2, X_2 \in \mathbb{R}), \\ \partial_t J_r(X_2,t) = G_r(X_2,t) & (X_2 \in \mathbb{R},\ r = 1,\ldots,N_R), \\ \partial_t G_r(X_2,t) = -\dfrac{1}{\gamma\rho_i}G_r(X_2,t) - \omega_r^2 J_r(X_2,t) + \mu_m\alpha_r^2\left(\partial_t + \dfrac{2}{\gamma\rho_i}\right)\langle\!\langle \Delta V\rangle\!\rangle_a + \left(\dfrac{\alpha_r}{\gamma\rho_i}\right)^2\langle\!\langle \operatorname{div}\boldsymbol{\Sigma}\rangle\!\rangle_a & \\ \qquad\qquad (X_2 \in \mathbb{R},\ r = 1,\ldots,N_R), \\ [\![V]\!]_a = \widetilde{\mathcal{B}}_1\langle\!\langle \partial_{X_1} V\rangle\!\rangle_a + \widetilde{\mathcal{B}}_2\langle\!\langle \partial_{X_2} V\rangle\!\rangle_a & (X_2 \in \mathbb{R}), \\ [\![\Sigma_1]\!]_a = \widetilde{C}_{11}\langle\!\langle \partial_{X_1}\Sigma_1\rangle\!\rangle_a + \widetilde{C}_{12}\langle\!\langle \partial_{X_2}\Sigma_1\rangle\!\rangle_a + \widetilde{C}_{22}\langle\!\langle \partial_{X_2}\Sigma_2\rangle\!\rangle_a + \widetilde{D}_0\langle\!\langle V\rangle\!\rangle_a - h\sum_{r=1}^{N_R} J_r & (X_2 \in \mathbb{R}), \end{cases} \tag{3.102}$$

with the new parameter $\widetilde{D}_0 = (h\rho_m\alpha_0)/(\gamma\rho_i)$ due to dissipation. When $\gamma = +\infty$, then the inviscid case (3.3) is recovered.

3.6.2 Numerical approximation of the ghost values in 1D

The system (3.3) is recast in 1D for all t as

$$\begin{cases} \partial_t \Sigma(X,t) = \mu_m \, \partial_X V(X,t) & (|X| \geq a/2) \\ \partial_t V(X,t) = \dfrac{1}{\rho_m} \partial_X \Sigma(X,t) & (|X| \geq a/2) \\ \partial_t J_r(t) = G_r(t) & (r = 1, \dots, N_R) \\ \partial_t G_r(t) = -\dfrac{1}{\gamma \rho_i} G_r(t) - \omega_r^2 J_r(t) + \mu_m \alpha_r^2 \left(\partial_t + \dfrac{2}{\gamma \rho_i} \right) \langle\!\langle \partial_{XX}^2 V \rangle\!\rangle_a + \left(\dfrac{\alpha_r}{\gamma \rho_i} \right)^2 \langle\!\langle \partial_X \Sigma \rangle\!\rangle_a \\ [\![V]\!]_a = \widetilde{\mathcal{B}}_1 \, \langle\!\langle \partial_X V \rangle\!\rangle_a \\ [\![\Sigma]\!]_a = \widetilde{C}_{11} \, \langle\!\langle \partial_X \Sigma \rangle\!\rangle_a + \widetilde{D}_0 \, \langle\!\langle V \rangle\!\rangle_a - h \sum_{r=1}^{N_R} J_r. \end{cases} \tag{3.103}$$

The method to derive the numerical approximations of the ghost values, see Sections 3.2.4 and 3.2.5 and Approximation 1, is unchanged but the expressions of the matrices are modified compared to the case $\gamma = +\infty$. Their expressions is given below for $q = 3$.

$$\begin{cases} \mathbb{C}_\pm^3[i,i] = 1, & \mathbb{C}_\pm^3[5,1] = \mp \dfrac{\widetilde{D}_0}{2}, \\ \mathbb{C}_\pm^3[1,2] = \mp \dfrac{\widetilde{B}_1}{2}, & \mathbb{C}_\pm^3[5,6] = \mp \dfrac{\widetilde{C}_{11}}{2}, \\ \mathbb{C}_\pm^3[2,3] = \mp \dfrac{\widetilde{C}_{11}}{2}, & \mathbb{C}_\pm^3[6,7] = \mp \dfrac{\widetilde{B}_1}{2}, \\ \mathbb{C}_\pm^3[2,6] = \mp \dfrac{\widetilde{D}_0}{2\rho_m \mu_m}, & \mathbb{C}_\pm^3[7,3] = \mp \dfrac{h \rho_m}{\gamma \rho_i} \left(\dfrac{\alpha_0}{2} - \sum_{r=1}^{N_R} \alpha_r^2 \right), \\ \mathbb{C}_\pm^3[3,4] = \mp \dfrac{\widetilde{B}_1}{2}, & \mathbb{C}_\pm^3[7,6] = \pm \dfrac{h}{2(\gamma \rho_i c_m)^2} \sum_{r=1}^{N_R} \alpha_r^2, \\ \mathbb{C}_\pm^3[4,3] = \mp \dfrac{h}{2(\gamma \rho_i c_m)^2} \sum_{r=1}^{N_R} \alpha_r^2, & \mathbb{C}_\pm^3[7,8] = \mp \dfrac{1}{2} \left(\widetilde{C}_{11} - h \sum_{r=1}^{N_R} \alpha_r^2 \right), \\ \mathbb{C}_\pm^3[4,6] = \mp \dfrac{h}{2\mu_m c_m^2 (\gamma \rho_i)^3} \sum_{r=1}^{N_R} \alpha_r^2, & \mathbb{C}_\pm^3[i,j] = 0 \text{ else.} \\ \mathbb{C}_\pm^3[4,8] = \mp \dfrac{h}{2\mu_m \gamma \rho_i} \left(\alpha_0 - \sum_{r=1}^{N_R} \alpha_r^2 \right), \end{cases} \tag{3.104}$$

$$\begin{cases} \mathbb{Q}^3[2,j] = -\dfrac{h}{\mu_m} & \text{if } j \in \{N_R+1,...,2N_R\}, \\ \mathbb{Q}^3[4,j] = -\dfrac{h\omega_j^2}{\mu_m c_m^2 \gamma \rho_i} & \text{if } j \in \{1,...,N_R\}, \\ \mathbb{Q}^3[4,j] = \dfrac{h}{\mu_m c_m^2}\left(\omega_{j-N_R}^2 - \dfrac{1}{(\gamma\rho_i)^2}\right) & \text{if } j \in \{N_R+1,...,2N_R\}, \\ \mathbb{Q}^3[5,j] = -h & \text{if } j \in \{1,...,N_R\}, \\ \mathbb{Q}^3[7,j] = \dfrac{h\omega_j^2}{c_m^2} & \text{if } j \in \{1,...,N_R\}, \\ \mathbb{Q}^3[7,j] = \dfrac{h}{c_m^2\gamma\rho_i} & \text{if } j \in \{N_R+1,...,2N_R\}, \\ \mathbb{Q}^3[i,j] = 0 & \text{else.} \end{cases} \tag{3.105}$$

$$\boldsymbol{R}_\pm^3[4] = \mp\frac{1}{2}\Big(\widetilde{C}_{11} - h\sum_{r=1}^{N_R}\alpha_r^2\Big)\partial_X^4 V_\pm, \quad \boldsymbol{R}_\pm^3[8] = \mp\frac{\widetilde{B}_1}{2}\partial_X^4\Sigma_\pm, \quad \boldsymbol{R}_\pm^3[i] = 0 \text{ else.} \tag{3.106}$$

When $\gamma = +\infty$, one recovers the equations (3.14), (3.15) and (3.16) of the inviscid case.

3.6.3 Computation of the auxiliary variables in 1D

Compared with the inviscid case, the computation of the auxiliary variables is substantially changed by dissipation, since the equation satisfied by the auxiliary variables is modified. Since it is a second-order equation, there are three different possible cases depending on the sign of the discriminant. From now on we will focus on only one of these cases. Indeed, the following assumption is used regarding the dissipation parameter γ:

Assumption 3.2

$\gamma > \gamma^\star = 1/(2\,\rho_i\,\omega_1)$.

The infinite set of resonant frequencies is strictly increasing, see (1.23). Hence Assumption 3.2 implies that $\gamma > 1/(2\rho_i\omega_r)$ for all $r \geq 1$. The case of high dissipation, such that $\gamma \leq \gamma^\star$, yields a finite set of purely damped eigenmodes. The forthcoming calculations, where low dissipation is assumed, can easily be adapted to this regime. We introduce

$$\begin{cases} \xi^1 = -1/(2\gamma\rho_i) \\ \xi_r^2 = \sqrt{4\,\omega_r^2 - 1/(\gamma\rho_i)^2}\,/\,2 \\ \varphi(\tau) = \mu_m\alpha_r^2\left(\partial_t + \dfrac{2}{\gamma\rho_i}\right)\langle\partial_X^2 V\rangle_a(\tau) + \left(\dfrac{\alpha_r}{\gamma\rho_i}\right)^2\langle\partial_X\Sigma\rangle_a(\tau). \end{cases} \tag{3.107}$$

Zero initial conditions are assumed for J_r and G_r. Using Assumption 3.2, then the auxiliary fields write

$$\begin{cases} J_r(t_n) &= e^{\xi^1 t_n}\left[-\Lambda_r^1(t_n)\cos(\xi_r^2 t_n) + \Lambda_r^2(t_n)\sin(\xi_r^2 t_n)\right], \\ G_r(t_n) &= e^{\xi^1 t_n}\left[\Lambda_r^1(t_n)(\xi_r^2\sin(\xi_r^2 t_n) - \xi^1\cos(\xi_r^2 t_n)) + .\Lambda_r^2(t_n)(\xi_r^2\cos(\xi_r^2 t_n) + \xi^1\sin(\xi_r^2 t_n))\right], \end{cases} \tag{3.108}$$

where one has for $k = 1, 2$:

$$\Lambda_r^k(t_n) = \frac{1}{\xi_r^2}\int_0^{t_n} \ell_r^k(\tau)\,\mathrm{d}\tau \quad \text{with} \quad \begin{cases} \ell_r^1(\tau) = \varphi(\tau)\sin(\xi_r^2\tau)\mathrm{e}^{-\xi^1\tau}, \\ \ell_r^2(\tau) = \varphi(\tau)\cos(\xi_r^2\tau)\mathrm{e}^{-\xi^1\tau}. \end{cases} \tag{3.109}$$

This leads to an iterative computation of the functions Λ_r^k:

$$\begin{cases} \Lambda_r^k(t_0) = 0, \\ \Lambda_r^k(t_{n+1}) = \Lambda_r^k(t_n) + \dfrac{1}{\xi_r^2}\displaystyle\int_{t_n}^{t_{n+1}} \ell_r^k(\tau)\,\mathrm{d}\tau, \end{cases} \tag{3.110}$$

where $t_0 = 0$. As in the inviscid case, the integral is computed using the extrapolative Newton-Cotes formula (3.37) and the temporal derivative in (3.107) using the finite-difference approximation (3.38). The numerical approximation of the traces at $t_s \leq t_n$ is computed thanks to the numerical approximations $(\boldsymbol{U}_\pm^q)^s$, see (3.41) for the velocity.
To compute the numerical approximation $(\Lambda_r^k)^{n+1}$ of $\Lambda_r^k(t_{n+1})$, the following iterative relation is thus used:

$$\begin{cases} (\Lambda_r^k)^0 = 0, \\ (\Lambda_r^k)^{n+1} = (\Lambda_r^k)^n + \dfrac{\alpha_r^2\Delta t}{\xi_r^2}\displaystyle\sum_{w=0}^{q_I-2}\delta_w \times \\ \qquad \left[\dfrac{\mu_m}{\Delta t}\displaystyle\sum_{z=0}^{q_D}\beta_z(\langle\partial_X^2 V\rangle_a)^{n-w-z} + \dfrac{2\mu_m}{\gamma\rho_i}(\langle\partial_X^2 V\rangle_a)^{n-w} + \dfrac{1}{(\gamma\rho_i)^2}(\langle\partial_X \Sigma\rangle_a)^{n-w}\right](\kappa_r^k)^{n-w}, \end{cases} \tag{3.111}$$

with $(\kappa_r^1)^s = \sin(\xi_r^2 t_s)\mathrm{e}^{-\xi^1 t_s}$, $(\kappa_r^2)^s = \cos(\xi_r^2 t_s)\mathrm{e}^{-\xi^1 t_s}$, $(\langle\partial_X^2 V\rangle_a)^s$ and $(\langle\partial_X \Sigma\rangle_a)^s$ given by:

$$\begin{cases} (\langle\partial_X^2 V\rangle_a)^s = \dfrac{1}{2}\left((\boldsymbol{U}_-^q)^s + (\boldsymbol{U}_+^q)^s\right)[3], \\ (\langle\partial_X \Sigma\rangle_a)^s = \dfrac{1}{2}\left((\boldsymbol{U}_-^q)^s + (\boldsymbol{U}_+^q)^s\right)[q+3]. \end{cases} \tag{3.112}$$

Then, the numerical approximation of the auxiliary variables writes:

Result 3.6: Numerical approximations of the auxiliary variables with dissipation

$$\begin{cases} J_r^n = \mathrm{e}^{\xi^1 t_n}\left[-(\Lambda_r^1)^n\cos(\xi_r^2 t_n) + (\Lambda_r^2)^n\sin(\xi_r^2 t_n)\right], \\ G_r^n = \mathrm{e}^{\xi^1 t_n}\left[(\Lambda_r^1)^n(\xi_r^2\sin(\xi_r^2 t_n) - \xi^1\cos(\xi_r^2 t_n)) + (\Lambda_r^2)^n(\xi_r^2\cos(\xi_r^2 t_n) + \xi^1\sin(\xi_r^2 t_n))\right]. \end{cases} \tag{3.113}$$

It follows the vector $\boldsymbol{Z}^n$ and consequently the ghost values. In the inviscid case, the local truncation error was analysed in Section 3.3. The steps of the proof can be adapted directly to the dissipative case, and are not repeated here. The result of Property 5 then still holds for the dissipative case.

3.6.4 Overview of the 2D case

The computation of the ghost values in the two-dimensional case has been detailed in the inviscid case in Section 3.4. Compared with the one-dimensional case, a significant change occurs when the jump conditions are derived q times. Indeed, the q-th order jump conditions are derived not only by differentiating in time the jump conditions but also by differentiating with respect to the curvilinear

abscissa s, see Section 3.4.3. For the inviscid case, as discussed in Section 3.4.5, one only needs to compute $(q-2)(q-1)\times N_R$ auxiliary variables since the second member of the equation defining (J_r, G_r) only involves the third-order derivative term. In the damped case, first-order derivatives are also involved which requires the computation of $q(q+1)\times N_R$ auxiliary variables. In particular, the case $q=3$ used in practice does not require to introduce additional auxiliary variables in the inviscid case. Such technicalities cannot be avoided with dissipation and 12 auxiliary variables have to be computed.

Without dissipation, the matrices in the ESIM separate the terms of stress and velocity, which have very different orders of magnitude. In the dissipative case, these terms are mixed, which induces a bad conditioning of the jump condition matrices and leads to numerical instabilities. To overcome this difficulty, normalized physical parameters are used in our simulation software when dissipation is considered. These quantities are denoted by tildes in the following. We define the normalized time $\tilde{t} = \mathcal{N} t$ and frequency $\tilde{f} = f/\mathcal{N}$ and the normalized physical parameters $\tilde{\rho} = \mathcal{N}^3\rho$, $\tilde{\mu} = \mathcal{N}\mu$, $\tilde{c} = c/\mathcal{N}$, $\tilde{\gamma} = \gamma/\mathcal{N}^2$. The value of $\mathcal{N}$ is chosen so that all the normalized quantities are of the same order of magnitude.

3.6.5 Numerical experiments

3.6.5.1 Setting

Numerical experiments are then performed to assess the validity of the numerical method when dissipation is considered. The effective parameters are the ones of Tables 2.1 and 2.2, with $a = 1.3838\,\mathrm{m}$, $\mu_m = 10^{10}\ \mathrm{kg}\cdot\mathrm{m}^{-1}\cdot\mathrm{s}^{-2}$ and $c_m = 1500\,\mathrm{m}\cdot\mathrm{s}^{-1}$. In this configuration, the limit value of Assumption 3.2 is $\gamma^\star = 1.87\cdot 10^{-7}\,\mathrm{kg}^{-1}\cdot\mathrm{m}^3\cdot\mathrm{s}$. The value of the dissipation parameter is thus chosen to be $\gamma = 2\cdot 10^{-6}\,\mathrm{kg}^{-1}\cdot\mathrm{m}^3\cdot\mathrm{s} > \gamma^\star$.

The central frequency is $f_0 = 72$ Hz in the source function (2.57) used in the initial conditions (2.59). The point $\boldsymbol{X}_I = (-2, 0)\,\mathrm{m}$ is chosen such that the initial conditions do not intersect the enlarged interface. The initial profile (normalized by its maximum) of the velocity is displayed in Figure 3.11a.

The numerical parameters are $\Delta X = 0.2\,\mathrm{m}$ for the mesh size and $\Delta t = \zeta\Delta X/c_m$ for the time step. The CFL number $\zeta = 0.95 < 1$ is chosen and ensures the stability of the ADER-4 scheme in a homogeneous medium. The order of the ESIM is $q = 3$, and one chooses $(q_D, q_I) = (2, 3)$ for the computation of the auxiliary variables. The normalization parameter is set to $\mathcal{N} = 10^3$.

3.6.5.2 1D case

One first uses the 1D numerical method and the profile of the numerical approximation of this homogenized model is displayed at the final time $t_f = 31.7\,\mathrm{ms}$ together with a semi-analytical solution V_{ref} in Figure 3.11b. The computation of this semi-analytical solution is detailed in Section 3.A.1.

The discrepancy between the numerical and semi-analytical homogenized solutions is measured in the L^2-norm for $X \in [-50; -5]\,\mathrm{m}$. The relative error in Figure 3.11b, i.e. for $\Delta X = 0.2$ m, is of 0.7%. The relative error is then represented in Figure 3.12 as a function of ΔX whose slope in a log-log scale graph characterizes the global order of the scheme. This figure is obtained with the relative position of the enlarged interface in the uniform Cartesian grid being kept while the mesh size ΔX increases. The errors obtained with the numerical method previously described in the inviscid case are also included in the figure for comparison and denoted by the legend $\gamma = +\infty$. As theoretically predicted, order 2 of convergence is measured.

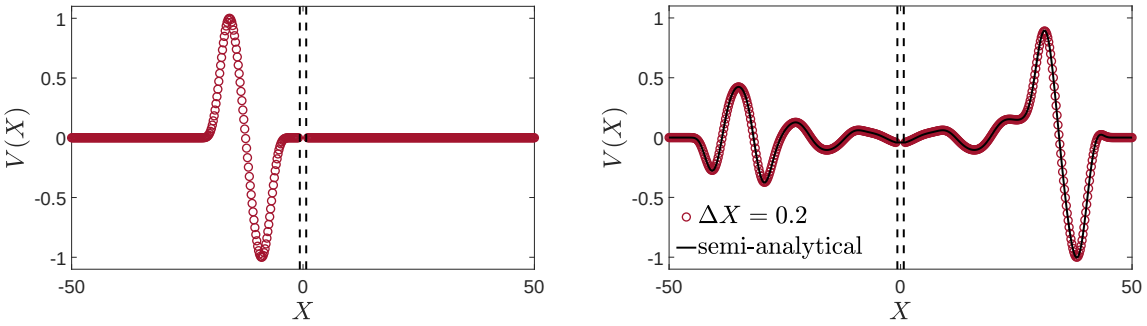

(a) $t = 0$ (b) $t = t_f$

Figure 3.11 – Velocity profiles of the homogenized problem at time $t = 0$ and time $t = t_f$ for a plane wave at normal incidence with $f_0 = 72\,\text{Hz}$. The dashed lines denote the positions of the enlarged interface.

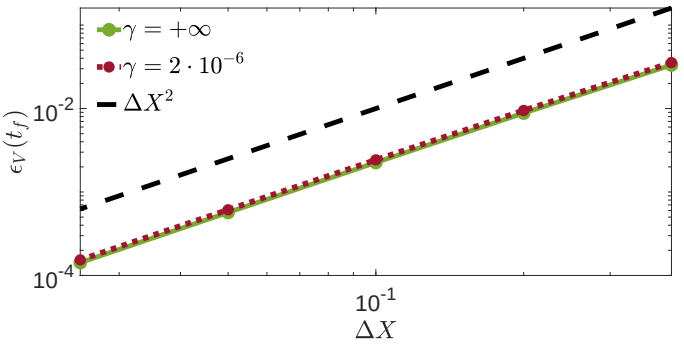

Figure 3.12 – Relative error between the 1D numerical and semi-analytical velocities of the homogenized problem in a log-log scale.

3.6.5.3 2D case

We still consider the same configuration of an incident plane wave at normal incidence but the full 2D algorithm is used for the homogenized problem. The same numerical parameters as in 1D are used and periodic conditions are imposed at the top and the bottom of the computational domain. Figure 3.13 shows the velocity fields at the initial time $t = 0$ and the final time $t = t_f = 31.7\,\text{ms}$. The profiles along $X_2 = -1\,\text{m}$ of the numerical and semi-analytical solutions of the homogenized problem are displayed at t_f in Figure 3.14a. The discrepancy is of same order as in 1D, with a relative error of 1%. This relative error is displayed as a function of ΔX in Figure 3.14b and confirms an order of 2. Consequently, we observe the same orders of accuracy as in 1D even if the 2D numerical method is much more intricate, involving 12 auxiliary variables computed instead of 2 for the one-dimensional problem.

3.7 Conclusion and perspectives

In this chapter, our objective was to handle enlarged interfaces characterized by frequency-dependent jump conditions and consequently jump conditions that are non-local in time when formulated in the time domain. A time-domain numerical method was proposed and implemented for this type of model. The proposed approach relies on the following key points: (i) A set of auxiliary variables is introduced locally along the enlarged interface, which allows to formulate a first-order system in time with jump conditions that are local in time. (ii) An immersed interface

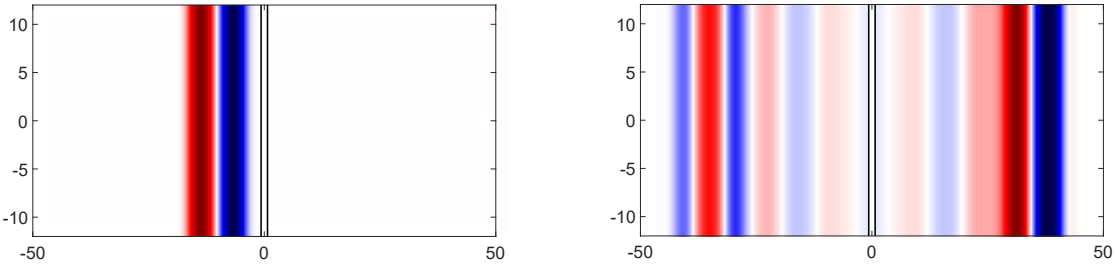

(a) $t = 0$ (b) $t = t_f$

Figure 3.13 – Velocity fields of the homogenized problem at time $t = 0$ and time $t = t_f$ at normal incidence with $f_0 = 72$ Hz. The black lines denote the enlarged interface.

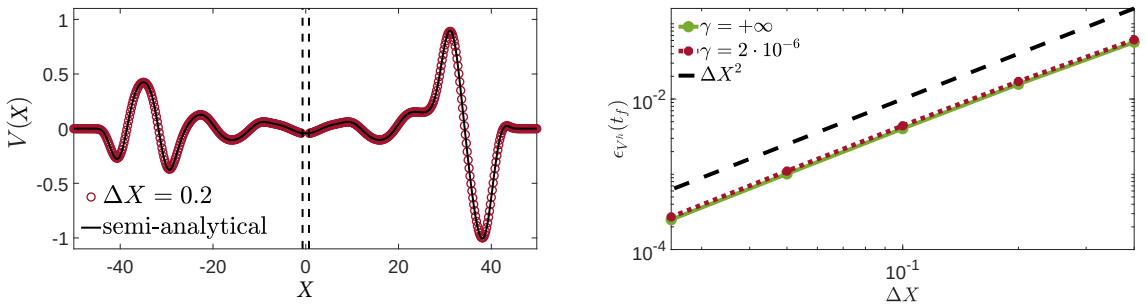

(a) Homogenized velocity profiles (b) Relative errors

Figure 3.14 – Numerical and semi-analytical velocity profiles (a) of the homogenized problem at time $t = t_f$ at normal incidence with $f_0 = 72$ Hz and corresponding relative errors (b).

method is developed to handle numerically such a system by using a high-order finite differences scheme on a Cartesian grid through a proper discretization of the enlarged interface.

Local error estimates were derived to assess the optimal values of the featured numerical parameters. The proposed numerical method was then illustrated and validated considering 1D and 2D configurations involving plane waves illuminating straight or curved enlarged interfaces. Moreover, semi-analytical solutions to these problems were derived and used for quantitative comparisons. Eventually, in line with the previous chapter, the modifications induced by the incorporation of dissipation in the resonant model was presented. Indeed, the computation of the auxiliary variables is substantially changed and the 2D numerical experiments require the computation of additional auxiliary variables.

This numerical method has been programmed from scratch in C++ (about 13000 lines) and will be implemented in the PROSPERO platform (http://prospero-software.science/) in a near future.

Different follow-ups can be identified at the end of this chapter from the mathematical, numerical and modeling standpoints:

- In the inviscid case, the auxiliary variables $\{\hat{J}_r\}$ are defined through (3.1) for all $\omega \neq \omega_r$. Therefore, in order to apply the inverse Fourier transform, care must be taken and a suitable approach relies on the introduction of an artificial damping parameter that is taken to zero once in the time domain. Studying such a limit amounts to investigate the question of the existence of a limiting absorption principle for the system considered (Cassier et al., 2017b). This has been omitted in this chapter and the inverse Fourier transform has only been applied

formally.

- Regarding stability in the framework of the ESIM method, the classical Von Neumann analysis cannot be applied, as it is only valid in homogeneous media. Energy methods, valid in the case of variable coefficients, are well suited to discretizations arising from a variational formulation, which is not the case for this method. A way to study the stability is the GKS analysis by discrete normal modes. This issue has been tackled in Lombard, 2010 for 1D problems with linear jump conditions. An attempt could be made to adapt it to cases of resonant jump conditions. This would not give a theoretical expression as the classical CFL condition but it could provide a numerical tool to test the stability for a given set of numerical and physical parameters.

- The treatment of the boundaries in the direction of the microstructured layer has been disregarded: we consider either periodic conditions, or impose the semi-analytical solution on the boundaries, or perform simulations on a sufficiently large domain so that the results in the domain of interest are not affected by boundaries phenomena. A perspective could be to add adequate Perfectly Matched Layers (Alvarez-Aramberri, Pardo, & Barucq, 2014)

- Some of the perspectives mentioned in the previous chapter concerning the homogenization step would naturally lead to perspectives regarding the numerical method: extension to the three dimensional case or to other dissipation models for example.

3.A Semi-analytical solutions for plane waves on a resonant meta-interface

In this appendix, semi-analytical solutions are computed for resonant meta-interfaces. They are used to inspect the validity of the numerical method developped in Chapter 3 and to compute the reflexion and transmission coefficients of the homogenized problem in Chapter 2.

3.A.1 Semi-analytical solution for a slanted plane wave on a tilted plane interface

In this subsection, the analytical solution is computed in the general case where dissipation is considered. One only has to take $\gamma = +\infty$ in the expression of $\mathscr{D}_\gamma$ to obtain the inviscid case. We consider an incident plane wave at an angle θ_I with the horizontal axis and an enlarged interface located between the *physical* points $X_1 = -a/2$ and $X_1 = a/2$, see Figure 3.15. The initial conditions are given in (3.100). To calculate the solution to the 2D problem (3.102) in this configuration, we consider its frequency-domain formulation (2.63). The wavefield solution $\hat{\boldsymbol{U}}(\boldsymbol{X}, \omega)$ is then decomposed into incident $\hat{\boldsymbol{U}}_I$, reflected $\hat{\boldsymbol{U}}_R$ and transmitted $\hat{\boldsymbol{U}}_T$ waves, ie $\hat{\boldsymbol{U}} = \hat{\boldsymbol{U}}_I + \hat{\boldsymbol{U}}_R + \hat{\boldsymbol{U}}_T$. It is assumed that these are plane waves that write

$$\begin{cases} \hat{\boldsymbol{U}}_I = \begin{pmatrix} 1/\mu_m \\ -\cos\theta_I/c_m \\ -\sin\theta_I/c_m \end{pmatrix} \exp(-\mathrm{i}\boldsymbol{k}_I \cdot (\boldsymbol{X} - \boldsymbol{X}_I))\, \hat{F}(\omega), \\ \hat{\boldsymbol{U}}_R = \begin{pmatrix} 1/\mu_m \\ -\cos\theta_R/c_m \\ -\sin\theta_R/c_m \end{pmatrix} \exp(-\mathrm{i}(\boldsymbol{k}_R \cdot \boldsymbol{X} - \boldsymbol{k}_I \cdot \boldsymbol{X}_I))\, \hat{F}(\omega)\, \mathcal{R}(\omega), \\ \hat{\boldsymbol{U}}_T = \begin{pmatrix} 1/\mu_m \\ -\cos\theta_T/c_m \\ -\sin\theta_T/c_m \end{pmatrix} \exp(-\mathrm{i}\boldsymbol{k}_T \cdot (\boldsymbol{X} - \boldsymbol{X}_I))\, \hat{F}(\omega)\, \mathcal{T}(\omega), \end{cases} \tag{3.114}$$

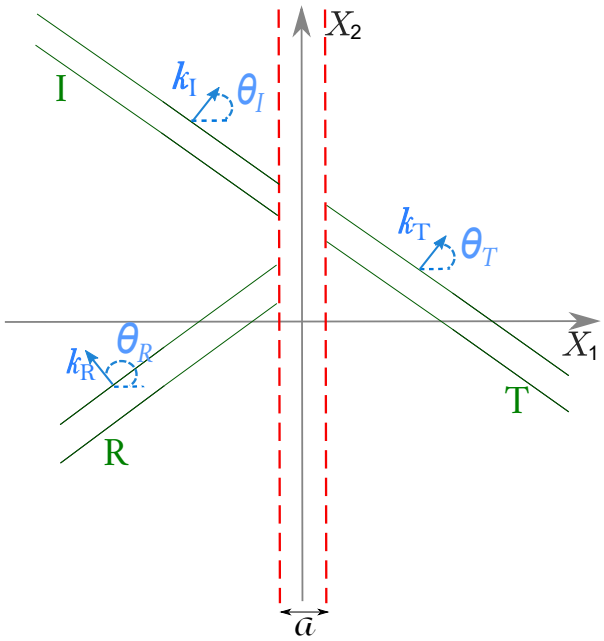

Figure 3.15 – Incident plane wave (I) illuminating the enlarged interface and leading to reflected (R) and transmitted (T) plane waves.

with $\theta_R = \pi - \theta_I$ and $\theta_T = \theta_I$, and $\boldsymbol{k}_I$, $\boldsymbol{k}_R$ and $\boldsymbol{k}_T$ being the corresponding wavevectors that are of norm ω/c_m and whose direction is normal to the wave fronts. Using the jump conditions in (2.63) and introducing the following parameters

$$\begin{cases} \alpha_1(\omega) = \dfrac{h}{2c_m^2}\left(\left(\mathcal{S} + \mathscr{D}_\gamma(\omega)\right)\cos(\theta_R)^2 + C_1 \sin\theta_R \cos\theta_R + \left(C_2 + \mathscr{D}_\gamma(\omega)\right)\sin(\theta_R)^2\right), \\ \alpha_2(\omega) = \dfrac{h}{2c_m^2}\left(\left(\mathcal{S} + \mathscr{D}_\gamma(\omega)\right)\cos(\theta_T)^2 + C_1 \sin\theta_T \cos\theta_T + \left(C_2 + \mathscr{D}_\gamma(\omega)\right)\sin(\theta_T)^2\right), \\ \beta_1 = -\dfrac{h}{2c_m}\left(\mathcal{B}\cos\theta_R + \mathcal{B}_2 \sin\theta_R\right), \\ \beta_2 = -\dfrac{h}{2c_m}(\mathcal{B}\cos\theta_T + \mathcal{B}_2 \sin\theta_T), \\ \delta(\omega) = \exp\left(-\mathrm{i}\dfrac{\omega}{c_m} a\cos\theta_I\right), \end{cases} \tag{3.115}$$

then we get the following system for the reflected coefficient $\mathcal{R}(\omega)$ and transmitted coefficient $\mathcal{T}(\omega)$:

$$\begin{cases} \left(\dfrac{\cos\theta_R}{c_m} - \mathrm{i}\omega\,\alpha_1(\omega)\right)\delta(\omega)\mathcal{R}(\omega) - \left(\dfrac{\cos\theta_T}{c_m} + \mathrm{i}\omega\,\alpha_2(\omega)\right)\delta(\omega)\mathcal{T}(\omega) = -\dfrac{\cos\theta_I}{c_m} + \mathrm{i}\omega\,\alpha_2(\omega), \\ \left(1 + \mathrm{i}\omega\,\beta_1\right)\delta(\omega)\mathcal{R}(\omega) - \left(1 - \mathrm{i}\omega\beta_2\right)\delta(\omega)\mathcal{T}(\omega) = -1 - \mathrm{i}\omega\,\beta_2. \end{cases} \tag{3.116}$$

One makes use of $\mathcal{B}_2 = \mathcal{C}_1$, see Property 1, and introduces the parameters

$$\begin{cases} \mathscr{L}(\omega) = h\left((-\mathcal{S}+\mathcal{B})\cos(\theta_I)^2 - \mathcal{C}_2\sin(\theta_I)^2 - \mathscr{D}_\gamma(\omega)\right), \\ \mathscr{G} = -h(\mathcal{C}_1+\mathcal{B}_2)\cos(\theta_I)\sin(\theta_I), \\ \mathscr{Z} = 2c_m\cos\theta_I, \\ \mathscr{N}(\omega) = h\left(\mathcal{S}\cos(\theta_I)^2 + \mathcal{C}_2\sin(\theta_I)^2 + \mathcal{B}\cos(\theta_I)^2 + \mathscr{D}_\gamma(\omega)\right), \\ \mathscr{M}(\omega) = \dfrac{h^2}{2c_m}\left(\mathcal{B}\mathcal{S}\cos(\theta_I)^2 - \mathcal{B}_2\mathcal{C}_1\sin(\theta_I)^2 + \mathcal{B}\mathcal{C}_2\sin(\theta_I)^2 + \mathcal{B}\mathscr{D}_\gamma(\omega)\right)\cos(\theta_I), \end{cases} \tag{3.117}$$

to get the reflection coefficient and the transmission coefficient

$$\begin{cases} \mathcal{R}(\omega) = \dfrac{\mathrm{i}\omega\,\mathscr{L}(\omega)}{\mathscr{Z}+\mathrm{i}\omega\,\mathscr{N}(\omega)-\omega^2\mathscr{M}(\omega)}\exp\left(\mathrm{i}\dfrac{\omega}{c_m}a\cos\theta_I\right), \\ \mathcal{T}(\omega) = \dfrac{\mathscr{Z}+\mathrm{i}\omega\,\mathscr{G}+\omega^2\mathscr{M}(\omega)}{\mathscr{Z}+\mathrm{i}\omega\,\mathscr{N}(\omega)-\omega^2\mathscr{M}(\omega)}\exp\left(\mathrm{i}\dfrac{\omega}{c_m}a\cos\theta_I\right). \end{cases} \tag{3.118}$$

These expressions used in (3.114) give the sought expression for $\hat{\boldsymbol{U}}(\boldsymbol{X},\omega)$. An inverse discrete Fourier transform in time provides the semi-analytical time-domain solution considered in Sections 3.5 and 3.6. It can be shown that the 1D semi-analytical solution is recovered when setting $\theta_I = 0$, $X_2 = 0$ and $\Sigma_2 = 0$ in the 2D solution.

Remark 13. *When the enlarged interface is tilted of an angle $-\phi$ with the horizontal axis then the calculation of the associated scattering coefficients follows the same lines in the rotated coordinate system $(\zeta,\eta) = (\cos\phi\,X_1 - \sin\phi\,X_2, \sin\phi\,X_1 + \cos\phi\,X_2)$. A rotation of angle $-\phi$ is then necessary after the inverse discrete Fourier transform to express the vectorial field $\boldsymbol{\Sigma}$ in the basis (X_1, X_2).*

3.A.2 Semi-analytical solution for a plane wave on a circular interface

We consider an incident plane wave at an angle θ_I with the horizontal axis and an enlarged circular interface defined by two circles of centers (x_c, y_c) and radii a^- and a^+, with $a^- > a^+$. The initial conditions are given in (3.100). The approach presented here applies to the particular interface parameter values $\mathcal{B}_2 = \mathcal{C}_1 = \alpha_0 = 0$, the other parameters being arbitrary. The method employed in Lombard and Piraux, 2004 for fluid-solid circular interface is applied here: to calculate the solution, we consider its frequency-domain formulation (1.19). The wavefield solution $\hat{\boldsymbol{U}}(\boldsymbol{X},\omega)$ is then decomposed into incident, reflected and transmitted waves. They are written on a truncated basis of Bessel functions using the Jacobi-Anger decomposition and the associated diffraction coefficients are derived from the jump conditions. We start by introducing a polar coordinates system (r,ϕ) such as $X_1 = x_c + r\cos\phi$ and $X_2 = y_c + r\sin\phi$, and the harmonic potential $\hat{\Psi}$ such that

$$\hat{V} = \mathrm{i}\frac{\omega}{\mu_m}\hat{\Psi}, \qquad \hat{\Sigma}_\nu = \partial_r\hat{\Psi}, \qquad \hat{\Sigma}_\tau = \frac{1}{r}\partial_\phi\hat{\Psi}. \tag{3.119}$$

The harmonic potential of the incident plane wave is:

$$\hat{\Psi}_I(X_1,X_2,\omega) = \exp\left(-\frac{\mathrm{i}\omega}{c_m}\left(X_1\cos\theta_I + X_2\sin\theta_I\right)\right)\frac{\hat{F}(\omega)}{\mathrm{i}\omega}. \tag{3.120}$$

The above potential reads:

$$\hat{\Psi}_I(X_1,X_2,\omega) = GS\exp\left(-\mathrm{i}kr\cos\alpha\right), \tag{3.121}$$

with $G = \hat{F}(\omega)/\mathrm{i}\omega$, $S = \exp(-\mathrm{i}k(x_c \cos\theta_I + y_c \sin\theta_I)$, $\alpha = \phi - \theta_I$ and $k = \omega/c_m$. The Bessel functions of the first-kind $\mathcal{J}_n$ satisfy the Jacobi-Anger expansion, see e.g. Harvey, Morse, and Feschbach, 1955:

$$\exp(-\mathrm{i}r\cos\alpha) = \sum_{n=0}^{\infty} \epsilon_n (-\mathrm{i})^n \cos(n\alpha)\mathcal{J}_n(r), \tag{3.122}$$

with $\epsilon_n = 1$ if $n = 0$, 2 else. From (3.121) and (3.122), we therefore express the potential $\hat{\Psi}_I$ as:

$$\hat{\Psi}_I(X_1, X_2, \omega) = GS \sum_{n=0}^{\infty} \epsilon_n (-\mathrm{i})^n \cos(n\alpha)\, \mathcal{J}_n(kr). \tag{3.123}$$

To satisfy the Sommerfeld condition of the radiated wavefield at infinity in the acoustic medium, the harmonic potential $\hat{\Psi}_R$ of the reflected wave is written on the basis of Hankel functions of the second-kind $\mathcal{H}_n$. To prevent singularities from occurring at $r = 0$, the harmonic potential $\hat{\Psi}_T$ of transmitted waves is written on the basis of the Bessel functions of the first-kind, i.e.

$$\hat{\Psi}_R(X_1, X_2, \omega) = \sum_{n=0}^{\infty} R_n \cos(n\alpha)\, \mathcal{H}_n(kr), \qquad \hat{\Psi}_T(X_1, X_2, \omega) = \sum_{n=0}^{\infty} T_n \cos(n\alpha)\, \mathcal{J}_n(kr), \tag{3.124}$$

where R_n and T_n are the coefficients of reflexion and transmission that have to be determined. The stress vector $\hat{\boldsymbol{\Sigma}} = (\hat{\Sigma}_\nu, \hat{\Sigma}_\tau)^\top$ and the velocity $\hat{V}$ are deduced from the potential $\hat{\Psi}$ using (3.121). From (3.119), (3.123) and (3.124), we deduce the components of the incident, reflected and transmitted waves as follows:

$$\begin{cases} \hat{V}_I = \mathrm{i}\dfrac{\omega}{\mu_m} GS \displaystyle\sum_{n=0}^{\infty} \epsilon_n (-\mathrm{i})^n \cos(n\alpha)\, \mathcal{J}_n(kr), \\ \hat{\Sigma}_{I\nu} = k\, GS \displaystyle\sum_{n=0}^{\infty} \epsilon_n (-\mathrm{i})^n \cos(n\alpha) \mathcal{J}_n'(kr), \\ \hat{\Sigma}_{I\tau} = -\dfrac{1}{r} GS \displaystyle\sum_{n=0}^{\infty} \epsilon_n (-\mathrm{i})^n n \sin(n\alpha)\, \mathcal{J}_n(kr), \end{cases}$$

$$\begin{cases} \hat{V}_R = \mathrm{i}\dfrac{\omega}{\mu_m} \displaystyle\sum_{n=0}^{\infty} R_n \cos(n\alpha) \mathcal{H}_n(kr), \\ \hat{\Sigma}_{R\nu} = k \displaystyle\sum_{n=0}^{\infty} R_n \cos(n\alpha) \mathcal{H}_n'(kr), \\ \hat{\Sigma}_{R\tau} = -\dfrac{1}{r} \displaystyle\sum_{n=0}^{\infty} R_n n \sin(n\alpha) \mathcal{H}_n(kr), \end{cases} \tag{3.125}$$

$$\begin{cases} \hat{V}_T = \mathrm{i}\dfrac{\omega}{\mu_m} \displaystyle\sum_{n=0}^{\infty} T_n \cos(n\alpha) \mathcal{J}_n(kr), \\ \hat{\Sigma}_{T\nu} = k \displaystyle\sum_{n=0}^{\infty} T_n \cos(n\alpha) \mathcal{J}_n'(kr), \\ \hat{\Sigma}_{T\tau} = -\dfrac{1}{r} \displaystyle\sum_{n=0}^{\infty} T_n n \sin(n\alpha) \mathcal{J}_n(kr). \end{cases}$$

In the case where $\mathcal{B}_2 = \mathcal{C}_1 = \alpha_0 = 0$ an identification is possible, then the coefficients R_n and T_n are deduced from the jump conditions in (1.19), which for all $0 \le \phi \le 2\pi$ read:

$$\hat{V}_T(a^+, \phi) - (\hat{V}_I + \hat{V}_R)(a^-, \phi) = \frac{h\mathcal{B}}{2}(\partial_r \hat{V}_T(a^+, \phi) + (\partial_r \hat{V}_I + \partial_r \hat{V}_R)(a^-, \phi)),$$

and

$$\hat{\Sigma}_{Tv}(a^+,\phi)-(\hat{\Sigma}_{Iv}+\hat{\Sigma}_{Rv})(a^-,\phi)=\frac{h\mathcal{S}}{2}(\partial_r\hat{\Sigma}_{Tv}(a^+,\phi)+(\partial_r\hat{\Sigma}_{Iv}+\partial_r\hat{\Sigma}_{Rv})(a^-,\phi))$$
$$+\frac{hC_2}{2}\left(\frac{1}{a^+}\partial_\phi\hat{\Sigma}_{T\tau}(a^+,\phi)+\frac{1}{a^-}(\partial_\phi\hat{\Sigma}_{I\tau}+\partial_\phi\hat{\Sigma}_{R\tau})(a^-,\phi)\right)+\frac{k^2h\mathscr{D}_\infty(\omega)}{2}(\hat{V}_T(a^+,\phi)+(\hat{V}_I+\hat{V}_R)(a^-,\phi)).$$

Then, one obtains the following system satisfied by the coefficients R_n and T_n for all $n\geq 0$:

$$\begin{cases}\left[k\mathcal{J}_n'(ka^+)-\frac{h\mathcal{S}}{2}k^2\mathcal{J}_n''(ka^+)+\frac{hC_2}{2}\left(\frac{n}{a^+}\right)^2\mathcal{J}_n(ka^+)-k^2\frac{h}{2}\mathscr{D}_\infty(\omega)\mathcal{J}_n(ka^+)\right]T_n\\ +\left[-k\mathcal{H}_n'(ka^-)-\frac{h\mathcal{S}}{2}k^2\mathcal{H}_n''(ka^-)+\frac{hC_2}{2}\left(\frac{n}{a^-}\right)^2\mathcal{H}_n(ka^-)-k^2\frac{h}{2}\mathscr{D}_\infty(\omega)\mathcal{H}_n(ka^-)\right]R_n\\ =GS\epsilon_n(-\mathrm{i})^n\left[k\mathcal{J}_n'(ka^-)+\frac{h\mathcal{S}}{2}k^2\mathcal{J}_n''(ka^-)-\frac{hC_2}{2}\left(\frac{n}{a^-}\right)^2\mathcal{J}_n(ka^-)+k^2\frac{h}{2}\mathscr{D}_\infty(\omega)\mathcal{J}_n(ka^-)\right],\\ \left[\mathcal{J}_n(ka^+)-\frac{h\mathcal{B}}{2}k\mathcal{J}_n'(ka^+)\right]T_n+\left[-\mathcal{H}_n(ka^-)-\frac{h\mathcal{B}}{2}k\mathcal{H}_n'(ka^-)\right]R_n\\ =GS\epsilon_n(-\mathrm{i})^n\left[\mathcal{J}_n(ka^-)+\frac{h\mathcal{B}}{2}k\mathcal{J}_n'(ka^-)\right].\end{cases}\tag{3.126}$$

In practice, one considers a finite number N_{Bessel} of modes. The coefficients R_n and T_n are computed from the associated systems (3.126) and (3.125) is finally used to obtain the wavefield solution $\hat{\boldsymbol{U}}(\boldsymbol{X},\omega)$ in the frequency domain. A discrete inverse Fourier transform in time yields the semi-analytical solution considered in Section 3.5.2.3.

CHAPTER 4

Topological optimization of the effective dynamics of microstructured interfaces

In the context of metamaterials, the optimization is an important step in order to determine the designs that exhibit interesting macroscopic behaviours. It can consist in optimizing the physical or geometric parameters if the geometry of the metamaterial is fixed (e.g. Helmholtz resonators (Romero-Garcia et al., 2021), multi-mass resonators (Palermo et al., 2018), slotted cylinders (Lagarrigue et al., 2013)). As discussed in introduction, in this chapter, we are rather interested in the topological optimization and this work was performed in collaboration with Rémi Cornaggia (now at Institut Jean Le Rond d'Alembert, Sorbonne Université).

More precisely, we consider the topological optimization of thin microstructured layers based on the corresponding homogenized models. Contrary to the previous two chapters, the row of inclusions is considered in the *non-resonant* case, i.e. with a low contrast of the physical parameters, see Assumption 1.1. Topological optimization in the case of resonant microstructures is an involved task that we consider beyond the scope of this thesis.

In Section 4.1, we precise the considered optimization process based on the homogenized model. In Section 4.2, the topological derivatives of the effectives parameters defining the homogenized

model are computed. They allow to describe the sensitivity of the effective parameters to topological perturbations in the unit cell. Section 4.3 describes the numerical methods used for the optimization process. Indeed, the computation of the effectives parameters requires to solve cell problems on an infinite strip. Their computation on a bounded cell is performed thanks to a FFT-based method with boundary correctors. The strategy to update the material properties based on the knowledge of the topolgical derivative is also described in this section. This is based either on a naive pixel by pixel update or by a level-set method. Finally, some preliminary numerical results are presented in Section 4.4.

4.1 Problem statement

We first recall the microstructured configuration and the associated homogenized model, and then introduce the topological optimization framework.

4.1.1 Physical configuration and homogenized model

Let us consider again the propagation of *scalar* waves in 2D across a periodic row of inclusions $\cup_i \Omega_i$ embedded within a homogeneous matrix Ω_m. The configuration is the one of Section 1.2.2.2 and Section 1.2.2.3. Consequently, compared to the previous two chapters, we consider here the *non-resonant* case, i.e. we assume a low contrast for both the mass density and the shear modulus, see Assumption 1.1. We first recall the results of the associated homogenization process (Marigo et al., 2017a), see Section 1.2.2.3 and especially the jump conditions 1.1.

To do so, we introduce for $j = 1, 2$ the fields $\Phi^{(j)}$ which are y_2-periodic and solutions of the following cell problems:

$$\begin{cases} \nabla_{\boldsymbol{y}} \cdot \left(\mu(\boldsymbol{y}) \left(\nabla_{\boldsymbol{y}} \Phi^{(j)}(\boldsymbol{y}) + \boldsymbol{e}_j \right) \right) = 0 \text{ in } \Omega, \\ \mu(\boldsymbol{y}) [\nabla_{\boldsymbol{y}} \Phi^{(j)}(\boldsymbol{y}) + \boldsymbol{e}_j] \cdot \boldsymbol{n} \text{ and } \Phi^{(j)} \text{ continuous on } \partial\Omega_i, \\ \lim\limits_{y_1 \to \pm\infty} \nabla_{\boldsymbol{y}} \Phi^{(j)}(y_1, y_2) = \boldsymbol{0}, \end{cases} \tag{4.1}$$

with Ω the elementary cell $\mathbb{R} \times [-1/2, 1/2]$. Then, the following constants are defined, for $j = 1, 2$:

$$\begin{cases} \mathcal{B}_j = \lim\limits_{y_1 \to +\infty} \left[\Phi^{(j)}(y_1, y_2) - \Phi^{(j)}(-y_1, y_2) \right], \\ C_j = \int_\Omega \dfrac{\mu(\boldsymbol{y})}{\mu_m} \dfrac{\partial \Phi^{(j)}}{\partial y_2}(\boldsymbol{y}) \, \mathrm{d}\boldsymbol{y}. \end{cases} \tag{4.2}$$

From Marigo et al., 2017a, we know that the homogenization at order $\mathcal{O}(\eta)$ of such a configuration yields the following homogenized model:

$$\begin{cases} \dfrac{\partial \boldsymbol{\Sigma}}{\partial t} = \mu_m \nabla V & (|X_1| \geq a/2,\ X_2 \in \mathbb{R}), \\ \rho_m \dfrac{\partial V}{\partial t} = \operatorname{div} \boldsymbol{\Sigma} & (|X_1| \geq a/2,\ X_2 \in \mathbb{R}), \\ [\![V]\!]_a = h \left\{ \mathcal{B} \left\langle\!\!\left\langle \dfrac{\partial V}{\partial X_1} \right\rangle\!\!\right\rangle_a + \mathcal{B}_2 \left\langle\!\!\left\langle \dfrac{\partial V}{\partial X_2} \right\rangle\!\!\right\rangle_a \right\} & (X_2 \in \mathbb{R}), \\ [\![\Sigma_1]\!]_a = h \left\{ \mathcal{S} \langle\!\langle \operatorname{div} \boldsymbol{\Sigma} \rangle\!\rangle_a - C_1 \left\langle\!\!\left\langle \dfrac{\partial \Sigma_1}{\partial X_2} \right\rangle\!\!\right\rangle_a - C \left\langle\!\!\left\langle \dfrac{\partial \Sigma_2}{\partial X_2} \right\rangle\!\!\right\rangle_a \right\} & (X_2 \in \mathbb{R}). \end{cases} \tag{4.3}$$

As in the resonant case, it consists in jump conditions for the velocity and the normal component of the stress vector on an effective enlarged interface of width $a \geq e$. However, due to the fact

that there is no scaling in η between μ_i and μ_m, the expressions of the effective parameters used in (4.3) are not the same and are recalled here:

$$\begin{cases} \mathcal{B} = \dfrac{a}{h} + \mathcal{B}_1, \\ \mathcal{C} = \dfrac{a}{h} + \left(\dfrac{\mu_i}{\mu_m} - 1\right) \displaystyle\int_{\Omega_i} \mathrm{d}\boldsymbol{y} + \mathcal{C}_2, \\ \mathcal{S} = \dfrac{a}{h} + \left(\dfrac{\rho_i}{\rho_m} - 1\right) \displaystyle\int_{\Omega_i} \mathrm{d}\boldsymbol{y}. \end{cases} \tag{4.4}$$

The effective parameters characterizing the homogenized medium are collected in $\boldsymbol{m}_{\text{eff}}$ as:

$$\boldsymbol{m}_{\text{eff}} = (\mathcal{B}, \mathcal{B}_2, \mathcal{S}, \mathcal{C}_1, \mathcal{C}). \tag{4.5}$$

4.1.2 Topological optimization

As already mentionned, the thickness a of the enlarged effective interface in $\boldsymbol{X}$-coordinates is always chosen such that $a \geq e$ with e the thickness of the microstructured array. We introduce the reference cell Ω^a which is the bounded subset in $\boldsymbol{y}$-coordinates of Ω defined by

$$\Omega^a = \left[-\frac{a}{2h}; \frac{a}{2h}\right] \times \underbrace{\left[-\frac{1}{2}; \frac{1}{2}\right]}_{I} \qquad \text{such that} \qquad \boldsymbol{m}(\boldsymbol{y}) = (\rho(\boldsymbol{y}), \mu(\boldsymbol{y})) = (\rho_m, \mu_m) \ \forall \boldsymbol{y} \in \Omega \backslash \Omega^a. \tag{4.6}$$

One aims at generating the phase distribution $\boldsymbol{m}_{\text{opt}}$ in this bounded cell Ω^a that defines a microstructure that optimizes an objective cost functional $\mathcal{J}(\boldsymbol{m}_{\text{eff}})$ that depends on the macroscopic behavior. Based on the homogenized model, this macroscopic behaviour is described by the effective parameters $\boldsymbol{m}_{\text{eff}}$ (4.5) that themselves depend on $\boldsymbol{m}$. We therefore consider the following optimization problem:

$$\text{Find} \qquad \boldsymbol{m}_{\text{opt}} = \arg\min_{\boldsymbol{m}} \tilde{\mathcal{J}}(\boldsymbol{m}) \qquad \text{with} \qquad \tilde{\mathcal{J}}(\boldsymbol{m}) = \mathcal{J}(\boldsymbol{m}_{\text{eff}}). \tag{4.7}$$

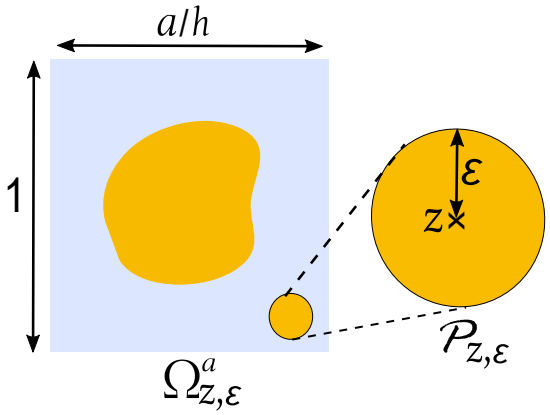

Figure 4.1 – Cell $\Omega^a_{z,\varepsilon}$ perturbed by the introduction of the inhomogeneity $\mathcal{P}_{z,\varepsilon}$.

To solve the problem (4.7), we allow topological perturbations of the microstructure. A perturbation is a small inhomogeneity $\mathcal{P}_{z,\varepsilon} = z + \varepsilon\mathcal{P}$ of size ε, normalized shape $\mathcal{P}$ and physical parameters $(\mu + \Delta\mu, \rho + \Delta\rho)$ introduced at a point $z \in \Omega^a$. The material perturbation is $\Delta\boldsymbol{m} = (\Delta\rho, \Delta\mu)$

with $\Delta\mu > -\min_{y\in\Omega^a}\mu(y)$ and $\Delta\rho > -\min_{y\in\Omega^a}\rho(y)$ to satisfy the physical constraints. The resulting perturbed cell is $\Omega^a_{z,\varepsilon}$ of parameters $m_{z,\varepsilon} = (\mu_{z,\varepsilon}, \rho_{z,\varepsilon}) = (\mu + \Delta\mu\chi_{\mathcal{P}_{z,\varepsilon}}, \rho + \Delta\rho\chi_{\mathcal{P}_{z,\varepsilon}})$, with $\chi_{\mathcal{P}_{z,\varepsilon}}$ the characteristic function of the perturbation domain $\mathcal{P}_{z,\varepsilon}$.

Let f be a function of the material properties. In this context, the so-called topological derivative of a given function f denoted by $\mathcal{D}f$ is defined thanks to the following asymptotic expansion in 2D:

$$f_{z,\varepsilon} := f(m_{z,\varepsilon}) \underset{\varepsilon\to 0}{=} f(m) + \varepsilon^2 \mathcal{D}f(m, z, \mathcal{P}, \Delta m) + o(\varepsilon^2). \tag{4.8}$$

It describes the influence on the functional f of a perturbation located at z, of shape $\mathcal{P}$ and material perturbation Δm. Therefore, the more negative $\mathcal{D}f(m, z, \mathcal{P}, \Delta m)$ is, the more efficient a perturbation at z would be to decrease f.

In this context, and given the optimization problem (4.7), one looks for the topological derivative $\mathcal{D}\tilde{\mathcal{J}}$. If $\mathcal{J}$ is differentiable with respect to the effective parameters, $\mathcal{D}\tilde{\mathcal{J}}$ is computed thanks to the chain rule:

$$\mathcal{D}\tilde{\mathcal{J}} = \frac{\partial\mathcal{J}}{\partial\mathcal{B}}\mathcal{D}\mathcal{B} + \frac{\partial\mathcal{J}}{\partial\mathcal{B}_2}\mathcal{D}\mathcal{B}_2 + \frac{\partial\mathcal{J}}{\partial\mathcal{S}}\mathcal{D}\mathcal{S} + \frac{\partial\mathcal{J}}{\partial\mathcal{C}_1}\mathcal{D}\mathcal{C}_1 + \frac{\partial\mathcal{J}}{\partial\mathcal{C}}\mathcal{D}\mathcal{C}. \tag{4.9}$$

The final objective is to have at hand an optimization algorithm in order to compute the optimal material distribution in the sense of (4.7).

4.1.3 Main strategy

The main strategy follows Cornaggia and Bellis, 2020. This involves different steps:

1. Initialization: definition of the initial material properties $m(y)$ for all $y \in \Omega^a$
2. Definition of the geometry $\mathcal{P}$ of the perturbation and its material properties $(\Delta\rho, \Delta\mu)$.
3. Definition of a stopping criterion
4. Until the stopping criterion is satisfied, iteration of the following process:
   (a) Computation of the cell problems solutions (4.1) which will appear in the expression of the topological derivatives
   (b) Computation of the topological derivatives of the effective parameters
   (c) Computation of the topological derivative of the cost functional $\mathcal{D}\tilde{\mathcal{J}}$ in Ω^a from (4.9).
   (d) The material properties are updated thanks to the information provided by $\mathcal{D}\tilde{\mathcal{J}}$

The topological derivatives of the effectives parameters $(\mathcal{D}\mathcal{B}, \mathcal{D}\mathcal{B}_2, \mathcal{D}\mathcal{S}, \mathcal{D}\mathcal{C}_1, \mathcal{D}\mathcal{C})$ are computed in Section 4.2 based on the expansion (4.8) and following Bonnet et al., 2018. The computation of the cell problems is detailed in Section 4.3.1. The update of the material properties following typically a gradient descent algorithm is discussed in Section 4.3.2.

4.2 Topological sensitivities of the effective parameters

For numerical purposes, since the optimization process will require the computation of many cell problems, one wants to compute the cell problems in a bounded domain which is not the case of the formulation (4.1). Consequently, we first reformulate the cell problem in a bounded cell in Section 4.2.1. Then, one looks for an expansion of the cell problem solution $\Phi_{z,\varepsilon}$ in the perturbed cell Ω^a_ε in Section 4.2.2. This finally allows the computation of the topological sensitivities of the parameters $\mathcal{D}\mathcal{B}$, $\mathcal{D}\mathcal{S}$ and $\mathcal{D}\mathcal{C}$ in Sections 4.2.3, 4.2.4 and 4.2.5, respectively.

4.2.1 Equivalent cell problem in a bounded cell

One introduces the vector $\boldsymbol{\Phi} = (\Phi^{(1)}, \Phi^{(2)})^T$ to work with compact notations. Due to (4.1), the problem posed in an infinite strip for $\boldsymbol{\Phi}$ reads

$$\begin{cases} \operatorname{div}\left(\mu(\boldsymbol{y})\left(\boldsymbol{\nabla}_{\boldsymbol{y}}\boldsymbol{\Phi}(\boldsymbol{y}) + \boldsymbol{I}_2\right)\right) = \boldsymbol{0} \text{ in } \Omega, \\ \mu(\boldsymbol{y})[\boldsymbol{\nabla}_{\boldsymbol{y}}\boldsymbol{\Phi}(\boldsymbol{y}) + \boldsymbol{I}_2]\cdot\boldsymbol{n} \text{ and } \boldsymbol{\Phi} \text{ continuous on } \partial\Omega_i, \\ \boldsymbol{\Phi} \ y_2 \text{ periodic}, \\ \lim\limits_{y_1\to\pm\infty} \boldsymbol{\nabla}_{\boldsymbol{y}}\boldsymbol{\Phi}(y_1, y_2) = \boldsymbol{0}, \end{cases} \tag{4.10}$$

with $\boldsymbol{I}_2$ the identity tensor. We remind that the variations of the physical parameters are restricted to Ω^a due to its definition in (4.6). We define the half-strips $\Omega_a^+ = [\frac{a}{2h}, +\infty[\times I$ and $\Omega_a^- =]-\infty, -\frac{a}{2h}]\times I$, see Figure 4.2, such that the restrictions $\boldsymbol{\Phi}^\pm = \boldsymbol{\Phi}_{|\Omega_a^\pm}$ satisfy:

$$\begin{cases} \boldsymbol{\Delta}\boldsymbol{\Phi}^\pm = 0 \text{ in } \Omega_a^\pm, \\ \boldsymbol{\Phi}^\pm \ y_2 \text{ periodic}, \\ \lim\limits_{y_1\to\pm\infty} \boldsymbol{\nabla}_{\boldsymbol{y}}\boldsymbol{\Phi}^\pm(y_1, y_2) = \boldsymbol{0}. \end{cases} \tag{4.11}$$

One writes the classical modal decomposition, also used in Marigo et al., 2017a, for $\boldsymbol{\Phi}^\pm$, which is harmonic in $\Omega_a^\pm$:

$$\boldsymbol{\Phi}^\pm(y_1, y_2) = \sum_{n\in\mathbb{Z}} \boldsymbol{\varphi}_{\boldsymbol{n}}^\pm \mathrm{e}^{\mp|\xi_n|\left(y_1 \mp \frac{a}{2h}\right)}\Psi_n(y_2), \quad \text{with} \quad \Psi_n(y_2) = \mathrm{e}^{\mathrm{i}\xi_n y_2}, \quad \xi_n = 2n\pi. \tag{4.12}$$

The modes $\{\Psi_n\}$ are orthonormal for the L^2 scalar product on the vertical section I, i.e. they

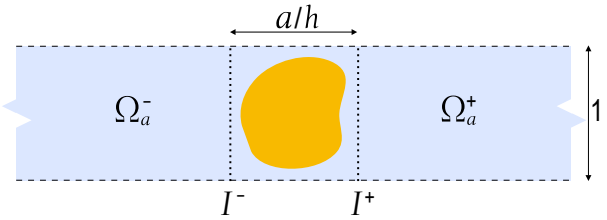

Figure 4.2 – Half strips $\Omega_a^+ = [\frac{a}{2h}, +\infty[\times I$ and $\Omega_a^- =]-\infty, -\frac{a}{2h}]\times I$.

satisfy:

$$\left(\Psi_p, \Psi_q\right)_I = \delta_{pq} \quad \text{with} \quad \left(f, g\right)_I := \int_I f(y_2)\overline{g(y_2)}\mathrm{d}y_2. \tag{4.13}$$

Consequently, choosing the particular section $I^+ = \left\{(y_1, y_2) \in \Omega_a^+,\ y_1 = \frac{a}{2h}\right\}$, see Figure 4.2, yields the expression of the modal coefficients in the right half-strip:

$$\boldsymbol{\varphi}_{\boldsymbol{n}}^+ = \left(\boldsymbol{\Phi}^+\left(\frac{a}{2h}, \cdot\right), \Psi_n\right)_I = \int_I \boldsymbol{\Phi}^+\left(\frac{a}{2h}, y_2\right)\overline{\Psi_n(y_2)}\mathrm{d}y_2. \tag{4.14}$$

One differentiates the decomposition (4.12) with respect to y_1 and uses the expression of the coefficients (4.14) to get the following *Dirichlet-to-Neumann* (DtN) operator linking the trace of $\boldsymbol{\Phi}$ and of its normal derivative on the section I^+ where $\boldsymbol{\Phi} = \boldsymbol{\Phi}^+$:

$$\partial_{y_1}\boldsymbol{\Phi}\left(\frac{a}{2h}, \cdot\right) = \boldsymbol{\Lambda}^+\left[\boldsymbol{\Phi}\left(\frac{a}{2h}, \cdot\right)\right], \tag{4.15}$$

where

$$\boldsymbol{\Lambda}^+[\boldsymbol{f}](y_2) = -\sum_{n\in\mathbb{Z}} (\boldsymbol{f}, \Psi_n)_I\, |\xi_n|\Psi_n(y_2). \tag{4.16}$$

Similarly, one can choose the particular section $I^- = \left\{(y_1, y_2) \in \Omega_a^-,\ y_1 = -\frac{a}{2h}\right\}$, see Figure 4.2, to get the expression of the left modal coefficients

$$\boldsymbol{\varphi}_n^- = \left(\boldsymbol{\Phi}^-\left(-\frac{a}{2h}, \cdot\right), \Psi_n\right)_I = \int_I \boldsymbol{\Phi}^-\left(-\frac{a}{2h}, y_2\right)\overline{\Psi_n(y_2)}\mathrm{d}y_2 \tag{4.17}$$

and thus the left DtN relation

$$-\partial_{y_1}\boldsymbol{\Phi}\left(-\frac{a}{2h}, \cdot\right) = \boldsymbol{\Lambda}^-\left[\boldsymbol{\Phi}\left(-\frac{a}{2h}, \cdot\right)\right], \tag{4.18}$$

where

$$\boldsymbol{\Lambda}^-[f](y_2) = -\sum_{n\in\mathbb{Z}}(f, \Psi_n)_I\,|\xi_n|\Psi_n(y_2). \tag{4.19}$$

From (4.15) and (4.18), one can write the following DtN relation for both interfaces $I^\pm$

$$\partial_{\boldsymbol{n}}\boldsymbol{\Phi}\left(\pm\frac{a}{2h}, \cdot\right) = \boldsymbol{\Lambda}\left[\boldsymbol{\Phi}\left(\pm\frac{a}{2h}, \cdot\right)\right], \quad \text{where } \boldsymbol{\Lambda} = \boldsymbol{\Lambda}^+ = \boldsymbol{\Lambda}^- \quad \text{and } \partial_{\boldsymbol{n}} = \pm\partial y_1. \tag{4.20}$$

The problem posed in the infinite band (4.10) can thus be rewritten as a problem with DtN boundary conditions on the bounded cell (4.6)

$$\begin{cases} \boldsymbol{\nabla}\cdot\left(\mu(\boldsymbol{y})\left(\boldsymbol{\nabla}\boldsymbol{\Phi} + \boldsymbol{I}_2\right)\right) = \boldsymbol{0} \text{ in } \Omega^a, \\ \boldsymbol{\Phi}\ \ y_2 \text{ periodic}, \\ \partial_n\boldsymbol{\Phi}\left(\pm\frac{a}{2h}, \cdot\right) = \boldsymbol{\Lambda}\left(\boldsymbol{\Phi}\left(\pm\frac{a}{2h}, \cdot\right)\right) \text{ on } I^\pm. \end{cases} \tag{4.21}$$

We then establish a formal relation which will be used several times to compute the topological derivatives. To do so, we consider a function $v \in H^1(\Omega^a;\mathbb{R})$, v y_2-periodic. The first equation of (4.21) is then multiplied by v and integrated by parts. Using the periodic condition and the boundary condition in (4.21), one obtains after a division by μ_m:

$$\boldsymbol{\mathcal{A}}_\mu(\boldsymbol{\Phi}, v) = -\boldsymbol{F}_\mu(v) + \boldsymbol{J}(v) \qquad \forall v \in H^1(\Omega^a;\mathbb{R}),\ v\ y_2\text{-periodic}. \tag{4.22}$$

This required the introduction of the following functions

$$\begin{cases} \boldsymbol{\mathcal{A}}_\mu(\boldsymbol{u}, v) = \displaystyle\int_{\Omega^a}\frac{\mu(\boldsymbol{y})}{\mu_m}\boldsymbol{\nabla}\boldsymbol{u}(\boldsymbol{y})^\top\cdot\boldsymbol{\nabla}v(\boldsymbol{y})\mathrm{d}\boldsymbol{y} + \mathcal{L}^-(\boldsymbol{u}, v) + \mathcal{L}^+(\boldsymbol{u}, v), \\ \boldsymbol{F}_\mu(v) = \displaystyle\int_{\Omega^a}\frac{\mu(\boldsymbol{y})}{\mu_m}\boldsymbol{\nabla}v(\boldsymbol{y})\mathrm{d}\boldsymbol{y}, \\ \boldsymbol{J}(v) = \displaystyle\int_I\left[v\left(\frac{a}{2h}, y_2\right) - v\left(-\frac{a}{2h}, y_2\right)\right]\boldsymbol{e}_1\mathrm{d}y_2, \end{cases} \tag{4.23}$$

with

$$\begin{cases} \mathcal{L}^-(\boldsymbol{u}, v) = \displaystyle\sum_{n>0}\beta_n\left(\psi_n, v\right)_I\left(\boldsymbol{u}, \psi_n\right)_I, \\ \mathcal{L}^+(\boldsymbol{u}, v) = -\displaystyle\sum_{n<0}\beta_n\left(\psi_n, v\right)_I\left(\boldsymbol{u}, \psi_n\right)_I. \end{cases} \tag{4.24}$$

This vector-valued weak-formulation is a short-hand notation for the two uncoupled equations satisfied by $\Phi^{(1)}$ and $\Phi^{(2)}$.

4.2.2 Approximation of the solution of the cell problem in the perturbed cell

To begin with, due to (4.22), the field $\boldsymbol{\Phi}_{z,\varepsilon}$ satisfies for all $v \in H^1(\Omega^a;\mathbb{R})$, v y_2-periodic:

$$\mathcal{A}_{\mu_{z,\varepsilon}}(\boldsymbol{\Phi}_{z,\varepsilon}, v) = -\boldsymbol{F}_\mu(v) - \boldsymbol{\delta F}_{z,\varepsilon}(v) + \boldsymbol{J}(v), \tag{4.25}$$

with

$$\boldsymbol{\delta F}_{z,\varepsilon}(v) = \frac{\Delta\mu}{\mu_m}\int_{\mathcal{P}_{z,\varepsilon}} \nabla v(\boldsymbol{y})\mathrm{d}\boldsymbol{y}. \tag{4.26}$$

Then, one introduces the Green's function $G(\cdot,\boldsymbol{x})$ created by a point source at $\boldsymbol{x} \in \Omega^a$ and solution of

$$\begin{cases} -\operatorname{div}_y\left(\dfrac{\mu(\boldsymbol{y})}{\mu_m}\nabla_y G(\boldsymbol{y},\boldsymbol{x})\right) = \delta(\boldsymbol{y}-\boldsymbol{x}) \quad \forall \boldsymbol{y} \in \Omega^a, \\ G(\cdot,\boldsymbol{x}) \ y_2\text{-periodic}, \\ -\boldsymbol{n}\cdot\nabla_y G(\boldsymbol{y},\boldsymbol{x})\Big|_{y_1=\pm\frac{a}{2h}} = \Lambda^{\pm}\left[G(\boldsymbol{y},\boldsymbol{x})\right]\Big|_{y_1=\pm\frac{a}{2h}} \quad \forall \boldsymbol{y} \in I^{\pm}. \end{cases} \tag{4.27}$$

It can be decomposed as

$$G(\boldsymbol{y},\boldsymbol{x}) = G_\infty\left(\boldsymbol{y}-\boldsymbol{x};\frac{\mu(\boldsymbol{x})}{\mu_m}\right) + G_c(\boldsymbol{y},\boldsymbol{x}) \quad \text{with} \quad G_\infty(r;\mu) = -\frac{1}{2\pi\mu}\ln(|r|), \tag{4.28}$$

where G_∞ is the full-space Green's tensor and G_c is the complementary part to the Green's function solution so that the boundary conditions are satisfied. For $\boldsymbol{w}$ sufficiently smooth, one gets from (4.27) the integral representation for all $\boldsymbol{x} \in \Omega^a$:

$$\boldsymbol{w}(x) = \mathcal{A}_\mu(\boldsymbol{w}, G(\cdot,\boldsymbol{x})) \tag{4.29}$$

with $\mathcal{A}_\mu$ defined in (4.23). One introduces

$$\boldsymbol{\mathcal{N}}_{z,\varepsilon}\boldsymbol{f}(\boldsymbol{x}) = \frac{\Delta\mu}{\mu_m}\int_{\mathcal{P}_{z,\varepsilon}} \nabla_y G(\boldsymbol{y},\boldsymbol{x})\cdot\nabla\boldsymbol{f}(\boldsymbol{y})\mathrm{d}\boldsymbol{y}. \tag{4.30}$$

Taking $v = G(\cdot,\boldsymbol{x})$ in (4.25) together with the definition (4.23) of $\mathcal{A}_\mu$ then yields

$$\begin{aligned} \mathcal{A}_\mu(\boldsymbol{\Phi}_{z,\varepsilon}, G(\cdot,\boldsymbol{x})) + \boldsymbol{\mathcal{N}}_{z,\varepsilon}\boldsymbol{\Phi}_{z,\varepsilon}(\boldsymbol{x}) &= -\boldsymbol{F}_\mu(G(\cdot,\boldsymbol{x})) - \boldsymbol{\delta F}_{z,\varepsilon}(G(\cdot,\boldsymbol{x})) + \boldsymbol{J}(G(\cdot,\boldsymbol{x})) \\ &= \mathcal{A}_\mu(\boldsymbol{\Phi}, G(\cdot,\boldsymbol{x})) - \boldsymbol{\delta F}_{z,\varepsilon}(G(\cdot,\boldsymbol{x})). \end{aligned} \tag{4.31}$$

where in the last line we used $v = G(\cdot,\boldsymbol{x})$ in (4.22). Finally, one considers $\boldsymbol{w} = \boldsymbol{\Phi}_{z,\varepsilon}$ and $\boldsymbol{w} = \boldsymbol{\Phi}$ in (4.29). Together with (4.31) this leads to:

$$(\boldsymbol{I} + \boldsymbol{\mathcal{N}}_{z,\varepsilon})(\boldsymbol{\Phi}_{z,\varepsilon})(\boldsymbol{x}) = \boldsymbol{\Phi}(\boldsymbol{x}) - \boldsymbol{\delta F}_{z,\varepsilon}(G(\cdot,\boldsymbol{x})). \tag{4.32}$$

Let introduce the scaled coordinates $\boldsymbol{x} = \boldsymbol{z} + \varepsilon\bar{\boldsymbol{x}}$ and assume the following expansion for all $\boldsymbol{x} \in \mathcal{P}_{z,\varepsilon}$:

$$\boldsymbol{\Phi}_{z,\varepsilon}(\boldsymbol{x}) = \boldsymbol{\Phi}(\boldsymbol{z}) + \varepsilon\boldsymbol{\Phi}_1(\bar{\boldsymbol{x}}) + o(\varepsilon). \tag{4.33}$$

One also writes the following Taylor expansion for the cell function

$$\boldsymbol{\Phi}(\boldsymbol{x}) = \boldsymbol{\Phi}(\boldsymbol{z}) + \varepsilon\bar{\boldsymbol{x}}\nabla\boldsymbol{\Phi}(\boldsymbol{z}) + o(\varepsilon). \tag{4.34}$$

Inserting (4.33) and (4.34) in (4.32) yields, since $\boldsymbol{\mathcal{N}}_{z,\varepsilon}\boldsymbol{\Phi}(\boldsymbol{z}) = \boldsymbol{0}$:

$$(\boldsymbol{I} + \boldsymbol{\mathcal{N}}_{z,\varepsilon})\left(\varepsilon\boldsymbol{\Phi}_1\left(\frac{\cdot - \boldsymbol{z}}{\varepsilon}\right)\right)(\boldsymbol{x}) = \varepsilon\bar{\boldsymbol{x}}\nabla\boldsymbol{\Phi}(\boldsymbol{z}) - \boldsymbol{\delta F}_{z,\varepsilon}(G(\cdot,\boldsymbol{x})). \tag{4.35}$$

Due to (4.28), the function G in (4.27) satisfies

$$\nabla_y G(\boldsymbol{y}, \boldsymbol{x}) = \varepsilon^{-1} \nabla G_\infty \left(\bar{\boldsymbol{y}} - \bar{\boldsymbol{x}}; \frac{\mu(z)}{\mu_m} \right) + o(\varepsilon^{-1}), \tag{4.36}$$

since ∇G_∞ is homogeneous and $G_c(\cdot, \boldsymbol{x})$ is C^∞. Once inserted in (4.35), one performs a change of variable to rewrite the integral on $\mathcal{P}$. Then, an identification of the contributions in $O(\varepsilon)$ leads to:

$$(\boldsymbol{I} + \boldsymbol{\mathcal{M}})(\tilde{\boldsymbol{\Phi}}_1)(\bar{\boldsymbol{x}}) = \bar{\boldsymbol{x}} \cdot (\nabla \boldsymbol{\Phi}(z) + \boldsymbol{I}), \tag{4.37}$$

with $\tilde{\boldsymbol{\Phi}}_1(\bar{\boldsymbol{x}}) = \boldsymbol{\Phi}_1(\bar{\boldsymbol{x}}) + \bar{\boldsymbol{x}}$ and $\boldsymbol{\mathcal{M}}$ defined by

$$\boldsymbol{\mathcal{M}} f(\bar{\boldsymbol{x}}) = \frac{\Delta \mu}{\mu_m} \int_{\mathcal{P}} \nabla G_\infty \left(\bar{\boldsymbol{y}} - \bar{\boldsymbol{x}}; \frac{\mu(z)}{\mu_m} \right) \cdot \nabla f(\bar{\boldsymbol{y}}) \mathrm{d}\bar{\boldsymbol{y}}. \tag{4.38}$$

Consequently, if one introduces $\boldsymbol{R}$ solution of

$$(\boldsymbol{I} + \boldsymbol{\mathcal{M}}) \boldsymbol{R}(\bar{\boldsymbol{x}}) = \bar{\boldsymbol{x}} \tag{4.39}$$

then

$$\tilde{\boldsymbol{\Phi}}_1(\bar{\boldsymbol{x}}) = \boldsymbol{R}(\bar{\boldsymbol{x}}) \cdot (\nabla \boldsymbol{\Phi}(z) + \boldsymbol{I}). \tag{4.40}$$

One inserts this in (4.33) to get at order $O(\varepsilon)$

$$\boldsymbol{\Phi}_{z,\varepsilon}(\boldsymbol{x}) = \boldsymbol{\Phi}(z) + \varepsilon (\boldsymbol{R}(\bar{\boldsymbol{x}}) \cdot (\nabla \boldsymbol{\Phi}(z) + \boldsymbol{I}) - \bar{\boldsymbol{x}}) + o(\varepsilon). \tag{4.41}$$

4.2.3 Computation of $\mathcal{DB} = (\mathcal{DB}, \mathcal{DB}_2)$

To begin with, one wants to rewrite the parameters $\mathcal{B}_1$ and $\mathcal{B}_2$ defined in (4.2) on the bounded cell Ω^a. One considers the limit $y_1 \longrightarrow \pm\infty$ in the decompositions (4.12), then the expression of the coefficients (4.14) and (4.17) yields:

$$\lim_{y_1 \to \pm\infty} \boldsymbol{\Phi}^{\pm}(y_1, y_2) = \boldsymbol{\varphi}_0^{\pm} = \int_I \boldsymbol{\Phi}^{\pm} \left(\pm \frac{a}{2h}, y_2 \right) \mathrm{d}y_2. \tag{4.42}$$

The effective parameter $\boldsymbol{\mathcal{B}} = (\mathcal{B}, \mathcal{B}_2)$, with $\mathcal{B}$ defined in (4.4), is thus expressed on the bounded cell Ω^a as:

$$\boldsymbol{\mathcal{B}}(\boldsymbol{m}) = \frac{a}{h} \boldsymbol{e}_1 + \int_I \left[\boldsymbol{\Phi} \left(\frac{a}{2h}, y_2 \right) - \boldsymbol{\Phi} \left(-\frac{a}{2h}, y_2 \right) \right] \mathrm{d}y_2. \tag{4.43}$$

Consequently, the effective parameter $\boldsymbol{\mathcal{B}}_{z,\varepsilon}$ associated with the perturbed cell writes

$$\boldsymbol{\mathcal{B}}_{z,\varepsilon} = \boldsymbol{\mathcal{B}}(\boldsymbol{m}) + \int_I \left[\delta \boldsymbol{\Phi}_{z,\varepsilon} \left(\frac{a}{2h}, y_2 \right) - \delta \boldsymbol{\Phi}_{z,\varepsilon} \left(-\frac{a}{2h}, y_2 \right) \right] \mathrm{d}y_2, \tag{4.44}$$

with the pertubation for the solution of the cell problem $\delta \boldsymbol{\Phi}_{z,\varepsilon}$ defined by

$$\delta \boldsymbol{\Phi}_{z,\varepsilon} = \boldsymbol{\Phi}_{z,\varepsilon} - \boldsymbol{\Phi}. \tag{4.45}$$

The left-hand-side of (4.25) writes

$$\mathcal{A}_{\mu_{z,\varepsilon}}(\boldsymbol{\Phi}_{z,\varepsilon}, v) = \mathcal{A}_\mu(\boldsymbol{\Phi}, v) + \mathcal{A}_\mu(\delta \boldsymbol{\Phi}_{z,\varepsilon}, v) + \frac{\Delta \mu}{\mu_m} \int_{\mathcal{P}_{z,\varepsilon}} \nabla \boldsymbol{\Phi}_{z,\boldsymbol{\varepsilon}}(\boldsymbol{y})^\top \cdot \nabla v(\boldsymbol{y}) \mathrm{d}\boldsymbol{y}. \tag{4.46}$$

Inserting this equation in (4.25) and using (4.22), one gets for for all $v \in H^1(\Omega^a; \mathbb{R})$, v y_2-periodic:

$$\mathcal{A}_\mu(\delta \boldsymbol{\Phi}_{z,\varepsilon}, v) + \frac{\Delta \mu}{\mu_m} \int_{\mathcal{P}_{z,\varepsilon}} \nabla \boldsymbol{\Phi}_{z,\boldsymbol{\varepsilon}}(\boldsymbol{y})^\top \cdot \nabla v(\boldsymbol{y}) \mathrm{d}\boldsymbol{y} = -\delta \boldsymbol{F}_{z,\varepsilon}(v). \tag{4.47}$$

Furthermore, $\beta = \Phi^{(1)} + y_1$ satisfies for all $\boldsymbol{w} \in H^1(\Omega^a; \mathbb{R}^2)$, $\boldsymbol{w}$ y_2-periodic

$$\mathcal{A}_\mu(\boldsymbol{w}, \beta) = \int_I \left[\boldsymbol{w}\left(\frac{a}{2h}, y_2\right) - \boldsymbol{w}\left(-\frac{a}{2h}, y_2\right) \right] \mathrm{d}y_2. \tag{4.48}$$

Taking $v = \beta$ in (4.47) and $\boldsymbol{w} = \boldsymbol{\delta\Phi}_{z,\varepsilon}$ in (4.48), the expansion (4.44) writes

$$\mathcal{B}_{z,\varepsilon} = \mathcal{B}(\boldsymbol{m}) - \frac{\Delta\mu}{\mu_m} \int_{\mathcal{P}_{z,\varepsilon}} \nabla\beta(\boldsymbol{y}) \cdot (\nabla\boldsymbol{\Phi}_{z,\varepsilon}(\boldsymbol{y}) + \boldsymbol{I}) \mathrm{d}\boldsymbol{y}. \tag{4.49}$$

Consequently, one looks for an asymptotic expansion for $\nabla\boldsymbol{\Phi}_{z,\varepsilon}$. For this purpose, one uses the final expansion (4.41) of the previous section. One also writes the expansion $\nabla\beta(\boldsymbol{y}) = \nabla\beta(\boldsymbol{z}) + o(1)$ for all $\boldsymbol{y} \in \mathcal{P}_{z,\varepsilon}$ and expresses the integral in the scaled coordinates as

$$\mathcal{B}_{z,\varepsilon} = \mathcal{B}(\boldsymbol{m}) - \frac{\Delta\mu}{\mu_m} \int_{\mathcal{P}} \nabla\beta(\boldsymbol{z}) \cdot \left(\frac{1}{\varepsilon} \nabla\boldsymbol{\Phi}_{z,\varepsilon}(\bar{\boldsymbol{y}}) + \boldsymbol{I} \right) \varepsilon^2 \mathrm{d}\bar{\boldsymbol{y}} + o(\varepsilon^2). \tag{4.50}$$

Inserting the expansion (4.41) in the above equation yields

$$\mathcal{B}_{z,\varepsilon} = \mathcal{B}(\boldsymbol{m}) - \varepsilon^2 \frac{\Delta\mu}{\mu_m} \nabla\beta(\boldsymbol{z}) \cdot \int_{\mathcal{P}} \nabla_{\bar{\boldsymbol{y}}} \boldsymbol{R}(\bar{\boldsymbol{y}}) \mathrm{d}\bar{\boldsymbol{y}} \cdot (\nabla\boldsymbol{\Phi}(\boldsymbol{z}) + \boldsymbol{I}) + o(\varepsilon^2). \tag{4.51}$$

We introduce the so-called polarization tensor $\boldsymbol{A}$ defined as

$$\boldsymbol{A}(\mathcal{P}, \mu(\boldsymbol{z}), \Delta\mu) = \frac{\Delta\mu}{\mu_m} \int_{\mathcal{P}} \nabla_{\bar{\boldsymbol{y}}} \boldsymbol{R}(\bar{\boldsymbol{y}}) \mathrm{d}\bar{\boldsymbol{y}}. \tag{4.52}$$

The dependancy in $\mu(\boldsymbol{z})$ comes from the equation (4.39) satisfied by $\boldsymbol{R}$. This polarization tensor have been used in previous studies (Cedio-Fengya, Moskow, & Vogelius, 1998; Ammari & Kang, 2007; Bonnet et al., 2018). In particular, it is symmetric and it is known analytically for an elliptic perturbation of semiaxes lengths $(1, \gamma)$ and directions $(\boldsymbol{a}_1, \boldsymbol{a}_2)$. In this case, its expression is given by:

$$\boldsymbol{A}(\mathcal{P}, \mu(\boldsymbol{z}), \Delta\mu) = \pi\gamma(\gamma+1) \frac{\Delta\mu}{\mu_m} \left(\frac{1}{1 + \gamma + \gamma\frac{\Delta\mu}{\mu(\boldsymbol{z})}} \boldsymbol{a}_1 \otimes \boldsymbol{a}_1 + \frac{1}{1 + \gamma + \frac{\Delta\mu}{\mu(\boldsymbol{z})}} \boldsymbol{a}_2 \otimes \boldsymbol{a}_2 \right). \tag{4.53}$$

Finally, the topological derivative of $\mathcal{B}$ writes

Result 4.1: Topological derivative of $\mathcal{B}$

$$\mathcal{DB}(\boldsymbol{m}, \boldsymbol{z}, \mathcal{P}, \Delta\boldsymbol{m}) = -(\nabla\Phi_1(\boldsymbol{z}) + \boldsymbol{e}_1) \cdot \boldsymbol{A}(\mathcal{P}, \mu(\boldsymbol{z}), \Delta\mu) \cdot (\nabla\boldsymbol{\Phi}(\boldsymbol{z}) + \boldsymbol{I}), \tag{4.54}$$

where we used the definition of $\beta = \Phi_1 + y_1$.

4.2.4 Computation of $\mathcal{DS}$

We first notice that, owing to the definition of $\mathcal{S}$ in (4.4), one has

$$\mathcal{S}(\boldsymbol{m}) = \int_{\Omega^a} \frac{\rho(\boldsymbol{y})}{\rho_m} \mathrm{d}\boldsymbol{y}. \tag{4.55}$$

Consequently, one gets

$$\begin{aligned} \mathcal{S}_{z,\varepsilon} &= \mathcal{S}(\boldsymbol{m}) + \int_{\mathcal{P}_{z,\varepsilon}} \frac{\Delta\rho}{\rho_m} \mathrm{d}\boldsymbol{y} \\ &= \mathcal{S}(\boldsymbol{m}) + \varepsilon^2 \frac{\Delta\rho}{\rho_m} |\mathcal{P}| \end{aligned} \tag{4.56}$$

which yields by identification with (4.8) the following result

Result 4.2: Topological derivative of $\mathcal{S}$

$$\mathcal{DS}(\boldsymbol{m}, z, \mathcal{P}, \Delta\boldsymbol{m}) = \frac{\Delta\rho}{\rho_m}|\mathcal{P}|. \tag{4.57}$$

4.2.5 Computation of $\mathcal{DC} = (\mathcal{DC}_1, \mathcal{DC})$

One wants to express the effective parameter $\boldsymbol{C} = (C_1, C)$ on the bounded cell Ω^a. To do so, one notices that only Ω^a contributes to the integral that defines C_1 and C_2 in (4.2). Indeed, the decomposition (4.12) yields for all $y_1^* > \frac{a}{2h}$

$$\int_{[\frac{a}{2h}, y_1^*]\times I} \frac{\mu(\boldsymbol{y})}{\mu_m}\frac{\partial\boldsymbol{\Phi}}{\partial y_2}(\boldsymbol{y})\mathrm{d}\boldsymbol{y} = \boldsymbol{0} \tag{4.58}$$

and the same holds for the integral on $\left[y_1^*, -\frac{a}{2h}\right] \times I$ with $y_1^* < -\frac{a}{2h}$. Therefore, $\boldsymbol{C}$ writes:

$$\boldsymbol{C}(\boldsymbol{m}) = \int_{\Omega^a} \frac{\mu(\boldsymbol{y})}{\mu_m}\left(\frac{\partial\boldsymbol{\Phi}}{\partial y_2}(\boldsymbol{y}) + \boldsymbol{e}_2\right)\mathrm{d}\boldsymbol{y}. \tag{4.59}$$

Consequently, the effective parameter $\boldsymbol{C}_{z,\varepsilon}$ associated with the perturbed cell writes

$$\boldsymbol{C}_{z,\varepsilon} = \boldsymbol{C}(\boldsymbol{m}) + \int_{\Omega^a} \frac{\mu(\boldsymbol{y})}{\mu_m}\frac{\partial\boldsymbol{\delta\Phi}_{z,\varepsilon}}{\partial y_2}(\boldsymbol{y})\mathrm{d}\boldsymbol{y} + \frac{\Delta\mu}{\mu_m}\int_{\mathcal{P}_{z,\varepsilon}}\left(\frac{\partial\boldsymbol{\Phi}_{z,\varepsilon}}{\partial y_2}(\boldsymbol{y}) + \boldsymbol{e}_2\right)\mathrm{d}\boldsymbol{y}. \tag{4.60}$$

We know that Φ_2 satisfies for all $\boldsymbol{w} \in H^1(\Omega^a; \mathbb{R}^2)$, $\boldsymbol{w}$ y_2-periodic

$$\mathcal{A}_\mu(\boldsymbol{w}, \Phi_2) = -\int_{\Omega^a} \frac{\mu(\boldsymbol{y})}{\mu_m}\frac{\partial\boldsymbol{w}}{\partial y_2}(\boldsymbol{y})\mathrm{d}\boldsymbol{y}. \tag{4.61}$$

One takes $v = \Phi_2$ in (4.47) and $\boldsymbol{w} = \boldsymbol{\delta\Phi}_{z,\varepsilon}$ in (4.61) and gets

$$\int_{\Omega^a} \frac{\mu(\boldsymbol{y})}{\mu_m}\frac{\partial\boldsymbol{\delta\Phi}_{z,\varepsilon}}{\partial y_2}(\boldsymbol{y})\mathrm{d}\boldsymbol{y} = \frac{\Delta\mu}{\mu_m}\int_{\mathcal{P}_{z,\varepsilon}} \nabla\Phi_2(\boldsymbol{y})\cdot(\nabla\boldsymbol{\Phi}_{z,\varepsilon}(\boldsymbol{y}) + \boldsymbol{I})\mathrm{d}\boldsymbol{y}, \tag{4.62}$$

which yields

$$\boldsymbol{C}_{z,\varepsilon} = \boldsymbol{C}(\boldsymbol{m}) + \frac{\Delta\mu}{\mu_m}\int_{\mathcal{P}_{z,\varepsilon}} (\nabla\Phi_2(\boldsymbol{y}) + \boldsymbol{e}_2)\cdot(\nabla\boldsymbol{\Phi}_{z,\varepsilon}(\boldsymbol{y}) + \boldsymbol{I})\mathrm{d}\boldsymbol{y}. \tag{4.63}$$

Once again, we use the Taylor expansion $\nabla\Phi_2(\boldsymbol{y}) = \nabla\Phi_2(z) + o(1)$ for all $\boldsymbol{y}$ in $\mathcal{P}_{z,\varepsilon}$, the expression of the integral in the scaled coordinates and the expansion (4.41) to get the final expression for the topological derivative

Result 4.3: Topological derivative of C

$$\mathcal{DC}(\boldsymbol{m}, z, \mathcal{P}, \Delta\boldsymbol{m}) = (\nabla\Phi_2(z) + \boldsymbol{e}_2)\cdot\boldsymbol{A}(\mathcal{P}, \mu(z), \Delta\mu)\cdot(\nabla\boldsymbol{\Phi}(z) + \boldsymbol{I}). \tag{4.64}$$

4.2.6 Numerical validation

To validate numerically the found expressions of the topological derivatives, we can compute the error made by the approximation of $\boldsymbol{\mathcal{B}}_{z,\varepsilon}$ and $\boldsymbol{C}_{z,\varepsilon}$ by $\boldsymbol{\mathcal{B}} + \varepsilon^2\boldsymbol{\mathcal{DB}}$ and $\boldsymbol{C} + \varepsilon^2\boldsymbol{\mathcal{DC}}$, respectively. Indeed, due to (4.51) and (4.63), this error should be of order ε^2 at least.

One starts with an initial reference configuration ($\varepsilon = 0$), computes the solutions of the cell problems (4.21) (their computation will be tackled in the next section), and thus the value of $\mathcal{B}$ and $\mathcal{C}$ from (4.43) and (4.59). The initial configuration is chosen to be heterogenous in order to avoid simplifications than can occur with a homogeneous medium as initialization. More precisely, we choose a homogenous medium of physical parameters $(\rho_m, \mu_m) = (2500\,\mathrm{kg}\cdot\mathrm{m}^{-3}, 12\cdot 10^9\,\mathrm{Pa})$, containing a circular inclusion of center $(-0.35\,\mathrm{m}, 0.35\,\mathrm{m})$, radius $0.1\,\mathrm{m}$ and physical parameters $(\rho_i, \mu_i) = (7800\,\mathrm{kg}\cdot\mathrm{m}^{-3}, 78\cdot 10^9\,\mathrm{Pa})$ (typical of steel in concrete).

Then one inserts a perturbation at $z = (0, 0)$. Its physical parameters are (ρ_i, μ_i). Its shape is a disk of radius ε. For $\varepsilon = 0.3$, the configuration is plotted in Figure 4.3a. For a given value of ε, one computes the perturbed cell problems and thus the exact effective parameters $\mathcal{B}_{z,\varepsilon}$ and $\mathcal{C}_{z,\varepsilon}$ from (4.43) and (4.59). Their first-order approximations $\mathcal{B} + \varepsilon^2\mathcal{D}\mathcal{B}$ and $\mathcal{C} + \varepsilon^2\mathcal{D}\mathcal{C}$ are computed from (4.54) and (4.64).

The errors between both the exact and approximated values are plotted as functions of ε in log-log scale in Figure 4.3b. Since $\mathcal{B}_2 = \mathcal{C}_1$, the results for only one of these parameters are plotted. The dotted line stands for an error of $\mathcal{O}(\varepsilon^4)$. It seems that this is the actual order of approximation of the effective parameters, the small variations for low values of ε being probably due to numerical errors in the computation of the coefficients. This underlines the fact that the leading order term and consequently the topological derivatives are well accounted for and that the terms of order ε^3 in the expansions (4.51) and (4.63) are probably equal to zero. This was already observed for the volumic case in Bonnet et al., 2018, with the intuition that it occurs for perturbations with a central symmetry. This remains however to be proved.

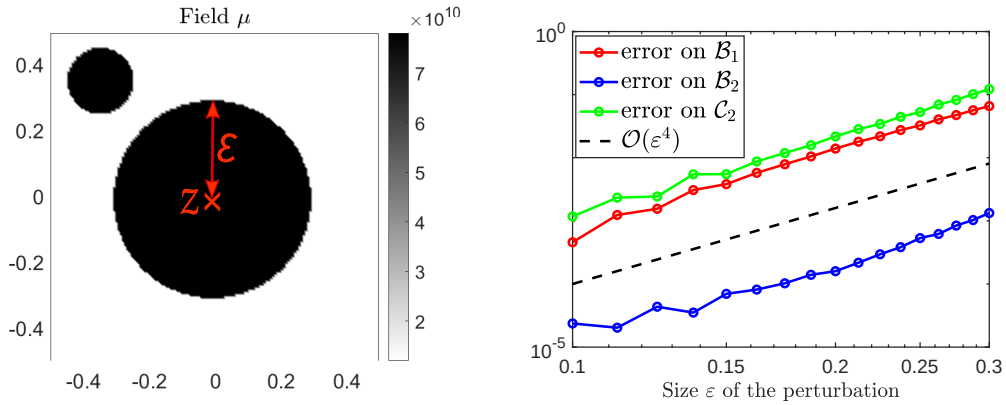

(a) (b)

Figure 4.3 – Test case for a circular perturbation: (a) Configuration for $\varepsilon = 0.3$. (b) Relative error between the exact and approximated effectives parameters as a function of ε in a log-log scale.

4.3 Numerical methods

4.3.1 FFT-based computation of the cell problems with boundary correctors

The optimization process requires the computation of numerous cell problems since the update of the material properties leads to new cell problems to solve at each iteration. The particularity in the framework of thin microstructured layers is that they are band cell problems in an infinite strip. In the case of cell problems with periodic conditions in a bounded domain, there are different ways of computing numerically the solutions. One possibility is the Finite Element Method based on weak formulations. Another possibility is to use a Fourier based formulation of the cell problem

and an algorithm accelerated by Fast Fourier Transform (FFT) (Moulinec & Suquet, 1998).

The Fourier based formulation is used here for the band cell problems. In Section 4.2.1, these cell problems have been reduced to cell problems in a bounded cell thanks to the introduction of DtN operators. Therefore, their computation requires to adapt the FFT-based computation in order to take into account the boundary conditions related to the DtN operators instead of the classical conditions of periodicity.

One first introduces the following decomposition:

$$\boldsymbol{\Phi} = \boldsymbol{\Phi}_{\text{per}} + \boldsymbol{\Phi}_{\text{bound}}. \tag{4.65}$$

The two terms of this decomposition are

- The bi-periodic function $\boldsymbol{\Phi}_{\text{per}}$ that satisfies:

$$\boldsymbol{\nabla} \cdot \left(\mu(\boldsymbol{y}) \left(\boldsymbol{I}_2 + \boldsymbol{\nabla}\boldsymbol{\Phi}_{\text{bound}} + \boldsymbol{\nabla}\boldsymbol{\Phi}_{\text{per}}\right)\right) = \boldsymbol{0} \text{ in } \Omega^a. \tag{4.66}$$

  This is an usual cell problem, which appears in homogenization of bi-periodic media, with a source term that is given by $\boldsymbol{I}_2 + \boldsymbol{\nabla}\boldsymbol{\Phi}_{\text{bound}}$. For a given function $\boldsymbol{\Phi}_{\text{bound}}$, this problem is solved using a FFT-accelerated algorithm. This method is detailed in Section 4.3.1.1.

- The boundary corrector $\boldsymbol{\Phi}_{\text{bound}}$ that ensures that the boundary conditions associated to the DtN operator are satisfied:

$$(\partial_{\boldsymbol{n}} - \boldsymbol{\Lambda})\, \boldsymbol{\Phi}_{\text{bound}} \left(\pm\frac{a}{2h}, \cdot\right) = -\,(\partial_{\boldsymbol{n}} - \boldsymbol{\Lambda})\, \boldsymbol{\Phi}_{\text{per}} \left(\pm\frac{a}{2h}, \cdot\right). \tag{4.67}$$

  An analytical expression of $\boldsymbol{\Phi}_{\text{bound}}$ can be obtained and is presented in Section 4.3.1.2.

In this setting, one strategy to compute $\boldsymbol{\Phi}$ is then to use a fixed-point algorithm detailed in Section 4.3.1.3:

1. Choose initial fields $\boldsymbol{\Phi}_{\text{per}}^{(0)}$ and $\boldsymbol{\Phi}_{\text{bound}}^{(0)}$.
2. Knowing $\boldsymbol{\Phi}_{\text{bound}}^{(i)}$, compute $\boldsymbol{\Phi}_{\text{per}}^{(i+1)}$ satisfying (4.66) (using a FFT-accelerated method).
3. Knowing $\boldsymbol{\Phi}_{\text{per}}^{(i+1)}$, find $\boldsymbol{\Phi}_{\text{bound}}^{(i+1)}$ satisfying (4.67).

The convergence of this fixed-point algorithm has not been investigated theoretically but it has been observed to converge in practice in numerical examples shown hereafter.

4.3.1.1 The classical FFT-accelerated algorithm

The approach of Moulinec and Suquet, 1998 used to solve cell problems with periodic conditions has been used in Cornaggia and Bellis, 2020 for the 2D antiplane case and is briefly described in this subsection. Let us consider the following cell problem

$$\begin{cases} \boldsymbol{S}(\boldsymbol{y}) = \mu(\boldsymbol{y})\,(\boldsymbol{E}(\boldsymbol{y}) + \boldsymbol{\nabla}\boldsymbol{P}(\boldsymbol{y})) \quad \forall \boldsymbol{y} \in \Omega^a, \\ \boldsymbol{\nabla} \cdot \boldsymbol{S}(\boldsymbol{y}) = \boldsymbol{0} \quad \forall \boldsymbol{y} \in \Omega^a, \\ \boldsymbol{P} \text{ periodic and } \boldsymbol{S} \cdot \boldsymbol{n} \text{ anti-periodic on } \partial\Omega^a, \\ \langle \boldsymbol{P} \rangle = \boldsymbol{0}. \end{cases} \tag{4.68}$$

with $\boldsymbol{E}$ an imposed prestrain and $\boldsymbol{P}$ the unknown. One introduces a reference medium with constant shear modulus $\mu_\star$ such that $\boldsymbol{S}$ can be rewritten as:

$$\boldsymbol{S}(\boldsymbol{y}) = \mu_\star \boldsymbol{\nabla}\boldsymbol{P}(\boldsymbol{y}) + \boldsymbol{T}(\boldsymbol{y}) \quad \text{with} \quad \boldsymbol{T}(\boldsymbol{y}) = \mu(\boldsymbol{y})\boldsymbol{E}(\boldsymbol{y}) + \delta\mu(\boldsymbol{y})\boldsymbol{\nabla}\boldsymbol{P}(\boldsymbol{y}) \tag{4.69}$$

and $\delta\mu(\boldsymbol{y}) = \mu(\boldsymbol{y}) - \mu_\star$.
First, the Fourier transform in space of a function $g(\boldsymbol{x})$ is defined by:

$$\mathscr{F}[g](\boldsymbol{\xi}) = \hat{g}(\boldsymbol{\xi}) = \int_{\mathbb{R}^2} g(\boldsymbol{x}) e^{-\mathrm{i}\boldsymbol{\xi}\cdot\boldsymbol{x}} \,\mathrm{d}\boldsymbol{x}, \tag{4.70}$$

where $\boldsymbol{\xi}$ is the wavenumber in the Fourier space. Using the Fourier Transform, (4.68) and (4.69), yields in the Fourier space

$$\begin{cases} \hat{\boldsymbol{P}}(\boldsymbol{0}) = \boldsymbol{0}, \\ \hat{\boldsymbol{P}}(\boldsymbol{\xi}) = \hat{\boldsymbol{\Gamma}}^0(\hat{\boldsymbol{T}})(\boldsymbol{\xi}) := \dfrac{1}{\mu_\star |\boldsymbol{\xi}|^2} \left(\mathrm{i}\boldsymbol{\xi} \cdot \hat{\boldsymbol{T}}(\boldsymbol{\xi})\right) \quad \forall \boldsymbol{\xi} \neq \boldsymbol{0} \end{cases} \tag{4.71}$$

The unit cell Ω^a is discretized into a regular grid of $N_1 \times N_2$ pixels. The coordinates of the pixels are:

$$\boldsymbol{y}_d(i_1, i_2) = \left(-\frac{a}{2h} + (i_1 - 1)\frac{a}{hN_1}, -\frac{1}{2} + (i_2 - 1)\frac{1}{N_2}\right), \quad i_1 = 1, \cdots, N_1, \quad i_2 = 1, \cdots, N_2. \tag{4.72}$$

If the N_j, $j = 1, 2$ are odd, the corresponding $N_1 \times N_2$ wavenumbers in the Fourier space are:

$$\boldsymbol{\xi}_d(r, s) = \left(\frac{\xi_r h}{a}, \xi_s\right) = \left(\frac{2\pi r h}{a}, 2\pi s\right), \quad \text{with} \begin{cases} r = -\dfrac{N_1 - 1}{2}, \cdots, -1, 0, 1, \cdots, \dfrac{N_1 - 1}{2}, \\ s = -\dfrac{N_2 - 1}{2}, \cdots, -1, 0, 1, \cdots, \dfrac{N_2 - 1}{2}. \end{cases} \tag{4.73}$$

In our case, we will always take odd values for the N_j, so that the maximum positive frequency is equal in absolute value to the minimum negative frequency.
The idea is to use alternatively (4.69) and (4.71) in the real and Fourier space with the following fixed-point algorithm:

1. Initialization for all $\boldsymbol{y}_d$:
   (a) $\boldsymbol{\epsilon}^0(\boldsymbol{y}_d) = \boldsymbol{E}(\boldsymbol{y}_d)$
   (b) $\boldsymbol{\sigma}^0(\boldsymbol{y}_d) = \mu(\boldsymbol{y}_d)\boldsymbol{\epsilon}^0(\boldsymbol{y}_d)$
2. Iterate until convergence
   (a) $\hat{\boldsymbol{\sigma}}^i = FFT(\boldsymbol{\sigma}^i)$
   (b) $\hat{\boldsymbol{P}}^{i+1}(\boldsymbol{\xi}_d) = \hat{\boldsymbol{P}}^i(\boldsymbol{\xi}_d) + \hat{\boldsymbol{\Gamma}}^0(\hat{\boldsymbol{\sigma}}^i)(\boldsymbol{\xi}_d) \;\forall\, \boldsymbol{\xi}_d \neq \boldsymbol{0}$ and $\hat{\boldsymbol{P}}^{i+1}(\boldsymbol{0}) = \boldsymbol{0}$
   (c) $\hat{\boldsymbol{\epsilon}}^{i+1}(\boldsymbol{\xi}_d) = \mathrm{i}\boldsymbol{\xi}_d \hat{\boldsymbol{P}}^{i+1}(\boldsymbol{\xi}_d)$
   (d) $\boldsymbol{\epsilon}^{i+1} = FFT^{-1}(\hat{\boldsymbol{\epsilon}}^{i+1})$
   (e) $\boldsymbol{\sigma}^{i+1}(\boldsymbol{y}_d) = \boldsymbol{\sigma}^0(\boldsymbol{y}_d) + \mu(\boldsymbol{y}_d)\boldsymbol{\epsilon}^{i+1}(\boldsymbol{y}_d)$

where "FFT" stands for the use of Fast Fourier Transform. Following Moulinec and Suquet, 1998, the reference shear modulus is chosen as $\mu_\star = (\mu_m + \mu_i)/2$ to ensure convergence of the fixed-point. The algorithm is applied for each component of $\boldsymbol{P}$ and the associated stopping criteria adopted here are

$$\frac{||P_j^{n+1} - P_j^n||_{L^2(\Omega^a)}}{||P_j^n||_{L^2(\Omega^a)}} < \delta_{FFT}, \tag{4.74}$$

where δ_{FFT} is a user chosen parameter.
This method will be used to compute $\boldsymbol{\Phi}_{\text{per}}$ with a prestrain $\boldsymbol{E} = \boldsymbol{I}_2 + \boldsymbol{\nabla}\boldsymbol{\Phi}_{\text{bound}}$ which to be updated at each time step thanks to the analytical expression developped in the next section.

4.3.1.2 Analytical expression for the boundary corrector

The function $\boldsymbol{\Phi}_{\text{per}}$ is discretized using the Fourier representation:

$$\boldsymbol{\Phi}_{\text{per}}(y_1, y_2) = \sum_p \sum_q \boldsymbol{\varphi}_{pq} \Psi_p^a(y_1) \Psi_q(y_2), \quad \text{with} \quad \begin{cases} \Psi_q(y_2) = \mathrm{e}^{\mathrm{i}\xi_q y_2} \\ \Psi_p^a(y_1) = \Psi_p(h y_1/a) \end{cases} \tag{4.75}$$

where $\xi_p = 2p\pi$, p ranges from $-(N_1-1)/2$ to $(N_1-1)/2$, and q ranges from $-(N_2-1)/2$ to $(N_2-1)/2$ The boundary corrector $\boldsymbol{\Phi}_{\text{bound}}$ is written on the basis of harmonic solutions in the infinite strip (same convention as (4.12)) as

$$\boldsymbol{\Phi}_{\text{bound}}(y_1, y_2) = y_1 z_0 + \sum_{q \neq 0} \left(z_q^- \mathrm{e}^{|\xi_q|(y_1 + a/(2h))} + z_q^+ \mathrm{e}^{-|\xi_q|(y_1 - a/(2h))} \right) \Psi_q(y_2). \tag{4.76}$$

One introduces the notation:

$$e_q = \mathrm{e}^{|\xi_q| a/h} \tag{4.77}$$

so that the boundary conditions (4.20) write at $y_1 = -\frac{a}{2h}$:

$$-z_0 - \sum_{q \neq 0} |\xi_q| \left(z_q^- - z_q^+ e_q \right) \Psi_q + \sum_{q \neq 0} |\xi_q| \left(z_q^- + z_q^+ e_q \right) \Psi_q = \sum_p \sum_q (-1)^p \left[\frac{\mathrm{i}\xi_p h}{a} - |\xi_q| \right] \boldsymbol{\varphi}_{pq} \Psi_q \tag{4.78}$$

and at $y_1 = \frac{a}{2h}$

$$z_0 + \sum_{q \neq 0} |\xi_q| \left(z_q^- e_q - z_q^+ \right) \Psi_q + \sum_{q \neq 0} |\xi_q| \left(z_q^- e_q + z_q^+ \right) \Psi_q = \sum_p \sum_q (-1)^p \left[-\frac{\mathrm{i}\xi_p h}{a} - |\xi_q| \right] \boldsymbol{\varphi}_{pq} \Psi_q. \tag{4.79}$$

Projecting onto Ψ_q, one gets the following equations for the coefficients (z_0, z_q^-, z_q^+):

$$\begin{cases} z_0 = -\sum_p (-1)^p \mathrm{i} \dfrac{\xi_p h}{a} \boldsymbol{\varphi}_{p0} = -\boldsymbol{S}_0^{(2)} \dfrac{a}{h}, \\ z_q^- = \dfrac{1}{2e_q} \sum_p (-1)^p \left[-\dfrac{\mathrm{i}\xi_p h}{a|\xi_q|} - 1 \right] \boldsymbol{\varphi}_{pq} = \dfrac{1}{2e_q} \left(-\dfrac{h}{a|\xi_q|} \boldsymbol{S}_q^{(2)} - \boldsymbol{S}_q^{(1)} \right), \\ z_q^+ = \dfrac{1}{2e_q} \sum_p (-1)^p \left[\dfrac{\mathrm{i}\xi_p h}{a|\xi_q|} - 1 \right] \boldsymbol{\varphi}_{pq} = \dfrac{1}{2e_q} \left(\dfrac{h}{a|\xi_q|} \boldsymbol{S}_q^{(2)} - \boldsymbol{S}_q^{(1)} \right), \end{cases} \tag{4.80}$$

where $\boldsymbol{S}_q^{(1)}$ and $\boldsymbol{S}_q^{(2)}$ are weighted sums of the Fourier coefficients of $\boldsymbol{\Phi}_{\text{per}}$:

$$\begin{cases} \boldsymbol{S}_q^{(1)} = \sum_p (-1)^p \boldsymbol{\varphi}_{pq}, \\ \boldsymbol{S}_q^{(2)} = \mathrm{i} \sum_p (-1)^p \xi_p \boldsymbol{\varphi}_{pq}. \end{cases} \tag{4.81}$$

Remark 4.1. *Since $\boldsymbol{\Phi}$ is a real-valued function, (4.65),(4.75) and (4.76) imply that $\boldsymbol{\varphi}_{pq} = \overline{\boldsymbol{\varphi}_{(-p)q}}$. Therefore $\boldsymbol{S}_q^{(1)}$ and $\boldsymbol{S}_q^{(2)}$ are real, and so are (z_0, z_q^-, z_q^+).*

4.3.1.3 Final fixed-point algorithm

We summarize here the main steps to compute the cell problems (4.10) in the case of a thin microstructured array.

1. Initialization for all $\boldsymbol{y}_d$:
   (a) $\boldsymbol{\epsilon}^0(\boldsymbol{y}_d) = \boldsymbol{I}_2$
   (b) $\boldsymbol{\sigma}^0(\boldsymbol{y}_d) = \mu(\boldsymbol{y}_d)\boldsymbol{\epsilon}^0(\boldsymbol{y}_d)$
2. Iterate until convergence with stopping criterion (4.74):
   (a) $\hat{\boldsymbol{\sigma}}^i = FFT(\boldsymbol{\sigma}^i)$
   (b) $\hat{\boldsymbol{\Phi}}^{i+1}_{\text{per}}(\boldsymbol{\xi}_d) = \hat{\boldsymbol{\Phi}}^{i}_{\text{per}}(\boldsymbol{\xi}_d) + \hat{\boldsymbol{\Gamma}}^0(\hat{\boldsymbol{\sigma}}^i)(\boldsymbol{\xi}_d) \;\forall\, \boldsymbol{\xi}_d \neq \boldsymbol{0}$ and $\hat{\boldsymbol{\Phi}}^{i+1}_{\text{per}}(\boldsymbol{0}) = \boldsymbol{0}$
   (c) $\hat{\boldsymbol{\epsilon}}^{i+1}(\boldsymbol{\xi}_d) = \mathrm{i}\boldsymbol{\xi}_d \hat{\boldsymbol{\Phi}}^{i+1}_{\text{per}}(\boldsymbol{\xi}_d)$
   (d) $\boldsymbol{\epsilon}^{i+1} = FFT^{-1}(\hat{\boldsymbol{\epsilon}}^{i+1})$
   (e) compute $\boldsymbol{\Phi}_{\text{bound}}$ from (4.76) and (4.80)
   (f) $\boldsymbol{\sigma}^{i+1}(\boldsymbol{y}_d) = \boldsymbol{\sigma}^0(\boldsymbol{y}_d) + \mu(\boldsymbol{y}_d)\left(\boldsymbol{\epsilon}^{i+1}(\boldsymbol{y}_d) + \boldsymbol{\nabla}\boldsymbol{\Phi}_{\text{bound}}(\boldsymbol{y}_d)\right)$.

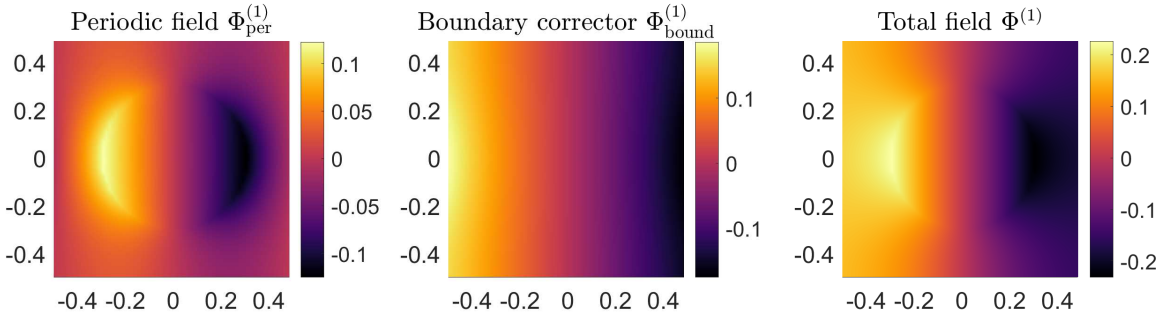

(a) First cell problem

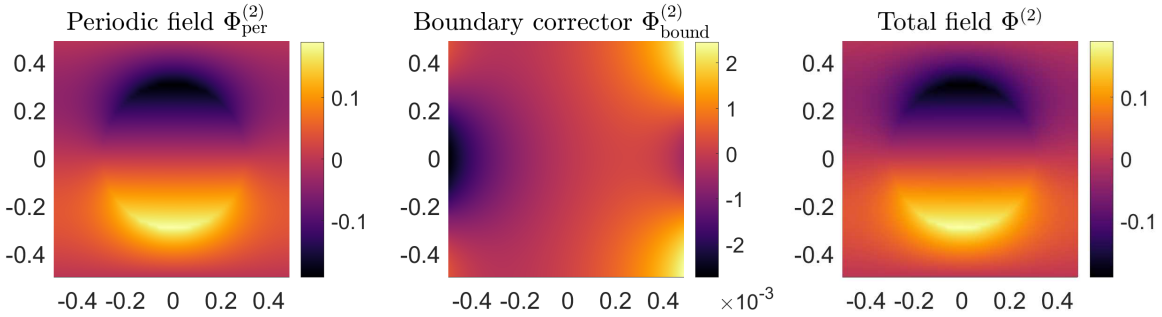

(b) Second cell problem

Figure 4.4 – Periodic part, boundary corrector and total fields $\boldsymbol{\Phi}$.

Figures 4.4a and 4.4b display the solutions of the cell problems for $\mu_m = 1.25$, $\mu_i = 7.69$, and a circular inclusion of radius $R = 0.3$. The cell Ω^a is $[-1/2;1/2] \times [-1/2;1/2]$. The numerical parameters are $\delta_{\text{FFT}} = 10^{-8}$ and $N_1 = N_2 = 77$. For both cell problems, the periodic part, the boundary correctors and the total fields are represented.

4.3.1.4 Comparison with a finite element approach

Another method to compute the band cell problems is to choose a domain $[-L;L]\times[-1/2;1/2]$ with L large enough and to consider the variational formulation of

$$\begin{cases} \nabla\cdot\left(\mu(\boldsymbol{y})\left(\nabla_{\boldsymbol{y}}\boldsymbol{\Phi}(\boldsymbol{y})+\boldsymbol{I}_2\right)\right)=\boldsymbol{0} \text{ in } [-L;L]\times[-1/2;1/2], \\ \mu(\boldsymbol{y})[\nabla_{\boldsymbol{y}}\boldsymbol{\Phi}(\boldsymbol{y})+\boldsymbol{I}_2]\cdot\boldsymbol{n} \text{ and } \boldsymbol{\Phi} \text{ continuous on } \partial\Omega_i, \\ \boldsymbol{\Phi} \ y_2 \text{ periodic}, \\ \nabla_{\boldsymbol{y}}\boldsymbol{\Phi}(\pm L, y_2)=\boldsymbol{0}. \end{cases} \tag{4.82}$$

The Neumann condition in (4.82) models the limit condition $\lim_{y_1\to\pm\infty}\nabla_{\boldsymbol{y}}\boldsymbol{\Phi}(y_1,y_2)=\boldsymbol{0}$ in (4.10). The formulation (4.82) allows a computation with a Finite Element Method in FreeFem++ (Hecht, 2012).

The results given by the fixed-point FFT algorithm with boundary correctors previously presented is compared with the solutions obtained with the Finite Element method. For the Finite Element method, we set $L=6$ while for the FFT method we chose $N_1=N_2=129$ and $\delta_{\text{FFT}}=10^{-8}$. With both methods, the physical parameters are $\mu_m=1.25$ and $\mu_i=7.69$, and we investigated two different geometries:

1. a rectangular inclusion, aligned with the axes, with length $L_1=0.9$ and height $L_2=0.6$. The results for this geometry are presented in Table 4.1.
2. an ellipsoidal inclusion, tilted of $40°$, with semiaxes $a_1=0.4$ and $a_2=0.24$. The associated results with both numerical methods are summarized in Table 4.2.

Table 4.1 – Comparison of the results given by the two methods for the rectangular inclusion.

Method	Finite Element Method	FFT
$[\min,\max]\Phi^{(1)}$	$[-0.351, 0.351]$	$[-0.351, 0.351]$
$[\min,\max]\Phi^{(2)}$	$[-0.196, 0.196]$	$[-0.199, 0.199]$
$(\mathcal{B}_1,\mathcal{B}_2)$	$(-0.645,\ -5.5\cdot10^{-7})$	$(-0.646,\ 0)$
$(\mathcal{C}_1,\mathcal{C}_2)$	$(7.0\cdot10^{-6},\ -1.71)$	$(0,\ -1.82)$

Table 4.2 – Comparison of the results given by the two methods for the ellipsoidal inclusion.

Method	Finite Element Method	FFT
$[\min,\max]\Phi^{(1)}$	$[-0.250, 0.250]$	$[-0.251, 0.251]$
$[\min,\max]\Phi^{(2)}$	$[-0.198, 0.198]$	$[-0.196, 0.196]$
$(\mathcal{B}_1,\mathcal{B}_2)$	$(-0.372,\ -7.36\cdot10^{-2})$	$(-0.371,\ -6.96\cdot10^{-2})$
$(\mathcal{C}_1,\mathcal{C}_2)$	$(7.00\cdot10^{-2},\ -0.976)$	$(6.96\cdot10^{-2},\ -1.01)$

For both geometries, the satisfying agreement of the results given by both methods allows to validate the methodology and computation of the fixed-point FFT algorithm. The main advantage of this strategy is that it allows to work with a bounded domain around the inclusion instead of a large truncated domain that approximates the limit condition. This method will be used later on when cell problems computations are required.

4.3.2 Optimization process and material updating

In the configuration mentioned above, there are only two phases: Ω_m which is the homogeneous matrix outside the microstructured array, and $\Omega_i\subset\Omega^a$ which are the inclusions phase. Consequently

the only material modification allowed in the optimization process is a phase conversion from (ρ_i, μ_i) to (ρ_m, μ_m) or conversely. Accordingly, the material perturbation $\boldsymbol{\Delta m}$ in the topological derivatives (4.57), (4.54) and (4.64) is chosen as:

$$\boldsymbol{\Delta m} = (\rho_i - \rho_m, \mu_i - \mu_m) \text{ in } \Omega_m \quad \text{and} \quad \boldsymbol{\Delta m} = (\rho_m - \rho_i, \mu_m - \mu_i) \text{ in } \Omega_i. \tag{4.83}$$

Moreover, the shape of the perturbation $\mathcal{P}$ is a disk so that the expression of the polarization tensor is given by (4.53) with $\gamma = 1$. The use of the boundary corrector approach described above requires that the phase at the boundaries $y_1 = \pm\frac{a}{2h}$ is Ω_m. Consequently, one define an optimization domain

$$\Omega^{\text{des}} = [-b; b] \times [-1/2; 1/2] \quad \text{with} \quad b < \frac{a}{2h}$$

in which material updates are allowed. The updating strategies for the material distribution are the same as in Cornaggia and Bellis, 2020 and are exposed in this section for the case of thin microstructured layers.

4.3.2.1 One pixel phase permutation

The simplest update of the optimization domain Ω^{des} is the following: a phase conversion is applied to the pixel $\boldsymbol{z}_P$ where the topological derivative $\mathcal{DJ}^{(n)}$ is the most negative i.e.

$$\boldsymbol{z}_P = \arg \min_{\boldsymbol{z} \in \Omega^{\text{des}}_-} \mathcal{DJ}(\boldsymbol{z}),$$

with $\Omega^{\text{des}}_- = \left\{\boldsymbol{z} \in \Omega^{\text{des}} \text{ such that } \mathcal{DJ}(\boldsymbol{z}) \leq 0\right\}$.
The correspondng stopping criterion is defined as:

$$\min_{\boldsymbol{z} \in \Omega^{\text{des}}} \mathcal{DJ}(\boldsymbol{z}) \geq 0.$$

If a phase change is applied at two consecutive iterations to the same pixel, one considers that the cost functional can not be decreased anymore even if a local minimum is not reached, and the algorithm is stopped.
This procedure is very easy to implement but can also be very slow if the initialization is far from an optimal microstructure and/or if the discretization is very fine.

4.3.2.2 Level-set method

Since the material is made of two phases, a common way to characterize it is to use a *level-set* function Ψ that satisfies:

$$\begin{cases} \Psi(\boldsymbol{z}) > 0 \text{ in } \Omega^{\text{des}} \cap \Omega_m \\ \Psi(\boldsymbol{z}) < 0 \text{ in } \Omega^{\text{des}} \cap \Omega_i \end{cases} \quad \text{and} \quad ||\Psi||_{L^2(\Omega^{\text{des}})} = 1. \tag{4.84}$$

A projection alogorithm introduced in Amstutz and Andrä, 2006 for topological optimization can then be used (Amstutz et al., 2010; Amstutz, 2011; Giusti et al., 2016; Oliver et al., 2017). The main steps are recalled in this subsection.
First, one defines a signed normalized topological derivative $\overline{\mathcal{DJ}}^{(n)}$ at iteration n as:

$$\overline{\mathcal{DJ}}^{(n)}(\boldsymbol{z}) = \begin{cases} \mathcal{DJ}^{(n)}(\boldsymbol{z}) / ||\mathcal{DJ}^{(n)}||_{L^2(\Omega^{\text{des}})} \text{ in } \Omega^{\text{des}} \cap \Omega_m \\ -\mathcal{DJ}^{(n)}(\boldsymbol{z}) / ||\mathcal{DJ}^{(n)}||_{L^2(\Omega^{\text{des}})} \text{ in } \Omega^{\text{des}} \cap \Omega_i. \end{cases} \tag{4.85}$$

When $\overline{\mathcal{DJ}}^{(n)}$ satisfies the sign condition (4.84), then $\mathcal{DJ}^{(n)}(\boldsymbol{z}) > 0$ is satisfied in the whole optimization domain Ω^{des}. Consequently, in this case, the leading-order approximation of the

cost functional $\mathcal{J}$ cannot be decreased anymore by a phase change in Ω^{des}. Therefore, $\overline{\mathcal{DJ}}^{(n)}$ satisfying (4.84), is a sufficient optimal condition that ensures that the material configuration corresponds to a local minimum of $\mathcal{J}$. The updating strategy of Amstutz and Andrä, 2006 aims at fulfilling this condition. At each iteration, the new level-set function $\Psi^{(n+1)}$ is computed as:

$$\Psi^{(n+1)}(z) = \frac{1}{\sin(\Theta^{(n)})}\left[\sin((1-\kappa^{(n)})\Theta^{(n)})\Psi^{(n)}(z) + \sin(\kappa^{(n)}\Theta^{(n)})\overline{\mathcal{DJ}}^{(n)}(z)\right], \tag{4.86}$$

with the angle $\Theta^{(n)}$ being defined by the projection

$$\Theta^{(n)} = \cos^{-1}\left(\overline{\mathcal{DJ}}^{(n)}, \Psi^{(n)}\right)_{L^2(\Omega^{\text{des}})}. \tag{4.87}$$

The parameter $\kappa^{(n)}$ in (4.86) is chosen so that the cost functional decreases at each iteration. In practice, it is initialized to $\kappa^{(0)} = 1$ and then at each iteration it is determined up to a minimal value κ_{min} within an inner optimization loop that writes as:

1. Initalization to $\kappa^{(n)} = \min(2, \kappa^{(n-1)})$
2. While the cost functional does not decrease
   - set $\kappa^{(n)} = \kappa^{(n)}/2$
   - if $\kappa < \kappa_{\text{min}}$, the level-set algorithm is stopped: the cost functional cannot be decreased by the level-set projection

The stopping criterion of the level-set method associated with the updating (4.86) is:

$$|\Theta^{(n)}| < \delta_\Theta \tag{4.88}$$

with δ_Θ a user-chosen tolerance parameter.

Remark 14. *Different initializations are possible for the level-set function $\Psi^{(0)}$, here we chose to compute it as $f/||f||_{L^2(\Omega^{des})}$ with f being defined by:*

$$f(z) = \begin{cases} \mu_\star - \mu(z) \text{ if } \mu_m < \mu_i, \\ \mu(z) - \mu_\star \text{ if } \mu_m > \mu_i, \end{cases} \tag{4.89}$$

where we recall that $\mu_\star = (\mu_m + \mu_i)/2$.

4.4 Numerical examples

This section is a work in progress. Accordingly, some preliminary results are presented below for different cost functionals to be minimized.
The unit cell is $\Omega^a = [-1/2; 1/2] \times [-1/2; 1/2]$ which is discretized with $N_1 = N_2 = 77$. The tolerance for the FFT algorithm (4.74) is $\delta_{\text{FFT}} = 10^{-3}$. The optimization domain is $\Omega^{\text{des}} = [-0.4; 0.4] \times [-1/2; 1/2]$. The phase Ω_i is represented in black and the phase Ω_m in white. More precisely, the color corresponds to the material at the center of each pixel delimited by four couples of coordinates.

4.4.1 Realizing some objective effective parameters

One chooses a reference configuration associated with some effective parameters $\boldsymbol{m}_{\text{eff}}^{\text{ref}}$ and introduces the following cost functional

$$\mathcal{J}(\boldsymbol{m}_{\text{eff}}) = \frac{\sum_{i=1}^{5} \left(\boldsymbol{m}_{\text{eff}}[i] - \boldsymbol{m}_{\text{eff}}^{\text{ref}}[i]\right)^2}{\sum_{i=1}^{5} \left(\boldsymbol{m}_{\text{eff}}^{\text{ref}}[i]\right)^2}. \tag{4.90}$$

Here, we consider a reference configuration made of a square inclusion Ω_i of side length 0.35, see Figure 4.5a. The physical parameters are chosen so that $\mu_i/\mu_m = \rho_m/\rho_i = 2$. Two initializations are considered in these figures: a circle of radius 0.18 (stricly included in the reference square), or a circle of radius 0.25 (strictly including the reference square). These two initializations are presented in Figures 4.5b and 4.5c.

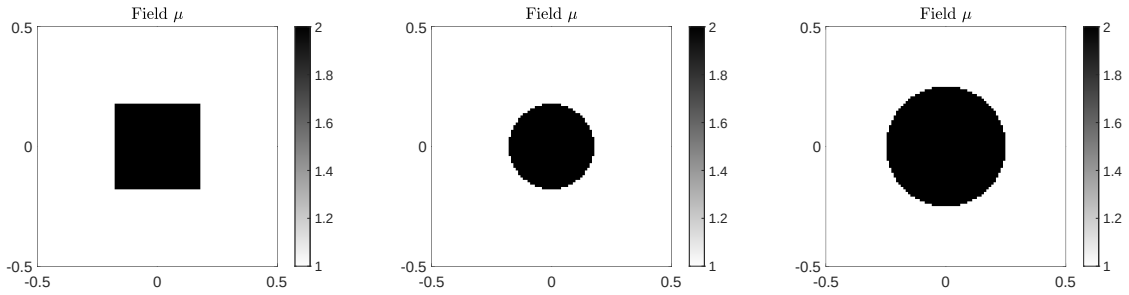

(a) Reference (b) First initialization (c) Second initialization

Figure 4.5 – Reference configuration and two different initializations.

The one-pixel phase permutation algorithm, see Section 4.3.2.1, is applied. The evolution of the cost functional is displayed in Figures 4.6a and Figures 4.6b for each initialization, respectively. In both cases, one can see that the cost functional decreases along the iterations. Figures 4.7a

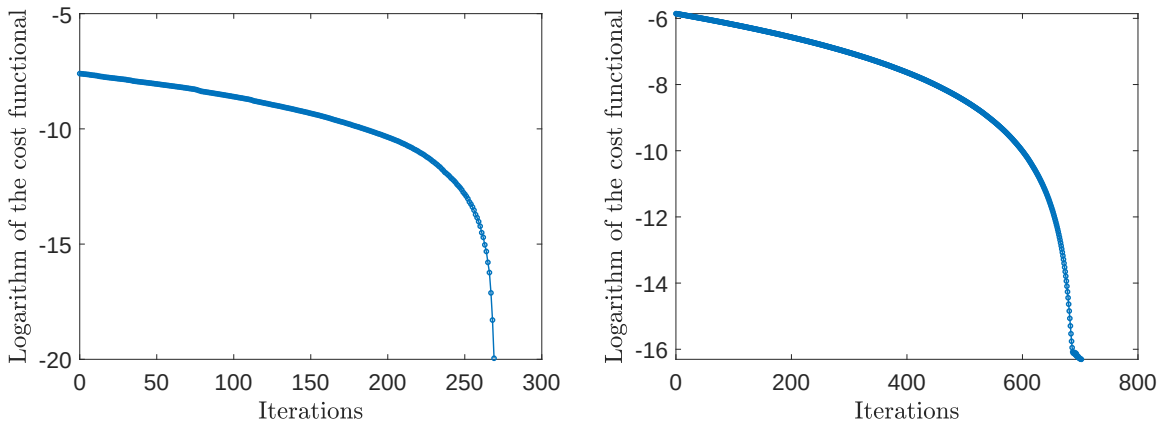

(a) First initialization (b) Second initialization

Figure 4.6 – Evolution of the cost functional along the iterations.

and 4.7b display the final configurations obtained at the end of the optimization process. One

should mention that the exact reference configuration is not reached in the second test. In the first example, the algorithm has converged to the exact reference configuration while in the second case, the cost-functional is greatly reduced (from $2.9 \cdot 10^{-3}$ to $8.3 \cdot 10^{-8}$), but the reference configuration is not reached.

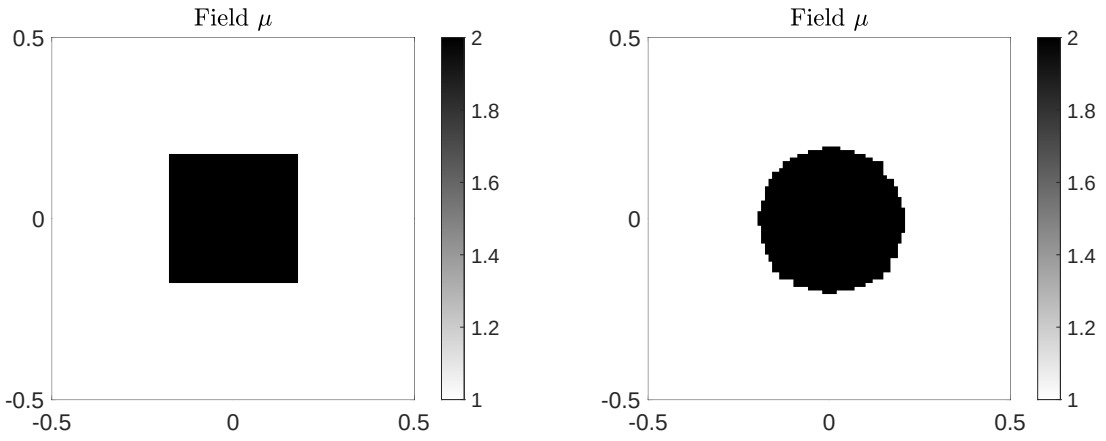

(a) First initialization (b) Second initialization

Figure 4.7 – Final configurations.

In fact, the algorithms only converge to a local minimum and there is no guarantee that the reference configuration is the only one. Consequently it strongly depends on the initialization. This is not really suprising since some of the first-order effective parameters do not seem to be very sensitive to the geometry to some extents. To illustrate this, Figure 4.8 displays the effective parameters for an inclusion Ω_i which is a tilted ellipse of fixed minor semi-axis 0.2, varying tilted angle (from 0 to $\pi/4$) and varying major semi-axis (from 0.2 to 0.5). It clearly underlines that some of the effective parameters are not very sensitive to the geometry and that the minimum is probably not unique.

4.4.2 Minimizing the reflexion or transmission coefficient

In this second case, one chooses N incident angles $(\theta_j)_{j=1,\cdots,N}$ in which we want to minimize the deviation from a target reflexion coefficient $\mathcal{R}_j^{\text{target}}$. To this end, one recalls that the reflexion coefficient for an incident plane wave of incident angle θ_j associated to the homogenized model (4.3) is given by:

$$\mathcal{R}(\theta_j, \omega) = \frac{\mathrm{i}\omega\, \mathscr{L}(\omega)}{\mathscr{Z} + \mathrm{i}\omega\, \mathscr{N}(\omega) - \omega^2 \mathscr{M}(\omega)} \exp\left(\mathrm{i}\frac{\omega}{c_m} a \cos\theta_j\right), \tag{4.91}$$

with

$$\begin{cases} \mathscr{L}(\omega) = h\left(\mathcal{B}\cos(\theta_j)^2 + \mathcal{C}\sin(\theta_j)^2 - \mathcal{S}\right), \\ \mathscr{Z} = 2c_m \cos\theta_j, \\ \mathscr{N}(\omega) = h\left(-\mathcal{C}\sin(\theta_j)^2 + \mathcal{B}\cos(\theta_j)^2 + \mathcal{S}\right), \\ \mathscr{M}(\omega) = \dfrac{h^2}{2c_m}\left(\mathcal{B}_2\mathcal{C}_1\sin(\theta_j)^2 - \mathcal{B}\mathcal{C}\sin(\theta_j)^2 + \mathcal{B}\mathcal{S}\right)\cos(\theta_j). \end{cases} \tag{4.92}$$

Its derivation follows the same steps as in Appendix 3.A.1 for the case of resonant effective interfaces. In fact, the result of the appendix can be transposed here with a formal change of

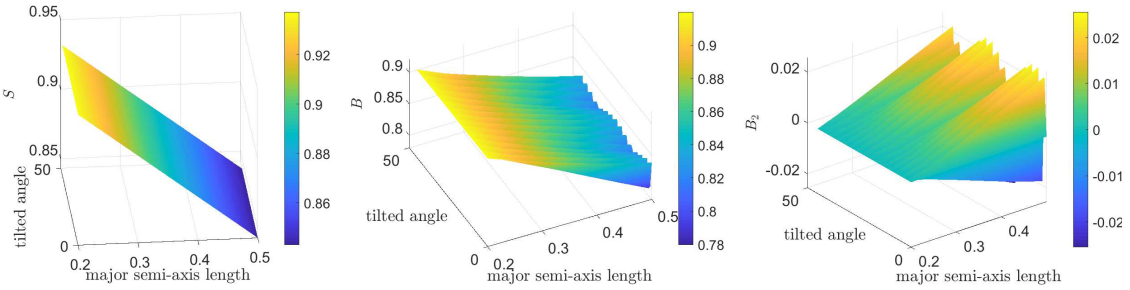

(a) $\mathcal{S}$ (b) $\mathcal{B}$ (c) $\mathcal{B}_2$

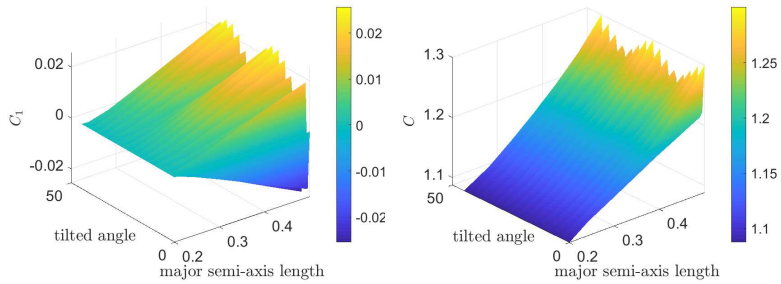

(d) C_1 (e) C

Figure 4.8 – Variation of the five effective parameters for a periodic cell containing an ellipse Ω_i of varying tilt angle and major semi-axis.

effective parameters.
Hence, we introduce the following cost functional

$$\mathcal{J}(\boldsymbol{m}_{\text{eff}}; \theta_1, \cdots, \theta_N, \omega) = \sum_{j=1}^{N} \alpha_j \left(|\mathcal{R}(\theta_j, \omega)| - \mathcal{R}_j^{\text{target}} \right)^2. \tag{4.93}$$

with α_j a coefficient to weight the contribution of the jth direction.

As first numerical investigations about this second cost functional, we consider $N = 1$ and $\mathcal{R}_1^{\text{target}} = \mathcal{R}^{\text{target}}$ is either equal to 0 or to 1 so that we aim at minimizing either the reflexion or the transmission, respectively. Since there is no requirement about the phase ratio, whatever the initialization is, we recover in one iteration of the level-set method the following expected results: a homogeneous cell with no phase Ω_i when $\mathcal{R}^{\text{target}} = 0$, or an optimization domain Ω^{des} entirely made of phase Ω_i when $\mathcal{R}^{\text{target}} = 1$.

■ *Volume constraint.* Furthermore, one can aim at minimizing this cost functional for a given objective ratio V_{target} between the two phases. In this case, one introduces the following modified cost functional

$$\mathcal{J}(\boldsymbol{m}_{\text{eff}}; \theta_1, \cdots, \theta_N, \omega) = \sum_{j=1}^{N} \alpha_j \left(|\mathcal{R}(\theta_j, \omega)| - \mathcal{R}_j^{\text{target}} \right)^2 + \lambda \left(\frac{V}{V_{\text{target}}} - 1 \right)^2 \tag{4.94}$$

where the parameter $V = |\Omega_i|/|\Omega_m|$ is the surface of the phase Ω_i divided by the total surface of the unit cell Ω^a.

The initialization of the Lagrange multiplier λ will be precised later on for each example. In these first numerical investigations, we considered the following naive updating strategy within the level-set method described in Section 4.3.2.2. First, one sets the following tolerance parameters:

$\delta_\Theta = 10^{-1}$, $\delta_{\text{Vol}} = 2 \cdot 10^{-1}$, $\kappa_{\text{min}} = 10^{-3}$. Secondly, the level-set method is applied and can be stopped for two reasons according to Section 4.3.2.2:

1. $|\Theta| < \delta_\Theta$: then,
   - if $\left(\frac{V}{V_{\text{target}}} - 1\right) < \delta_{\text{Vol}}$: the algorithm is stopped. A local minimum is found that satisfies the phase ratio requirement with the desired precision.
   - else, if $\left(\frac{V}{V_{\text{target}}} - 1\right) > \delta_{\text{Vol}}$: the parameter λ is reset to $\lambda = 2\lambda$, κ is reset to 1, and the level-set method is applied to the updated cost functional.
2. $\kappa < \kappa_{\text{min}}$: then,
   - if $\left(\frac{V}{V_{\text{target}}} - 1\right) > \delta_{\text{Vol}}$: the parameter λ is reset to $\lambda = 2\lambda$, κ is reset to 1, and the level-set method is applied to the updated cost functional.
   - else, if $\left(\frac{V}{V_{\text{target}}} - 1\right) < \delta_{\text{Vol}}$: the parameter λ is reset to $\lambda = \lambda/2.5$, κ is reset to 1 and the level-set method is applied to the updated cost functional.

We add an additional criterion which allows to stop the procedure if the cost functional cannot be decreased anymore: if at the ith update of λ, the configuration is the same as at its $(i-2)$th update, the algorithm is stopped.

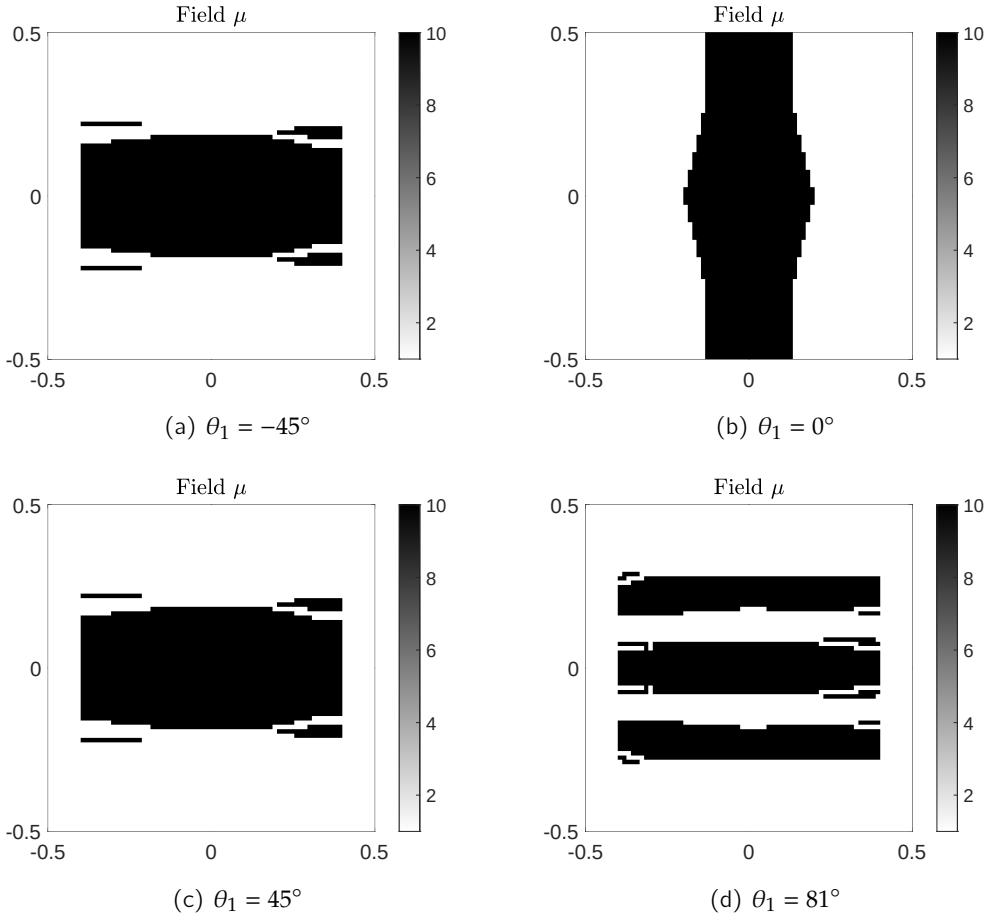

(a) $\theta_1 = -45°$ (b) $\theta_1 = 0°$

(c) $\theta_1 = 45°$ (d) $\theta_1 = 81°$

Figure 4.9 – Minimizing the reflexion coefficient under the constraint $V_{\text{target}} = 0.3$: final unit cells

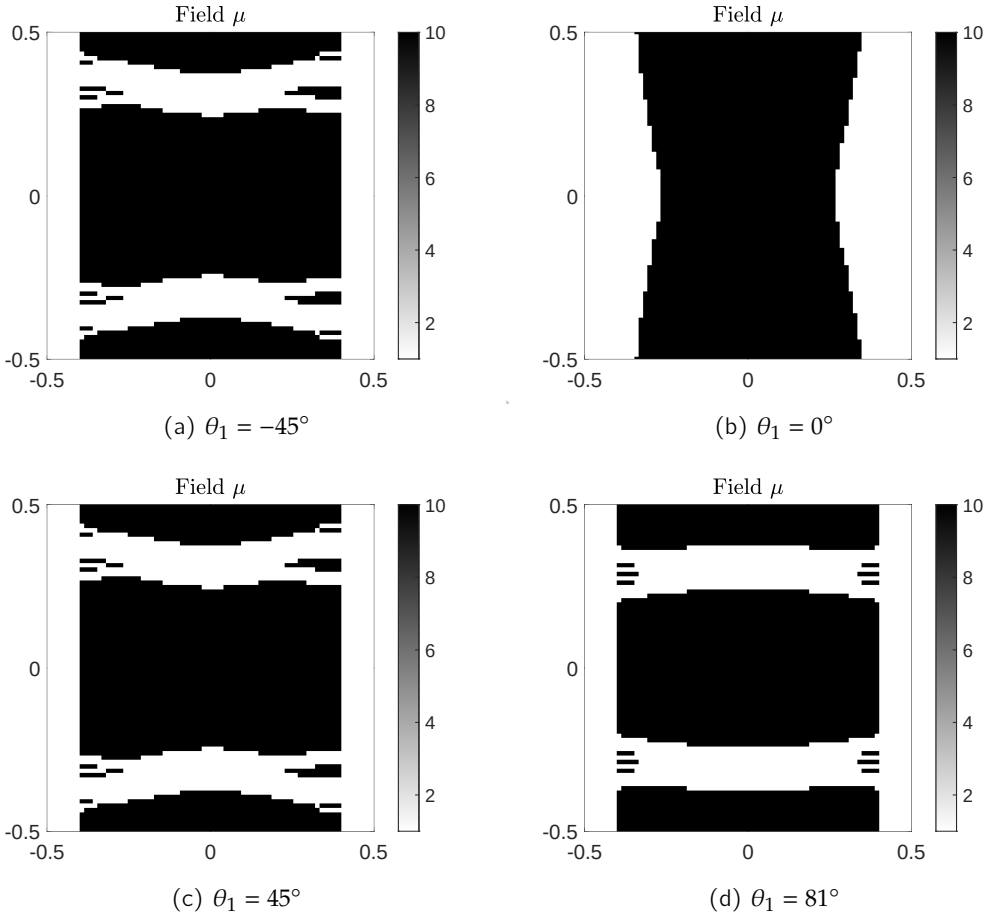

(a) $\theta_1 = -45°$ (b) $\theta_1 = 0°$

(c) $\theta_1 = 45°$ (d) $\theta_1 = 81°$

Figure 4.10 – Minimizing the reflexion coefficient under the constraint $V_{\text{target}} = 0.6$

We now consider a circular inclusion Ω_i of radius 0.23 as an initialization. The physical parameters are chosen so that $\mu_i/\mu_m = \rho_m/\rho_i = 10$ and $kh = \omega h/c_m = 0.45$. Figures 4.9 and 4.10 display the final configurations when one aims at minimizing the reflexion coefficient for $V_{\text{target}} = 0.3$ and $V_{\text{target}} = 0.6$, respectively. The associated microstructured layers are displayed in FIgures 4.11 and 4.12. In both examples, four incident angles $\theta_1 = -45°, 0°, 45°, 81°$ are considered. One can see a shift in the geometry as the incident angle increases and a symmetry with respect to the normal incidence. In each case, convergence was obtained with the desired phase ratio criterion after several updates of λ. To get the convergence, we have to play on the initial value of λ. For $V_{\text{target}} = 0.3$, we started with $\lambda = 5 \cdot 10^{-2}, 5 \cdot 10^{-3}, 5 \cdot 10^{-2}, 5 \cdot 10^{-2}$ for $\theta_1 = -45°, 0°, 45°, 81°$, respectively. For $V_{\text{target}} = 0.6$, the initialization was $\lambda = 5, 0.1, 5, 1$, for $\theta_1 = -45°, 0°, 45°, 81°$, respectively. To give an idea of the numerical cost, the result of Figure 4.9b was obtained in 23 iterations of the level-set and required the computation of 67 cell problems (4.10).

4.5 Conclusion and perspectives

In this chapter, we considered wave propagation across a row of inclusions in the *non-resonant* case, i.e. with a low contrast of the physical parameters. This microstructured configuration can be replaced by a homogenized model characterized by effective jump conditions on an effective enlarged interface. In this context, the objective was to propose a method to perform a topological optimization of this row of inclusions based on the associated first-order homogenized model. The

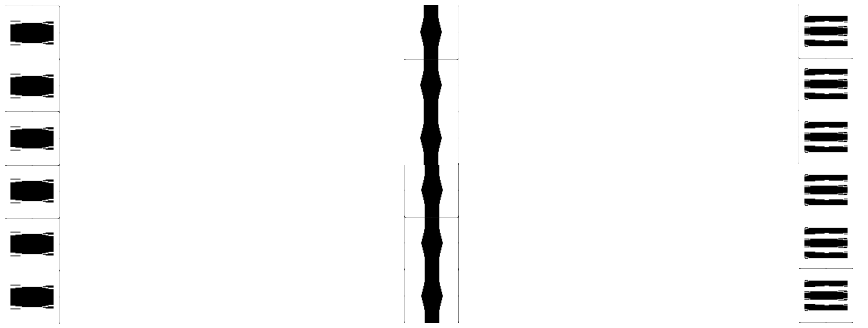

(a) $\theta_1 = -45°$ or $\theta_1 = 45°$ (b) $\theta_1 = 0°$ (c) $\theta_1 = 81°$

Figure 4.11 – Minimizing the reflexion coefficient under the constraint $V_{\text{target}} = 0.3$: final microstructured layers (six unit cells are shown)

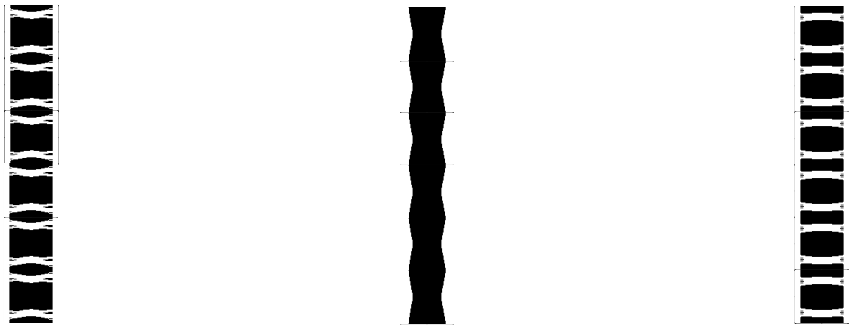

(a) $\theta_1 = -45°$ or $\theta_1 = 45°$ (b) $\theta_1 = 0°$ (c) $\theta_1 = 81°$

Figure 4.12 – Minimizing the reflexion coefficient under the constraint $V_{\text{target}} = 0.6$: final microstructured layers (six unit cells are shown)

latter involves five effective parameters that themselves require the resolution of a cell problem in an inifinite strip. Since, the optimization requires the resolution of numerous cell problems, a first step was therefore to write an equivalent formulation of the cell problems in a bounded cell. Then, the topological derivatives of the five effectives parameters were calculated. This step was validated numerically in the case of a circular perturbation. Then, the numerical methods used in the optimization process were presented. Each step of the optimization process requires the resolution of the cell problems which were solved thanks to a FFT-based method. This method was adapted to the case of the band cell problems through the introduction of boundary correctors. The material updating was handled thanks to one pixel phase permutations or to a level-set method. Eventually, some preliminary numerical results were presented for two kinds of cost functional.

Different perspectives or follow-ups can be highlighted:

- First, more numerical investigations are needed for example to see the influence of the choice of the wavenumber when minimizing the reflexion coefficient.
- When a volume constraint is considered, an automatic initialization and updating of the Lagrange multiplier can be carried out to replace the "user controlled" approach used for the moment.
- In addition, one may wish to have smoother final geometries than those presented for the minimisation of the reflexion coefficient. This can been obtained thanks to perimeter

constraint in the the level set (Ambrosio & Buttazzo, 1993; Yamada, Izui, Nishiwaki, & Takezawa, 2010).

- Then one can consider $N > 1$ in the second cost functional. This could allow to minimize the reflexion for different incident angles, or to minimize the reflexion coefficient for one angle and the transmission for another.
- The quality of the final configurations obtained could be checked through time-domain simulations in the homogenized configuration with the final effective parameters.
- From a mathematical point of view, the topological derivatives are obtained thanks to the ansatz (4.33) for the cell problem solution in the perturbed cell. Their justification could be thought as already done for microstructures occupying the whole space (Bonnet et al., 2018).
- Another more demanding perspective concerns the fact that the effective parameters have been observed to be not very sensitive to the geometry. This could justify the derivation of a higher order homogenized model that could be more sensitive to the geometry which would be useful for optimization purposes.
- Eventually, one could be interested in the *resonant* case which was the framework of the previous chapters. It would require more work on the optimization process since the resonant homogenized model includes resonant frequencies that depend on the geometry of the microstructure, see Vondřejc et al., 2017 for shape optimization. Consequently, the extension of the topological derivatives calculation and their use in an optimization algorithm do not seem incremental but would be of particular interest for example in the context of noise reduction (Ma et al., 2014; Schwan et al., 2017).

Part II

Homogenization of periodic media with imperfect interfaces

CHAPTER 5

Low-frequency homogenization with imperfect interfaces

In this chapter, we are interested in the low-frequency homogenization of periodic media with imperfect contacts. Indeed, the contacts between the different solids are often not perfect: defects (e.g. air, cracks, voids) or thin layers of glue can be present. In this case, a jump of the displacement and of the stress have to be considered in the contact region (between an inclusion and the matrix or between two media). These situations have been modelled by *spring-mass* conditions (Jones & Whittier, 1967; Tattersall, 1973; Sevostianov, Rodriguez-Ramos, Guinovart-Diaz, Bravo-Castillero, & Sabina, 2012). These rheological models have been justified thanks to finite element simulations (Vlasie & Rousseau, 2003) or asymptotic expansions (Licht, Lebon, & Léger, 2009; Lebon & Rizzoni, 2018; Pham et al., 2021).

The homogenization of such periodic media with imperfect contacts has been conducted in the static regime (Hashin, 1990; Hashin, 2002; Donato, Faella, & Monsurrò, 2007; López-Realpozo et al., 2008; Argilaga, Papachristos, Caillerie, & Pont, 2016; Lochner & Peter, 2020) but it seems that dynamic homogenization has seldom been treated. An exception is Andrianov, Danishevs'kyy, Topol, and Weichert, 2011 which investigates theoretically the macroscopic motion of waves in a 1D periodic array of coated inclusions in a matrix, with both the media and the interfaces behaving non-linearly. In this chapter, we rather consider a linear material, possibly heterogeneous, with

imperfect interfaces that are possibly governed by a smooth non-linear law. Furthermore, the stress is also possibly discontinuous and time-domain simulations are presented.

The low-frequency homogenization of a 1D periodic medium with linear interfaces is first conducted in Section 5.1. It allows to present the methodology in a simple way. This work has led to an extension to non-linear contacts in Bellis et al., 2021. The framework and the main results of this paper are also presented in Section 5.2. The homogenized model is eventually derived in higher space dimensions in Section 5.3 in the elastic case where the contacts are linear.

5.1 1D array of linear interfaces

5.1.1 Microstructured problem

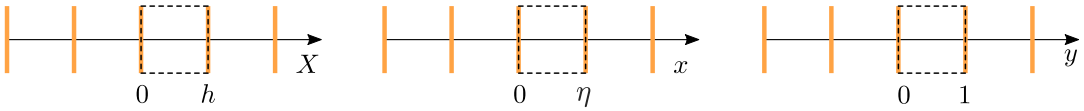

Figure 5.1 – Geometry settings in the X, x and y variables. A periodic cell is highlighted with a dashed line.

We consider the propagation of transient waves in a 1D h-periodic elastic medium containing imperfect interfaces located at $X_n = nh$ with $n \in \mathbb{Z}$, see left part of Figure 5.1. The medium is assumed to be linear elastic with mass density $\rho_h(X)$ and Young's modulus $\mu_h(X)$. Given a source term F, the displacement field U_h is governed by the time-domain wave equation

$$\begin{cases} \rho_h(X)\dfrac{\partial^2 U_h}{\partial t^2}(X,t) = \dfrac{\partial \Sigma_h}{\partial X}(X,t) + F(X,t), \\ \Sigma_h(X,t) = \mu_h(X)\dfrac{\partial U_h}{\partial X}(X,t), \end{cases} \tag{5.1}$$

with Σ_h being the stress field. The constitutive parameters characterizing the microstructured medium considered are possibly heterogeneous and assumed to satisfy the following mathematical assumptions.

Assumption 5.1

The mass density and the Young's modulus write $\rho_h(X) = \rho(X/h)$ and $\mu_h(X) = \mu(X/h)$, respectively, where

$$\rho, \mu \in L^\infty_{\text{per}}(0,1) := \Big\{ g \in L^\infty(\mathbb{R}),\ g(y+1) = g(y),\ \text{a.e. } y \in \mathbb{R} \Big\},$$
$$\text{with} \quad \rho \geq \rho_{\min} > 0, \quad \mu \geq \mu_{\min} > 0.$$

Moreover, the interfaces are assumed to be characterized by the interface *mass* and *rigidity* parameters $M \geq 0$ and $K > 0$, respectively, so that the following transmission conditions apply at any interface point X_n:

$$\begin{cases} M \left\langle\!\!\left\langle \dfrac{\partial^2 U_h}{\partial t^2}(\cdot,t) \right\rangle\!\!\right\rangle_{X_n} = \big[\!\big[\Sigma_h(\cdot,t) \big]\!\big]_{X_n}, & \text{(5.2a)} \\ \langle\!\langle \Sigma_h(\cdot,t) \rangle\!\rangle_{X_n} = K \big[\!\big[U_h(\cdot,t) \big]\!\big]_{X_n}, & \text{(5.2b)} \end{cases}$$

where, for any function $g(X)$, we define the jump and mean operators $[\![\cdot]\!]_{X_n}$ and $\langle\!\langle \cdot \rangle\!\rangle_{X_n}$ as

$$\big[\!\big[g \big]\!\big]_{X_n} = g(X_n^+) - g(X_n^-) \qquad \text{and} \qquad \big\langle\!\!\big\langle g \big\rangle\!\!\big\rangle_{X_n} = \frac{1}{2}\big(g(X_n^+) + g(X_n^-)\big). \tag{5.3}$$

In addition, both the displacement U_h and the stress field Σ_h are assumed to be continuous on the open intervals $]X_n, X_{n+1}[$.

Property 6. *The problem* (5.1) *together with* (5.2) *is well posed. Indeed, one introduces the* bulk *energy and the* interface *energy respectively as*

$$\begin{cases} \mathscr{E}_h^m(t) = \dfrac{1}{2}\displaystyle\int_I \left\{ \rho_h(X) V_h(X,t)^2 + \frac{1}{\mu_h(X)} \Sigma_h(X,t)^2 \right\} \mathrm{d}X, & \text{(5.4a)} \\ \mathscr{E}_h^i(t) = \displaystyle\sum_{n\in\mathbb{Z}/\ X_n\in I} \left\{ \frac{1}{2} M \left\langle\!\left\langle V_h(\cdot,t) \right\rangle\!\right\rangle_{X_n}^2 + \frac{1}{2K} \left\langle\!\left\langle \Sigma_h(\cdot,t) \right\rangle\!\right\rangle_{X_n}^2 \right\}, & \text{(5.4b)} \end{cases}$$

for an interval $I = [a,b]$ such that a and b do not coincide with an imperfect interface. Then, if the source term $F = 0$ and I is large enough so that the boundary terms vanish, the following conservation identity holds for the total energy

$$\frac{\mathrm{d}}{\mathrm{d}t}\left(\mathscr{E}_h^m + \mathscr{E}_h^i \right) = 0. \tag{5.5}$$

Proof. One introduces $V_h = \frac{\partial U_h}{\partial t}$, and one multiplies the first equation of (5.1) by V_h. Then, an integration by parts on I yields when $F = 0$

$$\int_I \rho_h \frac{\partial V_h}{\partial t} V_h \,\mathrm{d}X = \Big[\Sigma_h(\cdot,t) V_h(\cdot,t) \Big]_a^b - \sum_{n\in\mathbb{Z}/\ X_n\in I} [\![\Sigma_h V_h]\!]_{X_n} - \int_I \left\{ \Sigma_h \frac{\partial V_h}{\partial X} \right\} \mathrm{d}X. \tag{5.6}$$

The domain I is chosen large enough so that the boundary term vanishes. Due to the interface conditions (5.2), the jump term writes

$$\begin{aligned} [\![\Sigma_h V_h]\!]_{X_n} &= [\![\Sigma_h]\!]_{X_n} \left\langle\!\left\langle V_h \right\rangle\!\right\rangle_{X_n} + \left\langle\!\left\langle \Sigma_h \right\rangle\!\right\rangle_{X_n} [\![V_h]\!]_{X_n} \\ &= M \frac{\mathrm{d}}{\mathrm{d}t} \left\langle\!\left\langle V_h \right\rangle\!\right\rangle_{X_n} \left\langle\!\left\langle V_h \right\rangle\!\right\rangle_{X_n} + \frac{1}{K} \left\langle\!\left\langle \Sigma_h \right\rangle\!\right\rangle_{X_n} \frac{\mathrm{d}}{\mathrm{d}t} \left\langle\!\left\langle \Sigma_h \right\rangle\!\right\rangle_{X_n}. \end{aligned} \tag{5.7}$$

where one has assumed sufficient smoothness for $f = U_h$ or V_h so that

$$\left[\!\!\left[\frac{\partial f}{\partial t} \right]\!\!\right]_{X_n} = \frac{\mathrm{d}}{\mathrm{d}t} [\![f]\!]_{X_n} \qquad \text{and} \qquad \left\langle\!\!\left\langle \frac{\partial f}{\partial t} \right\rangle\!\!\right\rangle_{X_n} = \frac{\mathrm{d}}{\mathrm{d}t} \left\langle\!\left\langle f \right\rangle\!\right\rangle_{X_n}. \tag{5.8}$$

Then, using the second equation of (5.1), the last term in (5.6) writes

$$\int_I \Sigma_h(X) \frac{\partial V_h}{\partial X}(X) \mathrm{d}X = \int_I \frac{1}{\mu(X)} \Sigma_h(X) \frac{\partial \Sigma_h}{\partial t}(X) \mathrm{d}X \tag{5.9}$$

Consequently, the balance of energy holds. □

The framework of this chapter is again the low-frequency regime, and the corresponding assumption is recalled:

Assumption 5.2

We consider a reference wavelength $\lambda^\star$ and the following adimensionalized parameter is introduced

$$\eta = hk^\star, \qquad \text{with} \qquad k^\star = \frac{2\pi}{\lambda^\star} \tag{5.10}$$

being the reference wavenumber. One assumes that $\eta \ll 1$.

Our objective is to derive an effective dynamical model, up to the first-order, for the waves propagating in the periodic interface array considered. More precisely, we seek an approximation $U^{(1)}$ of the solution U_h to (5.1–5.2) of the form:

$$U_h(X,t) = U^{(1)}(X,t) + o(h).$$

5.1.2 Two-scale expansion

The derivation of the homogenized model follows the usual lines of two-scale asymptotic expansions, see for example Sánchez-Palencia, 1980; Boutin and Auriault, 1993; Wautier and Guzina, 2015 for homogenization in dynamics with perfect contacts.
To begin with, we consider some reference material parameters $\rho^\star$ and $E^\star$ that define the wavespeed $c^\star = \sqrt{E^\star/\rho^\star}$. These parameters will be specified later on. Accordingly and using (5.10), we introduce the following nondimensionalized space and time variables $x = k^\star X$ and $\tau = k^\star c^\star t$, respectively. One introduces the nondimensionalized fields

$$u_\eta(x,\tau) = k^\star U_h(X,t), \qquad v_\eta(x,\tau) = \frac{1}{c^\star} V_h(X,t) \qquad \text{and} \qquad \sigma_\eta(x,\tau) = \frac{1}{E^\star}\Sigma_h(X,t),$$

and the parameters

$$\begin{cases} \alpha = \dfrac{\rho}{\rho^\star}, \ \beta = \dfrac{\mu}{E^\star}, \\ f(x,\tau) = \dfrac{F(X,t)}{k^\star E^\star}, \\ \mathcal{M} = \dfrac{M}{h\rho^\star}, \quad \text{and} \quad \mathcal{K} = \dfrac{Kh}{E^\star}. \end{cases} \tag{5.11}$$

The wave equation (5.1) is recast as

$$\alpha\left(\frac{x}{\eta}\right)\frac{\partial^2 u_\eta}{\partial\tau^2}(x,\tau) = \frac{\partial}{\partial x}\left(\beta\left(\frac{x}{\eta}\right)\frac{\partial u_\eta}{\partial x}(x,\tau)\right) + f(x,\tau), \tag{5.12}$$

and the interface conditions (5.2) are recast as

$$\begin{cases} \mathcal{M}\,\eta\left\langle\!\!\left\langle \dfrac{\partial^2 u_\eta}{\partial\tau^2}(\cdot,\tau)\right\rangle\!\!\right\rangle_{x_n} = \left[\!\!\left[\beta\dfrac{\partial u_\eta}{\partial x}(\cdot,\tau)\right]\!\!\right]_{x_n}, \\ \left\langle\!\!\left\langle \beta\dfrac{\partial u_\eta}{\partial x}(\cdot,\tau)\right\rangle\!\!\right\rangle_{x_n} = \dfrac{\mathcal{K}}{\eta}\left[\!\!\left[u_\eta(\cdot,\tau)\right]\!\!\right]_{x_n}, \end{cases} \tag{5.13}$$

where we have extended the jump and mean notations at $x_n = nhk^\star = n\eta$. The equations (5.12) and (5.13) are the nondimensional counterparts of (5.1) and (5.2), respectively. As such, they fully highlight the contributions of the parameter η. Therefore, unless particular assumptions are made explicitly, the contribution of the terms in these equations, in particular that of the parameters α, β, $\mathcal{M}$ and $\mathcal{K}$, will be of order $O(1)$ in the forthcoming asymptotic expansion.

In the low-frequency regime, the material parameters α and β vary on a fine scale associated with the rescaled coordinate $y = x/\eta$, see Figure 5.1. The wavefield is also assumed to have small-scale features that are described by y, and slow continuous variations as well, which are described by the variable x. Accordingly, the field u_η is expanded using the following ansatz:

$$u_\eta(x,\tau) = \sum_{j\geq 0} \eta^j u_j(x, x/\eta, \tau). \tag{5.14}$$

The fields u_j are assumed to be continuous with respect to the first variable and 1-periodic with respect to the second variable, i.e.

$$u_j(x,y,\tau) = u_j(x,y+1,\tau)$$

for all $y \in]0,1[$. The fields u_j being potentially discontinuous at the points y_n, we extend at the micro-scale the jump and mean notations (5.3) for a function $g(x,y)$ as

$$\begin{aligned} \llbracket g \rrbracket_{y_n} &\equiv \llbracket g(x,\cdot) \rrbracket_{y_n} = g(x,y_n^+) - g(x,y_{n+1}^-), \\ \langle\!\langle g \rangle\!\rangle_{y_n} &\equiv \langle\!\langle g(x,\cdot) \rangle\!\rangle_{y_n} = \frac{1}{2}\big(g(x,y_n^+) + g(x,y_{n+1}^-)\big), \end{aligned} \tag{5.15}$$

where we used the y-periodicity. Moreover, due to peridic assumptions, the index will be dropped later on: the jump and mean will refer to the point $y_n = 0$. One also introduces the average on the unit periodic cell as

$$\langle g \rangle = \int_0^1 g(y)\,\mathrm{d}y. \tag{5.16}$$

In addition, for any continuous 1-periodic function on the open interval $]0,1[$, the following relation holds

$$\left\langle \frac{\mathrm{d}g}{\mathrm{d}y} \right\rangle = -\llbracket g \rrbracket. \tag{5.17}$$

As customary in two-scale analysis, partial differentiation with respect to x has to be rewritten as $\big(\partial/\partial x + \frac{1}{\eta}\partial/\partial y\big)$ due to the scale separation. Therefore, the nondimentionalized wave equation (5.12) writes

$$\alpha(y)\frac{\partial^2 u_\eta}{\partial \tau^2} = \frac{1}{\eta^2}\frac{\partial}{\partial y}\left(\beta(y)\frac{\partial u_\eta}{\partial y}\right) + \frac{1}{\eta}\left(\frac{\partial}{\partial y}\left(\beta(y)\frac{\partial u_\eta}{\partial x}\right) + \beta(y)\frac{\partial^2 u_\eta}{\partial x \partial y}\right) + \beta(y)\frac{\partial^2 u_\eta}{\partial x^2} + f(x,\tau), \tag{5.18}$$

and the associated interface conditions (5.13) are

$$\begin{cases} \mathcal{M}\,\eta \left\langle\!\!\left\langle \dfrac{\partial^2 u_\eta}{\partial \tau^2} \right\rangle\!\!\right\rangle = \left\llbracket \beta\left(\dfrac{\partial u_\eta}{\partial x} + \dfrac{1}{\eta}\dfrac{\partial u_\eta}{\partial y}\right) \right\rrbracket, & \text{(5.19a)} \\ \left\langle\!\!\left\langle \beta\left(\dfrac{\partial u_\eta}{\partial x} + \dfrac{1}{\eta}\dfrac{\partial u_\eta}{\partial y}\right) \right\rangle\!\!\right\rangle = \dfrac{\mathcal{K}}{\eta}\left\llbracket u_\eta \right\rrbracket, & \text{(5.19b)} \end{cases}$$

where the definitions (5.15) are being considered. Moreover, the continuity of the displacement and the stress field within the periodic cells implies that for all $j \geq 0$

$$u_j \text{ and } \beta\left(\frac{\partial u_{j+1}}{\partial y} + \frac{\partial u_j}{\partial x}\right) \text{ are continuous on every intervals }]y_n, y_{n+1}[. \tag{5.20}$$

5.1.3 Zeroth-order homogenization

5.1.3.1 Zeroth-order field

One identifies the terms of order $O(\eta^{-2})$ in (5.18) together with these of order $O(\eta^{-1})$ in (5.19a) and (5.19b). It leads to the following system for the zeroth-order field u_0:

$$\begin{cases} \dfrac{\partial}{\partial y}\left(\beta(y)\dfrac{\partial u_0}{\partial y}(x,y,\tau)\right) = 0, & \text{(5.21a)} \\ \left[\!\left[\beta\dfrac{\partial u_0}{\partial y}(x,\cdot,\tau)\right]\!\right] = 0, & \text{(5.21b)} \\ \left\langle\!\left\langle\beta\dfrac{\partial u_0}{\partial y}(x,\cdot,\tau)\right\rangle\!\right\rangle = \mathcal{K}\left[\!\left[u_0(x,\cdot,\tau)\right]\!\right]. & \text{(5.21c)} \end{cases}$$

Integration of (5.21a) with the continuity condition (5.21b) entails

$$\frac{\partial u_0}{\partial y}(x,y,\tau) = \frac{1}{\beta(y)}\mathcal{A}_0(x,\tau). \tag{5.22}$$

Using (5.17) and (5.22) yields

$$\left\langle\frac{1}{\beta}\right\rangle\mathcal{A}_0(x,\tau) = -\left[\!\left[u_0\right]\!\right].$$

Then using (5.21c) in the previous equation leads to

$$\begin{aligned}\left\langle\frac{1}{\beta}\right\rangle\mathcal{A}_0(x,\tau) &= -\frac{1}{\mathcal{K}}\left\langle\!\left\langle\beta\frac{\partial u_0}{\partial y}(x,\cdot,\tau)\right\rangle\!\right\rangle \\ &= -\frac{1}{\mathcal{K}}\,\mathcal{A}_0(x,\tau),\end{aligned}$$

where we used (5.22) in the last equation. Therefore, $\mathcal{A}_0(x,\tau) = 0$ and consequently

$$u_0(x,y,\tau) = u_0(x,\tau). \tag{5.23}$$

5.1.3.2 First-order field

Next, identifying the terms of order $O(\eta^{-1})$ in (5.18) together with those of order $O(1)$ in (5.19a) and (5.19b) leads to the following system for the first-order field u_1:

$$\begin{cases} \dfrac{\partial}{\partial y}\left(\beta(y)\left(\dfrac{\partial u_1}{\partial y}(x,y,\tau) + \dfrac{\partial u_0}{\partial x}(x,\tau)\right)\right) = 0, & \text{(5.24a)} \\ \left[\!\left[\beta\left(\dfrac{\partial u_1}{\partial y} + \dfrac{\partial u_0}{\partial x}\right)(x,\cdot,\tau)\right]\!\right] = 0, & \text{(5.24b)} \\ \left\langle\!\left\langle\beta\left(\dfrac{\partial u_1}{\partial y} + \dfrac{\partial u_0}{\partial x}\right)(x,\cdot,\tau)\right\rangle\!\right\rangle = \mathcal{K}\left[\!\left[u_1(x,\cdot,\tau)\right]\!\right]. & \text{(5.24c)} \end{cases}$$

Integration of (5.24a) with the continuity condition (5.24b) entails

$$\frac{\partial u_1}{\partial y}(x,y,\tau) = -\frac{\partial u_0}{\partial x}(x,\tau) + \frac{1}{\beta(y)}\sigma_0(x,\tau) \tag{5.25}$$

where σ_0 has to be determined. One sets

$$E^\star = \left\langle\frac{1}{\mu}\right\rangle^{-1} \qquad \text{so that} \qquad \left\langle\frac{1}{\beta}\right\rangle = 1, \tag{5.26}$$

due to the definition (5.11) of β. Averaging the equation (5.25) and using (5.17) leads to

$$-\left[\!\left[u_1(x,\cdot,\tau)\right]\!\right] = -\frac{\partial u_0}{\partial x}(x,\tau) + \sigma_0(x,\tau). \tag{5.27}$$

Inserting (5.27) in (5.24c) and using (5.25) entails

$$\sigma_0(x,\tau) = \frac{\mathcal{K}}{\mathcal{K}+1}\frac{\partial u_0}{\partial x}(x,\tau). \tag{5.28}$$

5.1.3.3 Second-order field

Considering the second-order field u_2, then identifying the terms of order $O(1)$ in (5.18) gives

$$\frac{\partial}{\partial y}\left(\beta(y)\left(\frac{\partial u_2}{\partial y}(x,y,\tau)+\frac{\partial u_1}{\partial x}(x,y,\tau)\right)\right)+\beta(y)\frac{\partial^2 u_1}{\partial x\partial y}(x,y,\tau)+\beta(y)\frac{\partial^2 u_0}{\partial x^2}(x,\tau)+f(x,\tau)$$
$$=\alpha(y)\frac{\partial^2 u_0}{\partial \tau^2}(x,\tau). \tag{5.29}$$

Collecting the terms of order $O(\eta)$ in (5.19a) leads to the jump conditions

$$\begin{cases} \left[\!\left[\beta\left(\dfrac{\partial u_2}{\partial y}+\dfrac{\partial u_1}{\partial x}\right)(x,\cdot,\tau)\right]\!\right] = \mathcal{M}\left\langle\!\left\langle\dfrac{\partial^2 u_0}{\partial \tau^2}(x,\tau)\right\rangle\!\right\rangle, & \text{(5.30a)} \\ \left\langle\!\left\langle\beta\left(\dfrac{\partial u_2}{\partial y}+\dfrac{\partial u_1}{\partial x}\right)(x,\cdot,\tau)\right\rangle\!\right\rangle = \mathcal{K}\left[\!\left[u_2(x,\cdot,\tau)\right]\!\right]. & \text{(5.30b)} \end{cases}$$

One averages the equation (5.29) on the unit periodic cell $]0,1[$ while using the identity (5.17). Given the continuity condition (5.20) for $j=1$, together with the jump condition (5.30a), it implies

$$-\mathcal{M}\left\langle\!\left\langle\frac{\partial^2 u_0}{\partial \tau^2}(x,\tau)\right\rangle\!\right\rangle+\frac{\partial}{\partial x}\left\langle\!\left\langle\beta\left(\frac{\partial u_1}{\partial y}(x,\cdot,\tau)+\frac{\partial u_0}{\partial x}(x,\tau)\right)\right\rangle\!\right\rangle+f(x,\tau)=\langle\alpha\rangle\frac{\partial^2 u_0}{\partial \tau^2}(x,\tau). \tag{5.31}$$

Moreover, as in (5.26), the reference mass density entering the definition (5.11) of α is chosen as

$$\rho^\star = \langle\rho\rangle \qquad \text{so that} \qquad \langle\alpha\rangle = 1. \tag{5.32}$$

Finally, owing to the continuity of the field u_0 and using (5.25) in (5.31) we obtain

$$(\mathcal{M}+1)\frac{\partial^2 u_0}{\partial \tau^2}(x,\tau) = \frac{\partial}{\partial x}\big(\sigma_0(x,\tau)\big)+f(x,\tau). \tag{5.33}$$

Using (5.28), one gets the following effective wave equation for the nondimensionalized macroscopic field u_0:

$$(\mathcal{M}+1)\frac{\partial^2 u_0}{\partial \tau^2}(x,\tau) = \frac{\mathcal{K}}{\mathcal{K}+1}\frac{\partial^2 u_0}{\partial x^2}(x,\tau)+f(x,\tau). \tag{5.34}$$

5.1.4 First-order homogenization

Then, one looks for an effective model up to the first-order. Its derivation will follow the lines of the previous section at the next order.

5.1.4.1 Third-order field

One identifies the terms of order $O(\eta)$ in (5.18):

$$\frac{\partial}{\partial y}\left(\beta(y)\left(\frac{\partial u_3}{\partial y}(x,y,\tau)+\frac{\partial u_2}{\partial x}(x,y,\tau)\right)\right)+\beta(y)\frac{\partial^2 u_2}{\partial x\partial y}(x,y,\tau)+\beta(y)\frac{\partial^2 u_1}{\partial x^2}(x,y,\tau) \\ =\alpha(y)\frac{\partial^2 u_1}{\partial \tau^2}(x,y,\tau). \quad (5.35)$$

The identification at the order $O(\eta^2)$ in (5.19a) leads to

$$\left[\!\left[\beta\left(\frac{\partial u_3}{\partial y}+\frac{\partial u_2}{\partial x}\right)(x,\cdot,\tau)\right]\!\right]=\mathcal{M}\left\langle\!\left\langle\frac{\partial^2 u_1}{\partial \tau^2}(x,\cdot,\tau)\right\rangle\!\right\rangle. \quad (5.36)$$

One averages (5.35) and uses (5.17), given the continuity condition (5.20) for $j=2$, which yields

$$-\mathcal{M}\left\langle\!\left\langle\frac{\partial^2 u_1}{\partial \tau^2}(x,\cdot,\tau)\right\rangle\!\right\rangle+\frac{\partial}{\partial x}\left\langle\beta\left(\frac{\partial u_2}{\partial y}(x,\cdot,\tau)+\frac{\partial u_1}{\partial x}(x,\cdot,\tau)\right)\right\rangle=\left\langle\alpha\,\frac{\partial^2 u_1}{\partial \tau^2}(x,\cdot,\tau)\right\rangle, \quad (5.37)$$

where we have made use of (5.36). This identity will be used to derive an equation for the mean field $\langle u_1\rangle$. We now look for an expression for the three terms in (5.37).

■ *First term.* First, the integration of (5.25), together with the continuity of y in $]0,1[$, yields the following explicit expression of u_1:

$$u_1(x,y,\tau)=-\frac{\partial u_0}{\partial x}(x,\tau)y+\sigma_0(x,\tau)b(y)+q_1(x,\tau), \quad (5.38)$$

with

$$b(y)=\int_0^y\frac{1}{\beta(z)}\,\mathrm{d}z, \quad (5.39)$$

and $q_1(x,\tau)$ that still needs to be determined.
Averaging the identity (5.38) gives the following expression for q_1:

$$q_1(x,\tau)=\langle u_1(x,\cdot,\tau)\rangle+\frac{1}{2}\frac{\partial u_0}{\partial x}(x,\tau)-\mathcal{B}\,\sigma_0(x,\tau) \quad (5.40)$$

with

$$\mathcal{B}=\langle b\rangle=\int_0^1\int_0^y\frac{1}{\beta(z)}\,\mathrm{d}z\,\mathrm{d}y.$$

Now, considering the first term in (5.37), one gets

$$\left\langle\!\left\langle\frac{\partial^2 u_1}{\partial \tau^2}(x,\cdot,\tau)\right\rangle\!\right\rangle=\frac{\partial^2}{\partial \tau^2}\left\langle\!\left\langle u_1(x,\cdot,\tau)\right\rangle\!\right\rangle.$$

Moreover, due to (5.15), (5.38) and (5.26), we have

$$\begin{aligned}\left\langle\!\left\langle u_1(x,\cdot,\tau)\right\rangle\!\right\rangle&=\frac{1}{2}\big(u_1(x,0^+,\tau)+u_1(x,1^-,\tau)\big)\\&=-\frac{1}{2}\frac{\partial u_0}{\partial x}(x,\tau)+\frac{1}{2}\sigma_0(x,\tau)+q_1(x,\tau)\\&=\langle u_1(x,\cdot,\tau)\rangle+\left(\frac{1}{2}-\mathcal{B}\right)\sigma_0(x,\tau),\end{aligned} \quad (5.41)$$

where we used the identity (5.40) in the last line. Consequently, the first term in (5.37) writes

$$\left\langle\!\left\langle\frac{\partial^2 u_1}{\partial \tau^2}(x,\cdot,\tau)\right\rangle\!\right\rangle=\frac{\partial^2}{\partial \tau^2}\langle u_1(x,\cdot,\tau)\rangle+\left(\frac{1}{2}-\mathcal{B}\right)\frac{\mathcal{K}}{\mathcal{K}+1}\frac{\partial^3 u_0}{\partial x\partial \tau^2}. \quad (5.42)$$

■ *Second term.* In order to deal with the second term in (5.37), one inserts (5.25) into (5.29) and one integrates the resulting equation to obtain:

$$\beta(y)\left(\frac{\partial u_2}{\partial y}(x,y,\tau)+\frac{\partial u_1}{\partial x}(x,y,\tau)\right)+\left(\frac{\partial \sigma_0}{\partial x}(x,\tau)+f(x,\tau)\right)y=a(y)\frac{\partial^2 u_0}{\partial \tau^2}(x,\tau)+p_2(x,\tau), \quad (5.43)$$

where the function $p_2(x,\tau)$ is to be determined and $a(y)$ is defined as

$$a(y)=\int_0^y \alpha(z)\,\mathrm{d}z.$$

To determine the function p_2, one divides (5.43) by β and one averages the resulting equation. The identities (5.17), together with (5.26), and the continuity of u_2 on $]0,1[$ provide

$$-\left[\!\left[u_2(x,\cdot,\tau)\right]\!\right]+\frac{\partial}{\partial x}\left\langle u_1(x,\cdot,\tau)\right\rangle+\left(\frac{\partial \sigma_0}{\partial x}(x,\tau)+f(x,\tau)\right)\left\langle\frac{y}{\beta}\right\rangle=\frac{\partial^2 u_0}{\partial \tau^2}(x,\tau)\left\langle\frac{a}{\beta}\right\rangle+p_2(x,\tau). \quad (5.44)$$

Moreover, from (5.30b) and taking the mean value of (5.43), one gets

$$\left[\!\left[u_2(x,\cdot,\tau)\right]\!\right]=\frac{1}{\mathcal{K}}\left\{\frac{1}{2}\frac{\partial^2 u_0}{\partial \tau^2}(x,\tau)-\frac{1}{2}\left(\frac{\partial \sigma_0}{\partial x}(x,\tau)+f(x,\tau)\right)+p_2(x,\tau)\right\}. \quad (5.45)$$

Inserting this last equation in (5.44) leads to the following expression of p_2:

$$\begin{aligned}p_2(x,\tau)=\frac{1}{\mathcal{K}+1}\Bigg\{&\mathcal{K}\frac{\partial}{\partial x}\left\langle u_1(x,\cdot,\tau)\right\rangle-\left(\frac{1}{2}+\mathcal{K}\left\langle\frac{a}{\beta}\right\rangle\right)\frac{\partial^2 u_0}{\partial \tau^2}(x,\tau)\\&+\left(\frac{1}{2}+\mathcal{K}\left\langle\frac{y}{\beta}\right\rangle\right)\left(\frac{\partial \sigma_0}{\partial x}(x,\tau)+f(x,\tau)\right)\Bigg\}. \quad (5.46)\end{aligned}$$

One averages (5.43) on $]0,1[$ and one uses the expression of p_2 (5.46) to get the following relation involving the second term of (5.37):

$$\begin{aligned}\left\langle\beta\left(\frac{\partial u_2}{\partial y}(x,\cdot,\tau)+\frac{\partial u_1}{\partial x}(x,\cdot,\tau)\right)\right\rangle=&\frac{\mathcal{K}}{\mathcal{K}+1}\frac{\partial}{\partial x}\left\langle u_1(x,\cdot,\tau)\right\rangle\\&+\left\{\mathcal{A}-\frac{1}{\mathcal{K}+1}\left(\frac{1}{2}+\mathcal{K}\left\langle\frac{a}{\beta}\right\rangle\right)\right\}\frac{\partial^2 u_0}{\partial \tau^2}(x,\tau)\\&+\left\{-\frac{1}{2}+\frac{1}{\mathcal{K}+1}\left(\frac{1}{2}+\mathcal{K}\left\langle\frac{y}{\beta}\right\rangle\right)\right\}\left(\frac{\partial \sigma_0}{\partial x}(x,\tau)+f(x,\tau)\right), \quad (5.47)\end{aligned}$$

where we have defined

$$\mathcal{A}=\langle a\rangle=\int_0^1\int_0^y \alpha(z)\,\mathrm{d}z\,\mathrm{d}y.$$

Finally, one uses (5.28) and (5.34) to express σ_0 in terms of u_0 in (5.47):

$$\begin{aligned}\left\langle\beta\left(\frac{\partial u_2}{\partial y}(x,\cdot,\tau)+\frac{\partial u_1}{\partial x}(x,\cdot,\tau)\right)\right\rangle=&\frac{\mathcal{K}}{\mathcal{K}+1}\frac{\partial}{\partial x}\left\langle u_1(x,\cdot,\tau)\right\rangle\\&+\left\{\mathcal{A}-\frac{1}{\mathcal{K}+1}\left(\frac{1}{2}+\mathcal{K}\left\langle\frac{a}{\beta}\right\rangle\right)+\left(-\frac{1}{2}+\frac{1}{\mathcal{K}+1}\left(\frac{1}{2}+\mathcal{K}\left\langle\frac{y}{\beta}\right\rangle\right)\right)(\mathcal{M}+1)\right\}\frac{\partial^2 u_0}{\partial \tau^2}(x,\tau). \quad (5.48)\end{aligned}$$

■ *Third term.* In a last step we focus on the right-hand side term in (5.37), i.e.

$$\left\langle \alpha \, \frac{\partial^2 u_1}{\partial \tau^2}(x,\cdot,\tau) \right\rangle = \frac{\partial^2}{\partial \tau^2} \left\langle \alpha \, u_1(x,\cdot,\tau) \right\rangle .$$

One uses the expression (5.38) for u_1 to obtain the following expression of $\langle \alpha u_1 \rangle$:

$$\left\langle \alpha \, u_1(x,\cdot,\tau) \right\rangle = -\frac{\partial u_0}{\partial x}(x,\tau) \left\langle \alpha \, y \right\rangle + \sigma_0(x,\tau) \left\langle \alpha \, b \right\rangle + q_1(x,\tau). \tag{5.49}$$

Eventually, the expression (5.40) for q_1 is used together with (5.28) in (5.49), which is then differentiated twice with respect to τ to get:

$$\left\langle \alpha \, \frac{\partial^2 u_1}{\partial \tau^2}(x,\cdot,\tau) \right\rangle \quad = \quad \left\langle u_1(x,\cdot,\tau) \right\rangle \; + \; \left(\frac{1}{2} - \left\langle \alpha \, y \right\rangle + \left(\left\langle \alpha \, b \right\rangle - \mathcal{B} \right) \frac{\mathcal{K}}{\mathcal{K}+1} \right) \frac{\partial^3 u_0}{\partial x \partial^2 \tau}(x,\tau). \tag{5.50}$$

5.1.4.2 Equation for the mean field associated with the first-order corrector

To conclude, the identities (5.42), (5.48) differentiated with respect to x, and (5.50) are used back in (5.37). Doing so we obtain the equation for the mean field $\langle u_1 \rangle$:

$$(\mathcal{M}+1) \frac{\partial^2}{\partial \tau^2} \left\langle u_1(x,\cdot,\tau) \right\rangle = \frac{\mathcal{K}}{\mathcal{K}+1} \frac{\partial^2}{\partial x^2} \left\langle u_1(x,\cdot,\tau) \right\rangle + s\big(u_0(x,\tau)\big), \tag{5.51}$$

where the source term $s\big(u_0(x,\tau)\big)$ is given by

$$s\big(u_0(x,\tau)\big) = \mathcal{G} \frac{\partial^3 u_0}{\partial x \partial \tau^2}(x,\tau), \tag{5.52}$$

with

$$\begin{aligned} \mathcal{G} = \mathcal{A} - \frac{1}{\mathcal{K}+1} \left(\frac{1}{2} + \mathcal{K} \left\langle \frac{a}{\beta} \right\rangle \right) + \left(-\frac{1}{2} + \frac{1}{\mathcal{K}+1} \left(\frac{1}{2} + \mathcal{K} \left\langle \frac{y}{\beta} \right\rangle \right) \right) (\mathcal{M}+1) \\ - \mathcal{M} \left(\frac{1}{2} - \mathcal{B} \right) \frac{\mathcal{K}}{\mathcal{K}+1} - \frac{1}{2} + \left\langle \alpha \, y \right\rangle - \left(\left\langle \alpha \, b \right\rangle - \mathcal{B} \right) \frac{\mathcal{K}}{\mathcal{K}+1}. \end{aligned} \tag{5.53}$$

By integration by parts one proves that

$$\begin{cases} \left\langle \dfrac{y}{\beta} \right\rangle = 1 - \mathcal{B}, \\ \left\langle \alpha y \right\rangle = 1 - \mathcal{A}, \\ \left\langle \alpha b \right\rangle = 1 - \left\langle \dfrac{a}{\beta} \right\rangle, \end{cases}$$

and consequently $\mathcal{G} = 0$. Then, the source term in (5.51) vanishes and the final equation for $\langle u_1 \rangle$ is

$$(\mathcal{M}+1) \frac{\partial^2}{\partial \tau^2} \left\langle u_1(x,\cdot,\tau) \right\rangle = \frac{\mathcal{K}}{\mathcal{K}+1} \frac{\partial^2}{\partial x^2} \left\langle u_1(x,\cdot,\tau) \right\rangle . \tag{5.54}$$

Finally, once the mean field is computed using the equation (5.54), then the local *corrector* u_1 at the micro-scale within the periodic array can be reconstructed by inserting (5.28) and (5.40) into (5.38) as

$$u_1(x,y,\tau) = \left\langle u_1(x,\cdot,\tau) \right\rangle + \left\{ \frac{1}{2} - y + \frac{\mathcal{K}}{\mathcal{K}+1} \big(b(y) - \mathcal{B} \big) \right\} \frac{\partial u_0}{\partial x}(x,\tau). \tag{5.55}$$

5.1.5 Final homogenized model

Now that the homogenized models have been obtained for both the zeroth and first-order terms u_0 and u_1 in the rescaled coordinate system, the final step is to formulate the sought first-order approximation of the solution U_h in the original coordinate system. Considering the ansatz (5.14), then from u_0 and u_1 we can define the approximation $u^{(1)}$ as

$$u^{(1)}(x,\tau) = u_0(x,\tau) + \eta u_1(x, x/\eta, \tau) = u_0(x,\tau) + hk^\star u_1(x, x/\eta, \tau).$$

Once transposed in the original coordinate system, and due to the definition of the nondimensionalized fields introduced in Section 5.1.2, one looks for an expression for $U^{(1)}(X,t) = u^{(1)}(x,\tau)/k^\star$. It is expressed as

$$U^{(1)}(X,t) = U_0(X,t) + hU_1(X,t), \tag{5.56}$$

where $U_0(X,t) = u_0(x,\tau)/k^\star$ and $U_1(X,t) = u_1(x, x/\eta, \tau)$. From the definition of the nondimensionalized variables and fields introduced in Section 5.1.2 and owing to (5.26) and (5.32), the equation (5.34) is transposed in the original coordinate system and the equation satisfied by U_0 writes:

Result 5.1: Zeroth-order homogenized field

$$\rho_{\text{eff}} \frac{\partial^2 U_0}{\partial t^2}(X,t) = \mu_{\text{eff}} \frac{\partial^2 U_0}{\partial X^2}(X,t) + F(X,t), \tag{5.57}$$

with the effective mass density and shear modulus being defined as

$$\rho_{\text{eff}} = \langle \rho \rangle + \frac{M}{h} \text{ and } \mu_{\text{eff}} = \frac{Kh}{Kh \langle 1/\mu \rangle + 1}. \tag{5.58}$$

Remark 15. *The case of perfect interfaces can be recovered by setting $K \to +\infty$ and $M \to 0$, which yields the well-known result $\rho_{\text{eff}} = \langle \rho \rangle$ and $\mu_{\text{eff}} = \langle 1/\mu \rangle^{-1}$.*

Considering the mean displacement field $\overline{U}_1(X,t) = \langle u_1(x,\cdot,\tau) \rangle$, and following the same transposition as for the zeroth-order field, then $\overline{U}_1$ turns out to be governed by the wave equation

Result 5.2: Mean field associated with the first-order homogenized field

$$\rho_{\text{eff}} \frac{\partial^2 \overline{U}_1}{\partial t^2}(X,t) = \mu_{\text{eff}} \frac{\partial^2 \overline{U}_1}{\partial X^2}(X,t). \tag{5.59}$$

Moreover, once the mean field $\overline{U}_1(X,t)$ has been computed then the associated local corrector is written. It is the *total field* $U_1(X,t) = u_1(x,y,\tau)$ that can be found by expressing (5.55) in the original coordinate system. One introduces $y = (X - nh)/h$ when X belongs to a given interval $\big(nh, (n+1)h\big)$, so that this local corrector writes

Result 5.3: First-order homogenized field

$$U_1(X,t) = \overline{U}_1(X,t) + \left\{ \frac{1}{2} - y + \big(b(y) - \mathcal{B}\big)\, \mu_{\text{eff}} \left\langle \frac{1}{\mu} \right\rangle \right\} \frac{\partial U_0}{\partial X}(X,t). \tag{5.60}$$

■ *Hyperbolicity.* One introduces

$$V_0 = \frac{\partial U_0}{\partial t} \quad \text{and} \quad \mathcal{E}_0 = \frac{\partial U_0}{\partial X}. \tag{5.61}$$

Then, it is straighforward to rewrite (5.57) as the following first-order system:

$$\begin{cases} \dfrac{\partial \mathcal{E}_0}{\partial t}(X,t) = \dfrac{\partial V_0}{\partial X}(X,t) \\ \dfrac{\partial V_0}{\partial t}(X,t) = \dfrac{1}{\rho_{\text{eff}}} \left\{ \mu_{\text{eff}} \dfrac{\partial \mathcal{E}_0}{\partial t}(X,t) + F(X,t) \right\}. \end{cases} \tag{5.62}$$

Upon introducing

$$\mathbb{G}_{\text{eff}} = \begin{pmatrix} 0 & -1 \\ -\frac{\mu_{\text{eff}}}{\rho_{\text{eff}}} & 0 \end{pmatrix} \quad \text{and} \quad \boldsymbol{F} = \begin{pmatrix} 0 \\ F/\rho_{\text{eff}} \end{pmatrix}, \tag{5.63}$$

it can be written in the condensend form as the strictly hyperbolic system

$$\frac{\partial}{\partial t} \boldsymbol{\Psi}_0(X,t) + \mathbb{G}_{\text{eff}} \frac{\partial}{\partial X} \boldsymbol{\Psi}_0(X,t) = \boldsymbol{F}(X,t) \qquad \text{with} \qquad \boldsymbol{\Psi}_0 = \big(\mathcal{E}_0, V_0\big)^{\top}. \tag{5.64}$$

The same can be done for the mean field associated with the first-order correction $\overline{U}_1$ which is solution of (5.59). Indeed, upon introducing

$$\overline{V}_1 = \frac{\partial \overline{U}_1}{\partial t} \quad \text{and} \quad \overline{\mathcal{E}}_1 = \frac{\partial \overline{U}_1}{\partial X}, \tag{5.65}$$

this can be recast as the first-order strictly hyperbolic system

$$\frac{\partial}{\partial t} \overline{\boldsymbol{\Psi}}_1(X,t) + \mathbb{G}_{\text{eff}} \frac{\partial}{\partial X} \overline{\boldsymbol{\Psi}}_1(X,t) = \boldsymbol{0} \qquad \text{with} \qquad \overline{\boldsymbol{\Psi}}_1 = \big(\overline{\mathcal{E}}_1, \overline{V}_1\big)^{\top}. \tag{5.66}$$

5.1.6 Numerical experiments

Numerical simulations are presented in this section to illustrate the first-order effective model obtained. The microstructured configuration has periodicity $h = 10\,\text{m}$, with a homogeneous periodic cell of physical parameters $\rho = 1200\,\text{kg/m}^3$, $\mu = 9.408 \cdot 10^9\,\text{Pa}$, $M = 0\,\text{Pa.s}^2/\text{m}$, and $K = 2.45 \cdot 10^9\,\text{Pa/m}$.

In both the microstructured and the homogenized configurations, numerical simulations are performed on a uniform grid using the Explicit Simplified Interface Method discussed in Section 1.3.2. The source term is defined as $F(X,t) = \delta(X - X_s)\, g(t)$, with $X_s = 505\,\text{m}$ and $g(t)$ given by:

$$g(t) = \begin{cases} A \displaystyle\sum_{m=1}^{4} a_m \, \sin(\beta_m \, \omega_c \, t) & \text{if } 0 < t < \dfrac{1}{f_c}, \\ 0 \;\; \text{otherwise,} \end{cases} \tag{5.67}$$

where $\beta_m = 2^{m-1}$ and the coefficients a_m being $a_1 = 1$, $a_2 = -21/32$, $a_3 = 63/768$, $a_4 = -1/512$ so that $g \in C^6([0,+\infty[)$. The central frequency f_c is associated to a dimensionless parameter $\eta = 2\pi f_c h \sqrt{\rho_{\text{eff}}/\mu_{\text{eff}}}$ which should be very small compared to 1 in order to satisfy Assumption 5.2.

Figure 5.2 corresponds to an excitation at the central frequency $f_c = 10\,\text{Hz}$, associated with the value $\eta = 0.26$, and amplitude $A = 0.1$. One can see a good agreement between the velocity in the microstructured configuration V_h and the result of the first-order homogenization $V^{(1)}$. More precisely, one notes in Figure 5.2d, at the scale of the microstructure, the local fluctuations of V_h

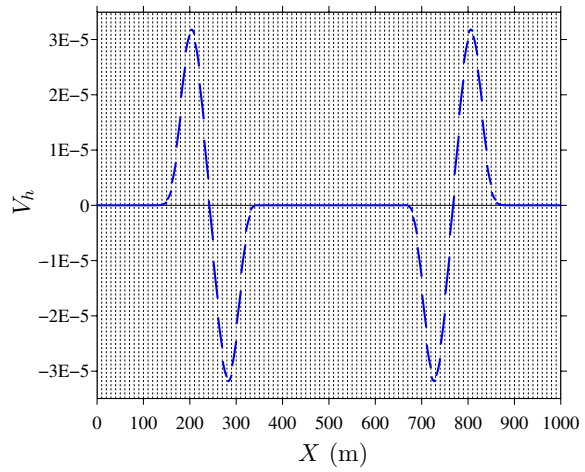

(a) Field V_h in the microstructured medium.

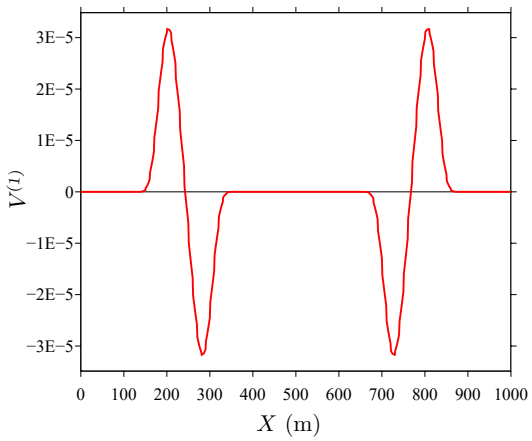

(b) First-order homogenized field $V^{(1)}$.

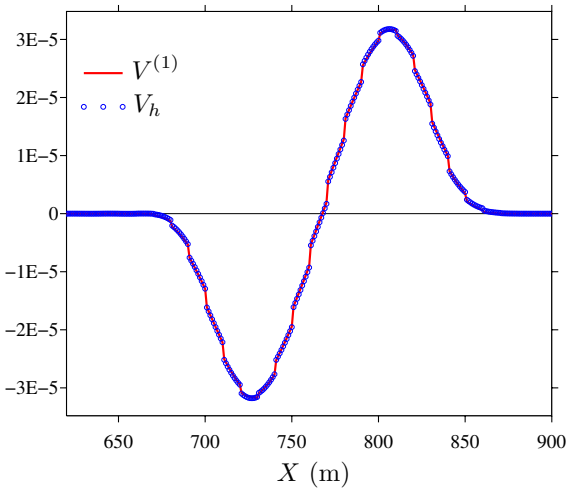

(c) Superposition of the fields V_h and $V^{(1)}$.

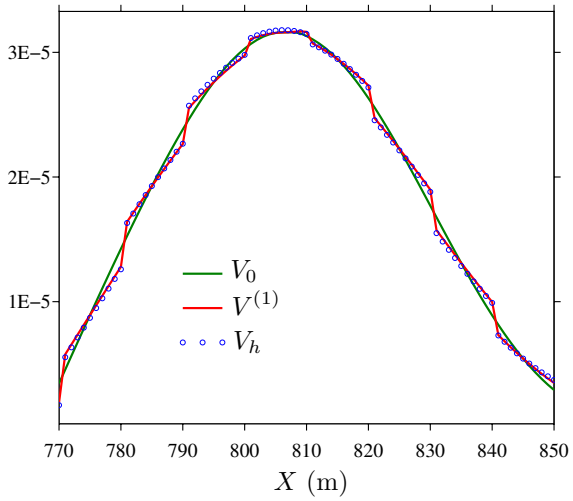

(d) Close-up showing the zeroth- and first-order homogenized fields V_0 and $V^{(1)}$, respectively, and V_h.

Figure 5.2 – Snapshots of the velocity fields (in m/s) at $t = 0.16\,\text{s}$ in the case of a homogeneous periodic cell and an excitation by a pulse with central frequency $f_c = 10\,\text{Hz}$ (i.e. $\eta = 0.26$)

are correctly captured by the first-order corrector but not by the zeroth-order effective field which only describes a mean field.

Figure 5.3 then illustrates the influence of the central frequency by considering two central frequencies, $f_c = 10\,\text{Hz}$ (i.e. $\eta = 0.26$), and $f_c = 20\,\text{Hz}$ (i.e. $\eta = 0.52$). The first-order corrector captures adequately the main wavefield variations. However, as expected, the agreement between V_h and $V^{(1)}$ is deteriorating as the frequency increases and η goes to 1. Indeed, one can notice that the homogenized model does not capture the high-frequency oscillations that appear after the passing of the main wave front.

5.2 Extension to non-linear interfaces

The previous results have been extended to the case of non-linear contacts in Bellis et al., 2021. Non-linear conditions can model complex interface phenomena, such as the generation of higher- or

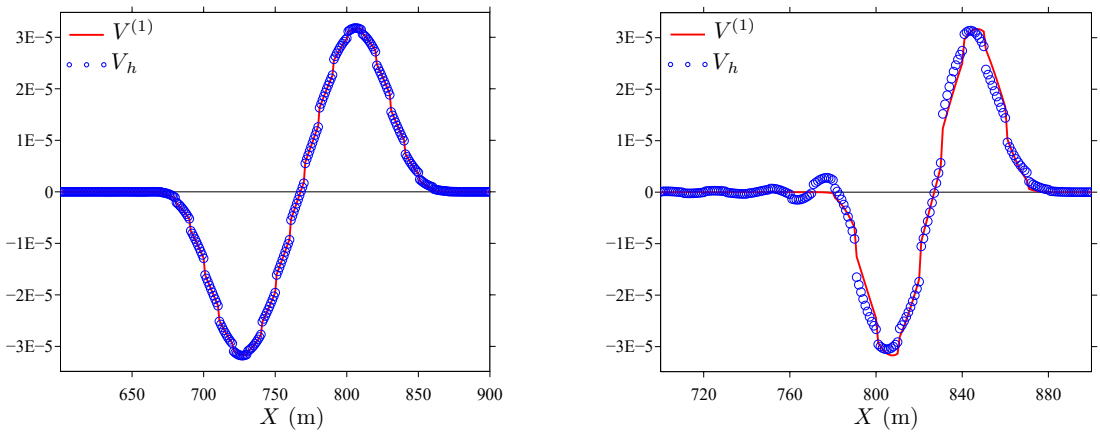

(a) $f_c = 10\,\text{Hz}$ (i.e. $\eta = 0.26$) (b) $f_c = 20\,\text{Hz}$ (i.e. $\eta = 0.52$)

Figure 5.3 – Superposition of the fields V_h and $V^{(1)}$ (in m/s) at $t = 0.16\,\text{s}$ in the case of a homogeneous periodic cell for two different central frequencies.

sub-harmonics, hysteretic or chaotic behaviors, slow dynamics (Gusev, Castagnède, & Moussatov, 2003; Pecorari, 2003; Broda, Staszewski, Martowicz, Uhl, & Silberschmidt, 2014). The study focused on smooth non-linear interface laws, such as those that model elastic interphases or joints (Achenbach & Norris, 1982; Bandis, Lumsden, & Barton, 1984).

5.2.1 Non-linear setting

More precisely, the interfaces are still characterized by the interface *mass* and *rigidity* parameters M and K, but also by a *non-linear*, constitutive relation $\mathcal{R}$, so that the following transmission conditions apply at any interface point X_n:

$$\begin{cases} M \left\langle\!\!\left\langle \dfrac{\partial^2 U_h}{\partial t^2}(\cdot,t) \right\rangle\!\!\right\rangle_{X_n} = \left[\!\left[\Sigma_h(\cdot,t) \right]\!\right]_{X_n} & \text{(5.68a)} \\ \langle\!\langle \Sigma_h(\cdot,t) \rangle\!\rangle_{X_n} = K\,\mathcal{R}\left(\left[\!\left[U_h(\cdot,t) \right]\!\right]_{X_n} \right). & \text{(5.68b)} \end{cases}$$

In this non-linear setting, the interface parameters satisfy the following assumption.

Assumption 5.3

The imperfect interfaces are such that $M \geq 0$ and $K > 0$, while $\mathcal{R}$ is a *smooth* function satisfying

$$\mathcal{R} : (-d, +\infty) \longrightarrow \mathbb{R} \quad \text{such that} \quad \mathcal{R}(0) = 0, \quad \mathcal{R}' > 0 \quad \text{and} \quad (\mathcal{R}'' < 0 \text{ or } \mathcal{R}'' = 0),$$

where $d \in \mathbb{R}_+ \cup \{+\infty\}$ is a *maximum compressibility length* and $\mathcal{R}'$, $\mathcal{R}''$ are the first and second derivatives of $\mathcal{R}$, respectively.

Remark 16. *The linear behaviour of Section 5.1 is obtained for $\mathcal{R}$ being defined as $\mathcal{R}(\zeta) = \zeta$. A simple non-linear model satisfying Assumptions 5.3 and used in practice in Bellis et al., 2021 is the hyperbolic model (Achenbach & Norris, 1982; Bandis et al., 1984) defined by*

$$\mathcal{R}(\zeta) = \frac{\zeta}{1 + \zeta/d}. \tag{5.69}$$

Assumption 5.4

Moreover, as in the linear case (5.1), a source term F is considered. However, contrary to the linear case, it is assumed that the forcing is of low-amplitude so that the amplitude does not involve an additional scaling in η, at least at short times.

Property 7. *These assumptions on the model parameters and constitutive function are sufficient for the well-posedness of the solution in the case of an array of non-linear interfaces. Indeed, as for Property 6, one can prove that the conservation energy (5.5) still holds in the non-linear case, upon changing the interface energy into:*

$$\mathscr{E}_h^i(t) = \sum_{n\in\mathbb{Z}/\,X_n\in I} \left\{ \frac{1}{2} M \left\langle\!\!\left\langle V_h(\cdot,t) \right\rangle\!\!\right\rangle_{X_n}^2 + K \int_0^{\mathcal{R}^{-1}\left(\langle\!\langle \Sigma_h(\cdot,t)\rangle\!\rangle_{X_n}/K\right)} \mathcal{R}(\zeta)\,\mathrm{d}\zeta \right\}. \tag{5.70}$$

5.2.2 Overview of the main homogenization results

A method similar to the one presented in the previous section for the linear case has been deployed in Bellis et al., 2021. An overview of the resulting model is presented in this section.

5.2.2.1 Zeroth-order homogenized field

It is only assumed that the leading-order term u_0 does not depend on the variable y whereas in the linear case it can be proven rigourously as in Section 5.1.3.1. Then, one can prove that the mean field $U_0(X,t)$ satisfies

Result 5.4: Zeroth-order homogenized field

$$\rho_{\text{eff}} \frac{\partial^2 U_0}{\partial t^2}(X,t) = \frac{\partial \Sigma_0}{\partial X}(X,t) + F(X,t), \tag{5.71}$$

with the effective mass density which is unchanged compared to the linear case and given by (5.58). The macroscopic stress field now satisfies the following local but non-linear strain-stress relation

$$\left\langle \frac{1}{\mu} \right\rangle \Sigma_0(X,t) + \frac{1}{h} \mathcal{R}^{-1}\left(\frac{1}{K} \Sigma_0(X,t) \right) = \mathcal{E}_0(X,t), \tag{5.72}$$

where $\mathcal{E}_0 = \partial U_0/\partial X$. The latter macroscopic strain field is therefore related to the macroscopic stress field Σ_0 by the effective *non-linear* constitutive relation (5.72), which we formally write as $\Sigma_0 = \mathcal{G}_{\text{eff}}(\mathcal{E}_0)$.

Remark 5.1. *In the case of the linear interface law, the effective strain-stress relation is linear and writes as*

$$\mathcal{G}_{\text{eff}}(\mathcal{E}_0) = C^{\ell}_{\text{eff}}\,\mathcal{E}_0 \qquad \textit{with} \qquad C^{\ell}_{\text{eff}} = \left(\left\langle \frac{1}{\mu} \right\rangle + \frac{1}{Kh} \right)^{-1}. \tag{5.73}$$

5.2.2.2 First-order homogenized field

Result 5.5: Mean field associated with the first-order homogenized field

The mean displacement field $\overline{U}_1(X,t)$ can be obtained as the solution of the following equation

$$\rho_{\text{eff}}\frac{\partial^2\overline{U}_1}{\partial t^2}(X,t)=\frac{\partial\overline{\Sigma}_1}{\partial X}(X,t)+\mathcal{S}\big(U_0(X,t)\big). \tag{5.74}$$

Here the macroscopic stress field $\overline{\Sigma}_1(X,t)$ satisfies the following *linear* and *heterogeneous* constitutive relation

$$\overline{\Sigma}_1(X,t)=\mathcal{G}'_{\text{eff}}\big(\mathcal{E}_0(X,t)\big)\frac{\partial\overline{U}_1}{\partial X}(X,t), \tag{5.75}$$

while the source term $\mathcal{S}(U_0)$ is given by

$$\mathcal{S}\big(U_0(X,t)\big)=\langle\rho\rangle\left\langle\frac{1}{\mu}\right\rangle\left\{\mathcal{B}-\langle\alpha\, b\rangle+\frac{M}{h\,\langle\rho\rangle}\left(\mathcal{B}-\frac{1}{2}\right)\right\}\mathcal{G}''_{\text{eff}}(\mathcal{E}_0)\left\{\left(\frac{\partial^2U_0}{\partial X\partial t}\right)^2-\frac{\partial^2U_0}{\partial X^2}\frac{\partial^2U_0}{\partial t^2}\right\}.$$

Eventually, the expression of the *total field* $U_1(X,t)=u_1(x,y,\tau)$ is

Result 5.6: First-order homogenized field

$$\begin{aligned}&U_1(X,t)=\overline{U}_1(X,t)+\mathcal{P}\big(y,\mathcal{E}_0(X,t)\big)\,\mathcal{E}_0(X,t),\\ \text{with}\qquad &\mathcal{P}\big(y,\mathcal{E}_0(X,t)\big)=\left(\frac{1}{2}-y\right)+\big(b(y)-\mathcal{B}\big)\left\langle\frac{1}{\mu}\right\rangle\frac{\mathcal{G}_{\text{eff}}\big(\mathcal{E}_0(X,t)\big)}{\mathcal{E}_0(X,t)}\end{aligned} \tag{5.76}$$

a *cell function* which depends explicitly and in a non-linear fashion on $\mathcal{E}_0(X,t)$.

5.2.2.3 Main properties

In Bellis et al., 2021, we have shown that the following properties hold in the non-linear case.

■ *Hyperbolicity.* As in the linear case in (5.64), the non-linear equations (5.71)–(5.72) for the zeroth-order mean field $U_0(X,t)$ can be written in condensed form as

$$\frac{\partial}{\partial t}\boldsymbol{\Psi}_0(X,t)+\frac{\partial}{\partial X}\Big(\mathbb{G}_{\text{eff}}\big(\boldsymbol{\Psi}_0(X,t)\big)\Big)=\boldsymbol{F}(X,t)\qquad\text{with}\qquad\boldsymbol{\Psi}_0=\big(\mathcal{E}_0,V_0\big)^{\top}, \tag{5.77}$$

and where $\mathbb{G}_{\text{eff}}$ is a function from $\mathbb{R}^2$ into itself, while $\boldsymbol{F}=\big(0,F/\rho_{\text{eff}}\big)^{\top}$. This is a first-order system which is strictly hyperbolic and whose characteristic speeds are the eigenvalues of the Jacobian matrix $\mathbb{G}'_{\text{eff}}$. They are strain-dependent and write as

$$v_{\pm}(\mathcal{E}_0)=\pm\sqrt{\frac{1}{\rho_{\text{eff}}}\frac{\partial\Sigma_0}{\partial\mathcal{E}_0}}.$$

Moreover, except in the limit case of linear interfaces, the system is *genuinely non-linear*. It implies in particular that there exists a solution to the Cauchy problem, see Dafermos, 2005, and that the waves connecting piecewise constant states are either shocks or rarefaction waves, a property that is at the foundation of some efficient numerical methods, see Godlewski and Raviart, 2013.

The equations (5.74–5.75) for the mean field $\overline{U}_1(X,t)$ can be recast as the following first-order system:

$$\frac{\partial}{\partial t}\overline{\boldsymbol{\Psi}}_1(X,t)+\frac{\partial}{\partial X}\Big(\mathbb{G}'_{\text{eff}}\big(\boldsymbol{\Psi}_0(X,t)\big)\,\overline{\boldsymbol{\Psi}}_1(X,t)\Big)=\boldsymbol{S}\big(\boldsymbol{\Psi}_0(X,t)\big)\qquad\text{with}\qquad\overline{\boldsymbol{\Psi}}_1=\big(\overline{\mathcal{E}}_1,\overline{V}_1\big)^{\top},\tag{5.78}$$

while $\boldsymbol{S}=\big(0,\mathcal{S}(U_0)/\rho_{\text{eff}}\big)^{\top}$. This is a linear and strictly hyperbolic system, whose characteristic speeds are identically equal to those of the first-order system (5.77) for the zeroth-order mean field $\big(\mathcal{E}_0,V_0\big)$.

■ *Energy analysis for the zeroth-order homogenized model.* For an interval $I\subset\mathbb{R}$ and a time $t\geq 0$, the effective energy $\mathscr{E}_0=\mathscr{E}_0^m+\mathscr{E}_0^i$ with

$$\begin{cases}\mathscr{E}_0^m(t)=\dfrac{1}{2}\displaystyle\int_I\left\{\big\langle\rho\big\rangle\,V_0^2+\left\langle\frac{1}{E}\right\rangle\Sigma_0^2\right\}\mathrm{d}X,&(5.79a)\\[2ex]\mathscr{E}_0^i(t)=\dfrac{1}{h}\displaystyle\int_I\left\{\frac{1}{2}MV_0^2+K\int_0^{\mathcal{R}^{-1}(\Sigma_0/K)}\mathcal{R}(\zeta)\,\mathrm{d}\zeta\right\}\mathrm{d}X,&(5.79b)\end{cases}$$

is the effective mechanical energy associated with the zeroth-order homogenized model. These terms are respectively associated with the bulk and interface energies of the microstructured problem, and satisfy $\mathscr{E}_0^m(t)\geq 0$ and $\mathscr{E}_0^i(t)\geq 0$ for all time $t\geq 0$.
Lastly, if V_0 and $\mathcal{E}_0$ are both sufficiently smooth and compactly supported at time $t=0$, then in the absence of source term, i.e. $F=0$, it holds $\frac{\mathrm{d}}{\mathrm{d}t}\mathscr{E}_0=0$ for all time t such that $\mathrm{supp}(V_0(\cdot,t))\subset I$ and $\mathrm{supp}(\mathcal{E}_0(\cdot,t))\subset I$.
A fundamental difference occurs between the microstructured and homogenized models, due to the non-linearity of the partial differential equation (5.77), which yields the formation of shocks in a finite time. The total effective energy $\mathscr{E}_0$ is conserved as long as shocks do not appear and then there is dissipation of energy contrary to the microstructured configuration.

■ *Estimation of the time of apparition of shocks.* At small strains, the effective stress-strain relation can be expanded at the second order as:

$$\Sigma_0\underset{\mathcal{E}_0\to 0}{\sim}\mathcal{G}'_{\text{eff}}(0)\,\mathcal{E}_0\,\big(1-\gamma\,\mathcal{E}_0\big)+o(\mathcal{E}_0^2)\qquad\text{with}\qquad\mathcal{G}'_{\text{eff}}(0)>0\text{ and }\gamma\geq 0,\tag{5.80}$$

since $\mathcal{G}_{\text{eff}}(0)=0$ and given that $\mathcal{G}_{\text{eff}}$ is a concave and strictly increasing function. Considering the small strains quadratic non-linear constitutive law (5.80), then P. Lax derived an estimated time $t^\star$ when shocks would appear, see Lax, 1957; Lax, 1964. Given a Cauchy problem with sinusoidal strain of amplitude $\mathcal{E}_{\text{max}}$ and angular frequency $\omega_c=2\pi f_c$, we obtain

$$t^\star\approx\frac{1}{\mathcal{E}_{\text{max}}\gamma\,\omega_c}+\frac{1}{2f_c},\tag{5.81}$$

with the additional term $1/(2f_c)$ being the time required for the source to generate a complete sinus arch. In the linear case, i.e. in the small strain limit, a monochromatic forcing of amplitude A leads to $\mathcal{E}_{\text{max}}=A\rho_{\text{eff}}/C_{\text{eff}}^{\ell}$.
Logically, $t^\star$ is inversely proportional to both the non-linearity coefficient γ of (5.80) and to the amplitude $\mathcal{E}_{\text{max}}$, as the larger these parameters are the stronger the non-linear effects are. Shocks occur beyond $t^\star$ and the total energy $\mathscr{E}_0$ then decreases, contrary to the case of the microstructured medium. Consequently, (5.81) can be interpreted as an upper bound of the duration of validity of the derived effective models.

5.2.3 Overview of the numerical results

Numerical simulations have been performed for the hyperbolic non-linear constitutive relation (5.69) of the interface function by Bruno Lombard in Bellis et al., 2021. An overview of the numerical results obtained for the monolayered case is given in this subsection to illustrate the zeroth- and first-order effective models presented previously. The microstructured configuration is the same as in Section 5.1.6. The additional parameter characterizing the non-linearity is $d = 10^{-4}$ m.

In both the microstructured and the homogenized configurations, numerical simulations are performed on a uniform grid using a finite-volume scheme with flux limiters (LeVeque, 2002). In the microstructured configuration, the interfaces are handled using the Explicit Simplified Interface Method (Lombard & Piraux, 2007; Junca & Lombard, 2009; Junca & Lombard, 2012) discussed in Section 1.3.2.

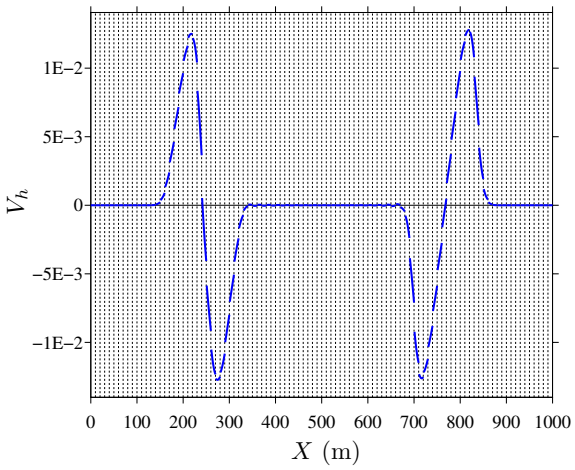

(a) Field V_h in the microstructured medium.

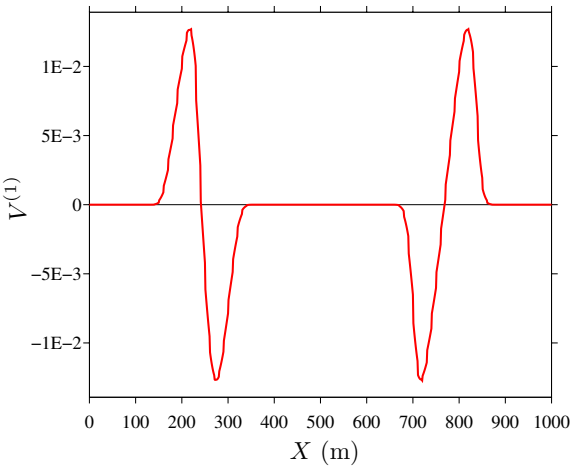

(b) First-order homogenized field $V^{(1)}$.

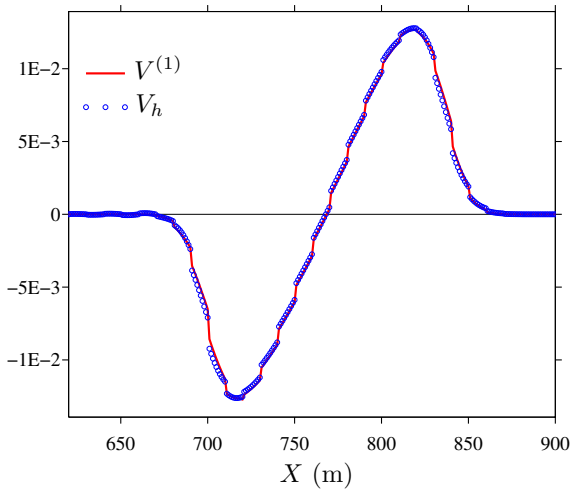

(c) Superposition of the fields V_h and $V^{(1)}$.

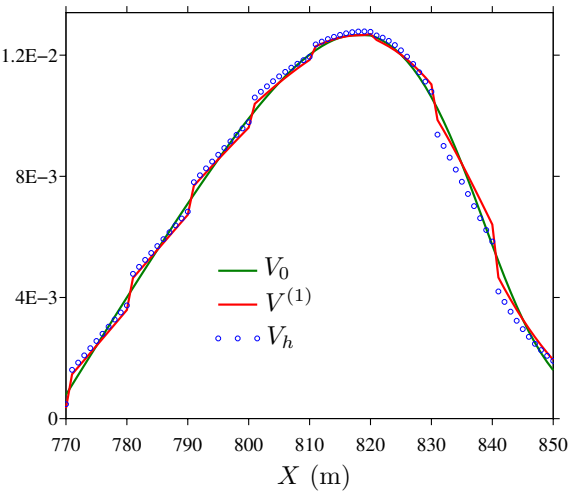

(d) Close-up showing the zeroth- and first-order homogenized fields V_0 and $V^{(1)}$, respectively, and V_h.

Figure 5.4 – Snapshots of the velocity fields (in m/s) at $t = 0.16$ s in the case of a homogeneous periodic cell and an excitation by a pulse with central frequency $f_c = 10$ Hz (i.e. $\eta = 0.26$) and amplitude $A = 40$.

The source term has been defined in (5.67). The difference in the non-linear case is that increasing the source amplitude A induces stronger non-linear phenomena. However, in the model derivation in Section 5.2.2, it is assumed that the forcing is of low-amplitude so that the amplitude

does not involve an additional scaling in η, at least at short times. This requirement does not occur in the linear case treated in Section 5.1. Consequently, the influence of the central frequency and the amplitude of the forcing is numerically investigated.

Figure 5.4 corresponds to an excitation at the central frequency $f_c = 10\,\text{Hz}$, associated with the value $\eta = 0.26$, and amplitude $A = 40$. As in the linear case, one can see a good agreement between the velocity in the microstructured configuration V_h and the result of the first-order homogenization $V^{(1)}$ with local fluctuations of V_h which are correctly captured by the first-order corrector but not by the zeroth-order effective field.

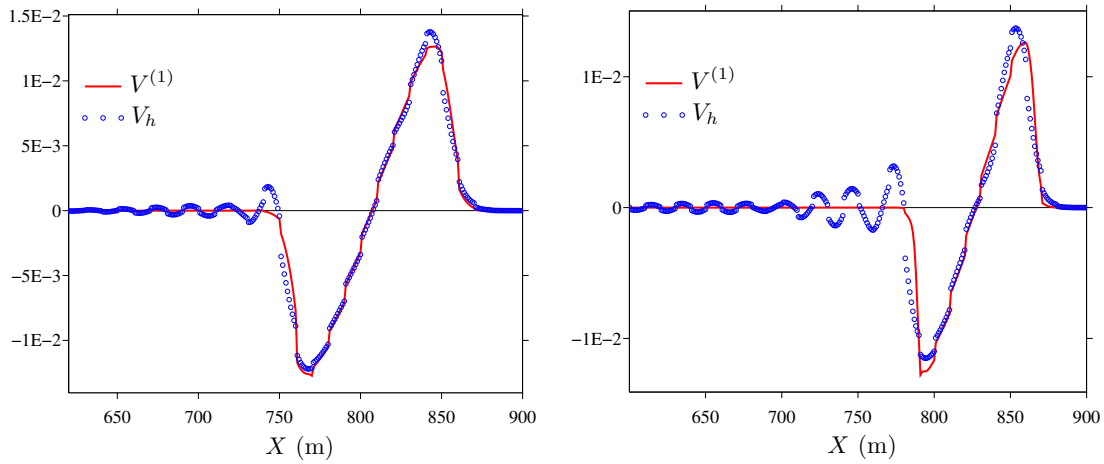

(a) $f_c = 15\,\text{Hz}$ (i.e. $\eta = 0.39$) (b) $f_c = 20\,\text{Hz}$ (i.e. $\eta = 0.52$)

Figure 5.5 – Superposition of the fields V_h and $V^{(1)}$ (in m/s) at $t = 0.16\,\text{s}$ with close-up on the right-going waves in the case of a homogeneous periodic cell and a source of amplitude $A = 40$, for two different central frequencies.

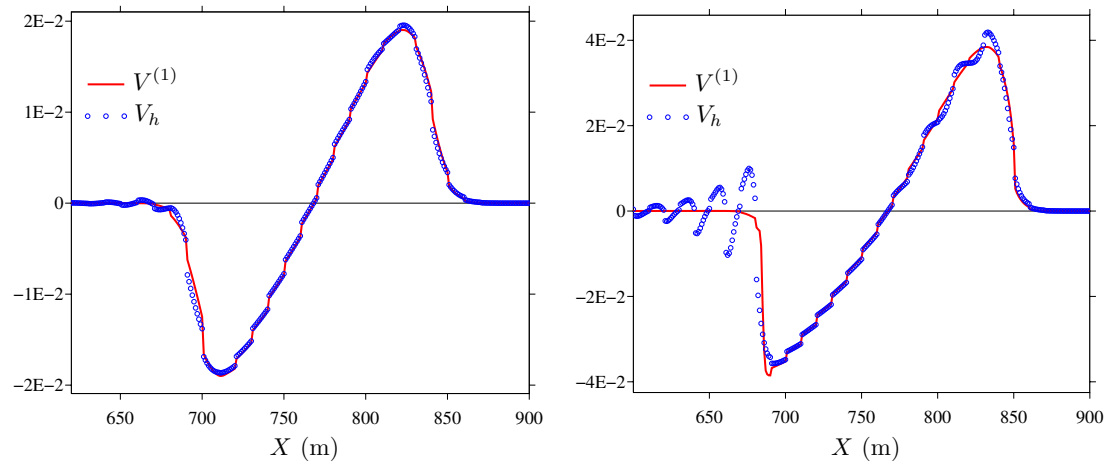

(a) $A = 60$. (b) $A = 120$.

Figure 5.6 – Superposition of the fields V_h and $V^{(1)}$ (in m/s) at $t = 0.16\,\text{s}$ with close-up on the right-going waves in the case of a homogeneous periodic cell and a source at central frequency $f_c = 10\,\text{Hz}$ (i.e. $\eta = 0.26$), for two different amplitudes.

■ *Influence of the central frequency.* At the amplitude value $A = 40$, as in Figure 5.4, Figure 5.5 illustrates the influence of the central frequency by considering relatively larger values of f_c and

consequently of the parameter η. For both frequencies, $f_c = 15\,\text{Hz}$ (i.e. $\eta = 0.39$) and $f_c = 20\,\text{Hz}$ (i.e. $\eta = 0.52$), the first-order corrector still captures adequately the main wavefield variations. However, this homogenized model is non-dispersive and does not capture the high-frequency oscillations that appear after the main wave front. As expected, at higher frequencies, the agreement between V_h and $V^{(1)}$ is deteriorating and dispersive effects increase with time of propagation.

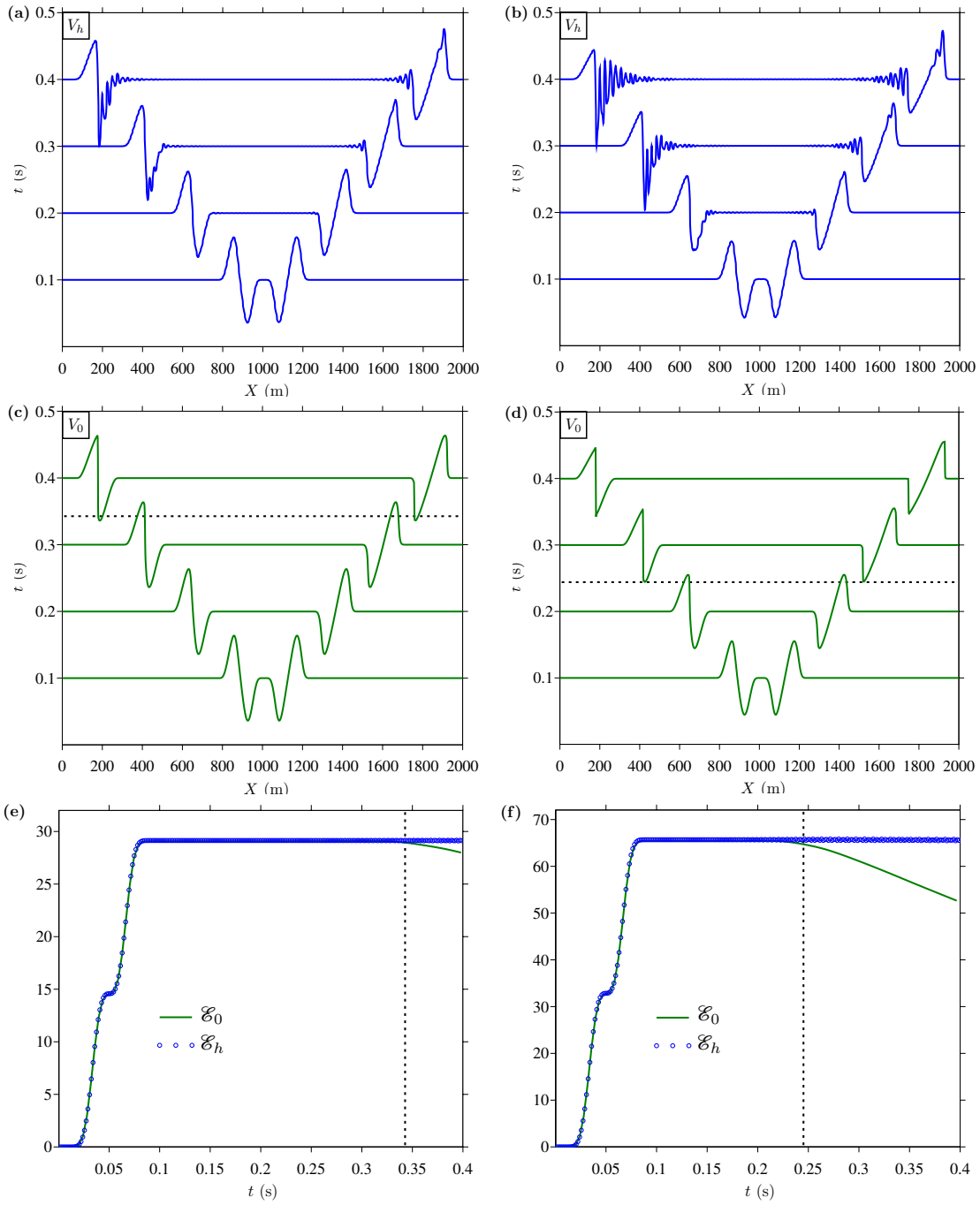

Figure 5.7 – Case of a homogeneous periodic cell and an excitation by a pulse centered at $f_c = 10\,\text{Hz}$ with amplitude $A = 40$ (left panels) and $A = 60$ (right panels). Top: seismograms of V_h in the microstructured medium. Middle: seismograms of the homogenized field V_0. Bottom: superposition and time evolution of the energies $\mathscr{E}_h$ and $\mathscr{E}_0$. The dotted lines denote the estimated time $t^\star$ for each case.

■ *Influence of the source amplitude.* Then, the central frequency is kept as in Figure 5.4, i.e. $f_c = 10\,\text{Hz}$ so that $\eta = 0.26$, but the source amplitude is now increased to $A = 60$ and $A = 120$ in Figure

5.6. As A increases, the stiffening of the wave fronts becomes more apparent and the oscillations increase at the scale of the microstructure. The latter are not captured by the homogenized model and this illustrates that the associated configurations are beyond the implicit assumption of a relatively low source amplitude in the non-linear case.

■ *Formation of shocks.* It has been discussed in Section 5.2.2.3 that the zeroth-order homogenized model allows the formation of shocks in a finite time, unlike the microstructured media. As it can be seen from the figures 5.5b and 5.6b, shocks can also develop in a finite time with the first-order model.
This discussion is now illustrated numerically in Figure 5.7. The computational domain is $[0, 2000]$ m and the source with central frequency $f_c = 10$ Hz and amplitude $A = 40$ (left column) or $A = 60$ (right column) is placed at $X_s = 1010$ m, i.e. at the center of a cell. The top (resp. middle) panels correspond to seismograms of the velocity field V_h (resp. V_0). The bottom panels show the temporal evolutions of the energies in the microstructured medium and in the homogenized one, i.e. $\mathscr{E}_h$ and $\mathscr{E}_0$ respectively.

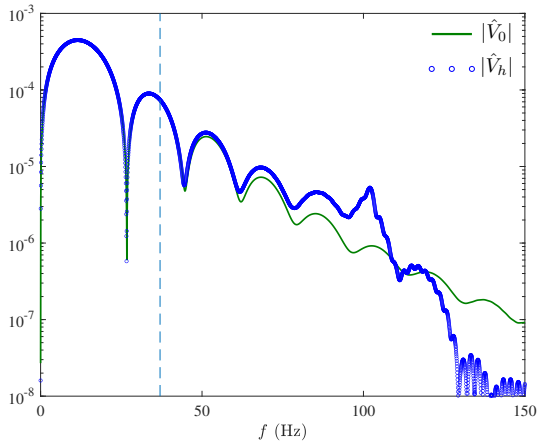

(a) $A = 40$ and X_{r1}.

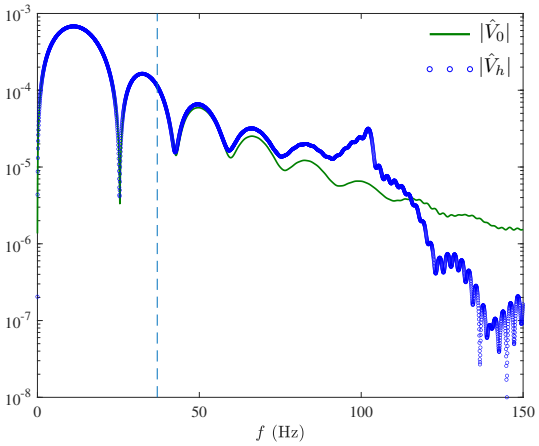

(b) $A = 60$ and X_{r1}.

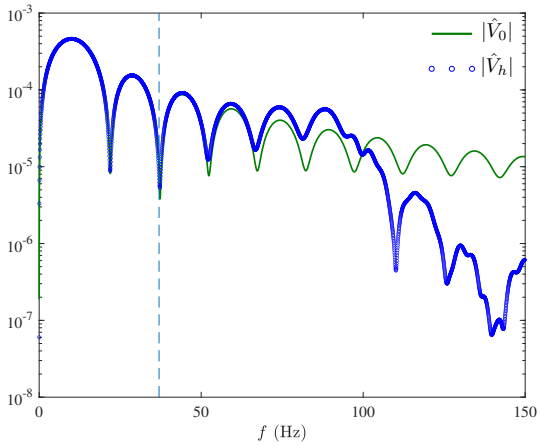

(c) $A = 40$ and X_{r2}.

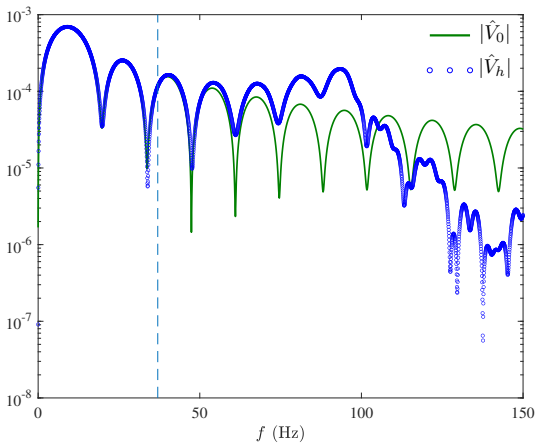

(d) $A = 60$ and X_{r2}.

Figure 5.8 – Case of a homogeneous periodic cell and an excitation by a pulse centered at $f_c = 10$ Hz with amplitude $A = 40$ (left panels) and $A = 60$ (right panels), as in Figure 5.7. Spectra of the velocity fields V_h and V_0 recorded at two receivers placed at $X_{r1} = 1205$ m and $X_{r2} = 1705$ m. The vertical dashed line indicates the value of the frequency that corresponds to $\eta = 1$.

In each case, the dotted lines denote the estimated time $t^\star$ which is an estimation of the time of apparition of shocks for the small strain limit and a monochromatic forcing (5.81). This time

is therefore assumed to be an estimation of the time of apparition of shocks and consequently of the duration of validity of the homogenized model. For $t < t^*$ a good agreement is observed for both the wavefields and the energies. Near $t = t^\star$, the effective energy $\mathscr{E}_0$ starts to decrease, which is typical of a shock formation, as can be observed in Fig. 5.7c and 5.7d. In the mean time, the energy $\mathscr{E}_h$ in the microstructured media is conserved, as expected. Dispersive effects are again clearly visible in Fig.5.7a and 5.7b with high-frequency oscillations.

Figure 5.8 illustrates the influence of the shocks on the spectral content of the waves. Considering the configuration of Figure 5.7, two receivers are placed at $X_{r1} = 1205\,\text{m}$ and $X_{r2} = 1705\,\text{m}$, i.e. both at the center of a cell near the source and further away. The propagation distance at X_{r1} (resp. X_{r2}) is about one (resp. three) wavelength relatively to the central frequency f_c. Figure 5.8 then represents the discrete Fourier spectra of the recorded time-domain signals for the two forcing amplitudes $A = 40$ and $A = 60$ considered. The waves reach the receiver X_{r1} before the time $t^\star$, so that no shock has formed yet in the homogenized media. We then note a satisfying agreement between the microstructured and the effective spectra at low frequency, see Fig. 5.8a and 5.8b. When recorded at the receiver X_{r2}, the wavefield V_0 has now formed a shock while V_h is characterized by stronger dispersive effects, as previously observed. Accordingly, we notice significant enrichments of the associated spectra, see Fig. 5.8c and 5.8d. In particular, the spectra associated with V_0 now behave as sinc functions, which is characteristic of the Fourier transforms of discontinuous functions. While at frequencies $f \geq 37\,\text{Hz}$, which corresponds to $\eta = 1$, the Fourier contents associated with these two models are clearly different, they still agree relatively well for lower frequencies $f \leq 37\,\text{Hz}$.

5.3 2D/3D elastic media with linear interfaces

In this section, we now generalize to $\mathbb{R}^N$, with $N = 2$ or 3 (see Figure 5.9 for $N = 2$), the results of Section 5.1 concerning linear interfaces. The space coordinate is denoted by $\boldsymbol{X}$ and one introduces $X_i = \boldsymbol{X} \cdot \boldsymbol{e}_i$, for $i \in \{1 \cdots N\}$. The 1D setting is particular in the sense that integrations can be performed explicitely instead of computing solutions of cell problems, which cannot be avoided in higher dimensions. Therefore, the extension to higher dimensions is not straightforward and is the subject of this section.

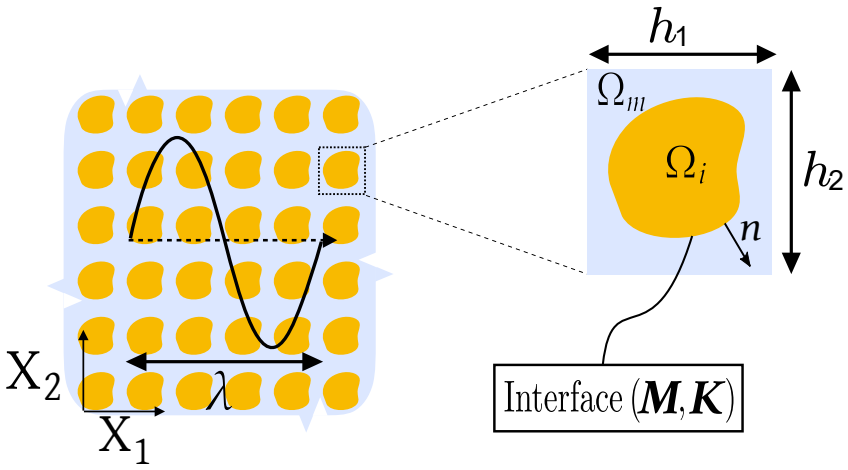

Figure 5.9 – Microstructured configuration in the 2D case with imperfect interfaces.

5.3.1 Setting

We consider the propagation of transient waves in a elastic medium made of inclusions $\cup_i \Omega_i$ embedded periodically in a homogeneous matrix Ω_m. The elastic medium is assumed to be $\boldsymbol{h}$-periodic, with $h_i = \boldsymbol{h}\cdot\boldsymbol{e}_i$ and $h = \max_{i=1,\cdots,N} h_i$. The medium is linear elastic with mass density $\rho_h(\boldsymbol{X})$ and fourth-order elasticity tensor $\boldsymbol{C}_h(\boldsymbol{X})$. Given a source term $\boldsymbol{F}$, the displacement field $\boldsymbol{U}_h$ is governed by the time-domain wave equation

$$\rho_h(\boldsymbol{X})\frac{\partial^2 \boldsymbol{U}_h}{\partial t^2}(\boldsymbol{X},t) = \nabla\cdot\boldsymbol{\Sigma}_h(\boldsymbol{X},t) + \boldsymbol{F}(\boldsymbol{X},t) \tag{5.82}$$

where

$$\boldsymbol{\Sigma}_h(\boldsymbol{X},t) = \boldsymbol{C}_h(\boldsymbol{X}) : \boldsymbol{\varepsilon}\left[\boldsymbol{U}_h\right](\boldsymbol{X},t), \tag{5.83}$$

with $\boldsymbol{\Sigma}_h$ being the stress tensor and $\boldsymbol{\varepsilon}_{\boldsymbol{X}}\left[\boldsymbol{U}_h\right]$ being the strain tensor. Moreover, the interfaces $\partial\Omega_i$ are assumed to be linear and characterized by the interface *mass* and *rigidity* second-order tensors $\boldsymbol{M}$ and $\boldsymbol{K}$ so that the following transmission conditions apply at each interface $\partial\Omega_i$:

$$\begin{cases} \boldsymbol{M}\cdot\left\langle\!\!\left\langle \dfrac{\partial^2\boldsymbol{U}_h}{\partial t^2}(\cdot,t)\right\rangle\!\!\right\rangle_{\boldsymbol{X}} = \left[\!\left[\boldsymbol{\Sigma}_h(\cdot,t)\cdot\boldsymbol{n}\right]\!\right]_{\boldsymbol{X}} & (\boldsymbol{X}\in\partial\Omega_i), \\ \left\langle\!\!\left\langle\boldsymbol{\Sigma}_h(\cdot,t)\cdot\boldsymbol{n}\right\rangle\!\!\right\rangle_{\boldsymbol{X}} = \boldsymbol{K}\cdot\left[\!\left[\boldsymbol{U}_h(\cdot,t)\right]\!\right]_{\boldsymbol{X}} & (\boldsymbol{X}\in\partial\Omega_i), \end{cases} \tag{5.84}$$

where $\boldsymbol{n}$ is the outward normal to the inclusion. For any function $g(\boldsymbol{X})$, one generalizes the definitions of the jump and mean in $\mathbb{R}^N$ as

$$\left[\!\left[g\right]\!\right]_{\boldsymbol{X}} = g(\boldsymbol{X}^+) - g(\boldsymbol{X}^-) \qquad \text{and} \qquad \left\langle\!\!\left\langle g\right\rangle\!\!\right\rangle_{\boldsymbol{X}} = \frac{1}{2}\left(g(\boldsymbol{X}^+) + g(\boldsymbol{X}^-)\right), \tag{5.85}$$

for $\boldsymbol{X}\in\partial\Omega_i$ and where the superscript + (resp. −) stands for the Ω_m (resp. Ω_i) side.
The constitutive parameters characterizing the microstructured medium considered satisfy the following mathematical assumptions.

Assumption 5.5

The mass density is expressed as $\rho_h(\boldsymbol{X}) = \rho(\boldsymbol{X}/h)$ and the fourth-order elasticity tensor reads $\boldsymbol{C}_h(\boldsymbol{X}) = \boldsymbol{C}(\boldsymbol{X}/h)$, where

$$\rho, C_{jklm} \in L^\infty_{\text{per}}(\boldsymbol{\mathcal{Y}}) := \left\{ g\in L^\infty(\mathbb{R}^N),\ \forall i\in\{1,\cdots,N\},\ g\left(\boldsymbol{y}+\frac{h_i}{h}\boldsymbol{e}_i\right) = g(\boldsymbol{y}) \text{ a.e. } \boldsymbol{y}\in\mathbb{R}^N \right\} \tag{5.86}$$

with $\rho \geq \rho_{\min} > 0$, and $\boldsymbol{C}$ positive definite.

Assumption 5.6

The second-order tensors $\boldsymbol{M}$ and $\boldsymbol{K}$ can be written $\boldsymbol{M} = M_n\,\boldsymbol{n}\otimes\boldsymbol{n} + M_t\,\boldsymbol{t}\otimes\boldsymbol{t}$ and $\boldsymbol{K} = K_n\,\boldsymbol{n}\otimes\boldsymbol{n} + K_t\,\boldsymbol{t}\otimes\boldsymbol{t}$ with $\boldsymbol{n}$ and $\boldsymbol{t}$ the normal and the tangent unitary vectors, respectively, at the interfaces matrix/inclusion. We assume that $M_n \geq 0$, $M_t \geq 0$, $K_n > 0$ and $K_t > 0$.

Property 8. *The problem* (5.82)–(5.83) *together with* (5.84) *is well posed. Indeed, one introduces the* bulk *energy and the* interface *energy respectively as*

$$\begin{cases} \mathscr{E}_h^m(t) = \dfrac{1}{2}\displaystyle\int_{\mathcal{D}} \left\{\rho_h(\boldsymbol{X})\boldsymbol{V}_h(\boldsymbol{X},t)^2 + \boldsymbol{\varepsilon}\left[\boldsymbol{U}_h\right](\boldsymbol{X},t) : \boldsymbol{C}_h(\boldsymbol{X}) : \boldsymbol{\varepsilon}\left[\boldsymbol{U}_h\right](\boldsymbol{X},t)\right\}\mathrm{d}\boldsymbol{X}, & \text{(5.87a)} \\ \mathscr{E}_h^i(t) = \displaystyle\sum_{\partial\Omega_i\in\mathcal{D}} \int_{\partial\Omega_i} \frac{1}{2}\left\{\left\langle\!\!\left\langle\boldsymbol{V}_h\right\rangle\!\!\right\rangle_{\boldsymbol{X}}\cdot\boldsymbol{M}\cdot\left\langle\!\!\left\langle\boldsymbol{V}_h\right\rangle\!\!\right\rangle_{\boldsymbol{X}} + \left[\!\left[\boldsymbol{U}_h\right]\!\right]_{\boldsymbol{X}}\cdot\boldsymbol{K}\cdot\left[\!\left[\boldsymbol{U}_h\right]\!\right]_{\boldsymbol{X}}\right\}\mathrm{d}\boldsymbol{X}, & \text{(5.87b)} \end{cases}$$

with $\boldsymbol{V}_h = \frac{\partial \boldsymbol{U}_h}{\partial t}$. *The domain* $\mathcal{D}$ *is chosen such that the boundary* $\partial\mathcal{D}$ *does not intersect an interface* $\partial\Omega_i$. *Then, if the source term* $\boldsymbol{F} = \boldsymbol{0}$, *and if* $\mathcal{D}$ *is large enough so that the boundary terms vanish, the following conservation identity holds for the total energy*

$$\frac{\mathrm{d}}{\mathrm{d}t}\left(\mathscr{E}_h^m + \mathscr{E}_h^i\right) = 0. \tag{5.88}$$

Proof. One considers the dot product of (5.82) and $\boldsymbol{V_h}$, one uses (5.83), and one integrates over $\mathcal{D}$. Then, when $\boldsymbol{F} = \boldsymbol{0}$ and when $\mathcal{D}$ is chosen large enough so that the boundary terms vanish, an integration by parts yields:

$$\int_{\mathcal{D}} \rho_h \frac{\partial \boldsymbol{V}_h}{\partial t} \cdot \boldsymbol{V}_h \,\mathrm{d}\boldsymbol{X} = -\sum_{\partial\Omega_i \in \mathcal{D}} \int_{\partial\Omega_i} [\![\boldsymbol{\Sigma}_h \cdot \boldsymbol{n} \cdot \boldsymbol{V}_h]\!]_X \,\mathrm{d}\boldsymbol{X} - \int_{\mathcal{D}} \boldsymbol{\varepsilon}[\boldsymbol{V}_h] : \boldsymbol{C}_h : \boldsymbol{\varepsilon}[\boldsymbol{U}_h]. \tag{5.89}$$

Due to the interface conditions (5.84), the jump term writes

$$\begin{aligned} [\![\boldsymbol{\Sigma}_h \cdot \boldsymbol{n} \cdot \boldsymbol{V}_h]\!]_X &= [\![\boldsymbol{\Sigma}_h \cdot \boldsymbol{n}]\!]_X \cdot \langle\!\langle \boldsymbol{V}_h \rangle\!\rangle_X + \langle\!\langle \boldsymbol{\Sigma}_h \cdot \boldsymbol{n} \rangle\!\rangle_X \cdot [\![\boldsymbol{V}_h]\!]_X \\ &= \left(\boldsymbol{M} \cdot \left\langle\!\left\langle \frac{\partial \boldsymbol{V}_h}{\partial t} \right\rangle\!\right\rangle_X\right) \cdot \langle\!\langle \boldsymbol{V}_h \rangle\!\rangle_X + (\boldsymbol{K} \cdot [\![\boldsymbol{U}_h]\!]_X) \cdot \left[\!\left[\frac{\boldsymbol{U}_h}{\partial t} \right]\!\right]_X. \end{aligned} \tag{5.90}$$

Furthermore, one assumes sufficient smoothness for $\boldsymbol{f} = \boldsymbol{U}_h$ or $\boldsymbol{V}_h$ so that

$$\left[\!\left[\frac{\partial \boldsymbol{f}}{\partial t} \right]\!\right]_X = \frac{\mathrm{d}}{\mathrm{d}t} [\![\boldsymbol{f}]\!]_X \qquad \text{and} \qquad \left\langle\!\left\langle \frac{\partial \boldsymbol{f}}{\partial t} \right\rangle\!\right\rangle_X = \frac{\mathrm{d}}{\mathrm{d}t} \langle\!\langle \boldsymbol{f} \rangle\!\rangle_X. \tag{5.91}$$

Consequently, the balance of energy holds. □

Eventually, the low-frequency hypothesis Assumption 5.2 $\eta = hk^\star \ll 1$ still holds.

5.3.2 Two-scale expansion

One considers some reference material parameters $\rho^\star$ and $E^\star$, for example (5.32) and (5.26), that define the wavespeed $c^\star = \sqrt{E^\star/\rho^\star}$. Then we follow the same steps as in the 1D case to establish the wave equation and interface conditions satisfied in the nondimensionalized coordinates. We present here the main steps in higher dimensions:

- Definition of non-dimensionalized variables, fields and parameters:

$$\begin{gathered} \boldsymbol{x} = k^\star \boldsymbol{X}, \quad \tau = k^\star c^\star t, \quad \boldsymbol{u}_\eta(\boldsymbol{x}, \tau) = k^\star \boldsymbol{U}_h(\boldsymbol{X}, t), \quad \boldsymbol{f}(\boldsymbol{x}, \tau) = \frac{\boldsymbol{F}(\boldsymbol{X}, t)}{k^\star E^\star}, \\ \alpha = \frac{\rho}{\rho^\star}, \quad \boldsymbol{\beta} = \frac{\boldsymbol{C}}{E^\star}, \quad \boldsymbol{\mathcal{M}} = \frac{\boldsymbol{M}}{h\,\rho^\star}, \quad \boldsymbol{\mathcal{K}} = \frac{\boldsymbol{K}h}{E^\star}. \end{gathered} \tag{5.92}$$

- The rescaled coordinate $\boldsymbol{y} = \boldsymbol{x}/\eta$ is introduced. The parameters α and $\boldsymbol{\beta}$ are assumed to vary on this fast fine scale.

- The field $\boldsymbol{u}_\eta$ is expanded using the following ansatz:

$$\boldsymbol{u}_\eta(\boldsymbol{x}, \tau) = \sum_{j \geq 0} \eta^j \boldsymbol{u}_j(\boldsymbol{x}, \boldsymbol{y}, \tau), \tag{5.93}$$

  where the fields $\boldsymbol{u}_j$ are assumed to be continuous with respect to the first variable and $\boldsymbol{h}/h$-periodic with respect to the second variable.

- The jump and mean notations are extended at the micro-scale as

$$\begin{aligned}\left[\!\left[u_j \right]\!\right]_y &\equiv \left[\!\left[u_j(x,\cdot,\tau) \right]\!\right]_y = u_j(x,y^+,\tau) - u_j(x,y^-,\tau),\\ \left\langle\!\left\langle u_j \right\rangle\!\right\rangle_y &\equiv \left\langle\!\left\langle u_j(x,\cdot,\tau) \right\rangle\!\right\rangle_y = \frac{1}{2}\big(u_j(x,y^+,\tau) + u_j(x,y^-,\tau)\big),\end{aligned} \tag{5.94}$$

  for $x \in \mathbb{R}^N$ and $y \in \partial\Omega_i$.

- The differential operator with respect to x is rewritten as

$$\nabla_x + \frac{1}{\eta}\nabla_y \quad \text{and} \quad \varepsilon_x + \frac{1}{\eta}\varepsilon_y.$$

- One also introduces the unit periodic cell

$$\mathcal{Y} := \left\{ y \in \mathbb{R}^N,\ \forall i \in \{1,\cdots,N\},\ y_i = y\cdot e_i \in \left[0, \frac{h_i}{h}\right] \right\} \tag{5.95}$$

  and later on, $\langle g \rangle = \int_{\mathcal{Y}} g(y)\,\mathrm{d}y$.

These steps yield the nondimentionalized wave equation

$$\begin{aligned}\alpha(y)\frac{\partial^2 u_\eta}{\partial\tau^2} = \frac{1}{\eta^2}\nabla_y\cdot\big(\beta(y) : \varepsilon_y[u_\eta]\big) + \frac{1}{\eta}\Big(\nabla_y\cdot\big(\beta(y) : \varepsilon_x[u_\eta]\big) + \nabla_x\cdot\big(\beta(y) : \varepsilon_y[u_\eta]\big)\Big)\\ + \nabla_x\cdot\big(\beta(y) : \varepsilon_x[u_\eta]\big) + f(x,\tau),\end{aligned} \tag{5.96}$$

and the associated interface conditions for $y \in \partial\Omega_i$

$$\begin{cases} \eta\,\mathcal{M}\cdot\left\langle\!\left\langle \dfrac{\partial^2 u_\eta}{\partial\tau^2} \right\rangle\!\right\rangle_y = \left[\!\left[\beta : \left(\varepsilon_x[u_\eta] + \dfrac{1}{\eta}\varepsilon_y[u_\eta]\right)\cdot n \right]\!\right]_y, & \text{(5.97a)}\\ \left\langle\!\left\langle \beta : \left(\varepsilon_x[u_\eta] + \dfrac{1}{\eta}\varepsilon_y[u_\eta]\right)\cdot n \right\rangle\!\right\rangle_y = \dfrac{1}{\eta}\mathcal{K}\cdot\left[\!\left[u_\eta \right]\!\right]_y. & \text{(5.97b)}\end{cases}$$

The equations (5.96) and (5.97) are used in the next section together with the ansatz (5.93) to derive a homogenized model.

5.3.3 Zeroth-order homogenization

5.3.3.1 Zeroth-order field

One identifies the terms at order $O(\eta^{-2})$ in (5.96) and $O(\eta^{-1})$ in (5.97a) and (5.97b) and gets the following system for the zeroth-order field u_0:

$$\begin{cases} \nabla_y\cdot\big(\beta : \varepsilon_y[u_0]\big) = 0 & (y \in \mathcal{Y}), & \text{(5.98a)}\\ \left[\!\left[\beta : \varepsilon_y[u_0]\cdot n \right]\!\right]_y = 0 & (y \in \partial\Omega_i), & \text{(5.98b)}\\ \left\langle\!\left\langle \beta : \varepsilon_y[u_0]\cdot n \right\rangle\!\right\rangle_y = \mathcal{K}\cdot\left[\!\left[u_0 \right]\!\right]_y & (y \in \partial\Omega_i). & \text{(5.98c)}\end{cases}$$

We take the dot product of (5.98a) and u_0 and integrate over the unit periodic cell $\mathcal{Y}$. Integrating by parts and using the periodicity conditions on the boundaries of the cell $\mathcal{Y}$ leads to:

$$\int_{\mathcal{Y}} \big(\beta : \varepsilon_y[u_0]\big) : \nabla_y u_0 + \int_{\partial\Omega_i} \left[\!\left[\big(\beta : \varepsilon_y[u_0]\cdot n\big)\cdot u_0 \right]\!\right]_y = 0. \tag{5.99}$$

The first term writes by minor symmetry of $\boldsymbol{\beta}$

$$\int_{\mathcal{Y}} (\boldsymbol{\beta} : \boldsymbol{\varepsilon}_y[\boldsymbol{u}_0]) : \boldsymbol{\nabla}_y \boldsymbol{u}_0 = \int_{\mathcal{Y}} \boldsymbol{\varepsilon}_y[\boldsymbol{u}_0] : \boldsymbol{\beta} : \boldsymbol{\varepsilon}_y[\boldsymbol{u}_0] \tag{5.100}$$

and the second one writes

$$\begin{aligned} \int_{\partial\Omega_i} \left[\!\left[(\boldsymbol{\beta} : \boldsymbol{\varepsilon}_y[\boldsymbol{u}_0] \cdot \boldsymbol{n}) \cdot \boldsymbol{u}_0 \right]\!\right]_y &= \int_{\partial\Omega_i} \left[\left[\!\left[\boldsymbol{\beta} : \boldsymbol{\varepsilon}_y[\boldsymbol{u}_0] \cdot \boldsymbol{n} \right]\!\right]_y \cdot \langle\!\langle \boldsymbol{u}_0 \rangle\!\rangle_y + \left\langle\!\left\langle \boldsymbol{\beta} : \boldsymbol{\varepsilon}_y(\boldsymbol{u}_0) \cdot \boldsymbol{n} \right\rangle\!\right\rangle_y \cdot \left[\!\left[\boldsymbol{u}_0 \right]\!\right]_y \right] \\ &= \int_{\partial\Omega_i} \left[\!\left[\boldsymbol{u}_0 \right]\!\right]_y \cdot \boldsymbol{\mathcal{K}} \cdot \left[\!\left[\boldsymbol{u}_0 \right]\!\right]_y , \end{aligned} \tag{5.101}$$

where we use the interface conditions (5.98b) and (5.98c). Both terms in (5.99) are thus positive owing to Assumptions 5.5 and 5.6. Therefore, the first term equals to 0 and from (5.100), one gets $\boldsymbol{\varepsilon}_y(\boldsymbol{u}_0) = \boldsymbol{0}$ in $\mathcal{Y}$. The decomposition of the gradient of $\boldsymbol{\nabla}_y \boldsymbol{u}_0$ into symmetric and antisymmetric parts reads:

$$\boldsymbol{\nabla}_y \boldsymbol{u}_0 = \boldsymbol{\varepsilon}_y(\boldsymbol{u}_0) + \boldsymbol{A}(\boldsymbol{u}_0),$$

with $\boldsymbol{A}(\boldsymbol{u}_0) = \frac{1}{2}\left(\boldsymbol{\nabla}_y \boldsymbol{u}_0 - \boldsymbol{\nabla}_y \boldsymbol{u}_0^\top\right)$. We know that the symmetric part vanishes, and the antisymmetric satisfies

$$\frac{\partial A_{ij}}{\partial y_k} = \frac{\partial \varepsilon_{ik}}{\partial y_j} - \frac{\partial \varepsilon_{jk}}{\partial y_i} = 0.$$

Together with the periodic conditions, this yields $\boldsymbol{\nabla}_y \boldsymbol{u}_0 = \boldsymbol{0}$. So, one obtains as in 1D:

$$\boldsymbol{u}_0(\boldsymbol{x}, \boldsymbol{y}, \tau) = \boldsymbol{u}_0(\boldsymbol{x}, \tau). \tag{5.102}$$

5.3.3.2 First-order field

Next, one identifies the terms of order $\mathcal{O}(\eta^{-1})$ in (5.96) together with those of order $\mathcal{O}(1)$ in (5.97a) and (5.97b). Given (5.102), this leads to the following system for the first-order field $\boldsymbol{u}_1$:

$$\begin{cases} \boldsymbol{\nabla}_y \cdot \left(\boldsymbol{\beta} : \boldsymbol{\varepsilon}_y[\boldsymbol{u}_1]\right) + \boldsymbol{\nabla}_y \cdot \left(\boldsymbol{\beta} : \boldsymbol{\varepsilon}_x[\boldsymbol{u}_0]\right) = \boldsymbol{0} & (\boldsymbol{y} \in \mathcal{Y}), & \text{(5.103a)} \\ \left[\!\left[\boldsymbol{\beta} : \left(\boldsymbol{\varepsilon}_y[\boldsymbol{u}_1] + \boldsymbol{\varepsilon}_x[\boldsymbol{u}_0]\right) \cdot \boldsymbol{n} \right]\!\right]_y = \boldsymbol{0} & (\boldsymbol{y} \in \partial\Omega_i), & \text{(5.103b)} \\ \left\langle\!\left\langle \boldsymbol{\beta} : \left(\boldsymbol{\varepsilon}_y[\boldsymbol{u}_1] + \boldsymbol{\varepsilon}_x[\boldsymbol{u}_0]\right) \cdot \boldsymbol{n} \right\rangle\!\right\rangle_y = \boldsymbol{\mathcal{K}} \cdot \left[\!\left[\boldsymbol{u}_1 \right]\!\right]_y & (\boldsymbol{y} \in \partial\Omega_i). & \text{(5.103c)} \end{cases}$$

Due to the linearity of (5.103a) and the separation of variables of the forcing term $\boldsymbol{\nabla}_y \cdot \boldsymbol{\beta} : \boldsymbol{\varepsilon}_x[\boldsymbol{u}_0]$, $\boldsymbol{u}_1$ can be written:

$$\boldsymbol{u}_1(\boldsymbol{x}, \boldsymbol{y}, \tau) = \boldsymbol{\mathcal{U}}_1(\boldsymbol{x}, \tau) + \boldsymbol{P}(\boldsymbol{y}) : \boldsymbol{\varepsilon}_x[\boldsymbol{u}_0], \tag{5.104}$$

with $\boldsymbol{P}$ a third-order tensor. The symmetry of $\boldsymbol{\varepsilon}_x[\boldsymbol{u}_0]$ implies the following symmetry for $\boldsymbol{P}$: $P_{ipq} = P_{iqp}$. We then introduce the vector $\boldsymbol{P}^{pq} = P_{ipq}\boldsymbol{e}_i$ which is the solution of the following cell-problem due to (5.103):

$$\begin{cases} \boldsymbol{\nabla}_y \cdot \left(\boldsymbol{\beta} : \boldsymbol{\varepsilon}_y[\boldsymbol{P}^{pq}]\right) + \boldsymbol{\nabla}_y \cdot \left(\boldsymbol{\beta} : \boldsymbol{I}^{pq}\right) = \boldsymbol{0} & (\boldsymbol{y} \in \mathcal{Y}), & \text{(5.105a)} \\ \left[\!\left[\boldsymbol{\beta} : \left(\boldsymbol{\varepsilon}_y[\boldsymbol{P}^{pq}] + \boldsymbol{I}^{pq}\right) \cdot \boldsymbol{n} \right]\!\right]_y = \boldsymbol{0} & (\boldsymbol{y} \in \partial\Omega_i), & \text{(5.105b)} \\ \left\langle\!\left\langle \boldsymbol{\beta} : \left(\boldsymbol{\varepsilon}_y[\boldsymbol{P}^{pq}] + \boldsymbol{I}^{pq}\right) \cdot \boldsymbol{n} \right\rangle\!\right\rangle_y = \boldsymbol{\mathcal{K}} \cdot \left[\!\left[\boldsymbol{P}^{pq} \right]\!\right]_y & (\boldsymbol{y} \in \partial\Omega_i), & \text{(5.105c)} \end{cases}$$

with $\boldsymbol{I}^{pq}$ the second-order tensor defined by $\boldsymbol{I}^{pq} = \boldsymbol{e}_p \otimes \boldsymbol{e}_q$. The fields $\boldsymbol{P}^{pq}$ and $\boldsymbol{\beta} : \left(\boldsymbol{\varepsilon}_y[\boldsymbol{P}^{pq}] + \boldsymbol{I}^{pq}\right) \cdot \boldsymbol{n}$ also satisfy the periodicity conditions on the boundaries of the periodic cell $\mathcal{Y}$. Moreover, $\boldsymbol{P}^{pq}$ is chosen such that $\langle \boldsymbol{P}^{pq} \rangle = \boldsymbol{0}$ and consequently $\langle \boldsymbol{u}_1 \rangle = \boldsymbol{\mathcal{U}}_1(\boldsymbol{x}, \tau)$.

5.3.3.3 Second-order field

One identifies the terms at order $O(1)$ in (5.96) and $O(\eta)$ in (5.97a) and (5.97b). It yields the following system for the second-order field $\boldsymbol{u}_2$:

$$\begin{cases} \nabla_y \cdot \left(\boldsymbol{\beta} : \left(\boldsymbol{\varepsilon}_y[\boldsymbol{u}_2] + \boldsymbol{\varepsilon}_x[\boldsymbol{u}_1]\right)\right) + \nabla_x \cdot \left(\boldsymbol{\beta} : \left(\boldsymbol{\varepsilon}_y[\boldsymbol{u}_1] + \boldsymbol{\varepsilon}_x[\boldsymbol{u}_0]\right)\right) + \boldsymbol{f}(\boldsymbol{x},\tau) = \alpha \dfrac{\partial^2 \boldsymbol{u}_0}{\partial \tau^2} \quad (\boldsymbol{y} \in \mathcal{Y}) & \text{(5.106a)} \\ \left[\!\left[\boldsymbol{\beta} : \left(\boldsymbol{\varepsilon}_y[\boldsymbol{u}_2] + \boldsymbol{\varepsilon}_x[\boldsymbol{u}_1]\right) \cdot \boldsymbol{n}\right]\!\right]_y = \boldsymbol{\mathcal{M}} \cdot \dfrac{\partial^2 \boldsymbol{u}_0}{\partial \tau^2} \quad (\boldsymbol{y} \in \partial\Omega_i) & \text{(5.106b)} \\ \left\langle\!\left\langle \boldsymbol{\beta} : \left(\boldsymbol{\varepsilon}_y[\boldsymbol{u}_2] + \boldsymbol{\varepsilon}_x[\boldsymbol{u}_1]\right) \cdot \boldsymbol{n}\right\rangle\!\right\rangle_y = \boldsymbol{\mathcal{K}} \cdot [\![\boldsymbol{u}_2]\!]_y \quad (\boldsymbol{y} \in \partial\Omega_i) & \text{(5.106c)} \end{cases}$$

5.3.3.4 Wave equation for the zeroth-order field

Averaging the equation (5.106a) over the unit periodic cell $\mathcal{Y}$, while using the periodicity conditions on its boundaries and the interface condition (5.106b), implies

$$\left(\langle\alpha\rangle \boldsymbol{I} + \int_{\partial\Omega_i} \boldsymbol{\mathcal{M}} \mathrm{d}\boldsymbol{y}\right) \cdot \frac{\partial^2 \boldsymbol{u}_0}{\partial \tau^2} = \nabla_x \cdot \left\langle \boldsymbol{\beta} : \left(\boldsymbol{\varepsilon}_y[\boldsymbol{u}_1] + \boldsymbol{\varepsilon}_x[\boldsymbol{u}_0]\right)\right\rangle + \boldsymbol{f}(\boldsymbol{x},\tau). \tag{5.107}$$

Result 5.7: Effective equation for the nondimensionalized zeroth-order field

One introduces the effective nondimensionalized fourth-order tensor $\bar{\boldsymbol{\beta}}$ defined by

$$\bar{\boldsymbol{\beta}} = \left\langle \beta_{ijmn} \left(\frac{\partial P_{nkl}}{\partial y_m} + \delta_{mk}\,\delta_{nl}\right)\right\rangle \boldsymbol{e}_i \otimes \boldsymbol{e}_j \otimes \boldsymbol{e}_k \otimes \boldsymbol{e}_l, \tag{5.108}$$

and the effective nondimensionalized mass density $\bar{\boldsymbol{\alpha}}$ defined by

$$\bar{\boldsymbol{\alpha}} = \left(\langle\alpha\rangle \boldsymbol{I} + \int_{\partial\Omega_i} \boldsymbol{\mathcal{M}} \mathrm{d}\boldsymbol{y}\right). \tag{5.109}$$

Finally, owing to (5.104) and (5.107) one obtains

$$\bar{\boldsymbol{\alpha}} \cdot \frac{\partial^2 \boldsymbol{u}_0}{\partial \tau^2} = \nabla_x \cdot \left(\bar{\boldsymbol{\beta}} : \boldsymbol{\varepsilon}_x[\boldsymbol{u}_0]\right) + \boldsymbol{f}(\boldsymbol{x},\tau). \tag{5.110}$$

This equation is the effective wave equation satisfied by the nondimensionalized macroscopic field $\boldsymbol{u}_0$ in the rescaled coordinate system.

■ *Symmetries of $\bar{\boldsymbol{\alpha}}$ and $\bar{\boldsymbol{\beta}}$.*

Result 5.8: Symmetries of the effective tensors

The effective tensor $\bar{\boldsymbol{\alpha}}$ is symmetric.
The effective tensor $\bar{\boldsymbol{\beta}}$ satisfies the usual minor symmetries and major symmetry.

Proof.

- The symmetry of $\boldsymbol{\mathcal{M}}$ yields the symmetry for $\bar{\boldsymbol{\alpha}}$
- $\boldsymbol{\beta}_{jikl} = \boldsymbol{\beta}_{ijkl}$ proves that $\bar{\boldsymbol{\beta}}_{jikl} = \bar{\boldsymbol{\beta}}_{ijkl}$.

- Using that $\boldsymbol{P}_{nlk} = \boldsymbol{P}_{nkl}$ and $\boldsymbol{\beta}_{ijlk} = \boldsymbol{\beta}_{ijkl}$ yields $\bar{\boldsymbol{\beta}}_{ijlk} = \bar{\boldsymbol{\beta}}_{ijkl}$.
- One considers the dot product of equation (5.105a) for $(p,q) = (i,j)$ and $\boldsymbol{P}^{kl}$. One integrates it by parts over $\mathcal{Y}$ and one uses the periodic conditions to get:

$$\left\langle \boldsymbol{\varepsilon}_{\boldsymbol{y}}[\boldsymbol{P}^{kl}] : \boldsymbol{\beta} : \left(\boldsymbol{\varepsilon}_{\boldsymbol{y}}[\boldsymbol{P}^{ij}] + \boldsymbol{I}^{ij} \right) \right\rangle + \int_{\partial\Omega_i} \left[\!\left[\boldsymbol{\beta} : \left(\boldsymbol{\varepsilon}_{\boldsymbol{y}}[\boldsymbol{P}^{ij}] + \boldsymbol{I}^{ij} \right) \cdot \boldsymbol{n} \cdot \boldsymbol{P}^{kl} \right]\!\right] = \boldsymbol{0}. \tag{5.111}$$

Due to the jump conditions (5.105b)–(5.105c), this writes:

$$\left\langle \boldsymbol{\varepsilon}_{\boldsymbol{y}}[\boldsymbol{P}^{kl}] : \boldsymbol{\beta} : \left(\boldsymbol{\varepsilon}_{\boldsymbol{y}}[\boldsymbol{P}^{ij}] + \boldsymbol{I}^{ij} \right) \right\rangle + \int_{\partial\Omega_i} \left[\!\left[\boldsymbol{P}^{kl} \right]\!\right] \cdot \boldsymbol{\mathcal{K}} \cdot \left[\!\left[\boldsymbol{P}^{ij} \right]\!\right] = \boldsymbol{0}. \tag{5.112}$$

Similarly, the dot product of equation (5.105a) for $(p,q) = (k,l)$ and $\boldsymbol{P}^{ij}$ yields

$$\left\langle \boldsymbol{\varepsilon}_{\boldsymbol{y}}[\boldsymbol{P}^{ij}] : \boldsymbol{\beta} : \left(\boldsymbol{\varepsilon}_{\boldsymbol{y}}[\boldsymbol{P}^{kl}] + \boldsymbol{I}^{kl} \right) \right\rangle + \int_{\partial\Omega_i} \left[\!\left[\boldsymbol{P}^{ij} \right]\!\right] \cdot \boldsymbol{\mathcal{K}} \cdot \left[\!\left[\boldsymbol{P}^{kl} \right]\!\right] = \boldsymbol{0}. \tag{5.113}$$

Due to the symmetries of $\boldsymbol{\beta}$ and $\boldsymbol{\mathcal{K}}$, the difference of the two resulting equations yields

$$\left\langle \beta_{ijmn} \frac{\partial P_{nkl}}{\partial y_m} \right\rangle = \left\langle \beta_{klmn} \frac{\partial P_{nij}}{\partial y_m} \right\rangle.$$

Combined with the fact that $\beta_{ijkl} = \beta_{klij}$, this leads to the major symmetry $\bar{\boldsymbol{\beta}}_{klij} = \bar{\boldsymbol{\beta}}_{ijkl}$.

□

5.3.4 First-order homogenization

The purpose of this section is to derive an effective model up to the first order. The latter will enrich the model obtained in the previous section that only involves a zeroth-order mean field.

5.3.4.1 An explicit form for the second-order field

Due to (5.106a), $\boldsymbol{u}_2$ can be written as

$$\boldsymbol{u}_2(\boldsymbol{x},\boldsymbol{y},\tau) = \boldsymbol{\mathcal{U}}_2(\boldsymbol{x},\tau) + \boldsymbol{P}(\boldsymbol{y}) : \boldsymbol{\varepsilon}_{\boldsymbol{x}}[\boldsymbol{\mathcal{U}}_1] + \boldsymbol{Q}(\boldsymbol{y}) \vdots \boldsymbol{\nabla}_{\boldsymbol{x}} \boldsymbol{\varepsilon}_{\boldsymbol{x}}[\boldsymbol{u}_0] + \boldsymbol{G}(\boldsymbol{y}) \cdot \boldsymbol{f}(\boldsymbol{x},\tau), \tag{5.114}$$

where $\vdots$ is the notation when contracting three indices, $\boldsymbol{Q}$ is a fourth-order tensor, and $\boldsymbol{G}$ a second-order tensor. One can assume that $Q_{pqrs} = Q_{pqsr}$ due to the symmetries of $\boldsymbol{\nabla}_{\boldsymbol{x}} \boldsymbol{\varepsilon}_{\boldsymbol{x}}[\boldsymbol{u}_0]$.
We introduce $\boldsymbol{Q}^{qrs} = Q_{pqrs}\, \boldsymbol{e}_p$ and $\boldsymbol{G}^s = G_{ps} \boldsymbol{e}_p$. Using (5.106), $\boldsymbol{Q}^{qrs}$ is solution of the following equation for $\boldsymbol{y} \in \mathcal{Y}$

$$\bar{\boldsymbol{\alpha}} \cdot \left[\boldsymbol{\nabla}_{\boldsymbol{y}} \cdot \left(\boldsymbol{\beta} : \boldsymbol{\varepsilon}_{\boldsymbol{y}}[\boldsymbol{Q}^{qrs}] + \boldsymbol{\beta} \cdot \boldsymbol{e}_q \cdot \boldsymbol{P}^{rs} \right) + \left(\boldsymbol{\beta} : \boldsymbol{\varepsilon}_{\boldsymbol{y}}[\boldsymbol{P}^{rs}] \right) \cdot \boldsymbol{e}_q + \boldsymbol{\beta} \vdots \boldsymbol{I}^{qrs} \right] = \alpha \bar{\boldsymbol{\beta}}^{qrs}, \tag{5.115}$$

together with the interface conditions for $\boldsymbol{y} \in \partial\Omega_i$

$$\begin{cases} \bar{\boldsymbol{\alpha}} \cdot \left[\!\left[\left(\boldsymbol{\beta} : \boldsymbol{\varepsilon}_{\boldsymbol{y}}[\boldsymbol{Q}^{qrs}] + \boldsymbol{\beta} \cdot \boldsymbol{e}_q \cdot \boldsymbol{P}^{rs} \right) \cdot \boldsymbol{n} \right]\!\right]_{\boldsymbol{y}} = \boldsymbol{\mathcal{M}} \cdot \bar{\boldsymbol{\beta}}^{qrs}, & \text{(5.116a)} \\ \left\langle\!\!\left\langle \left(\boldsymbol{\beta} : \boldsymbol{\varepsilon}_{\boldsymbol{y}}[\boldsymbol{Q}^{qrs}] + \boldsymbol{\beta} \cdot \boldsymbol{e}_q \cdot \boldsymbol{P}^{rs} \right) \cdot \boldsymbol{n} \right\rangle\!\!\right\rangle_{\boldsymbol{y}} = \boldsymbol{\mathcal{K}} \cdot \left[\!\left[\boldsymbol{Q}^{qrs} \right]\!\right]_{\boldsymbol{y}}, & \text{(5.116b)} \end{cases}$$

with $\bar{\boldsymbol{\beta}}^{qrs} = \bar{\beta}_{pqrs}\, \boldsymbol{e}_p$ and $\boldsymbol{I}^{qrs} = \boldsymbol{e}_q \otimes \boldsymbol{e}_r \otimes \boldsymbol{e}_s$. Similarly, $\boldsymbol{G}^s$ satisfies the following cell-problem

$$\begin{cases} \bar{\boldsymbol{\alpha}} \cdot \left(\boldsymbol{\nabla}_{\boldsymbol{y}} \cdot \left(\boldsymbol{\beta} : \boldsymbol{\varepsilon}_{\boldsymbol{y}}[\boldsymbol{G}^s] \right) \right) = (\alpha \boldsymbol{I} - \bar{\boldsymbol{\alpha}}) \cdot \boldsymbol{e}_s & (\boldsymbol{y} \in \mathcal{Y}), & \text{(5.117a)} \\ \bar{\boldsymbol{\alpha}} \cdot \left[\!\left[\boldsymbol{\beta} : \boldsymbol{\varepsilon}_{\boldsymbol{y}}[\boldsymbol{G}^s] \cdot \boldsymbol{n} \right]\!\right]_{\boldsymbol{y}} = \boldsymbol{\mathcal{M}} \cdot \boldsymbol{e}_s & (\boldsymbol{y} \in \partial\Omega_i), & \text{(5.117b)} \\ \left\langle\!\!\left\langle \boldsymbol{\beta} : \boldsymbol{\varepsilon}_{\boldsymbol{y}}[\boldsymbol{G}^s] \cdot \boldsymbol{n} \right\rangle\!\!\right\rangle_{\boldsymbol{y}} = \boldsymbol{\mathcal{K}} \cdot \left[\!\left[\boldsymbol{G}^s \right]\!\right]_{\boldsymbol{y}} & (\boldsymbol{y} \in \partial\Omega_i). & \text{(5.117c)} \end{cases}$$

5.3.4.2 Third-order field

Next, identifying the terms of order $\mathcal{O}(\eta)$ in (5.96) together with those of order $\mathcal{O}(\eta^2)$ in (5.97a) and (5.97b), leads to the following system for the third-order field $\boldsymbol{u}_3$:

$$\begin{cases} \nabla_y \cdot \left(\boldsymbol{\beta} : \left(\boldsymbol{\varepsilon}_y[\boldsymbol{u}_3] + \boldsymbol{\varepsilon}_x[\boldsymbol{u}_2]\right)\right) + \nabla_x \cdot \left(\boldsymbol{\beta} : \left(\boldsymbol{\varepsilon}_y[\boldsymbol{u}_2] + \boldsymbol{\varepsilon}_x[\boldsymbol{u}_1]\right)\right) = \alpha \dfrac{\partial^2 \boldsymbol{u}_1}{\partial \tau^2} \quad (\boldsymbol{y} \in \mathcal{Y}), & \text{(5.118a)} \\ \left[\!\left[\boldsymbol{\beta} : \left(\boldsymbol{\varepsilon}_y[\boldsymbol{u}_3] + \boldsymbol{\varepsilon}_x[\boldsymbol{u}_2]\right) \cdot \boldsymbol{n}\right]\!\right]_y = \boldsymbol{\mathcal{M}} \cdot \left\langle\!\!\left\langle \dfrac{\partial^2 \boldsymbol{u}_1}{\partial \tau^2} \right\rangle\!\!\right\rangle_y \quad (\boldsymbol{y} \in \partial\Omega_i), & \text{(5.118b)} \\ \left\langle\!\!\left\langle \boldsymbol{\beta} : \left(\boldsymbol{\varepsilon}_y[\boldsymbol{u}_3] + \boldsymbol{\varepsilon}_x[\boldsymbol{u}_2]\right) \cdot \boldsymbol{n} \right\rangle\!\!\right\rangle_y = \boldsymbol{\mathcal{K}} \cdot \left[\!\left[\boldsymbol{u}_3\right]\!\right]_y \quad (\boldsymbol{y} \in \partial\Omega_i). & \text{(5.118c)} \end{cases}$$

The equation (5.118a) is integrated over the unit periodic cell $\mathcal{Y}$ using the periodicity conditions on the boundaries of $\mathcal{Y}$ and the interface condition (5.118b):

$$-\int_{\partial\Omega_i} \boldsymbol{\mathcal{M}} \cdot \left\langle\!\!\left\langle \frac{\partial^2 \boldsymbol{u}_1}{\partial \tau^2} \right\rangle\!\!\right\rangle_y \mathrm{d}\boldsymbol{y} + \nabla_x \cdot \left\langle \boldsymbol{\beta} : \left(\boldsymbol{\varepsilon}_y[\boldsymbol{u}_2] + \boldsymbol{\varepsilon}_x[\boldsymbol{u}_1]\right) \right\rangle = \left\langle \alpha \frac{\partial^2 \boldsymbol{u}_1}{\partial \tau^2} \right\rangle. \tag{5.119}$$

The equations (5.104) and (5.114) are used in (5.119) and one obtains the equation below for the mean field $\boldsymbol{\mathcal{U}}_1$:

Result 5.9: Nondimensionalized mean field associated with the first-order corrector

$$\bar{\boldsymbol{\alpha}} \cdot \frac{\partial^2 \boldsymbol{\mathcal{U}}_1}{\partial \tau^2} = \nabla_x \cdot \left(\bar{\boldsymbol{\beta}} : \boldsymbol{\varepsilon}_x\left[\boldsymbol{\mathcal{U}}_1\right]\right) + \boldsymbol{\mathcal{S}}(\boldsymbol{u}_0), \tag{5.120}$$

where the source term $\boldsymbol{\mathcal{S}}(\boldsymbol{u}_0)$ depends explicitely on the zeroth-order field and is given by

$$\begin{aligned} \boldsymbol{\mathcal{S}}(\boldsymbol{u}_0) = &-\left(\langle \alpha \boldsymbol{P} \rangle + \int_{\partial\Omega_i} \boldsymbol{\mathcal{M}} \cdot \langle\!\langle \boldsymbol{P} \rangle\!\rangle_y \, \mathrm{d}\boldsymbol{y}\right) : \boldsymbol{\varepsilon}_x\left[\frac{\partial^2 \boldsymbol{u}_0}{\partial \tau^2}\right] \\ &+ \nabla_x \cdot \left\langle \boldsymbol{\beta} : \left(\boldsymbol{\varepsilon}_y\left[\boldsymbol{Q} \vdots \nabla_x \boldsymbol{\varepsilon}_x[\boldsymbol{u}_0]\right] + \boldsymbol{\varepsilon}_y\left[\boldsymbol{G} \cdot \boldsymbol{f}\right] + \boldsymbol{\varepsilon}_x\left[\boldsymbol{P} : \boldsymbol{\varepsilon}_x\left[\boldsymbol{u}_0\right]\right]\right) \right\rangle. \end{aligned} \tag{5.121}$$

Remark 17. *For numerical purposes, one can prefer an expression of the source term $\boldsymbol{\mathcal{S}}(\boldsymbol{u}_0)$ which is independant of the tensors $\boldsymbol{Q}$ and $\boldsymbol{G}$. Indeed, it seems less costly to avoid the computation of these additional cell problems to have a first-order homogenized field. Using (5.116) and (5.117) allows to get the following expression for the source term:*

$$\begin{aligned} \boldsymbol{\mathcal{S}}(\boldsymbol{u}_0)_j = &\left\langle \beta_{pqmn} \left(P_{mst} \frac{\partial P_{pjk}}{\partial y_q} - P_{mjk} \frac{\partial P_{pst}}{\partial y_q} \right) \right\rangle \frac{\partial^2 (\varepsilon_x[\boldsymbol{u}_0])_{st}}{\partial x_n \partial x_k} + \left\langle \beta_{jkmn} P_{mls} \right\rangle \frac{\partial^2 (\varepsilon_x[\boldsymbol{u}_0])_{ls}}{\partial x_n \partial x_k} \\ &- \left\langle \beta_{pqmn} P_{pjk} \right\rangle \frac{\partial^2 (\varepsilon_x[\boldsymbol{u}_0])_{mn}}{\partial x_q \partial x_k} + \int_{\partial\Omega_i} \mathcal{M}_{pq} \left\langle\!\!\left\langle P_{pjk} \right\rangle\!\!\right\rangle \mathrm{d}\boldsymbol{y} \, \frac{\partial^3 (u_0)_q}{\partial \tau^2 \partial x_k} \\ &- \int_{\partial\Omega_i} \mathcal{M}_{jn} \left\langle\!\!\left\langle P_{nkm} \right\rangle\!\!\right\rangle \mathrm{d}\boldsymbol{y} \, \frac{\partial^3 (u_0)_m}{\partial \tau^2 \partial x_k} + \left\langle \alpha P_{pjk} \right\rangle \frac{\partial^3 (u_0)_p}{\partial \tau^2 \partial x_k} - \left\langle \alpha P_{jkm} \right\rangle \frac{\partial^3 (u_0)_m}{\partial \tau^2 \partial x_k}. \end{aligned} \tag{5.122}$$

This expression avoids the computation of additional cell problems. However, it is more intricate so it will not be used in the following.

5.3.5 Final homogenized model

Following the same lines as in Section 5.1.5, one gets the following first-order approximation of the wavefield. Let define

$$\boldsymbol{U}^{(1)}(\boldsymbol{X}, t) = \boldsymbol{U}_0(\boldsymbol{X}, t) + h \boldsymbol{U}_1(\boldsymbol{X}, t).$$

It requires to introduce the effective fourth-order tensor

$$\bar{\boldsymbol{C}} = \left\langle C_{ijmn}\left(\frac{\partial P_{nkl}}{\partial y_m} + \delta_{mk}\,\delta_{nl}\right)\right\rangle \boldsymbol{e}_i \otimes \boldsymbol{e}_j \otimes \boldsymbol{e}_k \otimes \boldsymbol{e}_l, \tag{5.123}$$

and the effective mass density

$$\bar{\boldsymbol{\rho}} = \langle \rho \rangle \boldsymbol{I} + \frac{1}{h}\int_{\partial\Omega_i} \boldsymbol{M}\,\mathrm{d}\boldsymbol{y}. \tag{5.124}$$

Result 5.10: Final homogenized field

Then, the mean field $\boldsymbol{U}_0(\boldsymbol{X},t)$ is governed by the equation

$$\bar{\boldsymbol{\rho}} \cdot \frac{\partial^2 \boldsymbol{U}_0}{\partial t^2} = \boldsymbol{\nabla}_X \cdot \left(\bar{\boldsymbol{C}} \colon \boldsymbol{\varepsilon}_X\left[\boldsymbol{U}_0\right]\right) + \boldsymbol{F}(\boldsymbol{X},t). \tag{5.125}$$

The first order corrector $\boldsymbol{U}_1$ is computed from

$$\boldsymbol{U}_1(\boldsymbol{X},t) = \overline{\boldsymbol{U}}_1(\boldsymbol{X},t) + \boldsymbol{P}\left(\frac{\boldsymbol{X}}{h}\right) : \boldsymbol{\varepsilon}_X\left[\boldsymbol{U}_0\right]. \tag{5.126}$$

The latter is valid for $\boldsymbol{X} \in h\mathcal{Y}$ and the field for all $\boldsymbol{X} \in \mathbb{R}^N$ is recovered using the periodicity. The equation (5.126) requires the computation of $\boldsymbol{P}$, which is solution of the cell problem (5.105) and of the mean field $\overline{\boldsymbol{U}}_1(\boldsymbol{X},t)$ solution of

$$\bar{\boldsymbol{\rho}} \cdot \frac{\partial^2 \overline{\boldsymbol{U}}_1}{\partial t^2} = \boldsymbol{\nabla}_X \cdot \left(\bar{\boldsymbol{C}} \colon \boldsymbol{\varepsilon}_X\left[\overline{\boldsymbol{U}}_1\right]\right) + \boldsymbol{S}(\boldsymbol{U}_0), \tag{5.127}$$

where the source term is given by

$$\begin{aligned}\boldsymbol{S}(\boldsymbol{U}_0) = &-\left(\left\langle \rho \boldsymbol{P}\right\rangle + \frac{1}{h}\int_{\partial\Omega_i} \boldsymbol{M} \cdot \langle\!\langle \boldsymbol{P} \rangle\!\rangle_y \,\mathrm{d}\boldsymbol{y}\right) : \boldsymbol{\varepsilon}_X\left[\frac{\partial^2 \boldsymbol{U}_0}{\partial t^2}\right] \\ &+ \boldsymbol{\nabla}_X \cdot \left\langle \boldsymbol{C} : \left(\boldsymbol{\varepsilon}_y\left[\boldsymbol{Q} \vdots \boldsymbol{\nabla}_X \boldsymbol{\varepsilon}_X\left[\boldsymbol{U}_0\right]\right] + \boldsymbol{\varepsilon}_y\left[\boldsymbol{G} \cdot \boldsymbol{F}\right] + \boldsymbol{\varepsilon}_X\left[\boldsymbol{P} \colon \boldsymbol{\varepsilon}_X\left[\boldsymbol{U}_0\right]\right]\right)\right\rangle.\end{aligned} \tag{5.128}$$

Remark 18. *The case of perfect interfaces, see for example (Boutin & Auriault, 1993), can be recovered by setting $K = +\infty$ and $M = 0$ in the interface model considered when $\boldsymbol{F} = \boldsymbol{0}$.*

■ *Energy identity for the zeroth-order homogenized model.* For a domain $\mathcal{D}$ and a time $t \geq 0$, one defines

$$\mathscr{E}_0^m(t) = \frac{1}{2}\int_{\mathcal{D}} \left\{\left\langle \rho \right\rangle \boldsymbol{V}_0(\boldsymbol{X},t)^2 + \boldsymbol{\varepsilon}\left[\boldsymbol{U}_0\right](\boldsymbol{X},t) \colon \langle \boldsymbol{C} \rangle : \boldsymbol{\varepsilon}\left[\boldsymbol{U}_0\right](\boldsymbol{X},t)\right\} \mathrm{d}\boldsymbol{X}, \tag{5.129a}$$

$$\mathscr{E}_0^i(t) = \frac{1}{2}\int_{\mathcal{D}} \left\{\boldsymbol{V}_0(\boldsymbol{X},t) \cdot \boldsymbol{\rho}^{\mathrm{int}} \cdot \boldsymbol{V}_0(\boldsymbol{X},t) + \boldsymbol{\varepsilon}\left[\boldsymbol{U}_0\right](\boldsymbol{X},t) : \boldsymbol{C}^{\mathrm{int}} : \boldsymbol{\varepsilon}\left[\boldsymbol{U}_0\right](\boldsymbol{X},t)\right\} \mathrm{d}\boldsymbol{X}, \tag{5.129b}$$

with

$$\begin{cases} \boldsymbol{\rho}^{\mathrm{int}} = \dfrac{1}{h}\displaystyle\int_{\partial\Omega_i} \boldsymbol{M}\,\mathrm{d}\boldsymbol{y} \\ \boldsymbol{C}^{\mathrm{int}} = \left\langle C_{ijmn}\dfrac{\partial P_{nkl}}{\partial y_m}\right\rangle \boldsymbol{e}_i \otimes \boldsymbol{e}_j \otimes \boldsymbol{e}_k \otimes \boldsymbol{e}_l. \end{cases}$$

The effective energy $\mathscr{E}_0 = \mathscr{E}_0^m + \mathscr{E}_0^i$ is the effective mechanical energy associated with the zeroth-order homogenized model. The terms (5.129a) and (5.129b) are respectively associated with the

bulk and interface energies of the microstructured problem (5.87), and satisfy $\mathscr{E}_0^m(t) \geq 0$ and $\mathscr{E}_0^i(t) \geq 0$ for all time $t \geq 0$.
Lastly, if $\mathcal{D}$ is large enough and if $F = 0$, it holds $\frac{\mathrm{d}}{\mathrm{d}t}\mathscr{E}_0 = 0$ for all time t.

5.4 Conclusion

In this chapter, we studied periodic media with imperfect contact of the spring-mass type in the framework of low-frequency homogenization. We first considered a 1D periodic array of linear interfaces. Thanks to two-scale asymptotic expansions, a first-order homogenized model was obtained. The zeroth-order contribution of the displacement is a mean field that is solution of a wave equation with the original source term. This wave equation involves a homogeneous effective mass density and shear modulus that depend on the physical parameters, as in the case of perfect bonding, and on the interface parameters. The mean field associated with the first-order corrector is solution of the same wave equation without source term. The associated cell problem is found analytically due to 1D specificity.

Then, an overview of the extension of this work to non-linear interfaces was presented. In this case, the zeroth-order mean field is solution of a wave equation with non-linear constitutive stress-strain relation. Consequently, shocks occur in the homogenized model in finite time contrary to the case of the microstructured configuration. From the instant where shocks appear, there is dissipation of energy in the homogenized model contrary to the microstructured configuration. The first order corrector term involves a mean field solution of a wave equation and a corrector. The corrector, the source term for the mean field and its constitutive relation depend non-linearly on the zeroth-order field. Numerical experiments have shown a good agreement before shocks appear. This agreement deteriorates as the frequency or the amplitude of the source increase.

Eventually, the derivation of a first-oder homogenized model was tackled for the full elasticity configuration in $\mathbb{R}^N$ with $N = 2, 3$. The mean fields satisfy a wave equation involving an effective mass density which turns out to be a tensor and an effective tensor of elasticity which satisfies the usual properties of symmetry. Contrary to the 1D case, the source term for the first-order mean field does not vanish without further assumption. The computation of the solution to cell problems is also required.

This work raises the following open questions and perspectives:

- The first natural perspective is to complete the work started in the last section about the case of higher spatial dimensions. Indeed, the first-order homogenized model has been derived but we still need to perform numerical simulations in order to assess its valididty by comparisons with full-field simulations. While the computation of the zeroth-order homogenized field should not pose any difficulty, the computation of the first-order corrector with the resolution of cell problems in each point is more intricate. In this framework, we analized the symmetries of the effective tensors but we will also look at the properties of isotropy thanks to Christoffel tensor.

- Another perspective is the deployement of the homogenization method, with one time-scale and two length-scales, up to the second order, in the three cases studied. This is required in order to describe the dispersive nature of the fields. In linear dynamic homogenization, the long-term behavior of the microstructured wavefields is not well captured by first-order effective models, in particular due to the dispersive nature of the former that develops with time (Santosa & Symes, 1991; Lamacz, 2011). It is even more true in the non-linear case since the "long term" notion is correlated to the amplitude of the source. Another possibility

to the prospect of "long term" behaviour is to introduce a slow and a fast time-scales in the asymptotics (Chen & Fish, 2001).

- For non-linear interfaces, a relatively low amplitude of the source term is assumed. An effective model for waves of relatively larger amplitudes would also be interesting and would require the consideration of an additional scaling in the classical small parameter η relatively to the amplitude.

CHAPTER 6

High-frequency homogenization for a 1D medium with imperfect interfaces

The framework considered in this chapter is this of Section 1.2.3 with waves propagating in $h-$periodic media at angular frequencies that are not necessary small, which does not correspond to the setting of low-frequency homogenization. More precisely, we are interested in the dispersion relations in periodic media that describe how the angular frequency ω depends on the the Bloch wavenumbers k. These relations can be studied through dispersion diagrams that restrict the Bloch wavenumbers to the first Brillouin zone $[0, \pi/h]$ in the one-dimensional case. The version of *high-frequency homogenization* considered aims at approximating how the dispersion relation behaves near the edges of this Brillouin zone. Adopting the terminology of Guzina et al., 2019, we will refer to the homogenization near the left edge of the Brillouin zone $k \approx 0$ as Finite Frequency Low Wavenumber (FFLW), while the homogenization near the right edge ($k \approx \pi/h$) will be referred to as Finite Frequency Finite Wavenumber (FFFW). Accordingly, one introduces $\tilde{k}$ as

$$\text{(FFLW)} : \tilde{k} = k \quad \text{and} \quad \text{(FFFW)} : \tilde{k} = \pi/h - k, \tag{6.1}$$

In this chapter, following the methodology of Craster et al., 2010a, we apply the high-frequency homogenization technique to a one-dimensional periodic medium that have imperfect interfaces at the edges of the periodic cell. In line with the previous chapter, the imperfect contacts are modelled by linear spring-mass interface conditions. These imperfect conditions typically arise from the homogenization of a thin interphase. The results presented in the paper are hence relevant for wavelength comparable to the periodicity, but much larger than the thin interphase approximated by the imperfect contact laws.

In Section 6.1 the physical problem at hand is presented. The two-scale asymptotic expansion method is developed in Section 6.2. Then, Section 6.3 provides an approximation of both the dispersion diagram and the wavefield at the edges of the band gaps. The case where two branches of the dispersion diagrams intersect with non-zero slopes is studied in Section 6.4. Section 6.5 provides a smooth transition between the two previous cases and therefore provides an approximation in the case of narrow band gaps. Eventually, in Section 6.6 two examples are considered and treated both by a Bloch-Floquet analysis and by the approximation previously obtained. It illustrates the validity of the homogenization method.

6.1 Problem under study

6.1.1 Physical setting

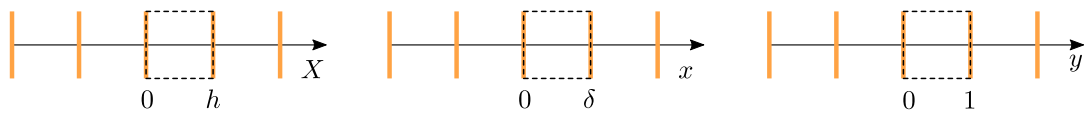

Figure 6.1 – Geometry settings in the X, x and y variables, a periodic cell is highlighted with a dashed line.

The medium is now one-dimensional with periodicity $h > 0$, and a macroscopic length $L > 0$ which can be seen as the modulation length. We denote the physical space variable X, the density $\rho_h(X)$ and the Young's modulus $\mu_h(X)$. The edges of the periodic cell are located at $X_n = nh$, with $n \in \mathbb{Z}$, see left part of Figure 6.1. The interfaces at the edges are assumed to be imperfect, of the linear spring-mass type. More precisely, they are characterized by a mass parameter and a stiffness parameter denoted M and K, respectively, see (5.2) in the previous chapter. Consequently, the governing equation and jump conditions for the displacement $U_h(X)$ read in the frequency

domain:

$$\begin{cases} \dfrac{\mathrm{d}}{\mathrm{d}X}\left(\mu_h(X)\dfrac{\mathrm{d}U_h}{\mathrm{d}X}\right) + \rho_h(X)\omega^2 U_h = 0 & (X \in \mathbb{R}), \\ [\![U_h]\!]_{X_n} = \dfrac{1}{K}\left\langle\!\!\left\langle \mu_h \dfrac{\mathrm{d}U_h}{\mathrm{d}X} \right\rangle\!\!\right\rangle_{X_n} & (n \in \mathbb{Z}), \\ \left[\!\!\left[\mu_h \dfrac{\mathrm{d}U_h}{\mathrm{d}X} \right]\!\!\right]_{X_n} = -M\omega^2 \langle\!\langle U_h \rangle\!\rangle_{X_n} & (n \in \mathbb{Z}), \end{cases} \tag{6.2}$$

with ω the angular frequency at which waves propagate in the medium, and the jump $[\![\cdot]\!]$ and the mean value $\langle\!\langle\cdot\rangle\!\rangle$ at the interface X_n being defined in (5.3).
Due to the h-periodicity, the physical parameters can be written $\rho_h(X) = \rho\left(\frac{X}{h}\right)$ and $\mu_h(X) = \mu\left(\frac{X}{h}\right)$, with ρ and μ some 1-periodic functions. They satisfy Assumption 5.1 as in the previous chapter. We also assume that, even if discontinuity is possible for the physical parameters in $]0,1[$, the displacement $U_h(X)$ and the stress $\mu_h(X)\frac{\mathrm{d}U_h}{\mathrm{d}X}$ are continuous on a periodic cell.

6.1.2 Bloch-Floquet analysis

The Bloch-Floquet analysis allows to study wave propagation in periodic media through a spectral problem in one single cell. It consists in seeking solutions propagating at the Bloch wavenumber k of the form

$$U_h(X) = \mathfrak{U}_h(X)e^{\mathrm{i}kX}, \tag{6.3}$$

with $\mathfrak{U}_h(X)$ being h-periodic. In some cases, see Sections 6.6.1 and 6.6.2, it is possible to get from this analysis an explicit dispersion relation between the frequency ω and the Bloch wavenumber k. Its graphical representation is the so-called dispersion diagram.
From (6.3), one notes that for $k = 0$, we have $U_h(X) = U_h(X + h)$, i.e. the solution is periodic, while for $k = \frac{\pi}{h}$, we have $U_h(X) = -U_h(X + h)$, i.e. the solution is antiperiodic. These values of k correspond to the edges of the so-called Brillouin zone. The aim of this chapter is to approximate the Bloch-Floquet solutions around these edges, i.e. close to $k = 0$ (FFLW) or $k = \frac{\pi}{h}$ (FFFW) with finite angular frequencies satisfying $\omega = O(1)$.

6.2 Methodology

6.2.1 Nondimensionalization

We start by a nondimensionalization of the physical problem (6.2). Firstly, we recall the characteristic density $\rho^\star = \langle\rho\rangle$, Young's modulus $\mu^\star = \langle 1/\mu\rangle^{-1}$ and wavespeed $c^\star = \sqrt{\mu^\star/\rho^\star}$, with the average operator $\langle\cdot\rangle$ defined in (5.16). Then, one can define the following non-dimensional quantities

$$x = \frac{X}{L},\ \delta = \frac{h}{L},\ \eta = \frac{\omega h}{c^\star},\ \kappa = Lk,\ \alpha = \frac{\rho}{\rho^\star},\ \beta = \frac{\mu}{\mu^\star},$$
$$\mathcal{K} = \frac{Kh}{\mu^\star},\ \mathcal{M} = \frac{M}{h\rho^\star},\ u_\delta(x) = \frac{U_h(X)}{L}. \tag{6.4}$$

Remark 19. *The non-dimensionalization of the parameters is the same as in the previous chapter, see (5.11). The differences are for the variables and the wavefield.*

Remark 20. *One notices that the notation η is consistent with the small parameter of the previous chapters. The difference in this chapter is that, in the framework of high-frequency homogenization,*

η is not supposed to be much smaller than one contrary to δ.

Remark 21. *The choice of $\rho^\star$ and $\mu^\star$ is arbitrary. They are chosen here to be the effective properties obtained by low-frequency homogenization, see Chapter 5. In practice, this implies that $\langle\alpha\rangle = \langle 1/\beta\rangle = 1$.*

Consequently, the physical parameters read

$$\rho_h(X) = \rho\left(\frac{X}{h}\right) = \rho\left(\frac{x}{\delta}\right) \quad \text{and} \quad \mu_h(X) = \mu\left(\frac{X}{h}\right) = \mu\left(\frac{x}{\delta}\right),$$

with x corresponding to the geometrical setting of Figure 6.1 (center). Using these quantities, (6.2) can be rewritten as the non-dimensional governing equation

$$\delta^2 \frac{\mathrm{d}}{\mathrm{d}x}\left(\beta\left(\frac{x}{\delta}\right)\frac{\mathrm{d}u_\delta}{\mathrm{d}x}(x)\right) + \eta^2\alpha\left(\frac{x}{\delta}\right)u_\delta(x) \;=\; 0, \tag{6.5}$$

subject to the jump conditions for $n \in \mathbb{Z}$:

$$\begin{cases} [\![u_\delta]\!]_{x_n} = \dfrac{\delta}{\mathcal{K}}\left\langle\!\!\left\langle \beta\left(\dfrac{x}{\delta}\right)\dfrac{\mathrm{d}u_\delta}{\mathrm{d}x}\right\rangle\!\!\right\rangle_{x_n}, \\ \delta\left[\!\!\left[\beta\left(\dfrac{x}{\delta}\right)\dfrac{\mathrm{d}u_\delta}{\mathrm{d}x}\right]\!\!\right]_{x_n} = -\mathcal{M}\eta^2\left\langle\!\left\langle u_\delta\right\rangle\!\right\rangle_{x_n}. \end{cases} \tag{6.6}$$

The equations (6.5)-(6.6) constitute our non-dimensional problem. They fully highlight the contributions of the parameter δ. In particular, the order of magnitude of the parameters α, β, $\mathcal{M}$ and $\mathcal{K}$ will be assumed to be of order $\mathcal{O}(1)$.
In this non-dimensional setting, the Bloch-Floquet analysis (6.3) consists in looking for solutions of the form

$$u_\delta(x) = \mathfrak{u}_\delta(x)e^{\mathrm{i}\kappa x}, \tag{6.7}$$

where κ is the non-dimensional Bloch wavenumber and $\mathfrak{u}_\delta$ is δ-periodic. It implies that u_δ and its derivative u'_δ satisfy

$$u_\delta(x+\delta) = u_\delta(x)e^{\mathrm{i}\kappa\delta} \quad \text{and} \quad u'_\delta(x+\delta) = u'_\delta(x)e^{\mathrm{i}\kappa\delta}. \tag{6.8}$$

Remark 6.1. *The FFLW case corresponds to $\kappa\delta \approx 0$ and the FFFW case corresponds to $\kappa\delta \approx \pi$. When $\kappa\delta$ is exactly 0 (resp. π), then the solution $u_\delta(x)$ is δ-periodic (resp. δ-antiperiodic).*

6.2.2 Two-scale asymptotic expansion

Assumption 6.1

As discussed in introduction, one assumes that the macroscopic characteristic length L is much larger than the periodicity h, implying that $\delta \ll 1$.

Then, the dimensionless material parameters α and β will vary on a fine scale associated with the rescaled coordinate $y = x/\delta$, see Figure 6.1 (right) for the associated geometrical configuration. Furthermore, the displacement field is also assumed to have small scale features described by y,

and slow continuous variations described by x. Following the two-scale expansion technique, we hence expand the wavefield u_δ and the reduced frequency η according to the following ansatzes:

$$u_\delta(x) = \sum_{j\geqslant 0} \delta^j u_j(x,y) \qquad \text{and} \qquad \eta^2 = \sum_{\ell\geqslant 0} \delta^\ell \eta_\ell^2. \tag{6.9}$$

According to Remark 6.1, u_j is assumed to be 1-periodic (resp. antiperiodic) in y in the FFLW (resp. FFFW) case. The space coordinates x and y are treated as two independent variables (scale separation), implying that

$$\frac{\mathrm{d}}{\mathrm{d}x} \to \frac{\partial}{\partial x} + \frac{1}{\delta}\frac{\partial}{\partial y}. \tag{6.10}$$

Inserting (6.9) and (6.10) in (6.5)–(6.6) yields

$$\sum_{j\geqslant 0}\left[\delta^j \frac{\partial}{\partial y}\left(\beta\frac{\partial u_j}{\partial y}\right) + \delta^{j+1}\left\{\beta\frac{\partial^2 u_j}{\partial x\partial y} + \frac{\partial}{\partial y}\left(\beta\frac{\partial u_j}{\partial x}\right)\right\} + \delta^{j+2}\beta\frac{\partial^2 u_j}{\partial x^2} + \sum_{\ell\geqslant 0}\delta^{\ell+j}\eta_\ell^2\alpha u_j\right] = 0, \tag{6.11}$$

subject to the jump conditions at $y_n = n$, $n \in \mathbb{Z}$:

$$\sum_{j\geqslant 0}\delta^j \left[\!\left[u_j(x,y)\right]\!\right]_{y_n} = \frac{\delta}{\mathcal{K}}\sum_{j\geqslant 0}\delta^j \left\langle\!\left\langle \beta(y)\left(\frac{\partial u_j}{\partial x} + \frac{1}{\delta}\frac{\partial u_j}{\partial y}\right)\right\rangle\!\right\rangle_{y_n}, \tag{6.12}$$

and

$$\delta\sum_{j\geqslant 0}\delta^j \left[\!\left[\beta(y)\left(\frac{\partial u_j}{\partial x} + \frac{1}{\delta}\frac{\partial u_j}{\partial y}\right)\right]\!\right]_{y_n} = -\mathcal{M}\left(\sum_{\ell\geqslant 0}\delta^\ell\eta_\ell^2\right)\left(\sum_{j\geqslant 0}\delta^j \left\langle\!\left\langle u_j\right\rangle\!\right\rangle_{y_n}\right). \tag{6.13}$$

For any function $g(x,y)$, the jump and mean brackets in y-coordinates are defined in (5.15). Due to the 1-periodicity (or anti-periodicity) in y for all the fields in (6.11)–(6.13), these three equations will be studied for $y \in]0,1[$. Consequently, the subscript y_n will be dropped later on since we will only consider the case $n = 0$. We also assume that the displacement and the stress are continuous within the unit cell. This leads to the following assumptions of continuity:

$$u_0,\ \beta\frac{\partial u_0}{\partial y},\ u_j \text{ and } \beta\left(\frac{\partial u_j}{\partial y} + \frac{\partial u_{j-1}}{\partial x}\right) \text{ for } j \geqslant 1 \text{ are continuous functions of } y \text{ on }]0,1[. \tag{6.14}$$

One recalls two properties of the jump and mean brackets that will be used later on. Firstly, for any two functions $f(x,y)$ and $g(x,y)$, the following relation holds:

$$\left[\!\left[fg\right]\!\right] = \left[\!\left[f\right]\!\right]\left\langle\!\left\langle g\right\rangle\!\right\rangle + \left\langle\!\left\langle f\right\rangle\!\right\rangle\left[\!\left[g\right]\!\right]. \tag{6.15}$$

Secondly, for any function $g^{\mathrm{per}}(x,y)$ that is 1-periodic in y

$$\left[\!\left[g^{\mathrm{per}}\right]\!\right] = g^{\mathrm{per}}(x,0^+) - g^{\mathrm{per}}(x,1^-) \quad \text{and} \quad \left\langle\!\left\langle g^{\mathrm{per}}\right\rangle\!\right\rangle = \frac{1}{2}(g^{\mathrm{per}}(x,0^+) + g^{\mathrm{per}}(x,1^-)) \tag{6.16}$$

while for a function $g^{\mathrm{anti}}(x,y)$ that is 1-antiperiodic in y

$$\left[\!\left[g^{\mathrm{anti}}\right]\!\right] = g^{\mathrm{anti}}(x,0^+) + g^{\mathrm{anti}}(x,1^-) \quad \text{and} \quad \left\langle\!\left\langle g^{\mathrm{anti}}\right\rangle\!\right\rangle = \frac{1}{2}(g^{\mathrm{anti}}(x,0^+) - g^{\mathrm{anti}}(x,1^-)). \tag{6.17}$$

In particular, (6.16) allows to relate the average operator (**??**) and the jump bracket for any function $g^{\mathrm{per}}(x,y)$ that is 1-periodic and continuous for $y \in]0,1[$ as:

$$\left\langle\frac{\partial g^{\mathrm{per}}}{\partial y}\right\rangle = -\left[\!\left[g^{\mathrm{per}}\right]\!\right] \tag{6.18}$$

Notation 6.2.1. *From now on, in order to efficiently deal with the FFLW (Finite Frequency Low Wavenumber, $\kappa\delta \approx 0$) and the FFFW (Finite Frequency Finite Wavenumber, $\kappa\delta \approx \pi$) cases simultaneously, we will assume that whenever the symbols $\pm$ or $\mp$ are used, the top sign corresponds to FFLW while the bottom sign corresponds to FFFW.*

An identification of the contributions of (6.11)–(6.13) at the orders δ^0, δ^1 and δ^2 is now performed to derive the sought approximations.

6.2.3 Zeroth-order field: an eigenvalue problem

At the leading order δ^0 in (6.11)–(6.13), the system obtained is:

$$\begin{cases} \dfrac{\partial}{\partial y}\left(\beta\dfrac{\partial u_0}{\partial y}\right) + \eta_0^2\alpha u_0 = 0 & (x\in\mathbb{R},\ y\in]0,1[), \quad (6.19a)\\ [\![u_0]\!] = \dfrac{1}{\mathcal{K}}\left\langle\!\!\left\langle \beta\dfrac{\partial u_0}{\partial y}\right\rangle\!\!\right\rangle & (x\in\mathbb{R}), \quad (6.19b)\\ \left[\!\!\left[\beta\dfrac{\partial u_0}{\partial y}\right]\!\!\right] = -\mathcal{M}\eta_0^2\langle\!\langle u_0\rangle\!\rangle & (x\in\mathbb{R}). \quad (6.19c) \end{cases}$$

The eigenvalue in the boundary condition (6.19c) is a bit unusual compared to classical eigenvalue problems where η_0^2 appears only in the governing equation (6.19a). Hence,one introduces the inner product $(\cdot|\cdot)$ defined for some functions $f(y)$ and $g(y)$ (either both FFLW or both FFFW) by

$$(f\,|\,g) = \langle \alpha f\bar{g}\rangle + \mathcal{M}\left\langle\!\!\left\langle f\right\rangle\!\!\right\rangle\left\langle\!\!\left\langle \bar{g}\right\rangle\!\!\right\rangle, \tag{6.20}$$

ant the (Sturm-Liouville) differential operator

$$\mathcal{L} = \frac{-1}{\alpha}\frac{\mathrm{d}}{\mathrm{d}y}\left(\beta\frac{\mathrm{d}}{\mathrm{d}y}\right). \tag{6.21}$$

Property 9. *The system (6.19) constitutes an eigenvalue problem for $\mathcal{L}$ using the tailored inner product* (6.20).

Proof. The system (6.19) can be formulated as follows: find λ such that

$$\begin{cases} \mathcal{L}[f] = \lambda f, & (6.22a)\\ [\![f]\!] = \dfrac{1}{\mathcal{K}}\left\langle\!\!\left\langle \beta\dfrac{\mathrm{d}f}{\mathrm{d}y}\right\rangle\!\!\right\rangle, & (6.22b)\\ \left[\!\!\left[\beta\dfrac{\mathrm{d}f}{\mathrm{d}y}\right]\!\!\right] = -\mathcal{M}\lambda\left\langle\!\!\left\langle f\right\rangle\!\!\right\rangle, & (6.22c) \end{cases}$$

for some function f that is periodic (FFLW) or antiperiodic (FFFW). The second jump condition (6.22c) is rewritten so that it does not involve λ explicitely anymore:

$$\begin{cases} \mathcal{L}[f] = \lambda f, & (6.23a)\\ [\![f]\!] = \dfrac{1}{\mathcal{K}}\left\langle\!\!\left\langle \beta\dfrac{\mathrm{d}f}{\mathrm{d}y}\right\rangle\!\!\right\rangle, & (6.23b)\\ \left[\!\!\left[\beta\dfrac{\mathrm{d}f}{\mathrm{d}y}\right]\!\!\right] = -\mathcal{M}\left\langle\!\!\left\langle \mathcal{L}[f]\right\rangle\!\!\right\rangle. & (6.23c) \end{cases}$$

One wants to prove that finding (λ, f) satisfying (6.23) with f periodic or antiperiodic is an eigenvalue problem. For this purpose, one needs to prove that the operator $\mathcal{L}$ subjected to the jump and periodicity conditions is both symmetric and non-negative for the inner product (6.20).

■ *Symmetry.* Proving the symmetry consists in proving that $\big(\mathcal{L}[f]\big|g\big) = \big(f\big|\mathcal{L}[g]\big)$ for any functions f and g satisfying both jump and periodic (FFLW) or antiperiodic (FFFW) conditions. We will hence prove that the quantity $\mathrm{Sym}(f,g) = \big(\mathcal{L}[f]\big|g\big) - \big(f\big|\mathcal{L}[g]\big)$ is zero. First by definition of the inner product (6.20) we have

$$\begin{aligned}\mathrm{Sym}(f,g) &= \langle \alpha \mathcal{L}[f]\bar{g}\rangle + \mathcal{M}\left\langle\!\left\langle \mathcal{L}[f]\right\rangle\!\right\rangle \left\langle\!\left\langle \bar{g}\right\rangle\!\right\rangle - \langle \alpha f \overline{\mathcal{L}[g]}\rangle - \mathcal{M}\left\langle\!\left\langle f\right\rangle\!\right\rangle \left\langle\!\left\langle \overline{\mathcal{L}[g]}\right\rangle\!\right\rangle \\ &= \left\langle f \frac{\mathrm{d}}{\mathrm{d}y}\left(\beta\frac{\mathrm{d}\bar{g}}{\mathrm{d}y}\right) - \frac{\mathrm{d}}{\mathrm{d}y}\left(\beta\frac{\mathrm{d}f}{\mathrm{d}y}\right)\bar{g}\right\rangle + \left\langle\!\left\langle f\right\rangle\!\right\rangle \left[\!\left[\beta\frac{\mathrm{d}\bar{g}}{\mathrm{d}y}\right]\!\right] - \left[\!\left[\beta\frac{\mathrm{d}f}{\mathrm{d}y}\right]\!\right]\left\langle\!\left\langle \bar{g}\right\rangle\!\right\rangle, \end{aligned} \tag{6.24}$$

where we have used the equation (6.23c) and the definition (6.21). Now, using the fact that

$$f\frac{\mathrm{d}}{\mathrm{d}y}\left(\beta\frac{\mathrm{d}\bar{g}}{\mathrm{d}y}\right) - \frac{\mathrm{d}}{\mathrm{d}y}\left(\beta\frac{\mathrm{d}f}{\mathrm{d}y}\right)\bar{g} = \frac{\mathrm{d}}{\mathrm{d}y}\left(f\beta\frac{\mathrm{d}\bar{g}}{\mathrm{d}y} - \beta\frac{\mathrm{d}f}{\mathrm{d}y}\bar{g}\right),$$

the equation (6.24) becomes

$$\begin{aligned}\mathrm{Sym}(f,g) &= \left\langle \frac{\mathrm{d}}{\mathrm{d}y}\left(f\beta\frac{\mathrm{d}\bar{g}}{\mathrm{d}y} - \beta\frac{\mathrm{d}f}{\mathrm{d}y}\bar{g}\right)\right\rangle + \left\langle\!\left\langle f\right\rangle\!\right\rangle \left[\!\left[\beta\frac{\mathrm{d}\bar{g}}{\mathrm{d}y}\right]\!\right] - \left[\!\left[\beta\frac{\mathrm{d}f}{\mathrm{d}y}\right]\!\right]\left\langle\!\left\langle \bar{g}\right\rangle\!\right\rangle \\ &\underset{\text{Eq. (6.18)}}{=} -\left[\!\left[f\beta\frac{\mathrm{d}\bar{g}}{\mathrm{d}y} - \beta\frac{\mathrm{d}f}{\mathrm{d}y}\bar{g}\right]\!\right] + \left\langle\!\left\langle f\right\rangle\!\right\rangle \left[\!\left[\beta\frac{\mathrm{d}\bar{g}}{\mathrm{d}y}\right]\!\right] - \left[\!\left[\beta\frac{\mathrm{d}f}{\mathrm{d}y}\right]\!\right]\left\langle\!\left\langle \bar{g}\right\rangle\!\right\rangle \\ &\underset{\text{Eq. (6.15)}}{=} \left\langle\!\left\langle \beta\frac{\mathrm{d}f}{\mathrm{d}y}\right\rangle\!\right\rangle \left[\!\left[\bar{g}\right]\!\right] - \left[\!\left[f\right]\!\right]\left\langle\!\left\langle \beta\frac{\mathrm{d}\bar{g}}{\mathrm{d}y}\right\rangle\!\right\rangle \\ &\underset{\text{Jump (6.23b)}}{=} \mathcal{K}\left[\!\left[f\right]\!\right]\left[\!\left[\bar{g}\right]\!\right] - \mathcal{K}\left[\!\left[f\right]\!\right]\left[\!\left[\bar{g}\right]\!\right] = 0, \end{aligned}$$

and hence the problem is symmetric.

■ *Non-negativity.* The non-negativity property is satisfied if $\big(\mathcal{L}[f]\big|f\big) \geqslant 0$ for any functions f satisfying both jump and periodic (FFLW) or antiperiodic (FFFW) conditions. By definition of the inner product (6.20), we have

$$\big(\mathcal{L}[f]\big|f\big) = \langle \alpha\mathcal{L}[f]\bar{f}\rangle + \mathcal{M}\left\langle\!\left\langle \mathcal{L}[f]\right\rangle\!\right\rangle\left\langle\!\left\langle \bar{f}\right\rangle\!\right\rangle = -\left\langle \frac{\mathrm{d}}{\mathrm{d}y}\left(\beta\frac{\mathrm{d}f}{\mathrm{d}y}\right)\bar{f}\right\rangle - \left[\!\left[\beta\frac{\mathrm{d}f}{\mathrm{d}y}\right]\!\right]\left\langle\!\left\langle \bar{f}\right\rangle\!\right\rangle, \tag{6.25}$$

where we have used both (6.23c) and (6.21). Now, using the fact that

$$\frac{\mathrm{d}}{\mathrm{d}y}\left(\beta\frac{\mathrm{d}f}{\mathrm{d}y}\right)\bar{f} = \frac{\mathrm{d}}{\mathrm{d}y}\left(\beta\frac{\mathrm{d}f}{\mathrm{d}y}\bar{f}\right) - \beta\left|\frac{\mathrm{d}f}{\mathrm{d}y}\right|^2,$$

then the equation (6.25) becomes

$$\begin{aligned}\big(\mathcal{L}[f]\big|f\big) &= \left\langle \beta\left|\frac{\mathrm{d}f}{\mathrm{d}y}\right|^2\right\rangle - \left\langle \frac{\mathrm{d}}{\mathrm{d}y}\left(\beta\frac{\mathrm{d}f}{\mathrm{d}y}\bar{f}\right)\right\rangle - \left[\!\left[\beta\frac{\mathrm{d}f}{\mathrm{d}y}\right]\!\right]\left\langle\!\left\langle \bar{f}\right\rangle\!\right\rangle \\ &\underset{\text{Eq. (6.18)}}{=} \left\langle \beta\left|\frac{\mathrm{d}f}{\mathrm{d}y}\right|^2\right\rangle + \left[\!\left[\beta\frac{\mathrm{d}f}{\mathrm{d}y}\bar{f}\right]\!\right] - \left[\!\left[\beta\frac{\mathrm{d}f}{\mathrm{d}y}\right]\!\right]\left\langle\!\left\langle \bar{f}\right\rangle\!\right\rangle \\ &\underset{\text{Eq. (6.15)}}{=} \left\langle \beta\left|\frac{\mathrm{d}f}{\mathrm{d}y}\right|^2\right\rangle + \left\langle\!\left\langle \beta\frac{\mathrm{d}f}{\mathrm{d}y}\right\rangle\!\right\rangle \left[\!\left[\bar{f}\right]\!\right] \underset{\text{Jump (6.23b)}}{=} \left\langle \beta\left|\frac{\mathrm{d}f}{\mathrm{d}y}\right|^2\right\rangle + \mathcal{K}\big|\left[\!\left[f\right]\!\right]\big|^2 \geqslant 0, \end{aligned}$$

hence the problem is non-negative.
In conclusion, the operator $\mathcal{L}$, together with the jump and periodicity conditions, is self-adjoint and non-negative in both the FFLW and FFFW cases. □

Therefore the problem (6.22) has a discrete set of (possibly repeated) real positive eigenvalues associated to real eigenfunctions that are orthogonal for the inner product (6.20). We choose one of these eigenvalues, and denote its square root by η_0. This adimensionalized frequency η_0 corresponds to an intersection of the dispersion diagram with the left (FFLW) or the right (FFFW) border of the Brillouin zone. Our aim is to approximate the solutions for some parameters $(\eta, \tilde{\kappa})$ close to $(\eta_0, 0)$, where we define $\tilde{\kappa}$ to be

$$(\text{FFLW}) : \tilde{\kappa} = \kappa \quad \text{and} \quad (\text{FFFW}) : \tilde{\kappa} = \pi/\delta - \kappa, \tag{6.26}$$

allowing us to treat the FFLW and FFFW cases simultaneously.

6.3 Case of simple eigenvalues

6.3.1 A form for u_0

First, we assume in this section that η_0 is a simple eigenvalue (multiplicity 1) and $\hat{u}_0(y)$ is an associated eigenfunction that is either periodic (FFLW) or antiperiodic (FFFW). The case of a double eigenvalue will be treated in Section 6.4. Consequently, $(\lambda, f) = (\eta_0^2, \hat{u}_0)$ is solution of (6.22). The resulting solution u_0 to (6.19) can thus be written

$$u_0(x, y) = \mathcal{U}_0(x)\hat{u}_0(y), \tag{6.27}$$

for some function $\mathcal{U}_0(x)$.
The main aim of this section is to derive a differential equation with constant coefficients satisfied by $\mathcal{U}_0(x)$. Note that in the case of low-frequency homogenization, the zeroth-order field $u_0(x, y)$ h as been shown to be independent of y; this is one of the main differences between low- and high-frequency homogenization.

6.3.2 Proving that $\eta_1 = 0$

We now collect the terms of order δ^1 in (6.11)–(6.13) to obtain the following system governing the first-order field u_1:

$$\begin{cases} \dfrac{\partial}{\partial y}\left(\beta\left(\dfrac{\partial u_1}{\partial y} + \dfrac{\partial u_0}{\partial x}\right)\right) + \beta\dfrac{\partial^2 u_0}{\partial x \partial y} + \alpha(\eta_0^2 u_1 + \eta_1^2 u_0) = 0, & \text{(6.28a)} \\ [\![u_1]\!] = \dfrac{1}{\mathcal{K}}\left\langle\!\!\left\langle \beta\left(\dfrac{\partial u_0}{\partial x} + \dfrac{\partial u_1}{\partial y}\right)\right\rangle\!\!\right\rangle, & \text{(6.28b)} \\ \left[\!\!\left[\beta\left(\dfrac{\partial u_0}{\partial x} + \dfrac{\partial u_1}{\partial y}\right)\right]\!\!\right] = -\mathcal{M}(\eta_0^2 \langle\!\langle u_1 \rangle\!\rangle + \eta_1^2 \langle\!\langle u_0 \rangle\!\rangle). & \text{(6.28c)} \end{cases}$$

We will show below that $\eta_1 = 0$. Following Craster et al., 2010a, we consider $\langle u_1 \cdot (6.19a) - u_0 \cdot (6.28a)\rangle$. The terms in $\alpha\eta_0^2 u_0 u_1$ cancel out, and using the fact that

$$u_1\frac{\partial}{\partial y}\left(\beta\frac{\partial u_0}{\partial y}\right) - u_0\frac{\partial}{\partial y}\left(\beta\left(\frac{\partial u_1}{\partial y} + \frac{\partial u_0}{\partial x}\right)\right) = \frac{\partial}{\partial y}\left(u_1\beta\frac{\partial u_0}{\partial y} - u_0\beta\left(\frac{\partial u_1}{\partial y} + \frac{\partial u_0}{\partial x}\right)\right) + \beta\frac{\partial u_0}{\partial y}\frac{\partial u_0}{\partial x},$$

one obtains

$$\left\langle \frac{\partial}{\partial y}\left(u_1\beta\frac{\partial u_0}{\partial y} - u_0\beta\left(\frac{\partial u_1}{\partial y} + \frac{\partial u_0}{\partial x}\right)\right)\right\rangle = \underbrace{\left\langle \beta\left(u_0\frac{\partial^2 u_0}{\partial x \partial y} - \frac{\partial u_0}{\partial x}\frac{\partial u_0}{\partial y}\right)\right\rangle}_{=0} + \eta_1^2\langle \alpha u_0^2\rangle. \tag{6.29}$$

Due to (6.27), we have $u_0 \frac{\partial^2 u_0}{\partial x \partial y} - \frac{\partial u_0}{\partial x}\frac{\partial u_0}{\partial y} = 0$, so the first bracket in the right-hand side of the equation above is actually zero. Now, using (6.14) and (6.18), then (6.29) becomes

$$-\left[\!\left[u_1 \beta \frac{\partial u_0}{\partial y} - u_0 \beta \left(\frac{\partial u_1}{\partial y} + \frac{\partial u_0}{\partial x} \right) \right]\!\right] = \eta_1^2 \langle \alpha u_0^2 \rangle. \tag{6.30}$$

When perfect interfaces are considered, the jump bracket term in (6.30) is automatically zero, a fact that is used in (Craster et al., 2010a) to conclude that $\eta_1 = 0$. This jump bracket does not cancel out when imperfect interfaces are considered. Instead, one makes use of (6.15) to rewrite (6.30) as

$$\begin{aligned}\eta_1^2 \langle \alpha u_0^2 \rangle &= -\left[\!\left[u_1 \right]\!\right] \left\langle\!\!\left\langle \beta \frac{\partial u_0}{\partial y} \right\rangle\!\!\right\rangle - \left\langle\!\left\langle u_1 \right\rangle\!\right\rangle \left[\!\left[\beta \frac{\partial u_0}{\partial y} \right]\!\right] + \left[\!\left[u_0 \right]\!\right] \left\langle\!\!\left\langle \beta \left(\frac{\partial u_1}{\partial y} + \frac{\partial u_0}{\partial x} \right) \right\rangle\!\!\right\rangle + \left\langle\!\left\langle u_0 \right\rangle\!\right\rangle \left[\!\left[\beta \left(\frac{\partial u_1}{\partial y} + \frac{\partial u_0}{\partial x} \right) \right]\!\right] \\ &= -\mathcal{K} \left[\!\left[u_0 \right]\!\right] \left[\!\left[u_1 \right]\!\right] + \mathcal{M} \eta_0^2 \left\langle\!\left\langle u_1 \right\rangle\!\right\rangle \left\langle\!\left\langle u_0 \right\rangle\!\right\rangle + \mathcal{K} \left[\!\left[u_0 \right]\!\right] \left[\!\left[u_1 \right]\!\right] - \mathcal{M} \left\langle\!\left\langle u_0 \right\rangle\!\right\rangle \left(\eta_0^2 \left\langle\!\left\langle u_1 \right\rangle\!\right\rangle + \eta_1^2 \left\langle\!\left\langle u_0 \right\rangle\!\right\rangle \right),\end{aligned}$$

where the jump conditions (6.19b)–(6.19c) and (6.28b)–(6.28c) have been used. This yields

$$\eta_1^2 (\langle \alpha u_0^2 \rangle + \mathcal{M} \left\langle\!\left\langle u_0 \right\rangle\!\right\rangle^2) = 0, \tag{6.31}$$

implying that $\eta_1 = 0$, because $\mathcal{M}$ and α are strictly positive, and, in the representation (6.27), $\mathcal{U}_0$ cannot be identically zero and $\hat{u}_0$ is a real function.

6.3.3 A form for $u_1(x, y)$

We can now simplify the equation (6.28a) governing u_1 to

$$\frac{\partial}{\partial y} \left(\beta \frac{\partial u_1}{\partial y} \right) + \alpha \eta_0^2 u_1 = -\mathcal{U}_0'(x)(2\beta(y)\hat{u}_0'(y) + \beta'(y)\hat{u}_0(y)). \tag{6.32}$$

Upon noting that, because $\hat{u}_0$ is solution to (6.19a), the field $-y\mathcal{U}_0'(x)\hat{u}_0(y)$ is a particular solution to (6.32), and that the differential operator applied to u_1 is exactly the same as that of (6.19a), we can conclude that u_1 can be written as

$$u_1(x, y) = \mathcal{U}_1(x)\hat{u}_0(y) + \mathcal{U}_0'(x) \left(\mathrm{v}_1(y) - y\hat{u}_0(y) \right). \tag{6.33}$$

The function $\mathcal{U}_1(x)$ will be shown to play no role in what follows. We will also prove that the function $\mathrm{v}_1(y)$, that is another solution to (6.19a), independent of $\hat{u}_0(y)$, is chosen to ensure that the jump conditions

$$\begin{cases} \left[\!\left[u_1 \right]\!\right] = \dfrac{1}{\mathcal{K}} \left\langle\!\!\left\langle \beta \left(\dfrac{\partial u_0}{\partial x} + \dfrac{\partial u_1}{\partial y} \right) \right\rangle\!\!\right\rangle, & \text{(6.34a)} \\ \left[\!\left[\beta \left(\dfrac{\partial u_0}{\partial x} + \dfrac{\partial u_1}{\partial y} \right) \right]\!\right] = -\mathcal{M} \eta_0^2 \left\langle\!\left\langle u_1 \right\rangle\!\right\rangle, & \text{(6.34b)} \end{cases}$$

are satisfied. These jump conditions come from (6.28b)–(6.28c), where we have used that $\eta_1 = 0$. Note that because of (6.33), and the periodicity properties of u_1 and $\hat{u}_0$, the function $\mathrm{v}_1(y) - y\hat{u}_0(y)$ has to be periodic (FFLW) or antiperiodic (FFFW). Because this function will appear many times in what follows, it is worth giving it a name. Hence, we define

$$f_1(y) = \mathrm{v}_1(y) - y\hat{u}_0(y). \tag{6.35}$$

Inputting the form (6.33) into (6.34), leads to two conditions on f_1:

$$\begin{cases} \left[\!\left[f_1 \right]\!\right] = \dfrac{1}{\mathcal{K}} \left\langle\!\left\langle \beta f_1' \right\rangle\!\right\rangle + \dfrac{1}{\mathcal{K}} \left\langle\!\left\langle \beta \hat{u}_0 \right\rangle\!\right\rangle, & \text{(6.36a)} \\ -\mathcal{M} \eta_0^2 \left\langle\!\left\langle f_1 \right\rangle\!\right\rangle = \left[\!\left[\beta f_1' \right]\!\right] + \left[\!\left[\beta \hat{u}_0 \right]\!\right]. & \text{(6.36b)} \end{cases}$$

One should notice, in particular, that no terms involving $\mathcal{U}_1(x)$ appear in these conditions.

For practical computations of the function $\mathrm{v}_1(y)$, which are required when dealing with specific examples, we can use (6.16)–(6.16) to rewrite the two jump conditions (6.36a) and (6.36b) as

$$\mathcal{L}_1[\mathrm{v}_1] = \mathcal{K}_1[\hat{u}_0] \quad \text{and} \quad \mathcal{L}_2[\mathrm{v}_1] = \mathcal{K}_2[\hat{u}_0], \tag{6.37}$$

where

$$\begin{cases} \mathcal{L}_1[\mathrm{v}_1] = \mathrm{v}_1(0^+) \mp \mathrm{v}_1(1^-) - \dfrac{1}{2\mathcal{K}}\left(\beta(0^+)\mathrm{v}_1'(0^+) \pm \beta(1^-)\mathrm{v}_1'(1^-)\right), \\ \mathcal{K}_1[\hat{u}_0] = \mp\hat{u}_0(1^-) \mp \dfrac{1}{2\mathcal{K}}\beta(1^-)\hat{u}_0'(1^-), \\ \mathcal{L}_2[\mathrm{v}_1] = -\dfrac{\mathcal{M}\eta_0^2}{2}\left(\mathrm{v}_1(0^+) \pm \mathrm{v}_1(1^-)\right) - \left(\beta(0^+)\mathrm{v}_1'(0^+) \mp \beta(1^-)\mathrm{v}_1'(1^-)\right), \\ \mathcal{K}_2[\hat{u}_0] = \mp\dfrac{\mathcal{M}\eta_0^2}{2}\hat{u}_0(1^-) \pm \beta(1^-)\hat{u}_0'(1^-), \end{cases}$$

and Notation 6.2.1 has been used. Note that $\mathcal{L}_{1,2}$ are the same operators as those applied to $\hat{u}_0$ when determining η_0, though in this case the right-hand side was 0.

6.3.4 An ODE for $\mathcal{U}_0(x)$

We can now collect the terms of order δ^2 in (6.11)–(6.13) to obtain the following equations governing the second-order field u_2:

$$\begin{cases} \dfrac{\partial}{\partial y}\left(\beta\left(\dfrac{\partial u_2}{\partial y} + \dfrac{\partial u_1}{\partial x}\right)\right) + \eta_0^2\alpha u_2 + \beta\dfrac{\partial^2 u_1}{\partial x \partial y} + \beta\dfrac{\partial^2 u_0}{\partial x^2} + \eta_2^2\alpha u_0 = 0, & \text{(6.38a)} \\ [\![u_2]\!] = \dfrac{1}{\mathcal{K}}\left\langle\!\!\left\langle \beta\left(\dfrac{\partial u_2}{\partial y} + \dfrac{\partial u_1}{\partial x}\right)\right\rangle\!\!\right\rangle, & \text{(6.38b)} \\ \left[\!\!\left[\beta\left(\dfrac{\partial u_2}{\partial y} + \dfrac{\partial u_1}{\partial x}\right)\right]\!\!\right] = -\mathcal{M}(\eta_0^2\langle\!\langle u_2\rangle\!\rangle + \eta_2^2\langle\!\langle u_0\rangle\!\rangle). & \text{(6.38c)} \end{cases}$$

Similarly to the manipulation in (6.3.2) to prove $\eta_1 = 0$, we consider the quantity $\langle u_2 \cdot (6.19a) - u_0 \cdot (6.38a)\rangle$. The terms in $\alpha\eta_0^2 u_0 u_2$ cancel out, and, using the fact that

$$u_2\frac{\partial}{\partial y}\left(\beta\frac{\partial u_0}{\partial y}\right) - u_0\frac{\partial}{\partial y}\left(\beta\left(\frac{\partial u_2}{\partial y} + \frac{\partial u_1}{\partial x}\right)\right) = \frac{\partial}{\partial y}\left(u_2\beta\frac{\partial u_0}{\partial y} - u_0\beta\left(\frac{\partial u_2}{\partial y} + \frac{\partial u_1}{\partial x}\right)\right) + \beta\frac{\partial u_0}{\partial y}\frac{\partial u_1}{\partial x},$$

we obtain

$$\left\langle\frac{\partial}{\partial y}\left(u_2\beta\frac{\partial u_0}{\partial y} - u_0\beta\left(\frac{\partial u_2}{\partial y} + \frac{\partial u_1}{\partial x}\right)\right)\right\rangle = \left\langle\beta\left(u_0\frac{\partial^2 u_1}{\partial x\partial y} - \frac{\partial u_0}{\partial y}\frac{\partial u_1}{\partial x} + u_0\frac{\partial^2 u_0}{\partial x^2}\right)\right\rangle + \eta_2^2\langle\alpha u_0^2\rangle. \tag{6.39}$$

Now, by directly using (6.27), (6.33) and (6.35) we can show that

$$u_0\frac{\partial^2 u_1}{\partial x\partial y} - \frac{\partial u_0}{\partial y}\frac{\partial u_1}{\partial x} + u_0\frac{\partial^2 u_0}{\partial x^2} = \mathcal{U}_0(x)\mathcal{U}_0''(x)w_1(y), \tag{6.40}$$

where we define

$$w_1 = \hat{u}_0 f_1' - \hat{u}_0' f_1 + (\hat{u}_0)^2. \tag{6.41}$$

Moreover, the first bracket of (6.39) can be simplified using (6.14) and (6.18) and, therefore, using (6.40), the identity (6.39) becomes

$$-\left[\!\!\left[u_2\beta\frac{\partial u_0}{\partial y} - u_0\beta\left(\frac{\partial u_2}{\partial y} + \frac{\partial u_1}{\partial x}\right)\right]\!\!\right] = \mathcal{U}_0(x)\mathcal{U}_0''(x)\langle\beta w_1\rangle + \eta_2^2\langle\alpha u_0^2\rangle. \tag{6.42}$$

Remark 6.2. *Inputting (6.35) into (6.41), one shows that* $w_1 = \hat{u}_0 v_1' - \hat{u}_0' v_1$*, which is the Wronskian associated to the second-order ODE* $(\beta g')' + \eta_0^2 \alpha g = 0$*, and hence satisfies the first-order ODE* $(\beta w_1)' = 0$*. Moreover, the hypothesis made in (6.14) regarding potential material properties discontinuities within the interior of the unit cell implies that* $\hat{u}_0$*,* $\beta \hat{u}_0'$*,* u_1 *and* $\beta \left(\frac{\partial u_1}{\partial y} + \mathcal{U}_0'(x) \hat{u}_0 \right)$ *are continuous in* y *on* $]0,1[$*. Using the form (6.33) of* u_1*, this implies that both* v_1 *and* $\beta v_1'$ *should be continuous on* $]0,1[$*. Hence,* βw_1 *is continuous on* $]0,1[$*. Moreover, using the fact that* $(\beta w_1)' = 0$*, this implies that* βw_1 *is constant on* $]0,1[$*. Therefore* $\langle \beta w_1 \rangle = \beta(0^+) w_1(0^+)$ *and its computation does not require any integration. Moreover, since* $\hat{u}_0$ *and* v_1 *are independent, it is clear that* $\langle \beta w_1 \rangle \neq 0$*.*

As in Section 6.3.2, we can now make use of (6.15) to simplify the left-hand side of (6.42):

$$
\begin{aligned}
&- \left[\!\!\left[u_2 \beta \frac{\partial u_0}{\partial y} - u_0 \beta \left(\frac{\partial u_2}{\partial y} + \frac{\partial u_1}{\partial x} \right) \right]\!\!\right] && (6.43)\\
&= - [\![u_2]\!] \left\langle\!\!\left\langle \beta \frac{\partial u_0}{\partial y} \right\rangle\!\!\right\rangle - \langle\!\langle u_2 \rangle\!\rangle \left[\!\!\left[\beta \frac{\partial u_0}{\partial y} \right]\!\!\right] + [\![u_0]\!] \left\langle\!\!\left\langle \beta \left(\frac{\partial u_2}{\partial y} + \frac{\partial u_1}{\partial x} \right) \right\rangle\!\!\right\rangle + \langle\!\langle u_0 \rangle\!\rangle \left[\!\!\left[\beta \left(\frac{\partial u_2}{\partial y} + \frac{\partial u_1}{\partial x} \right) \right]\!\!\right] \\
&= -\mathcal{K} [\![u_2]\!] [\![u_0]\!] + \mathcal{M} \eta_0^2 \langle\!\langle u_2 \rangle\!\rangle \langle\!\langle u_0 \rangle\!\rangle + \mathcal{K} [\![u_0]\!] [\![u_2]\!] - \mathcal{M} \langle\!\langle u_0 \rangle\!\rangle (\eta_0^2 \langle\!\langle u_2 \rangle\!\rangle + \eta_2^2 \langle\!\langle u_0 \rangle\!\rangle) && (6.44)\\
&= -\mathcal{M} \eta_2^2 \langle\!\langle u_0 \rangle\!\rangle^2 , && (6.45)
\end{aligned}
$$

where the jump conditions (6.19b)–(6.19c) and (6.38b)–(6.38c) have been used. Finally, using (6.45) and dividing by $\mathcal{U}_0(x)$, (6.42) can be rewritten as

$$
T \mathcal{U}_0''(x) + \eta_2^2 \mathcal{U}_0(x) = 0, \qquad \text{where} \qquad T = \frac{\langle \beta w_1 \rangle}{\langle \alpha (\hat{u}_0)^2 \rangle + \mathcal{M} \langle\!\langle \hat{u}_0 \rangle\!\rangle^2}, \tag{6.46}
$$

which is the effective equation for $\mathcal{U}_0$ with η_2 that still needs to be determined

6.3.5 Computation of η_2 and final approximations

Note that in (6.46) $T \neq 0$, but it can be either negative or positive. Since we have assumed to be close to an edge of the Brillouin zone, we are looking for standing waves, we seek η_2^2 such that $\eta_2^2 / T \geqslant 0$. Remember that η_2 is a correction term to the reduced frequency η, such that $\eta^2 = \eta_0^2 + \delta^2 \eta_2^2 + o(\delta^2)$. This means that for each branch of the dispersion diagram (determined by our initial choice of eigenvalue η_0), we look for a function $\eta_2(\kappa)$ that will lead to an approximation of $\eta(\kappa)$ at the second order in δ, where κ is the reduced Bloch wavenumber. In particular, by definition of the FFLW and FFFW cases, we should have

$$
\text{(FFLW)} \quad \eta_2(\kappa) \underset{\kappa \to 0}{\to} 0 \quad \text{and} \quad \text{(FFFW)} \quad \eta_2(\kappa) \underset{\kappa \to \frac{\pi}{\delta}}{\to} 0. \tag{6.47}
$$

In order for our asymptotic representation (6.9) to be compatible with the fact that u_δ should satisfy the Bloch-Floquet conditions (6.8), it is sufficient to impose that all the $u_j\left(x, \frac{x}{\delta}\right)$ should also satisfy these conditions. For $j = 0$, this means that

$$
\mathcal{U}_0(x + \delta) \hat{u}_0 \left(\frac{x}{\delta} + 1 \right) = \mathcal{U}_0(x) \hat{u}_0 \left(\frac{x}{\delta} \right) e^{\mathrm{i} \kappa \delta}. \tag{6.48}
$$

Hence, due to fact that $\hat{u}_0$ is periodic (FFLW) or antiperiodic (FFFW), we can cancel out the terms in $\hat{u}_0$ in (6.48) to get

$$
\mathcal{U}_0(x + \delta) = \pm \mathcal{U}_0(x) e^{\mathrm{i} \kappa \delta}, \tag{6.49}
$$

where, in (6.49) and below, Notation 6.2.1 is being used. The second Bloch-Floquet condition in (6.8), combined with (6.49), implies that

$$\mathcal{U}_0'(x+\delta) = \pm \mathcal{U}_0'(x) e^{\mathrm{i}\kappa\delta}. \tag{6.50}$$

Furthermore, because $\mathcal{U}_0$ is solution to (6.46), it can be written $\mathcal{U}_0(x) = Ae^{\mathrm{i}\sqrt{\eta_2^2/T}x} + Be^{-\mathrm{i}\sqrt{\eta_2^2/T}x}$ for some constants A and B. The Bloch-Floquet conditions (6.49) and (6.50) lead to

$$A\left(1 \mp e^{\mathrm{i}\delta\left(\sqrt{\eta_2^2/T}-\kappa\right)}\right) = 0 \quad \text{and} \quad B\left(1 \mp e^{-\mathrm{i}\delta\left(\sqrt{\eta_2^2/T}+\kappa\right)}\right) = 0. \tag{6.51}$$

One recalls that κ is restricted to $\left[0, \frac{\pi}{\delta}\right]$, i.e. to the first Brillouin zone in the dispersion diagram. Moreover, it is assumed that $\eta_2^2/T \geqslant 0$, (6.51). These two points imply that, using (6.26), we have

$$\sqrt{\eta_2^2/T} = \tilde{\kappa} \quad \text{and} \quad \mathcal{U}_0(x) = e^{\pm \mathrm{i}\tilde{\kappa}x}, \tag{6.52}$$

which gives the following approximation for the reduced frequency $\eta(\kappa)$

$$\eta^2 = \eta_0^2 + T(\tilde{\kappa}\delta)^2 + o(\tilde{\kappa}^2\delta^2) \quad \text{or equivalently} \quad \eta = \eta_0 + \frac{T}{2\eta_0}(\tilde{\kappa}\delta)^2 + o(\tilde{\kappa}^2\delta^2). \tag{6.53}$$

The non-dimensional wavefield is approximated by

$$u_\delta(x) = \underbrace{\mathcal{U}_0(x)\hat{u}_0(x/\delta)}_{u_0(x,x/\delta)} + O(\tilde{\kappa}\delta). \tag{6.54}$$

In Section 6.6, we will find it more convenient to test the validity of (6.54) when it is written in terms of the variable y as follows

$$u_\delta(\delta y) = \underbrace{e^{\pm \mathrm{i}\tilde{\kappa}\delta y}\hat{u}_0(y)}_{u_0(\delta y, y)} + O(\tilde{\kappa}\delta), \tag{6.55}$$

with $\hat{u}_0$ the eigenfunction of (6.19) associated with either periodic or antiperiodic conditions. Hence, as anticipated, using (6.4), our results can be summarized in dimensional form by (1.26) and (1.27):

Result 6.1: Final approximations for a simple eigenvalue

$$\begin{cases} \omega^2 = \omega_0^2 + \mathcal{T}\tilde{k}^2h^2 + o\left(\dfrac{h^2\tilde{k}^2}{L^2}\right), \\ U_h(X) = U^{(0)}(X) + O\left(\dfrac{h\tilde{k}}{L}\right), \end{cases} \tag{6.56}$$

where the parameter $\mathcal{T}$ and the leading-order wavefield $U^{(0)}$ are given by

$$\mathcal{T} = \frac{(c^\star)^2}{h^2}T, \quad \omega_0 = \frac{c^\star\eta_0}{h} \quad \text{and} \quad U_h^{(0)}(X) = e^{\pm \mathrm{i}\tilde{k}X}\hat{u}_0(X/h).$$

These equations are the sought approximations in the case where η_0 is assumed to be a simple eigenvalue. The quality of these approximations will be investigated through two examples in Section 6.6. The purpose of the next section is to deal with the case of a double eigenvalue, i.e. when two branches of the dispersion diagrams intersect with non-zero slopes.

6.4 Case of a double eigenvalue

6.4.1 A new form for u_0

In order to write (6.27), we assumed that η_0 was a simple eigenvalue. If instead we assume that η_0 has multiplicity 2 say, then we write

$$u_0(x,y) = \underbrace{\mathcal{U}_0^{(1)}(x)\hat{u}_0^{(1)}(y)}_{u_0^{(1)}(x,y)} + \underbrace{\mathcal{U}_0^{(2)}(x)\hat{u}_0^{(2)}(y)}_{u_0^{(2)}(x,y)}, \tag{6.57}$$

where $\hat{u}_0^{(1,2)}(y)$ are two independent eigenfunctions associated with the double eigenvalue η_0 and $\mathcal{U}_0^{(1,2)}(x)$ are some functions of x to be determined. Note that both $\hat{u}_0^{(1)}(y)$ and $\hat{u}_0^{(2)}(y)$ satisfy (6.19). In what follows, for any $j \in \{1,2\}$, we will use the notation $(6.19)^{(j)}$ to specify that we consider (6.19) as applied to $\hat{u}_0^{(j)}(y)$.

6.4.2 In this case, we cannot conclude that $\eta_1 = 0$

We will now apply the same methodology as in Section 6.3.2 and consider the quantity $\langle u_1 \cdot (6.19a)^{(1)} - u_0^{(1)} \cdot (6.28a)\rangle$. The exact same reasoning leads to the following counterpart to (6.29):

$$\left\langle \frac{\partial}{\partial y}\left(u_1 \beta \frac{\partial u_0^{(1)}}{\partial y} - u_0^{(1)} \beta \left(\frac{\partial u_1}{\partial y} + \frac{\partial u_0}{\partial x} \right) \right) \right\rangle = \left\langle \beta \left(u_0^{(1)} \frac{\partial^2 u_0}{\partial x \partial y} - \frac{\partial u_0}{\partial x}\frac{\partial u_0^{(1)}}{\partial y} \right) \right\rangle + \eta_1^2 \langle \alpha u_0^{(1)} u_0 \rangle. \tag{6.58}$$

The only difference being that this time, the first bracket in the right-hand side of (6.58) is not zero. Instead, it can be shown directly using (6.57) that

$$u_0^{(1)} \frac{\partial^2 u_0}{\partial x \partial y} - \frac{\partial u_0}{\partial x}\frac{\partial u_0^{(1)}}{\partial y} = \mathcal{U}_0^{(1)}(x)\mathcal{U}_0^{(2)\prime}(x)\mathtt{w}_0(y), \tag{6.59}$$

where $\mathtt{w}_0$ is the Wronskian defined by

$$\mathtt{w}_0(y) = \hat{u}_0^{(1)}(y)\hat{u}_0^{(2)\prime}(y) - \hat{u}_0^{(1)\prime}(y)\hat{u}_0^{(2)}(y). \tag{6.60}$$

The same methodology to simplify the left-hand side bracket in (6.58) as that used in Section 6.3.2 can be used:

1. use (6.18) to reduce the average bracket to a jump bracket
2. use (6.15) to decompose the jump bracket into four simpler jump/mean brackets
3. compute them using the jump conditions $(6.19b)^{(1)}$–$(6.19c)^{(1)}$ and (6.28b)–(6.28c).

This leads to

$$-\mathcal{M}\eta_1^2 \langle\!\langle u_0^{(1)} \rangle\!\rangle \langle\!\langle u_0 \rangle\!\rangle = \mathcal{U}_0^{(1)}(x)\mathcal{U}_0^{(2)\prime}(x)\langle \beta \mathtt{w}_0 \rangle + \eta_1^2 \langle \alpha u_0^{(1)} u_0 \rangle, \tag{6.61}$$

which, upon regrouping the terms, dividing through by $\mathcal{U}_0^{(1)}(x)$ and using (6.57), can be rewritten as

$$\langle \beta \mathtt{w}_0 \rangle \mathcal{U}_0^{(2)\prime}(x) = -\eta_1^2 \left(\{\mathcal{M}B_1^2 + C_1\}\mathcal{U}_0^{(1)}(x) + \{\mathcal{M}B_1B_2 + D\}\mathcal{U}_0^{(2)}(x) \right), \tag{6.62}$$

where we have defined

$$B_1 = \langle\langle \hat{u}_0^{(1)} \rangle\rangle,\ B_2 = \langle\langle \hat{u}_0^{(2)} \rangle\rangle,\ C_1 = \langle \alpha (\hat{u}_0^{(1)})^2 \rangle,\ C_2 = \langle \alpha (\hat{u}_0^{(2)})^2 \rangle,\ D = \langle \alpha \hat{u}_0^{(1)} \hat{u}_0^{(2)} \rangle. \tag{6.63}$$

In the exact same way, we consider the quantity $\langle u_1 \cdot (6.19a)^{(2)} - u_0^{(2)} \cdot (6.28a) \rangle$ to obtain

$$\langle \beta \mathtt{w}_0 \rangle \mathcal{U}_0^{(1)\prime}(x) = \eta_1^2 \left(\{ \mathcal{M} B_1 B_2 + D \} \mathcal{U}_0^{(1)}(x) + \{ \mathcal{M} B_2^2 + C_2 \} \mathcal{U}_0^{(2)}(x) \right). \tag{6.64}$$

Note that $\mathtt{w}_0$ is the Wronskian associated with (6.19a), and $\beta \mathtt{w}_0$ can be shown to be continuous on the unit cell, hence we conclude that $\beta \mathtt{w}_0$ is actually constant, and hence we can see that $\langle \beta \mathtt{w}_0 \rangle = \beta(0^+)\mathtt{w}_0(0^+)$. Since $\hat{u}_0^{(1)}$ and $\hat{u}_0^{(2)}$ are linearly independent, $\mathtt{w}_0$ (being the associated Wronskian) is also non-zero and in this case, we cannot conclude that $\eta_1 = 0$.

6.4.3 A first-order ODE for the slow variations of the wavefield

Upon introducing the function vector $\boldsymbol{\mathcal{U}} = (\mathcal{U}_0^{(1)}, \mathcal{U}_0^{(2)})^T$, the two equations (6.62) and (6.64) can be recast as the first-order ODE system

$$\boldsymbol{\mathcal{U}}'(x) = \frac{\eta_1^2}{\langle \beta \mathtt{w}_0 \rangle} \mathbb{N} \boldsymbol{\mathcal{U}}(x), \quad \text{where} \quad \mathbb{N} = \begin{pmatrix} \mathcal{M} B_1 B_2 + D & \mathcal{M} B_2^2 + C_2 \\ -(\mathcal{M} B_1^2 + C_1) & -(\mathcal{M} B_1 B_2 + D) \end{pmatrix}. \tag{6.65}$$

The two eigenvalues $\lambda_{1,2}$ of $\mathbb{N}$ are given by

$$\lambda_j = \mathrm{i}(-1)^j \sqrt{(\mathcal{M} B_1^2 + C_1)(\mathcal{M} B_2^2 + C_2) - (\mathcal{M} B_1 B_2 + D)^2}, \tag{6.66}$$

where, by the Cauchy-Schwarz inequality associated to the inner product (6.20), the quantity inside the square root is positive. The associated eigenvectors are given by

$$\boldsymbol{\mathcal{U}}_{\lambda_1} = \left(\frac{-(\mathcal{M} B_1 B_2 + D) + \lambda_2}{\mathcal{M} B_1^2 + C_1}, 1 \right)^T \quad \text{and} \quad \boldsymbol{\mathcal{U}}_{\lambda_2} = \left(\frac{-(\mathcal{M} B_1 B_2 + D) + \lambda_1}{\mathcal{M} B_1^2 + C_1}, 1 \right)^T \tag{6.67}$$

and hence, upon introducing T_d to be

$$T_d = \langle \beta \mathtt{w}_0 \rangle / \sqrt{(\mathcal{M} B_1^2 + C_1)(\mathcal{M} B_2^2 + C_2) - (\mathcal{M} B_1 B_2 + D)^2}, \tag{6.68}$$

the solution to (6.65) can be written as

$$\begin{aligned} \boldsymbol{\mathcal{U}}(x) &= \mathfrak{c}_1 \boldsymbol{\mathcal{U}}_{\lambda_1} e^{\frac{\eta_1^2}{\langle \beta \mathtt{w}_0 \rangle} \lambda_1 x} + \mathfrak{c}_2 \boldsymbol{\mathcal{U}}_{\lambda_2} e^{\frac{\eta_1^2}{\langle \beta \mathtt{w}_0 \rangle} \lambda_2 x} \\ &= \mathfrak{c}_1 \boldsymbol{\mathcal{U}}_{\lambda_1} e^{-\mathrm{i} \frac{\eta_1^2}{T_d} x} + \mathfrak{c}_2 \boldsymbol{\mathcal{U}}_{\lambda_2} e^{\mathrm{i} \frac{\eta_1^2}{T_d} x}, \end{aligned}$$

for some constants $\mathfrak{c}_{1,2}$ and η_1 that still needs to be determined.

6.4.4 Computation of η_1

At this stage, we need to remember the Bloch-Floquet conditions (6.8), which, when applied to u_0, imply that

$$\hat{u}_0^{(1)}(y)\{ \pm \mathcal{U}_0^{(1)}(x + \delta) - e^{i\kappa\delta} \mathcal{U}_0^{(1)}(x) \} + \hat{u}_0^{(2)}(y)\{ \pm \mathcal{U}_0^{(2)}(x + \delta) - e^{i\kappa\delta} \mathcal{U}_0^{(2)}(x) \} = 0,$$

where Notation 6.2.1 has been used. Since $\hat{u}_0^{(1)}$ and $\hat{u}_0^{(2)}$ are linearly independent, this implies that $\pm\boldsymbol{\mathcal{U}}(x+\delta) = e^{i\kappa\delta}\boldsymbol{\mathcal{U}}(x)$. Applying this condition to (6.69), leads to the value of η_1^2 as follows

$$\begin{cases} \delta\eta_1^2 = \pm T_d\tilde{\kappa}\delta \\ \mathfrak{c}_1 = 0 \end{cases} \quad \text{or} \quad \begin{cases} \delta\eta_1^2 = \mp T_d\tilde{\kappa}\delta \\ \mathfrak{c}_2 = 0 \end{cases} \tag{6.69}$$

Hence, using (6.69) and (6.69) the value of $\boldsymbol{\mathcal{U}} = (\boldsymbol{\mathcal{U}}_0^{(1)}, \boldsymbol{\mathcal{U}}_0^{(2)})^T$ writes as

$$\boldsymbol{\mathcal{U}}(x) = \mathfrak{c}_1\boldsymbol{\mathcal{U}}_{\lambda_1}e^{\pm i\tilde{\kappa}x} \quad \text{or} \quad \boldsymbol{\mathcal{U}}(x) = \mathfrak{c}_2\boldsymbol{\mathcal{U}}_{\lambda_2}e^{\pm i\tilde{\kappa}x}. \tag{6.70}$$

Result 6.2: Final approximations for a double eigenvalue

Consequently, using (6.67), the non-dimensional wavefield (6.57) is written in terms of the variable y as:

$$u_0(\delta y, y) = \begin{cases} e^{\pm i\tilde{\kappa}\delta y}\left(\dfrac{-(\mathcal{M}B_1B_2 + D) + \lambda_2}{\mathcal{M}B_1^2 + C_1}\hat{u}_0^{(1)}(y) + \hat{u}_0^{(2)}(y)\right) \\ \quad \text{or} \\ e^{\pm i\tilde{\kappa}\delta y}\left(\dfrac{-(\mathcal{M}B_1B_2 + D) + \lambda_1}{\mathcal{M}B_1^2 + C_1}\hat{u}_0^{(1)}(y) + \hat{u}_0^{(2)}(y)\right) \end{cases} \tag{6.71}$$

with λ_j given by (6.66). And since $\eta^2 = \eta_0^2 + \delta\eta_1^2 + o(\delta)$, we obtain the linear approximations

$$\eta = \begin{cases} \eta_0 + \dfrac{T_d}{2\eta_0}(\tilde{\kappa}\delta) + o(\tilde{\kappa}\delta). \\ \quad \text{or} \\ \eta_0 - \dfrac{T_d}{2\eta_0}(\tilde{\kappa}\delta) + o(\tilde{\kappa}\delta). \end{cases} \tag{6.72}$$

Therefore, near each double eigenvalue η_0 of the dispersion diagram, we have two linear approximations with opposite slopes emerging from η_0. Such behaviour of the dispersion diagram corresponds to the so-called Dirac points (Ochiai & Onoda, 2009; Lee-Thorp et al., 2018; Guzina et al., 2019).

6.5 Case of two nearby eigenvalues

In what has been done above, there is no uniform transition from the simple eigenvalue case to the double eigenvalue case. As will be seen in the examples of Section 6.6, when two simple eigenvalues are close to each other, the agreement between the dispersion diagram and the asymptotic of Section 6.3 is somewhat short-lived. In order to remedy to this issue, following some ideas developed in Moukhomodiarov, Pichugin, and Rogerson, 2009; Guzina et al., 2019, we will derive an asymptotic expansion for two nearby eigenvalues.

6.5.1 Modified system at the zero-th order

Let us assume that we have two nearby eigenvalues $\eta_0^{(1)}$ and $\eta_0^{(2)}$ with their associated eigenfunctions $\hat{u}_0^{(1)}(y)$ and $\hat{u}_0^{(2)}(y)$ that solve (6.19) and such that $\eta_0^{(1)} < \eta_0^{(2)}$. Since we are seeking an

approximation that remains valid when two eigenvalues merge into one, we assume that $\eta_0^{(1,2)}$ both belong to the same side of the dispersion diagram, i.e. they are either both FFLW or both FFFW. Their proximity is characterised by a positive parameter $\gamma = O(1)$ defined by

$$\gamma = \frac{\left(\eta_0^{(2)}\right)^2 - \left(\eta_0^{(1)}\right)^2}{\delta}. \tag{6.73}$$

In the vicinity of these eigenvalues we seek expansions of the form (6.9), in which we choose $\eta_0 = \eta_0^{(1)}$. In order to consider the competing nature of the two eigenvalues, we seek u_0 in the form (6.57), introducing the functions $\mathcal{U}_0^{(1,2)}(x)$ and $u_0^{(1,2)}(x,y)$ accordingly. With such choice of u_0, one can show directly that we have

$$\begin{cases} \dfrac{\partial}{\partial y}\left(\beta \dfrac{\partial u_0}{\partial y}\right) + (\eta_0^{(1)})^2 \alpha u_0 = -\delta\gamma\alpha u_0^{(2)}, \\ [\![u_0]\!] = \dfrac{1}{\mathcal{K}}\left\langle\!\!\left\langle \beta \dfrac{\partial u_0}{\partial y}\right\rangle\!\!\right\rangle, \\ \left[\!\!\left[\beta \dfrac{\partial u_0}{\partial y}\right]\!\!\right] = -\mathcal{M}(\eta_0^{(1)})^2 \langle\!\langle u_0\rangle\!\rangle - \mathcal{M}\delta\gamma\langle\!\langle u_0^{(2)}\rangle\!\rangle. \end{cases} \tag{6.74}$$

6.5.2 A first-order ODE for $\mathcal{U}$

The terms involving δ in the right-hand sides of (6.74) should be considered when collecting the terms of order δ in (6.11)–(6.13) to obtain the equations governing u_1:

$$\frac{\partial}{\partial y}\left(\beta\left(\frac{\partial u_1}{\partial y} + \frac{\partial u_0}{\partial x}\right)\right) + \beta\frac{\partial^2 u_0}{\partial x \partial y} + \alpha\left(\left(\eta_0^{(1)}\right)^2 u_1 + \eta_1^2 u_0 - \gamma u_0^{(2)}\right) = 0, \tag{6.75a}$$

$$[\![u_1]\!] = \frac{1}{\mathcal{K}}\left\langle\!\!\left\langle \beta\left(\frac{\partial u_0}{\partial x} + \frac{\partial u_1}{\partial y}\right)\right\rangle\!\!\right\rangle, \tag{6.75b}$$

$$\left[\!\!\left[\beta\left(\frac{\partial u_0}{\partial x} + \frac{\partial u_1}{\partial y}\right)\right]\!\!\right] = -\mathcal{M}((\eta_0^{(1)})^2\langle\!\langle u_1\rangle\!\rangle + \eta_1^2\langle\!\langle u_0\rangle\!\rangle - \gamma\langle\!\langle u_0^{(2)}\rangle\!\rangle). \tag{6.75c}$$

After following the exact same strategy as in Section 6.4, consider first the term $\left\langle u_1 \cdot (6.19a)^{(1)} - u_0^{(1)} \cdot (6.75a)\right\rangle$, and then the term $\left\langle u_1 \cdot (6.19a)^{(2)} - u_0^{(2)} \cdot (6.75a)\right\rangle$, to obtain two equations that can be recast in the first-order ODE system

$$\boldsymbol{\mathcal{U}}'(x) = \frac{\eta_1^2}{\langle \beta \mathtt{w}_0\rangle}\mathbb{N}_\gamma \boldsymbol{\mathcal{U}}(x). \tag{6.76}$$

Here we used $\boldsymbol{\mathcal{U}} = (\mathcal{U}_0^{(1)}, \mathcal{U}_0^{(2)})^T$, the function $\mathtt{w}_0$ is defined as in (6.60) and $\mathbb{N}_\gamma$ is given by

$$\mathbb{N}_\gamma = \begin{pmatrix} \mathcal{M}B_1B_2 + D & \left(1 - \frac{\gamma}{\eta_1^2}\right)(\mathcal{M}B_2^2 + C_2) \\ -(\mathcal{M}B_1^2 + C_1) & -\left(1 - \frac{\gamma}{\eta_1^2}\right)(\mathcal{M}B_1B_2 + D) \end{pmatrix} = \mathbb{N} + \frac{\gamma}{\eta_1^2}\begin{pmatrix} 0 & -\mathcal{M}B_2^2 - C_2 \\ 0 & \mathcal{M}B_1B_2 + D \end{pmatrix}, \tag{6.77}$$

the parameters $B_{1,2}$, $C_{1,2}$ and D being defined as in (6.63). Note that when taking $\gamma \to 0$ in (6.76), we recover exactly (6.65), showing the consistency of our approach. Note that when deriving the second line of (6.76), we neglect the term $\delta\gamma\langle u_1, \hat{u}_0^{(2)}\rangle$ that occurs in the process since it is of order δ. The eigenvalues $\lambda_{1,2}^{(\gamma)}$ of $\mathbb{N}_\gamma$ are

$$\lambda_j^{(\gamma)} = \frac{1}{2\eta_1^2}\Big[(\mathcal{M}B_1B_2 + D)\gamma + (-1)^j\sqrt{(\mathcal{M}B_1B_2 + D)^2(\gamma - 2\eta_1^2)^2 + 4(\mathcal{M}B_1^2 + C_1)(\mathcal{M}B_2^2 + C_2)\eta_1^2(\gamma - \eta_1^2)}\Big],$$

while the associated eigenvectors are

$$\boldsymbol{\mathcal{U}}_{\lambda_1^{(\gamma)}} = \left(\frac{-(\mathcal{M}B_1B_2 + D) + \lambda_2^{(\gamma)}}{(\mathcal{M}B_1^2 + C_1)}, 1\right)^T \quad \text{and} \quad \boldsymbol{\mathcal{U}}_{\lambda_2^{(\gamma)}} = \left(\frac{-(\mathcal{M}B_1B_2 + D) + \lambda_1^{(\gamma)}}{(\mathcal{M}B_1^2 + C_1)}, 1\right)^T. \tag{6.78}$$

6.5.3 Computation of η_1

We can hence follow what we have done in Section 6.4.3, and use the Bloch-Floquet conditions to obtain

$$\begin{cases} \dfrac{\eta_1^2\lambda_2^{(\gamma)}}{\langle\beta \mathtt{w}_0\rangle} = \pm \mathrm{i}\tilde{\kappa} \\ \mathfrak{c}_1 = 0 \end{cases} \quad \text{or} \quad \begin{cases} \dfrac{\eta_1^2\lambda_1^{(\gamma)}}{\langle\beta \mathtt{w}_0\rangle} = \pm \mathrm{i}\tilde{\kappa} \\ \mathfrak{c}_2 = 0 \end{cases} \tag{6.79}$$

which are implicit relationships between η_1^2 and κ. Fortunately, these can be inverted exactly to obtain

$$\eta_1^2 = \begin{cases} \dfrac{1}{2}\left(\gamma - \sqrt{4T_d^2\tilde{\kappa}^2 + 4\mathrm{i}T_d^2\dfrac{(\mathcal{M}B_1B_2 + D)}{\langle\beta \mathtt{w}_0\rangle}\tilde{\kappa}\gamma + \gamma^2}\right), \\ \qquad \text{or} \\ \dfrac{1}{2}\left(\gamma + \sqrt{4T_d^2\tilde{\kappa}^2 + 4\mathrm{i}T_d^2\dfrac{(\mathcal{M}B_1B_2 + D)}{\langle\beta \mathtt{w}_0\rangle}\tilde{\kappa}\gamma + \gamma^2}\right), \end{cases} \tag{6.80}$$

where (6.26) has been used, and where T_d is defined as in (6.68). One issue with (6.80) is that, in its current form, it implies that η_1^2 is actually complex. However, this issue is settled by realizing that upon using the inner product defined in (6.20), we can write

$$\mathcal{M}B_1B_2 + D = \left\langle \hat{u}_0^{(1)}, \hat{u}_0^{(2)} \right\rangle.$$

Hence, since $\hat{u}_0^{(1,2)}$ correspond to two different eigenvalues, they are orthogonal and we get $\mathcal{M}B_1B_2 + D = 0$. Therefore, the complex part of (6.80) disappears and it simplifies to the following final approximation.

Result 6.3: Final approximation of the dispersion relation for two nearby eigenvalues

$$\delta\eta_1^2 = \begin{cases} \dfrac{1}{2}\left(\delta\gamma - \sqrt{4T_d^2(\tilde{\kappa}\delta)^2 + (\delta\gamma)^2}\right) \\ \qquad \text{or} \\ \dfrac{1}{2}\left(\delta\gamma + \sqrt{4T_d^2(\tilde{\kappa}\delta)^2 + (\delta\gamma)^2}\right) \end{cases} \tag{6.81}$$

and

$$\eta^2 = (\eta_0^{(1)})^2 + \delta\eta_1^2 + o(\delta).$$

In the limit $\gamma \longrightarrow \infty$ or $\tilde{\kappa} \longrightarrow 0$, then η_1^2 behaves like $\eta_1^2 \longrightarrow 0$ or $\eta_1^2 \sim \gamma$, depending on the sign chosen in (6.80). This allows us to conclude that the $-$ sign corresponds to the branch emanating from $\eta_0^{(1)}$, while the $+$ sign corresponds to the branch emanating from $\eta_0^{(2)}$. There are two other interesting limits to consider.

The first is to see what happens when two eigenvalues are merging, i.e., we fix $\tilde{\kappa}\delta$ and let $\delta\gamma \longrightarrow 0$. In this case (6.81) simplifies to $\eta^2 \approx (\eta_0^{(1)})^2 + \frac{\delta\gamma}{2} \mp T_d\tilde{\kappa}\delta$, which, when plotted against $\tilde{\kappa}\delta$ are two straight lines with opposite slopes emanating from a point between the two nearby eigenvalues. When the two eigenvalues merge (i.e. $\delta\gamma = 0$), we recover exactly the double eigenvalue approximation (6.69).

The second interesting limit case is to understand how well (6.81) approximates the dispersion diagram at the edges of the Brillouin zone for a given $\delta\gamma \neq 0$. So we fix $\delta\gamma$ and let $\tilde{\kappa}\delta \longrightarrow 0$. In this case, (6.81) simplifies to

$$\eta^2 \approx (\eta_0^{(1)})^2 + \frac{1}{2}\left(\delta\gamma \mp \delta\gamma\right) \mp \frac{T_d^2}{\delta\gamma}(\tilde{\kappa}\delta)^2. \tag{6.82}$$

Hence, for the lower branch it becomes $\eta^2 \approx (\eta_0^{(1)})^2 - \frac{T_d^2}{\delta\gamma}(\tilde{\kappa}\delta)^2$, while for the upper branch, it reads $\eta^2 \approx (\eta_0^{(2)})^2 + \frac{T_d^2}{\delta\gamma}(\tilde{\kappa}\delta)^2$. This approximation looks like (6.53), but with an incorrect quadratic coefficient (since in general $\mp\frac{T_d^2}{\delta\gamma} \neq T$), so (6.82) is only a first-order approximation, slightly less accurate than the simple eigenvalue approximation.

Hence, (6.81) is a *uniform approximation*, in the sense that it is valid for both the simple and the double eigenvalue cases. Moreover, we will see in the next section that using (6.81) leads to a much longer-lived fit to the exact dispersion diagram than the simple eigenvalue method.

Result 6.4: Final approximation of the wavefield for two nearby eigenvalues

Eventually, the zeroth order wavefield writes as

$$u_0(\delta y, y) = e^{\pm i\tilde{\kappa}\delta y}\left(\pm\frac{\langle\beta w_0\rangle}{(\mathcal{M}B_1^2 + C_1)}\frac{i\tilde{\kappa}\delta}{\delta\eta_1^2}\hat{u}_0^{(1)}(y) + \hat{u}_0^{(2)}(y)\right), \tag{6.83}$$

with the expression of $\delta\eta_1^2$ on the two branches given by (6.81).

6.6 Examples and numerical experiments

The theory developed above has the advantage to be valid for any spatially varying periodic material properties, even in cases when the dispersion diagram cannot be obtained analytically or is computationally intricate to obtain. However, in order to validate the method, we now consider two simple examples, for which the dispersion diagram can be obtained directly by the Bloch-Floquet analysis.

6.6.1 Monolayer

The simplest example that can be considered is the case of a monolayer material with imperfect interface. By this we mean that the density and Young's modulus are constant, so that $\rho_h(X) = \rho^\star$ and $\mu_h(X) = \mu^\star$. This implies that $\alpha = \beta = 1$. The geometry of the physical problem is represented in Figure 6.2.

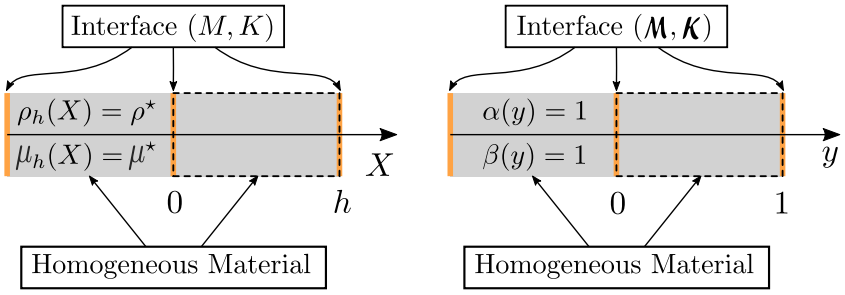

Figure 6.2 – Geometry of the monolayer problem in the physical (left) and nondimensional (right) settings.

The Bloch-Floquet analysis (see Appendix 6.A) gives the following dispersion relation

$$\cos(\kappa\delta) = \frac{1}{1+\frac{\mathcal{M}\eta^2}{4\mathcal{K}}}\left[\left(1-\frac{\mathcal{M}\eta^2}{4\mathcal{K}}\right)\cos(\eta) - \frac{1}{2}\left(\frac{\eta}{\mathcal{K}}+\mathcal{M}\eta\right)\sin(\eta)\right]. \tag{6.84}$$

Remark 22. *When $\mathcal{M} = 0$ and $\mathcal{K} = +\infty$ in 6.84, one recovers $\kappa = frac\eta\delta$ which holds for homogeneous media.*

The dispersion diagram classically displays band gaps as can be seen in Figure 6.3. We will now apply the high-frequency homogenization technique to derive an analytical approximation to the higher branches of the diagram and to the associated wavefields.

In the case of a single eigenvalue, using (6.19), we find that $\hat{u}_0$ can be written as $\hat{u}_0 = A\cos(\eta_0 y) + B\sin(\eta_0 y)$ for some constants A and B, and, using (6.16)–(6.17), it is subjected to the jump conditions

$$\begin{cases} \hat{u}_0(0^+) \mp \hat{u}_0(1^-) = \dfrac{1}{2\mathcal{K}}(\hat{u}_0'(0^+) \pm \hat{u}_0'(1^-)), \\ \hat{u}_0'(0^+) \mp \hat{u}_0'(1^-) = \dfrac{-\mathcal{M}\eta_0^2}{2}(\hat{u}_0(0^+) \pm \hat{u}_0(1^-)), \end{cases} \tag{6.85}$$

where here and throughout the section, Notation 6.2.1 is being used. This leads to the relation

$$\mathbb{M}^{\text{mo}}(A,B)^T = (0,0)^T, \tag{6.86}$$

where the 2×2 matrix $\mathbb{M}^{\text{mo}} = (\mathcal{M}_{ij}^{\text{mo}})$ is given by

$$\mathbb{M}^{\text{mo}} = \begin{pmatrix} 1 \mp \cos(\eta_0) \pm \frac{1}{2\mathcal{K}}\eta_0\sin(\eta_0) & \mp\sin(\eta_0) - \frac{\eta_0}{2\mathcal{K}}(1 \pm \cos(\eta_0)) \\ \mp\eta_0\sin(\eta_0) - \frac{\mathcal{M}\eta_0^2}{2}(1\pm\cos(\eta_0)) & -\eta_0(1\mp\cos(\eta_0)) \mp \frac{\mathcal{M}\eta_0^2}{2}\sin(\eta_0) \end{pmatrix}.$$

The only way for non-trivial solutions to (6.86) to exist is for the determinant of $\mathbb{M}^{\mathrm{mo}}$ to be zero, which after some algebraic manipulations, leads to a dispersion relation of the form

$$\begin{aligned}\mathcal{D}^{\mathrm{mo}}(\eta_0;\mathcal{M},\mathcal{K}) &= 2(1\mp\cos(\eta_0)) + \frac{\mathcal{M}}{2\mathcal{K}}\eta_0^2(1\pm\cos(\eta_0)) \pm \eta_0\sin(\eta_0)\left(\mathcal{M}+\frac{1}{\mathcal{K}}\right)\\ &= 0,\end{aligned}$$

where the fact that $\eta_0 \neq 0$ has been used (we are not here interested in the low frequency limit). In practice, when calculating η_0 and reconstructing $\hat{u}_0$, it can be useful to note that

$$\mathbb{M}^{\mathrm{mo}}[2,2] = \tfrac{\pm\sin(\eta_0)}{1\pm\cos(\eta_0)}\mathbb{M}^{\mathrm{mo}}[2,1], \quad \mathbb{M}^{\mathrm{mo}}[1,2] = \tfrac{1\pm\cos(\eta_0)}{\mp\sin(\eta_0)}\mathbb{M}^{\mathrm{mo}}[1,1], \tag{6.87}$$

$$\mathbb{M}^{\mathrm{mo}}[1,1]\mathbb{M}^{\mathrm{mo}}[2,1] = \mp\tfrac{\sin(\eta_0)}{2}\mathcal{D}^{\mathrm{mo}}(\eta_0;\mathcal{M},\mathcal{K}), \tag{6.88}$$

so that η_0 is either a zero of $\mathbb{M}^{\mathrm{mo}}[1,1]$ or $\mathbb{M}^{\mathrm{mo}}[2,1]$, and in the former (resp. latter) case, the top (resp bottom) line of $\mathbb{M}^{\mathrm{mo}}$ is zero (it can be shown that $\sin(\eta_0) \neq 0$). The computed eigenvalues coincide with the edges of the Brillouin zone of the dispersion diagram of Figure 6.3. To obtain $\hat{u}_0$, we set $A = 1$, so that $\hat{u}_0(0^+) = 1$, and compute B using the first (resp. second) line in (6.86) if $\mathbb{M}^{\mathrm{mo}}[1,1] \neq 0$ (resp. $\mathbb{M}^{\mathrm{mo}}[2,1] \neq 0$).

Because we are ultimately interested in the value of T in (6.53), we need to calculate $\langle \beta w_1 \rangle$ in (6.46). One reminds that $w_1 = \hat{u}_0 \mathrm{v}_1' - \hat{u}_0' \mathrm{v}_1$ and hence the computation of v_1 on the interval $]0,1[$ is required. It satisfies the same second-order equation (6.19a) as $\hat{u}_0$ and can hence be written $\mathrm{v}_1(y) = C\cos(\eta_0 y) + D\sin(\eta_0 y)$, for some constants C and D. These constants are determined using the jump conditions (6.37) satisfied by v_1. Thus, they can be found by solving $\mathbb{M}^{\mathrm{mo}}(C,D)^T = \boldsymbol{b}^{\mathrm{mo}}$, where

$$\boldsymbol{b}^{\mathrm{mo}} = \begin{pmatrix} \mp\hat{u}_0(1^-) \mp \frac{1}{2\mathcal{K}}\hat{u}_0'(1^-) \\ \mp\frac{\mathcal{M}\eta_0^2}{2}\hat{u}_0(1^-) \pm \hat{u}_0'(1^-) \end{pmatrix}. \tag{6.89}$$

Since $\mathbb{M}^{\mathrm{mo}}$ is singular, (6.89) does not have a unique solution so we set $C = 1$ say and use the non-trivial line of the system to determine D. This works well since it can be shown that $\boldsymbol{b}^{\mathrm{mo}}$ is such that $\boldsymbol{b}_j^{\mathrm{mo}} = 0$ whenever $\mathbb{M}[j,1] = 0$.

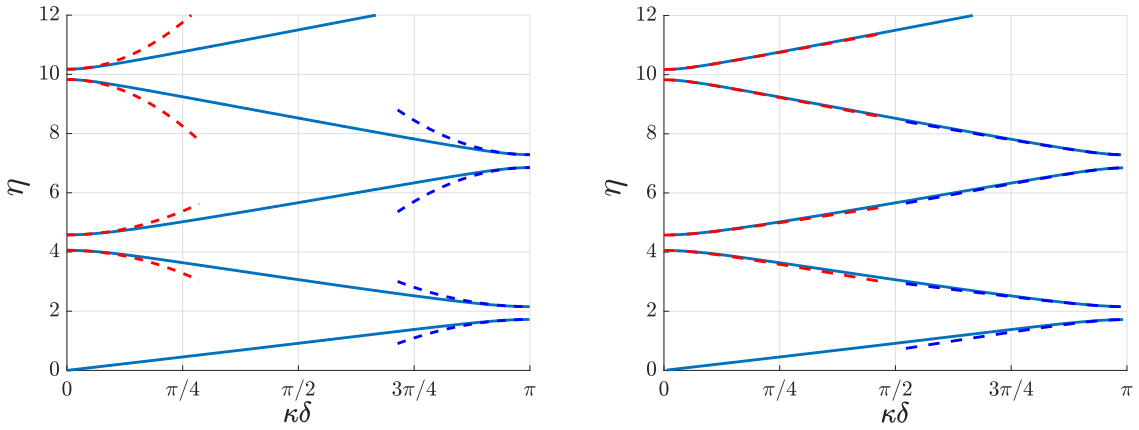

Figure 6.3 – Dispersion diagram for the monolayer case with $\mathcal{K} = 1$ and $\mathcal{M} = 0.5$. In red (resp. blue) dashed line are the periodic (resp. antiperiodic) second-order approximations (6.53) using the computed values of T (left) and nearby eigenvalue approximations (6.81) using the computed values of T_d and $\delta\gamma$ (right).

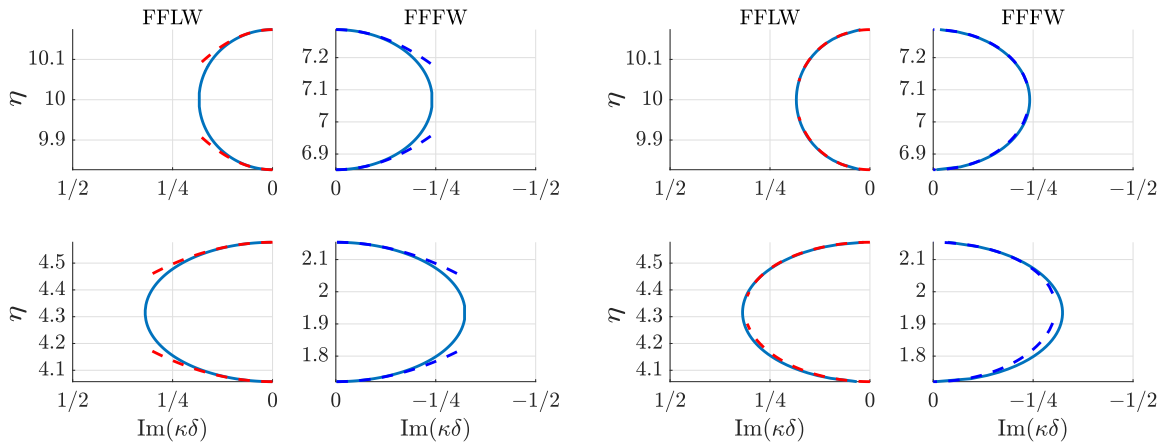

Figure 6.4 – Imaginary part of $\kappa\delta$ in the band gaps of the monolayer dispersion diagram for $\mathcal{K} = 1$ and $\mathcal{M} = 0.5$. In red (resp. blue) dashed lines are the periodic (resp. antiperiodic) second-order approximations (6.53) using the computed values of T (left) and nearby eigenvalue approximations (6.81) using the computed values of T_d and $\delta\gamma$ (right).

Once v_1 is found, the resulting value of T is directly obtained using (6.46). Note that, in this simple case, no numerical integration is required and calculations can be performed analytically. The resulting second-order approximations $\eta \approx \eta_0 + \frac{T}{2\eta_0}(\tilde{\kappa}\delta)^2$ are superposed to the dispersion diagram in Figure 6.3 (left), and one can see that they approximate well the branches in the vicinity of the edges of the Brillouin zone. One should also note that, as seen in Figure 6.4 (left), this approximation remains valid within the band gaps, where $\kappa\delta$ is complex and is such that $\mathrm{Re}(\kappa\delta) = 0$. This is expected since in these cases, $(\tilde{\kappa}\delta)^2$ remains real. Having computed all the eigenvalues and eigenfunctions, it is now straightforward to compute T_d as per (6.68) and $\delta\gamma$ as per (6.73), where the pairs of eigenvalues are chosen naturally according to the dispersion diagram (first-second) and (third-fourth) in both the FFLW and FFFW cases. Hence we can evaluate the nearby eigenvalue approximation (6.81) derived in Section 6.5. It is displayed in Figure 6.3 (right), and as can clearly be seen, even if this approximation is only first-order in the vicinity of the edges of the Brillouin zone, its agreement with the dispersion diagram is much longer lived than that of the simple eigenvalue approximation. Similar observations are true within the band gaps as can be seen in Figure 6.4 (right) We will now investigate the accuracy of the zeroth-order

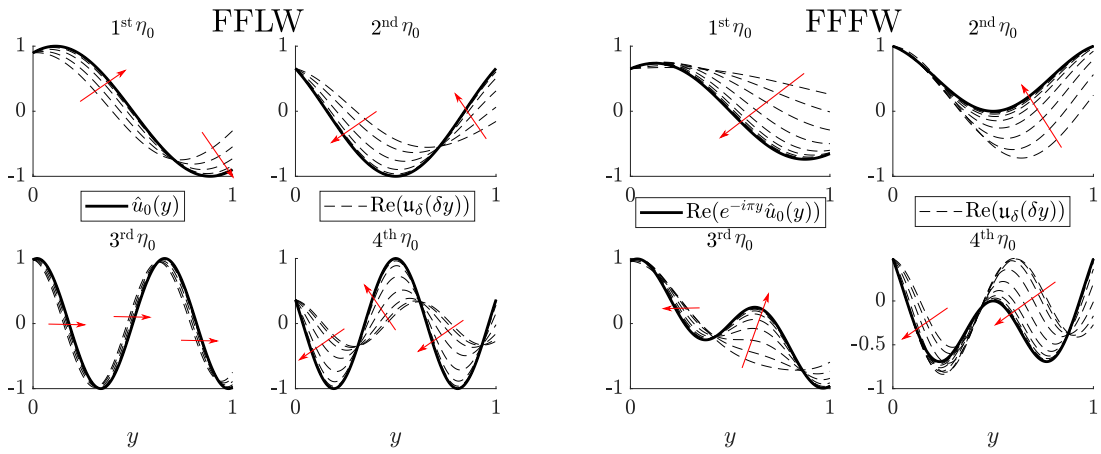

Figure 6.5 – Illustration of the convergence of the method in the monolayer case by comparing $\hat{u}_0$ and $\mathrm{u}_\delta(\delta y)$ in the FFLW (left) and the FFFW (right) cases. We plotted u_δ for 20 values of $\tilde{\kappa}\delta$ equidistributed in the log scale between 10^{-5} and 1. The red arrows indicate how $\mathrm{u}_\delta(\delta y)$ is changing as $\tilde{\kappa}\delta \to 0$.

field approximation obtained in the simple eigenvalue case. Using the Bloch-Floquet analysis (see Appendix 6.A), we can have access to the exact standing wavefield $u_\delta(x) = u_\delta(\delta y)$, and, to be compatible with the asymptotic expansion (6.9), we normalize it such that $u_\delta(0^+) = u_0(0, 0^+)$. Note that because of (6.7) and (6.55), the difference between the exact and approximated field can be written as

$$\begin{aligned} u_\delta(x) - u_0\left(x, \frac{x}{\delta}\right) &= u_\delta(\delta y) - u_0(\delta y, y) \\ &= \begin{cases} e^{i\kappa\delta y}(\mathfrak{u}_\delta(\delta y) - \hat{u}_0(y)) & \text{(FFLW)}, \\ e^{i\kappa\delta y}(\mathfrak{u}_\delta(\delta y) - e^{-i\pi y}\hat{u}_0(y)) & \text{(FFFW)}. \end{cases} \end{aligned} \tag{6.90}$$

To illustrate the validity of our approximation, we hence compare $\mathfrak{u}_\delta(\delta y)$ and $\hat{u}_0(y)$ for various values of $\kappa\delta$ in Figure 6.5, showing, as expected, that as $\tilde{\kappa}\delta$ gets smaller the zeroth-order field is a good approximation to the exact field.

A similar investigation can be carried out for the nearby eigenvalue approximation of the field. As can be seen in Figure 6.6, the approximation is good even for a value of $\tilde{\kappa}\delta = 0.5$ that is not particularly small, and for which the agreement of the simple eigenvalue zeroth-order field is poor.

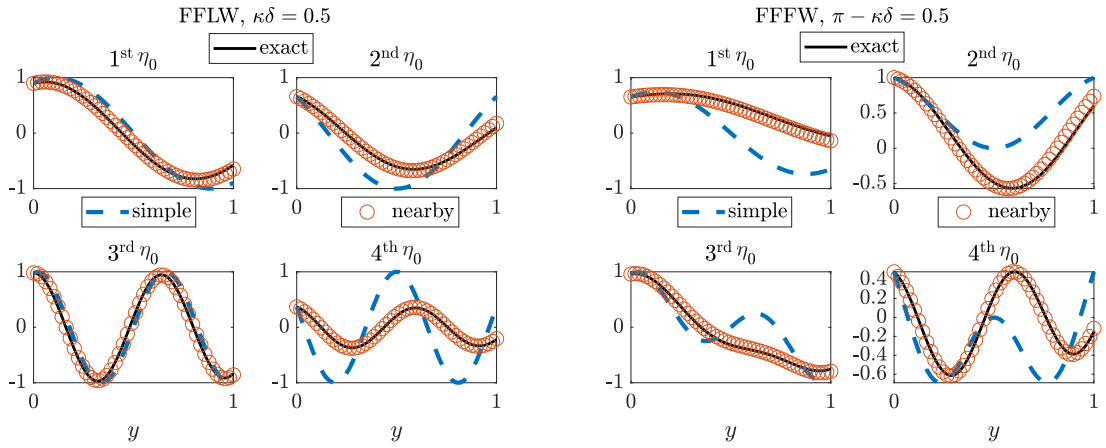

Figure 6.6 – Superposition of real parts of the exact ($\mathfrak{u}_\delta$), simple eigenvalue zeroth-order ($\hat{u}_0$) and nearby eigenvalue approximation normalised wavefields in the FFLW (left) and FFFW (right) for $\tilde{\kappa}\delta = 0.5$ in the monolayer case.

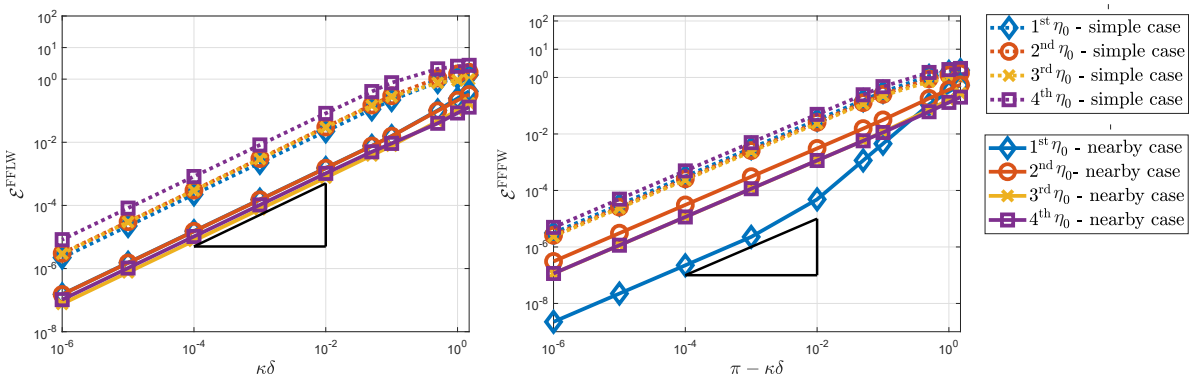

Figure 6.7 – Loglog plot of the error between the exact (Bloch Floquet) and the homogenized fields for various values of $\kappa\delta$ with $\mathcal{K} = 1$ and $\mathcal{M} = 0.5$ in the monolayer case. (Left) FFLW. (Right) FFFW. The slope depicted by a black triangle denotes a slope of 1. Dotted (resp. plain) lines correspond to the simple (resp. nearby) eigenvalue approximations.

In Figure 6.7, we plot the error between the exact field and the *homogenized* fields obtained using both the simple and nearby eigenvalue approximations. Due to the periodicity properties of $\mathfrak{u}_\delta$ and $\hat{u}_0$ and (6.90), the error is relatively easy to compute in the simple eigenvalue case and is defined as follows:

$$\text{(FFLW)}: \mathcal{E}^{\text{FFLW}}_{\text{simple}} = \max_{\mathbb{R}} |u_\delta(\delta y) - u_0(\delta y, y)| = \max_{[0,1]} |\mathfrak{u}_\delta(\delta y) - \hat{u}_0(y)|, \tag{6.91}$$

$$\text{(FFFW)}: \mathcal{E}^{\text{FFFW}}_{\text{simple}} = \max_{\mathbb{R}} |u_\delta(\delta y) - u_0(\delta y, y)| = \max_{[0,1]} |\mathfrak{u}_\delta(\delta y) - e^{-i\pi y}\hat{u}_0(y)|. \tag{6.92}$$

In the nearby eigenvalue approximation, using (6.83), the errors can be written as

$$\text{(FFLW)}: \mathcal{E}^{\text{FFLW}}_{\text{nearby}} = \max_{[0,1]} \left| \mathfrak{u}_\delta(\delta y) - \left(-\frac{\langle \beta \mathfrak{w}_0 \rangle}{(\mathcal{M}B_1^2 + C_1)} \frac{\mathrm{i}\tilde{\kappa}\delta}{\delta \eta_1^2} \hat{u}_0^{(1)}(y) + \hat{u}_0^{(2)}(y) \right) \right|, \tag{6.93}$$

$$\text{(FFFW)}: \mathcal{E}^{\text{FFFW}}_{\text{nearby}} = \max_{[0,1]} \left| \mathfrak{u}_\delta(\delta y) - e^{-i\pi y} \left(\frac{\langle \beta \mathfrak{w}_0 \rangle}{(\mathcal{M}B_1^2 + C_1)} \frac{i\tilde{\kappa}\delta}{\delta \eta_1^2} \hat{u}_0^{(1)}(y) + \hat{u}_0^{(2)}(y) \right) \right|. \tag{6.94}$$

One can see that we recover the expected behaviour $u_\delta(\delta y) = u_0(\delta y, y) + O(\tilde{\kappa}\delta)$, but that the nearby eigenvalue approximation performs much better for the whole range of values of $\tilde{\kappa}\delta$ used in Figure 6.7.

We now endeavour to study how the eigenvalues η_0 depend on $\mathcal{M}$ and $\mathcal{K}$. In order to visualise this we display a heat map of the first and second FFLW (periodic) $\eta_0(\mathcal{M}, \mathcal{K})$ in Figure 6.8. One can clearly see two distinct regions, on the left and on the right of the curve $\mathcal{K} = 1/\mathcal{M}$. On each side of these curves, the eigenvalue depend solely on one of the two parameters $(\mathcal{M}, \mathcal{K})$, which correspond to either the top or the bottom line of $\mathbb{M}^{\text{mo}}$ being zero. On the curve $\mathcal{K} = 1/\mathcal{M}$, both lines of $\mathbb{M}^{\text{mo}}$ are zero, and hence, the eigenvalue η_0 is a double eigenvalue.

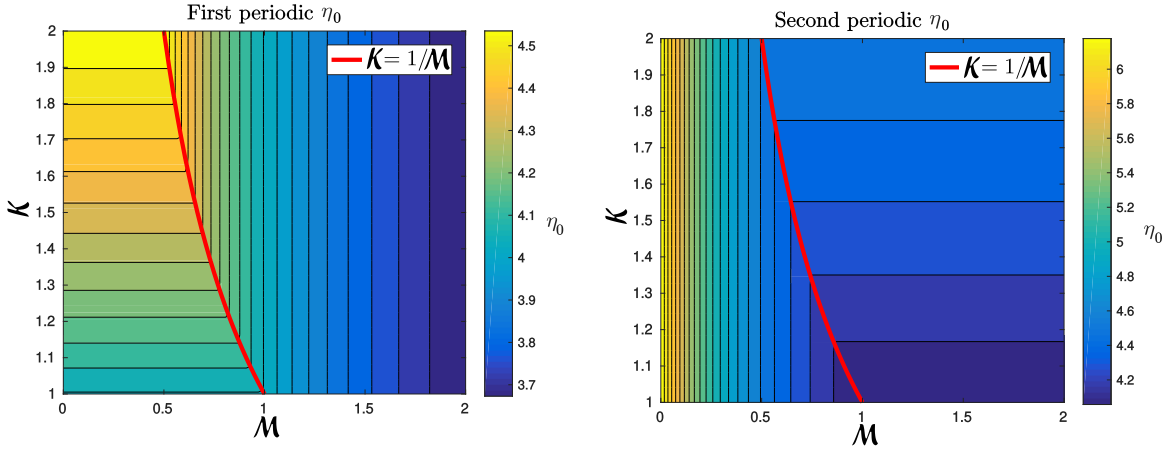

Figure 6.8 – Filled contour plot of the first (left) and second (right) periodic eigenvalues η_0 as $\mathcal{M}$ and $\mathcal{K}$ vary for the monolayer case. The thick red line represents the locus of double eigenvalues, while the thin black lines are isolines of η_0.

The other eigenvalues in the the FFLW (periodic) and FFFW (antiperiodic) case have very similar heatmaps, in particular they are all double eigenvalues when $\mathcal{K} = 1/\mathcal{M}$, as displayed on the dispersion diagram in Figure 6.9 (left).

In the case of a double eigenvalue, we have to follow the procedure of Section 6.4 by representing u_0 as in (6.57). We hence need to find two independent solutions $\hat{u}_0^{(1,2)}$ of (6.19), which can both be written $\hat{u}_0^{(1,2)}(y) = A^{(1,2)} \cos(\eta_0 y) + B^{(1,2)} \sin(\eta_0 y)$. Because of the dimension of the system,

any two independent vectors $(A^{(1)}, B^{(1)})^T$ and $(A^{(2)}, B^{(2)})^T$ would work, and we can hence choose $(A^{(1)}, B^{(1)})^T = (1,0)^T$ and $(A^{(2)}, B^{(2)})^T = (0,1)^T$. As seen in Section 6.4, the two functions $\mathcal{U}_0^{(1,2)}(x)$ appearing in (6.57) satisfy the first-order ODE system (6.65), where in our case we have

$$B_1 = \langle\!\langle \hat{u}_0^{(1)} \rangle\!\rangle = \frac{1 \pm \cos(\eta_0)}{2}, \qquad B_2 = \langle\!\langle \hat{u}_0^{(2)} \rangle\!\rangle = \frac{\pm \sin(\eta_0)}{2},$$
$$C_1 = \langle \alpha (\hat{u}_0^{(1)})^2 \rangle = \frac{\eta_0 + \sin(\eta_0)\cos(\eta_0)}{2\eta_0}, \quad C_2 = \langle \alpha (\hat{u}_0^{(2)})^2 \rangle = \frac{\eta_0 - \sin(\eta_0)\cos(\eta_0)}{2\eta_0},$$
$$D = \langle \alpha \hat{u}_0^{(1)} \hat{u}_0^{(2)} \rangle = \frac{\sin^2(\eta_0)}{2\eta_0}, \qquad \langle \beta \mathtt{w}_0 \rangle = \eta_0.$$

Using these, one can easily compute the associated eigenvalues $\lambda_{1,2}$ and eigenvectors $\boldsymbol{\mathcal{U}}_{\lambda_{1,2}}$ via (6.66) and (6.67). Note that in this case, one can show that

$$\mathcal{M} B_1 B_2 + D = 0 \quad \text{and} \quad \mathcal{M} B_1^2 + C_1 = \mathcal{M} B_2^2 + C_2,$$

so that the eigenvalues $\lambda_{1,2}$ and eigenvectors $\boldsymbol{\mathcal{U}}_{\lambda_{1,2}}$ of the matrix of the ODE system are simply

$$\lambda_j = i(-1)^j (\mathcal{M} B_1^2 + C_1) \quad \text{and} \quad \boldsymbol{\mathcal{U}}_{\lambda_j} = (-i(-1)^j, 1)^T,$$

and $T_d = \eta_0/(\mathcal{M} B_1^2 + C_1)$. We can hence superpose the resulting linear approximation (6.72) onto the dispersion diagram, revealing an excellent fit, as can be seen in Figure 6.9 (right). It is quite remarkable that in this case, every eigenvalues η_0 correspond to Dirac points. In fact this can be understood by considering a homogeneous material with only one spring-mass interface. Upon sending a wave onto this interface, one can naturally derive a coefficient of reflection $\mathrm{Ref}(\eta)$ and a coefficient of transmission $\mathrm{Trans}(\eta)$. It turns out that

$$\mathrm{Ref}(\eta) = \frac{-i\eta\left(\frac{1}{\mathcal{K}} - \mathcal{M}\right)}{2\left(1 - \frac{\mathcal{M}\eta^2}{4\mathcal{K}}\right) - i\eta\left(\frac{1}{\mathcal{K}} + \mathcal{M}\right)} \quad \text{and} \quad \mathrm{Trans}(\eta) = \frac{2\left(1 + \frac{\mathcal{M}\eta^2}{4\mathcal{K}}\right)}{2\left(1 - \frac{\mathcal{M}\eta^2}{4\mathcal{K}}\right) - i\eta\left(\frac{1}{\mathcal{K}} + \mathcal{M}\right)},$$

and therefore the reflection coefficient is zero if and only if the condition $\mathcal{K} = 1/\mathcal{M}$ is satisfied. Hence, in the periodic medium considered, no internal reflection can be present, no destructive/constructive interference can take place and no band gaps occur.

6.6.2 Bilayer

We now consider the case of a bilayer material characterised by the phase fraction $r \in]0,1[$, and hence provide the imperfect interface extension to the example given in Craster et al., 2010a. The unit cell is made up of two homogeneous materials. The first one has a length rh, density ρ_1 and Young's modulus μ_1, while the second has length $(1-r)h$, density ρ_2 and Young's Modulus μ_2. The two respective wave speeds are $c_1 = \sqrt{\mu_1/\rho_1}$ and $c_2 = \sqrt{\mu_2/\rho_2}$. The important non dimensional functions α and β are hence defined by

$$\alpha(y) = \begin{cases} \alpha^{(1)} = \rho_1/\rho^\star & \text{for} \quad y \in]0, r[, \\ \alpha^{(2)} = \rho_2/\rho^\star & \text{for} \quad y \in]r, 1[, \end{cases} \tag{6.95}$$

$$\beta(y) = \begin{cases} \beta^{(1)} = \mu_1/\mu^\star & \text{for} \quad y \in]0, r[, \\ \beta^{(2)} = \mu_2/\mu^\star & \text{for} \quad y \in]r, 1[, \end{cases} \tag{6.96}$$

where $\rho^\star = r\rho_1 + (1-r)\rho_2$ and $\mu^\star = (r/\mu_1 + (1-r)/\mu_2)^{-1}$. The interface at $y = r$ is assumed perfect, and the geometry of this physical problem is summarized in Figure 6.10.

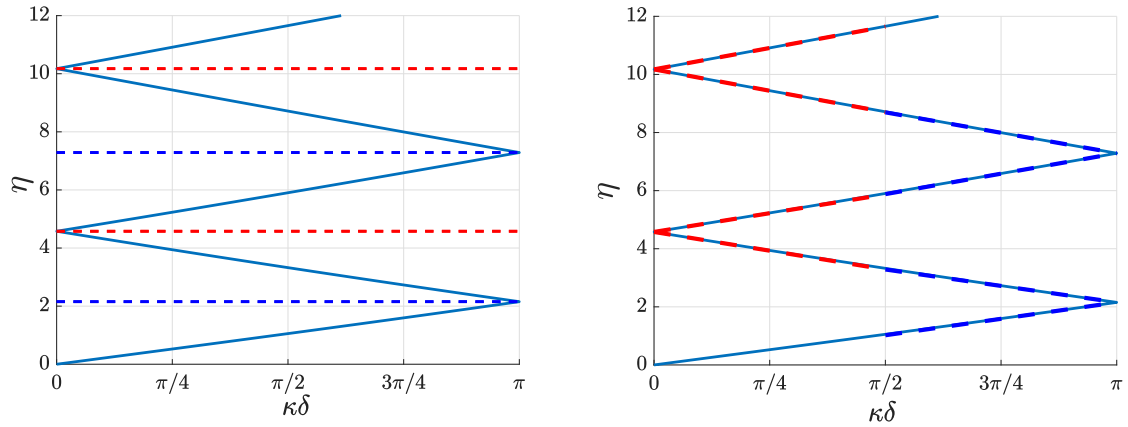

Figure 6.9 – Dispersion diagram for the monolayer case with $\mathcal{K} = 2$ and $\mathcal{M} = 0.5$ corresponding to double eigenvalues. (Left) In red (resp. blue) dashed lines are the periodic (resp. antiperiodic) eigenvalues η_0 calculated by finding the roots of (6.87). (Right) In red (resp. blue) dashed lines are the periodic (resp. antiperiodic) resulting first-order approximations (6.72).

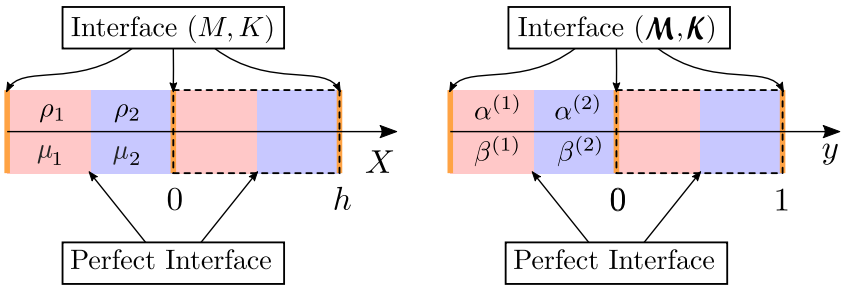

Figure 6.10 – Geometry of the bilayer problem (left) and non-dimensional (right) settings.

The classic Bloch-Floquet analysis will, in this case, give the following dispersion relation

$$\cos(\kappa\delta) = \frac{1}{1+\frac{\mathcal{M}\eta^2}{4\mathcal{K}}}\left[\left(1-\frac{\mathcal{M}\eta^2}{4\mathcal{K}}\right)\left(C_1C_2 - \frac{1}{2}\left(\frac{Z_1}{Z_2}+\frac{Z_2}{Z_1}\right)S_1S_2\right)\right.$$
$$\left. - \frac{\mathcal{M}\eta}{2}\left(\frac{S_1C_2Z^\star}{Z_1}+\frac{S_2C_1Z^\star}{Z_2}\right) - \frac{\eta}{2\mathcal{K}}\left(\frac{Z_1S_1C_2}{Z^\star}+\frac{Z_2S_2C_1}{Z^\star}\right)\right],$$

where $Z_i = \rho_i c_i$, $Z^\star = \rho^\star c^\star$, and $C_i = \cos(\eta H_i)$, $S_i = \sin(\eta H_i)$, $H_1 = rc^\star/c_1$, $H_2 = (1-r)c^\star/c_2$ and, naturally, $c^\star = \sqrt{\mu^\star/\rho^\star}$. As per the monolayer case, the dispersion diagram displays band gaps as can be seen in Figure 6.11. We will now apply the high-frequency homogenization technique to derive an analytical approximation to the higher branches of the diagram and to the associated wavefields.

Remark 23. *When $\mathcal{M} = 0$ and $\mathcal{K} = +\infty$ in (6.97), one recovers the dispersion relation for a bilayered medium with perfect interfaces.*

Using (6.19a) and (6.27), we find that $\hat{u}_0$ should satisfy

$$\begin{cases} \hat{u}_0'' + (\Omega^{(1)})^2\hat{u}_0 = 0 & \text{on }]0, r[, \\ \hat{u}_0'' + (\Omega^{(2)})^2\hat{u}_0 = 0 & \text{on }]r, 1[, \end{cases}$$

so that

$$\begin{cases} \hat{u}_0(y) = A^{(1)}\cos(\Omega^{(1)}y) + B^{(1)}\sin(\Omega^{(1)}y) & \text{on }]0, r[, \\ \hat{u}_0(y) = A^{(2)}\cos(\Omega^{(2)}y) + B^{(2)}\sin(\Omega^{(2)}y) & \text{on }]r, 1[, \end{cases} \tag{6.97}$$

where $A^{(1,2)}$ and $B^{(1,2)}$ are some constants to be determined, and $\Omega^{(1,2)} = \eta_0\sqrt{\frac{\alpha^{(1,2)}}{\beta^{(1,2)}}} = \eta_0\frac{c^\star}{c_{1,2}}$. The interface at $y = r$ is assumed perfect, and hence, $\hat{u}_0$ is also subject to the interface conditions

$$\begin{cases} \hat{u}_0(r^-) = \hat{u}_0(r^+), \\ \beta^{(1)}\hat{u}_0'(r^-) = \beta^{(2)}\hat{u}_0'(r^+), \end{cases} \quad \text{and} \quad \begin{cases} \hat{u}_0(0^+) \mp \hat{u}_0(1^-) = \frac{1}{2\mathcal{K}}(\beta^{(1)}\hat{u}_0'(0^+) \pm \beta^{(2)}\hat{u}_0'(1^-)), \\ \beta^{(1)}\hat{u}_0'(0^+) \mp \beta^{(2)}\hat{u}_0'(1^-) = -\frac{\mathcal{M}\eta_0^2}{2}(\hat{u}_0(0^+) \pm \hat{u}_0(1^-)), \end{cases}$$

where here and throughout this section, Notation 6.2.1 is being used. This results in a system of the form

$$\mathbb{M}^{\text{bi}}(A^{(1)}, B^{(1)}, A^{(2)}, B^{(2)})^T = (0,0,0,0)^T, \tag{6.98}$$

where the 4×4 matrix $\mathbb{M}^{\text{bi}}$ is given by

$$\begin{cases} \mathbb{M}^{\text{bi}}[1,1] = 1, & \mathbb{M}^{\text{bi}}[3,1] = -\cos(\Omega^{(1)}r), \\ \mathbb{M}^{\text{bi}}[1,2] = -\dfrac{\beta^{(1)}\Omega^{(1)}}{2\mathcal{K}}, & \mathbb{M}^{\text{bi}}[3,2] = -\sin(\Omega^{(1)}r), \\ \mathbb{M}^{\text{bi}}[1,3] = \mp\cos(\Omega^{(2)}) \pm \dfrac{\beta^{(2)}\Omega^{(2)}\sin(\Omega^{(2)})}{2\mathcal{K}}, & \mathbb{M}^{\text{bi}}[3,3] = \cos(\Omega^{(2)}r), \\ \mathbb{M}^{\text{bi}}[1,4] = \mp\sin(\Omega^{(2)}) \mp \dfrac{\beta^{(2)}\Omega^{(2)}\cos(\Omega^{(2)})}{2\mathcal{K}}, & \mathbb{M}^{\text{bi}}[3,4] = \sin(\Omega^{(2)}r), \\ \mathbb{M}^{\text{bi}}[2,1] = -\dfrac{\mathcal{M}\eta_0^2}{2}, & \mathbb{M}^{\text{bi}}[4,1] = \beta^{(1)}\Omega^{(1)}\sin(\Omega^{(1)}r), \\ \mathbb{M}^{\text{bi}}[2,2] = -\beta^{(1)}\Omega^{(1)}, & \mathbb{M}^{\text{bi}}[4,2] = -\beta^{(1)}\Omega^{(1)}\cos(\Omega^{(1)}r), \\ \mathbb{M}^{\text{bi}}[2,3] = \mp\beta^{(2)}\Omega^{(2)}\sin(\Omega^{(2)}) \mp \dfrac{\mathcal{M}\eta_0^2}{2}\cos(\Omega^{(2)}), & \mathbb{M}^{\text{bi}}[4,3] = -\beta^{(2)}\Omega^{(2)}\sin(\Omega^{(2)}r), \\ \mathbb{M}^{\text{bi}}[2,4] = \pm\beta^{(2)}\Omega^{(2)}\cos(\Omega^{(2)}) \mp \dfrac{\mathcal{M}\eta_0^2}{2}\sin(\Omega^{(2)}), & \mathbb{M}^{\text{bi}}[4,4] = \beta^{(2)}\Omega^{(2)}\cos(\Omega^{(2)}r). \end{cases}$$

The equation (6.98) can only have non-trivial solutions if $\det(\mathbb{M}^{\text{bi}}) = 0$, which gives a relation of the form

$$\mathcal{D}^{\text{bi}}(\eta_0; \mathcal{M}, \mathcal{K}, \beta^{(1)}, \beta^{(2)}, \Omega^{(1)}, \Omega^{(2)}, r) \quad = \quad 0, \tag{6.99}$$

the roots of which correspond to the eigenvalues η_0. The numerically computed eigenvalues coincide with the edges of the Brillouin zone on the dispersion diagram in Figure 6.11. To obtain $\hat{u}_0$, we find a vector in $\ker(\mathbb{M}^{\text{bi}})$ using the `null` function in Matlab, and use it as the coefficients $(A^{(1)}, B^{(1)}, A^{(2)}, B^{(2)})$.

We now need to find v_1 to obtain a second-order approximation. Since it is solution to the same equation (6.19a), we can write

$$\mathrm{v}_1(y) \quad = \quad \begin{cases} C^{(1)}\cos(\Omega^{(1)}y) + D^{(1)}\sin(\Omega^{(1)}y) & \text{on }]0, r[, \\ C^{(2)}\cos(\Omega^{(2)}y) + D^{(2)}\sin(\Omega^{(2)}y) & \text{on }]r, 1[. \end{cases} \tag{6.100}$$

Using (6.37) for the conditions at the unit cell interfaces, and remembering that, according to Remark 6.2, both v_1 and $\beta\mathrm{v}_1'$ should be continuous at $y = r$, one obtains a system of the form $\mathbb{M}^{\text{bi}}(C^{(1)}, D^{(1)}, C^{(2)}, D^{(2)})^T = \boldsymbol{b}^{\text{bi}}$, where

$$\boldsymbol{b}^{\text{bi}} \quad = \quad \left(\mp\hat{u}_0(1^-) \mp \frac{1}{2\mathcal{K}}\beta^{(2)}\hat{u}_0'(1^-), \mp\frac{\mathcal{M}\eta_0^2}{2}\hat{u}_0(1^-) \pm \beta^{(2)}\hat{u}_0'(1^-), 0, 0\right)^T.$$

Because the matrix $\mathbb{M}^{\text{bi}}$ is singular, we compute $(C^{(1)}, D^{(1)}, C^{(2)}, D^{(2)})^T$ via the Moore-Penrose Pseudo-inverse. Once v_1 is found, the resulting value of T is directly obtained using (6.46). The resulting approximations $\eta \approx \eta_0 + \frac{T}{2\eta_0}(\tilde{\kappa}\delta)^2$ are superposed to the Bloch-Floquet diagram in Figure 6.11 (left), and one can see that they approximate the branches well in the vicinity of the edges of the band gaps of the dispersion diagram. It is apparent from Figure 6.11 that the highest antiperiodic eigenvalue displayed seems to be a double eigenvalue (in fact we will see further that it is not exactly a double eigenvalue), and that the approximation is particularly short-lived in this neighbourhood. Having computed all the eigenvalues and eigenfunctions, we can once again evaluate the nearby eigenvalue approximation (6.81). It is displayed in Figure 6.11 (right), and as can clearly be seen, its agreement with the dispersion diagram is much longer-lived that of the simple eigenvalue approximation, even more so for the near-double eigenvalue.

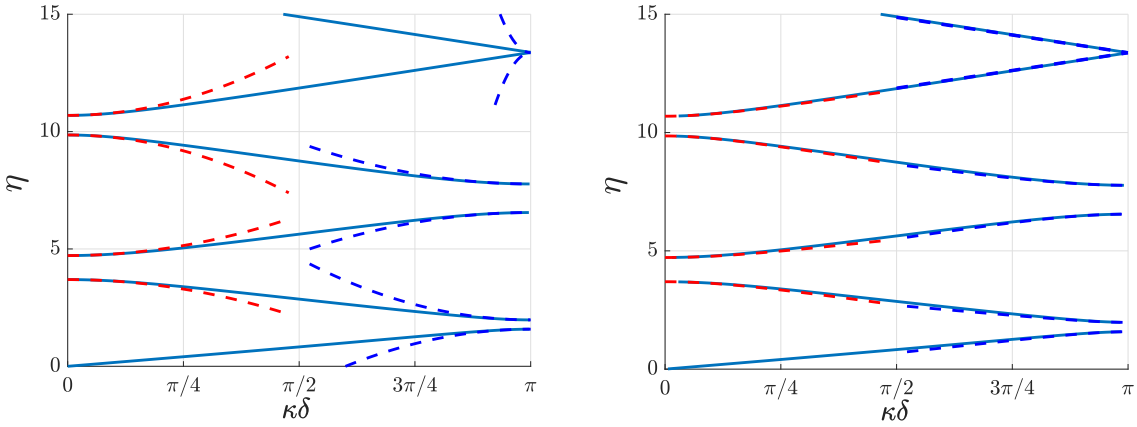

Figure 6.11 – Non-dimensional dispersion diagram for the bilayer case with $\rho_1 = 1200$ kg.m^{-3}, $\rho_2 = 1800$ kg.m^{-3}, $c_1 = 2800$m.s^{-1}, $c_2 = 3500$ m.s^{-1}, $\mu_1 = \rho_1 c_1^2$, $\mu_2 = \rho_2 c_2^2$, $M = 2 \times 10^4$ kg.m^2, $K = 2.45 \times 10^9$ Pa.m^{-1}, $r = 0.202$ and $h = 10$ m, corresponding to $\mathcal{K} \approx 1.41$ and $\mathcal{M} \approx 1.19$, $\alpha^{(1)} \approx 0.71$, $\alpha^{(2)} \approx 1.071$, $\beta^{(1)} \approx 0.54$ and $\beta^{(2)} \approx 1.27$. The red (resp. blue) dashed lines are the periodic (resp. antiperiodic) second-order approximations (6.53) using the computed values of T (left) and nearby eigenvalue approximations (6.81) using the computed values of T_d and $\delta\gamma$ (right).

Using the Bloch-Floquet analysis, in a very similar way to the monolayer case, we can have access to the exact standing wavefield $u_\delta(x) = u_\delta(\delta y)$, and we normalize it such that $u_\delta(0^+) = u_0(0, 0^+)$. As per the monolayer case, and because of (6.90), we illustrate the convergence of the simple eigenvalue method by comparing $u_\delta(\delta y)$ and $\hat{u}_0(y)$ for various values of $\kappa\delta$ in Figure 6.12.

A similar investigation can be carried out for the nearby eigenvalue approximation. As can be seen in Figure 6.13, the approximation is good even for a value of $\tilde{\kappa}\delta = 0.5$ that is not particularly small, and for which the agreement of the simple eigenvalue zeroth-order field is poor.

In Figure 6.14, we plot the error between the exact field and the *homogenized* fields obtained using both the simple and nearby eigenvalue approximations. The errors can be expressed as in (6.91)–(6.94). Again, one can see that we recover the expected behaviour $u_\delta(\delta y) = u_0(\delta y, y) + O(\tilde{\kappa}\delta)$, but that the nearby eigenvalue approximation performs better for the whole range of values of $\tilde{\kappa}\delta$ used in Figure 6.14.

As for the monolayer example displayed in Figure 6.9, it is possible to find physical parameters such that all the eigenvalues become simultaneously double eigenvalues (Dirac points). In order to do so one needs to ensure that $\mathcal{K} = 1/\mathcal{M}$, and that $\rho_1 c_1 = \rho_2 c_2$. The first condition imposes that the reflection coefficient due to the imperfect interface is zero, and the second imposes that the two homogeneous materials are "impedance matched" so that no reflection occurs from their perfect interface either.

However, for the bilayer, it appears that certain parameters lead to only two of the eigenvalues

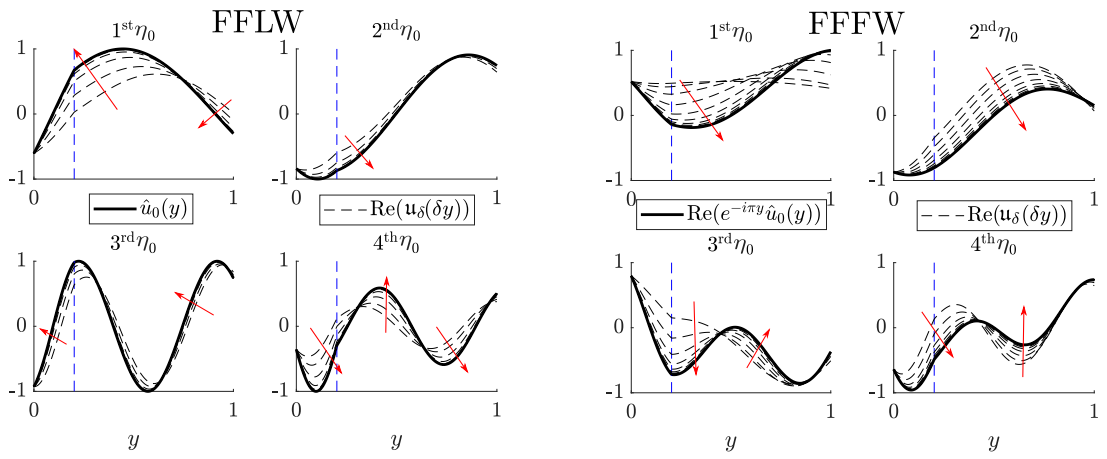

Figure 6.12 – Illustration of the convergence of the method in the bilayer case by comparing $\hat{u}_0$ and $\mathfrak{u}_\delta(\delta y)$ in the FFLW (left) and the FFFW (right) cases. We plotted $\mathfrak{u}_\delta$ for 20 values of $\tilde{\kappa}\delta$ equidistributed in the log scale between 10^{-5} and 1. The red arrows indicate how $\mathfrak{u}_\delta(\delta y)$ is changing as $\tilde{\kappa}\delta \to 0$, while the vertical dashed blue line indicates the position of the perfect interface between the two homogeneous materials.

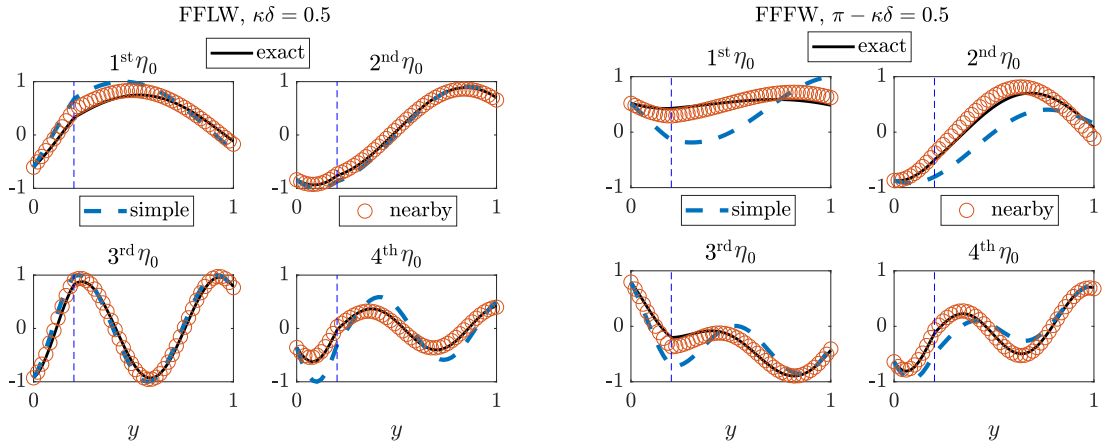

Figure 6.13 – Superposition of real parts of the exact ($\mathfrak{u}_\delta$), simple eigenvalue zeroth-order ($\hat{u}_0$) and nearby eigenvalue approximation normalised wavefields in the FFLW (left) and FFFW (right) for $\tilde{\kappa}\delta = 0.5$ in the bilayer case and for the same parameters used in Figure 6.11.

merging into a double eigenvalue, as appears to be the case in Figure 6.11. In order to visualize this phenomena, one could look at the evolution of the eigenvalues η_0 for fixed physical parameter, but for varying r within $]0,1[$. The results are displayed in Figure 6.15, and it seems that double eigenvalues or near-double eigenvalues may occur for some specific values of r, though, in this case, all the eigenvalues do not become double simultaneously. In fact, as illustrated in Figure 6.15, if one zooms on the areas of the graphs where eigenvalues seem to coincide, it appears that the curves do not actually touch each other. We will call these points *almost-Dirac points*. As highlighted above, the nearby eigenvalue approximation to the dispersion diagram is excellent for such almost-Dirac points, while the simple eigenvalue method leads to a very short-lived approximation, see Figure reffig:biBFdiag.

To explore the parameter space further, we will keep the values of r, $\alpha^{(1,2)}$ and $\beta^{(1,2)}$ used in Figure 6.11 and study the variation of the fifth and sixth antiperiodic eigenvalues η_0 that correspond to an almost-Dirac point according to Figure 6.15. As can be seen in Figure 6.16, in this case, we observe a similar behaviour as that of Figure 6.8, where two distinct regions seem to be separated by a smooth curve, on which the values of $\mathcal{M}$ and $\mathcal{K}$ chosen in Figure 6.11 (represented by a black star) seem to lie.

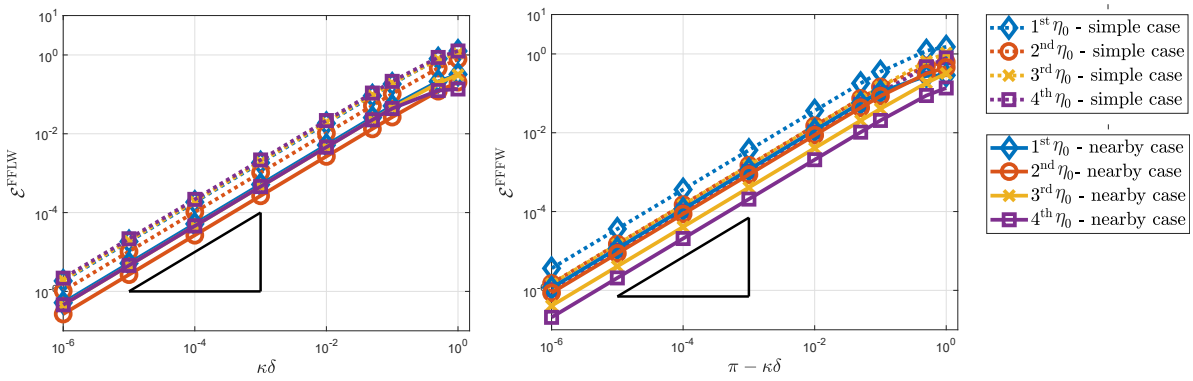

Figure 6.14 – Loglog plot of the error between the exact (Bloch Floquet) and the homogenized fields for various values of $\kappa\delta$ and for the same parameters of the bilayer case used in Figure 6.11. (Left) FFLW. (Right) FFFW. The slope depicted by a black triangle denotes a slope of 1. Dotted (resp. plain) lines correspond to the simple (resp. nearby) eigenvalue approximation.

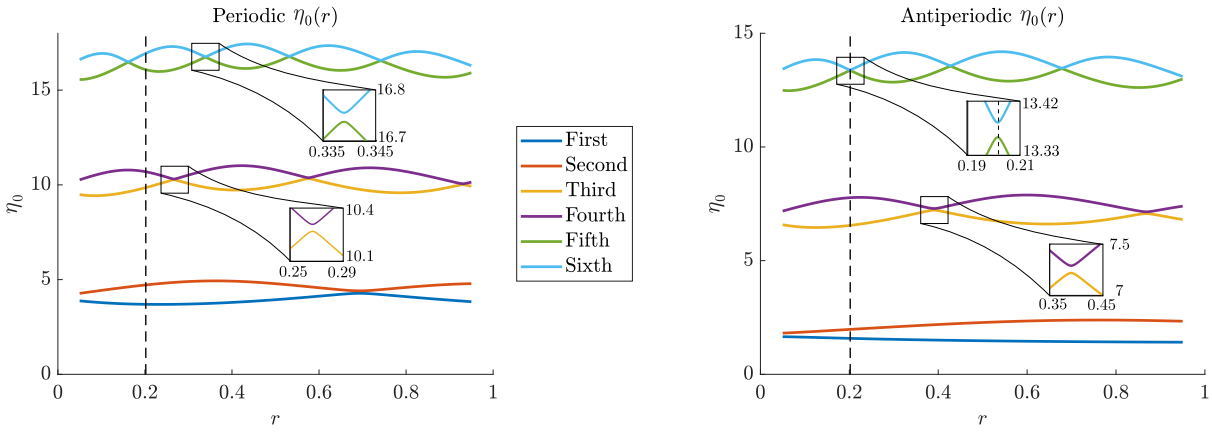

Figure 6.15 – Evolution of the first six FFLW (left) and FFFW (right) eigenvalues η_0 for the exact same parameters as those used in Figure 6.11, but for $r \in [0.05, 0.95]$. A vertical dashed line represents the value of r used in Figure 6.11. Zoom boxes are provided to show that near the almost-Dirac points, the eigenvalues remain simple

6.7 Conclusion

In this chapter, the high-frequency homogenization technique is extended to the case of one-dimensional periodic media with linear imperfect interfaces of the spring-mass type. The zeroth-order equations led to an eigenvalue problem and three cases were considered: a simple eigenvalue, a double eigenvalue, and two nearby eigenvalues. We obtained an approximation of both the wavefield and the dispersion diagram near the edges of the Brillouin zone. In the case of double eigenvalues, we then described the specific case of Dirac points whereas the nearby case allowed to propose a uniform approximation between the simple and the double case. We have illustrated the validity of the approximations with the two examples of monolayered and bilayered materials. In the case of the monolayered material, we quantified the error between the exact and the homogenized fields, and we found a simple condition on the nondimensional stiffness and mass values $\mathcal{K}$ and $\mathcal{M}$ for all the points at the edges of the Brillouin zone to become Dirac points. With both examples, we observed that the nearby eigenvalue approximation led to a much-longer-lived approximation to both the dispersion diagram and the wavefields.

The following perspectives can be considered:

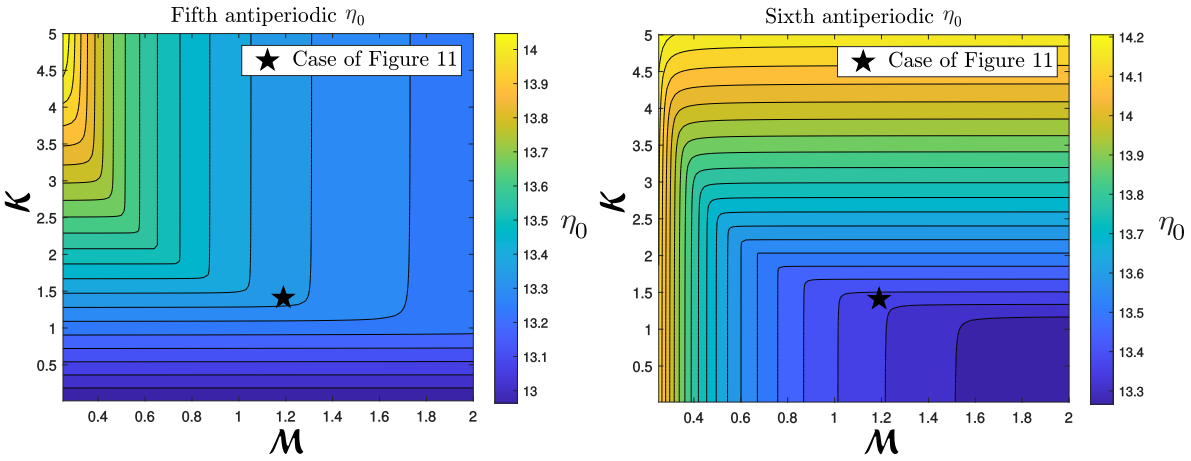

Figure 6.16 – Filled Contour Plot of the variations of the fifth (left) and sixth (right) antiperiodic eigenvalues in the bilayer case for the same values of r, $\alpha^{(1,2)}$ and $\beta^{(1,2)}$ used in Figure 6.11. The black star corresponds to the values of $\mathcal{M}$ and $\mathcal{K}$ used in Figure 6.11.

- the extension of this 1D work to multidimensional cases, see for example Guzina and Bonnet, 2021 for the anti-plane elasticity case. One main difference compared with the work of this chapter is that when the eigenvalue is repeated, its multiplicity can be higher than 2 which leads to a higher order system to compute the wavefield. Accordingly, in the nearby case, one has to consider a cluster of eigenvalues instead of two nearby eigenvalues. Eventually, numerical examples to validate the approximations obtained are more intricate to developp since analytical solutions are harder to obtain.
- in the spirit of the other chapters, it could be interesting to perform time-domain simulations to compare the agreement between homogenized and full-field simulations as time increases. This would require to formulate the homogenized problem in the time-domain (Harutyunyan et al., 2016) and to consider a source term, see Meng et al., 2020 for perfect interfaces.
- the extension of the asymptotics presented in this paper to higher order, i.e. to propose first- and maybe second-order corrections to the leading-order wavefields, see Guzina et al., 2019 for a first-order approximation with perfect interfaces.
- a more intricate possibility would be to consider non-linear imperfect interfaces as in the low-frequency framework of the previous chapter.
- another interesting direction is the consideration of scalings in the interface parameters, see Donato et al., 2007 in the static case where memory effects appear with an adequate scaling.

6.A Bloch-Floquet analysis of the monolayer case

In this case, u_δ satisfies (6.5)–(6.6) with $\alpha \equiv \beta \equiv 1$, hence, on $]0,\delta[$, we have

$$\begin{cases} u_\delta(x) = A_{\mathrm{BF}} \cos\left(\dfrac{\eta x}{\delta}\right) + B_{\mathrm{BF}} \sin\left(\dfrac{\eta x}{\delta}\right), & \text{(6.101a)} \\ u'_\delta(x) = -\dfrac{A_{\mathrm{BF}}\eta}{\delta} \sin\left(\dfrac{\eta x}{\delta}\right) + \dfrac{B_{\mathrm{BF}}\eta}{\delta} \cos\left(\dfrac{\eta x}{\delta}\right), & \text{(6.101b)} \end{cases}$$

subject to the two jump conditions

$$\begin{cases} [\![u_\delta]\!]^0 = \dfrac{\delta}{\mathcal{K}} \langle\!\langle u'_\delta \rangle\!\rangle^0, \\ \delta [\![u'_\delta]\!]^0 = -\mathcal{M}\eta^2 \langle\!\langle u_\delta \rangle\!\rangle^0, \end{cases} \tag{6.102}$$

relating the value of u_δ and u'_δ at 0^+ and 0^-. Moreover, according to Bloch-Floquet theory (6.7), we know that we can write $u_\delta(x) = \mathfrak{u}_\delta(x)e^{i\kappa x}$, for a δ-periodic function $\mathfrak{u}_\delta$, implying that, in particular, we have

$$\begin{cases} u_\delta(\delta^-) = u_\delta(0^-)e^{i\kappa\delta}, \\ u'_\delta(\delta^-) = u'_\delta(0^-)e^{i\kappa\delta}. \end{cases}$$

This, combined with the jump conditions (6.102), relates the values of u_δ and u'_δ at 0^+ and δ^-, and hence it gives two equations on A_{BF} and B_{BF}. These equations can be summarized by a matrix equation of the form $\mathbb{M}^{\mathrm{mo}}_{\mathrm{BF}}(\eta, \kappa\delta, \mathcal{M}, \mathcal{K})(A_{\mathrm{BF}}, B_{\mathrm{BF}})^T = (0,0)^T$, where

$$\begin{cases} \mathbb{M}^{\mathrm{mo}}_{\mathrm{BF}}[1,1] = 1 - e^{-i\kappa\delta}\cos(\eta) + \dfrac{\eta}{2\mathcal{K}}\sin(\eta)e^{-i\kappa\delta}, \\ \mathbb{M}^{\mathrm{mo}}_{\mathrm{BF}}[1,2] = -\sin(\eta)e^{-i\kappa\delta} - \dfrac{\eta}{2\mathcal{K}}(1+\cos(\eta)e^{-i\kappa\delta}), \\ \mathbb{M}^{\mathrm{mo}}_{\mathrm{BF}}[2,1] = -\eta\sin(\eta)e^{-i\kappa\delta} - \dfrac{\mathcal{M}\eta^2}{2}(1+\cos(\eta)e^{-i\kappa\delta}), \\ \mathbb{M}^{\mathrm{mo}}_{\mathrm{BF}}[2,2] = -\eta(1-\cos(\eta)e^{-i\kappa\delta}) - \dfrac{\mathcal{M}\eta^2}{2}\sin(\eta)e^{-i\kappa\delta}. \end{cases}$$

One notes that, as expected, for $\kappa\delta = 0$ or $\kappa\delta = \pi$ we have $\mathbb{M}^{\mathrm{mo}}_{\mathrm{BF}} = \mathbb{M}^{\mathrm{mo}}$ with the relevant sign. Of course, this system has only non-trivial solutions if $\det(\mathbb{M}^{\mathrm{mo}}_{\mathrm{BF}}) = 0$. One can show that

$$\det(\mathbb{M}^{\mathrm{mo}}_{\mathrm{BF}}) \quad = \quad \eta\left(-\mathcal{B} + 2e^{-i\kappa\delta}\left(\mathcal{C}\cos(\eta) - \frac{1}{2}\left(\frac{1}{\mathcal{K}} + \mathcal{M}\right)\eta\sin(\eta)\right) - \mathcal{B}e^{-2i\kappa\delta}\right),$$

where $\mathcal{B} = 1 + \frac{\mathcal{M}\eta^2}{4\mathcal{K}}$ and $\mathcal{C} = 1 - \frac{\mathcal{M}\eta^2}{4\mathcal{K}}$. Equating it to zero and multiplying by $e^{i\kappa\delta}/(\mathcal{B}\eta)$ leads to the dispersion relation (6.84).

For a value of η satisfying the dispersion relation, we have infinitely many possible vectors $(A_{\mathrm{BF}}, B_{\mathrm{BF}})^T$. To find one, just fix $A_{\mathrm{BF}} = 1$, and use either the first or second line of $\mathbb{M}^{\mathrm{mo}}_{\mathrm{BF}}$ to get B_{BF} as follows:

$$B_{\mathrm{BF}} = \frac{1 + e^{-i\kappa\delta}\left(-\cos(\eta) + \frac{\eta}{2\mathcal{K}}\sin(\eta)\right)}{\frac{\eta}{2\mathcal{K}} + e^{-i\kappa\delta}\left(\sin(\eta) + \frac{\eta}{2\mathcal{K}}\cos(\eta)\right)} \quad \text{or} \quad B_{\mathrm{BF}} = \frac{\frac{\mathcal{M}\eta}{2} + e^{-i\kappa\delta}\left(\sin(\eta) + \frac{\mathcal{M}\eta}{2}\cos(\eta)\right)}{-1 + e^{-i\kappa\delta}\left(\cos(\eta) - \frac{\mathcal{M}\eta}{2}\sin(\eta)\right)},$$

depending on which one has a non-zero denominator. It then leads to the exact Bloch-Floquet solution $u_\delta(x)$ on $]0,\delta[$. From this we recover $\mathfrak{u}_\delta(x) = u_\delta(x)e^{-i\kappa x}$ on $]0,\delta[$, which we can extend to $x \in \mathbb{R}$ by periodicity. We can therefore get $u_\delta(x)$ everywhere by $u_\delta(x) = \mathfrak{u}_\delta(x)e^{i\kappa x}$.

CHAPTER 7

Conclusion and perspectives

The design of media at a microscopic scale allows to control wave propagation in a fine way and to obtain exotic effects at the macroscopic scale. Thanks to homogenization methods, the microstructure can be advantageously replaced, at the macro scale, by a homogeneous effective medium. Then, as announced in the introduction, it raises the question of optimization tools in order to design the microstructure that allows to achieve a desired macroscopic effect. In this context, the consideration of interfaces (microstructured interfaces, imperfect interfaces) can lead to modifications in the homogenization methods, the numerical methods, or the optimization methods classically used. Therefore, the present thesis has focused on the study of waves propagation in microstructured media with interfaces through homogenization, time-domain simulations and optimization.

7.1 Conclusion

The first part of this thesis has focused on the propagation of waves across a periodic *row of inclusions*. The overall contribution on this topic is threefold:

- The aim was first to tackle the case of highly-contrasted inclusions that allow *local resonances* to occur. In Chapter 2, the homogenization process has been performed in the time-domain thanks to two-scale expansions and matched asymptotic methods. This has led to effective jump conditions that are non-local in time and that apply on the boundaries of an equivalent *enlarged* interface in which no field are defined anymore. Having the thickness of the effective interface larger than the width of the original microstructured array has been shown to be a sufficient condition to have a stable effective problem. The correspondence of this time-domain effective model with the frequency-dependent jump conditions developed in Pham et al., 2017 has also been established. Then, numerical examples have been provided to illustrate the model obtained and to compare its solutions with simulations involving the original microstructure. A good agreement has been found at low excitation frequency. This agreement deteriorates as the frequency increases and as the excitation consequently solicits resonant frequencies that are missed by the first order effective jump conditions. Eventually, dissipation of energy has been considered and for each resonant frequency taken into account in the homogenized model, Coherent Perfect Aborption was observed for a critical value of the dissipation parameter.

- The numerical method developped to simulate the interaction of transient waves with the effective resonant meta-interface has been described in Chapter 3. A set of auxiliary variables has been introduced locally along the enlarged interface in order to formulate an equivalent first-order system in time with jump conditions that are local in time. An immersed interface method has then been developed in 1D and 2D to handle numerically such a system by using a high-order finite differences scheme on a Cartesian grid. Local error estimates have been derived in 1D to assess the optimal values of the featured numerical parameters. The proposed numerical method has then been illustrated and validated considering 1D and 2D configurations involving plane waves illuminating both straight and curved enlarged interfaces. Moreover, the solutions to these problems have been derived analytically and used for quantitative comparisons. The modifications of the method induced by the consideration of dissipation of energy have also been presented.

- In Chapter 4, we have considered wave propagation across a row of inclusions in the *non-resonant* case, i.e. with a low contrast of the physical parameters. In this context, the objective was to propose a method to perform a topological optimization of this row of inclusions based on the associated non-resonant first-order homogenized model. The topological derivatives of the five scalar effective parameters have been calculated and this step have been validated numerically. As in the case of bulk microstructures, the expression of the effective parameters involves the solution to cell problems. However, in the case of a microstructured array, these cell problems are posed in an infinite strip. Since the optimization requires the resolution of numerous cell problems, the cell problems have been reformulated on a bounded cell. Then, a numerical method dedicated to this problem have been presented. This relies on the adaptation of the FFT-based method through the introduction of boundary correctors. Within the optimization process, the material update has then been handled thanks to one pixel phase permutations or to a level-set method. Eventually, some preliminary numerical results have been presented for two kinds of cost functional.

In a second part, we have studied media where imperfect interfaces are repeated periodically. The imperfect contact at these interfaces is modelled by *spring-mass* conditions. The contribution concerns two homogenization regimes:

- In Chapter 5, the *low-frequency* homogenization of these media was considered. We first considered a 1D periodic array of linear interfaces. Thanks to two-scale asymptotic expansions, a first-order homogenized model have been obtained: the mean fields satisfy a wave equation and the first-order corrector is found analytically. Then, an overview of the extension of this work to the case of non-linear interfaces has been presented. In this case, shocks occur and energy decreases in the homogenized model contrary to the microstructured configuration. For both linear and non-linear interfaces, numerical experiments have shown a good agreeement. As expected, this agreement deteriorates as the frequency increases in both the linear and non-linear cases. In the non-linear case, the same phenomenon has also been observed as the amplitude of the source increases. Eventually, the derivation of a first-oder homogenized model has been tackled for the full elasticity configuration in $\mathbb{R}^N$ with $N = 2, 3$. The mean fields then satisfy a wave equation involving an effective mass density which turns out to be a tensor and an effective elasticity tensor which satisfies the usual symmetry properties.

- The framework of *high-frequency homogenization* was at stake in Chapter 6. The technique has been extended to the case of one-dimensional periodic media with linear imperfect interfaces of the spring-mass type. The zeroth-order equations has led to an eigenvalue problem whose eigenvalues are the edges of the irreducible Brillouin zone corresponding to

standing waves. Three cases have been considered: a simple eigenvalue, a double eigenvalue, two nearby eigenvalues. In the three cases, an approximation of the dispersion diagram and the wave fields has been obtained for a frequency close to an eigenvalue and consequently to an edge of the Brillouin zone. In the case of double eigenvalues, we then described the specific case of Dirac points whereas the nearby case allowed to propose a uniform approximation between the simple and the double case. We have illustrated the validity of the approximations and we have observed that the nearby eigenvalue approximation led to a much-longer-lived approximation to both the dispersion diagram and the wave fields.

On the modeling side, several homogenized models have been derived: for a highly contrasted row of inclusions in the time domain at low-frequency, and for imperfect interfaces of the spring-mass type at either low-frequency or high-frequency. In the case of a row of low-contrasted inclusions, the topological optimization has also been studied based on the homogenized model available from the literature. The benefits of homogenization have also been observed: time-domain simulations for the homogenized model were much less costly in terms of computational time as full-field simulations in the microstructured configuration, and physical properties were explored analytically thanks to the effective model.
On the numerical side, a dedicated numerical method has been developped in 1D and 2D to simulate waves propagation in a homogeneous medium containing an enlarged interface on the boundaries of which resonant jump conditions apply. It has been programmed from scratch in C++ and its performance has been assessed. In a near future, the numerical method presented in this dissertation will be implemented in the PROSPERO platform http://prospero-software.science/.

7.2 Perspectives

Different follow-ups or perspectives have been identified and detailed at the end of each chapter. They can mostly be summarized in the following research lines.

1. In the very near future, two works in progress will be completed. Firstly, more numerical investigations and work on the final optimization algorithm has been identified in Chapter 4. Secondly, when imperfect interfaces are considered in the 2D or 3D case, we still need to perform numerical simulations in order to assess the validity of the homogenized model obtained by comparisons with full-field simulations.

2. A large part of the effective models obtained in this dissertation concerned a 1D configuration or the antiplane elasticity framework. The extension of this work to the full three dimensional elasticity case is a natural perspective that should not pose major technical difficulties, see Auriault and Bonnet, 1985; Auriault and Boutin, 2012; Comi and Marigo, 2019 for volumic microstructures in the resonant case or Guzina and Bonnet, 2021 for the anti-plane elasticity case in the high-frequency framework.

3. Another perspective is to perform the derivation of the effective models obtained in this thesis at higher order. In the resonant case, this could allow to account for the resonances associated with modes with zero mean, as discussed in Felbacq and Bouchitté, 2005; Pham et al., 2017. In the other low-frequency cases, this could be useful to describe the dispersive nature of the fields that appear when considering longer times (Santosa & Symes, 1991; Lamacz, 2011) or higher frequencies.

4. Another possibility is the consideration of additional scalings or small parameters. For example, to the prospect of "long term" behaviour, it is useful to introduce a slow and a fast time-scales in the asymptotics (Chen & Fish, 2001). For non-linear interfaces, a relatively low amplitude of the source term was assumed. An effective model for waves of relatively larger

amplitudes would also be interesting and would require the consideration of an additional scaling in the classical small parameter η relatively to the amplitude. For imperfect interfaces, another fruitful direction is the consideration of scalings in the mass and stiffness, see Donato et al., 2007 in the static case where memory effects appear with an adequate scaling.

5. In the first part of the dissertation, the microstructured array is assumed to be a single infinite array of inclusions. Perspectives regard the limitations of these geometric assumptions. Firstly, one could consider two rows of inclusions in order to play with two geometries and reach, for example, wide bands of high absorption instead of a unique value around each resonance. Secondly, the homogenization process could be performed for inclusions located along a curved line. The homogenized model would be more involved since, even in the non-resonant case, the local definition of the curvature will lead to a local expression of the effective parameters. Thirdly, as it is more realistic, it could be of interest to consider a layer of finite length. It requires to take into account both the boundary layer effects appearing near the microstructured layer and the corner singularities in the neighborhood of the extremities of the layer, see for example Semin et al., 2018 for a finite-length periodic array of holes.

6. Eventually, one could be interested in the topological optimization of thin microstructured arrays in the *resonant* case. It would require more work on the optimization process since the resonant homogenized model includes resonant frequencies that depend on the geometry of the microstructure, see Vondřejc et al., 2017 for shape optimization. Consequently, the extension of the topological derivatives calculation and their use in an optimization algorithm is a perspective in the longer term but would be of particular interest for example in the context of noise reduction (Ma et al., 2014; Schwan et al., 2017) or for coherent perfect absorption (Romero-Garcia et al., 2021).

References

Abdelmoula, R., Coutris, M., & Marigo, J.-J. (1998). Comportement asymptotique d''une interphase élastique mince. *Comptes Rendus de l'Académie des Sciences - Series IIB - Mechanics-Physics-Chemistry-Astronomy*, *326*(4), 237–242. doi:10.1016/s1251-8069(98)80032-8

Achenbach, J. D., & Norris, A. N. (1982). Loss of specular reflection due to nonlinear crack-face interaction. *Journal of Nondestructive Evaluation*, *3*(4), 229–239. doi:10.1007/bf00565867

Ahn, B., Lee, H., Lee, J. S., & Kim, Y. Y. (2019). Topology optimization of metasurfaces for anomalous reflection of longitudinal elastic waves. *Computer Methods in Applied Mechanics and Engineering*, *357*, 112582. doi:10.1016/j.cma.2019.112582

Allaire, G., de Gournay, F., Jouve, F., & Toader, A.-M. (2005). Structural optimization using topological and shape sensitivity via a level set method. *Control and Cybernetics*, *34*(1), 59–80.

Allaire, G., & Yamada, T. (2018). Optimization of dispersive coefficients in the homogenization of the wave equation in periodic structures. *Numerische Mathematik*, *140*(2), 265–326. doi:10.1007/s00211-018-0972-4

Allaire, G. (1992). Homogenization and two-scale convergence. *SIAM Journal on Mathematical Analysis*, *23*(6), 1482–1518. doi:10.1137/0523084

Alvarez-Aramberri, J., Pardo, D., & Barucq, H. (2014). Automatically adapted perfectly matched layers for problems with high contrast materials properties. *Procedia Computer Science*, *29*, 970–979. doi:10.1016/j.procs.2014.05.087

Ambrosio, L., & Buttazzo, G. (1993). An optimal design problem with perimeter penalization. *Calculus of Variations and Partial Differential Equations*, *1*(1), 55–69. doi:10.1007/bf02163264

Ammari, H., & Kang, H. (2007). *Polarization and moment tensors: with applications to inverse problems and effective medium theory*. Springer Science & Business Media.

Amstutz, S., Giusti, S. M., Novotny, A. A., & de Souza Neto, E. A. (2010). Topological derivative for multi-scale linear elasticity models applied to the synthesis of microstructures. *International Journal for Numerical Methods in Engineering*, *84*(6), 733–756. doi:10.1002/nme.2922

Amstutz, S. (2011). Analysis of a level set method for topology optimization. *Optimization Methods and Software*, *26*(4-5), 555–573. doi:10.1080/10556788.2010.521557

Amstutz, S., & Andrä, H. (2006). A new algorithm for topology optimization using a level-set method. *Journal of Computational Physics*, *216*(2), 573–588. doi:10.1016/j.jcp.2005.12.015

Andrianov, I., Danishevs'kyy, V., Topol, H., & Weichert, D. (2011). Homogenization of a 1d nonlinear dynamical problem for periodic composites. *ZAMM - Journal of Applied Mathematics and Mechanics / Zeitschrift für Angewandte Mathematik und Mechanik*, *91*(6), 523–534. doi:10.1002/zamm.201000176

Antonakakis, T., & Craster, R. V. (2012). High-frequency asymptotics for microstructured thin elastic plates and platonics. *Proceedings of the Royal Society A: Mathematical, Physical and Engineering Sciences*, *468*(2141), 1408–1427. doi:10.1098/rspa.2011.0652

Antonakakis, T., Craster, R., & Guenneau, S. (2014). Homogenisation for elastic photonic crystals and dynamic anisotropy. *Journal of the Mechanics and Physics of Solids*, *71*, 84–96. doi:10.1016/j.jmps.2014.06.006

Argilaga, A., Papachristos, E., Caillerie, D., & Pont, S. D. (2016). Homogenization of a cracked saturated porous medium: theoretical aspects and numerical implementation. *International Journal of Solids and Structures*, *94-95*, 222–237. doi:10.1016/j.ijsolstr.2016.03.017

Auriault, J.-L., & Bonnet, G. (1985). Dynamique des composites élastiques périodiques. *Arch Mech. 37*(4-5), 269–284.

Auriault, J.-L., & Boutin, C. (2012). Long wavelength inner-resonance cut-off frequencies in elastic composite materials. *International Journal of Solids and Structures*, *49*(23-24), 3269–3281. doi:10.1016/j.ijsolstr.2012.07.002

Bandis, S., Lumsden, A., & Barton, N. (1984). Fundamentals of rock joint deformation. *International Journal of Rock Mechanics and Mining Sciences & Geomechanics Abstracts*, *21*(2), 49. doi:10.1016/0148-9062(84)91255-5

Becache, E., Joly, P., & Tsogka, C. (2001). Fictitious domains, mixed finite elements and perfectly matched layers for 2-d elastic wave propagation. *Journal of Computational Acoustics*, *09*(03), 1175–1201. doi:10.1142/s0218396x01000966

Bellis, C., & Lombard, B. (2019). Simulating transient wave phenomena in acoustic metamaterials using auxiliary fields. *Wave Motion*, *86*, 175–194. doi:10.1016/j.wavemoti.2019.01.010

Bensoussan, A., Lions, J.-L., & Papanicolaou, G. (2011). *Asymptotic analysis for periodic structures*. AMS Chelsea Publishing.

Bonnet-Bendhia, A., Drissi, D., & Gmati, N. (2004). Simulation of muffler's transmission losses by a homogenized finite element method. *Journal of Computational Acoustics*, *12*(3), 447–474.

Bonnet, M., Cornaggia, R., & Guzina, B. B. (2018). Microstructural topological sensitivities of the second-order macroscopic model for waves in periodic media. *SIAM Journal on Applied Mathematics*, *78*(4), 2057–2082. doi:10.1137/17m1149018

Bouchitté, G., Bourel, C., & Felbacq, D. (2015, December 8). Homogenization near resonances and artificial magnetism in 3d dielectric metamaterials. doi:10.1007/s00205-017-1132-1. arXiv: 1512.02463 [math.AP]

Boutin, C., & Auriault, J. (1993). Rayleigh scattering in elastic composite materials. *International Journal of Engineering Science*, *31*(12), 1669–1689. doi:10.1016/0020-7225(93)90082-6

Boutin, C., Rallu, A., & Hans, S. (2014). Large scale modulation of high frequency waves in periodic elastic composites. *Journal of the Mechanics and Physics of Solids*, *70*, 362–381. doi:10.1016/j.jmps.2014.05.015

Broda, D., Staszewski, W., Martowicz, A., Uhl, T., & Silberschmidt, V. (2014). Modelling of nonlinear crack–wave interactions for damage detection based on ultrasound—a review.

Journal of Sound and Vibration, *333*(4), 1097–1118. doi:https://doi.org/10.1016/j.jsv.2013.09.033

Burel, A. (2014). *Contributions à la simulation numérique en élastodynamique: découplage des ondes p et s, modèles asymptotiques pour la traversée de couches minces* (Doctoral dissertation, Université Paris Sud - Paris XI).

Cai, W., Chettiar, U. K., Kildishev, A. V., & Shalaev, V. M. (2007). Optical cloaking with metamaterials. *Nature Photonics*, *1*(4), 224–227. doi:10.1038/nphoton.2007.28

Capdeville, Y., & Marigo, J.-J. (2012). A non-periodic two scale asymptotic method to take account of rough topographies for 2-d elastic wave propagation. *Geophysical Journal International*, *192*(1), 163–189. doi:10.1093/gji/ggs001

Carcione, J. M. (Ed.). (2007). *Wave fields in real media - wave propagation in anisotropic, anelastic, porous and electromagnetic media*. doi:10.1016/s0950-1401(07)x8002-9

Cassier, M., Hazard, C., & Joly, P. (2017a). Spectral theory for maxwell's equations at the interface of a metamaterial. part i: generalized fourier transform. *Communications in Partial Differential Equations*, *42*(11), 1707–1748. doi:10.1080/03605302.2017.1390675

Cassier, M., Joly, P., & Kachanovska, M. (2017b). Mathematical models for dispersive electromagnetic waves: an overview. *Computers & Mathematics with Applications*, *74*(11), 2792–2830. doi:10.1016/j.camwa.2017.07.025

Cedio-Fengya, D., Moskow, S., & Vogelius, M. (1998). Identification of conductivity imperfections of small diameter by boundary measurements. continuous dependence and computational reconstruction. *Inverse problems*, *14*(3), 553.

Chen, W., & Fish, J. (2001). A dispersive model for wave propagation in periodic heterogeneous media based on homogenization with multiple spatial and temporal scales. *Journal of Applied Mechanics*, *68*(2), 153. doi:10.1115/1.1357165

Chiavassa, G., & Lombard, B. (2011). Time domain numerical modeling of wave propagation in 2D heterogeneous porous media. *Journal of Computational Physics*, *230*(13), 5288–5309. doi:10.1016/j.jcp.2011.03.030

Cohen, G., & Joly, P. (1996). Construction analysis of fourth-order finite difference schemes for the acoustic wave equation in nonhomogeneous media. *SIAM Journal on Numerical Analysis*, *33*(4), 1266–1302. doi:10.1137/s0036142993246445

Collino, F., Joly, P., & Millot, F. (1997). Fictitious domain method for unsteady problems: *Journal of Computational Physics*, *138*(2), 907–938. doi:10.1006/jcph.1997.5849

Colombi, A., Roux, P., Guenneau, S., Gueguen, P., & Craster, R. V. (2016). Forests as a natural seismic metamaterial: rayleigh wave bandgaps induced by local resonances. *Scientific Reports*, *6*(1). doi:10.1038/srep19238

Colquitt, D. J., Craster, R. V., & Makwana, M. (2015). High frequency homogenisation for elastic lattices. *The Quarterly Journal of Mechanics and Applied Mathematics*, *68*(2), 203–230. doi:10.1093/qjmam/hbv005

Comi, C., & Marigo, J.-J. (2019). Homogenization approach and bloch-floquet theory for band-gap prediction in 2d locally resonant metamaterials. *Journal of Elasticity*, *139*(1), 61–90. doi:10.1007/s10659-019-09743-x

Cornaggia, R., & Bellis, C. (2020). Tuning effective dynamical properties of periodic media by FFT-accelerated topological optimization. *International Journal for Numerical Methods in Engineering*. doi:10.1002/nme.6352

Craster, R. V., Kaplunov, J., & Pichugin, A. V. (2010a). High-frequency homogenization for periodic media. *Proceedings of the Royal Society A: Mathematical, Physical and Engineering Sciences*, *466*(2120), 2341–2362. doi:10.1098/rspa.2009.0612

Craster, R. V., Kaplunov, J., & Postnova, J. (2010b). High-frequency asymptotics, homogenisation and localisation for lattices. *The Quarterly Journal of Mechanics and Applied Mathematics*, *63*(4), 497–519. doi:10.1093/qjmam/hbq015

Craster, R. V., & Guenneau, S. (Eds.). (2013). *Acoustic metamaterials*. doi:10.1007/978-94-007-4813-2

Craster, R. V., Kaplunov, J., Nolde, E., & Guenneau, S. (2011). High-frequency homogenization for checkerboard structures: defect modes, ultrarefraction, and all-angle negative refraction. *Journal of the Optical Society of America A*, *28*(6), 1032. doi:10.1364/josaa.28.001032

D'Alessandro, L., Belloni, E., D'Alo, G., Daniel, L., Ardito, R., Corigliano, A., & Braghin, F. (2017). Modelling and experimental verification of a single phase three-dimensional lightweight locally resonant elastic metamaterial with complete low frequency bandgap. In *2017 11th international congress on engineered materials platforms for novel wave phenomena (metamaterials)*. doi:10.1109/metamaterials.2017.8107842

Dafermos, C. M. (2005). *Hyperbolic conservation laws in continuum physics*. Springer.

Dal Maso, G. (2012). *An introduction to Γ-convergence*. Springer Science & Business Media.

David, M., Pideri, C., & Marigo, J.-J. (2012). Homogenized interface model describing inhomogeneities located on a surface. *Journal of Elasticity*, *109*(2), 153–187.

Delourme, B., Haddar, H., & Joly, P. (2012). Approximate models for wave propagation across thin periodic interfaces. *Journal de mathématiques pures et appliquées*, *98*(1), 28–71.

Delourme, B., Lunéville, E., Marigo, J.-J., Maurel, A., Mercier, J.-F., & Pham, K. (2021). A stable, unified model for resonant faraday cages. *Proceedings of the Royal Society A: Mathematical, Physical and Engineering Sciences*, *477*(2245), 20200668. doi:10.1098/rspa.2020.0668

Delourme, B., Haddar, H., & Joly, P. (2013). On the well-posedness, stability and accuracy of an asymptotic model for thin periodic interfaces in electromagnetic scattering problems. *Mathematical Models and Methods in Applied Sciences*, *23*(13), 2433–2464. doi:10.1142/s021820251350036x

Deymier, P. A. (2012). Introduction to phononic crystals and acoustic metamaterials. In *Acoustic metamaterials and phononic crystals* (pp. 1–12). doi:10.1007/978-3-642-31232-8_1

Donato, P., Faella, L., & Monsurrò, S. (2007). Homogenization of the wave equation in composites with imperfect interface: a memory effect. *Journal de Mathématiques Pures et Appliquées*, *87*(2), 119–143. doi:10.1016/j.matpur.2006.11.004

Dumont, S., Rizzoni, R., Lebon, F., & Sacco, E. (2018). Soft and hard interface models for bonded elements. *Composites Part B: Engineering*, *153*, 480–490. doi:10.1016/j.compositesb.2018.08.076

Felbacq, D., & Bouchitté, G. (2005). Theory of mesoscopic magnetism in photonic crystals. *Physical Review Letters*, *94*(18). doi:10.1103/physrevlett.94.183902

Fornet, B., & Guès, O. (2009). Penalization approach to semi-linear symmetric hyperbolic problems with dissipative boundary conditions. *Discrete & Continuous Dynamical Systems - A*, *23*(3), 827–845. doi:10.3934/dcds.2009.23.827

Geers, M., Kouznetsova, V., & Brekelmans, W. (2010). Multi-scale computational homogenization: trends and challenges. *Journal of Computational and Applied Mathematics*, *234*(7), 2175–2182. doi:10.1016/j.cam.2009.08.077

Giusti, S., Ferrer, A., & Oliver, J. (2016). Topological sensitivity analysis in heterogeneous anisotropic elasticity problem. theoretical and computational aspects. *Computer Methods in Applied Mechanics and Engineering*, *311*, 134–150. doi:10.1016/j.cma.2016.08.004

Giusti, S. M., Novotny, A. A., & de Souza Neto, E. A. (2010). Sensitivity of the macroscopic response of elastic microstructures to the insertion of inclusions. *Proceedings of the Royal Society A: Mathematical, Physical and Engineering Sciences*, *466*(2118), 1703–1723. doi:10.1098/rspa.2009.0499

Godlewski, E., & Raviart, P.-A. (2013). *Numerical approximation of hyperbolic systems of conservation laws*. Springer Science & Business Media.

Gralak, B., & Tip, A. (2010). Macroscopic maxwell's equations and negative index materials. *Journal of Mathematical Physics*, *51*(5), 052902. doi:10.1063/1.3374670

Gralak, B., & Maystre, D. (2012). Negative index materials and time-harmonic electromagnetic field. *Comptes Rendus Physique*, *13*(8), 786–799. doi:10.1016/j.crhy.2012.04.003

Gusev, V., Castagnède, B., & Moussatov, A. (2003). Hysteresis in response of nonlinear bistable interface to continuously varying acoustic loading. *Ultrasonics*, *41*(8), 643–654. doi:10.1016/s0041-624x(03)00179-3

Guzina, B., Meng, S., & Oudghiri-Idrissi, O. (2019). A rational framework for dynamic homogenization at finite wavelengths and frequencies. In *Advances in engineering materials, structures and systems: innovations, mechanics and applications* (pp. 362–366). doi:10.1201/9780429426506-63

Guzina, B. B., & Bonnet, M. (2021). Effective wave motion in periodic discontinua near spectral singularities at finite frequencies and wavenumbers. *Wave Motion*, *103*, 102729. doi:10.1016/j.wavemoti.2021.102729

Harutyunyan, D., Milton, G. W., & Craster, R. V. (2016). High-frequency homogenization for travelling waves in periodic media. *Proceedings of the Royal Society A: Mathematical, Physical and Engineering Sciences*, *472*(2191), 20160066. doi:10.1098/rspa.2016.0066

Harvey, R. B., Morse, P. M., & Feschbach, H. (1955). Methods of theoretical physics. *The Mathematical Gazette*, *39*(327), 80. doi:10.2307/3611130

Hashin, Z. (1990). Thermoelastic properties of fiber composites with imperfect interface. *Mechanics of Materials*, *8*(4), 333–348. doi:10.1016/0167-6636(90)90051-g

Hashin, Z., & Shtrikman, S. (1963). A variational approach to the theory of the elastic behaviour of multiphase materials. *Journal of the Mechanics and Physics of Solids*, *11*(2), 127–140. doi:10.1016/0022-5096(63)90060-7

Hashin, Z. (2002). Thin interphase/imperfect interface in elasticity with application to coated fiber composites. *Journal of the Mechanics and Physics of Solids*, *50*(12), 2509–2537. doi:10.1016/s0022-5096(02)00050-9

Hecht, F. (2012). New development in freefem++. *Journal of Numerical Mathematics*, *20*(3-4). doi:10.1515/jnum-2012-0013

Huang, S., Fang, X., Wang, X., Assouar, B., Cheng, Q., & Li, Y. (2019). Acoustic perfect absorbers via helmholtz resonators with embedded apertures. *The Journal of the Acoustical Society of America*, *145*(1), 254–262. doi:10.1121/1.5087128

Jiang, X., Li, Y., & Zhang, L. (2017). Thermoviscous effects on sound transmission through a metasurface of hybrid resonances. *The Journal of the Acoustical Society of America*, *141*(4), EL363–EL368. doi:10.1121/1.4979682

Jiménez, N., Huang, W., Romero-Garcia, V., Pagneux, V., & Groby, J.-P. (2016). Ultra-thin metamaterial for perfect and quasi-omnidirectional sound absorption. *Applied Physics Letters*, *109*(12), 121902. doi:10.1063/1.4962328

Jiménez, N., Romero-Garcia, V., Pagneux, V., & Groby, J.-P. (2017). Rainbow-trapping absorbers: broadband, perfect and asymmetric sound absorption by subwavelength panels for transmission problems. *Scientific Reports*, *7*(1). doi:10.1038/s41598-017-13706-4

Jones, J. P., & Whittier, J. S. (1967). Waves at a flexibly bonded interface. *Journal of Applied Mechanics*, *34*(4), 905–909. doi:10.1115/1.3607854

Junca, S., & Lombard, B. (2012). Interaction between periodic elastic waves and two contact nonlinearities. *Mathematical Models and Methods in Applied Sciences*, *22*(04), 1150022. doi:10.1142/s0218202511500229

Junca, S., & Lombard, B. (2009). Dilatation of a one-dimensional nonlinear crack impacted by a periodic elastic wave. *SIAM Journal on Applied Mathematics*, *70*(3), 735–761. doi:10.1137/080741021

Komatitsch, D., & Vilotte, J.-P. (1998). The spectral element method: an efficient tool to simulate the seismic response of 2d and 3d geological structures. *Bulletin of the Seismological Society of America*, *88*(2), 368–392.

Krushynska, A., Kouznetsova, V., & Geers, M. (2016). Visco-elastic effects on wave dispersion in three-phase acoustic metamaterials. *Journal of the Mechanics and Physics of Solids*, *96*, 29–47. doi:10.1016/j.jmps.2016.07.001

Lagarrigue, C., Groby, J. P., Tournat, V., Dazel, O., & Umnova, O. (2013). Absorption of sound by porous layers with embedded periodic arrays of resonant inclusions. *The Journal of the Acoustical Society of America*, *134*(6), 4670–4680. doi:10.1121/1.4824843

Lamacz, A. (2011). Dispersive effective models for waves in heterogeneous media. *Mathematical Models and Methods in Applied Sciences*, *21*(09), 1871–1899. doi:10.1142/s021820251100557x

Lapine, M., McPhedran, R. C., & Poulton, C. G. (2016). Slow convergence to effective medium in finite discrete metamaterials. *Physical Review B*, *93*(23). doi:10.1103/physrevb.93.235156

Lax, P. D. (1957). Hyperbolic systems of conservation laws II. *Communications on Pure and Applied Mathematics*, *10*(4), 537–566. doi:10.1002/cpa.3160100406

Lax, P. D. (1964). Development of singularities of solutions of nonlinear hyperbolic partial differential equations. *Journal of Mathematical Physics*, *5*(5), 611–613. doi:10.1063/1.1704154

Lebon, F., & Rizzoni, R. (2011). Asymptotic behavior of a hard thin linear elastic interphase: an energy approach. *International Journal of Solids and Structures*, *48*(3-4), 441–449. doi:10.1016/j.ijsolstr.2010.10.006

Lebon, F., & Rizzoni, R. (2018). Higher order interfacial effects for elastic waves in one dimensional phononic crystals via the lagrange-hamilton's principle. *European Journal of Mechanics - A/Solids*, *67*, 58–70. doi:10.1016/j.euromechsol.2017.08.014

Lee-Thorp, J. P., Weinstein, M. I., & Zhu, Y. (2018). Elliptic operators with honeycomb symmetry: dirac points, edge states and applications to photonic graphene. *Archive for Rational Mechanics and Analysis*, *232*(1), 1–63. doi:10.1007/s00205-018-1315-4

Leng, J., Gautier, F., Pelat, A., Picó, R., Groby, J.-P., & Romero-Garcia, V. (2019). Limits of flexural wave absorption by open lossy resonators: reflection and transmission problems. *New Journal of Physics*, *21*(5), 053003. doi:10.1088/1367-2630/ab1761

LeVeque, R. J. (2002). *Finite volume methods for hyperbolic problems (cambridge texts in applied mathematics)*. Cambridge University Press.

Lewińska, M., Kouznetsova, V., van Dommelen, J., Krushynska, A., & Geers, M. (2017). The attenuation performance of locally resonant acoustic metamaterials based on generalised viscoelastic modelling. *International Journal of Solids and Structures*, *126-127*, 163–174. doi:10.1016/j.ijsolstr.2017.08.003

Li, Y., Shen, C., Xie, Y., Li, J., Wang, W., Cummer, S. A., & Jing, Y. (2017). Tunable asymmetric transmission via lossy acoustic metasurfaces. *Physical Review Letters*, *119*(3). doi:10.1103/physrevlett.119.035501

Licht, C., Lebon, F., & Léger, A. (2009). Dynamics of elastic bodies connected by a thin adhesive layer. In *Springer proceedings in physics* (pp. 99–110). doi:10.1007/978-3-540-89105-5_9

Liu, Y., Liang, Z., Liu, F., Diba, O., Lamb, A., & Li, J. (2017). Source illusion devices for flexural lamb waves using elastic metasurfaces. *Physical Review Letters*, *119*(3). doi:10.1103/physrevlett.119.034301

Liu, Z. (2000). Locally resonant sonic materials. *Science*, *289*(5485), 1734–1736. doi:10.1126/science.289.5485.1734

Lochner, T., & Peter, M. A. (2020). Homogenization of linearized elasticity in a two-component medium with slip displacement conditions. *Journal of Mathematical Analysis and Applications*, *483*(2), 123648. doi:10.1016/j.jmaa.2019.123648

Lombard, B. (2010). *Modélisation numérique de la propagation et de la diffraction d'ondes mécaniques*. Habilitation à Diriger des Recherches de l'Université d'Aix-Marseille 2.

Lombard, B., Maurel, A., & Marigo, J.-J. (2017). Numerical modeling of the acoustic wave propagation across an homogenized rigid microstructure in the time domain. *Journal of Computational Physics*, *335*, 558–577.

Lombard, B., & Piraux, J. (2003). How to incorporate the spring-mass conditions in finite difference schemes. *SIAM Journal of Scientific Computing*, *24*(4), 1379–1407.

Lombard, B., Piraux, J., Gélis, C., & Virieux, J. (2008). Free and smooth boundaries in 2-D finite-difference schemes for transient elastic waves. *Geophysical Journal International*, *172*(1), 252–261. doi:10.1111/j.1365-246x.2007.03620.x

Lombard, B., & Piraux, J. (2007). Modeling 1-d elastic p-waves in a fractured rock with hyperbolic jump conditions. *Journal of Computational and Applied Mathematics*, *204*(2), 292–305. doi:10.1016/j.cam.2006.03.027

Lombard, B., & Piraux, J. (2006). Numerical modeling of elastic waves across imperfect contacts. *SIAM Journal on Scientific Computing*, *28*(1), 172–205. doi:10.1137/05062740x

Lombard, B., & Piraux, J. (2004). Numerical treatment of two-dimensional interfaces for acoustic and elastic waves. *Journal of Computational Physics*, *195*(1), 90–116. doi:10.1016/j.jcp.2003.09.024

López-Realpozo, J. C., Rodriguez-Ramos, R., Guinovart-Diaz, R., Bravo-Castillero, J., Fernández, L. P., Sabina, F. J., & Maugin, G. A. (2008). Effective properties of non-linear elastic laminated composites with perfect and imperfect contact conditions. *Mechanics of Advanced Materials and Structures*, *15*(5), 375–385. doi:10.1080/15376490801977742

Lorcher, F., & Munz, C.-D. (2006). Lax-wendroff-type schemes of arbitrary order in several space dimensions. *IMA Journal of Numerical Analysis*, *27*(3), 593–615. doi:10.1093/imanum/drl031

Ma, G., Yang, M., Xiao, S., Yang, Z., & Sheng, P. (2014). Acoustic metasurface with hybrid resonances. *Nature Materials*, *13*(9), 873–878. doi:10.1038/nmat3994

Marigo, J.-J., & Maurel, A. (2016a). Homogenization models for thin rigid structured surfaces and films. *The Journal of the Acoustical Society of America*, *140*(1), 260–273.

Marigo, J.-J., Maurel, A., Pham, K., & Sbitti, A. (2017a). Effective dynamic properites of a row of elastic inclusions: the case of scalar shear waves. *Journal of Elasticity*, *128*(2), 265–289.

Marigo, J.-J., & Pideri, C. (2011). The effective behaviour of elastic bodies containing microcracks or microholes localized on a surface. *International Journal of Damage Mechanics, SAGE Publications*, *20*, 1151–1177.

Marigo, J.-J., & Maurel, A. (2017b). An interface model for homogenization of acoustic metafilms. In *World scientific handbook of metamaterials and plasmonics* (pp. 599–645). doi:10.1142/9789813228702_0014

Marigo, J.-J., & Maurel, A. (2017c). Second order homogenization of subwavelength stratified media including finite size effect. *SIAM Journal on Applied Mathematics*, *77*(2), 721–743. doi:10.1137/16m1070542

Marigo, J.-J., & Maurel, A. (2016b). Two-scale homogenization to determine effective parameters of thin metallic-structured films. *Proceedings of the Royal Society A: Mathematical, Physical and Engineering Sciences*, *472*(2192), 20160068. doi:10.1098/rspa.2016.0068

Martin Ph. Bendsoe, O. S. (2003, December 1). *Topology optimization*. Springer Berlin Heidelberg. Retrieved from https://www.ebook.de/de/product/5640654/martin_ph_bendsoe_ole_sigmund_topology_optimization.html

Martinez-Sala, R., Sancho, J., Sanchez, J. V., Gomez, V., Llinares, J., & Meseguer, F. (1995). Sound attenuation by sculpture. *Nature*, *378*(6554), 241–241. doi:10.1038/378241a0

Matsushima, K., Isakari, H., Takahashi, T., & Matsumoto, T. (2020). A topology optimisation of composite elastic metamaterial slabs based on the manipulation of far-field behaviours. *Structural and Multidisciplinary Optimization*, *63*(1), 231–243. doi:10.1007/s00158-020-02689-y

Maurel, A., Mercier, J.-F., Pham, K., Marigo, J.-J., & Ourir, A. (2019a). Enhanced resonance of sparse arrays of helmholtz resonators—application to perfect absorption. *The Journal of the Acoustical Society of America*, *145*(4), 2552–2560. doi:10.1121/1.5098948

Maurel, A., Marigo, J.-J., Mercier, J.-F., & Pham, K. (2018). Modelling resonant arrays of the helmholtz type in the time domain. *Proceedings of the Royal Society A: Mathematical, Physical and Engineering Science*, *474*(2210), 20170894. doi:10.1098/rspa.2017.0894

Maurel, A., Marigo, J.-J., & Ourir, A. (2016). Homogenization of ultrathin metallo-dielectric structures leading to transmission conditions at an equivalent interface. *Journal of the Optical Society of America B*, *33*(5), 947. doi:10.1364/josab.33.000947

Maurel, A., Pham, K., & Marigo, J.-J. (2019b). Homogenization of thin 3d periodic structures in the time-domain effective boundary and jump conditions. In V. Romero-Garcia & A.-C. Hladky-Hennion (Eds.), *Fundamentals and applications of acoustic metamaterials*. doi:10.1002/9781119649182

Meng, S., Oudghiri-Idrissi, O., & Guzina, B. B. (2020, February 7). A convergent low-wavenumber, high-frequency homogenization of the wave equation in periodic media with a source term. arXiv: 2002.02838 [math.AP]

Mercier, J.-F., Marigo, J.-J., & Maurel, A. (2017). Influence of the neck shape for helmholtz resonators. *The Journal of the Acoustical Society of America*, *142*(6), 3703–3714. doi:10.1121/1.5017735

Moukhomodiarov, R., Pichugin, A., & Rogerson, G. (2009). The transition between neumann and dirichlet boundary conditions in isotropic elastic plates. *Mathematics and Mechanics of Solids*, *15*(4), 462–490. doi:10.1177/1081286509103781

Moulinec, H., & Suquet, P. (1998). A numerical method for computing the overall response of nonlinear composites with complex microstructure. *Computer Methods in Applied Mechanics and Engineering*, *157*(1-2), 69–94. doi:10.1016/s0045-7825(97)00218-1

Nassar, H., He, Q.-C., & Auffray, N. (2015). Willis elastodynamic homogenization theory revisited for periodic media. *Journal of the Mechanics and Physics of Solids*, *77*, 158–178. doi:10.1016/j.jmps.2014.12.011

Nguetseng, G. (1989). A general convergence result for a functional related to the theory of homogenization. *SIAM Journal on Mathematical Analysis*, *20*(3), 608–623. doi:10.1137/0520043

Noguchi, Y., & Yamada, T. (n.d.). Topology optimization of acoustic metasurfaces by using a two-scale homogenization method. *submitted*.

Noguchi, Y., Yamada, T., Izui, K., & Nishiwaki, S. (2018). Topology optimization for hyperbolic acoustic metamaterials using a high-frequency homogenization method. *Computer Methods in Applied Mechanics and Engineering*, *335*, 419–471. doi:10.1016/j.cma.2018.02.031

Nolde, E., Craster, R., & Kaplunov, J. (2011). High frequency homogenization for structural mechanics. *Journal of the Mechanics and Physics of Solids*, *59*(3), 651–671. doi:10.1016/j.jmps.2010.12.004

Ochiai, T., & Onoda, M. (2009). Photonic analog of graphene model and its extension: dirac cone, symmetry, and edge states. *Physical Review B*, *80*(15). doi:10.1103/physrevb.80.155103

Oliver, J., Ferrer, A., Cante, J. C., Giusti, S. M., & Lloberas-Valls, O. (2017). On multi-scale computational design of structural materials using the topological derivative. In *Computational methods in applied sciences* (pp. 289–308). doi:10.1007/978-3-319-60885-3_14

Ourir, A., Gao, Y., Maurel, A., & Marigo, J.-J. (2017). Homogenization of thin and thick metamaterials and applications. In *Metamaterials - devices and applications*. doi:10.5772/66035

Palermo, A., Vitali, M., & Marzani, A. (2018). Metabarriers with multi-mass locally resonating units for broad band rayleigh waves attenuation. *Soil Dynamics and Earthquake Engineering*, *113*, 265–277. doi:10.1016/j.soildyn.2018.05.035

Pecorari, C. (2003). Nonlinear interaction of plane ultrasonic waves with an interface between rough surfaces in contact. *The Journal of the Acoustical Society of America*, *113*(6), 3065. doi:10.1121/1.1570437

Pendry, J. B. (2000). Negative refraction makes a perfect lens. *Physical Review Letters*, *85*(18), 3966–3969. doi:10.1103/physrevlett.85.3966

Pham, K., Maurel, A., & Marigo, J.-J. (2017). Two scale homogenization of a row of locally resonant inclusions - the case of shear waves. *Journal of the Mechanics and Physics of Solids*, *106*, 80–94.

Pham, K., Maurel, A., & Marigo, J.-J. (2021). Revisiting imperfect interface laws for two-dimensional elastodynamics. *Proceedings of the Royal Society A: Mathematical, Physical and Engineering Sciences*, *477*(2245), 20200519. doi:10.1098/rspa.2020.0519

Pham, K., Mercier, J.-F., Fuster, D., Marigo, J.-J., & Maurel, A. (2020). Scattering of acoustic waves by a nonlinear resonant bubbly screen. *Journal of Fluid Mechanics*, *906*. doi:10.1017/jfm.2020.799

Rallu, A., Hans, S., & Boutin, C. (2018). Asymptotic analysis of high-frequency modulation in periodic systems. analytical study of discrete and continuous structures. *Journal of the Mechanics and Physics of Solids*, *117*, 123–156. doi:10.1016/j.jmps.2018.04.014

Rizzoni, R., Dumont, S., & Lebon, F. (2017). On saint venant - kirchhoff imperfect interfaces. *International Journal of Non-Linear Mechanics*, *89*, 101–115. doi:10.1016/j.ijnonlinmec.2016.12.002

Rizzoni, R., Dumont, S., Lebon, F., & Sacco, E. (2014). Higher order model for soft and hard elastic interfaces. *International Journal of Solids and Structures*, *51*(23-24), 4137–4148. doi:10.1016/j.ijsolstr.2014.08.005

Rizzoni, R., & Lebon, F. (2013). Imperfect interfaces as asymptotic models of thin curved elastic adhesive interphases. *Mechanics Research Communications*, *51*, 39–50. doi:10.1016/j.mechrescom.2013.04.008

Romero-Garcia, V., Jiménez, N., Groby, J.-P., Merkel, A., Tournat, V., Theocharis, G., ... Pagneux, V. (2020). Perfect absorption in mirror-symmetric acoustic metascreens. *Physical Review Applied*, *14*(5). doi:10.1103/physrevapplied.14.054055

Romero-Garcia, V., Jiménez, N., Theocharis, G., Achilleos, V., Merkel, A., Richoux, O., ... Pagneux, V. (2021). Design of acoustic metamaterials made of helmholtz resonators for perfect absorption by using the complex frequency plane. *Comptes Rendus. Physique*, *21*(7-8), 713–749. doi:10.5802/crphys.32

Romero-Garcia, V., Theocharis, G., Richoux, O., Merkel, A., Tournat, V., & Pagneux, V. (2016). Perfect and broadband acoustic absorption by critically coupled sub-wavelength resonators. *Scientific Reports*, *6*(1). doi:10.1038/srep19519

Sanchez-Hubert, J., & Sanchez-Palencia, E. (1992). *Introduction aux méthodes asymptotiques et à l'homogénéisation*. Collection Mathématiques Appliquées pour la Maîtrise.

Sánchez-Palencia, E. (1980). Non-homogeneous media and vibration theory. *Lecture notes in physics*, *127*.

Santosa, F., & Symes, W. W. (1991). A dispersive effective medium for wave propagation in periodic composites. *SIAM Journal on Applied Mathematics*, *51*(4), 984–1005. doi:10.1137/0151049

Schwan, L., Umnova, O., & Boutin, C. (2017). Sound absorption and reflection from a resonant metasurface: homogenisation model with experimental validation. *Wave Motion*, *72*, 154–172. doi:10.1016/j.wavemoti.2017.02.004

Schwartzkopff, T., Dumbser, M., & Munz, C.-D. (2004). Fast high order ADER schemes for linear hyperbolic equations. *Journal of Computational Physics*, *197*(2), 532–539. doi:10.1016/j.jcp.2003.12.007

Semin, A., Delourme, B., & Schmidt, K. (2018). On the homogenization of the helmholtz problem with thin perforated walls of finite length. *ESAIM: Mathematical Modelling and Numerical Analysis*, *52*(1), 29–67. doi:10.1051/m2an/2017030

Sevostianov, I., Rodriguez-Ramos, R., Guinovart-Diaz, R., Bravo-Castillero, J., & Sabina, F. (2012). Connections between different models describing imperfect interfaces in periodic fiber-reinforced composites. *International Journal of Solids and Structures*, *49*(13), 1518–1525. doi:10.1016/j.ijsolstr.2012.02.028

Su, X., Lu, Z., & Norris, A. N. (2018). Elastic metasurfaces for splitting SV- and p-waves in elastic solids. *Journal of Applied Physics*, *123*(9), 091701. doi:10.1063/1.5007731

Su, X., & Norris, A. N. (2016). Focusing, refraction, and asymmetric transmission of elastic waves in solid metamaterials with aligned parallel gaps. *The Journal of the Acoustical Society of America*, *139*(6), 3386–3394. doi:10.1121/1.4950770

Tattersall, H. G. (1973). The ultrasonic pulse-echo technique as applied to adhesion testing. *Journal of Physics D: Applied Physics*, *6*(7), 819–832. doi:10.1088/0022-3727/6/7/305

Tip, A. (1998). Linear absorptive dielectrics. *Physical Review A*, *57*(6), 4818–4841. doi:10.1103/physreva.57.4818

Vetterling, W. T., Teukolsky, S. A., Press, W. H., & Flannery, B. P. (1992). *Numerical recipes: the art of scientific computing*. Cambridge university press Cambridge.

Vinoles, V. (2016). *Problèmes d'interface en présence de métamatériaux : modélisation, analyse et simulations* (Doctoral dissertation, Université Paris-Saclay).

Vlasie, V., & Rousseau, M. (2003). Acoustical validation of the rheological models for a structural bond. *Wave Motion*, *37*(4), 333–349. doi:10.1016/s0165-2125(02)00092-6

Vondřejc, J., Rohan, E., & Heczko, J. (2017). Shape optimization of phononic band gap structures using the homogenization approach. *International Journal of Solids and Structures*, *113-114*, 147–168. doi:10.1016/j.ijsolstr.2017.01.038

Wautier, A., & Guzina, B. B. (2015). On the second-order homogenization of wave motion in periodic media and the sound of a chessboard. *Journal of the Mechanics and Physics of Solids*, *78*, 382–414. doi:10.1016/j.jmps.2015.03.001

Willis, J. R. (2011). Effective constitutive relations for waves in composites and metamaterials. *Proceedings of the Royal Society A: Mathematical, Physical and Engineering Sciences*, *467*(2131), 1865–1879. doi:10.1098/rspa.2010.0620

Willis, J. (1977). Bounds and self-consistent estimates for the overall properties of anisotropic composites. *Journal of the Mechanics and Physics of Solids*, *25*(3), 185–202. doi:10.1016/0022-5096(77)90022-9

Willis, J. (2016). Negative refraction in a laminate. *Journal of the Mechanics and Physics of Solids*, *97*, 10–18. doi:10.1016/j.jmps.2015.11.004

Willis, J. (1981). Variational principles for dynamic problems for inhomogeneous elastic media. *Wave Motion*, *3*(1), 1–11. doi:10.1016/0165-2125(81)90008-1

Xie, Y., Wang, W., Chen, H., Konneker, A., Popa, B.-I., & Cummer, S. A. (2014). Wavefront modulation and subwavelength diffractive acoustics with an acoustic metasurface. *Nature Communications*, *5*(1). doi:10.1038/ncomms6553

Xu, X., Barnhart, M. V., Li, X., Chen, Y., & Huang, G. (2019). Tailoring vibration suppression bands with hierarchical metamaterials containing local resonators. *Journal of Sound and Vibration*, *442*, 237–248. doi:10.1016/j.jsv.2018.10.065

Yamada, T., Izui, K., Nishiwaki, S., & Takezawa, A. (2010). A topology optimization method based on the level set method incorporating a fictitious interface energy. *Computer Methods in Applied Mechanics and Engineering*, *199*(45-48), 2876–2891. doi:10.1016/j.cma.2010.05.013

Yang, M., Ma, G., Yang, Z., & Sheng, P. (2015). Subwavelength perfect acoustic absorption in membrane-type metamaterials: a geometric perspective. *EPJ Applied Metamaterials*, *2*, 10. doi:10.1051/epjam/2015017

Zaccherini, R., Colombi, A., Palermo, A., Dertimanis, V. K., Marzani, A., Thomsen, H. R., ... Chatzi, E. N. (2019, December 2). Locally resonant metasurfaces for shear waves in granular media. arXiv: http://arxiv.org/abs/1912.00617v1 [physics.geo-ph]

Zhang, C., & LeVeque, R. J. (1997). The immersed interface method for acoustic wave equations with discontinuous coefficients. *Wave Motion*, *25*, 237–263.

Zhikov, V. V. (2000). On an extension of the method of two-scale convergence and its applications. *Sbornik: Mathematics*, *191*(7), 973–1014. doi:10.1070/sm2000v191n07abeh000491

Zhikov, V. V. (2005). On spectrum gaps of some divergent elliptic operators with periodic coefficients. *St. Petersburg Mathematical Journal*, *16*(05), 773–791. doi:10.1090/s1061-0022-05-00878-2

Zhu, H., & Semperlotti, F. (2016). Anomalous refraction of acoustic guided waves in solids with geometrically tapered metasurfaces. *Physical Review Letters*, *117*(3). doi:10.1103/physrevlett.117.034302

Published and submitted papers

Assier, R. C., Touboul, M., Lombard, B., & Bellis, C. (2020). High-frequency homogenization in periodic media with imperfect interfaces. *Proceedings of the Royal Society A: Mathematical, Physical and Engineering Sciences*, *476*(2244), 20200402. doi:10.1098/rspa.2020.0402

Bellis, C., Lombard, B., Touboul, M., & Assier, R. (2021). Effective dynamics for low-amplitude transient elastic waves in a 1d periodic array of non-linear interfaces. *Journal of the Mechanics and Physics of Solids*, *149*, 104321. doi:10.1016/j.jmps.2021.104321

Touboul, M., Gao, X., & Lombard, B. (2021). Damping in a row of locally-resonant inclusions: dynamic homogenization and scattering of transient shear waves. *Wave Motion*, *107*, 102811. doi:10.1016/j.wavemoti.2021.102811

Touboul, M., Lombard, B., & Bellis, C. (2020a). Time-domain simulation of wave propagation across resonant meta-interfaces. *Journal of Computational Physics*, *414*, 109474. doi:10.1016/j.jcp.2020.109474

Touboul, M., Pham, K., Maurel, A., Marigo, J.-J., Lombard, B., & Bellis, C. (2020b). Effective resonant model and simulations in the time-domain of wave scattering from a periodic row of highly-contrasted inclusions. *Journal of Elasticity*, *142*(1), 53–82. doi:10.1007/s10659-020-09789-2